

**Parametric Study for Non-Destructive Fatigue
Strength Evaluation of Offshore Tubular Welded Joints**

By

Enrong Chang BSc(Eng.) MSc(Eng.)

**A thesis Submitted for the Degree of
Doctor of Philosophy**

**Department of Mechanical Engineering
University College London**

October, 1997

ProQuest Number: 10105209

All rights reserved

INFORMATION TO ALL USERS

The quality of this reproduction is dependent upon the quality of the copy submitted.

In the unlikely event that the author did not send a complete manuscript and there are missing pages, these will be noted. Also, if material had to be removed, a note will indicate the deletion.



ProQuest 10105209

Published by ProQuest LLC(2016). Copyright of the Dissertation is held by the Author.

All rights reserved.

This work is protected against unauthorized copying under Title 17, United States Code.
Microform Edition © ProQuest LLC.

ProQuest LLC
789 East Eisenhower Parkway
P.O. Box 1346
Ann Arbor, MI 48106-1346

ABSTRACT

This thesis is concerned with the development of tools and methodologies for non-destructive fatigue strength evaluation of offshore tubular welded joints.

The sizing capability of new Non-Destructive Technique(NDT), alternating current field measurement(ACFM), was investigated. The University College London(UCL) underwater Probability Of Detection(POD) trial results were re-analysed to make them suitable for reliability fracture mechanics procedures.

Comprehensive thin shell finite element analyses were conducted for 660 tubular Y, T, X and DT-joints, with geometries typical of those used in offshore structures, subject to different modes of loading. The results have been used to produce a new set of stress parametric equations. These were assessed by comparing the predicted values with available test data. The equations can be used to predict hot spot Stress Concentration Factor(SCF) and Degree Of Bending(DOB) at all critical positions for X and DT-joints and also the full SCF distribution along both chord and brace toes for Y and T, X and DT-joints. Combination of these parametric equations with original UCL HCD equations allows one to recreate the full 2D stress distribution for tubular Y and T, X and DT-joints. Moreover, stress distribution concentration factor(SDCF) has been proposed and parametric equations were derived to predict average SCF and SDCF for Y and T, X and DT-joints.

Combining available weight functions and the UCL database of T-butt through-wall stress analysis results, a new set of weld toe Stress Intensity Factor(SIF) parametric equations were derived for both the deepest and surface points of semi-elliptical surface cracks in T-butt welded joints. Using thin pipe weight function as reference data, a novel weight function and the corresponding SIF solutions were derived for the deepest point of a semi-elliptical cracks at the saddle of tubular welded T-joints. A comparison of the predictions with the UCL experimental results, especially early fatigue crack growth data, showed that this new model can work well with the constant force shedding and the non-linear moment shedding derived from previous line spring FE analysis.

ACKNOWLEDGEMENT

On completing this work, I am deeply indebted to my supervisor, Prof. W. D. Dover, for providing me with this opportunity to carry out my PhD study at UCL, and his excellent supervision, invaluable guidance, keen support and constant encouragement. I wish to thank all staff in the Department of Mechanical Engineering at UCL , especially the NDE Centre for their help and advice.

Special thanks are also due to Dr. F. B. Brennan for providing the T-butt finite element stress analysis results and Dr. C. C. Monahan, Dr. A. T. Smith, Mr. P. Myers and Mr. L. S. Etube for their permission to use their test data for validation of the models developed in this study. Dr. A. Dier is thanked for his carefully checking up of this thesis and providing many useful comments.

I would like to acknowledge the generous financial support from Committee of Vice-Chancellors and Principals of the Universities of the United Kingdom and K. C. Wong Education Foundation during the course of this work.

I would like to express my sincere love to my wife Shuang, for her support and endless patience which has helped me to complete this work in the end.

Finally, I would like to dedicate this thesis to my parents for all their sacrifices, understanding and enormous love.

TABLE OF CONTENTS

	<u>Page</u>
Abstract	2
Acknowledgement	3
Table of Contents	4
List of Tables	9
List of Figures	15

CHAPTER ONE

INTRODUCTION AND LITERATURE REVIEW

1.1 Introduction	27
1.2 Fatigue Cracks in Tubular Welded Joints	29
1.3 Non Destructive Measurement and Underwater Inspection Reliability	30
1.4 Stress Analysis	33
1.5 Fatigue Strength Assessment	43
1.6 Research Objective and Scope of Thesis	72

CHAPTER TWO

IMPROVED FATIGUE CRACK SIZING USING ACFM

2.1 Introduction	82
2.2 Crack Measurement using Non-Destructive Techniques	83
2.3 Underwater Inspection Reliability of Non-Destructive Techniques	87
2.4 Conclusions	93

CHAPTER THREE

STRESS CONCENTRATION FACTOR PARAMETRIC EQUATIONS FOR TUBULAR X AND DT-JOINTS

3.1 Introduction	115
3.2 Finite Element Analyses	116
3.3 Deriving Parametric Equations by Regression Analyses	123
3.4 Validation	124
3.5 Conclusions	127

CHAPTER FOUR

PARAMETRIC EQUATIONS TO PREDICT STRESS DISTRIBUTIONS THROUGH THE THICKNESS AND ALONG THE INTERSECTION OF TUBULAR X AND DT-JOINTS

4.1 Introduction	157
4.2 Prediction of Degree of Bending in Tubular X and DT-joints	158
4.3 Parametric Equations to Predict the Stress Distribution along the Intersection	161
4.4 Conclusions	164

CHAPTER FIVE

STRESS PARAMETRIC EQUATIONS FOR TUBULAR Y AND T-JOINTS

5.1 Introduction	184
5.2 Systematic Finite Element Analyses	185
5.3 Deriving stress distribution parametric equations	187
5.4 Assessment	188
5.5 Concluding Remarks	191

CHAPTER SIX

CHARACTERISTIC PARAMETERS FOR STRESS DISTRIBUTION ALONG THE INTERSECTION OF TUBULAR Y, T, X AND DT-JOINTS

6.1 Introduction	225
6.2 Characteristic Parameters for Stress Distribution along Intersection of tubular Joints	226
6.3 Regression Analyses	228
6.4 Conclusions	229

CHAPTER SEVEN

DEEPEST POINT SIF PARAMETRIC EQUATIONS FOR THE SEMI-ELLIPTICAL CRACKS IN T-BUTT WELDED JOINTS

7.1 Introduction	234
7.2 Niu-Glinka Weight Function	235
7.3 Systematic SIF Calculation	236
7.4 Deriving Parametric Equations	238
7.5 Validation	239
7.6 Conclusions	241

CHAPTER EIGHT

SURFACE POINT SIF PARAMETRIC EQUATIONS FOR SEMI-ELLIPTICAL CRACKS IN T-PLATE WELDED JOINTS

8.1 Introduction	263
8.2 Wang-Lambert Weight Function	263
8.3 Deriving SIF Parametric Equations	265
8.4 Validation	267
8.5 Conclusions	268

CHAPTER NINE

SIF PARAMETRIC EQUATIONS FOR SEMI-ELLIPTICAL CRACKS AT THE SADDLE OF TUBULAR WELDED T-JOINTS

9.1 Introduction	279
9.2 Weight Function for Semi-elliptical Cracks at the Saddle of Tubular Welded T-Joints	280
9.3 SIF Parametric Equations for the Deepest Point of Semi-elliptical Surface Cracks at the Saddle of Tubular Welded T-Joints	284
9.4 Models for Load Shedding and Crack Shape Development	286
9.5 Validation	288
9.6 Conclusions	290

CHAPTER TEN

CONCLUSIONS

11.1 Overall Summary	303
11.2 Recommendations for Further Research	307

References	310
-------------------	-----

Appendices

Appendix A: The Stress Concentration Factor Parametric Equations for Tubular X and DT-Joints	319
Appendix B: Parametric Equations of Degree of Bending for Tubular X and DT-Joints	326
Appendix C: Parametric Equations of Stress Distribution along the intersection of Tubular X and DT-Joints	329
Appendix D: Parametric Equations of Stress Distribution along the intersection of Tubular Y and T-Joints	336

Appendix E:	The Average SCF Parametric Equations for Tubular Y and T-Joints	341
Appendix F:	The Average SCF Parametric Equations for Tubular X and DT-Joints	343
Appendix G:	Parametric Equations of Stress Distribution Concentration Factor(SDCF) for Tubular Y and T-Joints	345
Appendix H:	Parametric Equations of Stress Distribution Concentration Factor(SDCF) for Tubular X and DT-Joints	347
Appendix I:	The Deepest Point SIF Parametric Equations for Semi-elliptical Surface Cracks in T-Plate Welded Joints	349
Appendix J:	The Surface Point SIF Parametric Equations for Semi-elliptical Surface Cracks in T-Plate Welded Joints	352
Appendix K:	The Deepest Point SIF Parametric Equations for Semi-elliptical Surface Cracks in Tubular Welded Joints	356

LIST OF TABLES

	<u>Page</u>
Table 2.1	Comparison of In-air ACPD Characterised Data using U7 Crack Microgauge and Old Underwater ACFM Sizing Results using TSC U11 ACFM for Three Library Cracks
	95
Table 2.2	Comparison of New ACPD Measurement Results using U7 and U10 with In-air ACPD Characterised data for Three Library Cracks
	95
Table 2.3	Comparison of New and Old ACFM Measurement Results using U10 and U11 (In-air and Underwater) for Three Library Cracks
	96
Table 2.4	TSC U11 ACFM Missed Defects Analysis for Classification 'A' Cracks
	97
Table 2.5	Comparison of Ten Largest Spurious Indications Between TSC U11 ACFM and MPI Underwater POD trials for Classification 'A' Cracks
	97
Table 2.6	Comparison of Total Number of Spurious Indication Between TSC U11 ACFM and MPI Underwater POD TRIAL for Classification 'A' Cracks
	97
Table 3.1	Comparison Between SCFs around Upper Intersection from Coarse to Fine X Joint Meshes to Show Extent of Convergence ($\alpha=10$, $\beta=0.6$, $\gamma=20$, $\tau=0.5$, $\theta=60^\circ$)
	129
Table 3.2	Summary of Degree of Fit for SCF Parametric Equations
	130
Table 3.3	Comparison Between Predicted and Recorded SCF Data at Chord Crown Position for Single IPB Loaded X and DT-Joints
	131
Table 3.4	Comparison Between Predicted and Recorded SCF Data at Brace Saddle Position for Single OPB Loaded X and DT-Joints
	131
Table 3.5	Comparison Between Predicted and Recorded SCF Data at Chord Saddle Position for Single OPB Loaded X and DT-Joints
	131
Table 3.6	Comparison Between Predicted and Recorded SCF Data at Brace Crown Position for Balanced Axially Loaded X and DT-Joints
	132
Table 3.7	Comparison Between Predicted and Recorded SCF Data at Brace Saddle Position for Balanced Axially Loaded X and DT-Joints
	132

Table 3.8	Comparison Between Predicted and Recorded SCF Data at Chord Crown Position for Balanced Axially Loaded X and DT-Joints	133
Table 3.9	Comparison Between Predicted and Recorded SCF Data at Chord Saddle Position for Balanced Axially Loaded X and DT-Joints	134
Table 3.10	Comparison Between Predicted and Recorded SCF Data on Brace Side for Balanced IPB Loaded X and DT-Joints	135
Table 3.11	Comparison Between Predicted and Recorded SCF Data on Chord Side for Balanced IPB Loaded X and DT-Joints	136
Table 3.12	Comparison Between Predicted and Recorded SCF Data on Brace Side for Balanced OPB Loaded X and DT-Joints	137
Table 3.13	Comparison Between Predicted and Recorded SCF Data on Chord Side for Balanced OPB Loaded X and DT-Joints	138
Table 3.14	Validation of SCF Parametric Equation for X joint under Balanced Axial at Brace Crown Position	139
Table 3.15	Validation of SCF Parametric Equation for X joint under Balanced Axial at Brace Saddle Position	140
Table 3.16	Validation of SCF Parametric Equation for X joint under Balanced Axial at Chord Crown Position	141
Table 3.17	Validation of SCF Parametric Equation for X joint under Balanced Axial Loading at Chord Saddle Position	142
Table 3.18	Validation of SCF Parametric Equation for X joint under Balanced IPB Loading on Brace Side	143
Table 3.19	Validation of SCF parametric Equation for X joint under Balanced IPB Loading on Chord Side	144
Table 3.20	Validation of SCF Parametric Equation for X-joint under Balanced OPB Loading on Brace Side	145
Table 3.21	Validation of SCF Parametric Equation for X joint under Balanced OPB on Chord Side	146
Table 4.1	Comparison between DOBs around upper Intersection from Coarse to Fine X joint Meshes to Show Extent of Convergence ($\alpha=10$, $\beta=0.6$, $\gamma=20$, $\tau=0.5$, $\theta=60^\circ$)	165
Table 4.2	Summary of Degree of Fit for DoB Parametric Equations	166
Table 4.3	Comparison of DoB Data between the Predictions from Parametric Equations and Experimental Results for Tubular DT-Joints under Single OPB Loading	166

Table 4.4	Summary of Degree of Fit for the Parametric Equations of SCF Distribution around the Intersection of Tubular X and DT-joints	167
Table 4.5	Comparison between the predictions from the SCF and SCF Distribution Equations with the Recorded SCF data at chord crown position for single IPB Loaded X and DT-joints	168
Table 4.6	Comparison between the Predictions from the SCF and SCF Distribution Equations with the Recorded SCF data at Brace Saddle position for Single OPB Loaded X and DT-joints	168
Table 4.7	Comparison between the Predictions from the SCF and SCF Distribution Equations with the Recorded SCF data at Chord Saddle position for Single OPB Loaded X and DT-joints	168
Table 4.8	Comparison between the Predictions from the SCF and SCF Distribution Equations with Recorded SCF data at Brace Crown position for Balanced Axially Loaded X and DT-joints	169
Table 4.9	Comparison between the Predictions from the SCF and SCF Distribution Equations with Recorded SCF data at Brace Saddle position for Balanced Axially Loaded X and DT-joints	169
Table 4.10	Comparison between the Predictions from the SCF and SCF Distribution Equations with Recorded SCF data at Chord Crown position for Balanced Axially Loaded X and DT-joints	170
Table 4.11	Comparison between the Predictions from the SCF and SCF Distribution Equations with the Recorded data at Chord Saddle position for Balanced Axially Loaded X and DT-joints	170
Table 4.12	Comparison between the Predictions from the SCF and SCF Distribution Equations with the Recorded SCF data on Brace Side for Balanced IPB Loaded X and DT-joints	171
Table 4.13	Comparison between the Predictions from the SCF and SCF Distribution Equations with the Recorded SCF data on Chord Side for Balanced IPB Loaded X and DT-joints	171
Table 4.14	Comparison between the Predictions from the SCF and SCF Distribution Equations with the Recorded SCF data on Brace Side for Balanced OPB Loaded X and DT-joints	172
Table 4.15	Comparison between the Predictions from the SCF and SCF Distribution Equations with the Recorded SCF data on Chord Side for Balanced OPB Loaded X and DT-joints	172

Table 4.16	Validation of SCF Distribution Parametric Equation for X-joint under Balanced Axial at Brace Saddle Position	173
Table 4.17	Validation of SCF Distribution Parametric Equation for X-joint under Balanced Axial Loading at Chord Saddle Position	173
Table 4.18	Validation of SCF Distribution Parametric Equation for X-joint under Balanced IPB Loading on Brace Crown Position	173
Table 4.19	Validation of SCF Distribution Parametric Equation for X-joint under Balanced IPB Loading on Chord Crown Position	174
Table 4.20	Validation of SCF Distribution Parametric Equation for X-joint under Balanced OPB Loading on Brace Saddle Position	174
Table 4.21	Validation of SCF Distribution Parametric Equation for X joint under Balanced OPB on Chord Saddle Position	174
Table 5.1	Comparison between DOBs around upper Intersection from Coarse to Fine X joint Meshes to Show Extent of Convergence ($\alpha=10.39$, $\beta=0.5$, $\gamma=12.9$, $\tau=0.5$, $\theta=90^0$)	193
Table 5.2	Summary of Degree of Fit for the Parametric Equations of SCF Distribution around the Intersection of Tubular Y and T-joints	194
Table 5.3	Comparison between the Predictions from the SCF Distribution and HCD Equations with the Recorded data at Brace Crown position for Axially Loaded Y and T-joints	195
Table 5.4	Comparison between the Predictions from the SCF Distribution and HCD Equations with the Recorded data at Brace Saddle position for Axially Loaded Y and T-joints	195
Table 5.5	Comparison between the Predictions from the SCF Distribution and HCD Equations with the Recorded Data at Chord Crown position for Axially Loaded Y and T-joints	197
Table 5.6	Comparison between the Predictions from the SCF Distribution and HCD Equations with the Recorded Data at Chord Saddle position for Axially Loaded Y and T-joints	198
Table 5.7	Comparison between the Predictions from the SCF Distribution and HCD Equations with the Recorded Data on Brace Side for IPB loaded Y and T-joints	200
Table 5.8	Comparison between the Predictions from the SCF Distribution and HCD Equations with the Recorded Data on Chord Side for IPB loaded Y and T-joints	201

Table 5.9	Comparison between the Predictions from the SCF Distribution and HCD Equations with the Recorded Data on Brace Side for OPB loaded Y and T-joints	202
Table 5.10	Comparison between the Predictions from the SCF Distribution and HCD Equations with the Recorded Data on Chord Side for OPB loaded Y and T-joints	203
Table 5.11	Validation of SCF Distribution Parametric Equation for Y and T-joint under Axial Loading at Brace Crown Position	205
Table 5.12	Validation of SCF Distribution Parametric Equation for Y and T-joint under Axial Loading at Brace Saddle Position	205
Table 5.13	Validation of SCF Distribution Parametric Equation for Y and T-joint under Axial Loading at Chord Crown Position	205
Table 5.14	Validation of SCF Distribution Parametric Equation for Y and T-joint under Axial Loading at Chord Saddle Position	206
Table 5.15	Validation of SCF Distribution Parametric Equation for Y and T-joint under IPB Loading on Brace Side	206
Table 5.16	Validation of SCF Distribution Parametric Equation for Y and T-joint under IPB Loading on Chord Side	206
Table 5.17	Validation of SCF Distribution Parametric Equation for Y and T-joint under OPB Loading on Brace Side	207
Table 5.18	Validation of SCF Distribution Parametric Equation for Y and T-joint under OPB Loading on Chord Side	207
Table 6.1	Summary of Degree of Fit for Parametric Equations for Average SCF Along the Intersection of Tubular Y and T-Joints	230
Table 6.2	Summary of Degree of Fit for Parametric Equations for Average SCF Along the Intersection of Tubular X and DT-Joints	230
Table 6.3	Summary of Degree of Fit for Parametric Equations of Stress Distribution Concentration Factor Along the Intersection of Tubular Y and T-Joints	231
Table 6.4	Summary of Degree of Fit for Parametric Equations of Stress Distribution Concentration Factor Along the Intersection of Tubular X and DT-Joints	231
Table 6.5	Comparison of Predicted Average SCF with Test Data for Tubular Joints	232

Table 7.1	Summary of Degree of Fit for the SIF Parametric Equations for Semi-elliptical Crack in T-butt Welded Joints	242
Table 7.2	Comparison of the validated parameter ranges for N&G*S and PD6493(Mk) methods together with available FE data	243
Table 8.1	Summary of Degree of Fit for the SIF Parametric Equations for Semi-elliptical Crack in T-butt Welded Joints	269
Table 9.1	Summary of Fitting Degree for the SIF Parametric Equations for the Deepest point of Semi-elliptical Crack at Saddle Position of Tubular Welded Joint	291
Table 9.2	The Details of UCL Steel Tests for Tubular Joints	291
Table 10.1	Stress Parametric Equations for Simple Tubular Joints	308
Table 10.2	SIF Solutions for Semi-elliptical Cracks in Welded Joints	308

LIST OF FIGURES

	<u>Page</u>
Figure 1.1	Typical Jacket Structure(<u>Fatigue Handbook 1985</u>) 75
Figure 1.2	Examples of Simple Tubular Welded Joints 75
Figure 1.3	Geometric Notation for Simple Tubular Joint(UEG 1985) 76
Figure 1.4	Modes of Loading on Tubular Joint 76
Figure 1.5	Geometric Parameters of Weldments(Niu 1987) 77
Figure 1.6	The 'Hot-Spot' Stress Definition by UKOSRP I(Irvine 1981) 77
Figure 1.7	Location of the Points for Linear Extrapolation(Irvine 1981) 78
Figure 1.8	Typical Stress Distribution Through the Chord Wall (Dharmavasan and Dover 1988) 78
Figure 1.9	Typical Stress Distributions around the intersection of Tubular T-joint under Different Modes of Loading(Austin 1994) 79
Figure 1.10	Crack Deformation Modes 79
Figure 1.11	Schematic Diagram of Fatigue Crack Growth Behaviour 80
Figure 1.12	Embedded Crack in an Infinite Body 80
Figure 1.13	Surface Crack in a Flat Plate 81
Figure 1.14	Irregular Shape Crack Embedded in an Infinite Three Dimensional Body Defining the Weight Function 81
Figure 2.1	Fatigue Crack Profiles using ACPD Technique 98
Figure 2.2	Effect of using Different WAMI Versions for the ACFM Crack Depth Sizing Results 99
Figure 2.3	One Example of Comparison of the Destructive Test data with the Corresponding ACFM Signals for fatigue crack in Tubular Joint 100
Figure 2.4	A example to decide the physical lengths using three different procedures 101
Figure 2.5	Comparison of ACFM Depth Predictions against Destructive and Characterised data using Different Procedures 102
Figure 2.6	Effect of the Background Bx on ACFM Depth Predictions using Procedure 3 102
Figure 2.7	The ACFM Depth Predictions using Procedure 3 and the revised Background Bx 103
Figure 2.8	Effect of the Nature and Size of the Sample on the POD Curve 103
Figure 2.9	Crack Classifications 104

Figure 2.10	The Possible Outcome of an Inspection	105
Figure 2.11	Magnetic Particle Inspection, Effect of Depth Threshold on POD against Crack Length using Classification 'D'	106
Figure 2.12	EMD III Eddy Current Inspection, POD Against Crack Length for Cracks ≥ 1 mm deep using Classification 'D'	106
Figure 2.13	Hocking Eddy Current Inspection, Effect of Length Ratio on POD against Crack Length using Classification 'D'	107
Figure 2.14	Magnetic Particle Inspection, POD against Maximum Crack Depth using Classification 'D'	107
Figure 2.15	EMD III Eddy Current Inspection, POD against Maximum Crack Depth using Classification 'D'	108
Figure 2.16	Hocking Eddy Current Inspection, Effect of Length Ratio on POD against Maximum Crack Depth using Classification 'D'	108
Figure 2.17	Magnetic Particle Inspection, POD against Maximum Crack Depth using Classification 'B'	109
Figure 2.18	Magnetic Particle Inspection, Effect of Length Ratio on POD against Maximum Crack Depth using Classification 'B'	109
Figure 2.19	Magnetic Particle Inspection, POD against Maximum Crack Depth using Classification 'B1'	110
Figure 2.20	Magnetic Particle Inspection, Effect of Length Ratio on POD against Maximum Crack Depth using Classification 'B1'	110
Figure 2.21	Types of Missed Cracks using Classification 'A'	111
Figure 2.22	Comparison of TSC U11 ACFM and Underwater MPI, POD against Crack Length using Classification 'B1' for All Cracks	112
Figure 2.23	Comparison of TSC U11 ACFM and Underwater MPI, POD against Crack Length using Classification 'B1' for Cracks ≥ 1 mm deep	112
Figure 2.24	Comparison of TSC U11 ACFM and Underwater MPI, POD against Crack Length using Classification 'A' for All Cracks	113
Figure 2.25	Comparison of TSC U11 ACFM and Underwater MPI, POD against Crack Length using Classification 'A' for Cracks ≥ 1.5 mm deep	113
Figure 2.26	Comparison of POD against Crack Depth using Classification 'B1' Between TSC U11 ACFM and Underwater MPI	114
Figure 2.27	Comparison of Experimental POD against Crack Depth using Classification 'B1' Between TSC U11 ACFM and Underwater MPI	114
Figure 3.1	Geometric Notation for Tubular X-joint	147
Figure 3.2	Two Kinds of Thin-Shell Elements used in this Study	148

Figure 3.3	Typical Example of Finite Element Mesh Used to Model Tubular Joint ($\alpha=10$, $\beta=0.6$, $\gamma=20$, $\tau=0.5$, $\theta=60^\circ$)	148
Figure 3.4	Modes of Loading Used for Finite Element Joint Analyses	149
Figure 3.5	The Boundary Conditions for All Modes of Loading	150
Figure 3.6	Effect of α_b on the SCF Distribution on Brace Side of Intersection for Single Axial Loading X Joint ($\alpha=10$, $\beta=0.6$, $\gamma=20$, $\tau=0.5$, $\theta=60^\circ$)	151
Figure 3.7	Effect of α_b on the SCF Distribution on Brace Side of Intersection for Single IPB Loading X Joint ($\alpha=10$, $\beta=0.6$, $\gamma=20$, $\tau=0.5$, $\theta=60^\circ$)	151
Figure 3.8	Effect of α_b on the SCF Distribution on Brace Side of Intersection for Single OPB Loading X Joint ($\alpha=10$, $\beta=0.6$, $\gamma=20$, $\tau=0.5$, $\theta=60^\circ$)	152
Figure 3.9	Effect of α_b on the SCF Distribution on Chord Side of Intersection for Single Axial Loading X Joint ($\alpha=10$, $\beta=0.6$, $\gamma=20$, $\tau=0.5$, $\theta=60^\circ$)	152
Figure 3.10	Effect of α_b on the SCF Distribution on Chord Side of Intersection for Single IPB Loading X Joint ($\alpha=10$, $\beta=0.6$, $\gamma=20$, $\tau=0.5$, $\theta=60^\circ$)	153
Figure 3.11	Effect of α_b on the SCF Distribution on Chord Side of Intersection for Single OPB Loading X Joint ($\alpha=10$, $\beta=0.6$, $\gamma=20$, $\tau=0.5$, $\theta=60^\circ$)	153
Figure 3.12	The Deformed Mesh Superimposed upon the Unloaded Mesh for Single Axial Loading X Joint ($\alpha=10$, $\beta=0.6$, $\gamma=20$, $\tau=0.5$, $\theta=60^\circ$, $\alpha_b=6.09$)	154
Figure 3.13	The Deformed Mesh Superimposed upon the Unloaded Mesh for Single IPB Loading X Joint ($\alpha=10$, $\beta=0.6$, $\gamma=20$, $\tau=0.5$, $\theta=60^\circ$, $\alpha_b=6.09$)	154
Figure 3.14	The Deformed Mesh Superimposed upon the Unloaded Mesh for Single OPB Loading X Joint ($\alpha=10$, $\beta=0.6$, $\gamma=20$, $\tau=0.5$, $\theta=60^\circ$, $\alpha_b=6.09$)	155
Figure 3.15	The Deformed Mesh Superimposed upon the Unloaded Mesh for Balanced Axial Loading X Joint ($\alpha=10$, $\beta=0.6$, $\gamma=20$, $\tau=0.5$, $\theta=60^\circ$, $\alpha_b=6.09$)	155
Figure 3.16	The Deformed Mesh Superimposed upon the Unloaded Mesh for Balanced IPB Loading X Joint ($\alpha=10$, $\beta=0.6$, $\gamma=20$, $\tau=0.5$, $\theta=60^\circ$, $\alpha_b=6.09$)	156
Figure 3.17	The Deformed Mesh Superimposed upon the Unloaded Mesh for Balanced OPB Loading X Joint ($\alpha=10$, $\beta=0.6$, $\gamma=20$, $\tau=0.5$, $\theta=60^\circ$, $\alpha_b=6.09$)	156

Figure 4.1	Illustration of Tubular X and DT-Joints	175
Figure 4.2	Plot of Typical External Stress Distribution around the Intersection of Tubular X-joint under Single Brace Axial Loading	176
Figure 4.3	Plot of Typical External Stress Distribution around the Intersection of Tubular X-joint under Single Brace IPB Loading	177
Figure 4.4	Plot of Typical External Stress Distribution around the Intersection of Tubular X-joint under Single Brace OPB Loading	178
Figure 4.5	Comparison of Predicted Normalised External Surface SCF Distribution on Chord Toe with Steel Model Test Results for the Single IPB Loaded DT-joints($\alpha=7.48$, $\beta=0.64$, $\gamma=10.2$, $\tau=0.5$, $\theta=90^\circ$)	179
Figure 4.6	Comparison of Predicted Normalised External Surface SCF Distribution on Chord Toe with Steel Model Test Results for the Single IPB Loaded DT-joint($\alpha=7.48$, $\beta=0.64$, $\gamma=10.2$, $\tau=0.5$, $\theta=90^\circ$)	179
Figure 4.7	Comparison of Predicted Normalised External Surface SCF Distribution on Brace Toe with Steel Model Test Results for the Single OPB Loaded DT-joint($\alpha=9.9$, $\beta=0.8$, $\gamma=10.6$, $\tau=1.0$, $\theta=90^\circ$)	180
Figure 4.8	Comparison of Predicted Normalised External Surface SCF Distribution on Chord Toe with Steel Model Test Results for the Single OPB Loaded DT-joint($\alpha=9.9$, $\beta=0.8$, $\gamma=10.6$, $\tau=1.0$, $\theta=90^\circ$)	180
Figure 4.9	Comparison of Predicted Normalised External Surface SCF Distribution on Chord Toe with Steel Model Test Results for the Single OPB Loaded DT-joint($\alpha=7.48$, $\beta=0.64$, $\gamma=10.2$, $\tau=0.5$, $\theta=90^\circ$)	181
Figure 4.10	Comparison of Predicted Normalised External Surface SCF Distribution on Chord Toe with Steel Model Test Results for the Balanced Axial Loaded DT-joint($\alpha=4.4$, $\beta=0.51$, $\gamma=10.0$, $\tau=0.44$, $\theta=90^\circ$)	181
Figure 4.11	Comparison of Predicted Normalised External Surface SCF Distribution on Chord Toe with Steel Model Test Results for the Balanced Axial Loaded DT-joint($\alpha=5.33$, $\beta=0.61$, $\gamma=14.28$, $\tau=0.54$, $\theta=90^\circ$)	182
Figure 4.12	Comparison of Predicted Normalised External Surface SCF Distribution on Chord Toe with Steel Model Test Results for the Balanced Axial Loaded DT-joint($\alpha=6.67$, $\beta=0.76$, $\gamma=12.0$, $\tau=0.5$, $\theta=90^\circ$)	182
Figure 4.13	Comparison of Predicted Normalised External Surface SCF Distribution on Chord Toe with Steel Model Test Results for the Balanced Axial Loaded DT-joint($\alpha=7.02$, $\beta=0.71$, $\gamma=11.4$, $\tau=0.64$, $\theta=90^\circ$)	183
Figure 5.1	Geometric Notation for Tubular Y-Joint	208

Figure 5.2	Typical Example of Finite Element Mesh Used to Model Tubular Joint ($\alpha=10$, $\beta=0.5$, $\gamma=24$, $\tau=0.8$, $\theta=60^\circ$)	208
Figure 5.3	Plot of Typical External Stress Distribution around the Intersection of Tubular Y-joint under Axial Loading	209
Figure 5.4	Plot of Typical External Stress Distribution around the Intersection of Tubular Y-joint under IPB Loading	210
Figure 5.5	Plot of Typical External Stress Distribution around the Intersection of Tubular Y-joint under OPB Loading	211
Figure 5.6	Comparison of Predicted External Surface SCF Distribution on Brace Toe with Acrylic Model Test Results for the Axially Loaded Y-joint($\alpha=9.33$, $\beta=0.67$, $\gamma=15.0$, $\tau=0.8$, $\theta=45^\circ$)	212
Figure 5.7	Comparison of Predicted Normalised External Surface SCF Distribution on Brace Toe with Acrylic Model Test Results for the Axially Loaded Y-joint($\alpha=9.33$, $\beta=0.67$, $\gamma=15.0$, $\tau=0.8$, $\theta=45^\circ$)	212
Figure 5.8	Comparison of Predicted External Surface SCF Distribution on Chord Toe with Acrylic Model Test Results for the Axially Loaded Y-joint($\alpha=9.33$, $\beta=0.67$, $\gamma=15.0$, $\tau=0.8$, $\theta=45^\circ$)	213
Figure 5.9	Comparison of Predicted Normalised External Surface SCF Distribution on Chord Toe with Acrylic Model Test Results for the Axially Loaded Y-joint($\alpha=9.33$, $\beta=0.67$, $\gamma=15.0$, $\tau=0.8$, $\theta=45^\circ$)	213
Figure 5.10	Comparison of Predicted External Surface SCF Distribution on Chord Toe with Steel Model Test Results for the Axially Loaded T-joint($\alpha=7.26$, $\beta=0.71$, $\gamma=14.28$, $\tau=1.0$, $\theta=90^\circ$)	214
Figure 5.11	Comparison of Predicted Normalised External Surface SCF Distribution on Chord Toe with Steel Model Test Results for the Axially Loaded T-joint($\alpha=7.26$, $\beta=0.71$, $\gamma=14.28$, $\tau=1.0$, $\theta=90^\circ$)	214
Figure 5.12	Comparison of Predicted External Surface SCF Distribution on Chord Toe with Recently Steel Model Test Results for the Axially Loaded T-joint($\alpha=7.26$, $\beta=0.71$, $\gamma=14.28$, $\tau=1.0$, $\theta=90^\circ$)	215
Figure 5.13	Comparison of Predicted Normalised External Surface SCF Distribution on Chord Toe with Recently Steel Model Test Results for the Axially Loaded T-joint($\alpha=7.26$, $\beta=0.71$, $\gamma=14.28$, $\tau=1.0$, $\theta=90^\circ$)	215
Figure 5.14	Comparison of Predicted External Surface SCF Distribution on Brace Toe with Acrylic Model Test Results for the IPB-Loaded Y-joint($\alpha=9.33$, $\beta=0.67$, $\gamma=15.0$, $\tau=0.8$, $\theta=45^\circ$)	216

Figure 5.15	Comparison of Predicted Normalised External Surface SCF Distribution on Brace Toe with Acrylic Model Test Results for the IPB-Loaded Y-joint($\alpha=9.33$, $\beta=0.67$, $\gamma=15.0$, $\tau=0.8$, $\theta=45^\circ$)	216
Figure 5.16	Comparison of Predicted External Surface SCF Distribution on Chord Toe with Acrylic Model Test Results for the IPB-Loaded Y-joint($\alpha=9.33$, $\beta=0.67$, $\gamma=15.0$, $\tau=0.8$, $\theta=45^\circ$)	217
Figure 5.17	Comparison of Predicted Normalised External Surface SCF Distribution on Chord Toe with Acrylic Model Test Results for the IPB-Loaded Y-joint($\alpha=9.33$, $\beta=0.67$, $\gamma=15.0$, $\tau=0.8$, $\theta=45^\circ$)	217
Figure 5.18	Comparison of Predicted External Surface SCF Distribution on Brace Toe with Steel Model Test Results for the IPB-Loaded T-joint($\alpha=8.01$, $\beta=0.71$, $\gamma=14.28$, $\tau=0.78$, $\theta=90^\circ$)	218
Figure 5.19	Comparison of Predicted Normalised External Surface SCF Distribution on Brace Toe with Steel Model Test Results for the IPB-Loaded T-joint($\alpha=8.01$, $\beta=0.71$, $\gamma=14.28$, $\tau=0.78$, $\theta=90^\circ$)	218
Figure 5.20	Comparison of Predicted External Surface SCF Distribution on Chord Toe with Steel Model Test Results for the IPB-Loaded T-joint($\alpha=8.01$, $\beta=0.71$, $\gamma=14.28$, $\tau=0.78$, $\theta=90^\circ$)	219
Figure 5.21	Comparison of Predicted Normalised External Surface SCF Distribution on Chord Toe with Steel Model Test Results for the IPB-Loaded T-joint($\alpha=8.01$, $\beta=0.71$, $\gamma=14.28$, $\tau=0.78$, $\theta=90^\circ$)	219
Figure 5.22	Comparison of Predicted External Surface SCF Distribution on Brace Toe with Acrylic Model Test Results for the OPB-Loaded Y-joint($\alpha=9.33$, $\beta=0.67$, $\gamma=15.0$, $\tau=0.8$, $\theta=45^\circ$)	220
Figure 5.23	Comparison of Predicted Normalised External Surface SCF Distribution on Brace Toe with Acrylic Model Test Results for the OPB-Loaded Y-joint($\alpha=9.33$, $\beta=0.67$, $\gamma=15.0$, $\tau=0.8$, $\theta=45^\circ$)	220
Figure 5.24	Comparison of Predicted External Surface SCF Distribution on Chord Toe with Acrylic Model Test Results for the OPB-Loaded Y-joint($\alpha=9.33$, $\beta=0.67$, $\gamma=15.0$, $\tau=0.8$, $\theta=45^\circ$)	221
Figure 5.25	Comparison of Predicted Normalised External Surface SCF Distribution on Chord Toe with Acrylic Model Test Results for the OPB-Loaded Y-joint($\alpha=9.33$, $\beta=0.67$, $\gamma=15.0$, $\tau=0.8$, $\theta=45^\circ$)	221

Figure 5.26	Comparison of Predicted External Surface SCF Distribution on Brace Toe with Steel Model Test Results for the OPB-Loaded T-joint($\alpha=8.01$, $\beta=0.71$, $\gamma=14.28$, $\tau=0.78$, $\theta=90^\circ$)	222
Figure 5.27	Comparison of Predicted Normalised External Surface SCF Distribution on Brace Toe with Steel Model Test Results for the OPB-Loaded T-joint($\alpha=8.01$, $\beta=0.71$, $\gamma=14.28$, $\tau=0.78$, $\theta=90^\circ$)	222
Figure 5.28	Comparison of Predicted External Surface SCF Distribution on Chord Toe with Steel Model Test Results for the OPB-Loaded T-joint($\alpha=8.01$, $\beta=0.71$, $\gamma=14.28$, $\tau=0.78$, $\theta=90^\circ$)	223
Figure 5.29	Comparison of Predicted Normalised External Surface SCF Distribution on Chord Toe with Steel Model Test Results for the OPB-Loaded T-joint($\alpha=8.01$, $\beta=0.71$, $\gamma=14.28$, $\tau=0.78$, $\theta=90^\circ$)	223
Figure 5.30	Comparison of Predicted External Surface SCF Distribution on Chord Toe with Recently Steel Model Test Results for the OPB-Loaded Y-joint($\alpha=10.85$, $\beta=0.71$, $\gamma=14.28$, $\tau=1.0$, $\theta=35^\circ$)	224
Figure 5.31	Comparison of Predicted External Surface SCF Distribution on Chord Toe with Recently Steel Model Test Results for the OPB-Loaded Y-joint($\alpha=10.85$, $\beta=0.71$, $\gamma=14.28$, $\tau=1.0$, $\theta=35^\circ$)	224
Figure 6.1	Typical Example of SCF Distribution along the Intersection of Tubular Y-Joint	232
Figure 6.2	Illustration of Characteristic Parameters for SCF Distribution along the Intersection of Tubular Joint	233
Figure 6.3	Comparison of Predictions from Derived Parametric Equations with Test Data for Average SCF along the Intersection of Tubular Joint	233
Figure 7.1	Semi-elliptical Crack in T-butt Welded Joint	244
Figure 7.2	Comparison of Deepest Point SIF Predictions from N&G*S for Semi-elliptical Cracks in T-Butt Welded Joint ($\alpha=45^\circ$, $\rho/T=0.02$ and $L/T=2$) with N&R for Flat Plate under Tension	245
Figure 7.3	Comparison of Deepest Point SIF Predictions from N&G*S for Semi-elliptical Cracks in T-Butt Welded Joint ($\alpha=45^\circ$, $\rho/T=0.02$ and $L/T=2$) with N&R for Flat Plate under Bending	246
Figure 7.4	Comparison of Deepest Point SIF Predictions from N&G*S and PD6493 for Semi-elliptical Cracks in T-Butt Welded Joint ($\alpha=45^\circ$, $\rho/T=0.01$ and $a/T=0.01$) against L/T under Tension	247

Figure 7.5	Comparison of Deepest Point SIF Predictions from N&G*S and PD6493 for Semi-elliptical Cracks in T-Butt Welded Joint ($\alpha=45^0$, $\rho/T=0.01$ and $a/T=0.01$) against L/T under Bending	248
Figure 7.6	Comparison of Deepest Point SIF Predictions from N&G*S and PD6493 with Bell's 3D FE Data($\rho/T=0$) for Semi-elliptical Cracks in T-Butt Welded Joint ($\alpha=45^0$, $L/T=2.3$ and $\rho/T=0.01$) under Tension	249
Figure 7.7	Comparison of Deepest Point SIF Predictions from N&G*S and PD6493 with Bell's 3D FE data($\rho/T=0$) for Semi-elliptical Cracks in T-Butt Welded Joint ($\alpha=45^0$, $L/T=2.3$ and $\rho/T=0.01$) under Bending	250
Figure 7.8	Comparison of Deepest Point SIF Predictions from N&G*S and PD6493 with Bell's 3D FE Data($\rho/T=0$) for Semi-elliptical Cracks in T-Butt Welded Joint ($\alpha=30^0$, $L/T=2.3$ and $\rho/T=0.01$) under Tension	251
Figure 7.9	Comparison of Deepest Point SIF Predictions from N&G*S and PD6493 with Bell's 3D FE data($\rho/T=0$) for Semi-elliptical Cracks in T-Butt Welded Joint ($\alpha=30^0$, $L/T=2.3$ and $\rho/T=0.01$) under Bending	252
Figure 7.10	Comparison of Deepest Point SIF Predictions from N&G*S with Bell's 3D FE Data($\alpha=70^0$, $\rho/T=0$) for Semi-elliptical Cracks in T-Butt Welded Joint($L/T=2.3$ and $\rho/T=0.01$) under Tension (Note: alpha - Weld Angle in degree)	253
Figure 7.11	Comparison of Deepest Point SIF Predictions from N&G*S with Bell's 3D FE Data($\alpha=70^0$, $\rho/T=0$) for Semi-elliptical Cracks in T-Butt Welded Joint($L/T=2.3$ and $\rho/T=0.01$) under Bending (Note: alpha - Weld Angle in degree)	254
Figure 7.12	Comparison of Deepest Point SIF Predictions from N&G*S with Nykanen FE Data($\rho/T=0.17$) for Semi-elliptical Cracks in T-Butt Welded Joint ($\alpha=45^0$, $L/T=1.952$ and $\rho/T=0.066$) under Tension	255
Figure 7.13	Comparison of Deepest Point SIF Predictions from N&G*S with Dijkstra'89 FE Data ($\alpha=70^0$) for Semi-elliptical Cracks in T-Butt Welded Joint under Tension (Note: alpha - Weld Angle in degree, rho - Weld Radius ρ)	256
Figure 7.14	Comparison of Deepest Point SIF Predictions from N&G*S with Dijkstra'89 FE Data ($\alpha=70^0$) for Semi-elliptical Cracks in T-Butt Welded Joint under Bending (Note: alpha - Weld Angle in degree, rho - Weld Radius ρ)	257

Figure 7.15	Comparison of Deepest Point SIF Predictions from N&G*S with Dijkstra'89 FE Data ($\rho/T=0.0071$) for Semi-elliptical Cracks in T-Butt Welded Joint ($a/c=0.2$, $\alpha=45^\circ$, $L/T=1.864$ and $\rho/T=0.01$) under Tension	258
Figure 7.16	Comparison of Deepest Point SIF Predictions from N&G*S with Dijkstra'89 FE Data ($\rho/T=0.0071$) for Semi-elliptical Cracks in T-Butt Welded Joint($a/c=0.2$, $\alpha=45^\circ$, $L/T=1.864$ and $\rho/T=0.01$) under Bending	258
Figure 7.17	Comparison of Deepest Point SIF Predictions from N&G*S with Dijkstra'93 FE Data($\alpha=70^\circ$, $\rho/T=0$) for Semi-elliptical Cracks in T-Butt Welded Joint ($a/c=0.2$, $\rho/T=0.01$) under Tension (Note: alpha - Weld Angle in degree)	259
Figure 7.18	Comparison of Deepest Point SIF Predictions from N&G*S with Dijkstra'93 FE Data($\alpha=70^\circ$, $\rho/T=0$) for Semi-elliptical Cracks in T-Butt Welded Joint($a/c=0.2$, $\rho/T=0.01$) under Bending (Note: alpha - Weld Angle in degree)	260
Figure 7.19	Comparison of Deepest Point SIF Predictions from N&G*S and H&D&T for Semi-elliptical Cracks in T-Butt Welded Joint ($\alpha=30^\circ$, $\rho/T=0.02$ and $L/T=2.8$) under Tension	261
Figure 7.20	Comparison of Deepest Point SIF Predictions from N&G*S and H&D&T for Semi-elliptical Cracks in T-Butt Welded Joint ($\alpha=30^\circ$, $\rho/T=0.02$ and $L/T=2.8$) under Bending	262
Figure 8.1	Semi-elliptical Crack in T-butt Welded Joint	270
Figure 8.2	Comparison of Surface Point SIF Predictions from W&L(FP)*S for Semi-elliptical Cracks in T-Butt Welded Joint ($\alpha=45^\circ$, $\rho/T=0.02$, $L/T=2$) with N&R for Flat Plate under Tension	271
Figure 8.3	Comparison of Surface Point SIF Predictions from W&L(FP)*S for Semi-elliptical Cracks in T-Butt Welded Joint ($\alpha=45^\circ$, $\rho/T=0.02$, $L/T=2$) with N&R for Flat Plate under Bending	272
Figure 8.4	Comparison of Surface Point SIF Predictions from W&L(FP)*S and Modified W&L(FP)*S with Bell's 3D data for Semi-elliptical Cracks in T-Butt Welded Joint ($\alpha=45^\circ$, $\rho/T=0.01$, $L/T=2.3$) under Tension	273
Figure 8.5	Comparison of Surface Point SIF Predictions from W&L(FP)*S and Modified W&L(FP)*S with Bell's 3D data for Semi-elliptical Cracks in T-Butt Welded Joint ($\alpha=45^\circ$, $\rho/T=0.01$, $L/T=2.3$) under Bending	274

Figure 8.6	Comparison of Surface Point SIF Predictions from W&L(FP)*S and Modified W&L(FP)*S with Bell's 3D data for Semi-elliptical Cracks in T-Butt Welded Joint ($\alpha=30^\circ$, $p/T=0.01$, $L/T=2.3$) under Tension	275
Figure 8.7	Comparison of Surface Point SIF Predictions from W&L(FP)*S and Modified W&L(FP)*S with Bell's 3D data for Semi-elliptical Cracks in T-Butt Welded Joint ($\alpha=30^\circ$, $p/T=0.01$, $L/T=2.3$) under Bending	276
Figure 8.8	Comparison of Surface Point SIF Predictions from W&L(FP)*S and Modified W&L(FP)*S with Bell's 3D data for Semi-elliptical Cracks in T-Butt Welded Joint ($\alpha=70^\circ$, $p/T=0.01$, $L/T=2.3$) under Tension	277
Figure 8.9	Comparison of Surface Point SIF Predictions from W&L(FP)*S and Modified W&L(FP)*S with Bell's 3D data for Semi-elliptical Cracks in T-Butt Welded Joint ($\alpha=70^\circ$, $p/T=0.01$, $L/T=2.3$) under Bending	278
Figure 9.1	External Longitudinal Semi-elliptical Surface Crack in Thin Pipe	292
Figure 9.2	Semi-elliptical Surface Crack at Saddle Position of Tubular Welded Joint	292
Figure 9.3	Comparison of Two Different Load Shedding Models for Tubular Joints	293
Figure 9.4	Comparison of Two Different fatigue Crack Shape Development Models for Tubular Joints	293
Figure 9.5	Comparison of Deepest Point SIF Predictions from N&G*S and TJ*S for Semi-elliptical Cracks in Welded Joint ($\alpha=45^\circ$, $p/T=0.02$ and $L/T=2$) with N&R for Flat Plate under Tension	294
Figure 9.6	Comparison of Deepest Point SIF Predictions from N&G*S and TJ*S for Semi-elliptical Cracks in Welded Joint ($\alpha=45^\circ$, $p/T=0.02$ and $L/T=2$) with N&R for Flat Plate under Bending	295
Figure 9.7	Comparison of Deepest Point SIF Predictions from N&G*S and TJ*S for Semi-elliptical Cracks in Tubular Welded T-Joint under Axial Loading ($\alpha=47^\circ$, $p/T=0.047$ and $L/T=1.294$)	296
Figure 9.8	Comparison of Deepest Point SIF Predictions from N&G*S and TJ*S for Semi-elliptical Cracks in Tubular Welded T-Joint under OPB Loading ($\alpha=47^\circ$, $p/T=0.047$ and $L/T=1.294$)	296
Figure 9.9	Comparison of Deepest Point SIF Predictions from N&G*S and TJ*S for Semi-elliptical Cracks in Tubular Welded DT-Joint(UCX1) under Axial Loading ($\alpha=47^\circ$, $p/T=0.017$ and $L/T=0.636$)	297

Figure 9.10	Comparison of Deepest Point SIF Predictions from N&G*S and TJ*S for Semi-elliptical Cracks in Tubular Welded DT-Joint(UCX2) under Axial Loading ($\alpha=47^0$, $\rho/T=0.021$ and $L/T=0.79$)	297
Figure 9.11	Comparison of Deepest Point SIF Predictions from N&G*S and TJ*S for Semi-elliptical Cracks in Tubular Welded DT-Joint(UCX3) under Axial Loading ($\alpha=47^0$, $\rho/T=0.03$ and $L/T=0.85$)	298
Figure 9.12	Comparison of Deepest Point SIF Predictions from N&G*S, TJ*S and TPM for Semi-elliptical Cracks in Tubular Welded Joint(T1-M) under OPB Loading ($\alpha=38^0$, $\rho/T=0.052$ and $L/T=1.125$)	298
Figure 9.13	Comparison of Deepest Point SIF Predictions from N&G*S, TJ*S and TPM for Semi-elliptical Cracks in Tubular Welded Joint(T2-M) under OPB Loading ($\alpha=39^0$, $\rho/T=0.039$ and $L/T=1.125$)	299
Figure 9.14	Comparison of Deepest Point SIF Predictions from N&G*S, TJ*S and TPM for Semi-elliptical Cracks in Tubular Welded Joint(T4b-DT) under OPB Loading ($\alpha=33^0$, $\rho/T=0.079$ and $L/T=1.5$)	299
Figure 9.15	Comparison of Deepest Point SIF Predictions from N&G*S, TJ*S and TPM for Semi-elliptical Cracks in Tubular Welded Joint(Y1a-M) under OPB Loading ($\alpha=40^0$, $\rho/T=0.051$ and $L/T=1.0$)	300
Figure 9.16	Comparison of Deepest Point SIF Predictions from N&G*S, TJ*S and TPM for Semi-elliptical Cracks in Tubular Welded Joint(Y1c-M) under OPB Loading ($\alpha=41^0$, $\rho/T=0.059$ and $L/T=1.0$)	300
Figure 9.17	Comparison of Deepest Point SIF Predictions from N&G*S, TJ*S and TPM for Semi-elliptical Cracks in Tubular Welded Joint(Y2a-M) under OPB Loading ($\alpha=41^0$, $\rho/T=0.043$ and $L/T=1.0$)	301
Figure 9.18	Comparison of Deepest Point SIF Predictions from N&G*S, TJ*S and TPM for Semi-elliptical Cracks in Tubular Welded Joint(Y2c-M) under OPB Loading ($\alpha=39^0$, $\rho/T=0.052$ and $L/T=1.0$)	301
Figure 9.19	Comparison of Deepest Point SIF Predictions from N&G*S, TJ*S and TPM for Semi-elliptical Cracks in Tubular Welded Joint(T1-M) under IPB Loading ($\alpha=54^0$, $\rho/T=0.04$ and $L/T=1.125$)	302
Figure 9.20	Comparison of Deepest Point SIF Predictions from N&G*S, TJ*S and TPM for Semi-elliptical Cracks in Tubular Welded DT-Joint(S) under OPB Loading ($\alpha=23^0$, $\rho/T=0.111$ and $L/T=2.632$)	302
Figure 10.1	Illustration of Non-Destructive Fatigue Strength Assessment Methodology for Offshore Tubular Joints	309

To My Parents

CHAPTER ONE

INTRODUCTION AND LITERATURE REVIEW

1.1 Introduction

In order to meet the demands of the world's energy requirements, many steel offshore platforms have been built for exploration and exploitation of oil and gas reserves from hydrocarbon reservoirs below the sea bed. The first steel offshore structure was installed off the Louisiana coast shortly after World War II. Presently, over 6000 offshore steel platforms are operational with predominant locations being the Gulf of Mexico(GOM) and the North Sea.

Hydrocarbon production is dominated by use of bottom supported fixed platforms. Among them, the most predominant type is the steel jacket or "template" platform pioneered in the GOM. It is a truss-work tower consisting of tubular members with a deck on the top and piles into the sea-bed (Figure 1.1). Tubular members are used extensively in jacket platforms because of their high strength to weight ratio and non-directional buckling and bending strength, and low wave resistance. Within the jacket structure, tubular members are welded together at their intersections in a variety of forms, normally classified as T, Y, K, X, etc. and these joints are referred as tubular joints. The complex intersection of these joints represents a structural discontinuity that gives rise to severe stress concentrations at the weld toe and may introduce possible fatigue failure. Therefore, the service life of offshore jacket platforms is dependent on the structural integrity of tubular joints. (Figure 1.2)

The detailed design of the framing for a jacket structure can vary considerably, mainly depending on requirements of strength and fatigue. For most jacket platforms in the GOM, where calm wave climate largely prevails only occasionally interrupted by hurricanes, fatigue criteria are not governing and an ultimate strength approach is used for the rarely occurring hurricane loading.

Exploitation and production of crude oil and natural gas moved to deeper and more hostile ocean environments following the discovery of oil in the North Sea in the early 1960s. The design of North Sea platforms has been traditionally based on the experience gained from platforms in GOM. However, the North Sea presents an entirely different situation. During a typical operational life, tubular joints experience up to 200 million waves that could produce fatigue damage. With the large proportion of the medium sized waves that produce fatigue

damaging stress cycles in the structures, North Sea oil production platforms had to be designed against fatigue crack growth.

As some of these platforms are now approaching the end of their design lives, the maintenance of offshore structural integrity becomes more important to the safety and operational reliability of offshore installations. Fatigue damage has been identified as one of the most important factors in causing degradation of these joints in the North Sea because of the significant levels of cyclic fatigue damage associated with oscillatory wave loading and lower fatigue strengths due to high stress concentrations at the weld toes. Therefore, periodic in-service inspections are required in order to ensure the structural integrity of offshore structures. To provide a cost effective inspection, maintenance and repair policy, accurate fracture mechanics modelling is needed so that one can predict the fatigue crack growth behaviour. This information needs to be linked to an understanding of the ability of non destructive techniques (NDT) to reliably detect and size fatigue cracks in tubular welded joints.

The fatigue performance of offshore tubular welded joints is of considerable importance both in the original design and also during service for the offshore jacket platforms in the North Sea. In response to this challenge, several major European research and development programmes, such as United Kingdom Offshore Steels Research Programme(UKOSRP) Phases I(HSE, 1988) and II(HSE, 1987), and European Coal and Steel Community(ECSC)(Steel in Marine Structures, 1987), have been carried out in order to understand the fatigue and fracture behaviour of these joints for past two decades. Meanwhile, a series of cohesive fatigue programmes(Fatigue of Offshore Structures, 1988) have been conducted under management from University College London(UCL) in the application of fracture mechanics to predict fatigue crack growth. These programmes produced a broad fatigue database and reliable methods of using such data for design and certification; this has significantly increased our understanding of fatigue damage for offshore welded tubular joints. The results from these programmes have been used to develop and update the standards and guidance(Department of Energy, 1984 a)(HSE, 1990)(API, 1993)(CAN/CSA-S473-92, 1992). Taking account of new fatigue data produced over recent years, the fatigue guidance of the Offshore Safety Division of the Health and Safety Executive(HSE) was recently revised(HSE, 1995).

This chapter will review the main findings from these research programmes in the following areas:

- i) Behaviour of the fatigue cracks in tubular joints
- ii) NDT techniques to detect and size these fatigue cracks and their reliability
- iii) Determination of stress distribution in tubular joint

iv) Assessment of fatigue strength for tubular joint.

The final section of this chapter will address the research objectives of this study and describe the scope of the rest of thesis.

1.2 Fatigue Cracks in Tubular Welded Joints

Tubular joints consist ordinarily of joints between main and secondary member tubes. The former, which are larger in diameter, are denoted as chord, and the latter, which consist of small sized tubes, are denoted as braces. The joints in the main structure of offshore steel jackets are often multiplane joints. Uniplane joints are found in the bracings between main legs in horizontal planes and in secondary structural elements. In the present state of the art the joints are normally classified and evaluated in terms of the simple uniplane joints (Figure 1.2), disregarding the effect of braces that are not lying in the considered planes. Figure 1.3 shows the non-dimensional geometrical parameters that define simple welded joints.

It should be emphasised that the classification should not be based only on the geometry of the nodes, but also on the load transfer mode. For the fatigue analysis of tubular joints it is convenient to separate the loads in multiples of three basic load cases, i.e. axial load, in-plane bending load and out-of-plane bending load (Figure 1.4).

The fatigue life is a combination of initiation life and crack propagation life. It is known that there are many different types of defects (i.e. undercuts, slag inclusions and porosity) caused by the welding process in the weld toes of these joints. Although these defects do not exceed the maximum limit permitted in codes, they cannot be eliminated or observed by present NDT techniques. Also the severe stress concentration occurs at an intersection of the steel tubes. As a result, the cracks initiate at the existing welding defects or stress concentration sites such as the weld toe. The first occurrence of detectable cracks occurs at a very small fraction of the service life of these joints.

Generally, fatigue cracks initiate at several locations around the weld toe in the form of multiple adjacent surface cracks in the chord toe. These cracks grow and eventually coalesce to form a single dominant crack. The propagation of this dominant crack will cause failure.

Crack propagation and fatigue damage may occur even at very low stress level. For tubular welded joints, propagation often forms a larger fraction of the total life than initiation. Experiments have shown that the surface cracks propagate along the weld toe of the intersection and in the wall thickness direction. The growth path direction of the weld toe cracks is a function of the principal stress field (Remzi and Blackburn, 1987). The through-wall principal stress direction generated by brace-chord load transfer varies with crack depth. This causes increasing curvature as the crack deepens. In general if a crack is subjected to a mixed mode

of deformation, under fatigue loading it curves to minimise the K_{II} and K_{III} values. In simple joints, fatigue cracks are usually found to have propagated through the chord thickness in a direction close to the radial direction (normal to the shell surface), but to curve towards the brace in the latter stages of crack penetration.

The fatigue strength of a tubular welded joint is mainly characterised by the hot-spot stress. The crack growth behaviour is influenced by both membrane stress and bending stress. Tubular joints having the same hot spot stress but with different through thickness stress will have different fatigue lives. A weld toe surface crack, growing in a predominantly membrane stress field, will grow rapidly and at an increasing rate to chord wall penetration. In contrast, for a predominantly bending stress field, the same crack would grow at a steady rate (Dover, 1992).

The thickness of the chord wall influences the fatigue life. The fatigue lives of larger joints are found to be less than that of smaller joints in the high cycle range. This thickness effect is mainly due to the varying stress intensity in the weld notch region and can be largely decreased or eliminated by reducing the weld toe angle (Niu, 1987). The thickness effect will be discussed in detail later on in this chapter.

In as-welded tubular joints, residual stresses of yield stress magnitude exist. Thus, any load, compressive or tensile, will be equally damaging (Vughts and Kinra, 1976). Post-weld heat treatment does significantly improve the fatigue life of tubular joints. This increase is believed to be due to an extension of the crack initiation phase in these joints (Reynolds, 1987).

Both weld angle and weld toe radius can influence the non-linear stress region close to the weld toe (Niu and Glinka, 1987). The weld toe radius is the most significant feature affecting fatigue crack initiation but the weld toe angle is more important for subsequent crack growth. Therefore, modifying the weld profile on these joints can improve the fatigue life.

1.3 Non-Destructive Measurement and Underwater Inspection Reliability

1.3.1 Non-Destructive Inspection Techniques

Offshore structures are subjected to periodic inspections, since in-service inspection is the main safeguard against uncertainties in fatigue life prediction. Inspections are frequently carried out in service on a selection of joints, based upon their assessed fatigue and criticality to system strength. Detection and sizing of any cracks which grow allows the fatigue model to be updated, as well as providing the opportunity to repair the crack. The inspection interval will be dependent on the quality and nature of the information coming from inspection techniques.

The important part of offshore structure inspection involves examination of the submerged part of the platform and this is mainly performed by divers. Over the last 20 years, there has been a considerable improvement in the effectiveness of underwater inspection. In the 1970s, underwater jacket weld inspection consisted mainly of cleaning and close visual inspection (CVI). It soon became apparent that CVI would only detect serious through-thickness cracks that were open at the surface. During the 1980s, use of non-destructive inspection methods considerably increased the effectiveness of underwater weld inspection. Additionally, flooded member detection (FMD) was introduced, and it has become very effective for checking through-thickness cracking.

A range of non-destructive inspection systems have been developed for the underwater inspection of tubular welded joints. In particular magnetic particle inspection (MPI) is commonly used for the crack detection and measurement of surface crack length. However, this technique relies heavily on the skill of the diver, and does not give crack depth. Also the use of MPI is time-consuming since it requires extensive cleaning of the area to a bright metal finish together with setting up of the encircling induction coils prior to inspection. If the defect is confirmed by MPI, the depth of crack is often measured by the alternating current potential drop (ACPD) technique which measures crack depth by a comparison of surface electrical potential differences in the cracked region. This technique has also been successfully used for continuous fatigue crack growth monitoring in array form in laboratory. However, electrical contact has to be maintained between the probe and the component being inspected for ACPD measurement.

Based on the theoretical developments at UCL of the ACPD technique, a new technique, termed alternating current field measurement (ACFM), has been developed recently. The basic principle of this technique is to generate a uniform electromagnetic field, to measure the magnetic fields in the region of a crack, and to perform calculations according to the developed theory to estimate the depth of a crack. ACFM technique is simpler in operation and gives a reliable estimate of crack depth in a single pass as it depends on the measurement of the near-surface magnetic fields rather than the surface electric fields like ACPD. Thus ACFM does not require electric contact with the metal surface. For this technique, the input current is induced into the specimen thus making the system fully non-contacting. Non-contacting probes are useful for the inspection of coated or painted surfaces in order to reduce the time spent on cleaning prior to inspection.

The main advantage of the ACPD and ACFM techniques is the ability to size cracks without the need for prior calibration. Both the ACPD and ACFM techniques are particularly suited for measurement of the depth of surface cracks and the ACFM technique can also be used for detection. However, the ACPD and ACFM techniques depend on a theoretical model for their accuracy. When the theoretical conditions are not met then corrections need to be

applied, if available. ACFM and also the eddy current system are recently used more often since they offer the possibility of similar performance but reduced time compared to MPI.

1.3.2 Reliability of Underwater Non-Destructive Inspection

The offshore structural integrity assessment relies very much on the information obtained in service by underwater non-destructive inspection. The performance of underwater non-destructive inspection systems is subject to variations and uncertainties. When the inspection does not reveal a crack it does not necessarily mean that no crack is present. For reliability fracture mechanics based inspection planning, it is necessary to know the reliability of the inspection method in detection and sizing. The reliability of a non-destructive inspection technique for defect detection in a particular application is normally expressed as a probability of detection (POD) curve which characterises the uncertainties of any particular technique. The POD of cracks, using a particular inspection method, is important in determining the likelihood of detecting cracks at a stage where they can be repaired before affecting the integrity of the structure.

Non destructive inspection technique capabilities can only be demonstrated through experiment. Producing fatigue cracks in tubular welded joints is obviously an expensive undertaking and could be prohibitively expensive if these samples were only used for one trial and then destroyed in order to yield the true crack sizes. As crack sizes could be reasonably accurately determined by laboratory non-destructive inspection techniques, a confidential library of tubular welded joints containing known fatigue cracks has been established in the underwater NDE Centre at UCL and this has been used for a series of trials.

Many research efforts have been made towards improving inspection techniques and assessing the reliability of various underwater NDT techniques to detect and size surface breaking fatigue cracks in tubular joints at the University College London(UCL) Non Destructive Evaluation(NDE) Centre. POD trials(Rudlin and Dover, 1990 a)(Rudlin and Dover, 1990 b) have been carried out by the UCL Underwater NDE Centre in collaboration with The City University as a series of joint industry projects. These were for many underwater non-destructive inspection techniques such as MPI and two well-known eddy current systems (Hocking AV100 and Thorburn EMD III), all of which have been successfully used offshore.

The result of above trials have been reported as POD against crack length. However, It is more appropriate to have POD data in terms of crack depth as the crack depth is the primary parameter for remaining life estimation and fracture mechanics based calculation of fatigue

crack growth. Thus POD data in terms of crack size have to be reinterpreted before they can be used in probabilistic based inspection scheduling.

1.4 Stress Analysis

1.4.1 Stresses Acting on Tubular Welded Joints

Because fatigue strength is controlled by the maximum local stress anywhere in a component, a greater understanding of the stress distribution particularly in regions where cracks are likely to initiate and grow would create a basis for the development of a fracture mechanics approach for the prediction of fatigue life and provide the essential information for stress/life(S-N) fatigue design approach.

The problem with tubular joints is that the stress distribution at the intersection between members is uneven with very high stress concentrations occurring at some points. These stresses can be as high as twenty times the nominal stress for the intersection and therefore have considerable impact upon the fatigue lives of the joints.

The stresses in tubular welded connections can be divided into three categories:

- a) Nominal stresses caused by the basic structural response of the system to applied loads
- b) Geometric stresses caused by the need to maintain compatibility between the tubes
- c) Notch stresses caused by highly localised deformations in part of the tube wall

The nominal stresses arise due to the tubes behaving as beam/columns, and may be calculated by frame analysis of the structure. Away from connections this gives an accurate assessment of stress levels.

In order to determine the nominal stresses acting on the structural members, a global stress analysis is normally performed on an offshore structure. At this level the structure is modelled as a simplified three-dimensional space frame using beam theory to determine the forces and moments acting on the joint. This global analysis will provide basic information on the stresses in the members, under the action of applied dynamic loading due to wind waves, etc.

Fatigue, however, is a local phenomenon. It depends on the stresses acting around the intersection of tubular joints. These local stresses are complex in nature but arise from the following two main sources.

The tube-to-tube intersection of a joint causes local bending of the tubular walls under loading. The differences in deformation between the chord and the brace due to this bending require the tube walls to bend so that the chord and the brace remain in contact at the weld. This bending effect results in stresses adjacent to the intersection known as the geometric stresses. The geometric stresses are dependent on geometric parameters of the joints, overall joint configuration and applied loading types.

Reinforcement due to the weld at the intersection locally stiffens the tube walls. The notch stresses arise because of the finite thickness of the tube walls and weldments. However, this effect is not propagated far through the wall thickness, and thus leads to a local region of three-dimensional stresses. The notch stresses are mainly determined by the parameters representing local weld geometry, such as weld toe angle and weld toe radius, as illustrated in Figure 1.5.

The stresses inside the notch region are important for fatigue crack initiation and early crack growth. However, they are not the controlling parameter as the cracks grow through the thickness because the presence of a crack will produce load redistribution. Also the notch stress varies according to the geometry of the weld, and in consequence it is difficult to provide a deterministic value of the peak stress. Instead it has been assumed that the most important stresses controlling the fatigue behaviour are the geometric stresses at the weld toe.

As a part of the UKOSRP programme initiated to investigate the fatigue behaviour of tubular joints, various joint geometries were studied using a combination of finite-element stress analyses, strain-gauged acrylic models and photo-elastic models, and subsequently compared with strain-gauge measurements from the steel tubular test pieces, together with the results derived from parametric equations. The results showed that the stress variation on the exterior surface close to the weld toe follows a general form, shown in Figure 1.6. Far from the weld toe the nominal stresses predominate, close to the weld toe the notch stresses due to the weld geometry dominate, between these two regions exists a region where the changes in the stress field are linear and this variation is thought to be due to the geometric stresses produced by the interaction of chord and brace. Thus, a fictitious stress, known as the "hot-spot" stress has been introduced into the analysis. According to the recommendation proposed by UKOSRP I(Irvine 1981), the hot-spot stress is defined as *"the greatest value around the brace/chord intersection of the extrapolation to the weld toe of the geometric stress distributions near the weld toe. This 'hot spot' stress incorporates the effects of overall joint geometry (i.e. the relative size of the brace and chord) but omits the stress concentrating effect of the weld itself which results in a local stress distribution."* This is the stress which may be derived by linearly extrapolating the geometric stress to the weld toe. The locations of the points recommended for linear extrapolation for

tubular welded T and X joints(Irvine, 1981) are illustrated in Figure 1.7. This definition of hot spot stress is now held to be the most realistic expression of the fatigue crack growth inducing stress acting on a tubular joint.

For convenience these geometric weld toe stresses are often expressed in the form of the stress concentration factor (SCF) where the SCF is defined as

$$SCF = \frac{\text{extrapolated weld toe stresses}}{\text{nominal stresses}} \quad (1 - 1)$$

In order to conduct fracture mechanics calculations of remaining fatigue life on tubular welded joints, it is necessary to have the information on the magnitude and distribution of the stress acting in the anticipated crack path, not just the peak stress at one location such as saddle and crown. In particular one could identify another two key pieces of information that are needed, as well as the SCF, for fatigue crack growth calculations. These are listed below.

1) Stress variation through the thickness. (Degree of Bending)

Figure 1.8 shows a typical stress distribution through the chord wall. The surface stress field is predominantly due to chord wall bending (linear) and the stress concentration due to the change in section at the weld toe (non-linear). For a deep crack the weld toe stress concentration region would have little effect. Also in the design stage, it is difficult to predict the non-linear distribution that is dependent on the weld and weld toe geometry. Therefore, most efforts have been concentrated on the linear through thickness distribution and in particular attempting to define the ratio of bending to tension. Thus the stress distribution across the wall thickness is assumed to be a linear combination of membrane and bending stress about the plane of the element. The stress distribution through the chord wall is often characterised by either the degree of bending(DoB), i.e. the ratio of bending stress over total external stress or the ratio of bending to membrane stress.

2) Stress variation along the weld toe between the crown and saddle sites. (Stress Distribution around Intersection)

Fracture mechanics calculations on tubular joints require a knowledge of the local stress distribution around the joint as the way in which the multiple cracks initiate and coalesce is very much dependent on this information. Apart from the hot spot stresses, the average stress around a joint(Dharmavasan and Dover 1987) has also been shown to play an important role during the fatigue crack propagation. The stress distributions along the intersection of tubular joint are shown in Figure 1.9 for a tubular T-joint under axial, IPB and OPB loading. One can see from this figure that each load case has its particular distribution of stresses along the intersection line and thereby its particular influence on the

fatigue life. Thus the accurate prediction of stress distribution around a joint is very important for fatigue strength assessment especially under multiple axes loading.

1.4.2 Stress Analysis Techniques

The determination of the stress distribution around the intersection in tubular joints by analytical techniques has proven to be costly as well as difficult due to the relative complexity of the geometrical configuration as well as the thin-shell theory governing their behaviour. But some partial solutions have been obtained. These theoretical methods range from elementary strength of materials approaches to mathematical theory approaches.

A simple punching shear model was proposed by Carter et al(1969). The load transfer from the brace to the chord is assumed to be via shear forces acting through the chord wall and the force is considered to be uniformly distributed around the intersection. The method ignores the local bending that may occur and this would be an important omission for elastic behaviour. However, if larger scale yielding occurred then the stress distribution through the chord wall becomes much more uniform and this particular model might be more relevant. This elementary strength of materials approach was used to calculate the static strength in design codes.

The stress and deflection distributions(Hoff et al., 1953)(Bijlaard, 1955)(Kellogg, 1956) in tubular chords caused by load transmitted through various attachments were studied using the classical thin shell equations for cylindrical shells, such as those presented by Donnell(1934) and Flugge(1934). The results show that the stress decays rapidly away from the point of load application and that the decay has a characteristic wave length. Although these attempts were limited to simple geometries such as T-joints and failed to account properly for the stiffening of the chord wall due to the presence of the branches, these models were useful because they have been used to provide a physical understanding of the joint behaviour that has led to the present definition of hot spot stress.

A more realistic analysis of T joint was developed by Dundrova(1965). She assumed that the chord were subjected only to forces directly parallel to the brace axis. The distribution of these forces was determined by imposing compatibility of the displacements in the brace axial direction between the brace and the chord. Although it did not completely model the connectivity of the branches to the chord, this is the first analytical solution which explicitly included the brace in the analysis.

However, fatigue fracture mechanics analysis of tubular joints needs a more detailed stress distribution around the intersection and with greater accuracy. It has proved to be necessary to use numerical and experimental techniques for the determination of the stress

distribution. In the next section, a brief review of the most commonly used stress analysis techniques for offshore tubular joints is presented.

1.4.2.1 Numerical methods

Numerical methods are, in principle, capable of solving any stress analysis problem, to an accuracy which is limited only by the computing resources available. Traditionally, Fourier series superposition was used to solve the governing equations (Bijlaard, 1955) (Scordelis and Bouwkamp, 1970). For example, Bijlaard's solution (Bijlaard, 1955) is based on a double Fourier series representation of the displacements: one Fourier series in the axial direction, and the other in the hoop direction. However, a large number of terms in this solution must be used to obtain a relatively accurate result. It required extensive computational efforts and has been largely superseded by more advanced methods.

Nowadays, the principal numerical techniques are the finite difference method, finite element method and boundary element method. The finite difference method leads to an approximate solution to the exact problem, while the finite element method and boundary element method give an exact solution to an approximation of the original problem. The basic difference between the finite element method and boundary element method is the solution strategy. The finite element method is probably the most versatile and most adequate tool to analyse tubular joints. Hence it has been widely used to obtain the stress distribution of tubular joints.

1.4.2.1.1 Finite Element Method

The finite element method is a numerical procedure which is ideal for solving physical problems, such as for complex structural components, whose closed form solutions are almost impossible to obtain. This technique uses the assumption that although a complex structure can not be analysed directly, it can be discretized into small, regular, or finite, elements from which the solution can be formulated. The governing differential equations for a continuous system are approximated with simpler algebraic equations applied to a discretized model of the continuous system. By solving the combined effect of loading and constraints of these elements through the nodal compatibility, the overall behaviour of the structure can be evaluated.

Early attempts to apply the finite element method to the stress analysis of tubular joints were difficult due to the relative crudity of the elements used and the lack of computational power in dealing with large numbers of elements. Earlier facet shell/plate elements were used to model the joint because of their simplicity. For example, using constant strain

elements superposed with a nine degree of freedom flat plate bending element, Greimann et al(1973) obtained results within 20% of the experimentally determined steel joint test results.

Facet shell/plate elements introduce geometrical errors and the coupling which exists in shells between the membrane forces and bending moments is not reproduced. In these formulations at the element level, it is necessary to use more advanced elements for tubular joint analysis.

With the development of curved shell elements, finite element stress analysis for tubular joint has improved tremendously. These curved shell may be categorised as follows:

1) the thin shell elements based on Kirchhoff assumptions.

The comprehensive studies of stress concentration in tubular joints using various thin shell elements were conducted by Kuang(1975) and Gibstein(1981). It is now generally accepted that isoparametric thin shell elements are the most useful elements for tubular joint stress analysis, since they combine relatively high accuracy with low cost.

2) the shell element based on Reissner-Mindlin theory which may be applied to both thin and thick shells. They include the Ahmad element(Ahmad et al, 1970) and the complex semi-loof element(Irons, 1976).

The difference between these two kinds of curved shell elements is that the latter permits shear deformation and is suited to thick shells whereas the former is not.

One significant disadvantage in the use of shell elements for stress analysis in tubular intersections is that the tubular joints are modelled as intersecting cylindrical tubes at the mid-surfaces of the walls. Thus the weld is not modelled and the three dimensional stresses in the joint are lost. This could lead to spurious local bending of the member walls to be induced, particular in the brace. However, the shell elements do provide, in many cases, an acceptable compromise between accuracy and computational cost. Because the spurious local bending at intersections can lead to significant difference between calculated and observed stresses in some cases(Dijkstra, 1981), it is recommended that shell elements should not be used for tubular joints for which β exceeds 0.8 unless the weld is also explicitly modelled.

In order to overcome the above difficulty, three dimensional brick elements have been used to model the whole tubular joint. Using this type of element, the weld toe profile could be modelled as a sharp notch. This method will provide more accurate and detailed stress behaviour near the intersection than a simple thin shell analysis. It is only limited by the computational costs involved.

Because the three dimensional elements are very inefficient for shell bending situations, Parkhouse(1981) combined them, to model the weld toe, in a conforming manner with shell elements to model the portions of the tubular remote from the intersection and obtained promising results on an X-joint. However, the interpretation of the results was difficult as, infinite stresses arise at the notch tip in theory. It is necessary to calculate the stresses at some characteristic distance from the intersection which has the additional advantage that this may be chosen to coincide with typical strain gauge positions used in laboratory tests. Thus some information would be lost in the region close to the weld toe.

The choice of an element for a tubular joint analysis depends on the geometry of the joint and the purpose for which the results of the analysis are to be used. Curved-shell elements are adequate for SCFs in joints for which β does not exceed 0.8. For certain applications which require detailed information in the vicinity of the weld and through the wall thickness of the members, such as fracture mechanics studies of small defects at tubular joints, three-dimensional elements are essential, preferably used in conjunction with conforming shell elements to model areas remote from the intersection.

The major difficulty is the generation of the mesh, particular in regions where the stresses are changing rapidly, and numerous elements may be required for accurate results. The actual mesh chosen is a compromise between achieving acceptable accuracy and reducing the cost of the analysis. An important aspect of mesh design is that badly distorted elements must be avoided. For an economical analysis, the planes of symmetry and asymmetry in each joint are used to reduce the mesh size. Although this resulted in the need for additional load cases, there is a net cost saving since the finite element solution cost varies to approximately the square of the number of nodes making up the problem. As a "branched" structure, the tubular joint lends itself naturally to the technique of substructuring. This technique may provide additional savings if a given substructure can be used more than once in the same analysis or in a series of analyses.

In general, the advantages of finite element method include the ability to provide information on the stress behaviour of an entire joint and the ease with which extra load cases may be analysed.

1.4.2.2 Experimental Methods

According to the modelling media, laboratory-based techniques are generally divided into the testing of steel models, acrylic models and photoelastic models. All other methods should be calibrated against such experimental methods.

1.4.2.2.1 Strain Gauged Steel Model

The steel tubular joints, to scale or full-scale, may be tested statically to obtain strain distributions at the joint intersections using strain gauges. In this technique, the global features of geometry, with the weld toe present, and loading can be realistically reproduced. Any steel tubular joint must be fabricated to standard offshore procedures e.g. AWI(1984). Care must be taken for scaled specimens in the scaling down of the weld size, since large welds will produce inaccurate results. Tolerances on dimension must be based on current offshore practice and the results must be viewed in light of the actual dimensions of the specimen.

In order to obtain the strain and stress produced by the application of a static load, strain gauges are used around the intersection. Usually, a set of rosette gauges are placed around the intersection to locate the positions of maximum stress. Then the extrapolation gauges can be mounted to obtain the hot spot stress.

Being the most definitive testing technique, steel model tests provide the most realistic and accurate evaluation of the stresses in tubular joints. Hence the results of the other methods are validated against them.

However, this technique is costly and time-consuming, because of the extensive and careful strain gauging, and the large loading equipment and testing rigs that are required for representatively sized specimens. The notch stress field is difficult to measure due to the physical size of the strain gauges. Also for the steel models, the through thickness stress distribution is usually unknown as the stress distribution on the inner surface is difficult to measure, especially for the small joints. The use of steel models is only feasible when further tests, such as fatigue testing, are to be carried out.

1.4.2.2.2 Strain Gauged Acrylic Model

The acrylic models are made from commercially available cast acrylic tubes and are normally much scaled down versions of the steel models. It is a low cost alternative to testing larger steel joints. The procedure adopted for obtaining the stress distribution is similar to that of the steel models.

Acrylic models of tubular joints provide a number of advantages. Firstly, since acrylic has a low Young's modulus(E) that is about $1/80$ of that of steel, low loads are required to produce a measurable strain and consequently the test rigs can be small. Secondly, welds can be included or excluded. The welds may be added by attaching acrylic 'weld' machined to shape. It is often desirable to carry out the test without any fillets. This is particularly beneficial and cost saving when carrying out parametric studies. Thirdly, as strain gauges

may be fitted before assembly, strain data may be obtained on the inner surfaces of the chord and brace walls. This would be very difficult in steel welded joints. Finally, additional load cases can be performed easily and the models are available for re-testing and modification. Generally acrylic models have shown good correlation with the large scale steel model results.

The main disadvantage in using acrylic is that it creeps under loading. In order to obtain consistent results, any strain gauge reading must therefore be taken at a fixed time (usually one minute) after the loading has been applied.

1.4.2.2.3 Photoelastic Method

The photoelastic method is the only technique that enables a complete three dimensional stress pattern including stress distributions on the exterior and interior surfaces and through the chord and brace walls in the region of intersection to be obtained. The brace-chord weld profiles are modelled, hence continuous stress information in this region is obtained. It is particularly useful for joints with complicated geometry and/or loading conditions.

The stress freezing method is the most commonly used photoelastic technique in analysing tubular joints. It consists of heating the joint under loading, followed by cooling, so that the stresses are effectively frozen in the model and can be used to determine the total tubular joint stress distribution.

The photoelastic method can provide a detailed and accurate assessment of the total stress distribution. However, the models must be carefully prepared and the analysis of the fringe counts obtained can be extremely time-consuming and expensive. Moreover, the information obtained from this technique is usually too detailed for use in design.

1.4.2.3 Concluding Remarks

As a summary of the above discussion, although the strain gauge steel model results are considered most accurate, the performance of other modelling methods investigated indicates that each can be used for accurate stress analysis for tubular joints, with appropriate care. The choice of the stress analysis techniques must be considered in terms of cost and accuracy. The advantages and disadvantages of above methods have been summarised (Clayton and Irine, 1978) (Connolly, 1986).

Photoelasticity and steel modelling give the ability of modelling weldments in detail and the former method allows the extraction of stress data from any part of the connection, rather than at points where strain gauges have been affixed. Also the stresses in the interior of the structure can be determined. Acrylic models have been found in particular to be reliable,

cheap and flexible. Without weld toe modelling, it reproduced primary membrane stresses in close agreement in shape to those obtained from corresponding steel models. The thin shell finite element method, which does not attempt to model notch stresses, produces stress outputs at the mid surface intersection which broadly agree in shape with the geometric stress obtained with steel models. It can significantly over-predict brace stresses.

1.4.3 Parametric Equations

For most design and re-certification work, it is quite expensive and time consuming to estimate the stresses, in particular the hot spot stresses, for tubular joints using any of the above methods except for a few very important joints. Therefore, parametric equations which express the hot spot stresses in the form of the non-dimensional parameters of joints, α , β , γ , τ , θ were developed for various joint geometries by carrying out extensive parametric studies.

In practise only finite elements and the strain-gauged acrylic model techniques have been used for economical reasons. The most widely used equations are the Kuang(Potvin et al, 1977), Efthymiou and Durkin(1988), Wordsworth and Smedley(1981), Wordsworth and Smedley as modified by UEG(UEG 1985), Lloyds Register(Smedley and Fisher 1991) and UCL HCD(Hellier Connolly and Dover 1990). Of these equations those by Kuang, Efthymiou and Durkin, and UCL HCD are based on finite element models of various types. The Wordsworth and Smedley equations are based on results of acrylic model tests, and UEG equations are based on the Wordsworth and Smedley equations with modifications based on the comparison of the equations with steel joint data. Lloyds Register equations have been derived only recently and are based on the database of measured SCFs from steel and acrylic joints.

The accuracy of parametric equations can be assessed by comparing their predictions with existing strain-gauged steel test results. Unfortunately, the amount of steel data are limited. For this reason the data from acrylic model test are often used as well. A steel and acrylic test database based on the Lloyds Register data and the UCL database (with the criteria developed for acceptance of SCF data) was established by MaTSU(MaTSU 1996). By comparing the results derived from all parametric equations against the database, the performances of all existing SCF parametric equations have been recently assessed by the Fatigue Guidance Review Panel supported by the HSE(DEn.)(MaTSU 1996). It has been concluded that only two sets of SCF equations for simple tubular (i.e. X, K and T/Y) joints, i.e. the Efthymiou and Lloyd's Register equations, are recommended in the revised fatigue guidance for the saddle and crown positions in the chord and brace under axial, in-plane bending and out-of-plane bending loading.

Tubular joints of differing geometry or mode of loading but with similar hot-spot stresses often exhibited significantly different numbers of cycles to failure. These differences are

thought to be attributable to changes in crack growth rate, this being dependent on the through-thickness stress distribution as well as the hot-spot stress. It is anticipated that a joint with a high proportion of through-thickness bending stress, for example, will have a longer fatigue life than one with a similar hot-spot stress, but with a greater component of through-thickness membrane stress. Despite the degree of bending being important for fracture mechanics based crack growth assessment, so far there is only one set of parametric equations(UCL)(Connolly et al 1990) to predict the through thickness stress distributions and these are for tubular Y and T-joints.

The fracture mechanics calculations on tubular joints also requires a knowledge of the local stress distribution around the joint. The simple interpolation formulae based on the peak local stress at saddle and crown were reported by UEG(1985) tubular joints programme. Similarly, the parametric equations were developed at UCL(Hellier et al 1990) for the stress distribution around the brace/chord intersection of tubular Y and T-joints. These formulations predict the distribution around a joint based on the peak stresses from parametric equations. The UCL equations allow the effect of a hot spot at a point other than the crown or saddle to be taken into account. After comparing the UEG equations with finite element analysis results, Vinas-Pich(1994) concluded that the stress distribution proposed in design guidelines is not accurate enough around the whole brace-chord intersection. The problem with the UCL HCD equations and the UEG equations, is that they were derived from only a limited number of typical sample results rather than whole database and therefore they can not provide enough accuracy to all other cases for detailed analyses.

Despite being borderline in terms of the assumed criteria, the UCL HCD equations are not recommended for SCF calculation in revised fatigue guidance. However, the UCL HCD equations are the only set of parametric equations that can predict the SCF, the bending to membrane ratio and stress distribution in tubular Y and T-joints. The predictions from UCL HCD equations are compatible as they are obtained from the same database. All these aspects are essential for the fatigue crack growth analysis by using fracture mechanics. Given the importance of these three sets of equations for crack growth analysis, it would be valuable to conduct the parametric study to derive a further comprehensive set of stress equations for other type of joints such as K, X and DT-joints etc..

1.5 Fatigue Strength Assessment

The fatigue strength assessment is a major consideration in the design and in-service assessment of offshore tubular welded joints in North Sea. There are two basic approaches used in the fatigue life assessment of these joints. The first method relies on the use of stress-life(S-N) curves obtained from carrying out constant amplitude fatigue tests on

tubular joints. The second method is based on linear elastic fracture mechanics and considers the details of how the cracks propagate under the applied loading.

1.5.1 S-N Approach

Historically, the fatigue design life of offshore tubular welded joints is predicted using the S-N approach, which relates the stress range at a point under consideration to the number of cycles to failure. It is necessary to define the two parameters that describe the S-N curves, i.e. stress range and failure criterion, prior to analysis of data. The hot-spot stress range was selected as a good representation of the stress range. As most of the tests ignored the details of the crack monitoring, the failure life is divided in three stages:

- 1) N_1 : the number of cycles to first discernible surface crack
- 2) N_2 : the number of cycles to first through wall crack
- 3) N_3 : the number of cycles to termination of the test which is normally when the test rig can no longer apply the desired load because of increasing compliance of the specimen due to extensive cracking

It has been found that once the crack has gone through the thickness of wall, the stiffness of the joint decreases rapidly and the crack accelerates (Dover and Petrie 1976). Also the complete severance of a joint (N_3) in service does not often happen because the load redistribution in the frame structure will make the joint redundant and possible non-load carrying when N_2 has been reached. For these reasons, N_2 has been defined as the end of fatigue life of a tubular joint.

Based on the results of the experimental test programmes initially as part of UKOSRP-I and ECSC tests and by consideration of some safety factors, the S-N curves for tubular welded joints was proposed by UK Department of Energy (1983) and revised in current fatigue guidance (MaTSU 1996). The new curve for tubular joints has been designated the T' curve. The chord wall thickness in the test series ranged from 16 to 75mm. The basic S-N curve to be adopted is for joints tested in air with a chord wall thickness up to 16mm. The basic design S-N T' curves for fatigue in air are expressed below.

$$\log_{10} N = 12.182 - 3 \log_{10} S_B \quad \text{when } S_B \geq 53 \text{ Mpa} \quad (1 - 2)$$

$$\log_{10} N = 15.637 - 5 \log_{10} S_B \quad \text{when } S_B \leq 53 \text{ Mpa} \quad (1 - 3)$$

This design curve was defined as that corresponding to a 2.3% probability of failure which is equivalent to two standard deviations of $\log_{10} N$ below the mean S-N curve since fatigue endurance is log-normally distributed.

given a similar nominal stress

It is generally recognised that the thicker chord wall gives a shorter fatigue life. Therefore an empirical relationship based on the experimental results of welded joints was suggested for the strength (S) of tubular joints with chord wall thickness (t):

$$S = S_{\beta} \left(\frac{16}{t} \right)^{0.3} \quad (1-4)$$

where S_{β} is the basic fatigue strength from the basic curve for a given life. A set of curves based on this concept can be obtained for different wall thickness.

For variable amplitude loading, it is assumed that each load cycle causes a damage proportional to the total fatigue life in that level of load. The proportional damages then accumulate to a level which results in failure. The Miner's linear damage summation rule (Miner 1945) is often used to calculate the total damage fractions. It is defined as:

$$D = \sum \frac{n_i}{N_i} \quad (1-5)$$

where D is the linear sum of damage fractions

n_i is the number of cycles at i stress range ΔS_i

N_i is the corresponding mean fatigue life under the stress range ΔS_i taken from the design S-N curve

The advantage of S-N approach is that only one value of stress range, i.e. the hot spot stress range, is used to estimate the fatigue life. Moreover, it is possible to accommodate complex conditions such as combined modes of loading, corrosion, size effect, stress relief and other conditions with simple modifications. The S-N approach has gained widespread acceptance in design codes because of its ease of application.

However, the S-N curves are limited to the range of tubular joint geometries and loading comprising the database from which they are derived. It can be a severe limitation due to the variety of tubular designs used. Also, these S-N curves can only be applied to notionally crack free joints and can not be used to predict how cracks grow and remaining life when cracking is detected in service in a tubular joint because they do not correlate the physical damage mechanism to the assessment.

1.5.2 Fracture Mechanics Approach

In common with all engineering structures, offshore structures contain flaws, ranging from microscopic material defects to macroscopic geometric imperfections introduced during fabrication and construction. Wave action on the submerged structure creates cyclic stresses throughout the structure. When these cyclic stresses are magnified by geometric features and coincide with pre-existing flaws, fatigue cracking can develop in offshore structures during

their service. It is important to predict the propagation of a pre-existing crack and decide whether remedial action is necessary. Whereas the S-N method can only predict the total fatigue life, an alternative approach, based on linear elastic fracture mechanics, allows fatigue crack growth to be modelled. This approach can be combined with non-destructive evaluation to assess the significance of defects found during inspections and to calculate the remaining life of an in-service cracked structure in order to make run, retirement or repair decisions. So it is becoming increasingly important to the design and subsequent operation of structures that may develop cracks during their service life.

It is known that the concept of elastic stress concentration factor breaks down as a stress singularity exists close to the crack tip. Fracture mechanics seeks to relate the conditions of stress and strain fields in the vicinity of a crack tip to the remote stress and the crack size. Using a stress function approach, Sneddon(1946) obtained the stress expression in the vicinity of the crack tip as following.

$$\sigma_x = \frac{K_I}{(2\pi r)^{1/2}} \cos\left(\frac{\theta}{2}\right) \left[1 - \sin\left(\frac{\theta}{2}\right) \sin\left(\frac{3\theta}{2}\right) \right] + \text{non-singular terms} \quad (1-6a)$$

$$\sigma_y = \frac{K_I}{(2\pi r)^{1/2}} \cos\left(\frac{\theta}{2}\right) \left[1 + \sin\left(\frac{\theta}{2}\right) \sin\left(\frac{3\theta}{2}\right) \right] + \text{non-singular terms} \quad (1-6b)$$

$$\tau_{xy} = \frac{K_I}{(2\pi r)^{1/2}} \cos\left(\frac{\theta}{2}\right) \sin\left(\frac{\theta}{2}\right) \cos\left(\frac{3\theta}{2}\right) + \text{non-singular terms} \quad (1-6c)$$

where (r, θ) are polar co-ordinates based on the right-hand crack tip, and σ_x , σ_y , τ_{xy} are the stress acting on the element so located.

It has been found that the distribution of the stresses and strains ahead of the crack tip is always of the same form and the magnitude of the stress field changes as a result of changes in applied stress or crack size. Under the assumptions of linear elasticity, the magnitude of the stress field ahead of the crack tip can be used to describe the strength of the singularity by a single parameter, K , termed the stress intensity factor(SIF). It is a measure of the stress occurring in the highly stressed region at the tip of the crack in an elastic solid.

Successful use of linear elastic fracture mechanics(LEFM) requires a knowledge of the stress intensity factor for the configuration being considered. The crack in a three dimensional body may be deformed in three independent ways (Figure 1.10): opening mode(mode I), shear mode(mode II) and tearing mode (mode III). The opening mode(mode I) is considered as the most important. In general the SIF can be normalised with a divisor $(\sigma\sqrt{\pi a})$ which is the SIF value corresponding to a crack of half length a in an infinite sheet under a constant normal load σ .

$$K = Y\sigma\sqrt{\pi a} \quad (1-7)$$

where Y is SIF calibration factor

σ is the representative stress

a is the half length of the crack

As a measure of how the geometry and loading of a particular configuration affect the SIF for a crack in an infinite plate, the SIF calibration factor Y is a function of the crack size and shape, and the geometry and boundary conditions of structure in which it is located. The aspect ratio (depth/surface length) is also an important factor because the surface cracks are always approximated as semi-elliptical ones in all analytical methods.

Most materials deform plastically once some critical combination of stress is achieved and therefore a plastic zone is introduced at the crack tip although the crack tip stress field remains predominantly elastic. Under cyclic loading this plastic zone which undergoes permanent deformation changes in size and results in crack growth. Since the size of this plastic zone is a function of stress field and hence SIF, the changes in the plastic zone can be characterised by ΔK ($K_{\max} - K_{\min}$). Therefore Paris et al(1963) suggested that the fatigue crack growth rate can expressed by the range of SIF as follows:

$$\frac{da}{dN} = C(\Delta K)^m \quad (1 - 8)$$

where da/dN is the crack growth rate (the crack extension per load cycle)

ΔK is the stress intensity factor range

C and m are the material constants

The key feature of the stress intensity factor is that it is possible to relate the materials' resistance to crack growth since the stress intensity factor provides a measure of the driving force for crack propagation. Experiments have shown that the crack growth can be classified into three regions according to the relative magnitude of the crack growth rates (Figure 1.11). Region A starts with a fatigue threshold, ΔK_{th} below which cracks do not propagate under cyclic loading, and continues until the slope of the curve becomes constant. Region B is a linear one where the behaviour can be represented by Paris law. Finally region C corresponds to the onset of unstable crack growth rate where ΔK approaches the material inherent fracture toughness K_c . The majority of fatigue crack growth in engineering structures can be considered as lying in region B. Although some investigators have modified the Paris law to incorporate the threshold level, environment and the nature of the cyclic loading (its mean value and other features), it is still most widely used in its original form to describe the crack growth rate for the intermediate range of ΔK .

The procedure for fracture mechanics fatigue assessment is based on linear elastic behaviour and development of crack propagation using the Paris law. The determination of the stress

intensity factor K is very important step in this process since it is a measure of the severity of the defect in a given cracked region. Once the SIF solution is known with the material constants C and m , the fatigue propagation life from an initial crack size a_i to a final crack size a_f can be determined from

$$N = \int_{a_i}^{a_f} \frac{da}{C(\Delta K)^m} \quad (1-9)$$

Linear elastic fracture mechanics uses the stress intensity factor concept to characterise conditions at the crack tip. In conjunction with empirically derived material crack growth data, this technique can be used to model fatigue behaviour.

1.5.3 SIF Evaluation Methods

Much effort has been put into the derivation of SIFs and a variety of methods have been developed to approach the problem. This section intend to review these method very briefly. However, the emphasis is on the weight function method which has been recently developing very rapidly.

1.5.3.1 Analytical Method

Analytical solutions are those which satisfy all the boundary conditions exactly. Based on the Airy stress function approach, analytical solutions for the stress field, and therefore the SIF, in a large number of 2D Mode I and II crack geometries have been derived in closed form using Westergaard and Muskhelishvili's complex stress function method. The advantage of this approach is that it extends the possible range of problems by using conformal mapping. For example it can map a circular hole into a crack subjected to general loading.

However, for an arbitrary region it will usually be impossible to calculate the SIF using the analytical method. Instead, weight function, numerical, and experimental methods are needed.

1.5.3.2 Weight Function Method

One of the most powerful methods for calculating SIF for a crack subjected to general (non-uniform) stress fields is the weight function method proposed by Bueckner(1970) and Rice(1972). It has received more and more attention for recent years due to its relative simplicity with which SIF can be calculated for arbitrary symmetric loading, while preserving accuracy.

The idea is that if the SIF and corresponding displacement field on all the boundaries of a cracked body are identified as functions of crack size, then the SIF for the same body subject to any other symmetrical load system can be determined directly. Based on the principle of the strain energy release rate, the weight function can be obtained from following expression for plane problems.

$$m(x,a) = \frac{H}{2K_{ref}} \frac{\partial u_{ref}(x,a)}{\partial a} \quad (1-10)$$

where $m(x,a)$ is the weight function for the cracked geometry

H is the generalised modulus of elasticity

$H=E$ for plane stress

$H=E/(1-\nu^2)$ for plane strain

where E is modulus of elasticity

ν is Poisson's ratio

a is the crack size

u_{ref} is the crack opening displacement field associated with the reference symmetric loading

K_{ref} is the stress intensity factor solution for the reference system.

It has been demonstrated that the weight function is a property of a particular crack geometry and is independent of loading. Once the weight function is known for the crack geometry, it may be used in the derivation of additional SIFs under different load cases by a simple integration.

$$K_{new} = \int_0^a \sigma_{new}(x) m(x,a) dx \quad (1-11)$$

where K_{new} is the new stress intensity factor.

σ_{new} represents the new stress field through the crack plane.

The only restriction on a new loading is that it must not have less symmetry than the original. For a more general two-dimensional problem, the boundary tractions and displacements will be functions of x and y and the integral is evaluated over all boundaries.

It has been shown that the weight function is equal to the SIF at a point along the crack front when a pair of opposite unit forces act on the crack surface. Thus it may be thought of as a form of the Green's function for a cracked body. This approach separates the effect of component geometry from that of the imposed loading. It is one of the indirect methods in which a stress analysis of unflawed body is performed initially, and making use of

superposition principles, the stresses acting on the crack surfaces are used in a separate calculation to compute the SIF.

Only one stress analysis is required for the uncracked body and the results may be used in all successive evaluations of the crack tip SIFs. Thus the weight function method offers a cheap alternative to the finite element method. However, the weight function and the stress distribution must be known a priori. Although the SIF solutions are available for a wide range of crack problems, the corresponding crack opening displacement solutions are very scarce in the literature. In order to overcome this difficulty, it is necessary to make some necessary approximations for the crack opening displacement function or weight function itself to derive the weight function for a two dimensional cracked geometry. By using different assumptions, three approaches have been developed to derive weight function and are reviewed as following.

i) Assuming a crack opening displacement (COD) function

An approximation for the crack opening displacement function is required to derive the weight function for a two dimensional cracked geometry. The most common approach is to assume an expression to define COD in terms of the crack dimensions and stress state. Based on correct behaviour and for simplicity in use, Petroski-Achenbach(1978) proposed the particular dependence of u_{ref} for plane problems as follows:

$$u_{ref} = \frac{\sigma_0}{H\sqrt{2}} \left[4F_{ref} \sqrt{a(a-x)} + \frac{G(a-x)^{3/2}}{\sqrt{a}} \right] \quad (1-12)$$

where F_{ref} is a known SIF calibration function for the reference state and σ_0 is a characteristic (or normal) stress magnitude.

$$F_{ref} = \frac{K_{ref}}{\sigma_0 \sqrt{\pi a}} \quad (1-13)$$

This is an approximation for edge cracks under mode I loading and is consistent with the behaviour of the crack profile near the crack tip and small crack. The only unknown parameter, G , can be determined from self-consistency of solution and expressed as below.

$$G = \frac{(I_1 - 4F_{ref} \sqrt{a} I_2) \sqrt{a}}{I_3} \quad (1-14)$$

$$I_1 = \sigma_0 \pi \sqrt{2} \int_0^a F_{ef}^2 a da \quad (1-15)$$

$$I_2 = \int_0^a \sigma_{ref}(x) (a-x)^{1/2} dx \quad (1-16)$$

$$I_3 = \int_0^a \sigma_{ref}(x)(a-x)^{3/2} dx \quad (1-17)$$

Thus the general form of weight functions derived by using the Petroski-Achenbach method can be expressed as the 'Bueckner type' function in following form.

$$m(x,a) = \frac{2}{\sqrt{2\pi(a-x)}} \left[1 + M_1 \left(\frac{a-x}{a} \right) + M_2 \left(\frac{a-x}{a} \right)^2 \right] \quad (1-18)$$

$$M_1 = \frac{8F'_{ref}a + 4F_{ref} + 3G}{4F_{ref}} \quad (1-19)$$

$$M_2 = \frac{2G'a - G}{4F_{ref}} \quad (1-20)$$

Therefore, the task of the derivation of a weight function for any particular geometry can be reduced to determination of parameters M_1 and M_2 only.

Although Petroski-Achenbach COD function is an approximation for edge cracks under Mode I loading, it has been widely used to derive the weight function for other more complicated cases due to lack of assumed COD function for three dimensional crack. Using this approach and choosing the Newman-Raju equations for tension as a reference SIF solution, Niu and Glinka(1987)(1989) derived a set of weight functions for the SIF at the deepest point of semi-elliptical surface cracks in finite-thickness plates with an angular corner.

Although only one reference SIF solution is needed, it is difficult to implement the above approach to derive the weight functions for any particular crack geometry due to the limitation of the assumptions and the complexity of heavy computation which involves numerical differentiation. Thus two approaches using multiple-reference state method has been developed and have reviewed by Brennan(1994).

ii) Assuming a weight function directly

Fett(1987) showed that the crack opening displacement(COD) could be accurately calculated from known SIFs and corresponding load states and expressed in terms of a

power series. Furthermore, Shen and Glinka derived the 'Bueckner type' function independent of the Petroski-Achenbach COD and expressed the weight function as follows.

$$m(x,a) = \frac{1}{\sqrt{2\pi(a-x)}} \left[1 + M_1 \left(\frac{a-x}{a} \right)^{1/2} + M_2 \left(\frac{a-x}{a} \right) + M_3 \left(\frac{a-x}{a} \right)^{3/2} \right] \quad (1-22)$$

The parameters M_1 , M_2 and M_3 for a particular cracked body can be determined by knowing at least two reference SIF solutions and corresponding stress states. These reference data must be linearly independent of each other. An extra relationship is required if there are only two reference data. This is supplied by the observation that the slope of the crack surface of central through edge cracks under symmetrical loading is zero at $x=0$, i. e.

$$\left. \frac{\partial u(x,a)}{\partial x} \right|_{x=0} = 0 \quad (1-23)$$

hence,

$$\left. \frac{\partial m(x,a)}{\partial x} \right|_{x=0} = 0 \quad (1-24)$$

For deep single edge cracks, due to rotation of the cracked section in a finite thickness body, the curvature of the crack mouth is zero, i.e.

$$\left. \frac{\partial^2 m(x,a)}{\partial x^2} \right|_{x=0} = 0 \quad (1-25)$$

By solving these constitutive equations simultaneously, the three unknowns M_1 , M_2 and M_3 specific to a particular cracked geometry may be found. Thus the knowledge of a second set of reference data can eliminate the necessity of a formal derivation of crack opening displacement.

iii) Assuming a crack opening displacement (COD) derivative function

As it is the derivative of crack opening displacement, not the actual crack profile, that is needed for deriving the weight function, another approach of multiple-reference data is suggested (Ojdovic Rasko and Petroski 1991) to directly define the derivative of crack opening displacement in the form of a series as below.

$$\frac{\partial u(a,x)}{\partial a} = \frac{4\sigma_0}{H} \sqrt{2} \sum_{j=0}^m C_j \left(1 - \frac{x}{a} \right)^{j-1/2} \quad (1-26)$$

where

$$C_0 = \frac{F_1^{ref}\left(\frac{a}{t}\right)}{2} = \frac{K_1^{ref}}{2\sigma_0\sqrt{\pi a}} \quad (1 - 27)$$

C_j are unknown coefficients. The number of terms can be assumed to be $m+1$ for convenience where m is the number of symmetrical loading states.

By substituting equation (1 - 26) into the following equation

$$\int_0^a \frac{H}{2} \sigma_i^{ref}(x) \frac{\partial u(a, x)}{\partial a} dx = K_i^{ref}(a) K_1^{ref}(a) \quad (1 - 28)$$

then

$$2\sqrt{2}\sigma_0 \int_0^a \sigma_i^{ref}(x) \sum_{j=0}^m C_j \left(1 - \frac{x}{a}\right)^{j-1/2} dx = K_i^{ref}(a) K_1^{ref}(a) \quad (1 - 29)$$

Letting

$$W_{ij} = \int_0^a \sigma_i^{ref}(x) \left(1 - \frac{x}{a}\right)^{j-1/2} dx \quad (1 - 30)$$

gives

$$\sum_{j=0}^m W_{ij} C_j = K_i^{ref}(a) \frac{F_1^{ref}\left(\frac{a}{t}\right)}{2} \sqrt{\frac{\pi a}{2}} \quad (1 - 31)$$

Knowing C_0 gives

$$\sum_{j=1}^m W_{ij} C_j = \frac{F_1^{ref}\left(\frac{a}{t}\right)}{2} \left[K_i^{ref} \sqrt{\frac{\pi a}{2}} - W_{i0} \right] \quad (1 - 32)$$

The unknown coefficients C_j could be determined by solving a system of m simultaneous linear equations with m unknowns (Ojdrovic Rasko and Petroski 1991) and the weight function is determined as:

$$m(a, x) = \frac{H}{2K_1^{ref}} \frac{\partial u(a, x)}{\partial a} = \frac{2\sigma_0}{K_1^{ref}(a)} \sqrt{2} \sum_{j=0}^m C_j \left(1 - \frac{x}{a}\right)^{j-1/2} \quad (1 - 33)$$

This approach is to directly define the derivative of COD in the form of a power series, not COD itself and determine the coefficients from one or more known SIF solutions. It avoids numerical differentiation and thus reduces computational effort significantly and increases accuracy.

After comparing the results using the above approaches with published "exact" solutions for simple cracked bodies, Brennan(1994) concluded that the multiple reference states is not

only less troublesome mathematically, but far more accurate and stable than the traditional assumed profile approach. However, the disadvantage of this approach is that it generally requires at least two known solutions where it is often difficult to get even one reference solution.

1.5.3.3 Finite Element Method

As one of the direct methods in which the calculation of the SIF is performed in a single-stage analysis, finite element method is most widely used to model the singular stress and strain behaviour in the crack tip region. There are two basic approaches for calculating the SIF, i.e. using non-singular crack tip representation or singular elements.

i) Non-singular crack tip representations

Early FE model involved the use of a very high density of conventional elements around the crack tip to get the stress, σ_y , or displacement, v , at some small distance, r , from the crack tip. SIF may be calculated by making use of the relationship between the SIF with the displaced shape of crack face or the stress field close to the crack tip as below.

$$K_I = \lim_{r \rightarrow 0} \frac{E' v}{4} \left(\frac{2\pi}{r} \right)^{1/2} \quad (1 - 34)$$

$$K_I = (2\pi r)^{1/2} \lim_{r \rightarrow 0} \sigma_y \quad (1 - 35)$$

where K_I is SIF in mode I

r is the distance from the crack tip, measured close to the crack tip

E' is effective elastic modulus, equal to E for plane stress conditions and $E/(1-\nu^2)$ for plane strain conditions, E is Young's modulus

σ_y is the stress normal to the crack plane ahead of the crack.

It has been found that the displacement method is consistently more accurate than the stress method (Yamamoto et al 1973), and typically yields SIFs within 5% of accurate solutions. However, this method requires very accurate stress analysis near the crack tip.

An alternative method, i.e. the energy approach, is widely used in order to avoid the need to approach the crack tip and reduce the requirement for large numbers of very small elements near the tip of crack. As SIF is a function of the energy release rate during an incremental crack extension, this approach calculate the SIF by using following relationship.

$$K_I = \sqrt{GE'} \quad (1 - 36)$$

where G is energy released per unit increase in crack size ($\delta W/\delta a$), W is energy, a is crack size.

In traditional approaches, finite element analyses have been repeated with every small change in crack size in order to calculate the energy change, G . The typical errors are of order 2%. A more efficient version of this approach, termed the virtual crack extension(VCE) method, was proposed by Parks(1974) to estimate the strain energy release rate, G . It does not require a re-analysis of the problem.

Both of the above methods require high or medium density finite element meshes to model the stress distribution around the crack tip where the stresses are changing very rapidly. It is necessary to develop the techniques which can model the singularity at the tip of the crack in order to increase accuracy and reduce the necessary computational facilities.

ii) Singular elements

Various crack tip singular elements have been developed to represent the singular behaviour surrounding the crack tip in the element formulation. The near-tip stress and displacement fields may be written in terms of stress functions due to Westergaard, Muskhelishvili and Williams. Based on these classical-solutions, the special elements can be formed to permit the evaluation of SIF directly. Using polynomial displacement functions, appropriate singularities may be introduced either by manipulation of element shapes(Levy et al 1971) or of displacement fields(Tracey and Cook 1977) to ease the numerical solution process.

By moving some nodes to the particular locations, a conventional eight-noded quadrilateral isoparametric element can be modified to obtain a singularity of order $r^{-1/2}$ on all rays emanating from the corner point in a full 3D FE analysis. Further development of this technique allows additional elements adjacent to the near-tip element to include the effects of the nearby singularity.

Extensive finite element work has been done on the use of finite elements to model the singular stress and strain behaviour in the crack tip region. The advantage of FE analysis of a cracked body is the inclusion of all geometric and restraint parameters. Crack modelling accounts for local load redistribution around the crack, so SIF calculations are based on the local cracked, rather than the uncracked, stress distribution. However, this method needs a complex mesh generation scheme. It usually is quite time consuming and expensive, because successive calculations of the stress distribution and the corresponding SIFs are required for each increment of crack growth.

1.5.3.4 Combining Literature Solutions using Superposition Techniques

By using above method, tables and graphs of SIFs for a wide range of cracked geometries under simple stress states have been printed in handbooks (Rook and Cartwright 1976) (Murakami 1987). It is possible to adapt these available standard solutions to practical problems. The principle of superposition can be used to combine one or more of the simple solutions in order to solve complicated 2D crack problems. Furthermore, If two or more different loadings are applied to the system, the effect of the combined loading is the sum of their individual effects. In particular, the stress intensity factor for a region under multiple loading is the sum of the SIFs for the region under each part of the load. It enables one to relate SIFs for different load cases when the geometries are the same.

1.5.4 SIF Solutions of Surface Cracks in Offshore Structures

Accurate fatigue crack growth modelling in tubular welded joints using fracture mechanics requires a suitable SIF solution. Unfortunately, it is impossible to calculate the SIF analytically due to complex geometry and the non-uniform stress distribution in tubular joints. As a consequence, cracks in tubular joints are sometime represented as planar cracks in plates or T-butt welded plates, subjected to a combined tension and bending through-thickness stress distribution. By using this assumption, the SIF solution in form of parametric equations have been proposed using different methods. Also attempts have been made to use finite element methods and semi-empirical models to obtain more accurate SIF solutions for tubular joints. These models will be reviewed as following.

1.5.4.1 SIF Solutions of Surface Fatigue Cracks in Plates

The first SIF solution for a flat elliptical crack embedded in an infinite elastic solid, under uniaxial tension (Figure 1.12), was first derived by Irwin (1962) and the SIF at the points along the crack front is given by

$$K_I = \frac{\sigma \sqrt{\pi a}}{E(k)} \left(\frac{a^2}{c^2} \cos^2 \phi + \sin^2 \phi \right)^{0.25} \quad (1 - 37)$$

where $E(k)$ is the complete elliptical integral of the second kind

a and c are the half lengths of the minor and major axis of the crack respectively

ϕ is the angle around the crack tip where $\phi = 0^\circ$ and $\phi = 90^\circ$ corresponds to the ends of the major and minor axis respectively

For a semi-elliptical surface crack in a plate of finite dimensions (Figure 1.13), the effect of free surfaces (front and back surfaces) and finite plate dimensions must be included in the

SIF solutions. However, the analytical solution for this problem has proved to be impossible due to the complexity of geometry. To account for these effects, some correction factors were used to derive the surface solutions from the embedded crack solution by using approximate techniques. The widely used ones are outlined here.

a) Newman-Raju Equations

With singular crack tip elements to model the rapidly changing stress distribution in the region of the crack tip, Raju and Newman(1979) presented an analysis on a variety of semi-elliptical surface crack shapes in flat plates of finite width by extensive three-dimensional FEM studies using pure tension and pure bending loadings. The relationship between K_I and stress values ahead of the crack tip was used to calculate values of SIF at the deepest point. They obtained modifications to the embedded crack results for a range of crack sizes and included a correction factor to account for the effects of the finite plate width.

The accuracy of this solution was verified by analysis of a series of embedded cracks and the results of the SIF were found to be within 3% of the exact solution. Also, fracture tests of surface crack in a brittle acrylic material agreed favourably with the finite element analysis.

Raju and Newman studied the boundary layer effect near the surface. They found that the SIF near the free surface decrease rapidly across the thin layer called the boundary layer and the singularity of the order of $r^{-1/2}$, which generally exists near the crack tip, does not occur at the surface point of semi-elliptical cracks. Their FEM results have shown the boundary layer is very thin and the maximum surface SIF is insensitive to the finite element mesh configuration.

Subsequently, their results have been used to derive the parametric equations which give the values of SIF for embedded and surface semi-elliptical cracks in flat plates in the cases of uniform tension and pure bending as a function of the angle around the intersection, the crack depth, the surface crack length, the plate thickness and the plate width(Newman and Raju 1981).

b) Holdbrook-Dover Equations

In order to model the physical situation more closely, Holdbrook and Dover carried out fatigue tests on specimens of finite dimensions, containing a surface crack under tensile loading. The SIF solutions(Holdbrook and Dover 1979) for the surface cracks were derived to correlate the results of these tests with the fatigue crack growth data in standard specimens. Based on the solution of surface cracks in a semi-finite body, these equations

provided the correction for the finite dimension effects. The correction included the effects of finite area, the end conditions, load eccentricity and the induced secondary bending produced by changes in the position of the neutral axis as the crack grows. These equations provide good correlation between the crack growth data for surface cracks and through thickness cracks in pure tension.

c) O-Integral

For cracks in flat plates, one of the most popular weight function has been proposed by Oore and Burns (Oore and Burns 1980), known as O-Integral. They derived a general form of the weight function for an enclosed crack of arbitrary shape in an infinite continuum subject to a variable stress field (Figure 1.14) as

$$g_{QQ'} = \frac{\sqrt{2}}{\pi l_{QQ'}^2 \left\{ \int_s \frac{ds}{\rho^2} \right\}^{1/2}} \quad (1-38)$$

where $g_{QQ'}$ is the stress intensity factor at a point Q' on the crack front due to a pair of unit forces acting at a point q on the crack face

Then the SIF at the point Q' due to a distributed pressure σ_Q on the crack face would be

$$K_{Q'} = \iint_A g_{QQ'} \sigma_Q dA_Q \quad (1-39)$$

where dA_Q is an infinitesimal area around the point Q

A is the area of the crack surface

σ_Q is the stress in the uncracked material

This expression allows for any variation of stress across the crack surface (via the parameter $l_{QQ'}$) and variation in crack shape (via the parameter ρ_Q), whereas earlier models assume constant stress across the crack surface and a simple crack shape. Its formulation, however, requires a numerical solution.

As the O-integral is only valid for embedded flaws in an infinite solid, it has to be modified for surface breaking cracks using the relationship:

$$K_{surface} = K_{embedded} \bullet M_f \quad (1-40)$$

where $K_{surface}$ is the SIF due to an irregular surface crack subjected to any stress distribution

$K_{embedded}$ is the SIF due to an embedded crack with the same half geometry and under the same half loading on both halves of the crack surface

M_f converts the embedded flaw to an equivalent surface breaking flaw. It is a constant and dependent on geometry but not on loading. Assuming that the crack shape is always semi-elliptical, this correction factor can be obtained from the ratio between Newman-Raju solutions for a surface crack and an enclosed crack subject to same uniform tension.

One advantage of this two dimensional solution over other methods is that both crack depth growth and crack length growth can be modelled at the same time.

d) Shen-Glinka and Wang Lambert Solutions

The weight functions of the surface and the deepest point of semi-elliptical crack in an infinitely wide plate of finite thickness (Shen and Glinka 1991) (Shen et al 1991) were derived by using two reference SIFs and the general weight function form. They were validated against finite element data and differences were less than 2% for the surface point and 5% for the deepest point. It has been noted that these weight functions are only suitable for semi-elliptical surface crack of relative depth within $0.2 \leq a/t \leq 0.8$ and aspect ratio $0.2 \leq a/c \leq 1$. However, the aspect ratio in a welded joint is often less than 0.2. In order to extend the use of above weight functions to real problems, three dimensional finite element analyses (Wang and Lambert 1995) have been conducted to calculate the SIFs for low aspect ratio semi-elliptical surface cracks. Based on these results and some existing FE data for high aspect ratios (Newman and Raju 1981) (Shiratori et al 1987), the weight functions for the deepest point and surface points were derived and verified by Wang and Lambert (1995) using a similar procedure to that of Shen and Glinka (1991). They are suitable for semi-elliptical surface cracks with aspect ratio in the range of $0 \leq a/c \leq 1$ and the relative depths $0.2 \leq a/t \leq 0.8$.

e) Concluding Remarks

Some plate solutions were assessed in terms of accuracy by comparison with known flat plate solution for uniform tension and simple bending by Haswell and Dover (1991). The Newman-Raju solution can be regarded as a suitable standard for checking other formulations. It has been found that O-integral is inaccurate for plate solutions at values of crack depth in excess of 30% of the plate thickness (0.3T). More recently, Burns provided correction factors for cracks in plates at depths exceeding 0.3T. Unfortunately the correction factors are only for the deepest point of the crack front.

The results from Holdbrook and Dover gave good agreement with Newman-Raju for tension but lower values of Y for bending. But Dover and Connolly (1986) obtained good agreement with the experimental data to predict the crack shape development in plates subjected to

tension and bending using Holdbrook and Dover equations. It suggested that Newman-Raju might be over-conservative in the bending case.

1.5.4.2 SIF Solutions of Surface Fatigue Cracks in Thin Wall Cylinders

The effect of curvature is not considered in the above plate solutions. However, it is important for pipes, pressure vessels and tubular joints. By using 3D finite elements, Raju and Newman(1982) and Shiratori(1989) obtained SIFs for constant, linear, parabolic or cubic stress distributions acting on the crack surface of internal and external longitudinal semi-elliptical surface cracks in pipes with a radius/thickness ratio of 10. Based on these reference data and using the generalised form of Mode I weight function expressions, Shen and Glinka(1993) derived the weight functions for the deepest and surface points of semi-elliptical cracks in thin pipe. However, these solution are restricted to the cracks with aspect ratios between 0.2 and 1.0. In order to overcome this difficulty, Wang and Lambert(1996) conducted a series of 3D FE analyses to obtain the low aspect ratio crack data. Using these results together with existing FE data for higher aspect ratios, they(Wang and Lambert 1996) derived the closed form weight functions for the deepest and surface points of longitudinal semi-elliptical surface cracks in thin pipes which are valid for aspect ratios in the whole region $0 \leq a / c \leq 1$.

1.5.4.3 SIF Solutions of Surface Fatigue Cracks in T-Butts

All joints in offshore platforms are welded. Fatigue cracking occurs in the form of surface cracks initiating from the weld toe in these welded joints. The presence of the weld usually gives rise to a stress concentration, which is function of weld geometry, in the vicinity of the weld toe. This stress concentration introduces changes in the stress distribution in a section at the weld toe. The T-butt welded plates are usually used in offshore structure and can be treated as a simple model of tubular joints. This section reviews some models for T-butt.

a) Mk Approach

Maddox(1975) suggested that for the surface cracks located at the weld toe, subjected to nominal bending or tension, the SIFs at the deepest point of the crack could be calculated from the equation

$$K_I = M_k Y_{plate} \sigma \sqrt{\frac{\pi a}{Q}} \quad (1 - 41)$$

where Y is the SIF calibration factor for a similar surface crack in a flat plate subjected to the same nominal loads. Hence the magnification factor M_k is the ratio of the SIF for a crack at the weld toe to the SIF for a similar crack in a flat plate subjected to the same nominal loads. M_k normally decreases with increase in crack depth, from a value equal to the stress concentration factor in the absence of a crack down to unity at crack depths of typically 30% of material thickness. The M_k factor was obtained from the 2D finite element analysis of edge cracks at the weld toe and comparing the results with the corresponding results for the same crack in a flat plate. By curve fitting these values, the analytical expressions for M_k have been derived. Much work was carried out to enhance the accuracy of M_k at The Welding Institute(TWI). The final results were included in PD6493(1991). It should be noted that this approach is limited to a weld angle of 45° and a sharp weld toe and only consider the variation of the ratio of overall weld attachment length to wall thickness(L/T). Dijkstra et al(1989) also reported M_k solutions for a range of surface cracks at the weld toe of a T-butt.

It is common practice to use the 2D M_k factors combined with the 3D flat plate solution to calculate the SIF for a semi-elliptical surface crack at the weld toe. For the surface point where the ends of the semi-elliptical crack meet the plate surface, the M_k factor should be obtained from 3D analysis and few solutions are available. It is normally assumed to be constant and equal to either the elastic stress concentration factor at the weld toe(K_t), or the value of M_k corresponding to a very small crack, such as $a=0.15\text{mm}$. The latter approach is compatible with the fact that in steels there are inherent crack-like flaws of this order at the weld toes. After an extensive review, Pang(1990) concluded that it is conservative when applied 2D M_k to 3D situation for calculating the SIFs at deepest point of semi-elliptical surface cracks in weld joints and the current practice of adopting a constant value for surface point, based on the 2D solution is over-conservative.

b) Niu-Glinka Equations

Based on Petroski-Achenbach crack opening displacement expression and using Newman-Raju solutions as the reference SIF solution, Niu-Glinka(1990) have derived a weight function in closed form for the calculation of SIF at the deepest point of a crack emanating from the weld toe of a T-butt welded connection. This weight function is capable of incorporating weld profile effects due to different weld angle α and weld toe radius ρ under any mode I type of loading as an important development of weight function technique.

Initially they derived a weight function for an edge crack emanating from the weld toe in a T-butt joint. They also carried out the stress analysis of the uncracked body of this type of joint and derived the stress distribution for a range of geometries(Niu and Glinka 1987). Niu

and Glinka derived a weight function for the deepest point of a surface crack in a plate from Newman-Raju solution (Niu and Glinka 1989). They assumed that:

$$K_s^w = \frac{K_e^w}{K_e^p} K_s^p \quad (1 - 42)$$

where K_s^w is the SIF for a surface crack in a welded joint

K_s^p is the SIF for a surface crack in a plate subjected to the same stress distribution

K_e^w is the SIF for an edge crack in a welded joint

K_e^p is the SIF for an edge crack in a plate subjected to the same stress distribution

This assumption enabled Niu and Glinka to calculate M_k factors and then derive a weight function for a surface crack emanating from the weld toe of a T-butt welded joint. Based on this weight function they calculated the stress intensity factors for this type of joints having a surface crack subjected to pure tension or bending. It has been found that the SIF for a semi-elliptical surface crack is more affected by the weld angle than by the weld toe radius. However, it also depends strongly on the crack aspect ratio and crack depth. In general, the weld profile effect can be neglected for cracks deeper than half the plate thickness.

By using the stress distribution equations, a set of parametric equations (Hall et al 1990) have been derived to calculate SIF at the deepest point under tension and bending respectively.

The result from Niu-Glinka weight function were found to be substantially the same as those from Newman-Raju for all values of a/T in a flat plate. This is because this weight function is based on the Newman-Raju solution. The Niu-Glinka weight function gives a good agreement with fatigue crack growth data from flat plate welded connections. It is very interesting to compare the results from Niu-Glinka and M_k approaches as both of them incorporate the weld angle.

1.5.4.4 SIF Models for Surface Fatigue Cracks in Tubular Welded Joints

The fracture mechanics based fatigue crack growth modelling for tubular joints requires a model for the prediction of the stress intensity factors in tubular joints. Even if one assumes that crack is always located at the saddle position of the joint, and that the crack shape is semi-elliptical with constant aspect ratio, the determination of SIFs for defects located in tubular joints is an extremely difficult task. However, it is possible to obtain an approximate solution of acceptable accuracy to describe the crack growth behaviour by combining numerous experimental, numerical and theoretical methods.

1.5.4.4.1 Semi-Empirical Models Based on Experiment Data

As discussed in the previous section, once Y is determined, the crack growth and fatigue life can be evaluated by integrating the instantaneous crack growth rates. There are two semi-empirical models for rapidly modelling Y of surface crack growth in simple tubular joints, namely the Average Stress Model (AVS) and the Two Phase Model (TPM). These models are based on the analysis of fatigue crack growth data obtained during tests on simple tubular joints carried out at University College London. The results of measurements of crack size during fatigue tests, has provided the data about the variation of crack size as a function of the number cycles and hence the crack growth rate. Thus the unique value of the stress intensity modification factor, Y can be determined by using the Paris Law.

Early fatigue tests have shown that the growth rate for a T-joint under axial loading was higher than that of a similar joint under out-of-plane bending for a similar hot spot stress range. It would seem that the hot spot stress range is not sufficient to describe the behaviour of crack growth under different type of loading. There are other several other parameters which influence the crack growth behaviour in tubular joints. These are the magnitude of hot spot stress, the stress distribution around the intersection, mode of loading, joint geometry and joint size. Assuming that the stress distribution was important, Dharmavasan and Dover (1987) proposed an AVS model based on early fatigue growth data of welded tubular joints and derived experimental Y as a function of relative depth (a/T).

$$Y = DT^p \left(\frac{T}{a} \right)^j \quad (1 - 43)$$

where a is the crack depth

T is the tubular wall thickness

The parameters D , P and j are functions of average stress around the intersection as followings:

$$D = 1.18 - 0.32 S \quad (1 - 44 a)$$

$$j = 0.24 + 0.06 S \quad (1 - 44 b)$$

$$P = 0.13 - 0.02 S \quad (1 - 44 c)$$

where $S = SCF_{hs} / SCF_{av}$

SCF_{hs} is hot-spot stress concentration factor

SCF_{av} is the average of stress concentration factors around the intersection

For in-plane bending SCF_{av} is given by:

$$SCF_{av} = \frac{1}{\pi} \int_{-\frac{\pi}{2}}^{\frac{\pi}{2}} SCF(\phi) d\phi \quad (1-45)$$

For axial and out-plane bending:

$$SCF_{av} = \frac{1}{\pi} \int_0^{\pi} SCF(\phi) d\phi \quad (1-46)$$

where $SCF(\phi)$ is the geometric SCF around the intersection and the angle, ϕ , is measured from the crown.

Realising the effect of increasing joint size is to reduce the crack initiation or early growth phase, this model was later modified to account for the two phase of crack initiation and propagation separately and is called as TPM(Kam et al 1987). The experimental Y factor could be adequately expressed as:

$$Y = MB \left(\frac{T}{a} \right)^k \quad (1-47)$$

where

$$M = \left(0.25 \frac{T}{a} \right)^{-p} \quad \text{for } a < 0.25T \text{ (initiation)} \quad (1-48a)$$

$$M=1 \quad \text{for } a > 0.25T \text{ (propagation)} \quad (1-48b)$$

and

$$P = 0.231 \left(\frac{T}{0.016} \right)^{-1.71} \beta^{0.31} SCF_{hs}^{0.18} \quad (1-49)$$

$$B = (0.669 - 0.1625S) \left(\frac{T}{0.016} \right)^{0.11} \quad (1-50)$$

$$k = (0.353 + 0.057S) \left(\frac{T}{0.016} \right)^{-0.099} \quad (1-51)$$

β is the ratio of brace diameter to chord diameter of a tubular joint

The TPM was formulated using data from nine large scale tubular joints of various configurations tested in air under different modes of loading and has found to be able to forecast the influence of the wall thickness correctly. This empirical model, derived from constant amplitude fatigue data has been successfully applied to variable amplitude fatigue crack growth data with modification.

One problem noted is that the right side of (1-43) is not non-dimensional as T is the chord wall thickness. Austin(1994) found that the AVS model tended to over-predict the

experimental Y factors by a factor of approximately 15%. He noted the range-counted equivalent stress range was used for the variable amplitude in-air test in order to derive AVS model. However, the rainflow method of cycle counting is shown to produce better correlation with constant amplitude growth rate data for BS 4360:50D steel rather than range counting. Thus, using the rainflow method to re-interpret the variable amplitude test data, he suggested the following modified AVS model.

$$Y = \frac{A}{1.15} \left(\frac{T}{a} \right)^j \quad (1 - 52)$$

where $A = 0.73 - 0.18S \quad (1 - 53 a)$

$j = 0.24 + 0.06S \quad (1 - 53 b)$

The predictions using this improved model achieved a better agreement for recent experimental data compared to the original model (Myers 1996).

1.5.4.4.2 Application of Simplified Models to Tubular Joints by using Load Shedding Model

Due to the complexity of tubular joints, the practical application of fracture mechanics analysis usually requires simplification of the structural problem. This difficulty is usually overcome by using various simplified models such as plate, thin cylinders or T-butt welded plates. These fracture mechanics models with semi elliptical cracks and arbitrary stress fields on the crack centreline were derived provided that the boundary conditions remain fixed. Therefore they are sufficiently accurate in the case of statically determinant structures or in situations where the nominal stress level driving the crack does not change significantly with the changes in stiffness of the cracked sections. These models can easily be incorporated into approximate tubular joint crack growth models. Comparison of plate model predictions with fatigue growth results from full scale tubular joints for the same through-thickness stress and crack shape have been done (Haswell and Dover 1991). The results from Newman-Raju and Oore-Burns show the divergence between the these plate models predictions and experimental results at values of a/T in excess of 0.3. It has been found that plate models consistently over predict the Y factor for tubular joints. A small improvement could be obtained using the Niu-Glinka approach if the notch stress distribution was also included. This improvement could be significant in early crack growth, but would probably not have a dramatic effect on results for deep cracks.

It is now believed that this over-prediction is due to the multiple load paths found in tubular joints and the load shedding that takes place during fatigue crack growth. The fixed boundary conditions is a reasonable assumption for plates. However, in the case of tubular

joints the stresses responsible for crack growth are the membrane and bending stresses which depend on the stiffness of the cross section near the weld and change as a consequence of the presence of the crack. Aaghaakouchak(1989) have shown that varying the boundary conditions from built-in to simply supported would require special consideration in order to reconcile the standard flat plate Y prediction with tubular joint data.

Haswell and Hopkins(1991) carried out a study using FE shell models with line spring crack modelling, compared the Y prediction for a T joint subject to axial load with Y predictions obtained from plate models with different boundary conditions. It has been found that the boundary conditions of a cracked plate model influence the load path across the crack plane and its compliance. The ability of the plate ends to rotate or the imposition of displacement control are of major importance. Plate end rotation is due to a through-thickness bending moment resulting from the neutral axis offset caused by the crack and the imposed bending stress. Controlled plate end rotation together with changes in the model compliance will influence the SIF prediction. A displacement controlled condition provides a better model of the tubular joint considered.

In case of tubular joints with a complex geometry the load shedding mechanism is not yet fully understood. As the crack grows, the cracked region could gradually lose the local bending stiffness and rotational constraints, and the excess bending load could be transmitted through the uncracked part of the joint. It is thought that the reduction in local bending moment due to cracking, and the allied increase in local flexibility can be modelled by a systematic moment release. Assuming the tensile stress component does not change while the bending stress component decreases, the moment release models have been proposed(Aaghaakouchak 1989). They include the parabolic and the linear releases models. The parabolic release model is from the studies of edge cracks in plates and rings. The linear moment release model is proposed as a "limiting case". The results show that linear release in conjunction with Niu-Glinka method accurately models axial load cases but still slightly over-predicts out-of-plane and in-plane bending results. Du and Hancock(1989) found the non-linear force and moment shedding in tubular joints by using line spring FE model.

Although the simplified model combined with linear moment release model gives good agreement with the experimental data, the linear moment release mode is not based on solid theoretical foundation. It could be that this improved agreement is due to the over-prediction of simplified SIF solution for tubular joint and severity of linear moment release model.

Experiments show that the K level remains beneath the fracture toughness level during the fatigue crack growth in tubular joints due to the load shedding. This is a quite important reason why the brittle fracture is not likely to happen during the tubular joint fatigue test. 22/

1.5.4.4.3 Finite Element Models

A most accurate evaluation of SIF for tubular joints could be obtained by a three dimensional(3D) modelling of the joints containing the crack using the finite element method. The advantage of FE analysis of a cracked tubular joint is the inclusion of all geometric and restraint parameters.

Two types of finite element models have been proposed for tubular joints and outlined as followings.

a) Complete Model

The complete tubular joint is modelled using a shell finite element representation with the crack and weld geometry modelled using 3D element. The crack front is represented by collapsed 3D quarter point elements.

Ritchie and Voerman(1987) used this method to analysis a few cases of tubular joints. In their finite element model of a T-joint subjected to axial loading, they introduced several cracks of varying sizes obtained from fatigue experiments, which are normal to the shell surface. They calculated the SIFs for points along the crack front for each crack shape. The SIFs were found to be highest at the surface and lowest at the deepest point of the crack which agree with what is suggested by the more rapid surface growth of the crack observed in experiments. The calculated SIF values for the surface and deepest points of the crack were in excellent agreement with the empirical data. Also, they calculated the contributions of the different modes and concluded that for the first part of crack growth, K_{II} and K_{III} were insignificant compared to K_I .

b) Simple Model

In this simple approach, the complete tubular joint can be modelled using a shell finite element representation, with the crack modelled using line spring elements. This technique has the advantage of modelling the overall geometry of the cracked tubular joint and provides a highly efficient numerical model for crack analysis. The limitation of the this model is that it cannot model the weld geometry which affects the results for shallow cracks.

The line spring model developed by Rice and Levy(1972) provides a well-established, computationally efficient method for the analysis of part-through cracks in plate and shell structures. Based on Rice and Levy's model, a finite element line spring formulation has been developed by Parks and White(1982).

In this model the surface crack was replaced by a part-through thickness crack where it can be represented in a shell FE model as a series of one-dimensional line spring finite elements along the line of crack. Having both stretching and bending resistance acted, it simulated the constraints provided by the net ligament of the crack and its stiffness varied along the crack depending on the surface crack depth.

The line spring elements introduce an additional freedom, which is calculated from existing solutions for single edge notched specimens in plane strain. The local solution dominated by the crack tip singularity is therefore included in the global response of the structural model. Relative displacements and rotations calculated from the analysis are then coupled with the respective compliance value to compute the SIF at the line spring element integration points.

Huang and Hancock(1988) analysed a shell FE model with line spring representation of a T joint. Although the shell model used does not include the weld, Hancock's comparison with both semi-empirical and 3D FE results demonstrates the validity of the FE line spring model for crack depths between $a/T=0.2$ and 0.8. However, as the weld has not been modelled, the SIF is under-predicted at shallow crack depths.

Clearly an FE analysis can accurately model geometry, loading and structural restraint. However, as SIFs are invariably used in fracture mechanics analysis of cracks in offshore structures, they must be supported by accurate information on crack propagation and shape development. This information is best obtained by experiment and consequently there is a need to combine the numerical analysis with comparable empirical data. This combination would allow both the numerical models to be validated and their accuracy in terms of fatigue predictions be quantified.

1.5.4.4 Concluding Remarks

The attempts have been made to use the modified simplified models and finite element method and derive semi-empirical models to obtain more accurate SIF solution for tubular joints. It seems that there are two reasonable methods for obtaining SIFs in cracked tubular joints. The first method is to use simplified models that are analytical and easy to apply. However, the SIF solutions derived from these simplified models are influenced by model boundary condition assumptions. Thus these simplified solutions cannot be directly applied to tubular joints as they do not model major effects such as load shedding. A linear moment release modification was found to be appropriate for use with flat plate SIF solutions to give predictions of Y for tubular joints(Aaghaakouchak 1989).

The second and more representative approach is an FE analysis of the full-scale joint. SIFs for cracked tubular joints obtained from 3D finite element analysis of a tubular joint are in

reasonable agreement with semi-empirical data. The results of Hancock and co-workers, using line spring elements to model the crack, indicate that the weld profile does not significantly affect the SIF obtained from numerical analysis for crack depths in the range 20-80% wall thickness. However, this analysis is slow and expensive.

Finally, it is possible to use the multiple reference weight function method developed recently to provide the SIF solutions for fatigue cracks in tubular joints.

1.5.5 Thickness Effect

A size effect was well known in notched machined components whereby fatigue strength decreases with increase in size. This effect was also found in welded joints in 1970s. Fatigue design curves for offshore structures were developed from the test results of laboratory specimens which generally are less than 25mm thick (typical thickness=12.7mm and diameter=500mm) due to the limitation of loading capability of testing machines. However, the size of offshore structures are usually larger than that of these laboratory specimens. Therefore, the size effect issue has been the subject of considerable research over the past decade. Significant advances have been made in the understanding of the mechanisms which govern this apparent reduction in fatigue strength with increasing size.

Plate material in the as-rolled condition also shows a thickness effect which is somewhat less than that for welded joints, but still significant. It can be explained statistically in that the number and severity of flaws is likely to increase with size. However, for welded joints, this statistical explanation is probably of lesser significance. Of particular importance is the influence of weld joint dimensions on stress concentration and through wall stress distribution. This geometry effect has been generally recognised as the major cause to thickness effect and can be explained by the following factors(Berge 1985):

- 1) the magnitude of the stress concentration at the weld toe which is mainly determined by the local weld geometry. The notches at the weld toe in large joints are relatively sharper. The toe of the weld has nearly always the same radius due to the welding process.
- 2) the gradient of the stress in the plane of crack growth which is mainly determined by the plate thickness. The stress gradients are less steep in large size joints, which means that in a large joint a crack of a certain dimension is in a higher strained area than in a smaller joint. Moreover the plastic zone size will be larger.
- 3) the number of cycles in crack growth through the region of a steep stress gradient, relative to the total number of cycles to failure which is mainly determined by the size of the initial crack and the crack ellipticity.

Based on theoretical fracture mechanics calculation and considering the effect of joint dimension on SIF and crack growth rates by using weld toe SIF correction factor(M_k) for fillet welded joints, Gurney(1979) proposed the following model:

$$S = S_B \left(\frac{T_B}{T} \right)^{1/4} \quad (1-54)$$

$$N = N_B \left(\frac{T_B}{T} \right)^{3/4} \quad (1-55)$$

where S_B is the stress range and N_B is the fatigue life at the reference thickness, T_B , while S is the stress range which results in the same fatigue endurance and N is the fatigue life which has the same stress range at a thickness T .

Using a simple fracture mechanics model, Berge(1985) got the same answer as Gurney by making following assumptions:

- 1) Welded joints of the same type in various plate thickness are geometrically similar.
- 2) Initial conditions of fatigue crack growth are independent of plate thickness(a_i constant).
- 3) Furthermore, the notch root at the weld toe may be of constant radius, $\rho = \text{constant}$ instead of $\frac{\rho}{T} = \text{constant}$ as they are largely determined by the condition of the last pass at the weld toe.

The experimental data from some plate as-welded joints with thickness from 16mm-100mm confirmed the above model. Supported by the experimental data, the model suggested by Gurney and Berge has been implemented in UK Department of Energy fatigue guidance in 1984. (B=22mm for welded plates and 32mm for tubular joints). Insufficient tubular joint test data (UKOSRP-I thickness 6.3mm-32mm diameter 168mm-914mm as-welded condition and some ECSC data) exist to investigate this effect. However, it is assumed that tubular joints will behave in the same way as other welded plates with respect to the influence of thickness.

With more data produced from extensive research programs in Europe including UKOSRP II data (chord diameter 1830 and thickness 75mm) available, it seems that it is possible to have a more reasonable model. By fitting S-N curves to these data at each thickness, a conservative thickness correction exponent of 0.3 is proposed in current fatigue guidance:

$$S = S_B \left(\frac{T_B}{T} \right)^{0.3} \quad (1-56)$$

Additionally, the base line thickness for thickness correction was extended to 16mm for tubular joints.

There is a debate about whether the thickness effect can be largely decreased or eliminated by improving weld profiles between the researchers in Europe and US. In the US view, the thickness effect can be compensated for by improving weld profiles in thick sections. Weld improvement leads to an increase of fatigue strength and a decrease of the thickness effect. This means that increasing rate of fatigue strength due to weld improvement becomes larger as the plate thickness increases. Use of an improved AWS weld on joints with equal attachment as base-plate thickness reduces the effect of thickness from a factor of over four to a factor of about two.

European research, especially from UK and Norway, found that the thickness effect is essentially the same for a wide range of welded joints and weld geometry. Welds with improved weld toe profile showed higher fatigue strength, however the strength decreased when the thickness was scaled up. For joints improved by weld toe grinding or TIG re-melting the fatigue strength in general is improved. However, test data indicate that the thickness effect is of the same magnitude as for unimproved joints.

Apart from this debate, it is noted that there are some secondary factors from research programmes and these are listed as follows:

1) attachment thickness

There is a reduction of the thickness influence if the attachment thickness is kept constant. but it is only secondary effect on fatigue strength compared to the effect of main plate thickness because the dominant parameter affecting weld toe SCF is the ratio of weld toe radius to main plate thickness, ($\frac{\rho}{T}$), which is not influenced by attachment thickness. The experimental data on tubular joints indicated that the fatigue endurance is proportional to $\tau^{-0.153}$ and it is small compared to that for chord thickness $T^{-0.9}$.

2) Loading mode

The thickness effect is stronger under bending than under axial loading.

3) High/low SCFs

Experimental results and fatigue predictions indicate that the thickness exponent decreases with decreasing value of the SCF. Welded joints with low SCFs(SCF<1.5) give a smaller thickness effect as compared with as-welded joints.

4) Fatigue Life

The thickness effect depends on fatigue life, and increases as the fatigue life becomes longer. In particular, this trend is remarkable in the as-welded proportional joints. Both crack initiation and propagation lives are reduced with increasing thickness for welded

joints. The thickness effect is larger for crack initiation life than for failure life, the thickness effect on crack propagation life is very small. The thickness effect of a welded joints is supposed to be determined by crack initiation behaviour and the growing process of a shallow crack to the depth of about 1mm.

However, the thickness effect appears to be the same, regardless of local weld geometry and loading. Also it represents the average performance of welded joints and therefore is not too conservative when the thickness effect is evaluated for individual data sets. So the design rules for welded joints should be amended to include some secondary factors such as a less severe thickness penalty for low SCF joint and a stronger thickness effect for high SCF joints. It seems that the best solution is to establish the accurate fracture mechanics model that can take account the thickness effect. Thus an accurate thickness exponent can be applied depend on local geometry and loading.

1.6 Research Objectives and Scope of Thesis

A considerable amount of research effort has been spent to develop the methodology for the assessment of fatigue behaviour of welded tubular and plate joints. Non destructive evaluation of offshore tubular welded joints involves crack detection, crack sizing, stress analysis and fracture mechanics based assessment of crack growth. So far a lot of significant developments have been achieved in each of these areas. However, each of these areas still poses challenging problems for the offshore industry as reviewed in previous sections. In order to use the existing methodology, it is crucial to have the accurate information such as POD in NDT reliability, SCF, DOB and stress distribution in stress analysis, and SIF in fracture mechanics analysis. However, the task to have these basic modelling tools is far from being finished. In this study, it is intended to concentrate on the computational aspect of fatigue strength assessment. It will try to provide more information on underwater NDT reliability and stress distribution for tubular joints in a format suitable for fracture mechanics analysis. With more information available, it will be possible provide the more accurate modelling that is needed to improve the accuracy of prediction of fatigue crack growth. So the final objective of this study is to develop the models to predict the stress intensity factor in welded T-butt joints. As a summary, this study aims to provide the POD information of underwater NDT in convenient format for reliability based scheduling and the more accurate models for stress analysis and fracture mechanics analysis by carrying out a parametric study.

This chapter overviews the several important aspects of non-destructive fatigue strength assessment of offshore tubular welded joints. The rest of the thesis can be split into the following three parts.

1) Underwater Non Destructive Inspection Reliability

Chapter 2 will report the work on underwater NDT reliability. Fatigue cracks on tubular welded joints were measured using ACPD and ACFM techniques in order to clarify some characterisation data in UCL crack library. The UCL underwater Non destructive inspection reliability trial results (POD data) were re-analysed to make them suitable for reliability fracture mechanics procedures for the first time and these were incorporated into the Reliability based inspection scheduling(RISC) system.

2) Deriving the Stress Parametric Equations for Simple Tubular Joints

Comprehensive thin shell finite element stress analyses have been carried out for 330 tubular X, DT, and Y, T-joints. Based on the results of these systematic analyses, a series of stress parametric equations have been derived by regression analysis and will be presented from Chapter 3 to Chapter 6. Chapter 3 is on the derivation of a set of comprehensive SCF parametric equations for tubular welded X, DT-joints. A set of parametric equations to predict the degree of bending and stress distribution around the intersection of tubular X and DT-joints are reported in Chapter 4. In Chapter 5, efforts have been made to derive a new set of parametric equations to predict the stress distribution along the intersection of tubular Y and T-joints in order to enhance the prediction capability of UCL HCD stress parametric equations. Chapter 6 deals with developing a set of characteristic parametric equations for tubular Y, T, X and DT-joints to represent the stress distribution around the intersection of simple tubular joints.

3) Developing a set of SIF Parametric Equations for T-butt and Tubular Welded Joints

A series of SIF parametric equations was derived for both the deepest and surface(corner) points of semi-elliptical surface cracks in T-butts and the deepest points of semi-elliptical surface cracks in tubular welded joints, by using the weight functions and the database of T-butt through wall stress analysis results. This aspect is addressed in Chapter 7 to Chapter 9. Chapter 7 is on derivation of the deepest point SIF parametric equations for T-butt using the Niu-Glinka weight function. Chapter 8 reports on the derivation of the surface point SIF parametric equations for T-butt using the Wang-Lambert weight functions. In Chapter 9, taking the Wang-Lambert weight function for longitudinal cracks on thin pipe as reference

data, a new weight function for tubular welded joints is proposed and the corresponding deepest point SIF parametric equations are derived. Combined with the non-linear load shedding model, this solution can be used to predict the fatigue crack growth in tubular joints and this is confirmed by the experimental data.

Finally, Chapter 10 presents the conclusions of the study and proposes the areas which need further research and investigation.

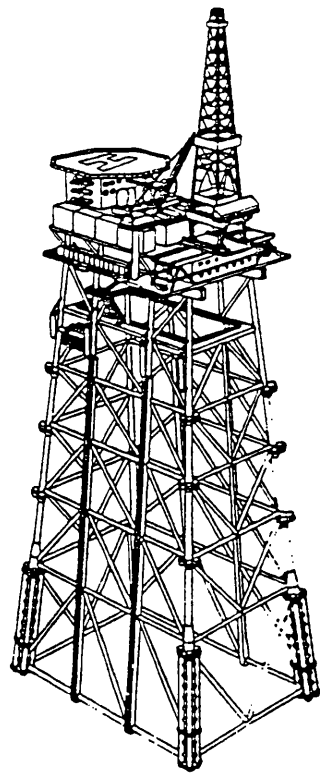
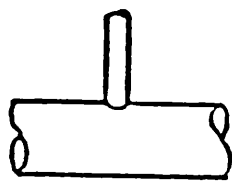
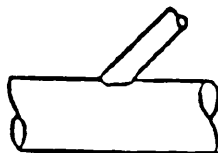


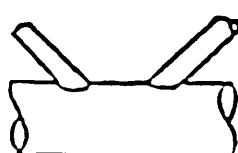
Figure 1.1 Typical Jacket Structure(Fatigue Handbook 1985)



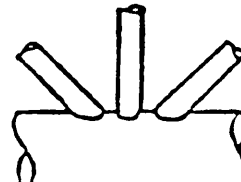
T Joint



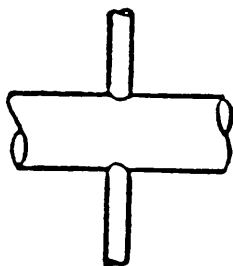
Y Joint



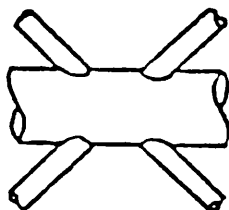
K Joint



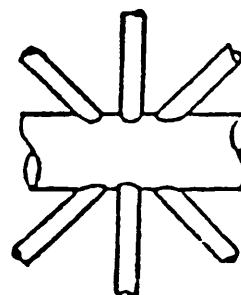
TK Joint



Double T Joint

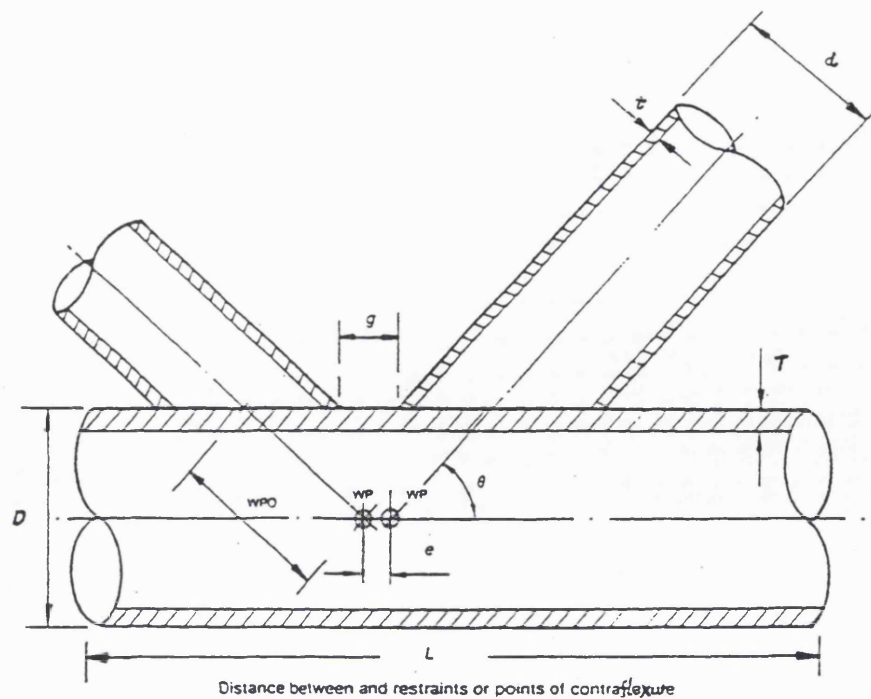


Double K Joint



Double TK Joint

Figure 1.2 Examples of Simple Tubular Welded Joints



Geometric ratios: $\alpha = \frac{2L}{D}$ $\beta = \frac{d}{D}$ $\gamma = \frac{D}{2T}$ $\tau = \frac{t}{T}$ $\zeta = \frac{g}{D}$

Figure 1.3 Geometric Notation for Simple Tubular Joint(UEG 1985)

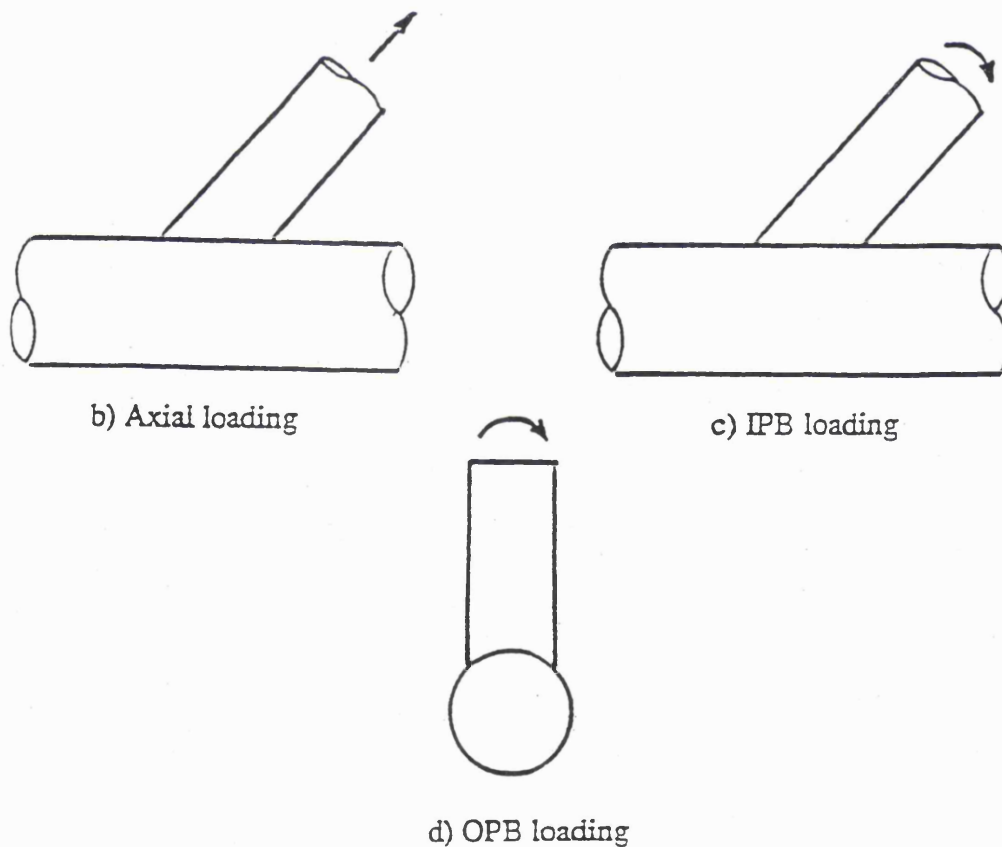


Figure 1.4 Modes of Loading on Tubular Joint

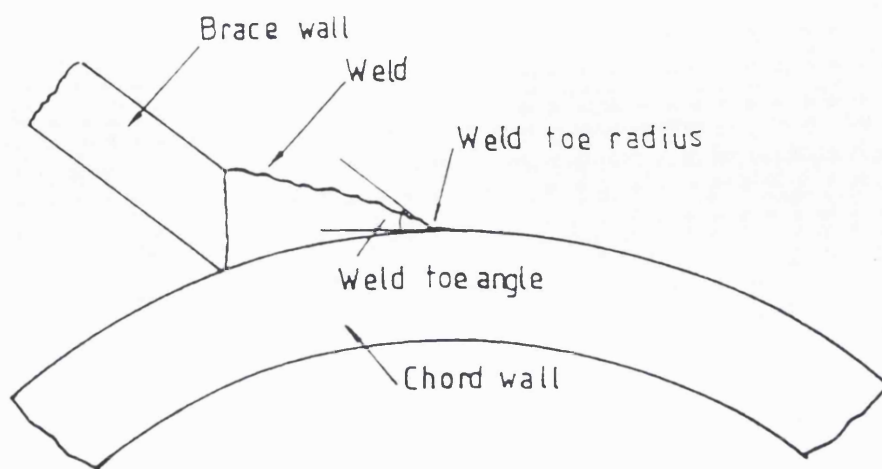


Figure 1.5 Geometric Parameters of Weldments(Niu 1987)

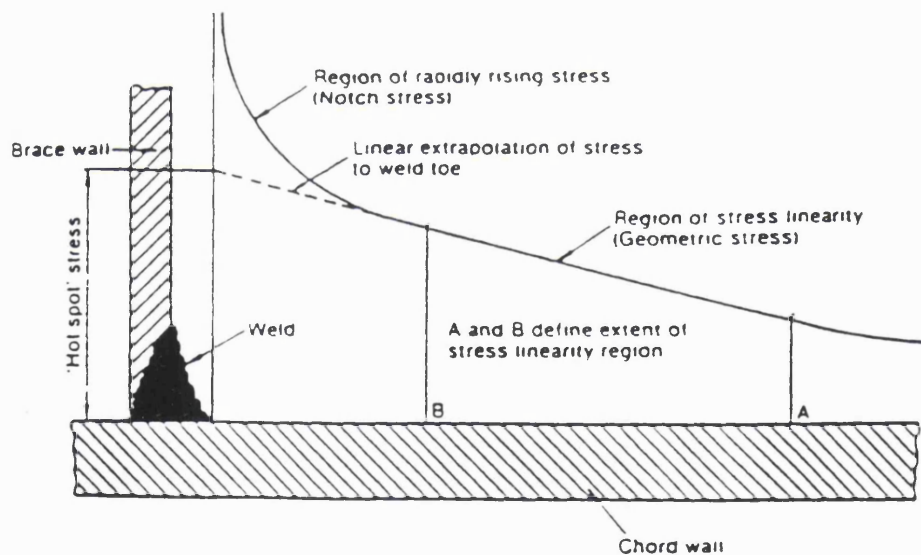


Figure 1.6 The 'Hot-Spot' Stress Definition by UKOSRP I(Irvine 1981)

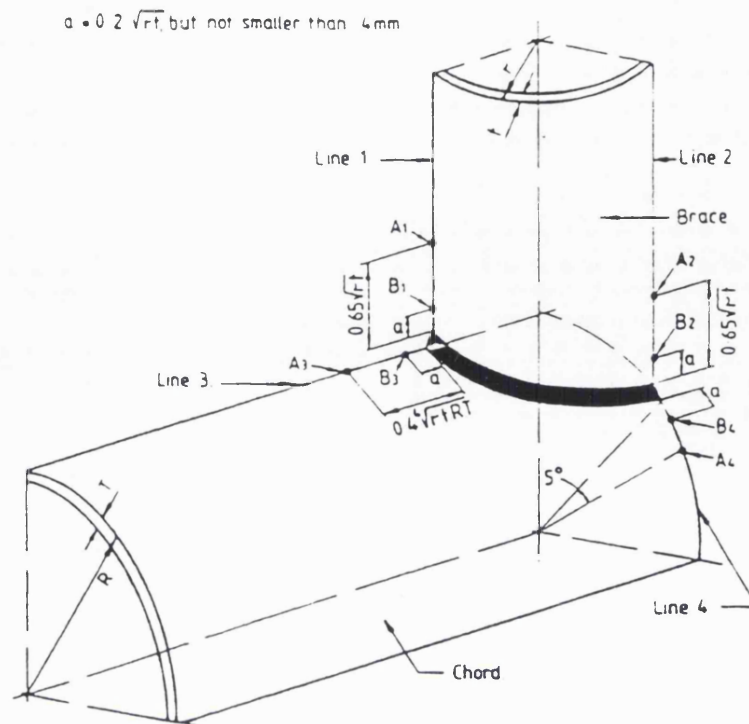


Figure 1.7 Location of the Points for Linear Extrapolation(Irvine 1981)

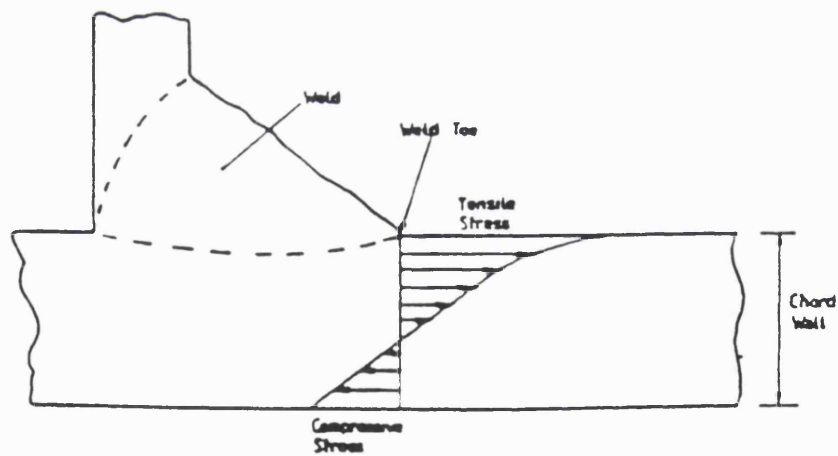


Figure 1.8 Typical Stress Distribution Through the Chord Wall
(Dharmavasan and Dover 1988)

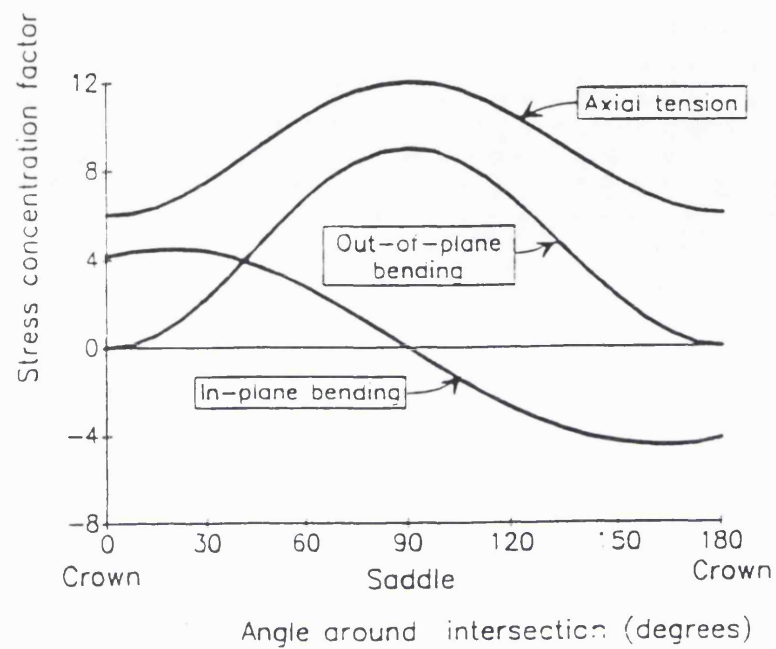


Figure 1.9 Typical Stress Distributions around the intersection of Tubular T-joint under Different Mode of Load(Austin 1994)

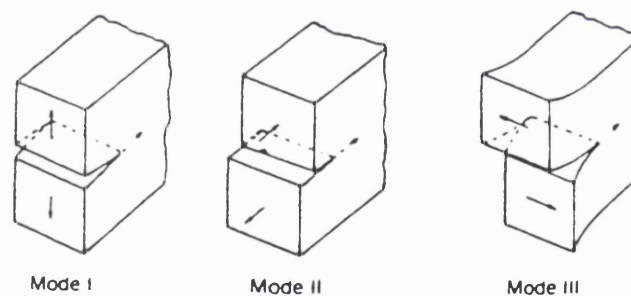


Figure 1.10 Crack Deformation Modes

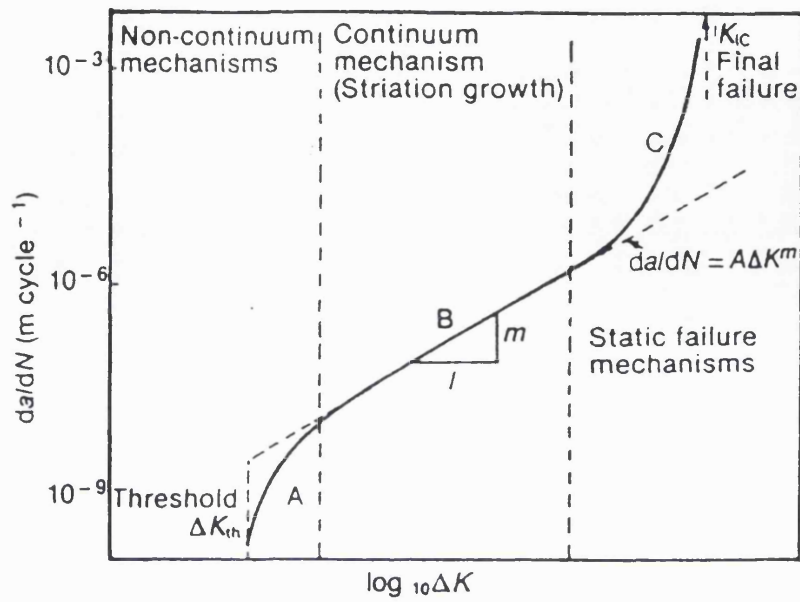


Figure 1.11 Schematic Diagram of Fatigue Crack Growth Behaviour

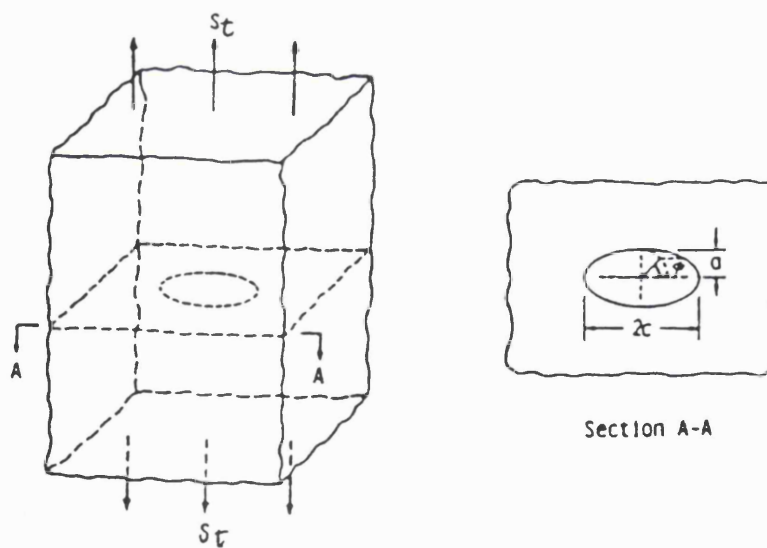


Figure 1.12 Embedded Crack in an Infinite Body

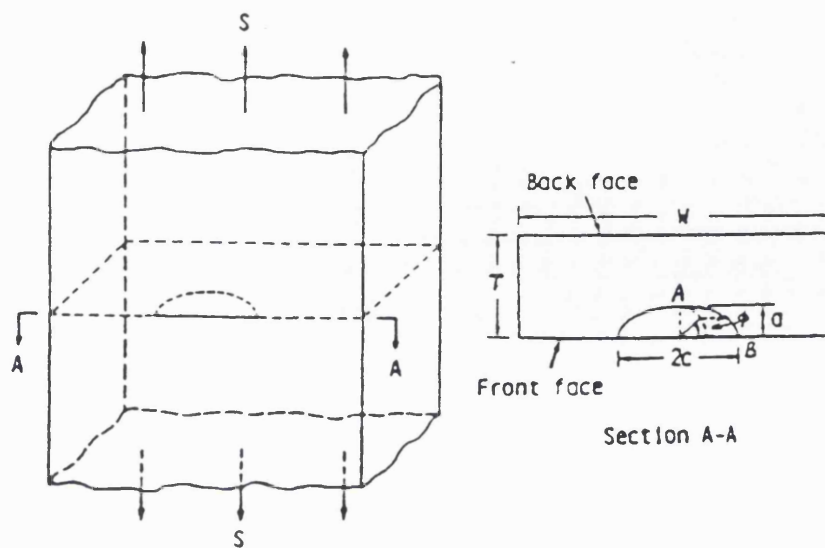


Figure 1.13 Surface Crack in a Flat Plate

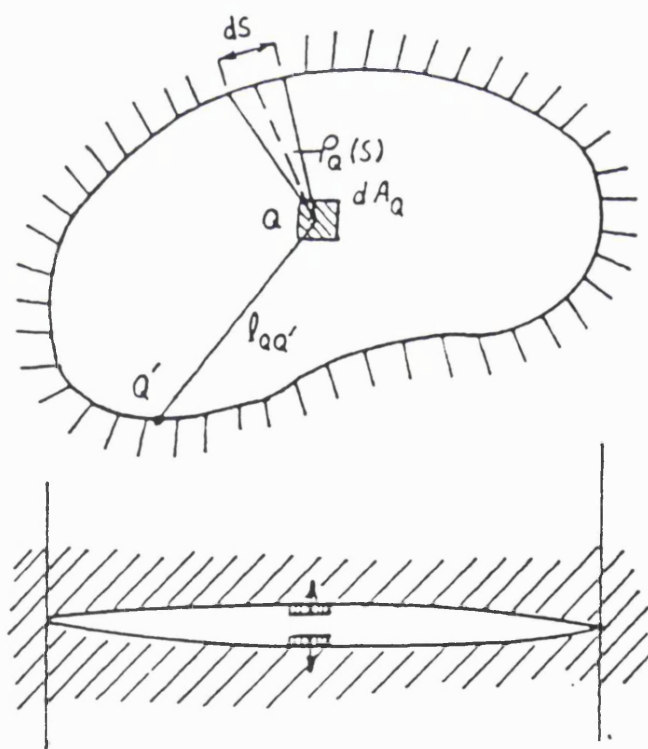


Figure 1.14 Irregular Shape Crack Embedded in an Infinite Three Dimensional Body Defining the Weight Function

CHAPTER TWO

IMPROVED FATIGUE CRACK SIZING USING ACFM

2.1 Introduction

Offshore fixed platforms, as used by the oil & gas industry, are designed to resist both static and cyclic loading (topside weight, wind and wave loading) and to have a design life often in excess of 100 years. Unfortunately the uncertainties in design and manufacture give rise to the possibility of fatigue cracking during service. Hence, regular inspections are required in order to ensure the structural integrity of offshore platforms. An important part of the inspection involves detecting and sizing the fatigue cracks in the submerged part of platforms. Originally it was mandatory to inspect platforms during a five year period but more recently cases based on rational inspection scheduling have become acceptable. These inspection schedules are based on fatigue fracture mechanics calculations which are in turn based on accurate stress analysis, stress intensity factor solutions, crack detection and crack sizing. This chapter is concerned with the last mentioned aspects, especially the Probability of Detection (POD) and accuracy of crack sizing.

In essence the strength of a cracked member is dependent on crack size or the size of the remaining ligament of material. Thus crack depth is the governing parameter and detection capability must be assessed in terms of performance with respect to crack depth. Conventionally POD data has been expressed in terms of crack length and the method was utilised in earlier UCL POD trials reporting. Moving to crack depth instead of length puts great emphasis on the quality of sizing data available with the trials data. In the circumstances it became apparent that the UCL crack library information needed to be reassessed in order to confirm the earlier results with ACPD and to improve confidence by using newer equipment. At the same time the non contacting version of ACPD, known ACFM, had become available and was being used widely in service. It would thus be valuable to investigate the sizing capability of ACFM. Given that ACFM was relatively new, this step also allowed procedure investigation. The final step was, that given the confirmed library crack sizes the POD data would be reanalysed in terms of POD versus crack depth.

2.2 Crack Measurement using Non-Destructive Techniques

2.2.1 Re-Measurement of Fatigue Cracks in Tubular Joints using ACPD and ACFM

As discussed in Chapter 1, the key idea in the UCL study on the reliability assessment of underwater non-destructive inspections is to set up a characterised fatigue crack library of tubular joints. The POD is a comparison of the underwater non destructive test results with the corresponding characterised library data. Whether this approach is successful is very much dependent on the accuracy of sizing these fatigue cracks in air.

Inspection of a large number of welded joints for fatigue cracks has been carried out in the underwater NDE Centre at UCL for the Inter-Calibration of Offshore NDT(ICON) project using several non-destructive inspection techniques. The data is expressed in terms of POD versus crack length but it is now considered desirable to reanalyse its data in terms of crack depth. Thus it is necessary to remeasure some cracks from the UCL library to give increased confidence. Development of the ACPD and ACFM technique has led to the introduction of new instruments, the Technical Software Consultants(TSC) crack microgauge model U10 (for both ACPD and ACFM) and U11(underwater version for ACFM). However, the underwater ACFM trials results indicated there were some large differences for three cracks on library of cracked nodes between in-air ACPD characterised data using U7 crack microgauge and the corresponding underwater ACFM sizing data using U11(Table 2.1). For these reason, a project was carried out to re-measurement of these cracks in air with ACPD and ACFM techniques using U7, U10 and U11 instruments.

The U7 ACPD measurements were repeated. An investigation has also been carried out to compare the behaviour between the U7 and U10 instruments. Finally a new non contacting sizing technique ACFM has become available and given its widely use in service, replacing ACPD, it was decided to include this approach as well. The details of measurement results were reported in reference(Chang et al, 1992 c). The main procedure is listed as below:

- i) Check chord and brace identification and record the information
- ii) Carry out MPI with magnetic yoke and mark position of crack ends
- iii) Size crack with ACPD technique using U7 and U10
- iv) Size crack with ACFM technique using U10 and U11
- v) Re-interpret the old underwater ACFM results using U11

The crack profiles were measured using ACPD technique based instruments U7 and U10 and they are illustrated in Figure 2.1. A comparison of new ACPD measurement results using U7 and U10 with in-air ACPD characterised data was made(Table 2.2). The corrected data were calculated using the revised calibration equation (2 - 1) for the ACPD

technique(Monahan 1991). It can be seen that the old ACPD data using U7 agree very well with the new ACPD results using U7. Although being slightly high, the ACPD data from U10 are very close to that from U7. The line contact behaviour is also consistent for U7 and U10. Thus it seems that the in-air ACPD data are reliable.

The ACFM measurements using U10 and U11 were carried out in-air for these library cracks. Old underwater ACFM data using U11 were re-analysed and some mistakes were found on interpreting crack depth from these data. Individual reasons for these mistakes were found. Some were due to bad scanning and others are caused by using the wrong physical length. After correcting these errors and using revised interpretation procedures, better results have been obtained. The detailed information for these measurement results were listed in Table 2.3. One can see that the underwater ACFM data using U11 are reliable, if one uses this instrument and the corresponding software in the correct way.

As a summary, the re-measurement results using ACPD by U7 and U10 agree reasonably well with those using ACFM by U10 and U11. Furthermore, some crack depth measurements have been carried out on T-butt samples. It has been found that the inferred depths from ACPD measurements are also very close to those from ACFM.

2.2.2 Effect of using Different WAMI Versions on Underwater ACFM Sizing Results

Containing theoretically-derived sizing algorithms, automated instrument control, data storage facilities and dedicated graphical output, the ACFM crack detection and sizing software(WAMI) was developed at TSC to interpret and size the results recorded during the underwater inspection using the ACFM technique. Initially, the crack sizing results in POD/Probability of Sizing(POS) for the TSC U11 ACFM crack microgauge report(Rudlin et al 1992) were obtained by using WAMI version 3.6b. A more recent version, WAMI 3.8b has become available since the completion of the trial. It has been found that there are some differences in the sizing estimates using the different versions of WAMI with same mean Bx, minimum Bx and same physical length. So it is necessary to report this difference.

WAMI version 3.8b has been used to calculate the underwater ACFM trial data again. Some mistakes in the old data were found and corrected. The new sizing results have been compared with the old data which were calculated with old version of WAMI and subsequently revised by TSC(Figure 2.2).

The comparison(Chang 1992 d) has shown that the new data tend to be slightly higher than the old data. The effect of using the different WAMI versions on underwater ACFM sizing results is basically small since the old data are quite close to the new data after correcting mistakes.

2.2.3 Investigation of Sizing Procedures for Underwater ACFM Inspection Results

It is well known that the fatigue cracking in tubular joint starts as a number of small semi-elliptical cracks that initially grow on different planes and subsequently coalesce by jumping from one plane to the another. This creates small steps or facets perpendicular to the main crack face and these facets act as line contacts. As far as alternating current field measurements are concerned, each line contact forms an electrical short circuit and the whole long crack acts as a series of shorter cracks. There are some long cracks in the UCL library. The ACFM sizing algorithm is based on a single crack with a semi-elliptical shape. However, the physical length used in initial depth sizing was the whole length of a defect indication. This may be one reason why the ACFM depth predictions are greater than the destructive and characterised data in most cases. Thus it is necessary to carry out the further investigation on the sizing procedure for the TSC U11 ACFM crack microgauge.

Since there are some difference between the sizing results with different versions of WAMI as discussed in section 2.2.2, only the latest version, WAMI 3.8b has been used in this investigation in order to update and standardise the results. The report from this investigation(Rudlin, Chang and Dover 1992 b) is a supplement to the POD/POS report on the TSC U11 crack microgauge(Rudlin et al 1992). It should be noted that the length estimates used to assess crack depth after the trials must be treated with reservation, as they will assume a constant scanning speed. The main steps of this investigation are listed as below:

- 1) Compare the destructive test data with the ACFM signals including the line contacts and other features. Based on these observation, develop the several different sizing procedures.
- 2) Apply these different procedures to the remainder of the library characterised cracks to see which procedure gives the best results.
- 3) Evaluate other effects on sizing accuracy, particular variations in the value of the background Bx.

A comparison of the ACFM signals including the line contacts with all available corresponding destructive test results was carried out. A typical example is shown in Figure 2.3. It was found that the signal between separate cracks always return to the background level. A line contact within a long crack can be recognised when the Bx signal does not return to the uncracked value and the butterfly tends to form a loop inside the long crack butterfly while the Bz signal responds by a peak and trough. One may locate a line contact by a Bx peak in the long crack dip in above circumstances.

As the physical length used in the initial depth sizing procedure in the trial was the length of the whole crack range, the sizing results showed that there is a tendency for this procedure to oversize the crack depth, particularly where line contacts were known to be present. Therefore, it is necessary to develop other procedures. Comparison with destructive test data tends to show that the depth predictions using the length between the large visible line contact indications or the length between the above line contact and the end of whole crack range are better than those using the initial procedure in the majority of cases. In order to find a more reasonable sizing procedure, three procedures have been formulated as following

Procedure 1: Treat the length between existing markers or whole crack range with Bz responding by a peak or trough as the physical length of independent crack.

Procedure 2: Treat the length between the line contact indications which are equal or greater than 90% of the Bx range (Bx background - Bx minimum) with Bz responding by a peak or trough (including the end of crack) or the length between above line contact and the end of whole crack range as the physical length of separate cracks. The Bx signal within this length should contain Bx minimum.

Procedure 3: Treating the length between the line contact indications which are equal and greater than 50% of Bx range (Bx background - Bx minimum) with Bz responding by a peak or trough (including the end of crack) or the length between above the line contact and the end of whole crack range as separate cracks. The Bx signal within this length should contain Bx minimum.

Using the value of the background Bx in initial sizing, a comparison has been carried out of the whole inspection results using the three different procedures with the destructive and characterised data. An example of the physical lengths obtained using the three different procedures is shown in Figure 2.4.

It was found that there is the geometry influence on ACFM signal, and the value of background Bx was overestimated in initial sizing for long cracks. Assuming that the influence on ACFM signal for the same geometry is same, the ACFM depth sizing was re-evaluated for the cracks at the saddle toe of three right angled braces in DT-joints having the same dimensions by using the Bx background in uncracked joints. Comparison of the ACFM predictions using this revised background Bx with those using initial background Bx was done.

Result details were reported in reference(Rudlin, Chang and Dover 1992 b). The investigation resulted in the following conclusions.

1) There are two important factors in underwater ACFM crack depth calculations. One is how to decide on the Bx background. The other is how to select the physical length, i.e.

what is the appropriate procedure. It has been found that the influence of the former is much larger and more sensitive than that of the latter.

2) Comparison of the destructive test results and characterised data with the corresponding underwater ACFM depth predictions using three different procedures is shown in Figure 2.5. One can see that the predictions using procedure 3 are better than the results using procedure 1 or 2, especially for the cracks with depth less than 17mm. The ACFM depth predictions using procedure 2 are close to those using procedure 1, although the former is a slightly better.

3) The underwater ACFM sizing results using revised background Bx are better than those using initial background Bx. They are closer to the destructive test results and characterised data(Figure 2.6).

4) When the effects of using procedure 3 and revised background Bx are combined, the underwater ACFM depth predictions agree very well to the destructive test results and characterised data(Figure 2.7).

2.3 Underwater Inspection Reliability of Non-destructive Techniques

The probability of detection(POD) has been identified as a primary tool for assessing the capability of NDT techniques. All inspection processes are uncertain due to inherent POD being less than 1 in the range of defect size of interest. The measure of this uncertainty always comes from blind trials. The true POD as a function of crack size will never be known exactly since NDT technique capabilities can only be demonstrated through the experiment. The objective of such an experiment is to provide a point estimate of POD over the whole population of any similar inspection area under investigation, and to provide the an estimate of how it may vary. There is relationship between the measured POD and true POD for the service situation. Statistical methods can be used to provide confidence limits on the true probabilities. In other words, the POD estimate can be made by setting a level of confidence that the results will be within certain limits. The lower bound of 90% population POD with 95% confidence has been chosen as the target. In other words, the objective of the POD trial is to estimate the crack size for which there is a 95% confidence that it can be detected by 90% of all cases.

It has been shown that both the magnitude and scatter in POD estimates are significantly influenced by crack size(Figure 2.8). A very large sample size would be required to reduce the "error" in the POD estimates in order to yield more precise crack length predictions of detection. Assuming a binomial distribution of the data, the number of cracks which need to be successfully detected in a trail within a crack size range can be shown to be 29 out of 29 to achieve a 90% at a 95% confidence limit.

2.3.1 UCL POD Trials

POD trials have been carried out by University College London Underwater NDE Centre for MPI(Rudlin and Dover 1990 a), two well-known eddy current systems, Hocking and EMD III(Rudlin and Dover 1990 b) and ACFM(Rudlin et al 1992), which have been successfully used offshore. As discussed above, more than 150 fatigue cracks in tubular welded joints are needed to produce the desired experimental POD curves. These fatigue cracks can be produced using a variety of fatigue test rigs capable of applying in-plane bending, out-plane bending and axial loading. Producing these pre-cracked tubular welded joints is obviously an expensive undertaking and could be prohibitively expensive if these samples were only used for one trial and then destroyed in order to yield the true crack sizes. Also, it has been shown that crack sizes could be reasonably accurately determined by laboratory NDT techniques. These consideration led to the concept of producing a library of precracked tubular joints which could be used for a series of trials. The confidential library of tubular welded joints containing known fatigue cracks have been established in underwater NDE Centre at UCL.

Therefore, it should be noted that the POD curves are produced in the way of comparing underwater non-destructive trial results using different underwater NDT techniques with the characterisation database of a confidential library of fatigue cracks formed by the laboratory techniques rather than by comparison of that with the destructive test results. The accuracy of POD is therefore dependent on the accuracy of the in-air crack measurement. So it requires a high level of confidence in the characterisation of cracks in library specimens to establish accurate POD curves. A reasonable estimate of crack size could be obtained by in air by MPI, ACPD and time of flight ultrasonic (TOFD). The first two are used to establish the length of a crack, whereas ACPD and TOFD can be used to establish the depth.

It is necessary to check on the quality of characterisation data of the above library cracks by carrying out a limited set of destructive tests since the measure POD values are obtained by comparing the air characterisation with the underwater results. Assessing the quality of air inspection results by means of destructive sectioning two double-brace T-joints belonging to the UCL confidential library of fatigue cracked tubular joints was therefore carried out(Monahan 1991). The results were used to evaluate the existing crack depth characterisation procedure for deep cracks and extended the ACPD calibration equation to include cracks less than 5mm in depth. The revised calibration equation for the ACPD technique which has been adopted for creating new characterisation database in the following analysis is listed as below:

$$d_m = 0.92 + 1.05d \quad (2 - 1)$$

where d_m is the 'true' or corrected depth (mm)

d is the predicted depth (mm) determined by laboratory NDT techniques.

2.3.2 Re-analysis of POD Trial Results using a New Classification

Cracks are often initiated in a number of places in the same region of a welded joint. The final appearance of a crack investigated by MPI may show a number of small indications. The criteria for grouping a number of small indications (appearances of cracks) determines the crack length. The classification A, B, B1 and C (Figure 2.9) have been used in the course of UCL underwater NDE Centre POD trials (Rudlin and Dover 1990 a) (Rudlin and Dover 1990 b). It is necessary to establish rules for the definition of a success. The resulting inspection performance will be strongly influenced by the success criteria chosen. The possible outcomes of an inspection are detection, missed (no detection) and spurious data (Figure 2.10). However, the detection is complicated by the fact that a number of small cracks can be detected together. The degree to which this happens depends on the classification. The classifications used in this thesis are outlined as below.

Classification A: Individual Crack Indications

Each small 'in-air' indication is treated as one crack. Cracks located in chord toe, brace toe or interbead are treated as the separate cracks.

There are two types of detection, namely isolated detection and combined detection. An isolated detection is where the indicated result from the diver corresponds to a single indication classified in air. The isolated detection can be further analysed by comparison of lengths. A combined detection is where the indicated results from the diver correspond to a number of indications in air. A spurious indication in these cases is one which does not overlap the in-air indication

Classification B: Dominant Defect in Defect Region

A defect region is defined as a part of the weld with defect indications separated from all other defect indications by at least 30 degrees of the circumference.

Classification B1: Dominant Defect in a Weld

As Classification B but expanded to include all the weld (i.e. the total weld area from brace toe to chord toe).

For Classification B and B1, a detection is defined as an indication from the diver within the cracked region. A spurious indication in these classification is a reported indication outside the cracked region. Where the lengths are compared, the length of the dominant crack, the

largest individual reported in-air crack indication in the cracked region, is used for comparison.

Several studies(Rudlin and Dover 1990 a)(Rudlin and Dover 1990 b) have been completed on the POD trials of various underwater NDT methods, using divers in a tank in underwater NDE Centre at UCL. For cracks which have an isolated detection, it is possible to carry out further comparison of the in-air and underwater results using the length ratio in order to get crack length sizing accuracy. The length ratio can provide a filter for the POD curves, by only admitting results of a certain accuracy as a positive detection.

However, the effect of length ratio on the POD can not be carried out on combined detection in the classification A, B, B1 and C. In order to facilitate further analysis of length ratio, the new classification D(Figure 2.9) has been introduced by the author and is defined as below:

Classification D: The Cracks where indications as in classification A are closer than 30 degrees are considered as a single crack. The Cracks in chord toe, brace toe or interbead locations are treated as separate cracks.

For this new classification, a detection is defined as an indication which overlap the in-air indications. A miss indication is one which does not overlap the in-air indications. A spurious data is the indication obtained underwater which have no corresponding indication in-air.

The POD trial data for underwater MPI, Hocking and EMD III Eddy Current Inspection methods have been re-analysed(Chang et al 1991a) using the new classification D. The POD curves in terms of crack length with depth information in the form of thresholds have been produced in this analysis. The existing UCL FORTRAN 77 programme was modified to calculate the lower bound estimate of the population POD with any specified confidence on the VAX/VMS system(Chang et al 1991b). So the lower bound estimates of population POD of 90% with 95% confidence level have also been calculated and included on the POD curves.

Typical examples are shown in Figure 2.11-2.13. It should be noted that all points are plotted on POD curves at the end of the crack size range. From the POD curves in terms of crack length with depth information in the form of thresholds, one can see that as the depth threshold increases the POD is generally higher. Sometimes, it can become irregular when the number of cracks is small at crack size ranges. Also the POD data with effect of length ratio threshold have shown that as the length ratio threshold increases, the POD level reduces. Increasing the length ratio threshold did not change the general shape of these curves. Comparing with the measured POD, the 95% confidence curve reduces but the general shape is maintained.

2.3.3 Re-analysis of POD Trial Results against Crack Depth

Historically, the NDT inspection reliability data have been based on the crack length as they are displayed as the variation of POD with surface crack length. It is realised that these data generated by the NDT inspection reliability investigations may not be used directly since they are not presented in a format readily for the reliability fatigue assessment which rather requires information on crack depth. The crack depth is the most important dimension used for remaining life prediction and the fracture mechanics based calculation of fatigue crack growth. Also, aspect ratios of fatigue cracks do not keep constant during fatigue crack growth in welded joints. The large scale test data have shown that different crack shapes occur (such as long shallow, long deep or short deep) due to different stress distributions in tubular welded joints. So, a fatigue damage assessment needs crack depth based POD information. In order to accommodate this requirement, POD curves versus crack depth is therefore required for various underwater NDT techniques.

Each characterised crack length in the UCL library for particular classification has a corresponding characterised maximum crack depth. This allows re-interpretation of the existing POD data. The POD trial data for underwater MPI, Hocking and EMD III Eddy Current Inspection methods have been re-analysed to make them suitable for reliability fracture mechanics procedures. These analyses (Chang and Dover 1991 c) (Chang and Dover 1992 a) (Chang and Dover 1992 b) have produced the POD in terms of crack length as well as the POD in terms of crack depth using a classification D. The lower bound estimate of population POD is included on the POD curves. The confidence level used was 95%. Furthermore, for the underwater MPI technique, the similar analyses to those described above have been done (Chang and Dover 1992 e) for classification B and B1. The underwater MPI trial results (Rudlin and Dover 1990 a) have been extended to include POD versus crack depth for the classification B and B1.

The results of all these studies formed a revised inspection reliability database and were incorporated into UCL RISC system (Chang and Dove 1994). Some examples are illustrated in Figures 2.14-2.20. The use of the different classifications is dependent on the particular application and the eventual remedial action to be taken. The classification B1 was decided to be used initially in inspection scheduling work as it is the commonest classification in use for a wide range of NDT system.

2.3.4 Comparison of Underwater POD Trial Data for ACFM and MPI

A variety of non-destructive techniques (NDT) are available for this purpose. It is important for an offshore operator to know the capabilities such as the minimum detectable crack size and often the reliability for detection of these different techniques. By comparison of the

performances of these individual NDT techniques, the most appropriate NDT technique may be chosen at the right price and to the appropriate accuracy. Furthermore, this information is crucial for rational inspection scheduling.

The underwater fatigue crack detection capability for the ACFM using TSC U11 Microgauge and MPI were compared in this section. To make this comparison, the results from the POD trials carried out at the UCL underwater NDE Centre on underwater ACFM(Rudlin et al 1992) and MPI(Rudlin and Dover 1990 a) have been used. Since some fatigue cracking had been carried out between the two trials, the new cracks have been removed from the original database as reported in the underwater ACFM trial document. The comparison has therefore been made on an identical database. These POD trials were carried out on the 80 brace/chord intersections of the UCL cracked node library, 24 of which had no fatigue damage. The others contained the cracks with varying length from 2mm to 643mm.

The classification A and B1(Figure 2.9) have been used in this analysis. It should be noted that the results using classification A are susceptible to missing of small defects by location error. This is due to using tape measurement on the weld and it has been observed that an error up to 20mm is possible. The classification A data give some idea of the capability for completing coverage of defects areas. On the other hand, the classification B1 data are much less susceptible to location error and may be used in further analysis as results of using a "first pass detection" criteria.

The information of the missed cracks is very important since a small number of the large missed defects can cause significant changes in POD curves. In order to further understand the classification A underwater ACFM trial results, the following types of missed defects have been introduced.

Type 1: a missed crack adjacent to a detected classification B1 dominant crack (in other words, a small crack missed at the end of the large crack which was detected)

Type 2: a missed crack running parallel to a detected classification B1 dominant crack (for example, an interbead crack is missed which runs parallel with a toe crack which was detected)

Type 3: a missed classification B1 dominant crack

Type 4: a missed crack where a classification B1 dominant crack missed nearby

A diagrammatic representation of the types of the missed defects is shown in Figure 2.21.

The comparison of the POD trial results in terms of crack length for the underwater MPI and underwater ACFM techniques has been carried out(Rudlin, Chang and Dover 1992 a). For the purpose of comparison, crack size ranges have been maintained the same. Comparison

on a "first pass detection" criteria(using classification B1) for the cracks with depth thresholds showed the POD curves(Figure 2.22-2.23) are similar for underwater ACFM and MPI. The small differences observed are no more than one crack in any size range. This is exaggerated slightly by the POD curve presentation because of the small number of cracks in the larger size range.

From the classification A comparison results, it showed that the POD curves reach 100% in the 50-108mm range for both techniques. The POD curve for ACFM is higher than MPI at range 29-49mm but lower below this range(Figure 2.24-2.25).

The relative frequency of different types of missed defects for ACFM trials was calculated as shown in Table 2.4. Examination of results showed the small cracks missed by underwater ACFM are mostly the cracks extending from the end of detected larger defects. Some of them may be due to location errors.

A comparison of the numbers of the spurious indications between these two techniques(Table 2.5-2.6) showed that the underwater ACFM technique has given a far superior performance in the trials for the non-reporting of spurious indications.

More recently, underwater ACFM POD data versus crack depth for classification B1 have been produced and compared with correspondent underwater MPI results(Dover, Chang and Rudlin 1994). Again, the POD versus crack depth curves(Figure 2.26) shows they are very close with underwater ACFM giving slightly better results. In order to see more detail, the cracks are grouped in blocks of 10 rather 29(Figure 2.27) and the conclusion remains the same.

As a summary, the POD performances for these two techniques are quite similar. The ACFM length measurement does not on a few occasions, include all the small cracks extending from the end of a crack. As giving superior performance in the trials for non-reporting of spurious indications and offering many advantages such as crack depth measurement, without prior calibration and requiring no electrical contact, the ACFM technique is preferred for underwater inspection.

2.4 Conclusions

The ACPD and ACFM techniques were used to size the fatigue cracks in tubular joints and the effect of using different versions of WAMI(ACFM crack detection and sizing software) and sizing procedures for the underwater ACFM results were investigated. Moreover, the underwater POD trials results for ACFM and MPI were compared. The POD performance for these two techniques is close. The ACFM is preferred as this technique offers many additional benefits for inspection of offshore structures. However, it does sometimes miss

the small cracks near the end of long crack. The sizing accuracy of ACFM technique depends on a theoretical model and the interpretation of ACFM inspection results is slightly complicated. Thus, it is important to use correct procedures.

A new crack classification D has been proposed. The POD in terms of both the crack length and the maximum crack depth for MPI and two well-known eddy current systems(Hocking and EMD III) using classification B, B1 and D were produced. These data, especially the crack depth based POD information, formed the inspection reliability database and has been directly used as input for reliability fracture mechanics based inspection planning of offshore jacket structures. Finally, it should be noted that the underwater NDT reliability assessment in current study at UCL aims to obtain the capability information for each technique and therefore do not include the human effect.

Table 2.1 Comparison of In-air ACPD Characterised Data using U7 Crack Microgauge and Old Underwater ACFM Sizing Results using TSC U11 ACFM for Three Library Cracks

Library Crack	Crack Location	Crack Depth (mm)	
		ACPD U7 (in-air)	ACFM U11 (underwater)
I	Chord Toe	18.4	35.8
II	Chord Toe	2.4	17.4
III	Chord Toe	18	9.8

Table 2.2 Comparison of New ACPD Measurement Results using U7 and U10 with In-air ACPD Characterised data for Three Library Cracks

Library Crack	Status	Instrument	Depth (mm)	Corrected Depth (mm)
I	Old	U7	16.28	18.01
	New	U7	16.63	18.38
	New	U10	18.9	20.77
II	Old	U7	2.4	3.44
	New	U7	2.44	3.48
	New	U10	2.56	3.61
III	Old	U7	18	19.82
	New	U7	17.36	19.15
	New	U10	17.65	19.45

Table 2.3 Comparison of New and Old ACFM Measurement Results using U10 and U11 (In-air and Underwater) for Three Library Cracks

Library Crack	Measurement Status	Circumference Total Length (mm)	Environment	Instrument	Start	Finish	Physical Length (mm)	Depth (mm)	Revised Length (mm)
I	Old	1610	underwater	U11	334	525	291	35.8	-
	Revised	1610	underwater	U11	334	525	191	18.6	200.1
	New	1583	in-air	U10	330	505	175	18.1	184
	New	1583	in-air	U11	330	505	175	17.9	184
	New	1583	in-air	MPI	325	516	-	-	191
II	Old	1610	underwater	U11	80	165	85	17.4	-
	Revised	1610	underwater	U11	155	165	10	1.7	11.1
	New	1580	in-air	U10	145	160	15	3.6	16.4
	New	1580	in-air	MPI	142	157	-	-	15
III	Old	1440	underwater	U11	220	510	290	9.8	-
	Revised	1440	underwater	U11	220	510	290	22.9	301.6
	New	1406	in-air	U10	174	480	306	20.9	320
	New	1406	in-air	MPI	167	513	-	-	346

Table 2.4 TSC U11 ACFM Missed Defects Analysis for Classification 'A' Cracks

Type of Missed Crack	1	2	3	4
No.	61	10	10	9
%	68	11	11	10

Notes:

Type 1: Classification B1 Dominant Crack Detected nearby

Type 2: Classification B1 Dominant Crack Detected on Deferent Positions across the Weld

Type 3: Classification B1 Dominant Crack Missed

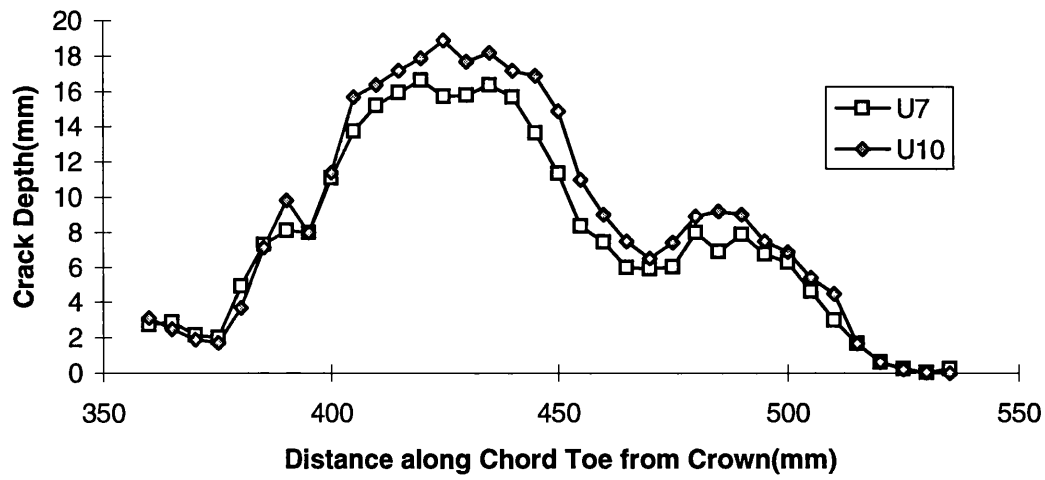
Type 4: Classification B1 Dominant Crack Missed nearby

Table 2.5 Comparison of Ten Largest Spurious Indications
Between TSC U11 ACFM and MPI Underwater POD trials
for Classification 'A' Cracks

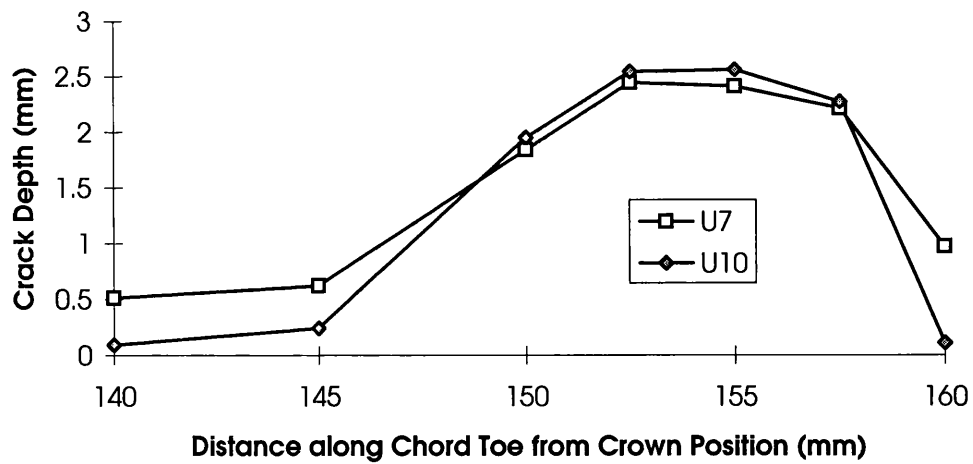
TSC U11 ACFM Length of Spurious Indication(mm)	MPI Length of Spurious Indication(mm)
23	280
23	280
22	170
21	101
18	100
17	90
16	60
15	30
14	30
11	25

Table 2.6 Comparison of Total Number of Spurious Indication
Between TSC U11 ACFM and MPI Underwater POD TRIAL
for Classification 'A' Cracks

	TSC U11 ACFM	MPI
Total Number	16	45

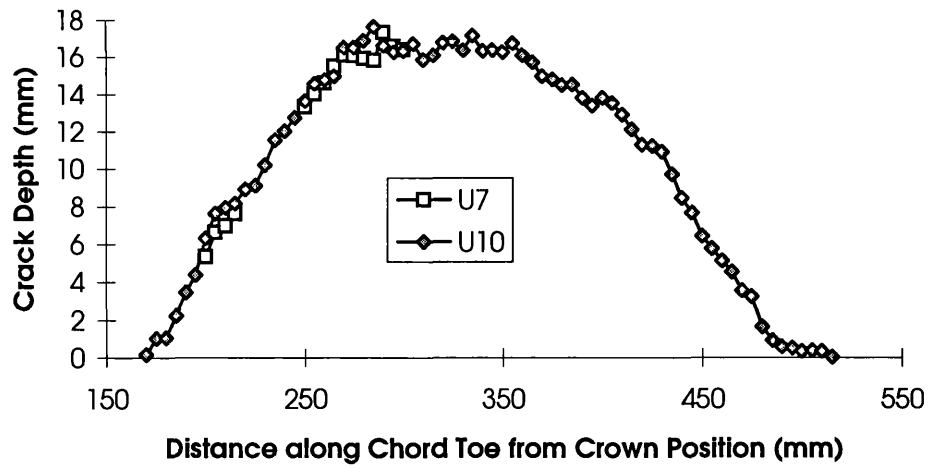


(a) Library Crack I



(b) Library Crack II

Figure 2.1 Fatigue Crack Profiles using ACPD Technique



(c) Library Crack III

Figure 2.1 Fatigue Crack Profiles using ACPD Technique (Continued)

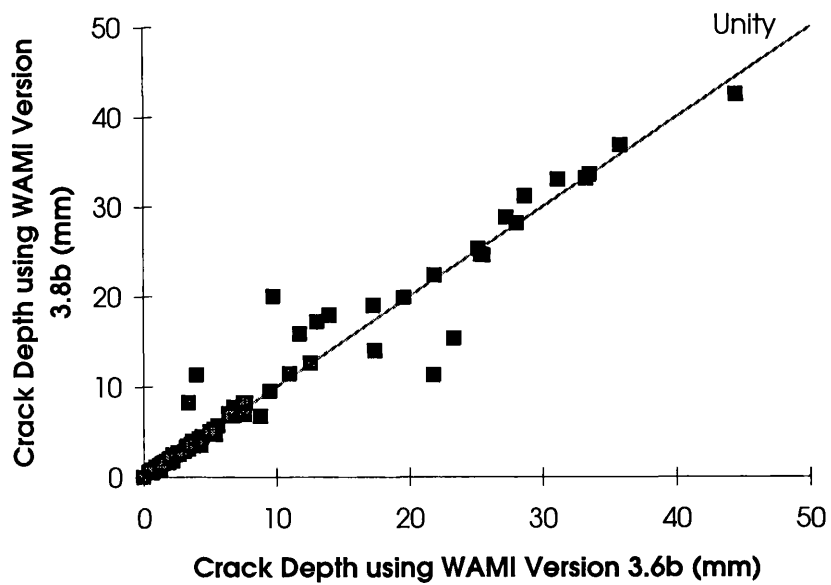


Figure 2.2 Effect of using Different WAMI Versions
for the ACFM Crack Depth Sizing Results

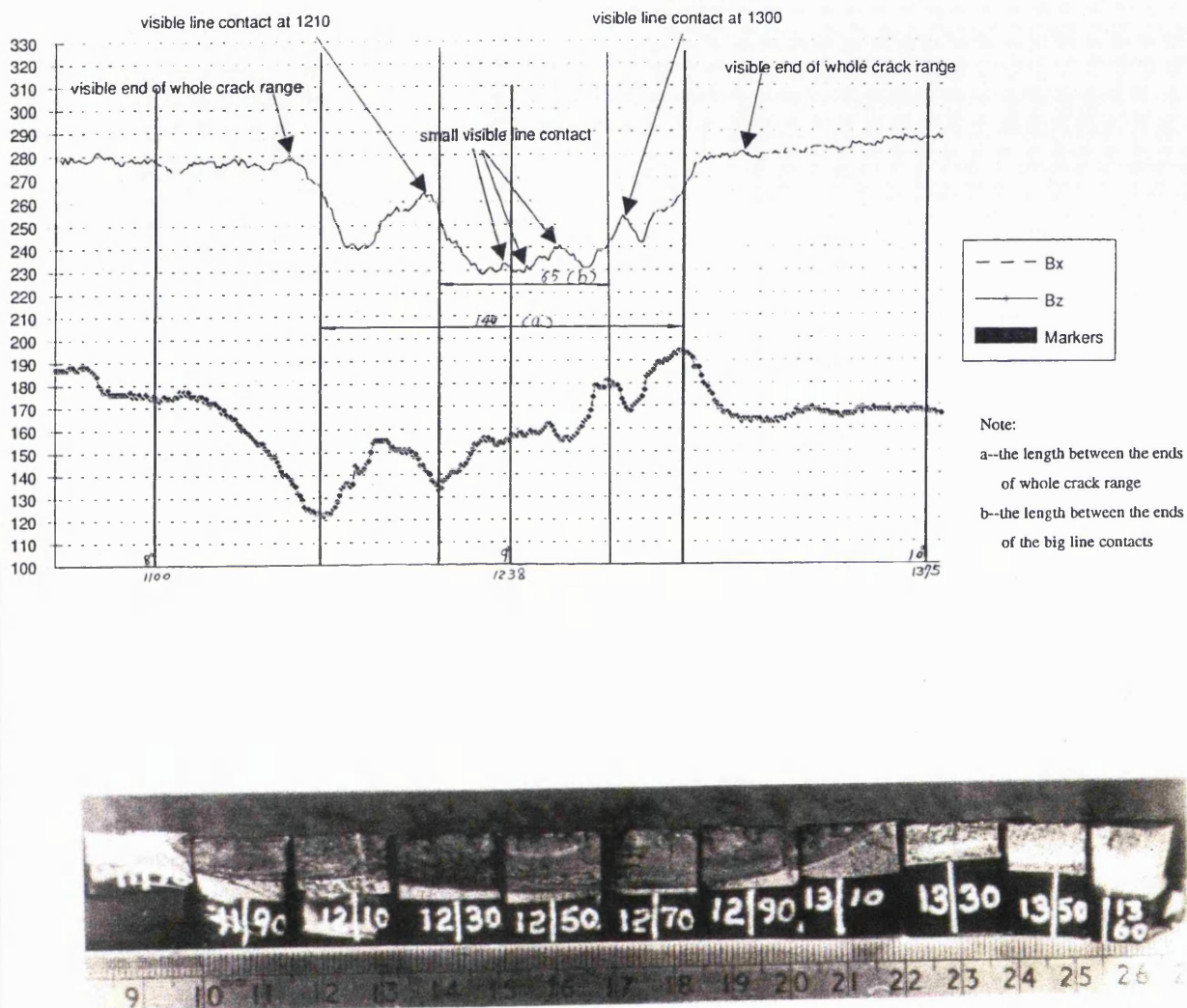
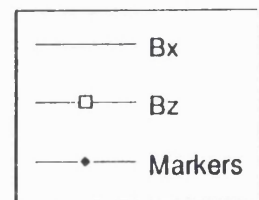
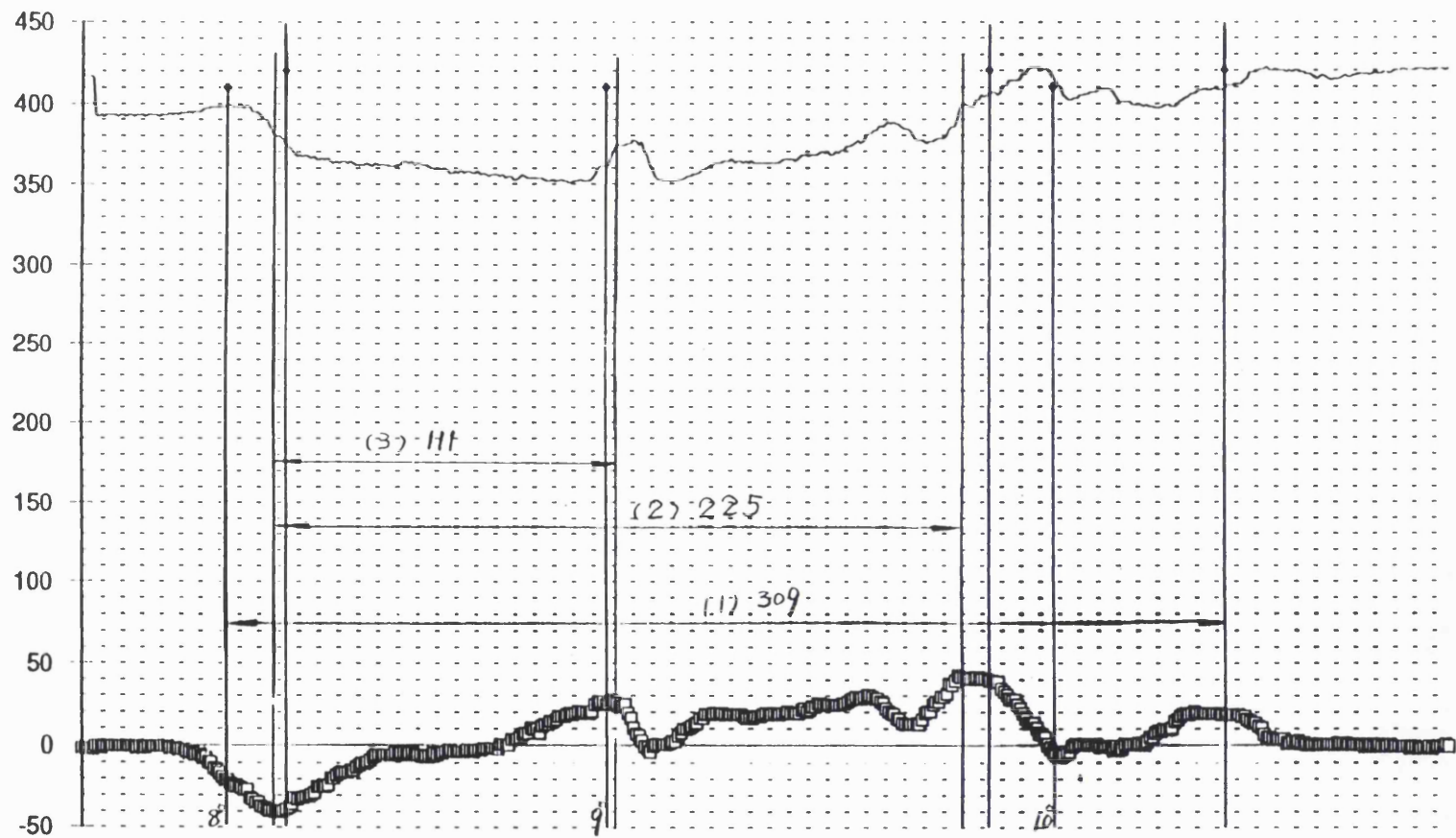


Figure 2.3 One Example of Comparison of the Destructive Test Data with Corresponding the ACFM Signal for Fatigue Crack in Tubular Joint



Note:

- (1)--the physical length using procedure 1
- (2)--the physical length using procedure 2
- (3)--the physical length using procedure 3

Figure 2.4 A example to decide the physical lengths using three different procedures

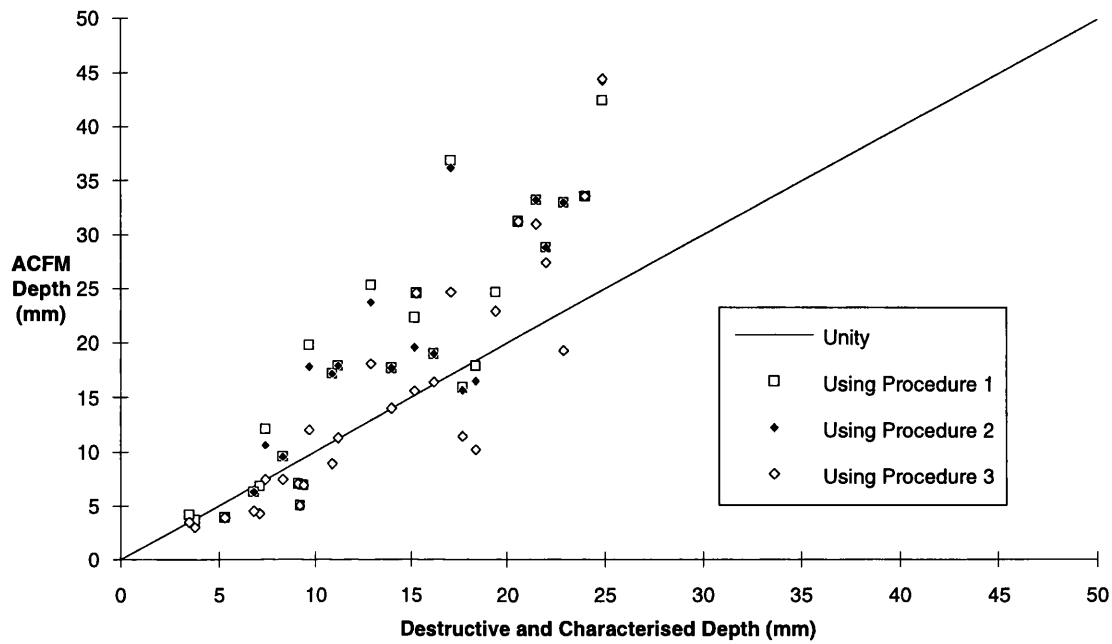


Figure 2.5 Comparison of ACFM Depth Predictions against Destructive and Characterised data using Different Procedures

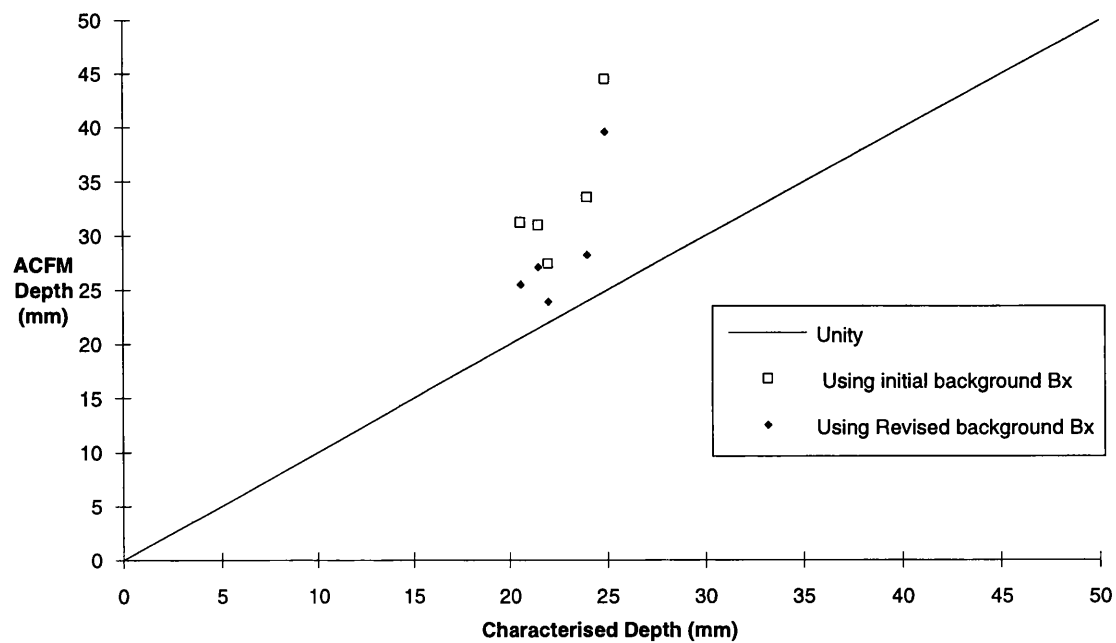


Figure 2.6 Effect of the Background Bx on ACFM Depth Predictions using Procedure 3

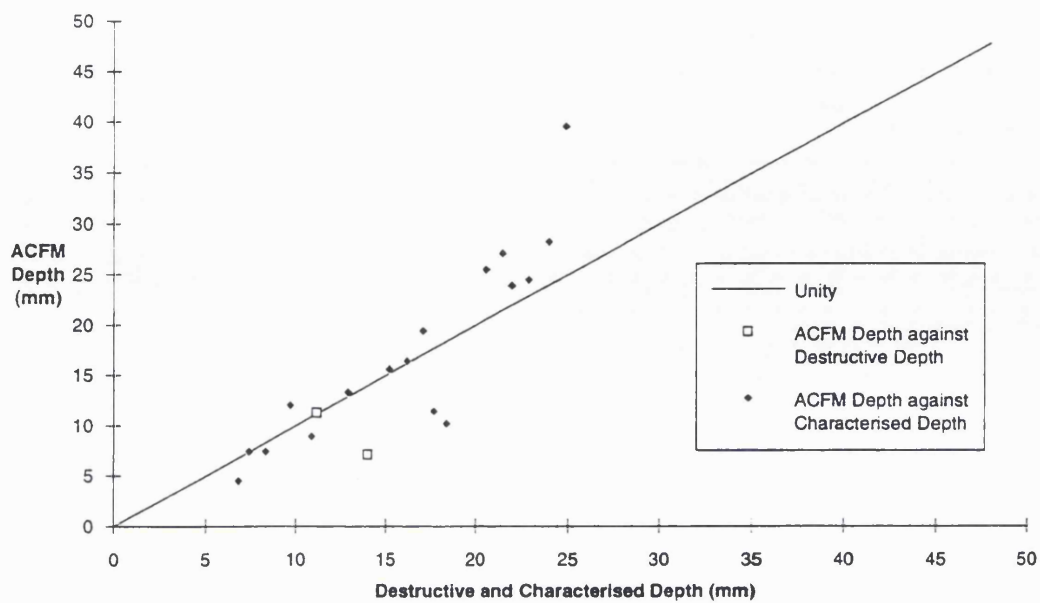


Figure 2.7 The ACFM Depth Predictions using
Procedure 3 and the revised Background Bx

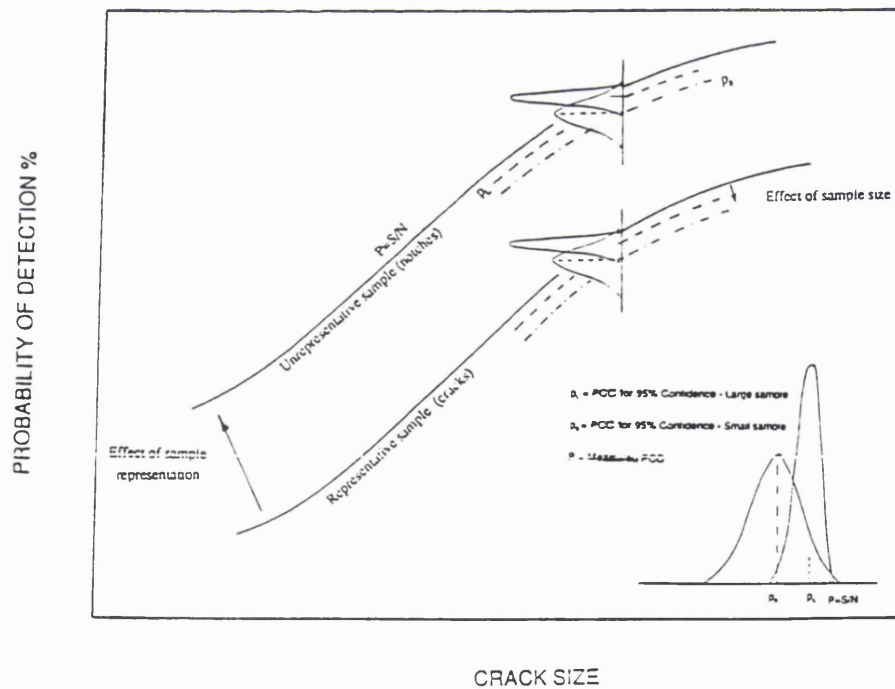


Figure 2.8 Effect of the Nature and Size of the Sample on the POD Curve

Overview	
Classification A	
Classification B	
Classification B1	
Classification D	

Figure 2.9 Crack Classifications












Characterisation	 Include all cracked region for Class 'B'					 Include all cracked region for Class 'B'
Detection	 Anywhere in cracked region for Class 'B'			 Anywhere in cracked region for Class 'B'		
Detection Type	Isolated	Isolated	Combined	Missed	Spurious	Missed + Spurious

Figure 2.10 The Possible Outcome of an Inspection

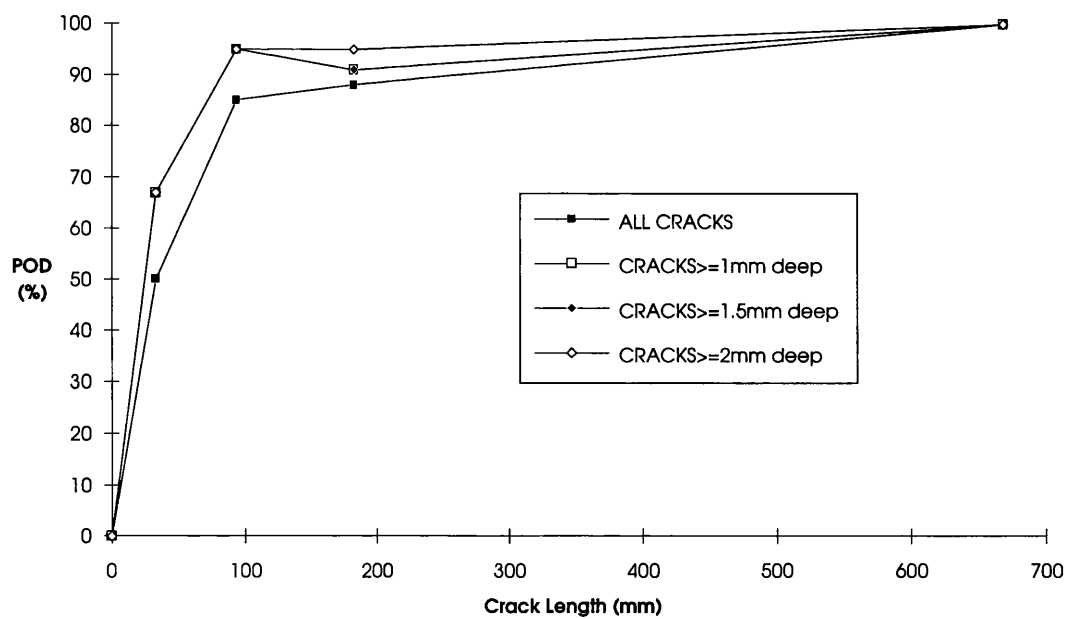


Figure 2.11 Magnetic Particle Inspection

Effect of Depth Threshold on POD against Crack Length using Classification 'D'

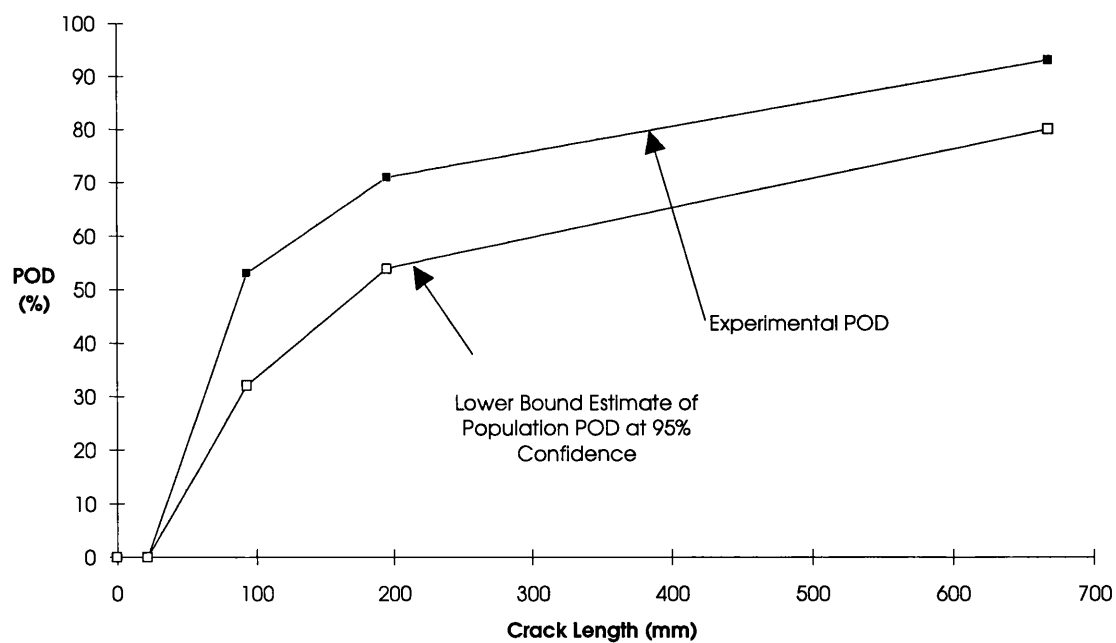


Figure 2.12 EMD III Eddy Current Inspection

POD Against Crack Length for Cracks ≥ 1 mm deep using Classification 'D'

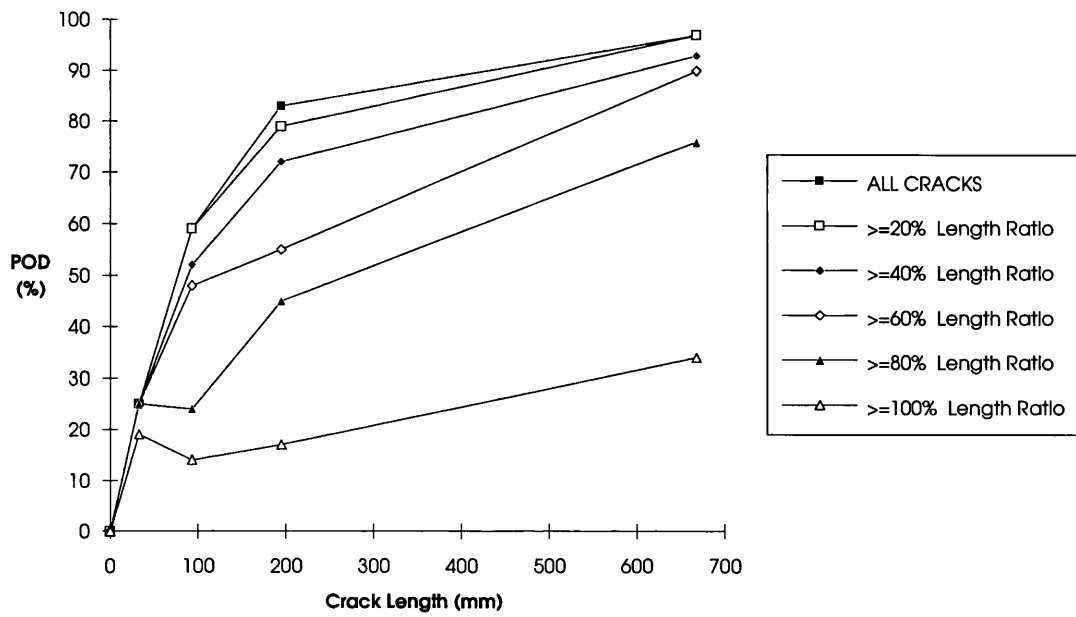


Figure 2.13 Hocking Eddy Current Inspection

Effect of Length Ratio on POD against Crack Length using Classification 'D'

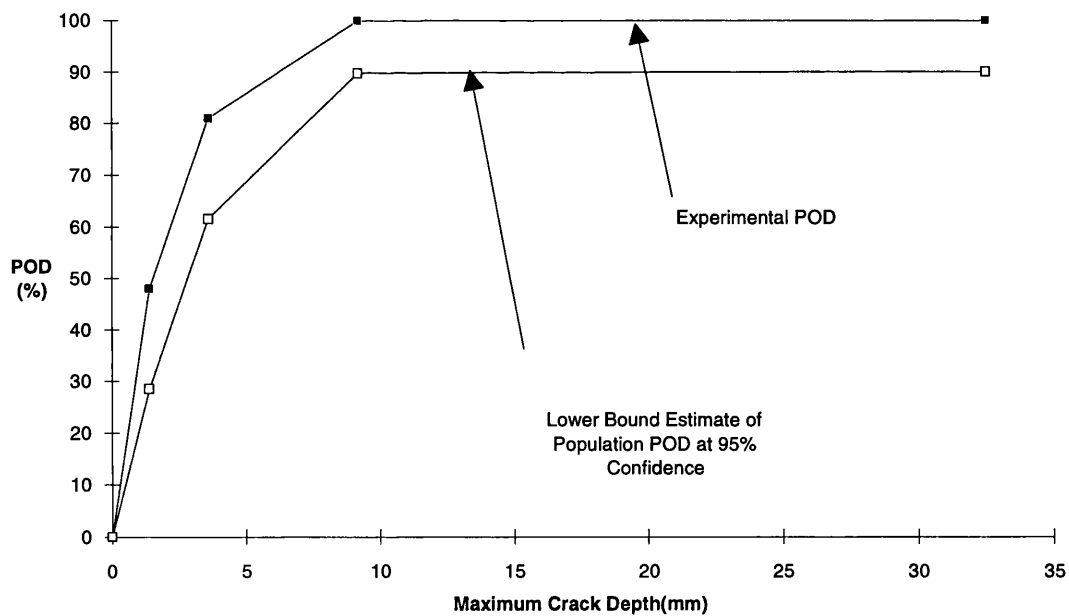


Figure 2.14 Magnetic Particle Inspection

POD against Maximum Crack Depth using Classification 'D'

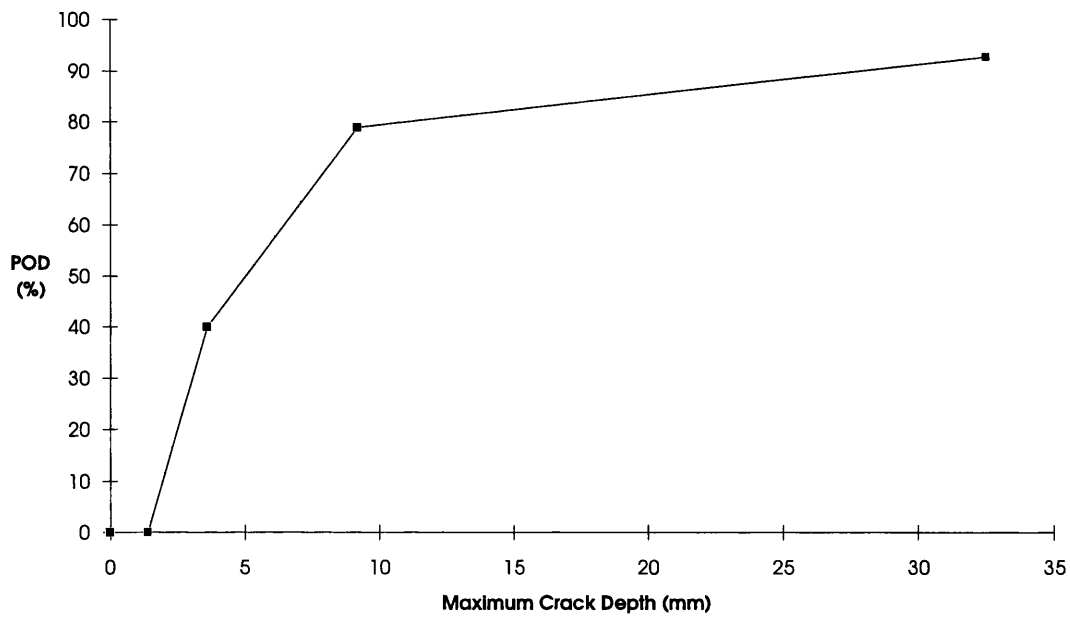


Figure 2.15 EMD III Eddy Current Inspection
POD against Maximum Crack Depth using Classification 'D'

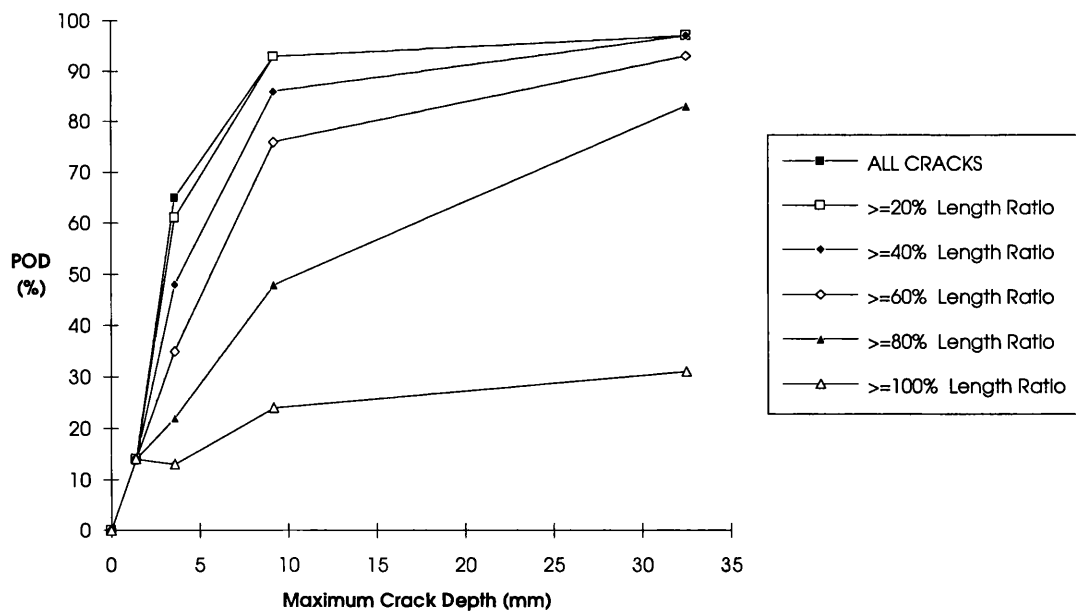


Figure 2.16 Hocking Eddy Current Inspection
Effect of Length Ratio on POD against Maximum Crack Depth using Classification 'D'

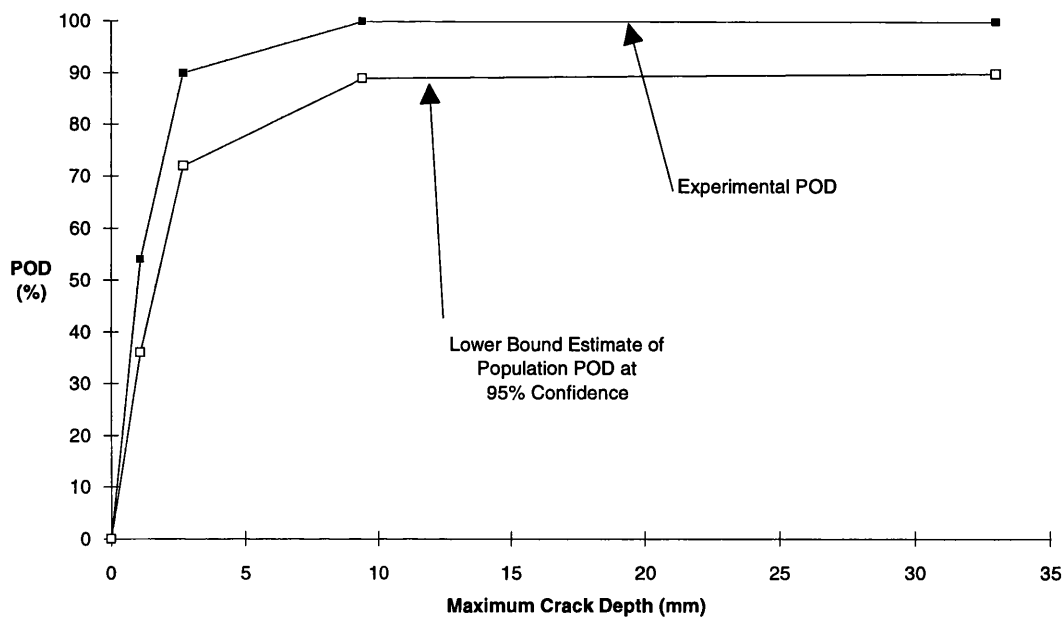


Figure 2.17 Magnetic Particle Inspection
POD against Maximum Crack Depth using Classification 'B'

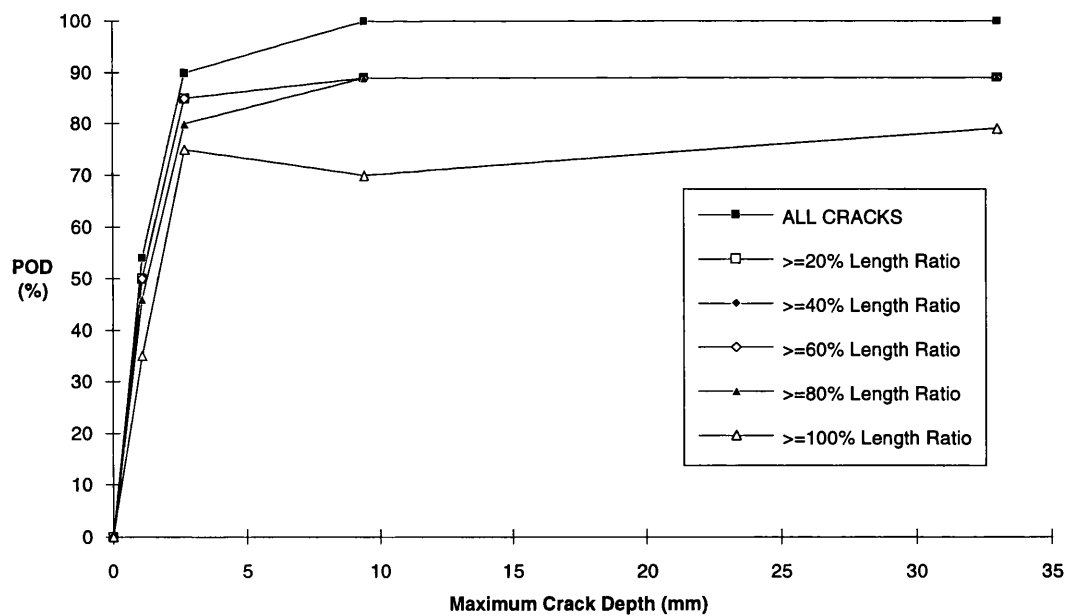


Figure 2.18 Magnetic Particle Inspection
Effect of Length Ratio on POD against Maximum Crack Depth using Classification 'B'

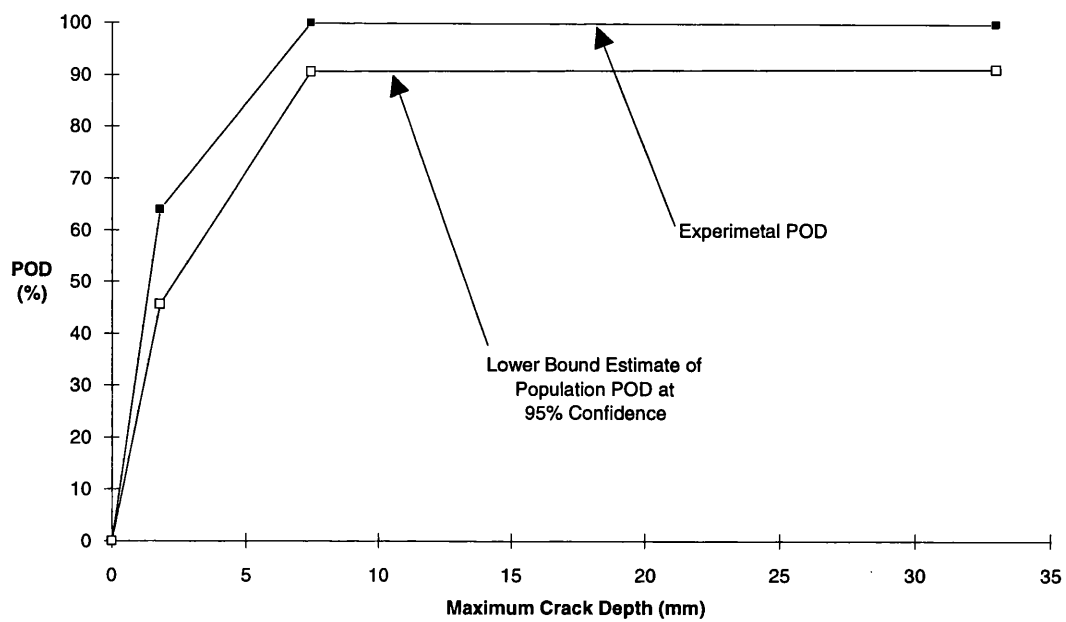


Figure 2.19 Magnetic Particle Inspection
POD against Maximum Crack Depth using Classification 'B1'

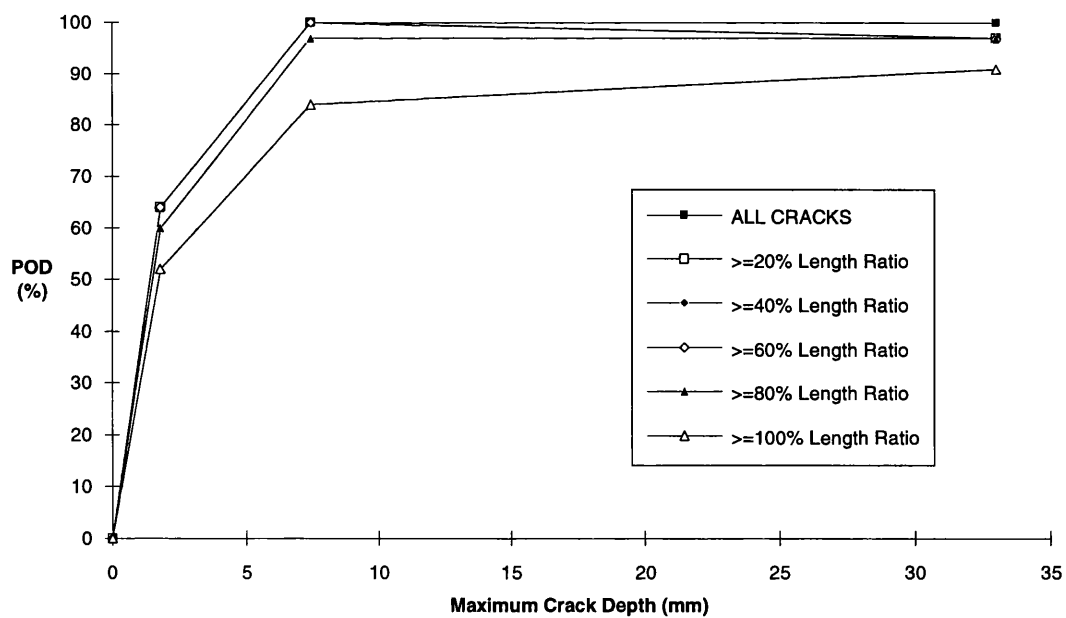


Figure 2.20 Magnetic Particle Inspection
Effect of Length Ratio on POD against Maximum Crack Depth using Classification 'B1'


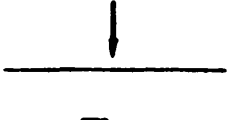




Characterisation	<p>Class B1 Dominant Crack</p> 	<p>Class B1 Dominant Crack</p> 	<p>Class B1 Dominant Crack</p> 	<p>Class B1 Dominant Crack</p> 
Detection				
Types of Missed Crack	<p>1 Class B1 Dominant Crack Detected nearby</p>	<p>2 Class B1 Dominant Crack Detected on Different Positions across the Weld</p>	<p>3 Class B1 Dominant Crack Missed</p>	<p>4 Class B1 Dominant Crack Missed nearby</p>

Figure 2.21 Types of Missed Cracks using Classification 'A'

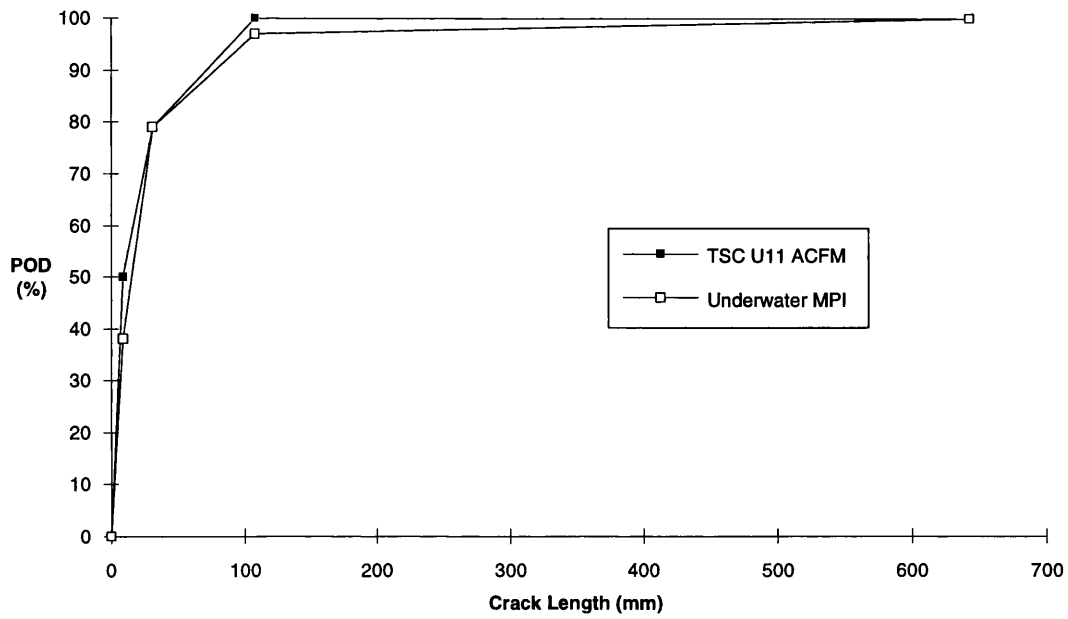


Figure 2.22 Comparison of TSC U11 ACFM and Underwater MPI
POD against Crack Length using Classification 'B1' for All Cracks

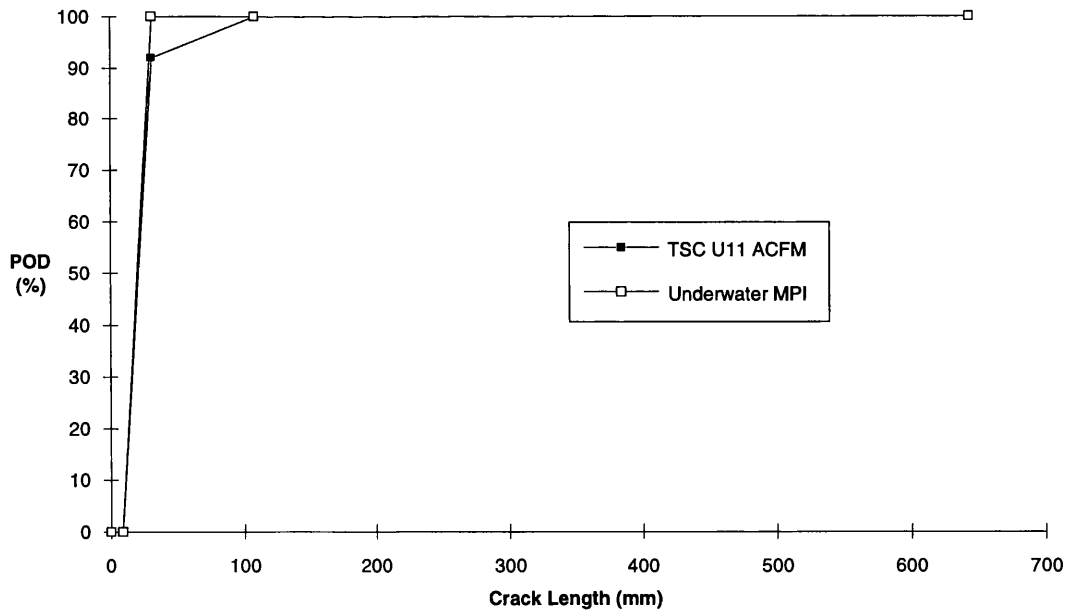


Figure 2.23 Comparison of TSC U11 ACFM and Underwater MPI
POD against Crack Length using Classification 'B1' for Cracks ≥ 1 mm deep

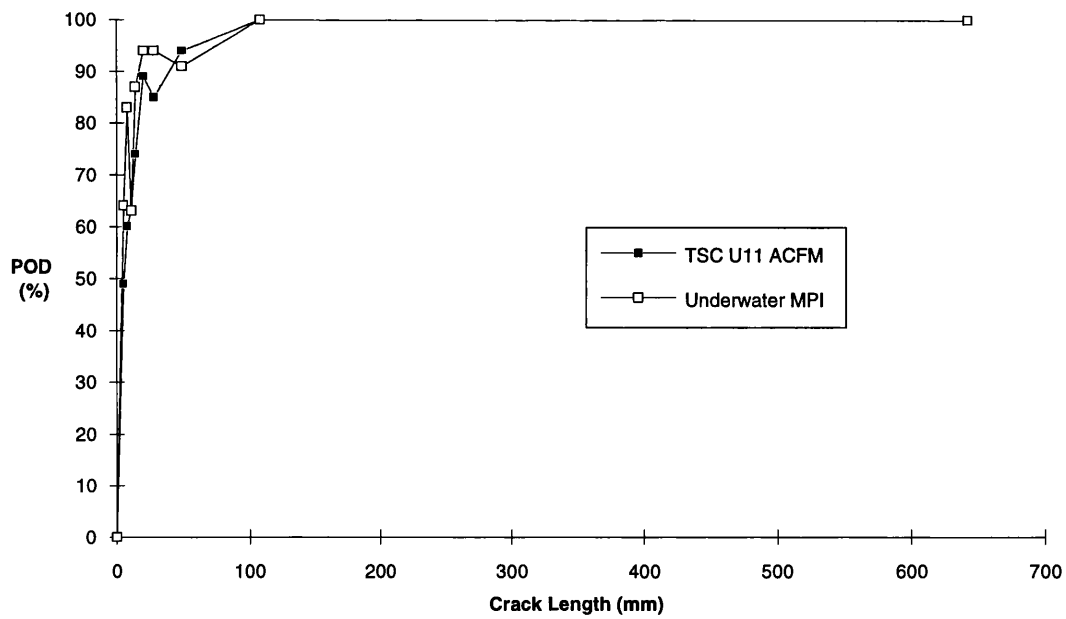


Figure 2.24 Comparison of TSC U11 ACFM and Underwater MPI
POD against Crack Length using Classification 'A' for All Cracks

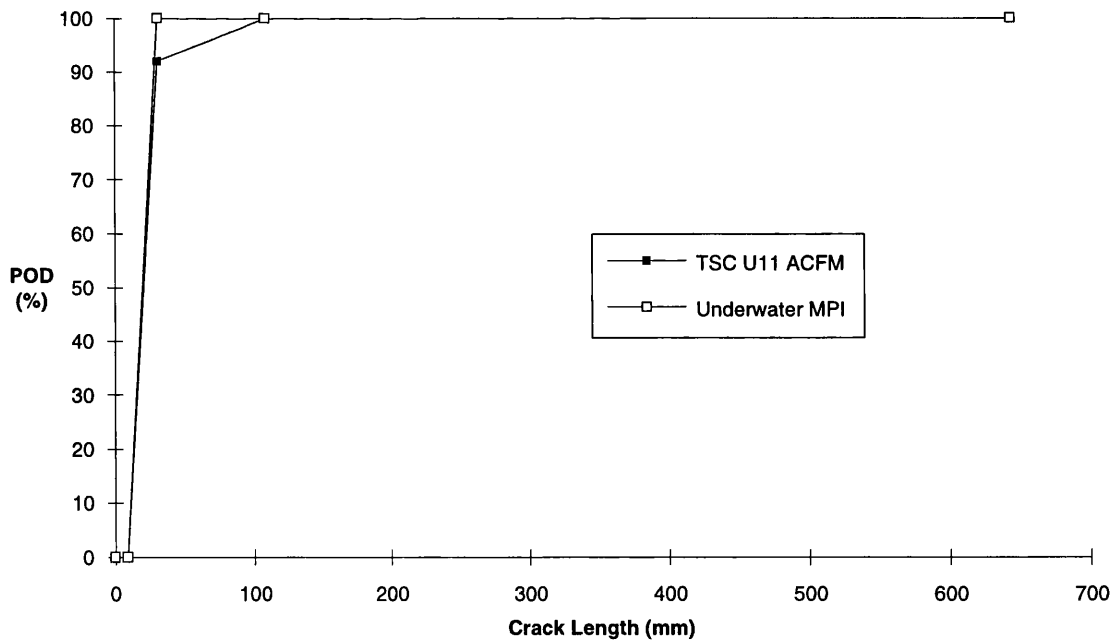


Figure 2.25 Comparison of TSC U11 ACFM and Underwater MPI
POD against Crack Length using Classification 'A' for Cracks ≥ 1.5 mm deep

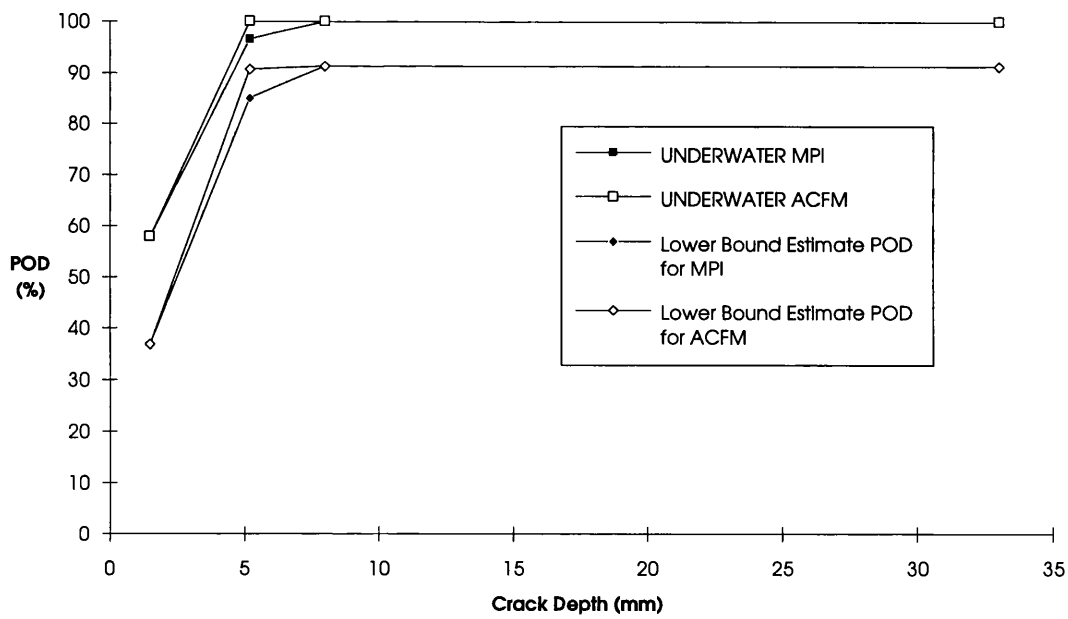


Figure 2.26 Comparison of POD against Crack Depth using Classification 'B1'
Between TSC U11 ACFM and Underwater MPI

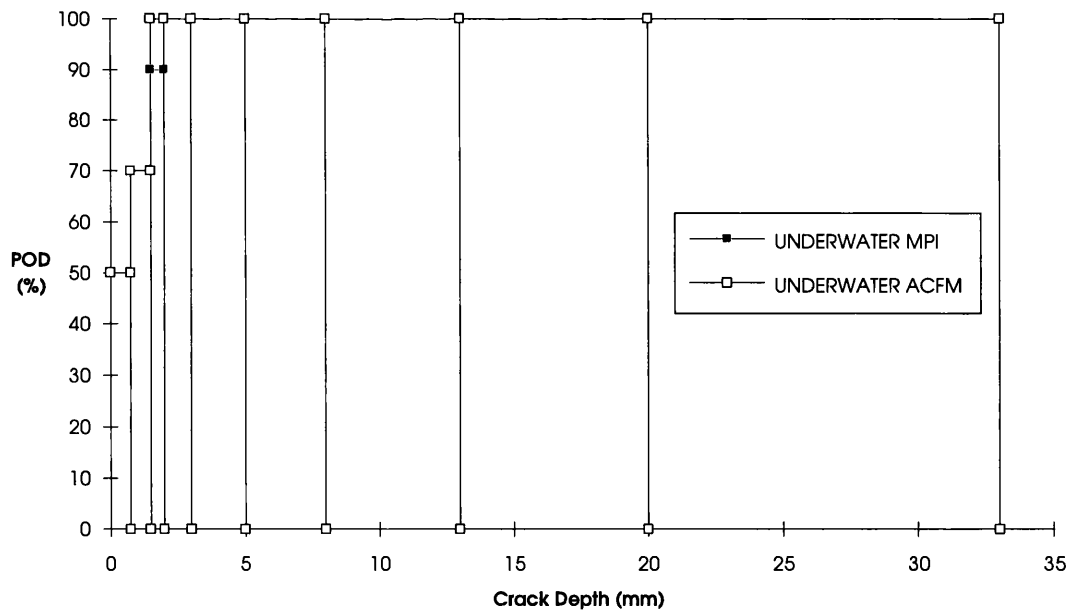


Figure 2.27 Comparison of Experimental POD against Crack Depth using Classification 'B1'
Between TSC U11 ACFM and Underwater MPI

CHAPTER THREE

STRESS CONCENTRATION FACTOR PARAMETRIC EQUATIONS FOR TUBULAR X AND DT-JOINTS

3.1 Introduction

Many kinds of offshore structures, such as jacket platforms, are constructed from tubular members welded together in a variety of forms (normally classified as T, Y, X, DT, K, etc.) because of their high strength to weight ratio and non-directional buckling and bending strength. The service life of these offshore platforms is dependent on the structural integrity of tubular joints. Fatigue damage has been identified as one of the most important factors in causing degradation of these joints in the North Sea because of the significant levels of cyclic fatigue damage associated with wave loading and the low fatigue strengths due to high stress concentrations at the weld toes. Therefore, periodic in-service inspections are required in order to ensure the structural integrity of offshore structures.

To provide a cost effective inspection, maintenance and repair policy, accurate fracture mechanics modelling, to predict the fatigue crack growth behaviour in tubular welded joints, is required. Fatigue strength is controlled by the local stress, and hence a greater understanding of the stress distribution, particularly in regions where cracks are likely to initiate and grow, is needed for the development of a fracture mechanics approach for the prediction of fatigue life. Stress information for tubular joints, including SCFs, stress distribution through the wall (degree of bending) and stress distribution around the intersection, are important elements in the prediction method.

The problem with tubular joints is that the stress distribution at the intersection between members is uneven with very high stress concentrations occurring at some points. These stresses can be as high as twenty times the nominal stress for the intersection and therefore have considerable impact upon the fatigue lives of the joints.

The fatigue performance of offshore tubular welded joints is also of considerable importance in the initial design. Historically, the fatigue design life is predicted using the Stress-Life(S-N) approach, which relates the stress range at a point under consideration to the number of cycles to failure. For tubular welded joints, the SCF can be used, with nominal loading, to calculate the magnitude of the local stress range, or as it is usually termed, the hot-spot stress range(HSS). HSS is a representative stress range for estimating the relative fatigue

strengths of tubular welded joints using an S-N approach. Therefore, much research effort has been directed towards the determination of SCFs for simple tubular joints.

Stress variation through the thickness and around the intersection has not attracted as much attention as SCFs. However, in order to conduct fracture mechanics calculations of remaining fatigue life on cracked tubular welded joints, information is required on the magnitude and distribution of the stress acting in the anticipated crack path, not just the peak stress at one location. It is therefore necessary to carry out a comprehensive study of stresses on various kinds of tubular welded joints.

For most design and re-certification work, parametric equations have been widely used to estimate the stresses and in particular the hot spot stresses for tubular joints. These equations are based on either extensive finite element (FE) stress analyses or experimental data from acrylic model tests. However, to date comprehensive stress studies have only been conducted on the Y and T-joints, using finite element method (Connolly et al 1990) (Hellier et al 1990 a) (Hellier et al 1990 b). For X and DT-joints as illustrated in Figure 3.1, there are some parametric equations for SCFs (Wordsworth 1987) (Efthymiou and Durkin 1988) (UEG 1985) (Smedley and Fisher 1991) but no equations exist for stress variation through the thickness and around the intersection. Even for SCF parametric equations, there is no full set of equations especially for single brace loading. Although in some cases one can get this information by using simplifying assumptions (i.e., using the solutions for Y and T-joints), but they may not always be appropriate. Also the three aspects of stress information should be obtained from the same sources in order to maintain the compatibility. All these considerations led to the present comprehensive study of stresses on X and DT-joints.

Nearly 2000 thin-shell finite element analyses have been conducted as a systematic study of stresses in tubular X and DT-joints. These analyses cover a wide range of joint geometries under six loading cases. This chapter aims to present the SCF parametric equations derived using regression analysis on the finite element analysis results. The parametric equations to predict the degree of bending and a full description of SCF distribution around the intersection will be addressed in the next chapter.

3.2 Finite Element Analyses

The determination of the stresses around tubular joints by analytical techniques, has proven to be very difficult due to the relative complexity of the geometrical configuration. Instead, parametric equations have been produced, which provide the SCF in terms of the non-dimensional parameters of joints, α , β , γ , τ , θ (see Figure 3.1). In practice for economical reason, only finite elements and the strain-gauged acrylic model techniques have been used to provide the input data for parametric equations.

The finite element method has been adopted in this study since this numerical procedure is ideal for solving physical problems, such as complex structural components, whose closed form solutions are difficult to obtain. It is by far the most common approach to determine the stress distribution and hot spot stress in tubular joints. The general-purpose finite element analysis package, ABAQUS/Standard(HKS 1992 a) was employed for this systematic study. ABAQUS/Post(HKS 1992 b) was used to post process the results from ABAQUS/Standard analyses.

Fatigue is a local phenomenon. It depends on the stresses acting around the intersection of tubular joints. These local stresses are complex in nature but are likely to arise from two main sources. Firstly, local bending under loading results in stresses adjacent to the intersection, known as the geometric stresses, in order to maintain compatibility between the tubes. They are dependent on geometric parameters of the joints, overall joint configuration and applied loading types. Secondly, notch stresses arise in highly localised regions in part of the tube wall since the weld toe is a region of rapidly varying shape. This effect is not propagated far through the wall thickness, however, and thus leads to a very localised region of high stresses. The notch stresses are mainly controlled by the weld geometry factors such as weld toe angle and weld toe radius.

The initial stresses inside the notch region, may be important for fatigue crack initiation. However they are not the controlling parameter as the cracks grow through the thickness. Also, as the notch stress varies according to the geometry of the weld, it is difficult to provide a deterministic value of the peak stress. For these reasons, only the geometric stresses at weld toe have been produced in this study. This is the conventional approach for SCF developed within the UK Department of Energy Guidance Notes(Department of Energy 1984 b). The hot-spot stress is defined as the largest value around the brace/chord intersection obtained by linear extrapolation to the weld toe of the geometric stress distribution near the weld toe. Ignoring the local stress arising from the weld profile, the hot spot stress is considerably lower than the peak stress but provides a consistent definition of fatigue stress for use with the traditional S-N design approach.

3.2.1 Pre-processing

3.2.1.1 Element Types

Shell elements are commonly used for tubular joint stress analysis, since they combine relatively high accuracy with low cost. Shell elements are based on shell theory which approximates a three-dimensional continuum with a two dimensional theory when the shell thickness is less than 1/10 of the typical shell global dimension. They are appropriate for modelling tubular joints. Shell elements are divided into two types, thin shell elements and

thick shell elements. The thin elements do not transmit shear forces, whereas the thick elements do. The choice of shell element type, thin or thick, is influenced by the importance of shear deformation in the structure. As the ratio of thickness to shell global dimension increase, shear deformation becomes more important. It has been shown (Connolly et al 1990) that there is little difference between results obtained using a thin shell finite element mesh and a thick shell element mesh for tubular joints since the ratio of wall thickness to diameter for tubular joints used for offshore structures are generally small (in other words, the tubes are thin walled). Thin-shell elements are commonly used for tubular joint analysis and have been chosen for this study.

The ABAQUS package offers a wide variety of shell elements. Two types of generally curved thin shell elements have been used to generate meshes for this study, namely quadrilateral eight-noded elements denoted 'S8R5' and triangular six-noded elements designated as 'STRI65'. They are fully compatible. These elements possess shape functions which make them suitable for any generally curved or folded shell problem and allows displacements normal to their surfaces and rotations about their edges. These displacements and rotations give rise to a stress distribution which varies linearly across the element. Stresses are initially calculated at the Gauss integration points and then extrapolated to obtain values at the nodal positions. The diagram of these elements are shown in Figure 3.2. They use five degrees of freedom (three displacement components u_x, u_y, u_z and two local in-surface rotation components ϕ_x, ϕ_y) at each node. In order to perform well in thin shell situations, a reduced integration technique is used with explicit integration through the element thickness. These elements are recommended for 'thin' shell applications since Kirchhoff constraints are imposed numerically in these elements.

One disadvantage in the use of shell elements for stress analysis in tubular intersections is that the tubular joints are modelled as intersecting cylindrical tubes at the mid-surfaces of the walls. Thus the weld is not modelled and some detail of the stresses are lost. This leads to hot spot stress locations which are different to steel models especially for the brace. For the chord the steel model location of the hot spot stress is close to that of the FE model. This is the reason why there are some discrepancies between the finite element results and those obtained from steel model test, especially at the brace side. However, the difference is generally quite small when comparing with results from strain-gauged acrylic models in which the weld is also omitted. The thin shell elements do provide, in many cases, an acceptable compromise between accuracy and computational cost except for situations where the chord and brace are of similar dimensions. For this reason the present study does not include SCFs in tubular joints for which β exceeds 0.8.

3.2.1.2 Mesh Generation

The main difficulty when using the finite element method is generation of the mesh, particular in regions where geometric discontinuities occur because stresses are changing rapidly in these regions. For the tubular joint, a geometric discontinuity occurs around the brace/chord intersection. Thus the stress gradients throughout the joint are not evenly distributed. Around the intersection the stress gradients are large, whilst in regions remote from the intersection the gradients are more evenly distributed.

In order to conduct a parametric study covering the majority of tubular joints used in offshore structures, a large number of finite element analyses must be performed. It is, therefore, preferable to use an automatic mesh generation program to produce the input files required for the ABAQUS finite element analysis. As mentioned before, this program should be capable of producing relatively fine elements in the vicinity of the brace/chord intersection, and coarse elements near the ends of the chord and brace, in order to obtain accurate results whilst avoiding unnecessary computational effect. Furthermore, the elements should not be excessively elongated and distorted in order to obtain the best numerical conditioning of the stiffness equations and to ensure maximum numerical accuracy.

An automatic mesh generation program for X and DT tubular joints (based on an existing program(Dharmavasan 1983) for T and Y tubular joints) has been developed in FORTRAN 77. This mesh generation program can reliably generate meshes for X and DT tubular joints having widely differing geometric parameters α , β , γ , τ and θ , and produce input files suitable for direct finite element analysis using ABAQUS/Standard. The program requires only a small amount of user input, usually only either absolute dimensions or non-dimensional geometric ratios.

When modelling the tubular joint, eight-noded quadrilateral elements were used in preference to triangular elements, since they are considerably more accurate. The latter were only used for reasons of geometric compatibility between adjoining regions. The sequence of steps executed in this mesh generation program was as follows. Firstly, the co-ordinates of the nodes at the intersection between the brace and chord were calculated and used to generate the brace nodes and elements. Secondly, the plug region was filled with a number of triangular elements. Thirdly, the remaining regions of the chord were generated.

Application of symmetry boundary conditions can simplify the finite element analysis saving CPU time and storage disk space. Only one half of each joint geometry needs to be modelled, owing to symmetry in the single/balanced axial loading and single/balanced in-plane bending cases. Although for single/balanced out-plane bending the situation is no longer symmetric, it was found(Connolly et al 1990) that satisfactory results could be obtained with the same meshes used for the other load cases by applying appropriate

restraints on the bisecting plane. A typical X joint mesh comprising 2167 nodes and 718 elements is shown in Figure 3.3. It took approximately 45 seconds of CPU time to generate on a DEC VAX/VMS workstation.

3.2.1.3 Loading and Boundary Conditions

There are two types of loading on tubular joints, single brace loading and double brace loading. The former loads are assumed to be axial loading, in-plane bending(IPB) and out-plane bending(OPB). Only balanced axial loading, balanced IPB and balanced OPB are considered in the latter since they are quite common in service. Figure 3.4 illustrates these six modes of loading.

In the case of single/balanced axial loading, the nominal stress was defined as the total applied load divided by the sectional area of the brace. Nominal stresses for moment loading were calculated from simple beam bending theory, using a moment arm measured from the brace end along its outer surface to the crown position for IPB, and to the saddle position for OPB. In order to make post processing easy, loads and moments applied to the brace end were always set to give unit nominal stress.

It is important to use the correct boundary conditions to obtain a realistic solution of stress distribution in tubular joints. The boundary conditions are summarised diagrammatically in Figure 3.5. The bottom brace end was rigidly fixed for balanced axial loading whereas both chord ends were rigidly fixed for all other load cases. Only one half of the joint was modelled owing to symmetry in the single/balanced axial and the single/balanced IPB cases, with no out-of-plane displacements and rotations permitted at nodes on the symmetry plane. For single/balanced OPB the situations are no longer symmetrical, but it has been found(Connolly et al 1990) that results of acceptable accuracy could be obtained by using the half-joint meshes with the in-plane displacements restrained over the bisecting plane.

3.2.2 Finite Element Calculation

The finite element analyses were run on a DEC VAX/VMS workstation. Young's modulus and Poisson's ratio were taken to be 207 Gpa and 0.3 respectively. Before the parametric study, a convergence test was performed in order to check that the meshes used for this study were sufficiently fine to predict the stresses at the brace/chord intersection with reasonable accuracy. Three meshes with 16, 20 and 24 elements respectively around the half intersection were analysed and the SCF results from these meshes are compared in Table 3.1. Comparison of SCF values obtained from these meshes generally has shown a good convergence. The coarsest mesh, having 16 elements around one half of the intersection,

was chosen for this study as an acceptable compromise between accuracy and the computational costs.

3.2.2.1 The Influence of brace length

Early studies showed that for balanced axial loading, the intersection stresses on either side were not identical. This was because only one brace end was rigidly fixed. It was found that a longer brace was needed in order to make the stresses on both sides of the chord identical. In order to save materials, most laboratory tests on joints have relatively short braces, these have been used to produce the experimental results which are used to assess parametric equations. The majority of tubular joints in offshore structures have relatively long braces. For this reason an additional study of the brace length effect on stress analyses of tubular joints has been conducted.

The geometric ratio $\alpha_b = 2l/d$ has been chosen to assess the effect of brace length on SCFs around the intersection, where l is the brace length (from centre of brace end to centre of plug) and d is the diameter of brace. A comparison of SCF distribution data for the tubular X-joints, with different α_b under single brace loading, is shown in Figures 3.6-3.11. These figures show that there is a critical α_b beyond which SCF data converge very quickly and α_b has little influence. For this case, critical α_b is about 6 and the corresponding l is around $0.36L$. This is probably the reason why α_b has not been included in any existing parametric equation. However, when α_b is below the critical α_b , the hot-spot stress can be under predicted for Axial and OPB loading and over predicted for IPB Loading. It is advisable that the α_b ratios of the tubular joints of SCF values be considered when comparing with the experimental database.

In the present study, it was decided to avoid the effect of short brace length. For this reason, joints with a brace length of about $0.4L$ were used. The long brace length did not increase the calculation work since coarse elements were used near the end of brace.

3.2.2.2 Parametric Finite Element Production

In order to produce parametric equations which are valid over the ranges of geometric joint parameters typically encountered in service, this study encompassed the following ranges of the geometric parameters:

$$6.0 \leq \alpha \leq 40.0 \quad (3-1)$$

$$0.2 \leq \beta \leq 0.8 \quad (3-2)$$

$$7.6 \leq \gamma \leq 32.0 \quad (3-3)$$

$$0.2 \leq \tau \leq 1.0 \quad (3 - 4)$$

$$0.1944\pi \leq \theta \leq \frac{\pi}{2} \quad (3 - 5)$$

Within the above parameter ranges, 330 joints were carefully chosen to give a representative coverage of joint sizes. In order to save CPU time, each joint was analysed consecutively for six load cases, without the need for recomputing the element stiffness matrices. Generally, it took about 3 hours of CPU time to analyse a typical joint. Figures 3.12-3.17 show typical examples of the deformed mesh superimposed upon the unloaded mesh for all modes of loading.

3.2.3 Post-processing

Stresses are linearly extrapolated through the Gauss integration points to the nodes by the nature of the elements chosen. The numerically greatest principal stress on the outer surface of the tube, at each node around the intersection, was used to calculate the SCF. Stresses at nodes shared by adjacent elements were averaged around, but not across the intersection. Since nominal stresses of value unity were chosen for the input files, the values of SCFs were obtained directly on both the chord and brace sides of the intersection from finite element output files.

The definition of hot-spot stress by Department of Energy (DEn) proposes linear extrapolation of the maximum principal stresses, outside the region of weld geometrical influence, to the weld toe. The sizes of the elements in the immediate vicinity of the intersection were carefully checked in order to make the linear stress distribution region similar to that as DEn recommend. However, shell elements are two-dimensional in nature, possessing thickness only in a mathematical sense needed to define the element stiffness matrix. A tubular joint analysed using these elements is actually modelled as the intersection between the brace and chord mid planes and the weld fillet can not be incorporated into this model. This means that the intersection stresses are calculated a small distance away from the point of interest. For the chord this distance is usually quite small. However it is relatively large for the brace. Therefore, it is necessary to verify the results by validating against the laboratory data and this will be addressed in later section.

In order to handle the large amount of data generated by the finite element runs, many batch files in VMS operating system have been written in order to read the required information from 330 ABAQUS output files and write them into a file which was used later in curve-fitting.

3.3 Deriving Parametric Equations by Regression Analyses

Using the database of finite element analysis results, parametric equations can be derived for the SCFs under six loading cases for both the chord and brace sides of the intersection. This was done using a statistical regression package known as 'MINITAB'(1991) which is capable of performing multiple regression and correlation analysis. The methodology used in deriving the equations was as follows.

a) The variations of the SCF were plotted as a function of the parameters α , β , γ and τ and θ in order to determine the best forms of the terms required, and also to ascertain if any cross-correlation existed between the terms.

b) A first attempt at the equation was made using the following simple form:

$$SCF = A_1 \alpha^{A_2} \beta^{A_3} \gamma^{A_4} \tau^{A_5} \theta^{A_6} \quad (3 - 6)$$

where A_1 to A_6 were determined from the regression analysis.

c) The above equations were then modified by using other (e.g. exponential) terms, and numerous regressions performed until a suitable equation with a large product moment correlation coefficient was obtained.

All the parametric equations obtained for each mode of loading and for both the chord and brace sides of the intersection are given in Appendices 1 to 12. These equations can predict the SCFs for tubular welded X and DT joints at a number of key locations around the brace and chord intersection. Also the equations describing angular location of the hot-spot stress site around the intersection are derived according the above regression methodology. Moreover, a summary of fitting quality for each parametric equations is presented in Table 3.2. For most equations, their correlation coefficient R^2 is greater than 90%, where a value of $R^2=100\%$ would imply that the equation fitted exactly all the variations in SCF.

It should be noted that all equations assume the loading direction shown in Figure 3.4. Therefore under single/balanced IPB loading negative hot-spot is at or close to crown toe while positive hot-spot lie at or near crown heel. In these loading cases, the SCFs on both brace and chord saddle positions were taken to be zero since they are generally very small. For the same reason, the SCFs on both brace and chord crown positions were also zero for single/balanced OPB cases. The hot-spot location in these loading cases was taken to be 90° because they were close to the saddle position. In order to avoid a large underprediction, a minimum SCF value of 1.5 was assigned irrespective of the prediction.

3.4. Validation

During the design stage, hot-spot stresses are usually estimated from parametric equations to assess the fatigue performance of tubular joints by an S-N approach. Underprediction of hot-spot stress can result in a significant reduction on fatigue life. It is therefore useful to examine the accuracy of prediction for all SCF parametric equations including this new set of parametric equations(UCL).

The most widely used equations for X and DT-joints are the Wordsworth and Smedley(WS)(Wordsworth 1987), Efthymiou(EFT)(Efthymiou and Durkin 1988), Wordsworth and Smedley as modified by UEG(UEG)(1985) and Lloyds Register(LR)(Smedley and Fisher 1991). Of these equations those by Efthymiou are based on 3-D shell finite element models. The Wordsworth and Smedley equations are based on results of acrylic model tests, and UEG equations are based on the Wordsworth and Smedley equations with modifications based on the comparison of the equations with steel joint data. Lloyds Register equations are derived recently and are based on the database of measured SCFs from steel and acrylic joints.

One way to assess the accuracy of parametric equations is to compare the predicted data with existing strain-gauged steel test results. Unfortunately, the amount of steel data for X and DT-joints is limited. For this reason the data from acrylic model test are often used as well. A steel and acrylic test database based on the Lloyds Register data and the UCL database (with the criteria developed for acceptance of SCF data) was established by MaTSU(1996). By comparing the results derived from all parametric equations against the database, the performances of all existing SCF parametric equations can be assessed. This was done recently by the Fatigue Guidance Review Panel supported by the HSE(DEn.)(MaTSU 1996). During the review, it was decided that only those recorded SCFs greater or equal to 1.5 would be included in the assessment. Also for each equation, ratios of predicted SCF(P) to the measured or recorded SCF(R) were determined for those joints having their geometric parameters within the recommended range of the particular equation. A ratio of 1.0 indicates an exact fit. The mean values of P/R were calculated, together with the standard deviation. In addition the percentage of joints for which P/R was less than both 1.0 and 0.8 was determined, representing the degree of underprediction of each equation. The percentage of joints for which $P/R > 1.5$ was also recorded, indicating the degree of overprediction. These values are given in table 3.13-3.21 for each combination of load case and measuring position.

Finally recommendations on the most suitable equations for use in design were made according to following criteria of acceptance.

i) If $\%[P/R < 1.0] \leq 25\%$ and $\%[P/R < 0.8] \leq 5\%$ then accept the parametric equation.

ii) If in addition to the above, $\%[P/R > 1.5] \geq 50\%$ then note the equation is generally conservative.

iii) If $\%[P/R < 1.0]$ is between 25% to 30% and/or the percentage of joints with values of $P/R < 0.8$ is slightly in excess of 5% then the equation was regarded as borderline and engineering judgement was used in assessing the validity of the equation. Otherwise the equation was rejected, since it was considered not acceptable.

Similar procedures and criteria to those described above have been adopted to validate this new set of parametric equations(UCL). Firstly, the prediction data from UCL equations together with other existing parametric equations are used to compare with steel and acrylic test results in order to test the relative accuracy. The results were all assessed in terms of the ratio P/R . Moreover, statistical properties such as mean, standard deviation, $\%[P/R < 0.8]$, $\%[P/R < 1.0]$ and $\%[P/R > 1.5]$ were also calculated. Based on these data, comments can be made about the performance of new UCL equations as a results of using the above criteria. Also these values were used to compare with those of other equations to test the relative accuracy. The assessment of the UCL equations is presented for each mode of loading in turn in following sections.

3.4.1 Single Brace Loading

For single brace subject loading modes, there are not enough test data to assess the accuracy of UCL parametric equations. Only a few strain-gauged steel test data for single brace subject IPB or OPB(Mshana 1993)(Smith 1995) can be found. Despite this the data have been used to compare the results from UCL parametric equations with Efthymiou equations(Tables 3.3-3.5). It should be noted that a number of SCFs for a given location on joints with same geometry were all included. Other than UCL, the Efthymiou set of equations is the only set of equations considering single brace subject loading. However, the Efthymiou equations are identical to those for T/Y-joints for IPB and OPB loading. From Tables 3.3-3.5 it can be seen that UCL predictions are consistently conservative when compared with these small set of steel test data. The predictions from the Efthymiou equations are generally slightly lower than those from UCL formulae (3 out of 4 cases studied).

3.4.2 Balanced Axial Loading

The comparison between the UCL equations and the steel and acrylic model results (together with other parametric equations) is shown in Tables 3.6-3.9 for balanced axial loading. The test results were obtained for models within the validity range of UCL equations. The statistical analyses were done for UCL equations at crown and saddle

positions for the brace and chord side respectively and are given in Tables 3.14-3.17 together with those of other parametric equations. All equations are accepted for brace saddle point (Table 3.15). However the UCL equation is regarded as conservative borderline whilst the Efthymiou one is only accepted as borderline unconservative. Table 3.17 shows that all of the equations except the Lloyds Register pass the criteria for chord saddle. For both brace and chord crown positions, UCL equations (Tables 3.14 & 3.16) cannot yet be recommended since there are less than 15 steel and acrylic joints in the SCF database. However, there is a tendency for the UCL equations to underpredict SCF data for the chord crown. A large underprediction of SCF, by 40%, for the chord crown was also found in previous work (Hamilton 1984). It seems that thin shell element method cannot model physical intersection of X and DT joints under balanced axial loading properly over a region near the chord crown. The UCL equation for a single brace subjected to axial loading (UCLS) at the chord crown was used to compare with the test database, although both chord ends were rigidly fixed in this loading case. The predictions were very much improved by using the UCLS equations. Therefore, the UCLS may be suggested to be used as a useful first estimate for SCF at the chord crown location.

3.4.3 Balanced IPB Loading

The test results and SCFs obtained from UCL and other equations are compared in Tables 3.10-3.11 for balanced IPB loading. The statistical analysis results for UCL equations at maximum SCF positions for the brace and chord side are given in Tables 3.18-3.19 together with those of other equations. It can be seen that UCL equations meet the given criteria like other equations on the chord side. On the brace side, the UCL equation is acceptable as it is not quite as conservative as the WS and UEG equations.

3.4.4 Balanced OPB Loading

Tables 3.12-3.13 contain the comparisons between the test results and SCFs values predicted by UCL and other equations for balanced OPB. Again the statistical properties of UCL equations were obtained at maximum SCF positions for brace and chord sides and are given in Tables 3.20-3.21 together with those of other equations. These tables show that UCL equations pass the criteria on both chord and brace sides like all of the other equations.

3.4.5 Summary

Predicting accurately hot-spot stresses is very important as existing S-N curves to estimate the fatigue life of tubular joints are based on those values. The finite element analysis is

virtually the only feasible numerical technique which can be used to compute SCFs of tubular joints(UEG 1985). Based on the results of the finite element analyses, the SCF parametric formulae, such as Kuang(Kuang et al. 1977), Gibstein(1978), Efthymiou(Efthymiou and Durkin 1988) and Hellier, Connolly and Dover(1990), have been widely used on current methods of design and assessment of offshore steel structures. The UCL equations were derived from the results of the stress linearly distributed thin-shell finite element analyses which do not include a weld fillet at the tubular joint intersection. This is the same as most of the equations quoted above. The SCFs used to derived the formulae were the maximum principal stresses at all locations.

The results show that using either 3D FE, shell element FE or strain gauged acrylic model data did not confer a consistent advantage in the prediction of SCF. In contrast the results show that all three methods of analysis can give acceptable accuracy in SCF prediction. For the new UCL equations, the predictions look to be acceptable across the range studied, except for the chord crown under balanced axial loading where single brace axial loading equation(UCLS) is recommended as a useful first estimate. Thus one could use any of the five quoted equations for calculation of SCF. However only in the case of the UCL equations will there be a set of parametric equations for the bending to membrane ratio and stress distribution obtained from the same database. Thus the new UCL equations are suitable for S/N calculations and remaining life fracture mechanics calculations.

As a summary of validation results, it can be seen that there are not enough data to assess UCL equations for single brace loading and those at the crown location for balanced axial loading. However, they can be used as a useful first estimate. The UCL equations are consistent in meeting the given criteria for estimating hot-spot SCFs for balanced loading. Hence they can be used in fatigue design and reassessment of offshore welded tubular X and DT-joints.

3.5 Conclusions

A systematic study of stresses in tubular X and DT joints based on nearly 2000 finite element analyses using thin-shell elements have been carried out. The results have been used to derive a full set of SCF parametric equations by regression analysis. These equations describe SCFs at a number of key locations as a function of non-dimensional joint geometric ratios α , β , γ , τ and θ for each mode of loading, and for both the chord and brace sides of the intersection in tubular welded X and DT joints. In order to test the accuracy, these parametric equations have been assessed by comparing the predicted values with results from steel and acrylic model tests and also with other predictions from existing parametric formulae given in the literature. It is concluded that this set of hot-spot SCF

equations can be used to predict hot-spot SCFs of tubular X and DT-joints under balanced loading.

Table 3.1 Comparison Between SCFs around Upper Intersection from Coarse to Fine X Joint Meshes to Show Extent of Convergence ($\alpha=10$, $\beta=0.6$, $\gamma=20$, $\tau=0.5$, $\theta=60^\circ$)

No. of elements around intersection	Chord		Brace	
	Crown Toe	Saddle	Crown Toe	Saddle
Single Axial Loading				
16	2.631	7.386	2.307	8.044
20	2.638	7.372	2.392	8.106
24	2.643	7.368	2.435	8.120
Single In-Plane Bending				
16	2.437	0.1583	2.843	0.000
20	2.439	0.1588	2.941	0.000
24	2.436	0.1588	2.990	0.000
Single Out-Plane Bending				
16	0.1851	6.540	0.3127	7.366
20	0.2072	6.524	0.2980	7.421
24	0.2220	6.512	0.2881	7.429
Balanced Axial Loading				
16	1.013	12.16	1.750	12.58
20	1.021	12.14	1.818	12.66
24	1.036	12.13	1.860	12.66
Balanced In-Plane Bending				
16	2.436	0.2048	2.862	0.000
20	2.438	0.2043	2.960	0.000
24	2.435	0.2038	3.009	0.000
Balanced Out-Plane Bending				
16	0.1811	6.351	0.3142	7.034
20	0.2024	6.336	0.2984	7.077
24	0.2164	6.325	0.2878	7.081

Table 3.2 Summary of Fitting Accuracy for SCF Parametric Equations

Location	Brace		Chord	
Circumferential position	R ² %	Equation	R ² %	Equation
Single Axial Loading				
Crown toe	81	Appendix A1.1	93.1	Appendix A2.1
Saddle	97.4	Appendix A1.2	97.4	Appendix A2.2
Crown heel	84.3	Appendix A1.3	92	Appendix A2.3
Hot-spot site	97.8	Appendix A1.4	97.6	Appendix A2.4
Position of hot-spot stress	90.1	Appendix A1.5	84.2	Appendix A2.5
Single In-Plane Bending				
Crown toe	88.2	Appendix A3.1	97.2	Appendix A4.1
Crown heel	84.6	Appendix A3.3	97.4	Appendix A4.3
Positive hot-spot site	95.3	Appendix A3.4	97	Appendix A4.4
Negative hot-spot site	93.7	Appendix A3.5	97.4	Appendix A4.5
Position of hot-spot stress	85.1	Appendix A3.6	82.2	Appendix A4.6
Position of hot-spot stress	83.5	Appendix A3.7	85.2	Appendix A4.7
Single Out-Plane Bending				
Saddle	97.2	Appendix A5.2	97.8	Appendix A6.2
Hot-spot site	97.2	Appendix A5.4	97.8	Appendix A6.4
Balanced Axial Loading				
Crown toe	88.1	Appendix A7.1	90.2	Appendix A8.1
Saddle	97.2	Appendix A7.2	97.4	Appendix A8.2
Crown heel	82.9	Appendix A7.3	85.6	Appendix A8.3
Hot-spot site	97.8	Appendix A7.4	97.8	Appendix A8.4
Position of hot-spot stress	86.9	Appendix A7.5	79.5	Appendix A8.5
Balanced In-Plane Bending				
Crown toe	89.7	Appendix A9.1	97.8	Appendix A10.1
Crown heel	86.7	Appendix A9.3	97.8	Appendix A10.3
Positive hot-spot site	95.3	Appendix A9.4	97.2	Appendix A10.4
Negative hot-spot site	93.7	Appendix A9.5	97.8	Appendix A10.5
Position of hot-spot stress	88	Appendix A9.6	81.1	Appendix A10.6
Position of hot-spot stress	84.8	Appendix A9.7	82.3	Appendix A10.7
Balanced Out-Plane Bending				
Saddle	95.8	Appendix A11.2	96.8	Appendix A12.2
Hot-spot site	95.8	Appendix A11.4	96.8	Appendix A12.4

Table 3.3 Comparison Between Predicted and Recorded SCF Data at Chord Crown Position for Single IPB Loaded X and DT-Joints

Ref.	Spec. no.	α	β	γ	τ	θ (deg)	Materials	Rec	UCL	EFT	UCL/Rec	EFT/Rec
Mshana 1993	IPB-1A	7.84	0.64	10.2	0.5	90	Steel	1.76	2.18	1.72	1.24	0.98
Mshana 1993	IPB-2A	7.84	0.64	10.2	0.5	90	Steel	1.76	2.18	1.72	1.24	0.98
Mshana 1993	IPB-1B	7.84	0.64	10.2	0.5	90	Steel	1.47	2.18	1.72	1.48	1.17
Mshana 1993	IPB-2B	7.84	0.64	10.2	0.5	90	Steel	1.68	2.18	1.72	1.30	1.03

Table 3.4 Comparison Between Predicted and Recorded SCF Data at Brace Saddle Position for Single OPB Loaded X and DT-Joints

Ref.	Spec. no.	α	β	γ	τ	θ (deg)	Materials	Rec	UCL	EFT	UCL/Rec	EFT/Rec
Smith 1995	W2	9.90	0.80	10.00	0.99	90	Steel	4.80	8.59	8.13	1.79	1.69
Smith 1995	W4	9.90	0.80	10.00	0.99	90	Steel	4.70	8.59	8.13	1.83	1.73

Table 3.5 Comparison Between Predicted and Recorded SCF Data at Chord Saddle Position for Single OPB Loaded X and DT-Joints

Ref.	Spec. no.	α	β	γ	τ	θ (deg)	Materials	Rec	UCL	EFT	UCL/Rec	EFT/Rec
Mshana 1993	OPB-1A	7.84	0.64	10.2	0.5	90	Steel	3.81	4.27	4.65	1.12	1.22
Mshana 1993	OPB-2A	7.84	0.64	10.2	0.5	90	Steel	3.09	4.27	4.65	1.38	1.50
Mshana 1993	OPB-1B	7.84	0.64	10.2	0.5	90	Steel	3.00	4.27	4.65	1.42	1.55
Mshana 1993	OPB-2B	7.84	0.64	10.2	0.5	90	Steel	3.66	4.27	4.65	1.17	1.27
Smith 1995	W1/W5	9.90	0.80	10.00	0.99	90	Steel	6.50	10.25	9.21	1.58	1.42
Smith 1995	W2	9.90	0.80	10.00	0.99	90	Steel	6.70	10.25	9.21	1.53	1.37
Smith 1995	W3/W6	9.90	0.80	10.00	0.99	90	Steel	6.70	10.25	9.21	1.53	1.37
Smith 1995	W4	9.90	0.80	10.00	0.99	90	Steel	6.40	10.25	9.21	1.60	1.44
Smith 1995	S1	9.90	0.80	10.00	0.99	90	Steel	6.40	10.25	9.21	1.60	1.44
Smith 1995	S2	9.90	0.80	10.00	0.99	90	Steel	6.00	10.25	9.21	1.71	1.53
Smith 1995	S3	9.90	0.80	10.00	0.99	90	Steel	6.60	10.25	9.21	1.55	1.39
Smith 1995	S4	9.90	0.80	10.00	0.99	90	Steel	6.20	10.25	9.21	1.65	1.48

Table 3.6 Comparison Between Predicted and Recorded SCF Data at Brace Crown Position for Balanced Axially Loaded X and DT-Joints

Spec. no.	α	β	γ	τ	θ (deg)	Materials	Rec	UCL	WS	EFT	UEG	LR	UCL/ Rec	WS/ Rec	EFT/ Rec	UEG/ Rec	LR/ Rec
E30	9.80	0.38	20.70	0.79	90	Steel	1.50	3.16	3.36	2.35	3.39	2.04	2.11	2.24	1.57	2.26	1.36
E36	9.80	0.38	20.50	0.81	90	Steel	1.70	3.16	3.40	2.36	3.43	2.05	1.86	2.00	1.39	2.02	1.21
E37	9.80	0.38	21.00	0.83	90	Steel	1.60	3.12	3.48	2.34	3.50	2.08	1.95	2.17	1.46	2.18	1.30
1U/1	10.00	0.26	12.00	0.75	90	Acrylic	1.70	3.93	3.10	2.96	3.10	1.95	2.31	1.82	1.74	1.82	1.15
1U/2	10.00	0.50	12.00	0.75	90	Acrylic	2.00	2.78	2.56	2.49	2.56	1.73	1.39	1.28	1.24	1.28	0.86
1U/3	10.00	0.80	12.00	0.75	90	Acrylic	1.70	1.50	1.89	2.35	1.89	1.54	0.88	1.11	1.38	1.11	0.90
1U/5	10.00	0.26	24.00	0.75	90	Acrylic	2.80	4.50	3.79	2.92	3.79	2.35	1.61	1.35	1.04	1.35	0.84
1U/9	10.00	0.26	32.00	0.75	90	Acrylic	3.40	4.19	4.15	2.88	4.34	2.58	1.23	1.22	0.85	1.28	0.76
2U/1	10.00	0.80	24.00	0.75	60	Acrylic	1.80	1.50	2.30	1.50	2.30	1.76	0.83	1.28	0.83	1.28	0.98

Table 3.7 Comparison Between Predicted and Recorded SCF Data at Brace Saddle Position for Balanced Axially Loaded X and DT-Joints

Spec. no.	α	β	γ	τ	θ (deg)	Material s	Rec	UCL	WS	EFT	UEG	LR	UCL/ Rec	WS/ Rec	EFT/ Rec	UEG/ Rec	LR/R ec
A	8.50	0.72	10.40	0.94	90	Steel	7.50	14.52	10.90	8.38	11.10	8.64	1.94	1.45	1.12	1.48	1.48
E30	9.80	0.38	20.70	0.79	90	Steel	10.60	22.70	15.30	14.13	15.44	15.04	2.14	1.44	1.33	1.46	1.46
E36	9.80	0.38	20.50	0.81	90	Steel	14.30	23.01	15.52	14.16	15.68	15.21	1.61	1.09	0.99	1.10	1.10
E37	9.80	0.38	21.00	0.83	90	Steel	12.40	24.03	16.24	14.65	16.36	16.02	1.94	1.31	1.18	1.32	1.32
X4	17.50	0.67	25.30	0.82	90	Steel	15.00	29.61	22.96	18.72	23.14	22.94	1.97	1.53	1.25	1.54	1.54
1U/1	10.00	0.26	12.00	0.75	90	Acrylic	7.60	13.10	6.77	6.81	6.77	6.00	1.72	0.89	0.90	0.89	0.89
1U/2	10.00	0.50	12.00	0.75	90	Acrylic	10.50	13.43	10.27	9.28	10.27	8.71	1.28	0.98	0.88	0.98	0.98
1U/3	10.00	0.80	12.00	0.75	90	Acrylic	9.10	13.67	8.90	7.55	9.38	7.30	1.50	0.98	0.83	1.03	1.03
1U/5	10.00	0.26	24.00	0.75	90	Acrylic	13.20	24.43	12.54	12.62	12.54	13.03	1.85	0.95	0.96	0.95	0.95
1U/6	10.00	0.50	24.00	0.75	90	Acrylic	19.20	25.05	19.54	17.55	19.54	19.70	1.30	1.02	0.91	1.02	1.02
1U/7	10.00	0.80	24.00	0.75	90	Acrylic	17.50	25.50	16.80	14.11	17.75	16.24	1.46	0.96	0.81	1.01	1.01
1U/9	10.00	0.26	32.00	0.75	90	Acrylic	21.90	31.64	16.39	16.49	17.31	18.40	1.44	0.75	0.75	0.79	0.79
1U/10	10.00	0.50	32.00	0.75	90	Acrylic	29.10	32.44	25.72	23.07	27.21	28.09	1.11	0.88	0.79	0.94	0.94
1U/11	13.30	0.80	32.00	0.75	90	Acrylic	28.90	33.52	22.07	18.47	24.68	23.06	1.16	0.76	0.64	0.85	0.85
2U/1	10.00	0.80	24.00	0.75	60	Acrylic	11.20	18.66	12.47	10.15	13.16	12.47	1.67	1.11	0.91	1.17	1.17

Table 3.8 Comparison Between Predicted and Recorded SCF Data at Chord Crown Position for Balanced Axially Loaded X and DT-Joints

Spec. no.	α	β	γ	τ	θ (deg)	Material s	Rec	UCL	UCLS	WS	EFT	UEG	LR	UCL/ Rec	UCLS/ Rec	WS/R ec	EFT/ Rec	UEG/ Rec	LR/ Rec
E30	9.80	0.38	20.70	0.79	90	Steel	3.30	2.09	4.70	3.75	3.46	3.79	3.61	0.63	1.42	1.14	1.05	1.15	1.09
E36	9.80	0.38	20.50	0.81	90	Steel	3.60	2.14	4.80	3.82	3.54	3.86	3.69	0.59	1.33	1.06	0.98	1.07	1.02
E37	9.80	0.38	21.00	0.83	90	Steel	3.30	2.15	4.93	3.93	3.65	3.96	3.76	0.65	1.50	1.19	1.11	1.20	1.14
1U/1	10.00	0.26	12.00	0.75	90	Acrylic	3.70	3.58	4.16	3.33	3.62	3.85	4.63	0.97	1.12	0.90	0.98	1.04	1.25
1U/2	10.00	0.50	12.00	0.75	90	Acrylic	2.20	1.76	3.83	2.48	2.28	2.86	2.41	0.80	1.74	1.13	1.04	1.30	1.09
1U/5	10.00	0.26	24.00	0.75	90	Acrylic	4.00	2.93	4.88	4.42	4.24	4.42	5.33	0.73	1.22	1.11	1.06	1.11	1.33
1U/9	10.00	0.26	32.00	0.75	90	Acrylic	4.10	3.15	5.22	5.00	4.53	5.30	5.54	0.77	1.27	1.22	1.11	1.29	1.35
2U/1	10.00	0.80	24.00	0.75	60	Acrylic	1.60	1.50	4.12	2.07	2.35	2.07	1.22	0.94	2.58	1.29	1.47	1.29	0.77
XJOINT2	16.00	0.33	24.00	1.00	45	Acrylic	10.30	3.91	6.36	6.90	5.27	6.90	11.85	0.38	0.62	0.67	0.51	0.67	1.15
XJOINT3	16.00	0.50	24.00	1.00	45	Acrylic	6.20	2.33	6.04	5.39	4.16	5.39	5.89	0.38	0.97	0.87	0.67	0.87	0.95
XJOINT5	16.00	0.83	24.00	1.00	45	Acrylic	2.00	1.50	5.67	2.45	3.55	2.44	1.73	0.75	2.83	1.22	1.77	1.22	0.86
XJOINT9	16.00	0.50	24.00	1.00	30	Acrylic	6.20	3.18	5.66	5.23	4.47	5.23	7.34	0.51	0.91	0.84	0.72	0.84	1.18

Table 3.9 Comparison Between Predicted and Recorded SCF Data at Chord Saddle Position for Balanced Axially Loaded X and DT-Joints

Spec. no.	α	β	γ	τ	θ (deg)	Materials	Rec	UCL	WS	EFT	UEG	LR	UCL/ Rec	WS/ Rec	EFT/ Rec	UEG/ Rec	LR/ Rec
18	6.70	0.76	12.00	0.50	90	Steel	7.70	8.10	9.10	8.64	9.43	7.64	1.05	1.18	1.12	1.23	0.99
19	7.00	0.71	11.40	0.64	90	Steel	10.20	10.78	11.86	11.23	12.06	9.89	1.06	1.16	1.10	1.18	0.97
20	6.70	0.76	12.00	0.50	90	Steel	7.70	8.10	9.10	8.64	9.43	7.64	1.05	1.18	1.12	1.23	0.99
34-35	10.00	0.50	14.30	0.50	90	Steel	10.90	9.97	11.69	11.25	11.69	10.75	0.91	1.07	1.03	1.07	0.99
39-40	10.00	0.50	14.30	0.50	90	Steel	11.20	9.97	11.69	11.25	11.69	10.75	0.89	1.04	1.00	1.04	0.96
A	8.50	0.72	10.40	0.94	90	Steel	10.90	16.74	15.71	14.88	16.03	12.73	1.54	1.44	1.37	1.47	1.17
E30	9.80	0.38	20.70	0.79	90	Steel	21.80	27.57	22.70	22.24	22.91	23.67	1.26	1.04	1.02	1.05	1.09
E36	9.80	0.38	20.50	0.81	90	Steel	20.80	28.24	23.05	22.58	23.29	23.96	1.36	1.11	1.09	1.12	1.15
E37	9.80	0.38	21.00	0.83	90	Steel	21.40	29.96	24.19	23.70	24.38	25.34	1.40	1.13	1.11	1.14	1.18
X4	17.50	0.67	25.30	0.82	90	Steel	29.50	37.05	34.86	33.01	35.14	37.17	1.26	1.18	1.12	1.19	1.26
X5	17.50	0.67	25.30	0.82	90	Steel	31.80	37.05	34.86	33.01	35.14	37.17	1.17	1.10	1.04	1.10	1.17
X6	17.50	0.35	25.00	0.81	90	Steel	24.00	35.98	26.43	26.03	26.45	29.26	1.50	1.10	1.08	1.10	1.22
1U/1	10.00	0.26	12.00	0.75	90	Acrylic	9.80	14.42	9.16	9.16	9.16	8.21	1.47	0.93	0.93	0.93	0.84
1U/2	10.00	0.50	12.00	0.75	90	Acrylic	13.10	14.42	14.72	14.16	14.72	12.84	1.10	1.12	1.08	1.12	0.98
1U/3	10.00	0.80	12.00	0.75	90	Acrylic	10.70	14.42	12.54	12.00	13.30	10.44	1.35	1.17	1.12	1.24	0.98
1U/5	10.00	0.26	24.00	0.75	90	Acrylic	18.50	30.07	18.32	18.32	18.31	20.23	1.63	0.99	0.99	0.99	1.09
1U/6	10.00	0.50	24.00	0.75	90	Acrylic	25.70	30.07	29.43	28.31	29.43	31.62	1.17	1.15	1.10	1.15	1.23
1U/7	10.00	0.80	24.00	0.75	90	Acrylic	24.10	30.07	25.08	24.01	26.59	25.71	1.25	1.04	1.00	1.10	1.07
1U/9	10.00	0.26	32.00	0.75	90	Acrylic	23.50	40.79	24.42	24.43	29.64	29.40	1.74	1.04	1.04	1.26	1.25
1U/10	10.00	0.50	32.00	0.75	90	Acrylic	39.90	40.79	39.25	37.75	39.80	45.96	1.02	0.98	0.95	1.00	1.15
1U/11	13.30	0.80	32.00	0.75	90	Acrylic	37.80	41.43	33.44	32.01	37.59	37.37	1.10	0.88	0.85	0.99	0.99
2U/1	10.00	0.80	24.00	0.75	60	Acrylic	17.00	22.42	18.20	18.80	19.30	19.28	1.32	1.07	1.11	1.14	1.13
XJOINT2	16.00	0.33	24.00	1.00	45	Acrylic	16.70	22.56	20.31	16.39	20.31	16.39	1.35	1.22	0.98	1.22	0.98
XJOINT3	16.00	0.50	24.00	1.00	45	Acrylic	14.80	22.56	19.97	20.94	19.96	21.08	1.52	1.35	1.41	1.35	1.42
XJOINT9	16.00	0.50	24.00	1.00	30	Acrylic	8.80	11.13	10.16	11.62	10.16	10.54	1.26	1.15	1.32	1.15	1.20

Table 3.10 Comparison Between Predicted and Recorded SCF Data on Brace Side for Balanced IPB Loaded X and DT-Joints

Spec. no.	α	β	γ	τ	θ (deg)	Materials	Rec	UCL	WS	EFT	UEG	LR	UCL/ Rec	WS/ Rec	EFT/ Rec	UEG /Rec	LR/R ec
AA	8.50	0.72	10.60	0.99	90	Steel	1.80	2.96	3.15	2.65	3.15	2.31	1.64	1.75	1.47	1.75	1.28
E30	9.80	0.38	20.70	0.79	90	Steel	2.50	4.33	3.78	3.52	3.81	2.76	1.73	1.51	1.41	1.52	1.10
E36	9.80	0.38	20.50	0.81	90	Steel	2.30	4.34	3.82	3.52	3.85	2.78	1.89	1.66	1.53	1.68	1.21
E37	9.80	0.38	21.00	0.83	90	Steel	2.40	4.41	3.92	3.60	3.94	2.85	1.84	1.63	1.50	1.64	1.19
1U/1	10.00	0.26	12.00	0.75	90	Acrylic	1.60	3.14	2.83	2.37	2.83	1.83	1.96	1.77	1.48	1.77	1.14
1U/2	10.00	0.50	12.00	0.75	90	Acrylic	2.30	3.29	2.95	2.67	2.95	2.16	1.43	1.28	1.16	1.28	0.94
1U/3	10.00	0.80	12.00	0.75	90	Acrylic	2.30	2.81	2.78	2.51	2.78	2.14	1.22	1.21	1.09	1.21	0.93
1U/5	10.00	0.26	24.00	0.75	90	Acrylic	3.10	4.33	3.77	3.55	3.77	2.54	1.40	1.22	1.14	1.22	0.82
1U/6	10.00	0.50	24.00	0.75	90	Acrylic	2.90	4.54	3.96	3.72	3.96	3.20	1.56	1.36	1.28	1.36	1.10
1U/7	10.00	0.80	24.00	0.75	90	Acrylic	3.80	3.87	3.69	3.09	3.69	3.17	1.02	0.97	0.81	0.97	0.83
1U/9	10.00	0.26	32.00	0.75	90	Acrylic	4.20	4.95	4.29	4.29	4.49	3.01	1.18	1.02	1.02	1.07	0.72
1U/10	10.00	0.50	32.00	0.75	90	Acrylic	5.20	5.18	4.51	4.33	4.73	3.90	1.00	0.87	0.83	0.91	0.75
1U/11	13.30	0.80	32.00	0.75	90	Acrylic	4.30	4.42	4.20	3.40	4.39	3.85	1.03	0.98	0.79	1.02	0.90
2U/1	10.00	0.80	24.00	0.75	60	Acrylic	2.70	3.26	3.61	3.01	3.61	2.77	1.21	1.34	1.11	1.34	1.03

Table 3.11 Comparison Between Predicted and Recorded SCF Data on Chord Side for Balanced IPB Loaded X and DT-Joints

Spec. no.	α	β	γ	τ	θ (deg)	Material s	Rec	UCL	WS	EFT	UEG	LR	UCL/ Rec	WS/ Rec	EFT/ Rec	UEG/ Rec	LR/ Rec
AA	8.50	0.72	10.60	0.99	90	Steel	3.20	4.66	3.41	3.45	3.41	3.31	1.46	1.06	1.08	1.06	1.04
E30	9.80	0.38	20.70	0.79	90	Steel	4.40	5.02	4.42	4.27	4.46	4.51	1.14	1.00	0.97	1.01	1.02
E36	9.80	0.38	20.50	0.81	90	Steel	4.00	5.13	4.48	4.33	4.53	4.56	1.28	1.12	1.08	1.13	1.14
E37	9.80	0.38	21.00	0.83	90	Steel	4.20	5.31	4.64	4.50	4.67	4.75	1.26	1.10	1.07	1.11	1.13
X4	17.50	0.67	25.30	0.82	90	Steel	2.80	5.59	5.04	4.76	5.05	4.84	2.00	1.80	1.70	1.80	1.73
X5	17.50	0.67	25.30	0.82	90	Steel	3.30	5.59	5.04	4.76	5.05	4.84	1.69	1.53	1.44	1.53	1.47
X6	17.50	0.35	25.00	0.81	90	Steel	4.40	5.59	5.00	4.93	5.01	5.51	1.27	1.14	1.12	1.14	1.25
1U/1	10.00	0.26	12.00	0.75	90	Acrylic	2.20	3.82	2.90	2.28	2.90	2.90	1.74	1.32	1.04	1.32	1.32
1U/2	10.00	0.50	12.00	0.75	90	Acrylic	2.80	3.76	3.10	2.93	3.10	2.80	1.34	1.11	1.05	1.11	1.00
1U/3	10.00	0.80	12.00	0.75	90	Acrylic	3.20	3.71	2.82	2.82	2.82	2.81	1.16	0.88	0.88	0.88	0.88
1U/5	10.00	0.26	24.00	0.75	90	Acrylic	4.20	5.13	4.39	4.04	4.39	5.73	1.22	1.05	0.96	1.05	1.36
1U/6	10.00	0.50	24.00	0.75	90	Acrylic	4.40	5.04	4.69	4.62	4.69	4.58	1.15	1.07	1.05	1.07	1.04
1U/7	10.00	0.80	24.00	0.75	90	Acrylic	4.00	4.97	4.27	3.87	4.27	4.14	1.24	1.07	0.97	1.07	1.03
1U/9	10.00	0.26	32.00	0.75	90	Acrylic	5.60	5.80	5.22	5.12	5.53	7.60	1.03	0.93	0.91	0.99	1.36
1U/10	10.00	0.50	32.00	0.75	90	Acrylic	5.70	5.69	5.58	5.59	5.91	5.61	1.00	0.98	0.98	1.04	0.98
1U/11	13.30	0.80	32.00	0.75	90	Acrylic	5.40	5.62	5.08	4.41	5.38	4.86	1.04	0.94	0.82	1.00	0.90
2U/1	10.00	0.80	24.00	0.75	60	Acrylic	3.60	4.51	4.14	3.50	4.14	3.85	1.25	1.15	0.97	1.15	1.07
XJOINT2	16.00	0.50	24.00	1.00	45	Acrylic	4.40	5.30	4.64	4.63	4.64	4.84	1.21	1.05	1.05	1.05	1.10
XJOINT9	16.00	0.50	24.00	1.00	30	Acrylic	5.00	4.19	3.64	3.64	3.64	4.07	0.84	0.73	0.73	0.73	0.81

Table 3.12 Comparison Between Predicted and Recorded SCF Data on Brace Side for Balanced OPB Loaded X and DT-Joints

Spec. no.	α	β	γ	τ	θ (deg)	Material s	Rec	UCL	WS	EFT	UEG	LR	UCL/ Rec	WS/ Rec	EFT/ Rec	UEG/ Rec	LR/ Rec
E30	9.80	0.38	20.70	0.79	90	Steel	3.80	9.07	7.06	7.40	7.12	7.05	2.39	1.86	1.95	1.87	1.86
E36	9.80	0.38	20.50	0.81	90	Steel	6.20	9.11	7.16	7.42	7.22	7.12	1.47	1.15	1.20	1.16	1.15
E37	9.80	0.38	21.00	0.83	90	Steel	5.00	9.44	7.46	7.67	7.51	7.48	1.89	1.49	1.53	1.50	1.50
X4	17.50	0.67	25.30	0.82	90	Steel	7.30	15.66	12.93	11.74	13.03	12.47	2.15	1.77	1.61	1.78	1.71
1U/1	10.00	0.26	12.00	0.75	90	Acrylic	2.50	4.53	3.30	3.25	3.30	3.00	1.81	1.32	1.30	1.32	1.20
1U/2	10.00	0.50	12.00	0.75	90	Acrylic	4.90	6.07	5.29	5.17	5.29	4.25	1.24	1.08	1.05	1.08	0.87
1U/3	10.00	0.80	12.00	0.75	90	Acrylic	5.10	7.48	5.91	4.77	6.20	3.90	1.47	1.16	0.93	1.22	0.77
1U/5	10.00	0.26	24.00	0.75	90	Acrylic	5.40	8.54	5.59	6.21	5.59	6.21	1.58	1.04	1.15	1.04	1.15
1U/6	10.00	0.50	24.00	0.75	90	Acrylic	11.00	11.43	9.59	9.64	9.58	9.36	1.04	0.87	0.88	0.87	0.85
1U/7	10.00	0.80	24.00	0.75	90	Acrylic	9.40	14.09	10.81	8.46	11.40	7.83	1.50	1.15	0.90	1.21	0.83
1U/9	10.00	0.26	32.00	0.75	90	Acrylic	10.10	11.11	7.13	8.10	7.49	8.84	1.10	0.71	0.80	0.74	0.87
1U/10	10.00	0.50	32.00	0.75	90	Acrylic	16.40	14.87	12.45	12.34	13.14	13.35	0.91	0.76	0.75	0.80	0.81
1U/11	13.30	0.80	32.00	0.75	90	Acrylic	16.90	19.16	14.08	12.33	15.71	13.62	1.13	0.83	0.73	0.93	0.81
2U/1	10.00	0.80	24.00	0.75	60	Acrylic	6.50	10.51	8.12	6.72	8.55	5.76	1.62	1.25	1.03	1.32	0.89

Table 3.13 Comparison Between Predicted and Recorded SCF Data on Chord Side for Balanced OPB Loaded X and DT-Joints

Spec. no.	α	β	γ	τ	θ (deg)	Material s	Rec	UCL	WS	EFT	UEG	LR	UCL/ Rec	WS/ Rec	EFT/ Rec	UEG/ Rec	LR/R ec
E30	9.80	0.38	20.70	0.79	90	Steel	7.70	11.52	9.62	9.32	9.71	10.85	1.50	1.25	1.21	1.26	1.41
E36	9.80	0.38	20.50	0.81	90	Steel	8.90	11.73	9.77	9.47	9.87	11.00	1.32	1.10	1.06	1.11	1.24
E37	9.80	0.38	21.00	0.83	90	Steel	8.30	12.35	10.26	9.93	10.34	11.61	1.49	1.24	1.20	1.25	1.40
X4	17.50	0.67	25.30	0.82	90	Steel	13.20	18.94	18.94	17.93	19.09	20.09	1.43	1.44	1.36	1.45	1.52
X5	17.50	0.67	25.30	0.82	90	Steel	16.80	18.94	18.94	17.93	19.09	20.09	1.13	1.13	1.07	1.14	1.20
X6	17.50	0.35	25.00	0.81	90	Steel	13.90	15.13	11.00	10.91	11.01	13.72	1.09	0.79	0.79	0.79	0.99
1U/1	10.00	0.26	12.00	0.75	90	Acrylic	3.70	5.59	3.65	3.63	3.65	3.71	1.51	0.99	0.98	0.99	1.00
1U/2	10.00	0.50	12.00	0.75	90	Acrylic	6.30	6.83	6.81	6.59	6.81	6.32	1.08	1.08	1.05	1.08	1.00
1U/3	10.00	0.80	12.00	0.75	90	Acrylic	6.20	7.89	7.79	7.15	8.26	5.76	1.27	1.26	1.15	1.33	0.93
1U/5	10.00	0.26	24.00	0.75	90	Acrylic	7.90	11.27	7.29	7.18	7.29	8.99	1.43	0.92	0.91	0.92	1.14
1U/6	10.00	0.50	24.00	0.75	90	Acrylic	13.40	13.76	13.63	12.72	13.63	14.76	1.03	1.02	0.95	1.02	1.10
1U/7	10.00	0.80	24.00	0.75	90	Acrylic	13.10	15.89	15.57	13.13	16.51	12.43	1.21	1.19	1.00	1.26	0.95
1U/9	10.00	0.26	32.00	0.75	90	Acrylic	10.80	15.07	9.72	9.50	10.31	12.94	1.40	0.90	0.88	0.95	1.20
1U/10	10.00	0.50	32.00	0.75	90	Acrylic	21.40	18.40	18.17	16.53	19.27	20.74	0.86	0.85	0.77	0.90	0.97
1U/11	13.30	0.80	32.00	0.75	90	Acrylic	22.40	22.10	20.77	19.41	23.34	21.39	0.99	0.93	0.87	1.04	0.95
2U/1	10.00	0.80	24.00	0.75	60	Acrylic	9.70	11.94	11.31	10.43	11.98	9.32	1.23	1.17	1.08	1.24	0.96
XJOINT2	16.00	0.33	24.00	1.00	45	Acrylic	7.80	8.95	8.36	7.02	8.36	7.63	1.15	1.07	0.90	1.07	0.98
XJOINT3	16.00	0.50	24.00	1.00	45	Acrylic	9.80	10.16	9.25	10.17	9.24	10.54	1.04	0.94	1.04	0.94	1.08
XJOINT9	16.00	0.50	24.00	1.00	30	Acrylic	6.30	5.10	4.70	5.84	4.70	5.27	0.81	0.75	0.93	0.75	0.84

Table 3.14 Validation of SCF Parametric Equation for X joint
under Balanced Axial at Brace Crown Position

Equation	Steel/ Acrylic	No of Pts	Database		Pred SCF/Recorded SCF			Decision
			Mean	%st dev of Enq	%P/R< 0.8	%P/R< 1.0	%P/R> 1.5	
Wordsworth & Smedley	Steel	3	2.13	12.0%	0.0%	0.0%	100%	accept but borderline conservative
	Acrylic	13	1.37	35.2%	0.0%	7.7%	38.5%	
	Pooled	16	1.51	44.1%	0.0%	6.3%	50.0%	
Efthymiou	Steel	3	1.47	9.2%	0.0%	0.0%	33.3%	accept but borderline
	Acrylic	13	1.45	40.2%	7.7%	7.7%	46.2%	
	Pooled	16	1.45	36.1%	6.3%	6.3%	43.8%	
UEG	Steel	3	2.15	12.0%	0.0%	0.0%	100%	accept but borderline conservative
	Acrylic	13	1.38	35.3%	0.0%	7.7%	38.5%	
	Pooled	16	1.52	44.5%	0.0%	6.3%	50.0%	
LR	Steel	3	1.29	7.7%	0.0%	0.0%	0.0%	accept
	Acrylic	13	1.12	12.3%	0.0%	7.7%	0.0%	
	Pooled	16	1.15	13.3%	0.0%	6.3%	0.0%	
UCL	Steel	3	1.97	12.7%	0.0%	0.0%	100%	too small database
	Acrylic	6	1.38	54.6%	0.0%	33.3%	33.3%	
	Pooled	9	1.57	52.9%	0.0%	22.2%	55.6%	

**Table 3.15 Validation of SCF Parametric Equation for X joint
under Balanced Axial at Brace Saddle Position**

Equation	Steel/ Acrylic	No of Pts	Database		Pred SCF/Recorded SCF			Decision
			Mean	%st dev of Enq	%P/R< 0.8	%P/R <1.0	%P/R >1.5	
Wordsworth & Smedley	Steel	4	1.34	18.8%	0.0%	0.0%	25.0%	accept
	Acrylic	12	1.19	18.0%	0.0%	16.7%	8.3%	
	Pooled	16	1.23	18.8%	0.0%	12.5%	12.5%	
Efthymiou	Steel	7	1.22	13.3%	0.0%	14.3%	0.0%	accept as borderline unconservative
	Acrylic	12	1.06	13.8%	8.3%	33.3%	0.0%	
	Pooled	19	1.12	15.4%	5.3%	26.3%	0.0%	
UEG	Steel	4	1.36	18.9%	0.0%	0.0%	25.0%	accept
	Acrylic	12	1.26	22.6%	0.0%	8.3%	16.7%	
	Pooled	16	1.29	21.6%	0.0%	6.3%	18.8%	
LR	Steel	6	1.32	17.7%	0.0%	0.0%	16.7%	accept
	Acrylic	12	1.14	14.4%	0.0%	25.0%	0.0%	
	Pooled	18	1.20	17.4%	0.0%	16.7%	5.6%	
UCL	Steel	5	1.92	19.3%	0.0%	0.0%	100%	accept but borderline conservative
	Acrylic	10	1.45	24.3%	0.0%	0.0%	30.0%	
	Pooled	15	1.61	31.8%	0.0%	0.0%	53.3%	

Table 3.16 Validation of SCF Parametric Equation for X joint
under Balanced Axial at Chord Crown Position

Equation	Steel/ Acrylic	No of Pts	Database		Pred SCF/Recorded SCF			Decision
			Mean	%st dev of Enq	%P/R< 0.8	%P/R< 1.0	%P/R> 1.5	
Wordsworth & Smedley	Steel	3	1.12	6.3%	0.0%	0.0%	0.0%	too small database
	Acrylic	9	1.14	24.3%	11.1%	44.4%	0.0%	
	Pooled	12	1.14	20.9%	8.3%	33.3%	0.0%	
Efthymiou	Steel	3	1.04	5.8%	33.3%	33.3%	0.0%	too small database
	Acrylic	9	1.15	44.2%	33.3%	33.3%	22.2%	
	Pooled	12	1.12	38.1%	33.3%	33.3%	16.7%	
UEG	Steel	3	1.14	6.2%	0.0%	0.0%	0.0%	too small database
	Acrylic	9	1.15	25.3%	11.1%	44.4%	0.0%	
	Pooled	12	1.15	21.7%	8.3%	33.3%	0.0%	
LR	Steel	3	1.07	5.7%	0.0%	0.0%	0.0%	too small database
	Acrylic	9	1.23	22.9%	0.0%	22.2%	11.1%	
	Pooled	12	1.19	21.0%	0.0%	16.7%	8.3%	
UCL	Steel	3	0.62	3.1%	100%	100%	0.0%	too small database
	Acrylic	9	0.69	22.1%	66.77%	100%	0.0%	
	Pooled	12	0.68	19.1%	75.0%	100%	0.0%	
UCLS	Steel	3	1.42	8.2%	0.0%	0.0%	0.0%	too small database
	Acrylic	9	1.48	76.3%	11.1%	33.3%	33.3%	
	Pooled	12	1.46	65.2%	8.3%	25.0%	25.0%	

Table 3.17 Validation of SCF Parametric Equation for X joint
under Balanced Axial Loading at Chord Saddle Position

Equation	Steel/ Acrylic	No of Pts	Database		Pred SCF/Recorded SCF			Decision
			Mean	%st dev of Enq	%P/R< 0.8	%P/R< 1.0	%P/R> 1.5	
Wordsworth & Smedley	Steel	8	1.10	4.6%	0.0%	0.0%	0.0%	accept
	Acrylic	17	1.29	27.1%	0.0%	5.9%	11.8%	
	Pooled	25	1.23	24.0%	0.0%	4.0%	8.0%	
Efthymiou	Steel	16	1.15	18.9%	0.0%	0.0%	12.5%	accept
	Acrylic	16	1.26	28.9%	0.0%	6.3%	12.5%	
	Pooled	32	1.21	24.7%	0.0%	3.2%	12.5%	
UEG	Steel	10	1.13	6.7%	0.0%	0.0%	0.0%	accept
	Acrylic	17	1.36	32.7%	0.0%	0.0%	17.6%	
	Pooled	27	1.27	28.3%	0.0%	0.0%	11.1%	
LR	Steel	15	1.09	15.0%	0.0%	46.7%	0.0%	reject
	Acrylic	17	1.24	20.4%	0.0%	11.8%	11.8%	
	Pooled	32	1.17	19.3%	0.0%	28.2%	6.3%	
UCL	Steel	12	1.20	21.7%	0.0%	16.7%	8.3%	accept
	Acrylic	13	1.33	21.4%	0.0%	0.0%	23.1%	
	Pooled	25	1.27	22.0%	0.0%	8.0%	16.0%	

Table 3.18 Validation of SCF Parametric Equation for X joint
under Balanced IPB Loading on Brace Side

Equation	Steel/ Acrylic	No of Pts	Database		Pred SCF/Recorded SCF			Decision
			Mean	%st dev of Enq	%P/R< 0.8	%P/R< 1.0	%P/R >1.5	
Wordsworth & Smedley	Steel	4	1.55	12.7%	0.0%	0.0%	75.0%	accept but conservative
	Acrylic	23	1.50	21.2%	0.0%	0.0%	60.9%	
	Pooled	27	1.51	20.1%	0.0%	0.0%	63.0%	
Efthymiou	Steel	6	1.33	25.6%	0.0%	16.7%	16.7%	accept
	Acrylic	23	1.29	22.4%	0.0%	4.3%	17.4%	
	Pooled	29	1.30	22.7%	0.0%	6.9%	17.2%	
UEG	Steel	4	1.57	10.7%	0.0%	0.0%	75.0%	accept but conservative
	Acrylic	23	1.51	20.0%	0.0%	0.0%	60.9%	
	Pooled	27	1.52	18.9%	0.0%	0.0%	63.0%	
LR	Steel	5	1.15	11.6%	0.0%	20.0%	0.0%	accept
	Acrylic	23	1.15	12.9%	0.0%	8.7%	0.0%	
	Pooled	28	1.15	12.5%	0.0%	10.7%	0.0%	
UCL	Steel	4	1.78	10.8%	0.0%	0.0%	100%	accept
	Acrylic	10	1.30	30.0%	0.0%	0.0%	20%	
	Pooled	14	1.44	33.8%	0.0%	0.0%	42.9%	

Table 3.19 Validation of SCF parametric Equation for X joint
under Balanced IPB Loading on Chord Side

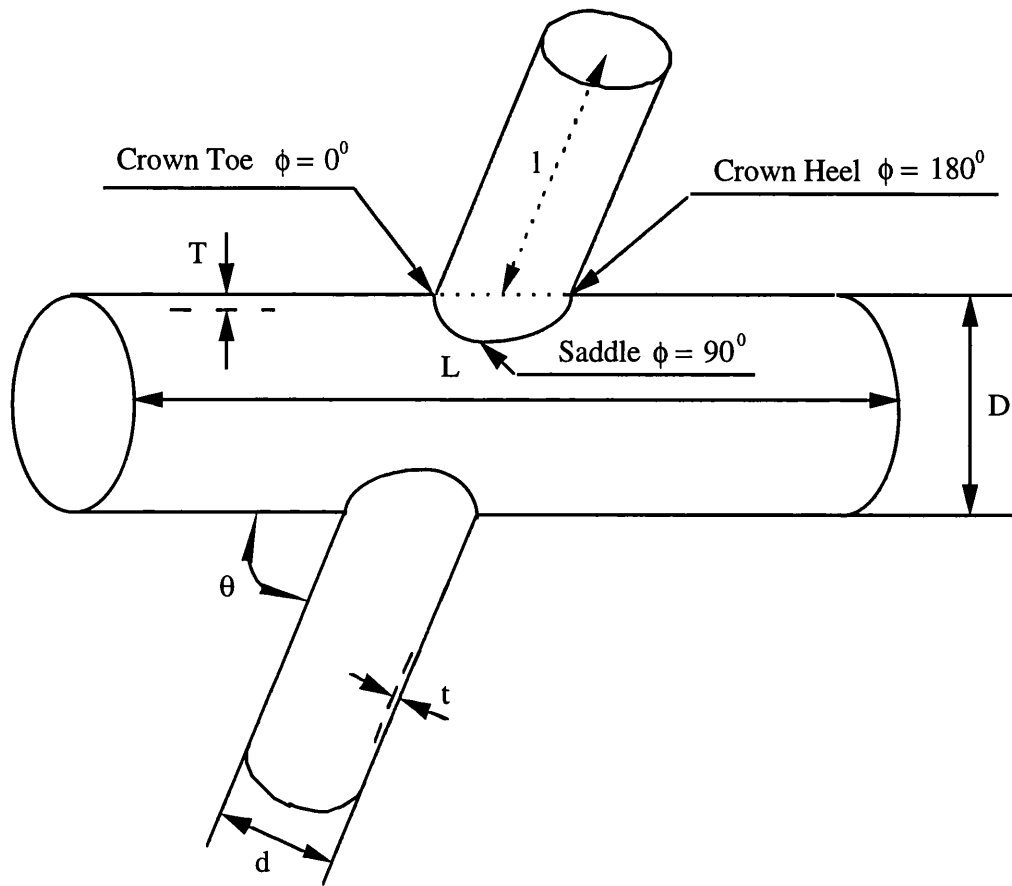
Equation	Steel/ Acrylic	No of Pts	Database		Pred SCF/Recorded SCF			Decision
			Mean	%st dev of Enq	%P/R< 0.8	%P/R< 1.0	%P/R> 1.5	
Wordsworth & Smedley	Steel	9	1.54	68.0%	0.0%	0.0%	44.4%	accept
	Acrylic	24	1.24	18.2%	0.0%	8.3%	8.3%	
	Pooled	33	1.32	39.7%	0.0%	6.1%	18.2%	
Efthymiou	Steel	12	1.33	37.9%	0.0%	8.3%	25.0%	accept
	Acrylic	24	1.17	15.7%	0.0%	12.5%	0.0%	
	Pooled	36	1.22	25.9%	0.0%	11.1%	8.3%	
UEG	Steel	9	1.56	73.4%	0.0%	0.0%	44.4%	accept
	Acrylic	24	1.25	17.8%	0.0%	8.3%	8.3%	
	Pooled	33	1.33	42.1%	0.0%	6.1%	18.2%	
LR	Steel	12	1.39	42.7%	0.0%	0.0%	16.7%	accept
	Acrylic	24	1.23	17.1%	0.0%	8.3%	8.3%	
	Pooled	36	1.28	28.7%	0.0%	6.1%	11.1%	
UCL	Steel	7	1.44	30.2%	0.0%	0.0%	28.6%	accept
	Acrylic	12	1.18	22.2%	0.0%	8.3%	8.3%	
	Pooled	19	1.28	27.7%	0.0%	5.3%	15.8%	

Table 3.20 Validation of SCF Parametric Equation for X-joint
under Balanced OPB Loading on Brace Side

Equation	Steel/ Acrylic	No of Pts	Database		Pred SCF/Recorded SCF			Decision
			Mean	%st dev of Enq	%P/R< 0.8	%P/R< 1.0	%P/R> 1.5	
Wordsworth & Smedley	Steel	4	1.57	31.2%	0.0%	0.0%	50.0%	accept
	Acrylic	12	1.35	34.3%	0.0%	16.7%	33.3%	
	Pooled	16	1.41	34.0%	0.0%	12.5%	37.5%	
Efthymiou	Steel	4	1.60	31.0%	0.0%	0.0%	75.0%	accept
	Acrylic	12	1.26	23.7%	0.0%	16.7%	16.7%	
	Pooled	16	1.35	28.9%	0.0%	12.5%	31.3%	
UEG	Steel	4	1.59	31.5%	0.0%	0.0%	75.0%	accept
	Acrylic	12	1.43	40.2%	0.0%	16.7%	33.3%	
	Pooled	16	1.47	37.9%	0.0%	12.5%	43.8%	
LR	Steel	4	1.59	30.3%	0.0%	0.0%	75.0%	accept
	Acrylic	12	1.21	19.9%	0.0%	16.7%	8.3%	
	Pooled	16	1.31	27.6%	0.0%	12.5%	25.0%	
UCL	Steel	4	1.97	39.2%	0.0%	0.0%	75.0%	accept
	Acrylic	10	1.34	29.6%	0.0%	10.0%	30.0%	
	Pooled	14	1.52	42.9%	0.0%	7.1%	42.9%	

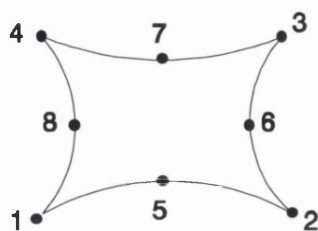
Table 3.21 Validation of SCF Parametric Equation for X joint
under Balanced OPB on Chord Side

Equation	Steel/ Acrylic	No of Pts	Database		Pred SCF/Recorded SCF			Decision
			Mean	%st dev of Enq	%P/R< 0.8	%P/R< 1.0	%P/R> 1.5	
Wordsworth & Smedley	Steel	6	1.16	21.7%	16.7%	16.7%	0.0%	accept
	Acrylic	17	1.28	37.4%	0.0%	17.6%	11.8%	
	Pooled	23	1.25	34.0%	4.3%	17.4%	8.7%	
Efthymiou	Steel	6	1.13	20.0%	16.7%	16.7%	0.0%	accept
	Acrylic	16	1.23	33.1%	0.0%	25.0%	18.8%	
	Pooled	23	1.20	30.0%	4.3%	21.7%	13.0%	
UEG	Steel	6	1.16	22.1%	16.7%	16.7%	0.0%	accept
	Acrylic	17	1.35	44.8%	0.0%	11.8%	17.6%	
	Pooled	23	1.30	40.5%	4.3%	13.0%	13.0%	
LR	Steel	6	1.32	20.4%	0.0%	16.7%	16.7%	accept
	Acrylic	17	1.23	16.6%	0.0%	5.9%	5.9%	
	Pooled	23	1.25	17.6%	0.0%	8.7%	8.7%	
UCL	Steel	6	1.33	18.1%	0.0%	0.0%	0.0%	accept
	Acrylic	13	1.15	21.4%	0.0%	15.4%	7.7%	
	Pooled	19	1.21	21.5%	0.0%	10.5%	5.3%	



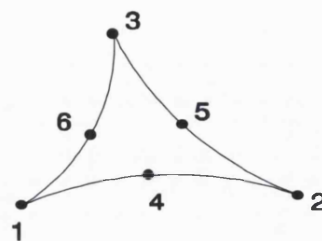
Geometric ratios: $\alpha = \frac{2L}{D}$ $\beta = \frac{d}{D}$ $\gamma = \frac{D}{2T}$ $\tau = \frac{t}{T}$ $\alpha_B = \frac{2l}{d}$

Figure 3.1 Geometric Notation for Tubular X-joint



(a) Typical Eight Noded Quadrilateral Double Curved

Curved Element (S8R5) with Reduced Integration,
using Five Degrees of Freedom per Node



(b) Typical Six Noded Triangular

Element (STRI65) using Five Degrees
of Freedom per Node

Figure 3.2 Two Kinds of Thin-Shell Elements used in this Study

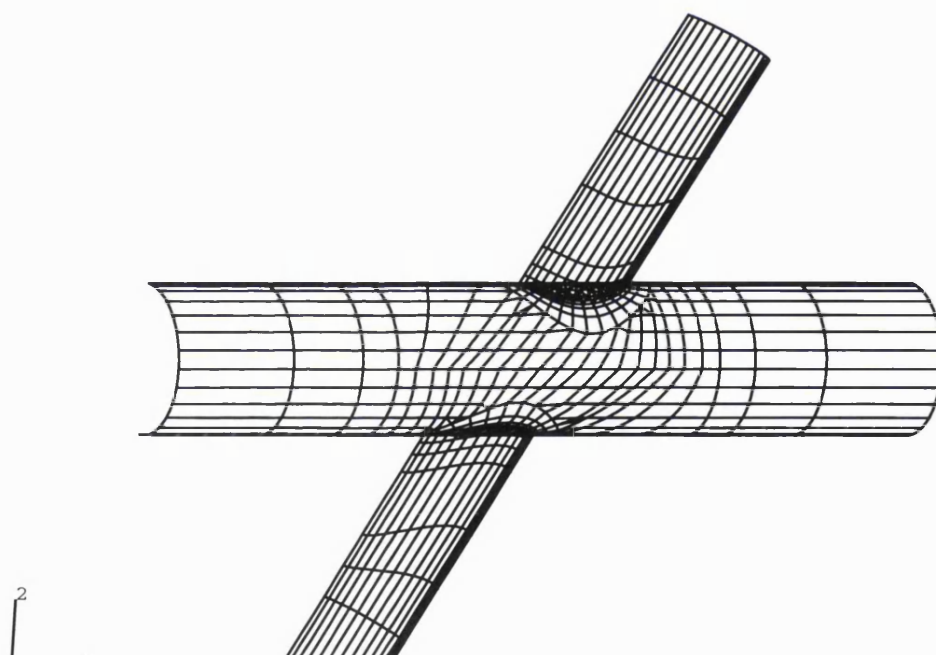
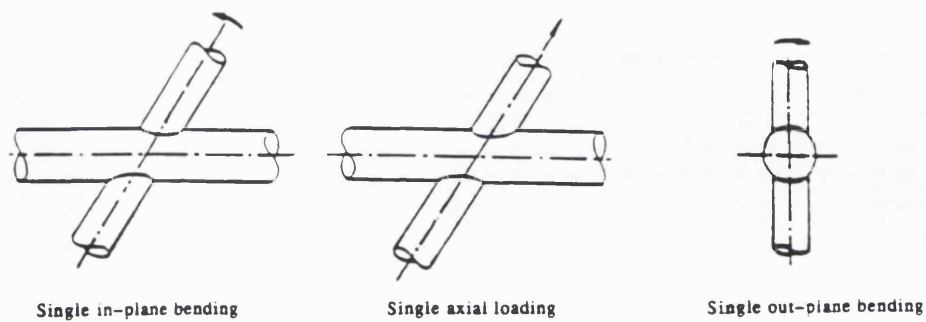
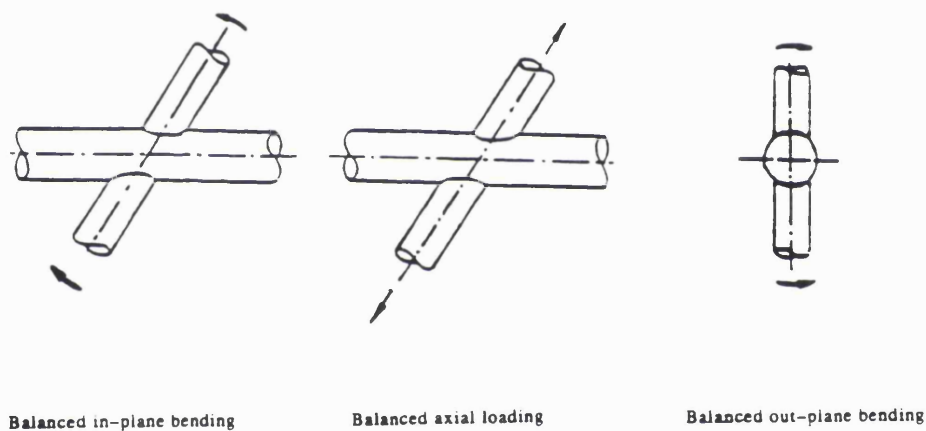


Figure 3.3 Typical Example of Finite Element Mesh Used to Model Tubular Joint

($\alpha=10$, $\beta=0.6$, $\gamma=20$, $\tau=0.5$, $\theta=60^\circ$)

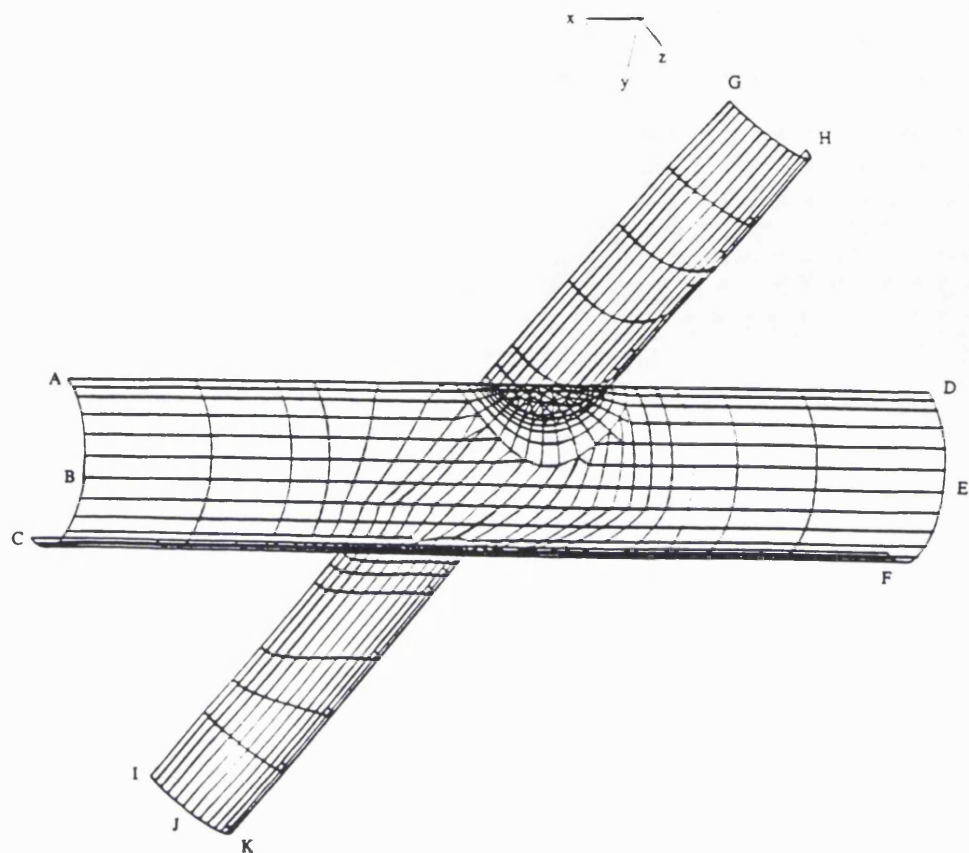


(a) Single brace loading



(b) Both brace loading

Figure 3.4 Modes of Loading Used for Finite Element Joint Analyses



Modes of Loading	Restraints on the following Planes			
	ABC	DEF	GACIKFDH	IJK
Single Axial	$u_x, u_y, u_z, \phi_x, \phi_y$	$u_x, u_y, u_z, \phi_x, \phi_y$	u_z, ϕ_x, ϕ_y	N/A
Single IPB	$u_x, u_y, u_z, \phi_x, \phi_y$	$u_x, u_y, u_z, \phi_x, \phi_y$	u_z, ϕ_x, ϕ_y	N/A
Single OPB	$u_x, u_y, u_z, \phi_x, \phi_y$	$u_x, u_y, u_z, \phi_x, \phi_y$	u_x, u_y	N/A
Balanced Axial	N/A	N/A	u_z, ϕ_x, ϕ_y	$u_x, u_y, u_z, \phi_x, \phi_y$
Balanced IPB	$u_x, u_y, u_z, \phi_x, \phi_y$	$u_x, u_y, u_z, \phi_x, \phi_y$	u_z, ϕ_x, ϕ_y	N/A
Balanced OPB	$u_x, u_y, u_z, \phi_x, \phi_y$	$u_x, u_y, u_z, \phi_x, \phi_y$	u_x, u_y	N/A

Figure 3.5 The Boundary Conditions for All Modes of Loading

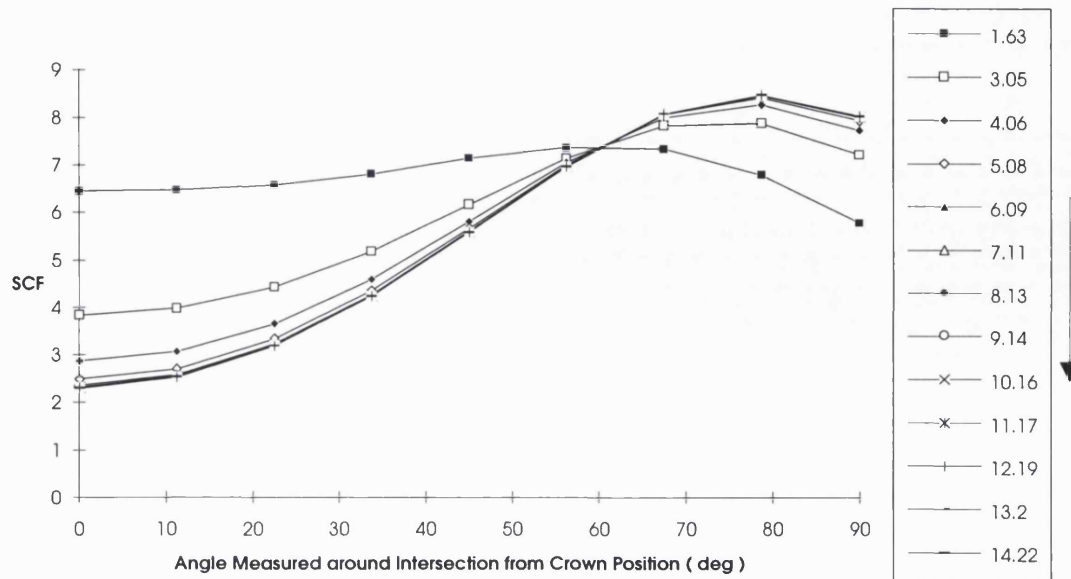


Figure 3.6 Effect of a_B on the SCF Distribution on Brace Side of Intersection
for Single Axial Loading X Joint ($\alpha=10$, $\beta=0.6$, $\gamma=20$, $\tau=0.5$, $\theta=60^\circ$)

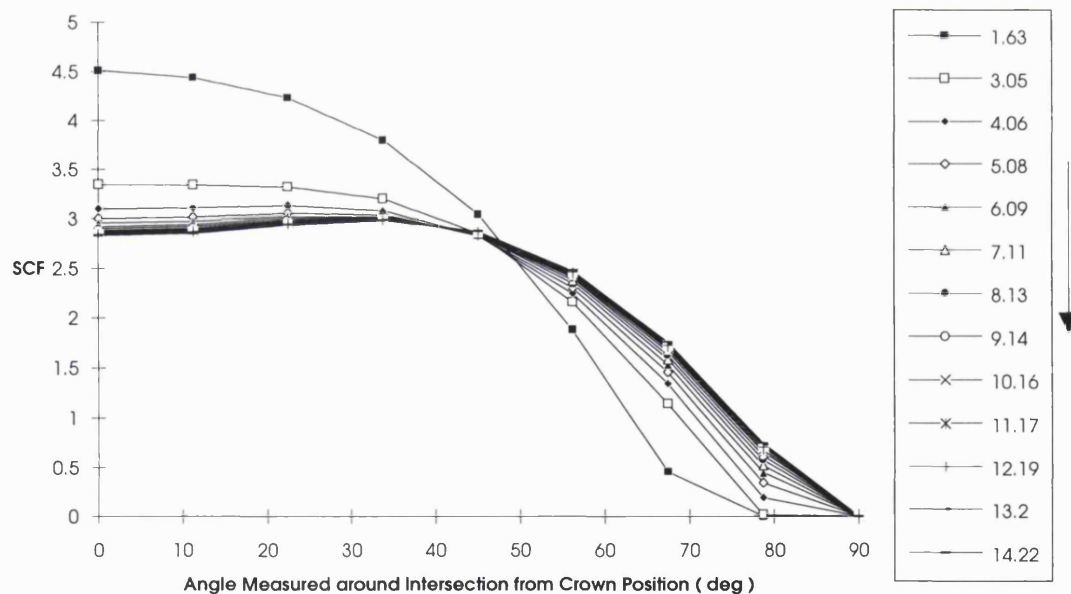


Figure 3.7 Effect of α_B on the SCF Distribution on Brace Side of Intersection
for Single IPB Loading X Joint ($\alpha=10$, $\beta=0.6$, $\gamma=20$, $\tau=0.5$, $\theta=60^\circ$)

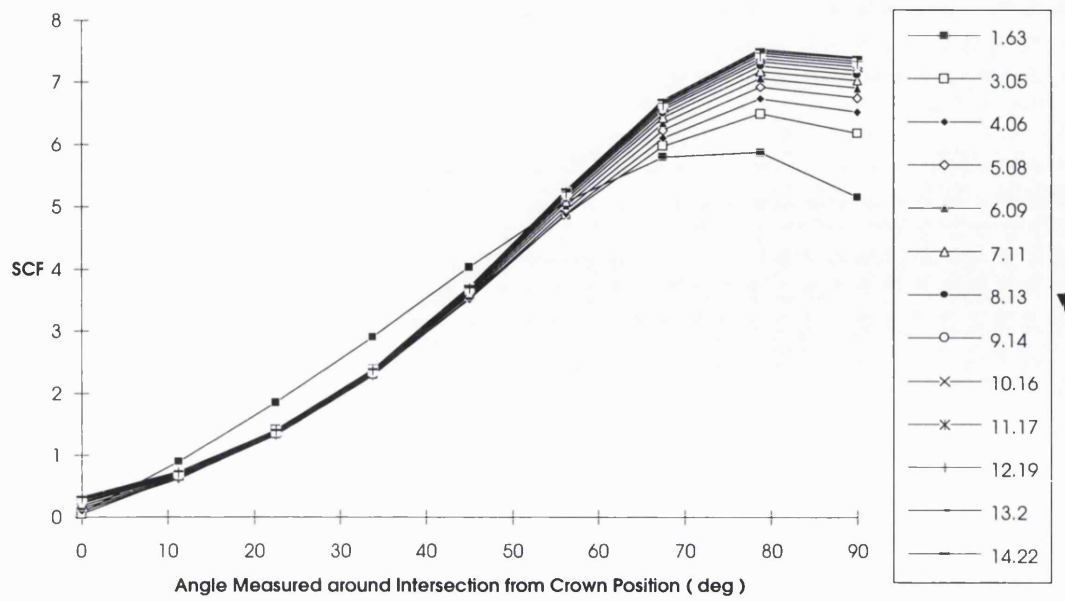


Figure 3.8 Effect of α_B on the SCF Distribution on Brace Side of Intersection

for Single OPB Loading X Joint ($\alpha=10, \beta=0.6, \gamma=20, \tau=0.5, \theta=60^\circ$)

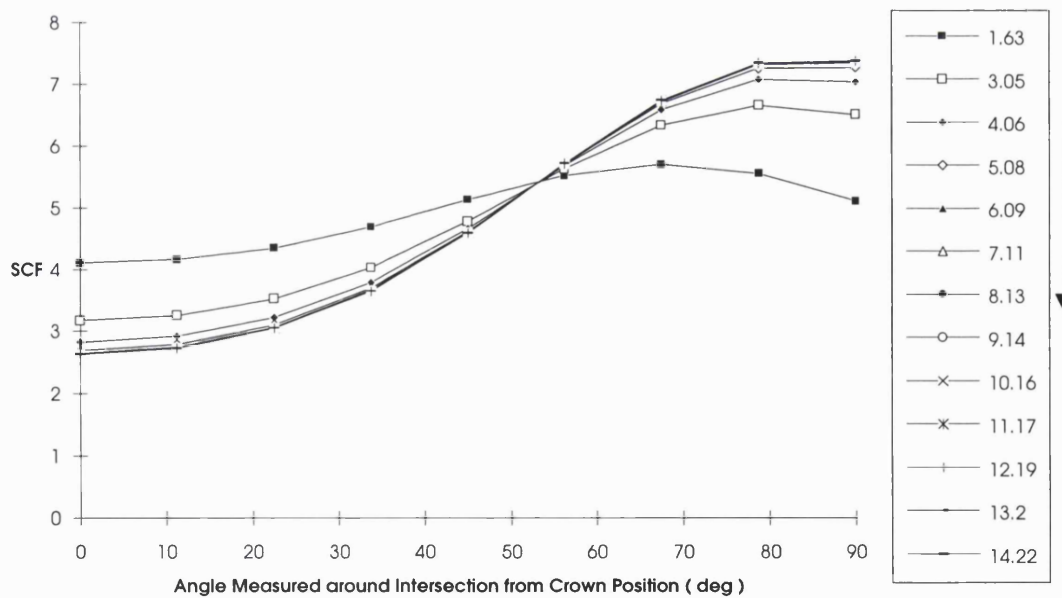


Figure 3.9 Effect of α_B on the SCF Distribution on Chord Side of Intersection

for Single Axial Loading X Joint ($\alpha=10, \beta=0.6, \gamma=20, \tau=0.5, \theta=60^\circ$)

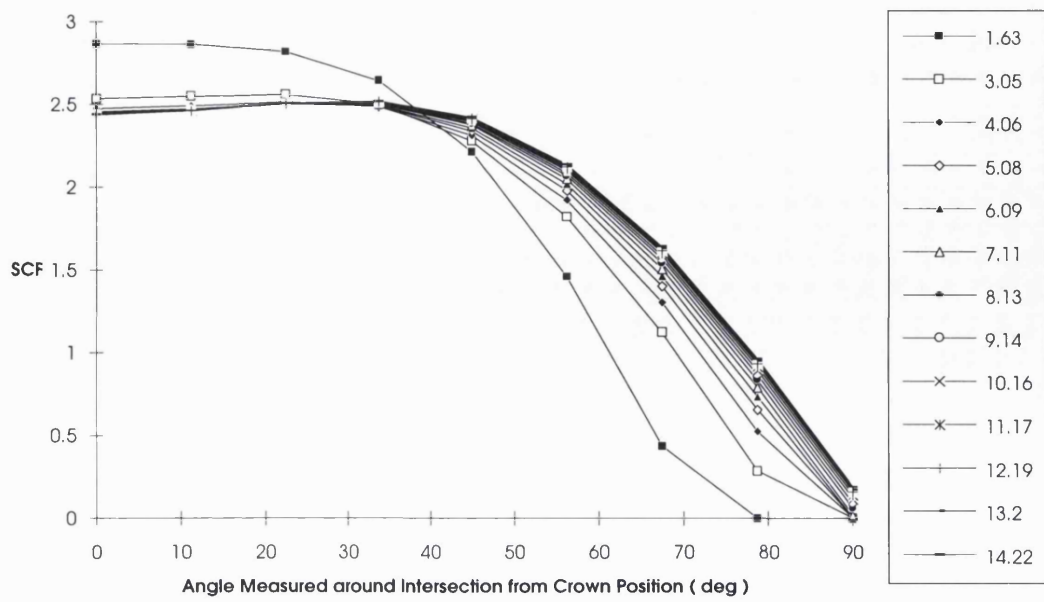


Figure 3.10 Effect of α_P on the SCF Distribution on Chord Side of Intersection

for Single IPB Loading X Joint ($\alpha=10$, $\beta=0.6$, $\gamma=20$, $\tau=0.5$, $\theta=60^\circ$)

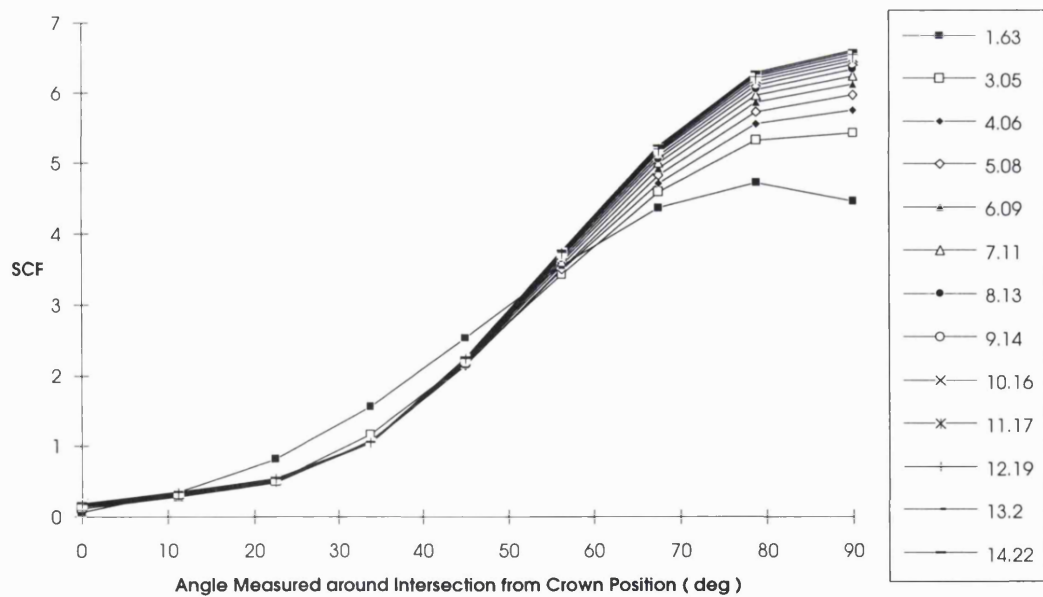


Figure 3.11 Effect of α_P on the SCF Distribution on Chord Side of Intersection

for Single OPB Loading X Joint ($\alpha=10$, $\beta=0.6$, $\gamma=20$, $\tau=0.5$, $\theta=60^\circ$)

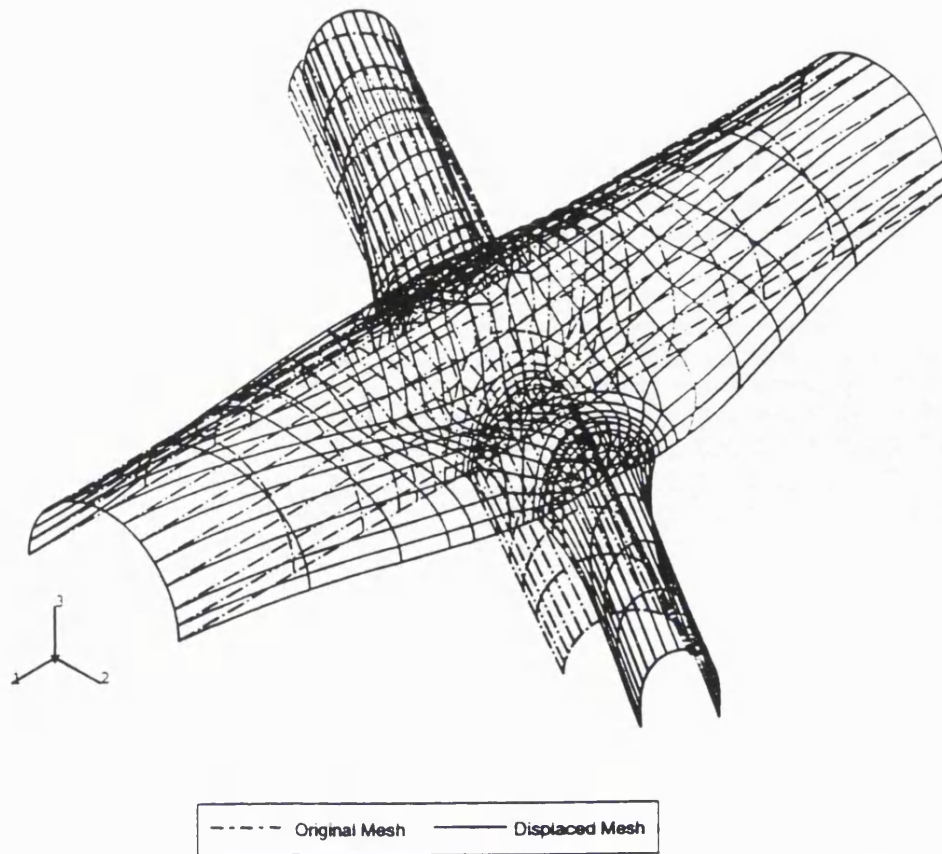


Figure 3.12 The Deformed Mesh Superimposed upon the Unloaded Mesh
for Single Axial Loading X Joint ($\alpha=10$, $\beta=0.6$, $\gamma=20$, $\tau=0.5$, $\theta=60^\circ$, $\alpha_B=6.09$)

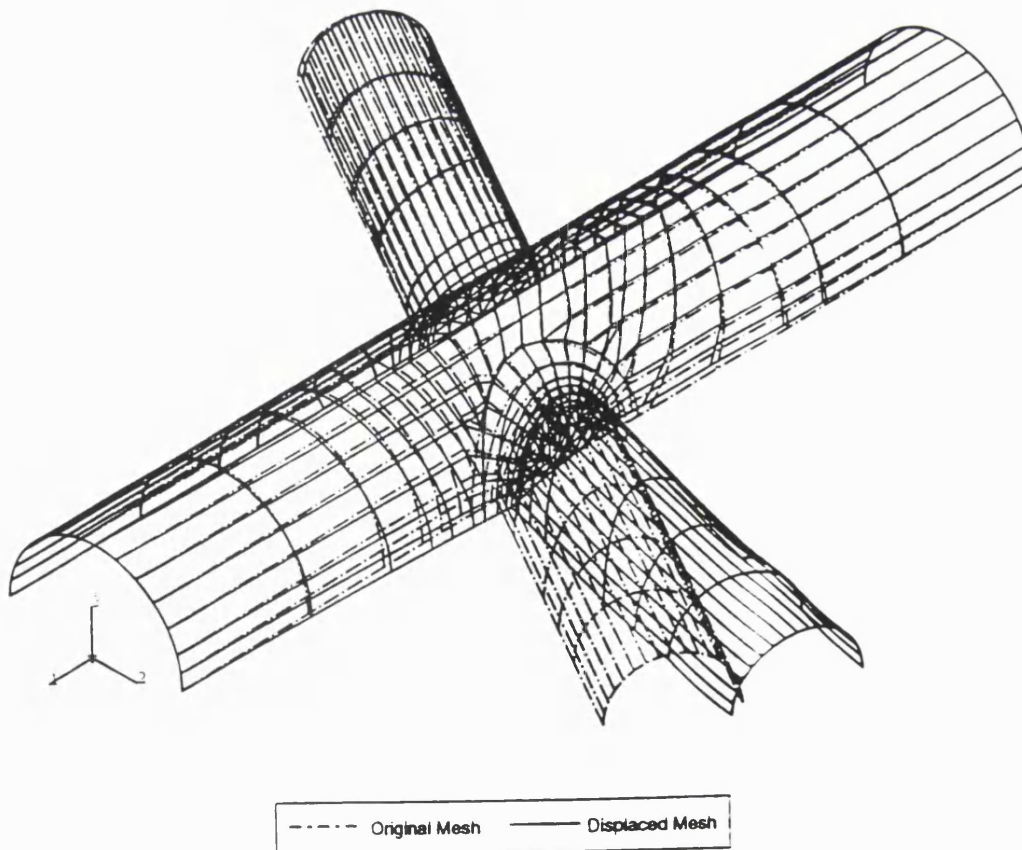


Figure 3.13 The Deformed Mesh Superimposed upon the Unloaded Mesh
for Single IPB Loading X Joint ($\alpha=10$, $\beta=0.6$, $\gamma=20$, $\tau=0.5$, $\theta=60^\circ$, $\alpha_B=6.09$)

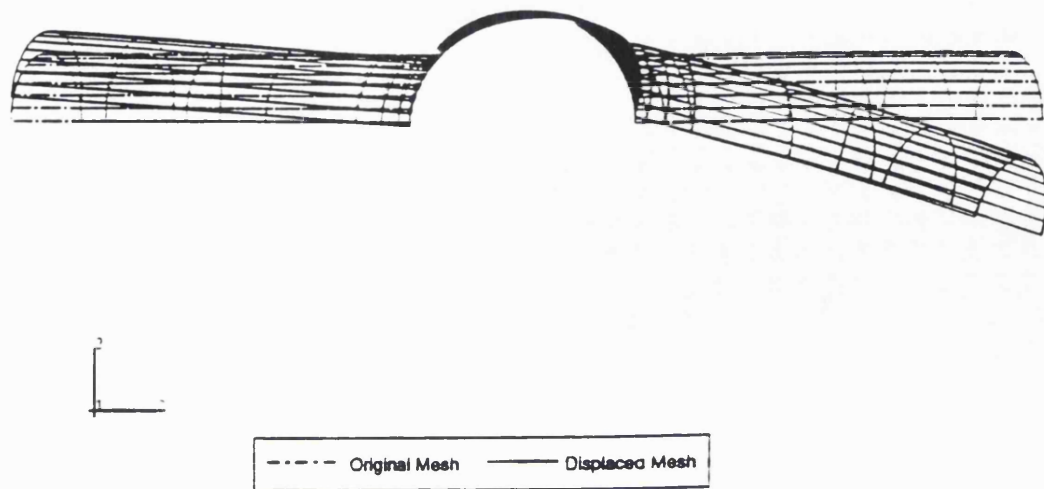


Figure 3.14 The Deformed Mesh Superimposed upon the Unloaded Mesh
for Single OPB Loading X Joint ($\alpha=10$, $\beta=0.6$, $\gamma=20$, $\tau=0.5$, $\theta=60^\circ$, $\alpha_B=6.09$)

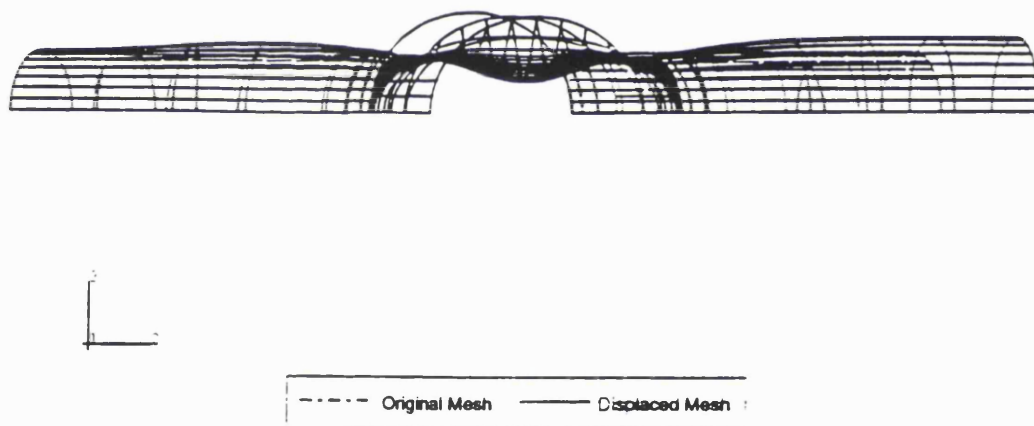


Figure 3.15 The Deformed Mesh Superimposed upon the Unloaded Mesh
for Balanced Axial Loading X Joint ($\alpha=10$, $\beta=0.6$, $\gamma=20$, $\tau=0.5$, $\theta=60^\circ$, $\alpha_B=6.09$)

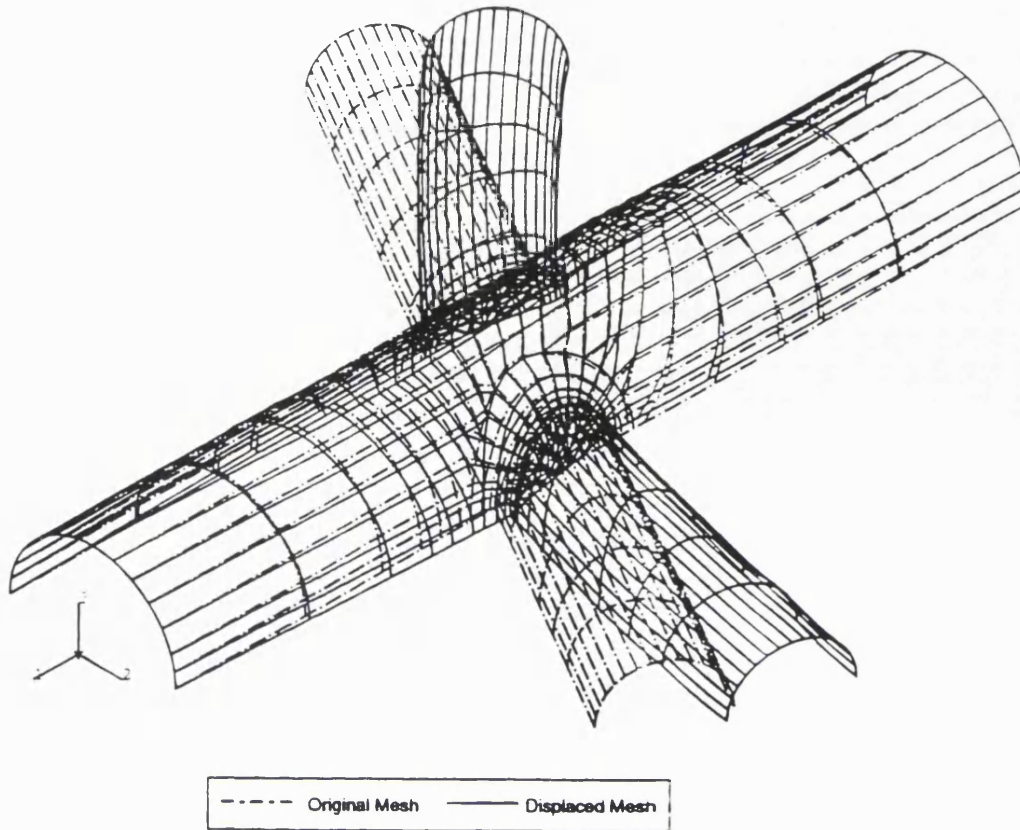


Figure 3.16 The Deformed Mesh Superimposed upon the Unloaded Mesh
for Balanced IPB Loading X Joint ($\alpha=10$, $\beta=0.6$, $\gamma=20$, $\tau=0.5$, $\theta=60^\circ$, $\alpha_B=6.09$)

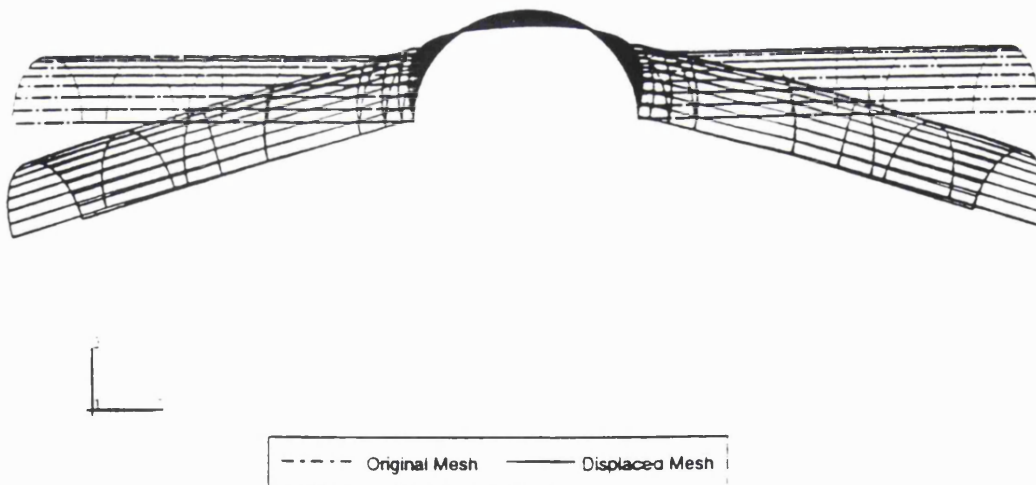


Figure 3.17 The Deformed Mesh Superimposed upon the Unloaded Mesh
for Balanced OPB Loading X Joint ($\alpha=10$, $\beta=0.6$, $\gamma=20$, $\tau=0.5$, $\theta=60^\circ$, $\alpha_B=6.09$)

CHAPTER FOUR

PARAMETRIC EQUATIONS TO PREDICT STRESS DISTRIBUTIONS THROUGH THE THICKNESS AND ALONG THE INTERSECTION OF TUBULAR X AND DT-JOINTS

4.1 Introduction

During the design stage, the hot spot stress based S-N approach is widely used to estimate the fatigue life of offshore tubular welded joints. As the hot spot stress is defined as a surface peak stress at the intersection, this method does not take the stress distribution into account. However, the analyses of a large number of fatigue tests of tubular welded joints have showed that fatigue behaviour is not dependent on the hot spot stress alone, but is also significantly influenced by the stress distribution around the intersection and particularly the through thickness stress distribution. It becomes apparent that the external surface hot spot stress is not enough to characterise all aspect of fatigue failure. Joints of differing geometries or modes of loading, but with similar hot spot stresses, may have different stress distributions and, as a result, they often exhibit significantly different numbers of cycles to failure. It is anticipated that a joint with a high proportion of through thickness bending stress will have a longer fatigue life than one with a similar hot spot stress, but with a greater component of through thickness membrane stress. Therefore the standard hot spot stress analysis may be unconservative for joints with a low degree of bending. Although one can use the lower bound S-N curve which is two standard deviations below the mean life curve through the experimental data, it can be over conservative for joints with a high degree of bending. It seems that the current standard hot spot stress based S-N approach has to be modified to include some parameters representing the stress distribution. Therefore stress distribution information is needed in order to have more accurate fatigue life prediction.

Another problem with the S-N approach is that this method gives only the total life and can not be used to predict how a crack grows or the remaining life when cracking is detected in service in a tubular joint. In order to deal with these problems, one has to use fracture mechanics since it correlates the physical damage mechanism to the assessment. However, the accurate determination of a Stress Intensity Factor(SIF) is the key for fracture mechanics calculations of remaining life, on cracked joints in service. It is well known that it is necessary to take the complex stress field in tubular welded joints into account in order to

have accurate SIF data. The information is required again on the magnitude and distribution of the stress acting in the anticipated crack path, not just the peak stress at one location. Fatigue crack propagation rates are important to reliability-based inspection scheduling, hence the need for this information is becoming more pressing.

In order to obtain the through thickness information from experiments, one has to access the inside of tubular joints to attach strain gauges. It is generally quite difficult, especially for the joints with small diameters in laboratory tests. The strain gauges are usually only placed on several points around the external surface hot spot stress region rather than at many points around the intersection. Thus the detailed stress distribution data, and especially through thickness information, are usually not available from tests. By using thin shell finite element method, parametric equations have been derived for Y and T joints in terms of peak stress (Hellier et al 1990 a), stress distribution (Hellier et al 1990 b) and bending to membrane ratio (Connolly et al 1990). However, for X and DT-joints, there are no parametric equations for stress variation through the thickness and around the intersection. For this reason, a comprehensive thin-shell FE analysis has been carried out for tubular X and DT-joints (Figure 4.1). The details of FE analyses is omitted in this chapter as it was reported in chapter three. The SCF parametric equations have been firstly derived and presented in the last chapter. This chapter will present the derivation and assessment of the parametric equations for predicting the stress variation through the wall (degree of bending) and stress distribution around the intersection for tubular X and DT-joints. In particular, new two dimensional regression methodology was adopted to fit full stress distribution along the intersection as a function of the geometric parameters α , β , γ , τ and θ . This new set of stress distribution equation can be used to predict the normalised distribution but also provide an alternative method for calculation of hot spot SCFs.

4.2 Prediction of Degree of Bending in Tubular X and DT-joints

As discussed in chapter 1, the through thickness stress field is predominantly due to linear chord wall bending and the non-linear stress concentration due to the change in section at the weld toe. The non-linear distribution around the weld toe stress concentration region is dependent on the weld and weld toe geometry and is difficult to predict during the design stage. It would have little effect for a deep crack. Thus, most efforts have been concentrated on the linear through thickness distribution and in particular attempting to define the ratio of bending to tension. The stress distribution across the wall thickness is assumed to be a linear combination of membrane and bending stress. The stress distribution through the chord wall is often characterised by either the degree of bending (DoB), i.e. the ratio of bending stress over total external stress or the ratio of bending to membrane stress.

The through wall thickness stress distribution data are important for fatigue strength assessment of tubular joints, particularly for fracture mechanics based remaining life calculation. Owing to the complexities introduced by the structural geometry and the nature of the local stress fields, it is impossible to calculate analytically the SIFs for defects located in tubular joints. This problem is often tackled by using the modified simplified models, such as the Newman-Raju flat plate solution, with an appropriate load shedding model. DoB has to be known before one can use these simplified SIF models to calculate the remaining fatigue life of tubular joints, as the high DoB in conjunction with load shedding mechanism, make the performance of fatigue crack growth in tubular welded joints different from other types of welded joints, such as T-butt.

Recently results of the SINTEF/TWI tubular joint fatigue tests (Eide 1993) confirmed the effect of DoB on fatigue life. For these self-reacted load in the double T specimens, a DoB of 0.69 was measured. It was found that there was a large difference between the experimentally measured fatigue life compared to predictions using S-N data. As the finite element analyses of tubular joints show that typical DoBs under axial and OPB loading are in the range of 0.8 - 0.9, this low DoB gives an additional membrane component in the chord wall. Thus, for any given hot spot stress, a more pronounced acceleration of crack growth and a shorter fatigue life may be expected for these specimens.

Fracture mechanics analyses were carried out (Eide 1993) by using both 3-D shell analysis with a Y compliance calibration based on line spring model computations, and a simplified two-dimensional analysis with a linear moment release load shedding model. They gave results in good agreement with the experimental data. The analyses showed that the fatigue life of tubular joints is not dependent on the hot spot stress alone, but is also significantly influenced by the through thickness distribution of stress. Consideration of load shedding makes the effect of DoB on fatigue life more pronounced as shedding of membrane stresses due to crack growth occurs at a much slower rate relative to the shedding of bending stresses in the same hot spot section. Assuming a "mean" DoB for the S/N tubular joints to be 0.85, the effect due to the DoB of 0.69 in the double T geometry was a factor on life of 1.5. With this correction the data come very close to the mean line of the current database.

As a summary, the DoB is an important parameter for the calculation of fatigue crack growth in tubular welded joints. So it is necessary to derive the parametric equations to predict the DoB information in tubular X and DT-joints by post processing the finite element analysis results reported in chapter 3. The section aims to report the derivation and assessment of these DoB parametric equations.

In order to make the results compatible, the numerically greatest principal stress on the outer surface and corresponding principal stress on the inner surface have been used to determine the relative amounts of through-thickness bending and membrane stress. A simple linear

interpolation between the stresses on the inner and outer tube walls was used in order to obtain the distribution of stresses through the joints intersection. A simple method of representing this linear interpolation is in terms of the ratio of bending to total stress, or degree of bending(DoB), expressed as

$$\frac{\sigma_B}{\sigma_T} = \frac{\sigma_B}{\sigma_B + \sigma_M} \quad (4-1)$$

where σ_B is the bending stress component

σ_T is the total stress on the outer tube surface

σ_M is the membrane stress, $\sigma_M = \sigma_T - \sigma_B$

From the above equation, it can be seen clearly that when the membrane stresses are tensile, the ratio σ_B/σ_T is less than one and greater than zero whereas it is greater than one when the membrane portion is compressive.

The results of DoB convergence tests(Table 4.1) showed that the coarsest mesh with 16 elements around the intersection could be used to obtain DoB with sufficient accuracy. The required information was obtained from the FE analysis results of 330 tubular X and DT-joints by using several batch files. They were used to calculate DoBs at the critical positions, such as saddle and crown position, under six modes of loading for both the chord and brace sides of the intersection.

Multiple regression analyses were performed on the database of finite element analysis results using a statistical package 'MINITAB'(1991) and the methodology used in deriving these equations is similar to that for SCF equations. The parametric equations of the ratio of bending to total stress(DoB) were derived at saddle and crown positions for each mode of loading and for both the chord and brace sides of the intersection. The equations are listed in Appendix B. A summary of fitting accuracy for all DoB equations is given in Table 4.2. The R^2 is greater than 94% for all the equations except those at brace saddle under single and balanced axial loading which are around 80%. As a value of $R^2=100\%$ would imply that the fitted equation captures all the variations in DoB, quite good correlation was achieved for the DoB equations derived.

In order to test the accuracy, this set of parametric equations was assessed by comparing the predicted values with results from acrylic and steel model tests. Due to the difficulty of accessing the inside of a tube, only one acrylic test data under single OPB loading was found and used for validation(Table 4.3). The prediction from the parametric equations for tubular T-joints is also included as a comparison. It can be seen that the prediction from this set of parametric equations for DT-joint is slighter higher than that for the T-joint. As both are conservative, the latter is closer to the experimental data.

The parametric equations have been derived to predict the DoBs at the critical positions of both the chord and brace sides of the intersection of tubular X and DT-joints under six modes of loading. However, the validation of this set of equations is very limited. The characterised equations for DoB distribution along the intersection (Cheaitani et al 1995) have been derived recently for tubular T-joints and they permit the interpolation of DoB between the crown and saddle positions. Combining these two sets of equations, the DoB at any position along the intersection of tubular X and DT-joints can be estimated.

4.3 Parametric Equations to Predict the Stress Distribution along the Intersection

Tubular joints of differing geometries or modes of loading have different stress distributions along the intersection. For a given joint, each load case has its own particular distribution of stresses along the intersection line and thereby a different influence on the fatigue life. Rigorous fracture mechanics calculations on tubular joints require a knowledge of the local stress distribution around the joint, i.e. stress variation along the weld toe between the crown and saddle sites. Experimental results show that the initiation and the subsequent coalescence of multiple cracks are very much dependent on the stress distribution. Apart from the use of hot spot stresses, the average stress around a joint (Dover and Dharmavasan 1987) have also been shown to play an important role during the fatigue crack propagation. Stress distribution equations would also be useful for calculating the average stress.

Some simple interpolation formulae have been reported by UEG (1985). Combined with the peak local stress at saddle and crown positions, they can be used to predict SCF variation along the brace/chord intersection of tubular joints. The parametric equations which were developed at UCL (Hellier et al 1990) for tubular Y and T-joints can provide similar information. All these formulations need the values of peak stresses obtained from SCF parametric equations. The UCL equations allow the effect of a hot spot at a point other than the crown or saddle to be taken into account. After comparing the UEG equations with FE results, Vinas-Pich (1994) concluded that the stress distribution proposed in the UEG design guidelines is not accurate enough around the whole brace-chord intersection. The problem with the UCL equations and the UEG equations is that they were derived by observing a limited number of typical sample results rather than whole database and therefore they can not provide enough accuracy to all other cases for detailed analyses. As they are only based on a restricted sample, they may be unconservative for some situations and this has been confirmed by Monahan (1994).

In order to overcome this difficulty, an effort has been made in this study to fit all the finite element results as function of all geometry ratio α , β , γ , τ and θ . The maximum principal stress on external surface along the intersection was chosen to derive the equations in order to maintain compatibility and be conservative. It should be noted that these maximum principal

stresses are often not perpendicular to the weld toe along the intersection. The database used to derive this set of equations is the same as that used for the previous two sets of equations. Typical plots of external surface stress distribution around the intersection of tubular X-joint are shown in Figures 4.2-4.4 for three different modes of single brace loading.

The regression analysis methodology is different from that used for the previous two sets of equations as it is a two-dimensional fitting process and can be split into the following two levels.

1) Performing numerous regressions until the best form of expression for the variations of the SCF, (i.e.) the equation with a large product moment correlation coefficient, was found for all joints under different modes of loading. After numerous tries, the following expressions were considered appropriate for both the chord and brace toes under each mode of loading.

For both brace and chord toes under single and balanced axial loading:

$$SCF(\phi) = C_0 + C_1\phi + C_2\cos\phi + C_3\cos2\phi \quad (0 \leq \phi \leq \pi) \quad (4-2)$$

For both brace and chord toes under single and balanced IPB loading:

$$SCF(\phi) = C_0 + C_1\cos\phi + C_2\cos2\phi \quad (0 \leq \phi \leq \pi) \quad (4-3)$$

For both brace and chord toes under single and balanced OPB loading:

$$SCF(\phi) = C_0 + C_1\sin\phi + C_2\sin2\phi + C_3\cos2\phi \quad (0 \leq \phi \leq \pi) \quad (4-4)$$

2) Fitting the coefficients in the above equations as a function of the parameters α , β , γ , τ and θ .

By carrying out regression analysis using the statistical package 'MINITAB'(1991), the parametric equations for SCF distribution equations have been derived for both chord and brace toes under six different modes of loading and are given in Appendix C. These equations can be easily programmed and enable the SCF value to be calculated at any angular location around both brace and chord toe for all modes of loading. A summary of the degree of fit for each equation is presented in Table 4.4. It shows that these equations fit the original FE data very well and the correlation coefficient R^2 is greater than 95% for the majority of cases including both fitting the form of equation and the coefficients. Assuming the loading directions shown in Figure 3.4, the negative hot-spot is at or close to the crown toe while the positive hot-spot lies at or near the crown heel under single/balanced IPB loading. In these loading cases, the SCFs on both brace and chord saddle positions were taken to be the average values from the equations from both sides in order to maintain the smooth transition of SCF. As the maximum principal stress were used to derive this set of equations, the SCFs on both brace and chord crown positions are not necessarily zero but are small values for single/balanced OPB cases. If the negative SCF value is predicted at crown positions under single/balanced axial and OPB loading, the compensation factor D

for the whole stress distribution is assigned for conservative reason. It should be also noted that a minimum of 1.5 was assigned when this set of equations are used to predict the SCF at critical points such as hot spot, saddle, crown toe and crown heel.

Aiming to produce the SCF distribution along the intersection, this set of equations also included the hot spot SCF information. Thus, the validation of this set of equations has been divided into the following two steps.

a) Hot spot SCF estimation

Firstly, following the same procedures described in last chapter, the predictions for hot spot SCFs from this set of equations are compared with the values from previous SCF parametric equations and together with all available experimental data in Lloyds and UCL database. They are presented in Table 4.5-4.15. Furthermore, statistical analyses were carried out for hot spot SCFs under the balanced loading which have relatively more data and are listed in Tables 4.16-4.21.

Since a different fitting methodology was used, the hot spot SCF predictions from these two set of equations are different despite the fact they are based on the same database. For single brace loading, the predictions from this set of equation are more close to experimental data compared with the predictions from the SCF equations but are still conservative (Tables 4.5-4.8) except for the cases with high β ratio at chord saddle position under single OPB loading (Table 4.8). The predictions of the SCFs at crown positions under balanced axial loading (Tables 4.8 and 4.10) are similar to those from SCF equations. From the results of comparison of hot spot SCF predictions with experimental data (Table 4.9, 4.11-4.21) for balanced loading, the tendency to have slightly reduced conservatism is also observed. The criteria described in the last chapter were used to validate these cases. As a results, all these equations are accepted.

Further examination showed again that most of the predictions that underpredict the test data are those with high β ratio. In terms of fitting original finite element hot spot SCF data, this set of equations may not be as good as the previously derived SCF equations, especially for high β ratio cases, as they aim to fit the distribution rather than hot spot alone. However, a comparison with experimental data shows that they can offer a reasonably good performance for predicting the hot spot SCF. As a summary, this set of equations shows a reduced degree of conservatism when used for hot spot SCF predictions but their predictions are still conservative. Care should be taken for those joints with high β ratio and the previous SCF equations can be used for these particular cases if necessary.

b) Normalised SCF distribution prediction

Since the predictions from the equations based on the finite element analysis results are generally conservative, the validation of distribution predictions are therefore based the

normalised SCF distribution data that can be obtained by dividing by the hot spot SCF. A comparison has been made between the normalised stress distribution predictions from this set of equations with all available UCL experimental test data(Mshana 1993)(Smith 1995)(Kam 1989) and this is shown in Figures 4.5-4.13. As can be seen from these figures, good agreement has been achieved for these cases. As the maximum principal stresses are used to derive the equations, the SCF predictions at the crown positions for OPB loading are not zero but small values(Figures 4.7-4.9). As can be seen from the Figures 4.7-4.8, the predictions agree very well with experimental data. However, the predicted curves for the OPB loading tend to be slightly high around the crown area for the high β ratio cases due to the nature of this three items expression. However, the high prediction is of a conservative nature, this effect is localised and far away from the hot spot area. As a summary, these equations provide a good normalised SCF distribution along the intersection. However, it should be noted that validation is limited as only these few test data were available.

4.4 Conclusions

For the accurate fatigue strength assessment of tubular joints, information is required on the magnitude and distribution of the stress acting in the anticipated crack path, not just the peak stress at one location. In order to meet this requirement, two sets of parametric equations have been derived to predict the degree of bending and stress distribution around the intersection respectively in tubular welded DT and X joints under six modes of loading as a function of the geometric parameters α , β , γ , τ and θ from nearly 2000 finite element analyses results. The stress distribution equations not only can be used to predict the normalised distribution for all cases but also have been proven to have capability to estimate the hot spot SCF under balanced brace loading. All these equations are directly compatible with each other and can be easily incorporated into fatigue life calculation codes. They provide a predictive capability for the stress acting on the anticipated crack plane, that is at the welded intersection of tubular X and DT-joints. Combination of these two sets of parametric equations allows one to recreate the 2D stress distribution around welded tubular X and DT-joints. However, it should be noted that the validation is very limited as so far only very few experimental data for DoB and stress distribution are available.

Table 4.1 Comparison between DOBs around upper Intersection from Coarse to Finite
X joint Meshes to Show Extent of Convergence ($\alpha=10$, $\beta=0.6$, $\gamma=20$, $\tau=0.5$, $\theta=60^\circ$)

No. of elements around intersection	Chord		Brace	
	Crown Toe	Saddle	Crown Toe	Saddle
Single Axial Loading				
16	-	0.872	-	0.786
20	-	0.872	-	0.788
24	-	0.872	-	0.789
Single In-Plane Bending				
16	0.778	-	0.764	-
20	0.778	-	0.770	-
24	0.779	-	0.774	-
Single Out-Plane Bending				
16	-	0.885	-	0.813
20	-	0.886	-	0.815
24	-	0.886	-	0.816
Balanced Axial Loading				
16	-	0.885	-	0.789
20	-	0.886	-	0.791
24	-	0.886	-	0.792
Balanced In-Plane Bending				
16	0.777	-	0.768	-
20	0.778	-	0.774	-
24	0.779	-	0.778	-
Balanced Out-Plane Bending				
16	-	0.886	-	0.807
20	-	0.887	-	0.810
24	-	0.887	-	0.810

Table 4.2 Summary of Degree of Fit for DoB Parametric Equations

Location	Brace		Chord	
Circumferential position	R ² %	Equation	R ² %	Equation
Single Axial Loading				
Saddle	81.1	Appendix B1.1	96.5	Appendix B1.2
Single In-Plane Bending				
Crown toe	94.9	Appendix B2.1	95.3	Appendix B2.2
Crown heel	94.7	Appendix B2.3	95.6	Appendix B2.4
Single Out-Plane Bending				
Saddle	96.0	Appendix B3.1	97.0	Appendix B3.2
Balanced Axial Loading				
Saddle	79.1	Appendix B4.1	94.0	Appendix B4.2
Balanced In-Plane Bending				
Crown toe	94.3	Appendix B5.1	96.0	Appendix B5.2
Crown heel	95.6	Appendix B5.3	95.6	Appendix B5.4
Balanced Out-Plane Bending				
Saddle	96.6	Appendix B6.1	96.8	Appendix B6.2

Table 4.3 Comparison of DoB Data between the Predictions from Parametric Equations
and Experimental Results for Tubular DT-Joints under Single OPB Loading

Ref.	Joint Geometry					DoB		
	α	β	γ	τ	$\theta(\text{deg})$	Chord Saddle		
						Parametric Equation for T and Y	Parametric Equation for X and DT	Exp.
Smith, 1995	9.9	0.8	10.6	1.0	90	0.849	0.862	0.888

Table 4.4 Summary of Degree of Fit for the Parametric Equations of SCF Distribution
around the Intersection of Tubular X and DT-joints

Mode of Loading/ Location	Equations	Form of Expression		C ₀	C ₁	C ₂	C ₃
		Descriptive Statistics (%)					
		Mean R ²	Std. Dev.	R ²			
Single Axial Loading							
Brace	Appendix C1.1	97.026	3.256	94.73	93.73	97.91	96.36
Chord	Appendix C1.2	96.423	4.663	97.67	90.02	93.29	96.13
Single In-Plane Bending							
Brace Toe Side	Appendix C2.1	98.690	1.673	98.29	98.22	98.57	N/A
Brace Heel Side	Appendix C2.1	99.242	0.96	98.46	98.39	98.49	N/A
Chord Toe Side	Appendix C2.2	99.79	0.210	97.53	98.83	98.06	N/A
Chord Heel Side	Appendix C2.2	98.97	0.962	97.98	98.08	97.69	N/A
Single Out-Plane Bending							
Brace	Appendix C3.1	97.754	2.160	98.34	97.62	96.45	98.52
Chord	Appendix C3.2	98.275	1.792	97.42	96.93	94.49	98.77
Balanced Axial Loading							
Brace	Appendix C4.1	96.162	3.886	93.18	91.31	97.41	99.08
Chord	Appendix C4.2	96.867	3.986	98.66	87.89	90.76	98.38
Balanced In-Plane Bending							
Brace Toe Side	Appendix C5.1	98.251	2.218	97.40	98.39	98.37	N/A
Brace Heel Side	Appendix C5.1	99.272	0.949	98.55	98.68	98.40	N/A
Chord Toe Side	Appendix C5.2	99.757	0.313	97.55	98.83	98.28	N/A
Chord Heel Side	Appendix C5.2	99.139	0.806	97.10	98.21	97.67	N/A
Balanced Out-Plane Bending							
Brace	Appendix C6.1	97.605	2.261	98.02	97.78	96.61	98.30
Chord	Appendix C6.2	98.115	1.858	98.05	97.52	90.22	98.27

Table 4.5 Comparison between the Predictions from the SCF and SCF Distribution Equations with the Recorded SCF data at Chord Crown position for Single IPB loaded X and DT-joints

Ref.	Spec. no.	α	β	γ	τ	θ (deg)	Mat	Rec	SCF Eq	SCF Dis Eq	SCF/Rec	SCF Dis /Rec
Mshana 1993	IPB-1A	7.84	0.64	10.2	0.5	90	Steel	1.76	2.18	2.03	1.24	1.15
Mshana 1993	IPB-2A	7.84	0.64	10.2	0.5	90	Steel	1.76	2.18	2.03	1.24	1.15
Mshana 1993	IPB-1B	7.84	0.64	10.2	0.5	90	Steel	1.47	2.18	2.03	1.48	1.38
Mshana 1993	IPB-2B	7.84	0.64	10.2	0.5	90	Steel	1.68	2.18	2.03	1.30	1.21

Table 4.6 Comparison between the Predictions from the SCF and SCF Distribution Equations with the Recorded SCF data at Brace Saddle position for Single OPB loaded X and DT-joints

Ref.	Spec. no.	α	β	γ	τ	θ (deg)	Mat	Rec	SCF Eq	SCF Dis Eq	SCF/Rec	SCF Dis /Rec
Smith 1995	W2	9.90	0.80	10.00	0.99	90	Steel	4.80	8.59	6.04	1.79	1.26
Smith 1995	W4	9.90	0.80	10.00	0.99	90	Steel	4.70	8.59	6.04	1.83	1.29

Table 4.7 Comparison between the Predictions from the SCF and SCF Distribution Equations with the Recorded SCF data at Chord Saddle position for Single OPB loaded X and DT-joints

Ref.	Spec. no.	α	β	γ	τ	θ (deg)	Mat	Rec	SCF Eq	SCF Dis Eq	SCF/Rec	SCF Dis /Rec
Mshana 1993	OPB-1A	7.84	0.64	10.2	0.5	90	Steel	3.81	4.27	4.08	1.12	1.07
Mshana 1993	OPB-2A	7.84	0.64	10.2	0.5	90	Steel	3.09	4.27	4.08	1.38	1.32
Mshana 1993	OPB-1B	7.84	0.64	10.2	0.5	90	Steel	3.00	4.27	4.08	1.42	1.36
Mshana 1993	OPB-2B	7.84	0.64	10.2	0.5	90	Steel	3.66	4.27	4.08	1.17	1.11
Smith 1995	W1/W5	9.90	0.80	10.00	0.99	90	Steel	6.50	10.25	6.1	1.58	0.94
Smith 1995	W2	9.90	0.80	10.00	0.99	90	Steel	6.70	10.25	6.1	1.53	0.91
Smith 1995	W3/W6	9.90	0.80	10.00	0.99	90	Steel	6.70	10.25	6.1	1.53	0.91
Smith 1995	W4	9.90	0.80	10.00	0.99	90	Steel	6.40	10.25	6.1	1.60	0.95
Smith 1995	S1	9.90	0.80	10.00	0.99	90	Steel	6.40	10.25	6.1	1.60	0.95
Smith 1995	S2	9.90	0.80	10.00	0.99	90	Steel	6.00	10.25	6.1	1.71	1.02
Smith 1995	S3	9.90	0.80	10.00	0.99	90	Steel	6.60	10.25	6.1	1.55	0.92
Smith 1995	S4	9.90	0.80	10.00	0.99	90	Steel	6.20	10.25	6.1	1.65	0.98

Table 4.8 Comparison between the Predictions from the SCF and SCF Distribution Equations with Recorded SCF data at Brace Crown position for Balanced Axially loaded X and DT-joints

Spec. no.	α	β	γ	τ	θ (deg)	Mat	Rec	SCF Eq	SCF Dis Eq	SCF/ Rec	SCF Dis/Rec
E30	9.80	0.38	20.70	0.79	90	Steel	1.50	3.16	2.14	2.11	1.42
E36	9.80	0.38	20.50	0.81	90	Steel	1.70	3.16	2.27	1.86	1.33
E37	9.80	0.38	21.00	0.83	90	Steel	1.60	3.12	2.22	1.95	1.39
1U/1	10.00	0.26	12.00	0.75	90	Acrylic	1.70	3.93	5.72	2.31	3.36
1U/2	10.00	0.50	12.00	0.75	90	Acrylic	2.00	2.78	2.98	1.39	1.49
1U/3	10.00	0.80	12.00	0.75	90	Acrylic	1.70	1.50	1.67	0.88	0.98
1U/5	10.00	0.26	24.00	0.75	90	Acrylic	2.80	4.50	5.57	1.61	1.99
1U/9	10.00	0.26	32.00	0.75	90	Acrylic	3.40	4.19	5.45	1.23	1.60
2U/1	10.00	0.80	24.00	0.75	60	Acrylic	1.80	1.50	11.07	0.83	6.15

Table 4.9 Comparison between the Predictions from the SCF and SCF Distribution Equations with Recorded SCF data at Brace Saddle position for Balanced Axially loaded X and DT-joints

Spec. no.	α	β	γ	τ	θ (deg)	Mat	Rec	SCF Eq	SCF Dis Eq	SCF/ Rec	SCF Dis/Rec
A	8.50	0.72	10.40	0.94	90	Steel	7.50	14.52	13.61	1.94	1.81
E30	9.80	0.38	20.70	0.79	90	Steel	10.60	22.70	21.73	2.14	2.05
E36	9.80	0.38	20.50	0.81	90	Steel	14.30	23.01	21.85	1.61	1.53
E37	9.80	0.38	21.00	0.83	90	Steel	12.40	24.03	22.53	1.94	1.82
X4	17.50	0.67	25.30	0.82	90	Steel	15.00	29.61	27.29	1.97	1.82
1U/1	10.00	0.26	12.00	0.75	90	Acrylic	7.60	13.10	13.50	1.72	1.78
1U/2	10.00	0.50	12.00	0.75	90	Acrylic	10.50	13.43	14.67	1.28	1.40
1U/3	10.00	0.80	12.00	0.75	90	Acrylic	9.10	13.67	11.16	1.50	1.23
1U/5	10.00	0.26	24.00	0.75	90	Acrylic	13.20	24.43	22.47	1.85	1.70
1U/6	10.00	0.50	24.00	0.75	90	Acrylic	19.20	25.05	25.55	1.30	1.33
1U/7	10.00	0.80	24.00	0.75	90	Acrylic	17.50	25.50	21.42	1.46	1.22
1U/9	10.00	0.26	32.00	0.75	90	Acrylic	21.90	31.64	28.64	1.44	1.31
1U/10	10.00	0.50	32.00	0.75	90	Acrylic	29.10	32.44	35.10	1.11	1.21
1U/11	13.30	0.80	32.00	0.75	90	Acrylic	28.90	33.52	29.33	1.16	1.01
2U/1	10.00	0.80	24.00	0.75	60	Acrylic	11.20	18.66	22.46	1.67	2.01

Table 4.10 Comparison between the Predictions from the SCF and SCF Distribution Equations with Recorded SCF data at Chord Crown position for Balanced Axially loaded X and DT-joints

Spec. no.	α	β	γ	τ	θ (deg)	Mat	Rec	SCF Eq	SCF Dis Eq	SCF/ Rec	SCF Dis/Rec
E30	9.80	0.38	20.70	0.79	90	Steel	3.30	2.09	1.5	0.63	0.45
E36	9.80	0.38	20.50	0.81	90	Steel	3.60	2.14	1.5	0.59	0.42
E37	9.80	0.38	21.00	0.83	90	Steel	3.30	2.15	1.5	0.65	0.45
1U/1	10.00	0.26	12.00	0.75	90	Acrylic	3.70	3.58	4.23	0.97	1.14
1U/2	10.00	0.50	12.00	0.75	90	Acrylic	2.20	1.76	1.50	0.80	0.68
1U/5	10.00	0.26	24.00	0.75	90	Acrylic	4.00	2.93	3.31	0.73	0.83
1U/9	10.00	0.26	32.00	0.75	90	Acrylic	4.10	3.15	1.72	0.77	0.42
2U/1	10.00	0.80	24.00	0.75	60	Acrylic	1.60	1.50	1.50	0.94	0.94
XJOINT2	16.00	0.33	24.00	1.00	45	Acrylic	10.3	3.91	3.52	0.38	0.34
XJOINT3	16.00	0.50	24.00	1.00	45	Acrylic	6.20	2.33	2.08	0.38	0.34
XJOINT5	16.00	0.83	24.00	1.00	45	Acrylic	2.00	1.50	1.65	0.75	0.82
XJOINT9	16.00	0.50	24.00	1.00	30	Acrylic	6.20	3.18	2.56	0.51	0.41

Table 4.11 Comparison between the Predictions from the SCF and SCF Distribution Equations with the Recorded data at Chord Saddle position for Balanced Axially loaded X and DT-joints

Spec. no.	α	β	γ	τ	θ (deg)	Mat	Rec	SCF Eq	SCF Dis Eq	SCF/ Rec	SCF Dis /Rec
18, 20	6.70	0.76	12.00	0.50	90	Steel	7.70	8.10	7.33	1.05	0.95
19	7.00	0.71	11.40	0.64	90	Steel	10.20	10.78	10.29	1.06	1.01
34-35, 39-40	10.00	0.50	14.30	0.50	90	Steel	11.05	9.97	10.46	0.90	0.95
A	8.50	0.72	10.40	0.94	90	Steel	10.90	16.74	15.95	1.54	1.46
E30	9.80	0.38	20.70	0.79	90	Steel	21.80	27.57	27.08	1.26	1.24
E36	9.80	0.38	20.50	0.81	90	Steel	20.80	28.24	27.61	1.36	1.33
E37	9.80	0.38	21.00	0.83	90	Steel	21.40	29.96	29.33	1.40	1.37
X4	17.50	0.67	25.30	0.82	90	Steel	29.50	37.05	34.69	1.26	1.18
X5	17.50	0.67	25.30	0.82	90	Steel	31.80	37.05	34.69	1.17	1.09
X6	17.50	0.35	25.00	0.81	90	Steel	24.00	35.98	33.43	1.50	1.39
1U/1	10.00	0.26	12.00	0.75	90	Acrylic	9.80	14.42	12.77	1.47	1.30
1U/2	10.00	0.50	12.00	0.75	90	Acrylic	13.10	14.42	15.11	1.10	1.15
1U/3	10.00	0.80	12.00	0.75	90	Acrylic	10.70	14.42	12.10	1.35	1.13
1U/5	10.00	0.26	24.00	0.75	90	Acrylic	18.50	30.07	24.31	1.63	1.31
1U/6	10.00	0.50	24.00	0.75	90	Acrylic	25.70	30.07	33.44	1.17	1.30
1U/7	10.00	0.80	24.00	0.75	90	Acrylic	24.10	30.07	24.83	1.25	1.03
1U/9	10.00	0.26	32.00	0.75	90	Acrylic	23.50	40.79	32.38	1.74	1.38
1U/10	10.00	0.50	32.00	0.75	90	Acrylic	39.90	40.79	46.44	1.02	1.16
1U/11	13.30	0.80	32.00	0.75	90	Acrylic	37.80	41.43	33.14	1.10	0.88
2U/1	10.00	0.80	24.00	0.75	60	Acrylic	17.00	22.42	19.73	1.32	1.16
XJOINT2	16.00	0.33	24.00	1.00	45	Acrylic	16.70	22.56	23.19	1.35	1.39
XJOINT3	16.00	0.50	24.00	1.00	45	Acrylic	14.80	22.56	24.98	1.52	1.69
XJOINT9	16.00	0.50	24.00	1.00	30	Acrylic	8.80	11.13	14.26	1.26	1.62

Table 4.12 Comparison between the Predictions from the SCF and SCF Distribution Equations with the Recorded SCF data on Brace Side for Balanced IPB Loaded X and DT-joints

Spec. no.	α	β	γ	τ	θ (deg)	Mat	Rec	SCF Eq	SCF Dis Eq	SCF/ Rec	SCF Dis/Re c
AA	8.50	0.72	10.60	0.99	90	Steel	1.80	2.96	3.03	1.64	1.68
E30	9.80	0.38	20.70	0.79	90	Steel	2.50	4.33	3.85	1.73	1.54
E36	9.80	0.38	20.50	0.81	90	Steel	2.30	4.34	3.83	1.89	1.67
E37	9.80	0.38	21.00	0.83	90	Steel	2.40	4.41	3.86	1.84	1.61
1U/1	10.00	0.26	12.00	0.75	90	Acrylic	1.60	3.14	3.0	1.96	1.88
1U/2	10.00	0.50	12.00	0.75	90	Acrylic	2.30	3.29	3.11	1.43	1.35
1U/3	10.00	0.80	12.00	0.75	90	Acrylic	2.30	2.81	2.57	1.22	1.12
1U/5	10.00	0.26	24.00	0.75	90	Acrylic	3.10	4.33	4.45	1.40	1.44
1U/6	10.00	0.50	24.00	0.75	90	Acrylic	2.90	4.54	3.54	1.56	1.22
1U/7	10.00	0.80	24.00	0.75	90	Acrylic	3.80	3.87	8.06	1.02	2.12
1U/9	10.00	0.26	32.00	0.75	90	Acrylic	4.20	4.95	5.42	1.18	1.29
1U/10	10.00	0.50	32.00	0.75	90	Acrylic	5.20	5.18	8.35	1.00	1.61
1U/11	13.30	0.80	32.00	0.75	90	Acrylic	4.30	4.42	9.57	1.03	2.23
2U/1	10.00	0.80	24.00	0.75	60	Acrylic	2.70	3.26	3.02	1.21	1.12

Table 4.13 Comparison between the Predictions from the SCF and SCF Distribution Equations with the Recorded SCF data on Chord Side for Balanced IPB Loaded X and DT-joints

Spec. no.	α	β	γ	τ	θ (deg)	Mat	Rec	SCF Eq	SCF Dis Eq	SCF/ Rec	SCF Dis/Re c
AA	8.50	0.72	10.60	0.99	90	Steel	3.20	4.66	4.21	1.46	1.32
E30	9.80	0.38	20.70	0.79	90	Steel	4.40	5.02	5.31	1.14	1.21
E36	9.80	0.38	20.50	0.81	90	Steel	4.00	5.13	5.47	1.28	1.37
E37	9.80	0.38	21.00	0.83	90	Steel	4.20	5.31	5.74	1.26	1.37
X4	17.50	0.67	25.30	0.82	90	Steel	2.80	5.59	3.60	2.00	1.29
X5	17.50	0.67	25.30	0.82	90	Steel	3.30	5.59	3.60	1.69	1.09
X6	17.50	0.35	25.00	0.81	90	Steel	4.40	5.59	5.80	1.27	1.32
1U/1	10.00	0.26	12.00	0.75	90	Acrylic	2.20	3.82	3.18	1.74	1.45
1U/2	10.00	0.50	12.00	0.75	90	Acrylic	2.80	3.76	3.73	1.34	1.33
1U/3	10.00	0.80	12.00	0.75	90	Acrylic	3.20	3.71	3.36	1.16	1.05
1U/5	10.00	0.26	24.00	0.75	90	Acrylic	4.20	5.13	5.16	1.22	1.23
1U/6	10.00	0.50	24.00	0.75	90	Acrylic	4.40	5.04	4.84	1.15	1.10
1U/7	10.00	0.80	24.00	0.75	90	Acrylic	4.00	4.97	4.56	1.24	1.14
1U/9	10.00	0.26	32.00	0.75	90	Acrylic	5.60	5.80	6.81	1.03	1.22
1U/10	10.00	0.50	32.00	0.75	90	Acrylic	5.70	5.69	7.88	1.00	1.38
1U/11	13.30	0.80	32.00	0.75	90	Acrylic	5.40	5.62	4.67	1.04	0.86
2U/1	10.00	0.80	24.00	0.75	60	Acrylic	3.60	4.51	3.63	1.25	1.01
XJOINT2	16.00	0.50	24.00	1.00	45	Acrylic	4.40	5.30	4.43	1.21	1.01

Table 4.14 Comparison between the Predictions from the SCF and SCF Distribution Equations with the Recorded SCF data on Brace Side for Balanced OPB Loaded X and DT-joints

Spec. no.	α	β	γ	τ	θ (deg)	Mat	Rec	SCF Eq	SCF Dis Eq	SCF/Rec	SCF Dis/Rec
E30	9.80	0.38	20.70	0.79	90	Steel	3.80	9.07	9.77	2.39	2.57
E36	9.80	0.38	20.50	0.81	90	Steel	6.20	9.11	9.73	1.47	1.57
E37	9.80	0.38	21.00	0.83	90	Steel	5.00	9.44	9.99	1.89	2.00
X4	17.50	0.67	25.30	0.82	90	Steel	7.30	15.66	17.02	2.15	2.33
1U/1	10.00	0.26	12.00	0.75	90	Acrylic	2.50	4.53	4.67	1.81	1.87
1U/2	10.00	0.50	12.00	0.75	90	Acrylic	4.90	6.07	6.98	1.24	1.43
1U/3	10.00	0.80	12.00	0.75	90	Acrylic	5.10	7.48	4.94	1.47	0.97
1U/5	10.00	0.26	24.00	0.75	90	Acrylic	5.40	8.54	7.16	1.58	1.33
1U/6	10.00	0.50	24.00	0.75	90	Acrylic	11.00	11.43	14.43	1.04	1.31
1U/7	10.00	0.80	24.00	0.75	90	Acrylic	9.40	14.09	10.74	1.50	1.14
1U/9	10.00	0.26	32.00	0.75	90	Acrylic	10.10	11.11	8.50	1.10	0.84
1U/10	10.00	0.50	32.00	0.75	90	Acrylic	16.40	14.87	19.86	0.91	1.21
1U/11	13.30	0.80	32.00	0.75	90	Acrylic	16.90	19.16	15.47	1.13	0.92
2U/1	10.00	0.80	24.00	0.75	60	Acrylic	6.50	10.51	7.44	1.62	1.15

Table 4.15 Comparison between the Predictions from the SCF and SCF Distribution Equations with the Recorded SCF data on Chord Side for Balanced OPB Loaded X and DT-joints

Spec. no.	α	β	γ	τ	θ (deg)	Mat	Rec	SCF Eq	SCF Dis Eq	SCF/Rec	SCF Dis/Rec
E30	9.80	0.38	20.70	0.79	90	Steel	7.70	11.52	10.90	1.50	1.42
E36	9.80	0.38	20.50	0.81	90	Steel	8.90	11.73	11.03	1.32	1.24
E37	9.80	0.38	21.00	0.83	90	Steel	8.30	12.35	11.67	1.49	1.41
X4	17.50	0.67	25.30	0.82	90	Steel	13.20	18.94	22.42	1.43	1.70
X5	17.50	0.67	25.30	0.82	90	Steel	16.80	18.94	22.42	1.13	1.33
X6	17.50	0.35	25.00	0.81	90	Steel	13.90	15.13	13.50	1.09	0.97
1U/1	10.00	0.26	12.00	0.75	90	Acrylic	3.70	5.59	4.86	1.51	1.31
1U/2	10.00	0.50	12.00	0.75	90	Acrylic	6.30	6.83	7.08	1.08	1.12
1U/3	10.00	0.80	12.00	0.75	90	Acrylic	6.20	7.89	3.97	1.27	0.64
1U/5	10.00	0.26	24.00	0.75	90	Acrylic	7.90	11.27	8.57	1.43	1.08
1U/6	10.00	0.50	24.00	0.75	90	Acrylic	13.40	13.76	16.54	1.03	1.23
1U/7	10.00	0.80	24.00	0.75	90	Acrylic	13.10	15.89	15.44	1.21	1.18
1U/9	10.00	0.26	32.00	0.75	90	Acrylic	10.80	15.07	12.96	1.40	1.20
1U/10	10.00	0.50	32.00	0.75	90	Acrylic	21.40	18.40	28.33	0.86	1.32
1U/11	13.30	0.80	32.00	0.75	90	Acrylic	22.40	22.10	29.45	0.99	1.31
2U/1	10.00	0.80	24.00	0.75	60	Acrylic	9.70	11.94	10.08	1.23	1.04
XJOINT2	16.00	0.33	24.00	1.00	45	Acrylic	7.80	8.95	9.34	1.15	1.20
XJOINT3	16.00	0.50	24.00	1.00	45	Acrylic	9.80	10.16	8.12	1.04	0.83
XJOINT9	16.00	0.50	24.00	1.00	30	Acrylic	6.30	5.10	6.79	0.81	1.08

Table 4.16 Validation of SCF Distribution Parametric Equation for X-joint
under Balanced Axial at Brace Saddle Position

Equation	Steel/ Acrylic	No of Pts	Database		Pred SCF/Recorded SCF			Decision
			Mean	%st dev of Enq	%P/R< 0.8	%P/R< 1.0	%P/R> 1.5	
SCF Eq	Steel	5	1.92	19.3%	0.0%	0.0%	100%	accept but borderline conservative
	Acrylic	10	1.45	24.3%	0.0%	0.0%	30.0%	
	Pooled	15	1.61	31.8%	0.0%	0.0%	53.3%	
SCF Dis Eq	Steel	5	1.81	18.5%	0.0%	0.0%	100.0%	accept but borderline conservative
	Acrylic	10	1.42	30.8%	0.0%	0.0%	30.0%	
	Pooled	15	1.55	32.6%	0.0%	0.0%	53.3%	

Table 4.17 Validation of SCF Distribution Parametric Equation for X-joint
under Balanced Axial Loading at Chord Saddle Position

Equation	Steel/ Acrylic	No of Pts	Database		Pred SCF/Recorded SCF			Decision
			Mean	%st dev of Enq	%P/R< 0.8	%P/R< 1.0	%P/R> 1.5	
SCF Eq	Steel	10	1.25	20.7%	0.0%	10.0%	10.0%	accept
	Acrylic	13	1.33	21.5%	0.0%	0.0%	23.1%	
	Pooled	23	1.29	21.1%	0.0%	4.3%	17.4%	
SCF Dis Eq	Steel	10	1.20	19.0%	0.0%	20.0%	0.0%	accept
	Acrylic	13	1.27	22.3%	0.0%	7.7%	15.4%	
	Pooled	23	1.24	20.8%	0.0%	13.0%	8.7%	

Table 4.18 Validation of SCF Distribution Parametric Equation for X-joint
under Balanced IPB Loading on Brace Crown Position

Equation	Steel/ Acrylic	No of Pts	Database		Pred SCF/Recorded SCF			Decision
			Mean	%st dev of Enq	%P/R< 0.8	%P/R< 1.0	%P/R> 1.5	
SCF Eq	Steel	4	1.78	10.8%	0.0%	0.0%	100%	accept
	Acrylic	10	1.30	30.0%	0.0%	0.0%	20%	
	Pooled	14	1.44	33.8%	0.0%	0.0%	42.9%	
SCF Dis Eq	Steel	4	1.63	6.5%	0.0%	0.0%	100%	accept
	Acrylic	10	1.54	40.8%	0.0%	0.0%	40.0%	
	Pooled	14	1.56	34.3%	0.0%	0.0%	57.1%	

Table 4.19 Validation of SCF Distribution Parametric Equation for X-joint
under Balanced IPB Loading on Chord Crwon Position

Equation	Steel/ Acrylic	No of Pts	Database		Pred SCF/Recorded SCF			Decision
			Mean	%st dev of Enq	%P/R< 0.8	%P/R< 1.0	%P/R> 1.5	
SCF Eq	Steel	7	1.44	30.2%	0.0%	0.0%	28.6%	accept
	Acrylic	11	1.22	20.3%	0.0%	0.0%	9.1%	
	Pooled	18	1.30	26.4%	0.0%	0.0%	16.7%	
SCF Dis Eq	Steel	7	1.28	10.0%	0.0%	0.0%	0.0%	accept
	Acrylic	11	1.16	17.9%	0.0%	9.1%	0.0%	
	Pooled	18	1.21	16.1%	0.0%	5.6%	0.0%	

Table 4.20 Validation of SCF Distribution Parametric Equation for X-joint
under Balanced OPB Loading on Brace Saddle Position

Equation	Steel/ Acrylic	No of Pts	Database		Pred SCF/Recorded SCF			Decision
			Mean	%st dev of Enq	%P/R< 0.8	%P/R< 1.0	%P/R> 1.5	
SCF Eq	Steel	4	1.97	39.2%	0.0%	0.0%	75.0%	accept
	Acrylic	10	1.34	29.6%	0.0%	10.0%	30.0%	
	Pooled	14	1.52	42.9%	0.0%	7.1%	42.9%	
SCF Dis Eq	Steel	4	2.12	43.3%	0.0%	0.0%	100.0%	accept
	Acrylic	10	1.22	29.7%	0.0%	30.0%	10.0%	
	Pooled	14	1.47	53.2%	0.0%	21.4%	35.7%	

Table 4.21 Validation of SCF Distribution Parametric Equation for X joint
under Balanced OPB on Chord Saddle Position

Equation	Steel/ Acrylic	No of Pts	Database		Pred SCF/Recorded SCF			Decision
			Mean	%st dev of Enq	%P/R< 0.8	%P/R< 1.0	%P/R> 1.5	
SCF Eq	Steel	6	1.33	18.1%	0.0%	0.0%	0.0%	accept
	Acrylic	13	1.15	21.4%	0.0%	15.4%	7.7%	
	Pooled	19	1.21	21.5%	0.0%	10.5%	5.3%	
SCF Dis Eq	Steel	6	1.35	24.0%	0.0%	16.7%	16.7%	accept
	Acrylic	13	1.12	19.7%	7.7%	15.4%	0.0%	
	Pooled	19	1.19	23.1%	5.3%	15.8%	5.3%	

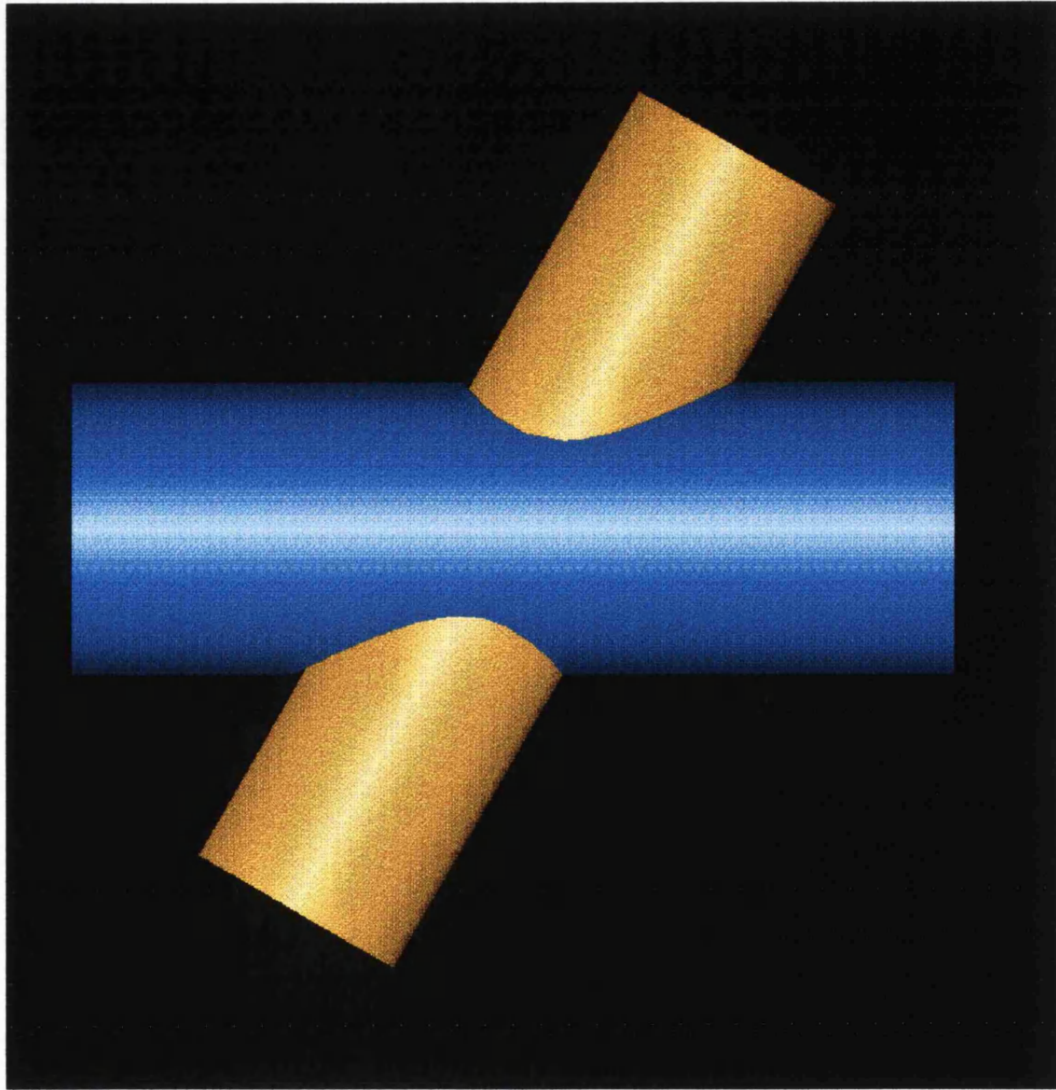


Figure 4.1 Illustration of Tubular X-joint

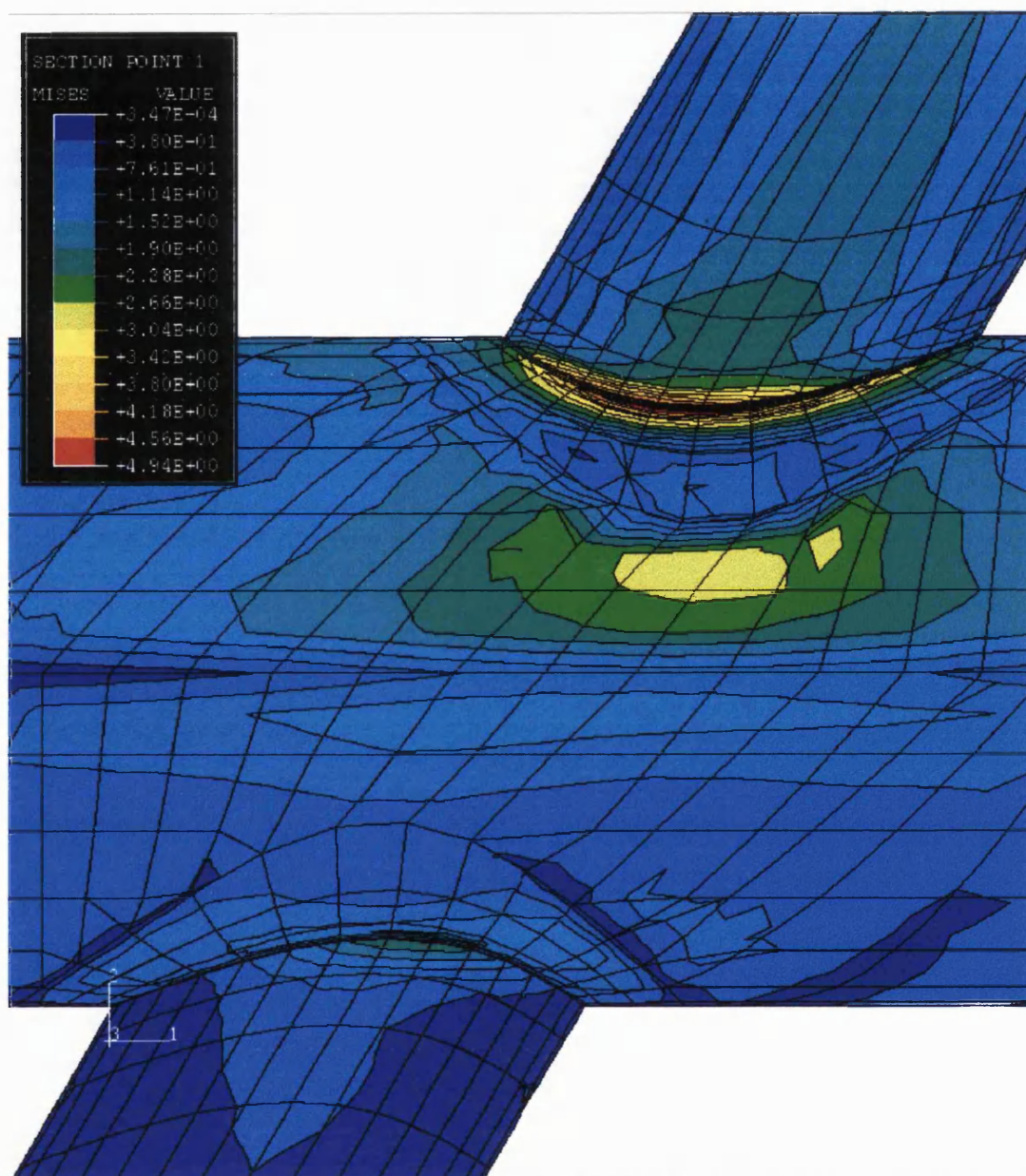


Figure 4.2 Plot of Typical External Stress Distribution around the Intersection of Tubular X-joint under Single Brace Axial Loading

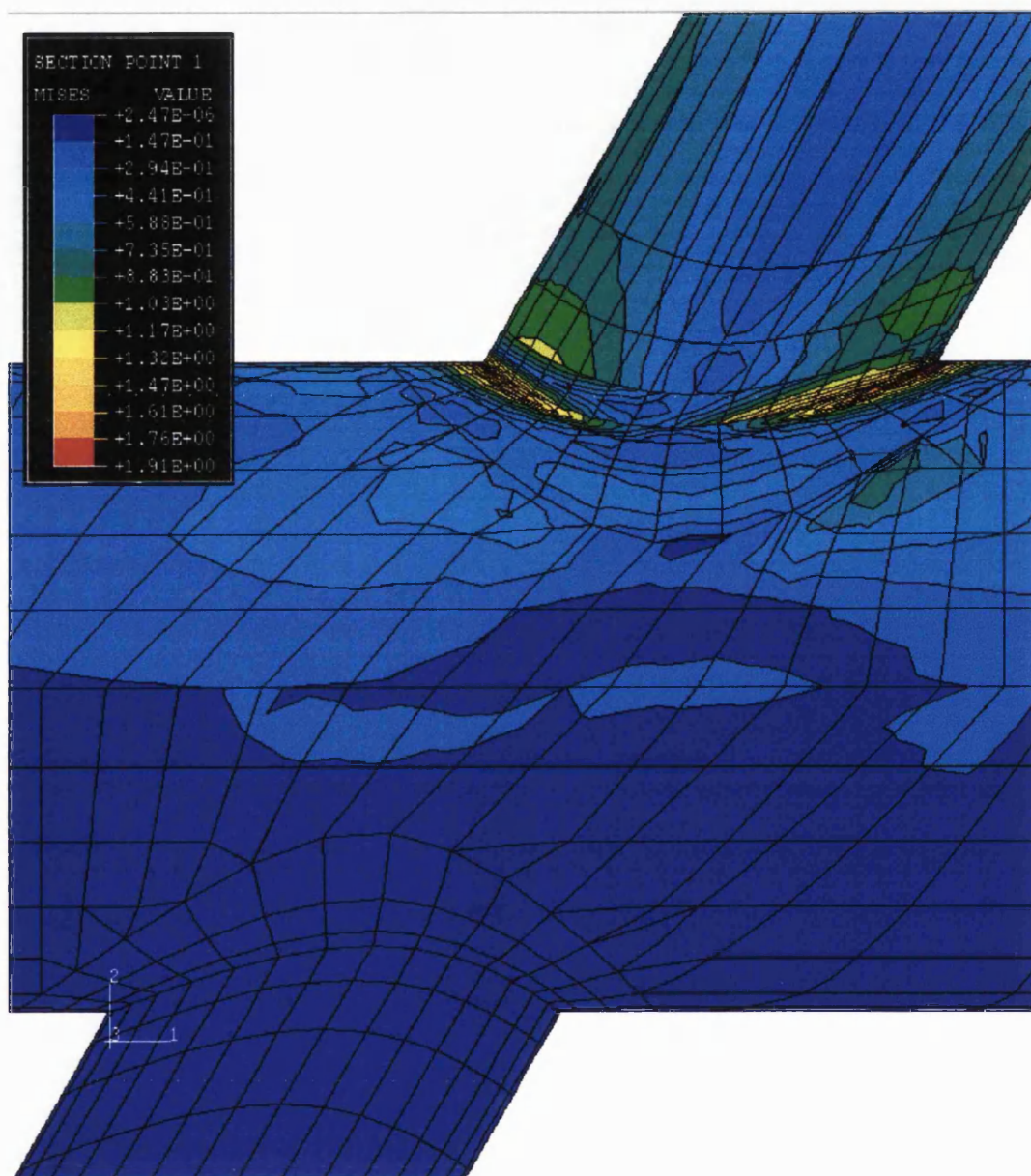


Figure 4.3 Plot of Typical External Stress Distribution around the Intersection of Tubular X-joint under Single Brace IPB Loading

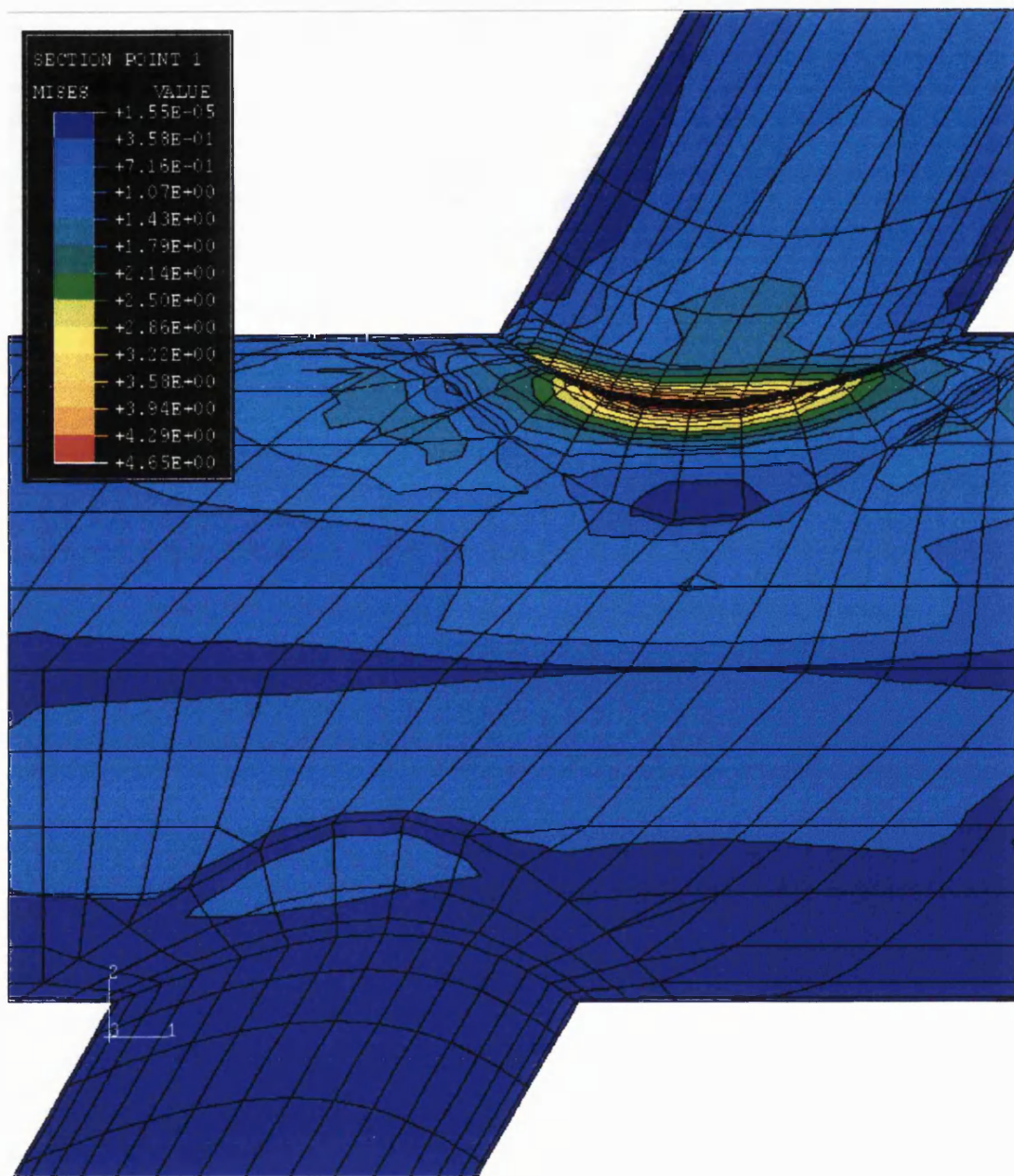


Figure 4.4 Plot of Typical External Stress Distribution around the Intersection of Tubular X-joint under Single Brace OPB Loading

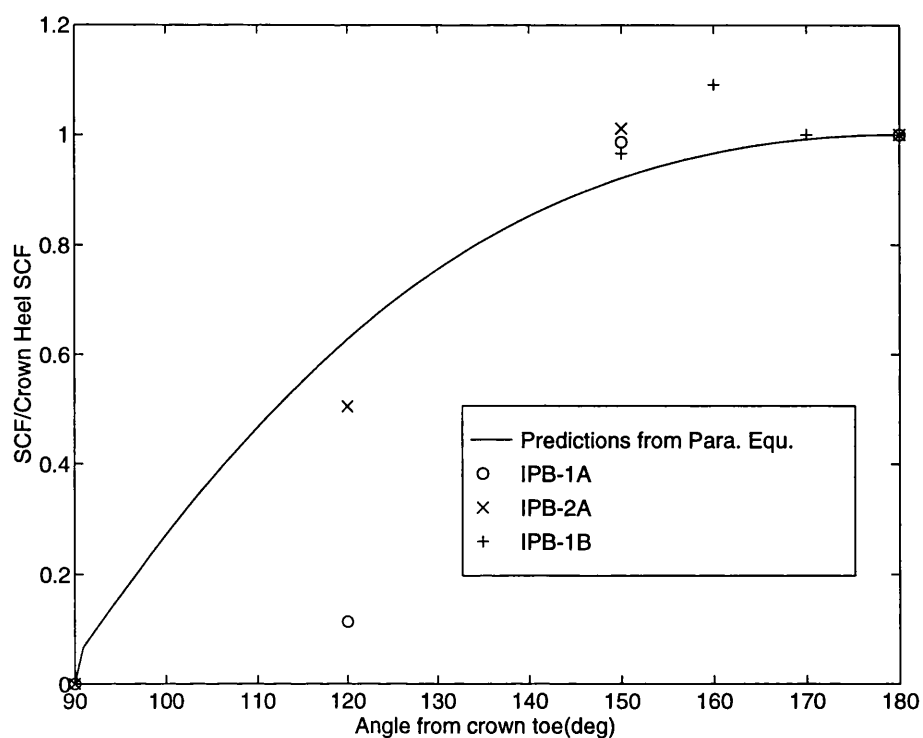


Figure 4.5 Comparison of Predicted Normalised External Surface SCF Distribution on Chord Toe with Steel Model Test Results for the Single IPB Loaded DT-joints ($\alpha=7.48$, $\beta=0.64$, $\gamma=10.2$, $\tau=0.5$, $\theta=90^\circ$)

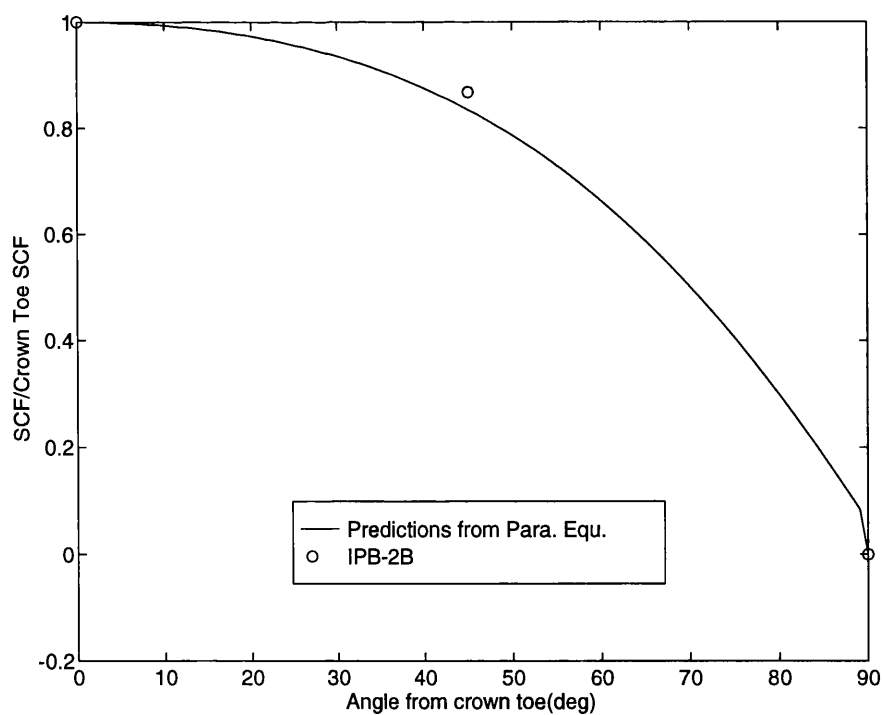


Figure 4.6 Comparison of Predicted Normalised External Surface SCF Distribution on Chord Toe with Steel Model Test Results for the Single IPB Loaded DT-joint ($\alpha=7.48$, $\beta=0.64$, $\gamma=10.2$, $\tau=0.5$, $\theta=90^\circ$)

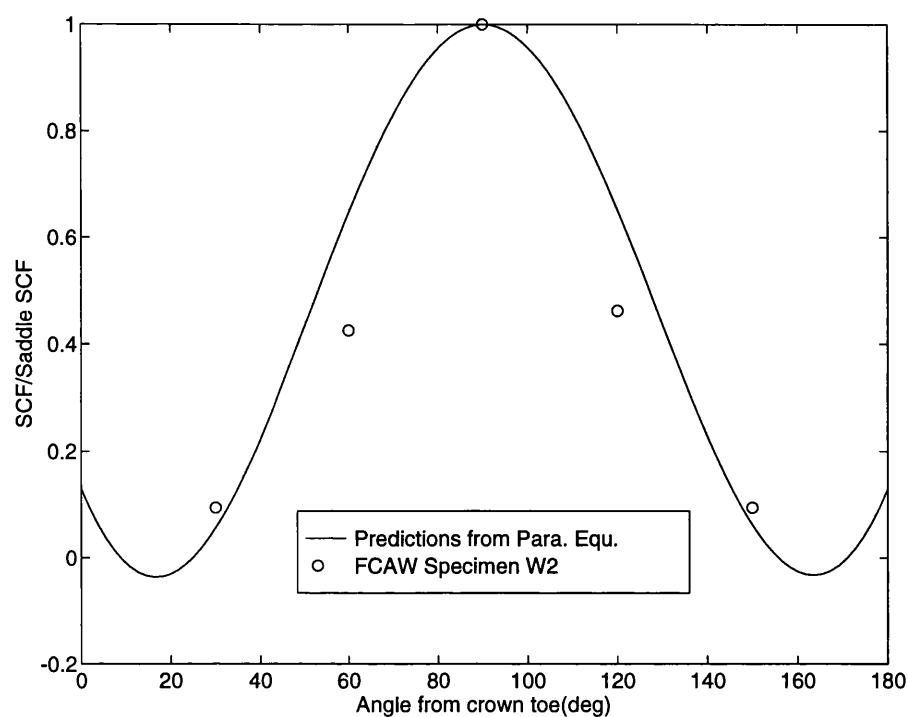


Figure 4.7 Comparison of Predicted Normalised External Surface SCF Distribution on Brace Toe with Steel Model Test Results for the Single OPB Loaded DT-joint ($\alpha=9.9$, $\beta=0.8$, $\gamma=10.6$, $\tau=1.0$, $\theta=90^\circ$)

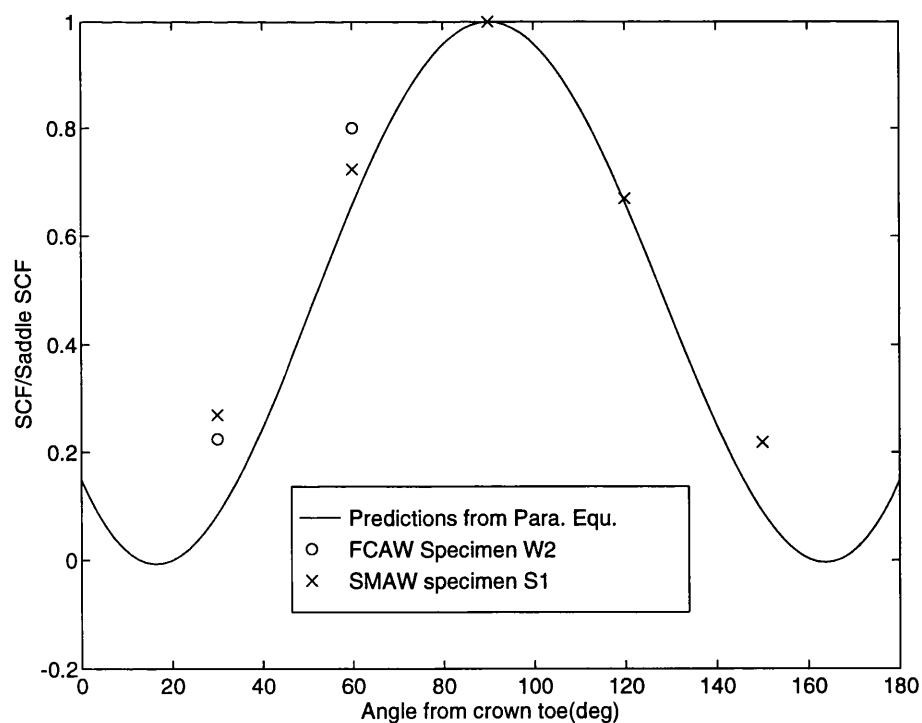


Figure 4.8 Comparison of Predicted Normalised External Surface SCF Distribution on Chord Toe with Steel Model Test Results for the Single OPB Loaded DT-joint ($\alpha=9.9$, $\beta=0.8$, $\gamma=10.6$, $\tau=1.0$, $\theta=90^\circ$)

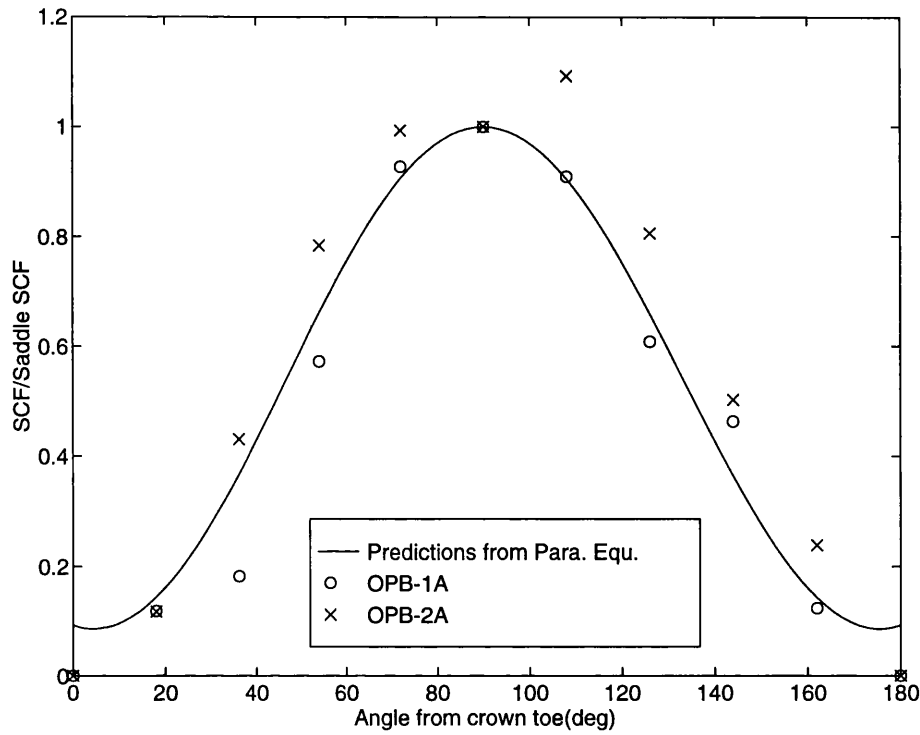


Figure 4.9 Comparison of Predicted Normalised External Surface SCF Distribution on Chord Toe with Steel Model Test Results for the Single OPB Loaded DT-joint ($\alpha=7.48$, $\beta=0.64$, $\gamma=10.2$, $\tau=0.5$, $\theta=90^\circ$)

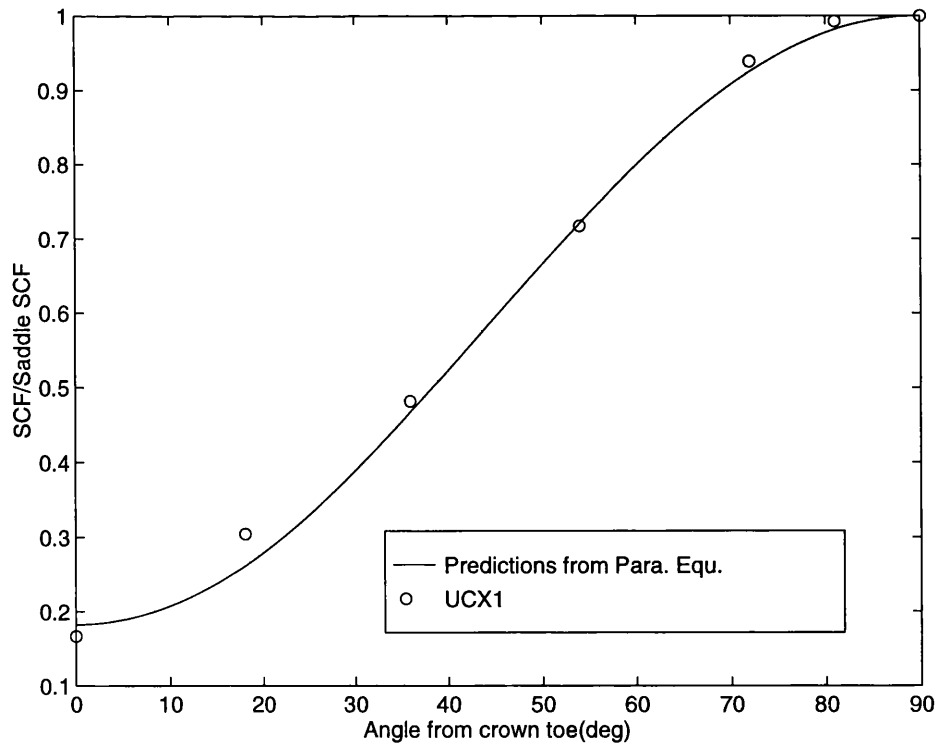


Figure 4.10 Comparison of Predicted Normalised External Surface SCF Distribution on Chord Toe with Steel Model Test Results for the Balanced Axial Loaded DT-joint ($\alpha=4.4$, $\beta=0.51$, $\gamma=10.0$, $\tau=0.44$, $\theta=90^\circ$)

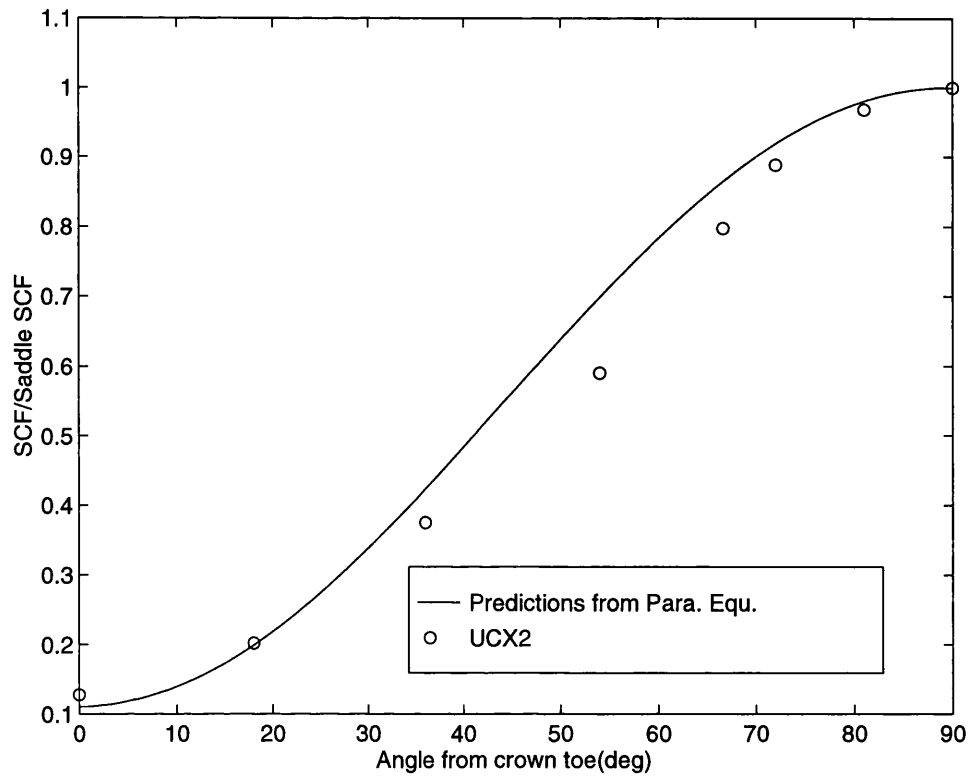


Figure 4.11 Comparison of Predicted Normalised External Surface SCF Distribution on Chord Toe with Steel Model Test Results for the Balanced Axial Loaded DT-joint ($\alpha=5.33$, $\beta=0.61$, $\gamma=14.28$, $\tau=0.54$, $\theta=90^\circ$)

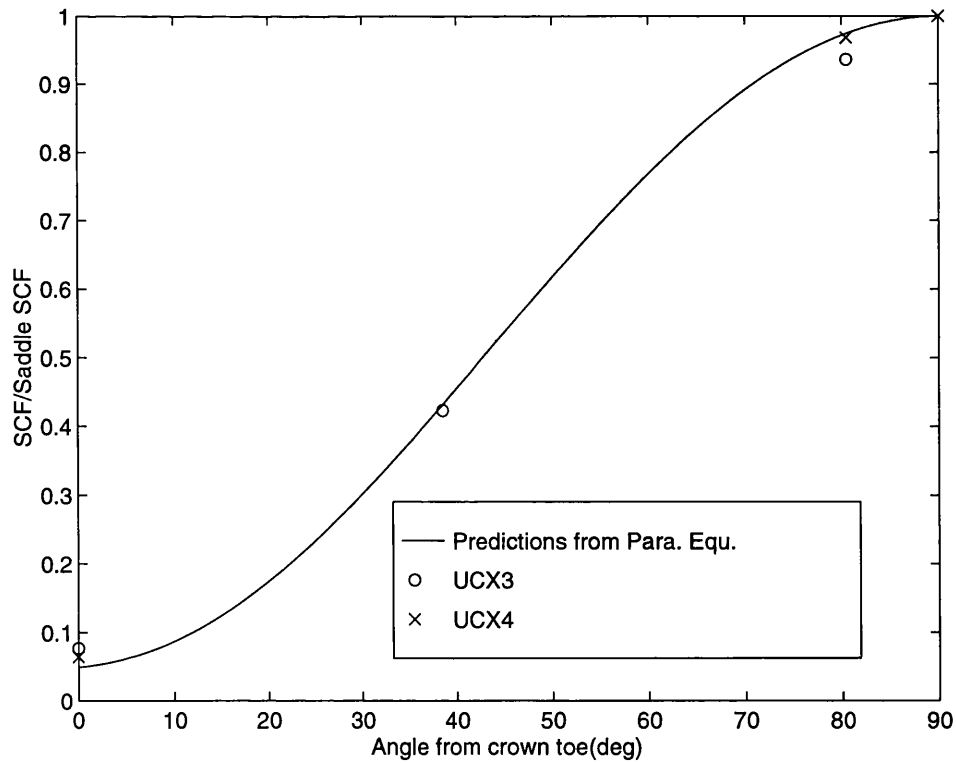


Figure 4.12 Comparison of Predicted Normalised External Surface SCF Distribution on Chord Toe with Steel Model Test Results for the Balanced Axial Loaded DT-joint ($\alpha=6.67$, $\beta=0.76$, $\gamma=12.0$, $\tau=0.5$, $\theta=90^\circ$)

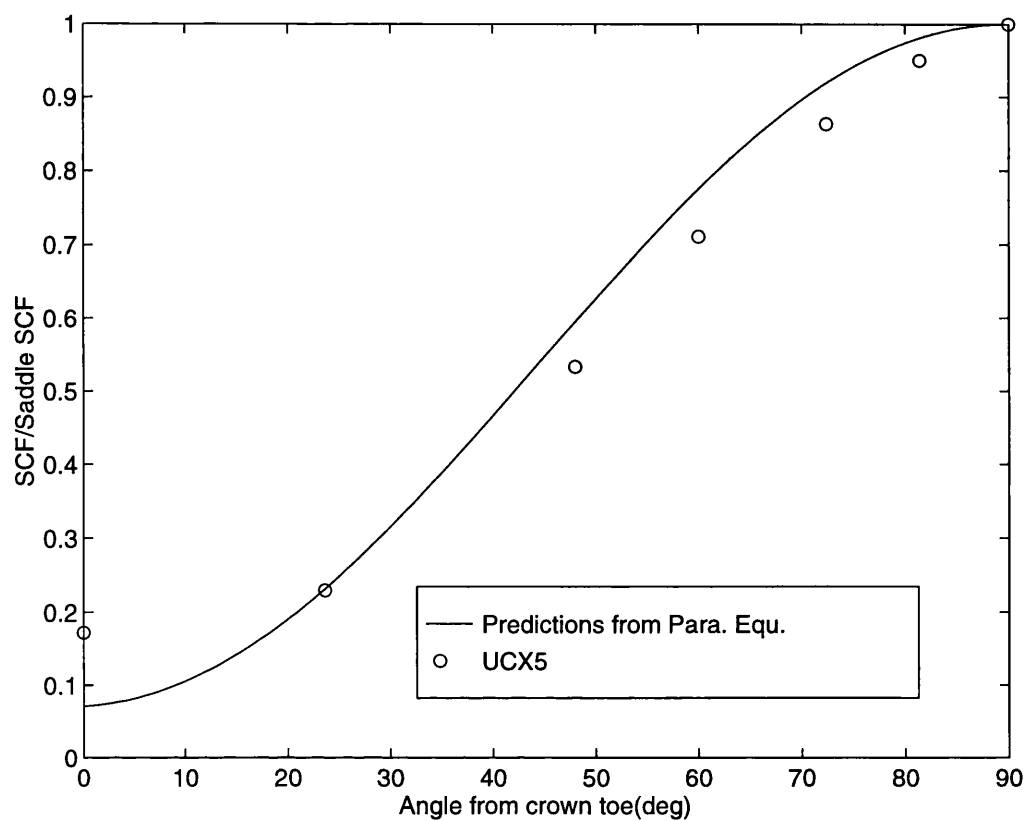


Figure 4.13 Comparison of Predicted Normalised External Surface SCF Distribution on Chord Toe with Steel Model Test Results for the Balanced Axial Loaded DT-joint ($\alpha=7.02$, $\beta=0.71$, $\gamma=11.4$, $\tau=0.64$, $\theta=90^\circ$)

CHAPTER FIVE

STRESS PARAMETRIC EQUATIONS FOR TUBULAR Y AND T-JOINTS

5.1 Introduction

The stress information needed for advanced fatigue strength assessment of tubular joints includes not only the hot spot SCF, but also the DoB and stress distribution along the intersection. Much research effort has been made to derive the stress parametric equations. Among them, the UCL HCD set of equations (Hellier et al 1990 a) (Hellier et al 1990 b) (Connolly et al 1990), is the only set of equations which can provide all these two dimensional stress information for tubular Y and T-joints. Others were not available for the fracture mechanics analysis. However, this set of equations was not recommended by fatigue panel (MaTSU 1996) to predict the hot spot SCF for tubular Y and T-joints as they do not pass the assessment criteria in some cases. The problem with the HCD stress distribution equations is that they were characteristic formulae and derived by observing a limited number of results rather than whole database. For this reason, they did not provide enough accuracy for all other cases for detailed analyses and may therefore be unconservative for some situations. Also the use of these stress distributions requires input on peak stresses. Thus it is desirable to enhance the stress prediction capability of this set of equations.

In the last chapter, it has been demonstrated that it is possible to derive a set of parametric equations to predict full stress distributions along the intersection of tubular X and DT-joints. These equations have the capability to estimate both the normalised SCF distributions and the hot spot SCFs. These new expressions are ideal for advanced fatigue assessment, especially during the design stage and for rigorous fracture mechanics analysis. Thus, an attempt has been made to derive similar equations for tubular Y and T-joints. Although systematic finite element analyses were performed for tubular Y and T-joint at UCL before, the original data were not available in electronic form now. With the dramatic advance in computing capability and the experience obtained in analysis of X and DT-joint, it is possible to obtain the new database very quickly. Using the similar procedure with same finite element package for the same joint database, the equations to be derived can be fully compatible with the equations for tubular X and DT-joints. All these consideration led to carry out over 1000 thin-shell finite element analyses. Being similar to that for X and DT-joints, the whole finite element analysis

process is only briefly presented in this chapter and the emphasis is placed on the curve-fitting these results and assessment of this new set of equations

5.2 Systematic Finite Element Analyses

A systematic study of stresses in tubular Y and T-joints(Figure 5.1) have been conducted using the general-purpose finite element analysis package, ABAQUS/Standard(HKS 1992 a). Two types of generally curved thin shell elements, namely quadrilateral eight-noded elements denoted 'S8R5' and triangular six-noded elements designated as 'STRI65', have been chosen to model tubular joint. They are fully compatible and allow displacements normal to their surfaces and rotations about their edges. These displacements and rotations give rise to a stress distribution which varies linearly across the element. Stresses are initially calculated at the Gauss integration points and then extrapolated to obtain values at the nodal positions.

It should be noted that the tubular joints are modelled as intersecting cylindrical tubes at the mid-surfaces of the walls. Thus the weld is not modelled and some detail of the stresses are lost. This leads to hot spot stress locations which are different to steel models especially for the brace. This is the reason why there are some discrepancies between the finite element results and those obtained from steel model test, especially on the brace side. However, the difference is generally quite small when comparing with results from strain-gauged acrylic models in which the weld is also omitted. The thin shell elements do provide, in many cases, an acceptable compromise between accuracy and computational cost except for situations where the chord and brace are of similar dimensions. For this reason the present study does not include SCFs in tubular joints for which β exceeds 0.8.

In order to conduct a parametric study, 330 different tubular Y and T-joints have been chosen for finite element analyses under axial, IPB and OPB loading respectively. Covering the majority of tubular joints used in offshore structures, they spanned the following ranges of the geometric parameters:

$$6.0 \leq \alpha \leq 40.0 \quad (5 - 1)$$

$$0.2 \leq \beta \leq 0.8 \quad (5 - 2)$$

$$7.6 \leq \gamma \leq 32.0 \quad (5 - 3)$$

$$0.2 \leq \tau \leq 1.0 \quad (5 - 4)$$

$$0.1944\pi \leq \theta \leq \frac{\pi}{2} \quad (5 - 5)$$

In the present study, the α_b for all joints was assigned to the realistic value of 8 in order to avoid the effect of short brace length.

Based on the mesh generation program for tubular X and DT-joints(Chang and Dover, 1996), a pre-processing program was developed to automatically produce the input files for finite analysis of tubular Y and T-joints in ABAQUS format. This program is capable of producing relatively fine elements in the vicinity of the brace/chord intersection, and coarse elements near the ends of the chord and brace, in order to obtain accurate results whilst avoiding unnecessary computational effect. It can reliably generate meshes for joints having widely differing geometric parameters α , β , γ , τ and θ . As the hot-spot stress is defined by Department of Energy(DEn) as the linear extrapolation to the maximum principal stresses, from outside the region of weld geometrical influence to the weld toe. So the size of the element in the immediate vicinity of the intersection was carefully chosen in order to make the linear stress distribution region similar to that as DEn recommended. The program requires only a small amount of user input, usually only either absolute dimensions or non-dimensional geometric ratios.

Figure 5.1 illustrates three modes of loading, i.e. axial, in-plane bending(IPB) and out-plane bending(OPB) loading. Only one half of each joint geometry needs to be modelled, owing to symmetry under axial and IPB loading. Although for out-plane bending the situation is no longer symmetric, it was found(Connolly et al 1990) that satisfactory results could be obtained with the same meshes used for the other load cases by applying appropriate restraints on the bisecting plane. A typical Y-joint mesh, shown in Figure 5.2, comprises 2178 nodes and 705 elements. It just took few seconds of CPU time to generate mesh on a DEC Alpha open VMS workstation.

In the case of axial loading, the nominal stress was defined as the total applied load divided by the sectional area of the brace. Nominal stresses for moment loading were calculated from simple beam bending theory, using a moment arm measured from the brace end along its outer surface to the crown position for IPB, and to the saddle position for OPB. In order to make post processing easy, loads applied to the brace end were always set to give a unit nominal stress.

It is important to use the correct boundary conditions to obtain a realistic solution of stress distribution in tubular joints. Both chord ends were rigidly fixed for all loading cases. Under axial and IPB, no out-of-plane displacements and rotations are permitted at nodes on the symmetry plane. For OPB the situations are no longer symmetrical, the in-plane displacements are restrained over the bisecting plane.

The finite element analyses were run on a DEC Alpha workstation with open VMS operating system. The Young's modulus and Poisson's ratio were taken to be 207 Gpa and 0.3 respectively. In order to save CPU time, each joint was analysed consecutively for three modes of loading cases, without the need for recomputing the element stiffness matrices.

A convergence test was performed firstly in order to check that the meshes used for this study were sufficiently fine to predict the stresses at the brace/chord intersection with reasonable accuracy. Three meshes with 16, 20 and 24 elements respectively around the half intersection were analysed and the SCF results from these meshes are compared in Table 5.1. Comparison of SCF values obtained from these meshes generally has shown a good convergence. The coarsest mesh, having 16 elements around one half of the intersection, was chosen for this study as an acceptable compromise between accuracy and the computational costs.

Systematic finite element analyses were carried out for 330 different tubular Y and T-joints under axial, IPB and OPB loading. With the powerful DEC Alpha workstation, it just took about 4 minutes of CPU time to analyse a typical joint. ABAQUS/Post(HKS 1992 b) was used to post process the results from ABAQUS/Standard analyses. Figures 5.3-5.5 show typical examples of the external stress distribution of a tubular Y-joint under three modes of loading respectively.

The numerically greatest principal stress on the outer surface of the tube, at each node around the intersection, was used to calculate the SCF. Stresses at nodes shared by adjacent elements were averaged around, but not across the intersection. The SCF distributions along the intersection have been extracted from the 330 ABAQUS output files for curve-fitting by using some batch files in open VMS operating system.

5.3 Deriving stress distribution parametric equations

The database of finite element analysis results was used to derive a new set of equations for the full stress distribution along the intersection of tubular Y and T-joints by using a statistical regression package known as 'MINITAB'(1991). The regression analysis methodology is similar to that used for X and DT-joints as described in the last chapter. The two-dimensional fitting process is split into the following two levels.

1) The best form of expression for the variations of the SCF were found for both the chord and brace toes under each mode of loading as below by numerous tries.

For both brace and chord toes under axial and OPB loading:

$$SCF(\phi) = C_0 + C_1\phi + C_2\cos 2\phi \quad (0 \leq \phi \leq \pi) \quad (5-6)$$

For both brace and chord toes under IPB loading:

$$SCF(\phi) = C_0 + C_1\cos \phi + C_2\cos 2\phi \quad (0 \leq \phi \leq \pi) \quad (5-7)$$

2) Performing numerous regressions to fit the coefficients in the above equations as a function of the parameters α , β , γ , τ and θ .

The parametric equations for SCF distribution have been derived for both chord and brace toes of tubular Y and T-joints under three different modes of loading by carrying out the

numerous regression analysis and they are given in Appendix D. A summary of degree of fit for each equation is presented in Table 5.2. It shows that these equations fit the original FE data very well and the correlation coefficient R^2 is greater than 95% for the majority cases including both the form of equation and the coefficients.

These equations can be easily programmed and enable the SCF value to be calculated at any angular location around both brace and chord toes for all modes of loading. Assuming the loading direction shown in Figure 5.1, the negative hot-spot is at or close to crown toe while the positive hot-spot lies at or near the crown heel under IPB loading. In this loading case, the SCFs on both brace and chord saddle positions were taken as the average values of two sides in order to maintain the smooth transition of SCF distribution curve. As the maximum principal stresses were used to derive this set of equations, the SCFs on both brace and chord crown positions are not necessary zero but small values for OPB loading. It should be noted that a minimum SCF of 1.5 should be assigned when this set of equations are used to predict the SCFs at critical points such as hot spot, saddle, crown toe and crown heel.

5.4 Assessment

A new set of equations has been produced to predict the full stress distribution along the intersection of tubular Y and T-joints. However, shell elements are two-dimensional in nature, possessing thickness only in a mathematical sense needed to define the element stiffness matrix. A tubular joint analysed using these elements is actually modelled as the intersection between the brace and chord mid planes and the weld fillet can not be incorporated into this model. This means that the intersection stresses are calculated a small distance away from the point of interest. For chord this distance is usually quite small. However it is relatively large for the brace. Therefore, it is necessary to verify the results by validating against laboratory data.

Although aiming to produce the SCF distribution along the intersection, this set of equations(SCF Dis) also provide an alternative way to predict the hot spot SCFs. Thus, the validation of this set of equations has been split into the following two aspects.

a) Hot spot SCF Estimation

As the SCF information is from the new database of finite element analysis results, which is different to that used to derive previous HCD equations, and also a new two dimensional fitting methodology was adopted to fit these data, the hot spot SCF prediction results from this set of equations are different with those from HCD equations. According to the same procedures described in chapter three, the predictions for hot spot SCFs from this set of equations are compared with the values from HCD SCF parametric equations and together with all available experimental data in the Lloyds and UCL database. They are presented in

Tables 5.3-5.10 for the SCF at critical points such as hot spot, saddle and crown positions on brace and chord toes under three modes of loading respectively. Furthermore, statistical analyses were carried out and the criteria described in chapter three were used to validate all these cases. The evaluation results are listed in Tables 5.11-5.18. The assessment of this new set of equations is presented for each mode of loading in turn as follows.

i) Axial Loading

The SCF predictions from this set of equation(SCF Dis) and HCD equations are compared with the steel and acrylic model test data at the crown and saddle positions on the brace toe(Tables 5.3-5.4 and 5.11-5.12). Both sets of equations pass the acceptance criteria. However, the HCD equation is only accepted as borderline at brace saddle position. The comparison between the SCF Dis and HCD predictions with the experimental data is shown in Tables 5.5-5.6 and 5.13-5.14 for SCFs at chord crown and saddle positions. Both SCF Dis and HCD equations are rejected at the chord crown position(Tables 5.5 and 5.13). The predictions from these two set of equations are generally smaller than the test data. Those from SCF Dis equations are worst. This underestimation for chord crown was also found in the previous the thin-shell finite element analysis(Chang and Dover, 1996). It may be due to the limitation in using thin shell finite elements. For the chord saddle position(Tables 5.6 and 5.14), the SCF Dis equation is accepted while the HCD equation is rejected.

ii) IPB loading

The experimental results and the SCFs from the SCF Dis and HCD equations are compared in Table 5.7-5.8 and 5.15-5.16). Both sets of equations are accepted for predicting hot spot SCFs at both brace and chord toes.

iii) OPB loading

A comparison is made between the experimental data and the predictions from the SCF Dis and HCD equations(Tables 5.9-5.10 and 5.17-5.18). Both sets of equations are accepted for predicting hot spot SCF on brace toe. For the chord saddle position, the HCD equation is accepted while the SCF Dis equation is rejected.

As a summary, the new set of equations(SCF Dis) are accepted to predict the hot spot SCF for all cases except for the chord saddle position under OPB loading. Further examination of this case(Table 5.10) showed that the main serious predictions($P/R < 0.8$) are those for joints with high β ratio. This set of equations may not be as good as the earlier one dimensional SCF equations, for fitting the original finite element database, especially for high β ratio cases, as it aims to fit the two dimensional distribution rather than the hot spot alone. However, a comparison with experimental data shows that it can offer reasonable good performance for predicting the hot spot SCF except for the high β cases at chord saddle position under OPB loading. Under these conditions, it can be replaced by the HCD SCF equation.

b) Normalised SCF Distribution Prediction

Since the capability of predicting hot spot SCFs was assessed for this new set of equations in the last section, the validation of stress distribution is therefore based on the normalised SCF distribution data that can be obtained by dividing the hot spot SCF. However, as associated information, the comparison of actual SCF values are also carried out for these two set of equations.

A comparison has been made between the original and normalised stress distribution predictions from the SCF Dis and HCD equations with the existing UCL acrylic and steel model test results(Hellier et al 1990 b) and recently UCL steel test data(Myers 1996)(Etube, 1996) and the results are shown in Figures 5.6-5.31. Again, the evaluation of stress distribution is presented for each mode of loading in turn as following.

i) Axial Loading

A comparison of the predicted actual values and normalised SCF distribution data from the SCF Dis equations and the HCD equations with experimental test results, is shown in Figures 5.6-5.13 for brace and chord toes respectively. As can be seen from these figures, a reasonably good agreement has been achieved for these cases for both equations. However, it has been noticed again that the predictions from the thin finite element analysis results based solutions including SCF Dis and HCD equations, underestimate the SCFs at the chord crown position.

ii) IPB loading

Figures 5.14-5.21 show the comparison between the predicted SCF distribution from these two set of equations with the acrylic and steel model test data for both brace and chord toes respectively. The figures show both actual values and normalised distributions. Again, both sets of equations provide a good predictions for stress distributions compared with experimental results. Moreover, the predictions from SCF Dis equations show a better correlation.

iii) OPB loading

A comparison has been made between the predicted actual values and normalised SCF distribution from both sets of equations with acrylic and steel test data for both brace and chord toes respectively(Figures 5.22-5.31). As can be seen from these figures, a good agreement has been achieved for these cases for both equations. As all the maximum principal stresses along the intersection are used to derive the equations, the predictions from SCF Dis equations agree very well with experimental data along the welds including the area away from hot spot. The SCF predictions at the crown positions from SCF Dis equations are not zero but small values while zero is assigned at crown position for HCD equations. Generally,

the predictions from SCF Dis equations show a better correlation. However, a slight underestimation from the SCF Dis equation was observed for the chord saddle in Figure 5.30.

As a summary, both sets of equations provide a reasonably good SCF distribution prediction along the intersection under all modes of loading compared with acrylic and steel test results, the predictions from the SCF Dis equations being a slightly better. However, it should be noted that validation is limited as only these few test data are available.

5.5 Concluding Remarks

Comprehensive stress distribution information is needed for the advanced fatigue strength assessment of tubular joints, especially under multiple axes loading. However, so far there is only one set of stress equations(UCL HCD) which can provide this whole information for tubular Y and T-joint. However, this set of equations was not recommended by the fatigue panel(MaTSU 1996) to predict the hot spot SCF as they did not pass the assessment criteria in some cases. Also the HCD stress distribution equations are only based on a limited sample of finite element results and require hot spot SCF input. They may not provide sufficient accuracy for all individual joints. In order to enhance the stress prediction capability, systematic finite element analyses have been carried out for 330 tubular Y and T-joints which are typically used offshore. Based on these finite element results, a new set of parametric equations have been derived to predict the full stress distribution along the intersection of tubular welded Y and T-joints under three modes of loading as a function of the geometric parameters α , β , γ , τ and θ . The stress distribution equations not only can predict the normalised distribution for all cases but also provide an alternative method for predicting the hot spot SCF.

A comprehensive assessment has been made by comparing the predictions from this set of equations(SCF Dis) and HCD equations with available acrylic and steel test results. As a result, the new set of equations has been proven to have the capability to reliably estimate the hot spot SCFs on both brace and chord toes under all modes of loading except for the chord saddle under OPB loading. For this particular case, the HCD SCF parametric equations can be used instead. Thus, combining with HCD equations, this new set of equations can be used to predict all hot spot SCFs for tubular Y and T-joints.

The assessment also shows that both SCF Dis and HCD equations can provide SCF distribution predictions along the intersection under all modes of loading with reasonably good accuracy compared with acrylic and steel test results. The predictions from SCF Dis equations perform somewhat better. However, it should be noted that the validation of the equations is very limited as so far only very a few experimental data for stress distributions are available.

The HCD parametric equations can be used to predict the DoBs at the critical positions of both the chord and brace sides of tubular Y and T-joints. The characterised equations for DoB distribution along the intersection (Cheaitani et al 1995) have been derived recently for tubular T-joints and they permit the interpolation of DoB between hot-spot position. Therefore, with these two set of equations, the DoB at any position along the intersection of tubular T-joints can be predicted and these equations may also be extended for use in tubular Y-joints as the first estimate.

Thus, combination of this new set of equations (SCF Dis) and HCD equations together with Cheaitani equations allows one to recreate the 2D stress distribution around welded tubular Y and T-joints. All these equations can be easily incorporated into fatigue life calculation codes and provide a predictive capability for the stress acting on the welded intersection, anticipated crack plane.

Table 5.1 Comparison between DOBs around upper Intersection from Coarse to Fine X joint Meshes to Show Extent of Convergence ($\alpha=10.39$, $\beta=0.5$, $\gamma=12.9$, $\tau=0.5$, $\theta=90^\circ$)

No. of elements	Chord		Brace	
around intersection	Crown	Saddle	Crown	Saddle
Axial Loading				
16	2.197	7.536	2.775	9.328
20	2.203	7.296	2.825	9.062
24	2.199	7.497	2.813	9.171
In-Plane Bending				
16	2.589	0.0548	3.360	0.1533
20	2.549	0.0523	3.322	0.1703
24	2.578	0.0557	3.330	0.1806
Out-Plane Bending				
16	0.1520	5.585	0.3842	6.733
20	0.1563	5.377	0.4168	6.445
24	0.1768	5.553	0.4341	6.621

Table 5.2 Summary of Degree of Fit for the Parametric Equations of SCF Distribution
around the Intersection of Tubular Y and T-joints

Mode of		Form of Expression		C ₀	C ₁	C ₂	C ₃
Loading/	Equations	Descriptive Statistics (%)					
Location		Mean R ²	Std. Dev.	R ²			
Axial Loading							
Brace	Appendix E1.1	91.34%	9.92%	97.72	93.85	98.35	N/A
Chord	Appendix E1.2	95.71%	5.29%	98.64	94.55	97.82	N/A
In-Plane Bending							
Brace Toe Side	Appendix E2.1	97.19%	3.39%	95.78	96.32	96.03	N/A
Brace Heel Side	Appendix E2.1	99.28%	1.26%	96.29	97.36	96.93	N/A
Chord Toe Side	Appendix E2.2	99.55%	0.57%	96.68	96.88	96.65	N/A
Chord Heel Side	Appendix E2.2	99.48%	0.46%	97.46	97.38	96.51	N/A
Out-Plane Bending							
Brace	Appendix E3.1	93.13%	8.68%	97.17	93.32	98.30	N/A
Chord	Appendix E3.2	95.69%	4.59%	98.08	93.37	98.11	N/A

Table 5.3 Comparison between the Predictions from the SCF Distribution and HCD Equations with the Recorded data at Brace Crown position for Axially Loaded Y and T-joints

Joint Ref	α	β	γ	τ	θ (Rad)	Mat	Rec	HCD	HCD/ Rec	SCF Dis	SCF Dis/ Rec
40/T	10.2	0.25	14.4	0.28	1.57	Steel	1.9	2.69	1.41	4.22	2.22
TG1	13.5	0.5	12	0.52	1.57	Acrylic	1.9	2.61	1.37	1.91	1.01
3U/1	10	0.26	12	0.75	1.57	Acrylic	1.6	3.65	2.28	4.35	2.72
3U/2	10	0.5	12	0.75	1.57	Acrylic	2	2.64	1.32	2.59	1.30
3U/3	10	0.8	12	0.75	1.57	Acrylic	2.1	2.30	1.09	1.80	0.86
3U/5	10	0.26	24	0.75	1.57	Acrylic	3	5.12	1.71	3.20	1.07
3U/9	10	0.26	32	0.75	1.57	Acrylic	3.2	7.27	2.27	3.24	1.01
9AU/2	10	0.8	24	1	0.79	Acrylic	1.9	2.14	1.13	2.92	1.54
9AU/3	10	0.8	24	1	1.05	Acrylic	2.1	1.82	0.86	2.14	1.02
9BU/1	10	0.8	24	1	1.57	Acrylic	1.5	1.57	1.05	1.50	1.00
11AU/1	10	0.5	12	1	1.57	Acrylic	1.5	2.52	1.68	2.70	1.80
14U/1	10	0.26	12	0.4	1.57	Acrylic	2.6	2.95	1.13	4.55	1.75
14U/2	10	0.5	12	0.4	1.57	Acrylic	2.2	2.47	1.12	2.94	1.34
14U/3	10	0.8	12	0.4	1.57	Acrylic	1.9	2.17	1.14	2.39	1.26
14U/4	10	0.26	24	0.4	1.57	Acrylic	3.1	4.13	1.33	3.14	1.01
14U/5	10	0.5	24	0.4	1.57	Acrylic	1.6	2.27	1.42	1.50	0.94
14DU/2	10	0.8	24	0.4	0.79	Acrylic	1.6	2.06	1.29	3.11	1.94
14DU/3	10	0.8	24	0.4	1.05	Acrylic	1.6	1.77	1.11	2.35	1.47

Table 5.4 Comparison between the Predictions from the SCF Distribution and HCD Equations with the Recorded data at Brace Saddle position for Axially Loaded Y and T-joints

Joint Ref	α	β	γ	τ	θ (Rad)	Mat	Rec	HCD	HCD/ Rec	SCF Dis	SCF Dis/ Rec
19/T	10.5	0.53	13.4	0.86	1.57	Steel	6.5	12.61	1.94	12.44	1.91
20/T	10	0.53	13.3	0.51	1.57	Steel	4.9	8.27	1.69	8.88	1.81
39/T	10.2	0.25	14.3	0.4	1.57	Steel	4.4	7.21	1.64	7.77	1.77
40/T	10.2	0.25	14.4	0.28	1.57	Steel	4.4	5.81	1.32	5.97	1.36
T-O	10	0.57	26.9	0.46	1.57	Steel	8.4	10.79	1.28	13.29	1.58
T-R	10	0.57	19.4	0.33	1.57	Steel	6.2	7.32	1.18	8.49	1.37
T(Steel)	6.3	0.5	24.1	1	1.57	Steel	12	19.35	1.61	16.62	1.39
1	6.9	0.66	23.1	0.91	0.79	Steel	6.5	8.66	1.33	8.49	1.31
TW2	12	0.4	19.7	0.5	1.57	Steel	9.1	10.73	1.18	12.32	1.35
T-ST	7.2	0.71	14.3	0.79	1.57	Steel	6	10.42	1.74	10.53	1.75
1.3	6.2	0.8	20.3	0.99	1.57	Steel	8.2	13.29	1.62	12.83	1.56
1.7	6.2	0.8	31.8	0.91	0.79	Steel	6.1	8.15	1.34	9.80	1.61
1.9	6.2	0.4	20.3	0.94	0.79	Steel	5	8.60	1.72	7.36	1.47

Table 5.4 Comparison between the Predictions from the SCF Distribution and HCD Equations with the Recorded Data at Brace Saddle position for Axially Loaded Y and T-joints
(Continued)

Joint Ref	α	β	γ	τ	θ (Rad)	Mat	Rec	HCD	HCD/ Rec	SCF Dis	SCF Dis/ Rec
TG1	13.5	0.5	12	0.52	1.57	Acrylic	6.3	8.05	1.28	8.97	1.42
3U/1	10	0.26	12	0.75	1.57	Acrylic	6	9.88	1.65	10.25	1.71
3U/2	10	0.5	12	0.75	1.57	Acrylic	8	10.68	1.34	10.77	1.35
3U/3	10	0.8	12	0.75	1.57	Acrylic	5.9	7.87	1.33	8.90	1.51
3U/5	10	0.26	24	0.75	1.57	Acrylic	10.7	14.66	1.37	17.18	1.61
3U/6	10	0.5	24	0.75	1.57	Acrylic	10.5	15.85	1.51	16.77	1.60
3U/7	10	0.8	24	0.75	1.57	Acrylic	13.6	11.66	0.86	14.10	1.04
3U/9	10	0.26	32	0.75	1.57	Acrylic	14.2	16.66	1.17	21.43	1.51
3U/10	10	0.5	32	0.75	1.57	Acrylic	17.4	18.01	1.04	20.09	1.15
3U/11	13.3	0.8	32	0.75	1.57	Acrylic	21.1	13.36	0.63	19.08	0.90
9AU/2	10	0.8	24	1	0.79	Acrylic	7.4	8.14	1.10	8.79	1.19
9AU/3	10	0.8	24	1	1.05	Acrylic	11.6	11.16	0.96	13.00	1.12
9BU/1	10	0.8	24	1	1.57	Acrylic	13.8	14.76	1.07	16.84	1.22
11AU/1	10	0.5	12	1	1.57	Acrylic	8.4	13.18	1.57	11.84	1.41
11AU/2	10	0.5	24	1	1.57	Acrylic	16.6	19.57	1.18	18.64	1.12
TJOINT 19	16	0.5	16	0.5	1.57	Acrylic	8	9.38	1.17	10.83	1.35
TJOINT 20	16	0.5	16	0.25	1.57	Acrylic	5.2	5.84	1.12	5.94	1.14
TJOINT 21	16	0.5	12	0.5	1.57	Acrylic	4.7	7.83	1.67	8.92	1.90
TJOINT 22	16	0.5	12	0.25	1.57	Acrylic	3.3	4.94	1.50	4.32	1.31
1T/0	8	0.5	12	1	1.57	Acrylic	11.6	13.10	1.13	10.78	0.93
14U/1	10	0.26	12	0.4	1.57	Acrylic	4.9	6.50	1.33	6.57	1.34
14U/2	10	0.5	12	0.4	1.57	Acrylic	6.4	6.54	1.02	6.85	1.07
14U/3	10	0.8	12	0.4	1.57	Acrylic	4.5	4.84	1.08	4.92	1.09
14U/4	10	0.26	24	0.4	1.57	Acrylic	9	9.57	1.06	12.27	1.36
14U/5	10	0.5	24	0.4	1.57	Acrylic	10.4	9.50	0.91	11.67	1.12
14U/6	10	0.8	24	0.4	1.57	Acrylic	9.2	6.95	0.76	8.93	0.97
14DU/2	10	0.8	24	0.4	0.79	Acrylic	4.6	3.89	0.84	3.28	0.71
14DU/3	10	0.8	24	0.4	1.05	Acrylic	8.1	5.33	0.66	6.07	0.75
TJOINT 6	16	0.5	16	1	1.57	Acrylic	12.7	16.01	1.26	16.99	1.34
TJOINT 10	16	0.33	24	1	1.57	Acrylic	16.2	18.88	1.17	22.35	1.38
TJOINT 12	16	0.67	24	1	1.57	Acrylic	21.5	17.84	0.83	19.96	0.93
2T/0	8	0.5	23.1	1	1.57	Acrylic	16.1	19.09	1.19	17.12	1.06
T-AC	9.3	0.67	15	0.8	1.57	Acrylic	7.6	11.45	1.51	11.83	1.56
Y-AC	9.3	0.67	15	0.8	0.79	Acrylic	6.1	6.34	1.04	6.06	0.99

Table 5.5 Comparison between the Predictions from the SCF Distribution and HCD Equations with the Recorded Data at Chord Crown position for Axially Loaded Y and T-joints

	α	β	γ	τ	θ (Rad)	Mat	R	HCD	HCD/ Rec	SCF Dis	SCF Dis/ Rec
19/T	10.5	0.53	13.4	0.86	1.57	Steel	5.2	4.26	0.82	3.86	0.74
20/T	10	0.53	13.3	0.51	1.57	Steel	2.8	2.84	1.01	2.58	0.92
39/T	10.2	0.25	14.3	0.4	1.57	Steel	2.4	2.75	1.14	3.22	1.34
Test	13	0.48	15.9	0.63	0.79	Steel	3.8	3.31	0.87	2.93	0.77
TG1	13.5	0.5	12	0.52	1.57	Acrylic	3.3	2.88	0.87	2.51	0.76
3U/1	10	0.26	12	0.75	1.57	Acrylic	4.5	4.49	1.00	4.68	1.04
3U/2	10	0.5	12	0.75	1.57	Acrylic	3.7	3.80	1.03	3.66	0.99
3U/3	10	0.8	12	0.75	1.57	Acrylic	4.5	3.59	0.80	3.14	0.70
3U/5	10	0.26	24	0.75	1.57	Acrylic	5.1	5.55	1.09	4.00	0.79
3U/6	10	0.5	24	0.75	1.57	Acrylic	3.9	4.42	1.13	2.75	0.71
3U/7	10	0.8	24	0.75	1.57	Acrylic	4.9	4.43	0.91	2.53	0.52
3U/9	10	0.26	32	0.75	1.57	Acrylic	5.3	6.39	1.21	3.95	0.75
3U/10	10	0.5	32	0.75	1.57	Acrylic	4.4	5.20	1.18	2.66	0.60
3U/11	13.3	0.8	32	0.75	1.57	Acrylic	6.4	5.17	0.81	2.91	0.45
9AU/2	10	0.8	24	1	0.79	Acrylic	6.4	5.29	0.83	4.62	0.72
9AU/3	10	0.8	24	1	1.05	Acrylic	6.3	5.28	0.84	3.82	0.61
9BU/1	10	0.8	24	1	1.57	Acrylic	6.6	5.31	0.80	2.94	0.45
11AU/1	10	0.5	12	1	1.57	Acrylic	6.7	4.70	0.70	4.86	0.73
11AU/2	10	0.5	24	1	1.57	Acrylic	5.5	5.82	1.06	3.95	0.72
14AU/1	10	0.26	12	0.4	1.57	Acrylic	2.8	2.61	0.93	3.36	1.20
14AU/2	10	0.5	12	0.4	1.57	Acrylic	2.6	2.30	0.88	2.35	0.90
14AU/3	10	0.8	12	0.4	1.57	Acrylic	2.6	2.26	0.87	2.20	0.85
14AU/4	10	0.26	24	0.4	1.57	Acrylic	2.5	3.23	1.29	2.53	1.01
14AU/5	10	0.5	24	0.4	1.57	Acrylic	2.2	2.72	1.24	1.50	0.68
14AU/6	10	0.8	24	0.4	1.57	Acrylic	2.9	2.80	0.97	2.17	0.75
14DU/2	10	0.8	24	0.4	0.79	Acrylic	2.8	2.55	0.91	2.55	0.91
14DU/3	10	0.8	24	0.4	1.05	Acrylic	2.9	2.70	0.93	2.27	0.78

Table 5.6 Comparison between the Predictions from the SCF Distribution and HCD Equations with the Recorded Data at Chord Saddle position for Axially Loaded Y and T-joints

Joint Ref	α	β	γ	τ	θ (Rad)	Mat	Rec	HCD	HCD/ Rec	SCF Dis	SCF Dis/ Rec
19/T	10.5	0.53	13.4	0.86	1.57	Steel	11.4	15.92	1.40	14.26	1.25
20/T	10	0.53	13.3	0.51	1.57	Steel	6.5	7.56	1.16	7.32	1.13
39/T	10.2	0.25	14.3	0.4	1.57	Steel	4.2	5.85	1.39	6.12	1.46
T-O	10	0.57	26.9	0.46	1.57	Steel	11.6	10.25	0.88	12.12	1.04
T-R	10	0.57	19.4	0.33	1.57	Steel	7.1	5.58	0.79	6.48	0.91
T(Steel)	6.3	0.5	24.1	1	1.57	Steel	18.5	29.04	1.57	25.57	1.38
Test	13	0.48	15.9	0.63	0.79	Steel	5.2	6.07	1.17	6.06	1.16
1	6.9	0.66	23.1	0.91	0.79	Steel	8.6	10.79	1.25	10.96	1.27
TW2	7.3	0.71	12	1	1.57	Steel	10	15.42	1.54	14.86	1.49
T250	12	0.5	19.7	0.5	1.57	Steel	10	9.80	0.98	10.81	1.08
T350	10	0.7	19.7	0.5	1.57	Steel	9.2	8.41	0.91	8.69	0.95
T-ST	7.2	0.71	14.3	0.79	1.57	Steel	8.7	11.86	1.36	11.46	1.32
2-3	10	0.5	13.4	0.5	1.57	Steel	5.7	7.48	1.31	7.32	1.28
4-10	10	0.5	14.3	0.5	1.57	Steel	6.7	7.85	1.17	7.78	1.16
11-12	10	0.25	14.3	0.39	1.57	Steel	4.7	5.67	1.21	5.88	1.25
13-17	10	0.5	14.3	0.5	1.57	Steel	7.7	7.85	1.02	7.78	1.01
SM-A	9.4	0.4	20	0.77	1.57	Steel	15.8	17.72	1.12	17.45	1.10
SM-B	9.3	0.6	19.8	0.75	1.57	Steel	16.1	16.08	1.00	15.18	0.94
SM-C	9.3	0.8	20.1	0.76	1.57	Steel	15.2	11.71	0.77	12.73	0.84
SR-A	9.4	0.4	20	0.75	1.57	Steel	15.2	17.07	1.12	16.93	1.11
SH-A	9.3	0.4	20.1	0.82	1.57	Steel	17.3	19.45	1.12	18.85	1.09
1.3	6.2	0.8	20.3	0.99	1.57	Steel	11.4	17.83	1.56	18.15	1.59
1.5	6.2	0.8	31.8	0.98	1.57	Steel	29	21.38	0.74	23.55	0.81
1.7	6.2	0.8	31.8	0.91	0.79	Steel	10.4	9.93	0.95	10.46	1.01
1.9	6.2	0.4	20.3	0.94	0.79	Steel	9.9	11.42	1.15	11.83	1.19
1	8	0.71	14.3	1	1.57	Steel	12.5	18.00	1.44	16.49	1.32
4-7	8.1	0.71	14.3	1	1.57	Steel	13.3	18.01	1.35	16.50	1.24
8	7.3	0.71	12	1	1.57	Steel	9.5	15.42	1.62	14.86	1.56
9-11	7.2	0.71	12	1	1.57	Steel	10.43	15.41	1.48	14.85	1.42
TG1	13.5	0.5	12	0.52	1.57	Acrylic	5.9	7.27	1.23	7.14	1.21
3U/1	10	0.26	12	0.75	1.57	Acrylic	7.6	11.02	1.45	11.62	1.53
3U/2	10	0.5	12	0.75	1.57	Acrylic	9.3	11.77	1.27	11.04	1.19
3U/3	10	0.8	12	0.75	1.57	Acrylic	7.5	8.03	1.07	8.74	1.17
3U/5	10	0.26	24	0.75	1.57	Acrylic	15.4	17.64	1.15	20.40	1.32
3U/6	10	0.5	24	0.75	1.57	Acrylic	17.3	18.85	1.09	18.97	1.10
3U/7	10	0.8	24	0.75	1.57	Acrylic	17.4	12.82	0.74	14.32	0.82
3U/9	10	0.26	32	0.75	1.57	Acrylic	20.4	19.98	0.98	25.74	1.26
3U/10	10	0.5	32	0.75	1.57	Acrylic	26.8	21.21	0.79	23.75	0.89
3U/11	13.3	0.8	32	0.75	1.57	Acrylic	25.8	15.03	0.58	18.27	0.71
9AU/2	10	0.8	24	1	0.79	Acrylic	11.7	9.78	0.84	11.49	0.98
9AU/3	10	0.8	24	1	1.05	Acrylic	19.3	14.48	0.75	16.12	0.84
9BU/1	10	0.8	24	1	1.57	Acrylic	21.9	20.16	0.92	21.25	0.97

Table 5.6 Comparison between the Predictions from the SCF Distribution and HCD Equations with the Recorded Data at Chord Saddle position for Axially Loaded Y and T-joints
(Continued)

Spec. no.	α	β	γ	τ	θ (Rad)	Mat	Rec	HCD	HCD/ Rec	SCF Dis	SCF Dis/ Rec
11AU/1	10	0.5	12	1	1.57	Acrylic	10.7	18.41	1.72	16.72	1.56
11AU/2	10	0.5	24	1	1.57	Acrylic	26.7	29.48	1.10	26.69	1.00
TJOINT 15	16	0.25	32	1	1.57	Acrylic	26.2	29.48	1.13	37.91	1.45
TJOINT 16	16	0.5	32	1	1.57	Acrylic	30	33.75	1.13	34.73	1.16
TJOINT 17	16	0.75	32	1	1.57	Acrylic	24	26.35	1.10	28.50	1.19
TJOINT 19	16	0.5	16	0.5	1.57	Acrylic	10	8.62	0.86	9.24	0.92
TJOINT 20	16	0.5	16	0.25	1.57	Acrylic	4	3.60	0.90	4.68	1.17
TJOINT 21	16	0.5	12	0.5	1.57	Acrylic	6.2	6.96	1.12	6.89	1.11
TJOINT 22	16	0.5	12	0.25	1.57	Acrylic	3.1	2.91	0.94	3.01	0.97
YJOINT 2	16	0.33	24	1	0.79	Acrylic	14.5	13.56	0.94	18.49	1.28
YJOINT 3	16	0.5	24	1	0.79	Acrylic	14.8	14.55	0.98	17.13	1.16
YJOINT 7	8	0.5	24	1	0.79	Acrylic	14.3	14.18	0.99	15.37	1.07
YJOINT 8	23	0.5	24	1	0.79	Acrylic	14.5	14.75	1.02	18.26	1.26
YJOINT 10	16	0.5	24	1	1.05	Acrylic	20	21.55	1.08	22.29	1.11
YJOINT 11	16	0.33	12	1	0.79	Acrylic	7.3	8.47	1.16	9.56	1.31
YJOINT 12	13.7	0.5	12	1	0.79	Acrylic	6	9.04	1.51	8.97	1.50
YJOINT 13	16	0.67	12	1	0.79	Acrylic	5	8.20	1.64	7.92	1.58
1T/0	8	0.5	12	1	1.57	Acrylic	14.5	18.26	1.26	16.47	1.14
14U/1	10	0.26	12	0.4	1.57	Acrylic	4.3	5.13	1.19	4.99	1.16
14U/2	10	0.5	12	0.4	1.57	Acrylic	4.6	5.20	1.13	5.05	1.10
14U/3	10	0.8	12	0.4	1.57	Acrylic	3.5	3.64	1.04	3.44	0.98
14U/4	10	0.26	24	0.4	1.57	Acrylic	7.7	8.19	1.06	10.68	1.39
14U/5	10	0.5	24	0.4	1.57	Acrylic	9.2	8.29	0.90	10.13	1.10
14U/5	10	0.8	24	0.4	1.57	Acrylic	8.9	5.80	0.65	6.69	0.75
14DU/2	10	0.8	24	0.4	0.79	Acrylic	4.3	3.09	0.72	2.55	0.59
14DU/3	10	0.8	24	0.4	1.05	Acrylic	7.4	4.35	0.59	4.34	0.59
TJONIT 1	16	0.25	12	1	1.57	Acrylic	10.8	16.37	1.52	18.44	1.71
TJONIT 2	16	0.5	12	1	1.57	Acrylic	12.2	18.74	1.54	17.00	1.39
TJONIT 3	16	0.75	12	1	1.57	Acrylic	11	14.63	1.33	14.33	1.30
TJONIT 5	16	0.25	16	1	1.57	Acrylic	15	20.71	1.38	22.50	1.50
TJONIT 6	16	0.5	16	1	1.57	Acrylic	18	23.71	1.32	20.71	1.15
TJONIT 7	16	0.75	16	1	1.57	Acrylic	16.2	18.51	1.14	17.32	1.07
TJONIT 10	16	0.33	24	1	1.57	Acrylic	24.2	27.95	1.16	29.87	1.23
TJONIT 11	16	0.5	24	1	1.57	Acrylic	25	30.00	1.20	27.94	1.12
TJONIT 12	16	0.67	24	1	1.57	Acrylic	27.5	27.08	0.98	24.96	0.91
2T/0	8	0.5	23.1	1	1.57	Acrylic	25	28.71	1.15	25.42	1.02
T-AC	9.3	0.67	15	0.8	1.57	Acrylic	8.8	13.63	1.55	12.71	1.44
Y-AC	9.3	0.67	15	0.8	0.79	Acrylic	7.2	6.97	0.97	6.49	0.90

Table 5.7 Comparison between the Predictions from the SCF Distribution and HCD Equations with the Recorded Data on Brace Side for IPB loaded Y and T-joints

Joint Ref	α	β	γ	τ	θ (Rad)	Mat	Rec	HCD	HCD/ Rec	SCF Dis	SCF Dis/ Rec
19/T	10.5	0.53	13.4	0.86	1.57	Steel	2.1	3.33	1.58	3.47	1.65
20/T	10	0.53	13.3	0.51	1.57	Steel	2.4	2.84	1.18	2.71	1.13
39/T	10.2	0.25	14.3	0.4	1.57	Steel	1.5	2.57	1.71	2.11	1.41
40/T	10.2	0.25	14.4	0.28	1.57	Steel	1.9	2.32	1.22	3.60	1.90
1	6.9	0.66	23.1	0.91	0.79	Steel	2.7	3.51	1.30	3.38	1.25
T-ST	7.2	0.71	14.3	0.79	1.57	Steel	2	3.34	1.67	3.25	1.63
Y-ST	7.2	0.71	14.3	0.79	0.79	Steel	2.5	2.91	1.16	2.64	1.06
TG1	13.5	0.5	12	0.52	1.57	Acrylic	2	2.75	1.37	2.70	1.35
3U/2	10	0.5	12	0.75	1.57	Acrylic	2.3	3.06	1.33	3.08	1.34
3U/3	10	0.8	12	0.75	1.57	Acrylic	2.1	3.09	1.47	2.89	1.37
3U/5	10	0.26	24	0.75	1.57	Acrylic	3	3.76	1.25	4.05	1.35
3U/6	10	0.5	24	0.75	1.57	Acrylic	2.8	3.95	1.41	4.22	1.51
3U/7	10	0.8	24	0.75	1.57	Acrylic	3.3	3.99	1.21	4.09	1.24
3U/9	10	0.26	32	0.75	1.57	Acrylic	3.6	4.18	1.16	4.56	1.27
3U/10	10	0.5	32	0.75	1.57	Acrylic	4.4	5.01	1.14	5.10	1.16
3U/11	13.3	0.8	32	0.75	1.57	Acrylic	4.2	4.44	1.06	5.01	1.19
9AU/2	10	0.8	24	1	0.79	Acrylic	2.4	3.51	1.46	3.36	1.40
9AU/3	10	0.8	24	1	1.05	Acrylic	2.9	4.14	1.43	3.90	1.34
9BU/1	10	0.8	24	1	1.57	Acrylic	2.6	4.34	1.67	4.40	1.69
11AU/1	10	0.5	12	1	1.57	Acrylic	2.1	3.33	1.59	2.89	1.37
11AU/2	10	0.5	24	1	1.57	Acrylic	3.2	4.30	1.34	4.98	1.56
1T/0	8	0.5	12	1	1.57	Acrylic	3.1	3.33	1.07	3.73	1.20
14U/1	10	0.26	12	0.4	1.57	Acrylic	1.9	2.39	1.26	1.98	1.04
14U/2	10	0.5	12	0.4	1.57	Acrylic	2.1	2.54	1.21	2.46	1.17
14U/3	10	0.8	12	0.4	1.57	Acrylic	2.2	2.57	1.17	2.48	1.13
14U/4	10	0.26	24	0.4	1.57	Acrylic	3	3.12	1.04	3.72	1.24
14U/5	10	0.5	24	0.4	1.57	Acrylic	2.7	3.28	1.21	3.07	1.14
14U/6	10	0.8	24	0.4	1.57	Acrylic	2.2	3.31	1.50	3.10	1.41
14DU/2	10	0.8	24	0.4	0.79	Acrylic	2	3.14	1.57	2.40	1.20
14DU/3	10	0.8	24	0.4	1.05	Acrylic	2.3	3.17	1.38	2.81	1.22
TJOINT 2	16	0.5	12	1	1.57	Acrylic	3.2	3.34	1.04	3.83	1.20
TJOINT 6	16	0.5	16	1	1.57	Acrylic	3.2	3.71	1.16	3.74	1.17
2T/0	8	0.5	23.1	1	1.57	Acrylic	4.3	4.23	0.98	4.85	1.13
T-AC	9.3	0.67	15	0.8	1.57	Acrylic	2	3.41	1.70	3.40	1.70
Y-AC	9.3	0.67	15	0.8	0.79	Acrylic	2.2	2.94	1.34	2.80	1.27

Table 5.8 Comparison between the Predictions from the SCF Distribution and HCD Equations with the Recorded Data on Chord Side for IPB loaded Y and T-joints

Joint Ref	α	β	γ	τ	θ (Rad)	Mat	Rec	HCD	HCD /Rec	SCF Dis	SCF Dis/ Rec
19/T	10.5	0.53	13.4	0.86	1.57	Steel	2.5	4.18	1.67	4.49	1.80
20/T	10	0.53	13.3	0.51	1.57	Steel	1.7	2.64	1.56	3.04	1.79
1	6.9	0.66	23.1	0.91	0.79	Steel	3.3	4.33	1.31	4.49	1.36
TW2	7.3	0.71	12	1	1.57	Steel	3	4.68	1.56	4.43	1.48
T-ST	7.2	0.71	14.3	0.79	1.57	Steel	3.1	4.15	1.34	3.97	1.28
Y-ST	7.2	0.71	14.3	0.79	0.79	Steel	2.7	2.99	1.11	4.01	1.49
TG1	13.5	0.5	12	0.52	1.57	Acrylic	1.8	2.51	1.40	3.00	1.67
3U/1	10	0.26	12	0.75	1.57	Acrylic	2.3	2.79	1.21	3.48	1.51
3U/2	10	0.5	12	0.75	1.57	Acrylic	2.7	3.48	1.29	3.89	1.44
3U/3	10	0.8	12	0.75	1.57	Acrylic	3.4	3.65	1.07	3.43	1.01
3U/5	10	0.26	24	0.75	1.57	Acrylic	4	5.01	1.25	5.09	1.27
3U/6	10	0.5	24	0.75	1.57	Acrylic	3.9	4.97	1.27	5.22	1.34
3U/7	10	0.8	24	0.75	1.57	Acrylic	4	4.91	1.23	4.83	1.21
3U/9	10	0.26	32	0.75	1.57	Acrylic	5.3	6.83	1.29	6.90	1.30
3U/10	10	0.5	32	0.75	1.57	Acrylic	5.1	5.73	1.12	6.16	1.21
3U/11	13.3	0.8	32	0.75	1.57	Acrylic	4.2	5.50	1.31	6.14	1.46
9AU/2	10	0.8	24	1	0.79	Acrylic	3.4	6.38	1.88	5.46	1.61
9AU/3	10	0.8	24	1	1.05	Acrylic	4.2	5.81	1.38	6.21	1.48
9BU/1	10	0.8	24	1	1.57	Acrylic	4.1	6.45	1.57	6.16	1.50
11AU/1	10	0.5	12	1	1.57	Acrylic	3.4	4.46	1.31	4.88	1.43
11AU/2	10	0.5	24	1	1.57	Acrylic	5.3	6.52	1.23	7.18	1.36
TJOINT 16	16	0.5	32	1	1.57	Acrylic	7	7.54	1.08	8.43	1.20
TJOINT 21	16	0.5	12	0.5	1.57	Acrylic	2.2	2.42	1.10	2.92	1.33
YJOINT 2	16	0.33	24	1	0.79	Acrylic	3.9	4.68	1.20	7.12	1.83
YJOINT 3	16	0.5	24	1	0.79	Acrylic	4.3	4.73	1.10	5.62	1.31
YJOINT 10	16	0.5	24	1	1.05	Acrylic	5	5.74	1.15	6.45	1.29
YJOINT 11	16	0.33	12	1	0.79	Acrylic	2.6	2.90	1.11	5.02	1.93
YJOINT 12	13.7	0.5	12	1	0.79	Acrylic	3.2	3.22	1.01	4.15	1.30
YJOINT 13	16	0.67	12	1	0.79	Acrylic	2.7	3.33	1.23	3.67	1.36
1T/0	8	0.5	12	1	1.57	Acrylic	3.8	4.48	1.18	4.88	1.28
14U/1	10	0.26	12	0.4	1.57	Acrylic	1.6	1.62	1.01	2.65	1.66
14U/2	10	0.5	12	0.4	1.57	Acrylic	1.8	2.01	1.12	2.54	1.41
14U/3	10	0.8	12	0.4	1.57	Acrylic	1.5	2.10	1.40	2.18	1.46
14U/4	10	0.26	24	0.4	1.57	Acrylic	2.4	2.88	1.20	4.17	1.74
14U/5	10	0.5	24	0.4	1.57	Acrylic	2.1	2.74	1.30	3.21	1.53
14U/6	10	0.8	24	0.4	1.57	Acrylic	2.1	2.71	1.29	2.44	1.16
14DU/2	10	0.8	24	0.4	0.79	Acrylic	2.1	2.34	1.12	2.19	1.04
14DU/3	10	0.8	24	0.4	1.05	Acrylic	2.1	2.47	1.17	2.38	1.13
TJOINT 2	16	0.5	12	1	1.57	Acrylic	4	4.43	1.11	4.88	1.22
TJOINT 6	16	0.5	16	1	1.57	Acrylic	4.5	5.16	1.15	5.67	1.26
TJOINT 11	16	0.5	24	1	1.57	Acrylic	6.6	6.53	0.99	7.18	1.09
2T/0	8	0.5	23.1	1	1.57	Acrylic	4.6	6.40	1.39	7.06	1.54
T-AC	9.3	0.67	15	0.8	1.57	Acrylic	2.9	4.26	1.47	4.20	1.45
Y-AC	9.3	0.67	15	0.8	0.79	Acrylic	2.4	3.07	1.28	2.83	1.18

Table 5.9 Comparison between the Predictions from the SCF Distribution and HCD Equations with the Recorded Data on Brace Side for OPB loaded Y and T-joints

Joint Ref	α	β	γ	τ	θ (Rad)	Mat	Rec	HCD	HCD/ Rec	SCF Dis	SCF Dis/R ec
T23/1-3	14	0.25	14.3	0.39	1.57	Steel	2.07	3.07	1.48	3.58	1.73
T24/1-3	14	0.25	14.3	0.28	1.57	Steel	1.73	2.62	1.52	2.42	1.40
T-ST	7.2	0.71	14.3	0.79	1.57	Steel	5.1	8.77	1.72	9.25	1.81
1.3	6.2	0.8	20.3	0.99	1.57	Steel	7.3	13.51	1.85	13.08	1.79
1.5	6.2	0.8	31.8	0.98	1.57	Steel	10.6	19.67	1.86	18.09	1.71
1.7	6.2	0.8	31.8	0.91	0.79	Steel	6.2	9.19	1.48	10.16	1.64
1.9	6.2	0.4	20.3	0.94	0.79	Steel	3.6	5.26	1.46	5.98	1.66
TG1	13.5	0.5	12	0.52	1.57	Acrylic	5.4	5.46	1.01	6.31	1.17
3U/1	10	0.26	12	0.75	1.57	Acrylic	2.5	3.77	1.51	4.43	1.77
3U/2	10	0.5	12	0.75	1.57	Acrylic	5	6.47	1.29	7.31	1.46
3U/3	10	0.8	12	0.75	1.57	Acrylic	6.7	7.61	1.14	7.79	1.16
3U/5	10	0.26	24	0.75	1.57	Acrylic	5.3	6.79	1.28	9.70	1.83
3U/6	10	0.5	24	0.75	1.57	Acrylic	9.2	11.65	1.27	12.75	1.39
3U/7	10	0.8	24	0.75	1.57	Acrylic	13.2	13.70	1.04	13.28	1.01
3U/9	10	0.26	32	0.75	1.57	Acrylic	9	8.66	0.96	11.94	1.33
3U/10	10	0.5	32	0.75	1.57	Acrylic	14.8	14.87	1.01	15.18	1.03
3U/11	13.3	0.8	32	0.75	1.57	Acrylic	19.8	17.51	0.88	15.74	0.80
9AU/2	10	0.8	24	1	0.79	Acrylic	6.8	7.58	1.12	8.80	1.29
9AU/3	10	0.8	24	1	1.05	Acrylic	10.4	11.26	1.08	12.19	1.17
9BU/1	10	0.8	24	1	1.57	Acrylic	12.2	15.68	1.29	15.18	1.24
11AU/1	10	0.5	12	1	1.57	Acrylic	5	7.41	1.48	7.13	1.43
11AU/2	10	0.5	24	1	1.57	Acrylic	11.6	13.34	1.15	13.56	1.17
TJOINT 19	16	0.5	16	0.5	1.57	Acrylic	6	6.85	1.14	7.97	1.33
TJOINT 20	16	0.5	16	0.25	1.57	Acrylic	4.2	4.95	1.18	5.29	1.26
TJOINT 21	16	0.5	12	0.5	1.57	Acrylic	4	5.37	1.34	6.23	1.56
TJOINT 22	16	0.5	12	0.25	1.57	Acrylic	3.6	3.88	1.08	3.67	1.02
1T/0	8	0.5	12	1	1.57	Acrylic	7.4	7.40	1.00	7.07	0.96
14U/1	10	0.26	12	0.4	1.57	Acrylic	2.2	2.81	1.28	2.66	1.21
14U/2	10	0.5	12	0.4	1.57	Acrylic	4.4	4.82	1.10	5.20	1.18
14U/3	10	0.8	12	0.4	1.57	Acrylic	4.4	5.67	1.29	5.03	1.14
14U/4	10	0.26	24	0.4	1.57	Acrylic	4.5	5.05	1.12	7.56	1.68
14U/5	10	0.5	24	0.4	1.57	Acrylic	8.3	8.68	1.05	9.61	1.16
14U/6	10	0.8	24	0.4	1.57	Acrylic	9.2	10.20	1.11	9.14	0.99
14DU/2	10	0.8	24	0.4	0.79	Acrylic	5.1	4.94	0.97	5.23	1.02
14DU/3	10	0.8	24	0.4	1.05	Acrylic	8.3	7.33	0.88	7.11	0.86
TJOINT 6	16	0.5	16	1	1.57	Acrylic	9	9.48	1.05	9.57	1.06
TJOINT 10	16	0.33	24	1	1.57	Acrylic	9.2	10.06	1.09	11.09	1.21
TJOINT 11	16	0.5	24	1	1.57	Acrylic	13.2	13.37	1.01	13.76	1.04
TJOINT 12	16	0.67	24	1	1.57	Acrylic	18	15.01	0.83	15.20	0.84
2T/0	8	0.5	23.1	1	1.57	Acrylic	12.2	12.90	1.06	13.06	1.07
T-AC	9.3	0.67	15	0.8	1.57	Acrylic	6.2	9.05	1.46	9.70	1.56
Y-AC	9.3	0.67	15	0.8	0.79	Acrylic	4.1	4.49	1.10	5.98	1.46

Table 5.10 Comparison between the Predictions from the SCF Distribution and HCD Equations
with the Recorded Data on Chord Side for OPB loaded Y and T-joints

Joint Ref	α	β	γ	τ	θ (Rad)	Mat	Rec	HCD	HCD /Rec	SCF Dis	SCF Dis/ Rec
T703/1-3	17.1	0.53	13.4	0.86	1.57	Steel	8.03	9.70	1.21	8.97	1.12
T704/1-3	17.1	0.53	13.4	0.51	1.57	Steel	5.27	5.75	1.09	5.43	1.03
T23/1-3	14	0.25	14.3	0.39	1.57	Steel	2.5	3.23	1.29	3.32	1.33
T24/1-3	14	0.25	14.3	0.28	1.57	Steel	1.7	2.32	1.36	2.65	1.56
T204C,T211C	5	0.5	14.3	0.5	1.57	Steel	5.1	5.93	1.16	5.36	1.05
T223	5	0.5	28.6	1	1.57	Steel	22	25.39	1.15	20.49	0.93
TW2	7.3	0.71	12	1	1.57	Steel	8.5	10.01	1.18	12.58	1.48
24	5.6	0.5	16.5	0.82	1.57	Steel	8.6	11.40	1.33	10.73	1.25
T-ST	7.2	0.71	14.3	0.79	1.57	Steel	9.1	9.59	1.05	9.80	1.08
1.5	6.2	0.8	31.8	0.98	1.57	Steel	18.5	28.59	1.55	23.14	1.25
1.7	6.2	0.8	31.8	0.91	0.79	Steel	10.9	12.37	1.13	10.75	0.99
1.9	6.2	0.4	20.3	0.94	0.79	Steel	6.2	7.88	1.27	8.11	1.31
2-3	10.9	0.71	14.3	0.78	0.61	Steel	3.3	3.54	1.07	2.91	0.88
TG1	13.5	0.5	12	0.52	1.57	Acrylic	4.9	5.16	1.05	4.94	1.01
3U/1	10	0.26	12	0.75	1.57	Acrylic	3.7	5.41	1.46	5.25	1.42
3U/2	10	0.5	12	0.75	1.57	Acrylic	6.4	7.41	1.16	7.51	1.17
3U/3	10	0.8	12	0.75	1.57	Acrylic	8.9	7.56	0.85	7.78	0.87
3U/5	10	0.26	24	0.75	1.57	Acrylic	8	11.57	1.45	10.40	1.30
3U/6	10	0.5	24	0.75	1.57	Acrylic	13.3	15.85	1.19	13.32	1.00
3U/7	10	0.8	24	0.75	1.57	Acrylic	18.5	16.17	0.87	14.00	0.76
3U/9	10	0.26	32	0.75	1.57	Acrylic	10.8	15.86	1.47	14.49	1.34
3U/10	10	0.5	32	0.75	1.57	Acrylic	21.6	21.73	1.01	17.47	0.81
3U/11	13.3	0.8	32	0.75	1.57	Acrylic	26.7	22.25	0.83	19.73	0.74
4U/1	5	0.5	28.6	1	1.57	Acrylic	24.2	25.39	1.05	20.49	0.85
4U/2	5	0.5	28.6	0.5	1.57	Acrylic	10.4	12.69	1.22	8.55	0.82
9AU/2	10	0.8	24	1	0.79	Acrylic	12.3	10.46	0.85	11.03	0.90
9AU/3	10	0.8	24	1	1.05	Acrylic	19	15.19	0.80	15.35	0.81
9BU/1	10	0.8	24	1	1.57	Acrylic	21.4	21.56	1.01	19.92	0.93
11AU/1	10	0.5	12	1	1.57	Acrylic	7	9.88	1.41	10.84	1.55
11AU/2	10	0.5	24	1	1.57	Acrylic	18.7	21.13	1.13	18.70	1.00

Table 5.10 Comparison between the Predictions from the SCF Distribution and HCD Equations
with the Recorded Data on Chord Side for OPB loaded Y and T-joints

(Continued)

Joint Ref	α	β	γ	τ	θ (Rad)	Mat	Rec	HCD	HCD /Rec	SCF Dis	SCF Dis/ Rec
TJOINT 15	16	0.25	32	1	1.57	Acrylic	14	20.06	1.43	21.22	1.52
TJOINT 16	16	0.5	32	1	1.57	Acrylic	24.5	29.16	1.19	25.85	1.06
TJOINT 17	16	0.75	32	1	1.57	Acrylic	23.7	29.71	1.25	27.00	1.14
TJOINT 19	16	0.5	16	0.5	1.57	Acrylic	7.7	6.81	0.88	6.39	0.83
TJOINT 20	16	0.5	16	0.25	1.57	Acrylic	3.5	3.41	0.97	4.08	1.17
TJOINT 21	16	0.5	12	0.5	1.57	Acrylic	5.2	4.97	0.96	4.69	0.90
TJOINT 22	16	0.5	12	0.25	1.57	Acrylic	2.5	2.48	0.99	2.73	1.09
YJOINT 2	16	0.33	24	1	0.79	Acrylic	8.5	9.29	1.09	9.57	1.13
YJOINT 3	16	0.5	24	1	0.79	Acrylic	10	10.31	1.03	11.19	1.12
YJOINT 10	16	0.5	24	1	1.05	Acrylic	15.5	14.98	0.97	15.05	0.97
YJOINT 11	16	0.33	12	1	0.79	Acrylic	3.5	4.80	1.37	3.67	1.05
YJOINT 12	13.7	0.5	12	1	0.79	Acrylic	4.6	5.31	1.15	5.44	1.18
YJOINT 13	16	0.67	12	1	0.79	Acrylic	5.4	5.41	1.00	5.23	0.97
1T/0	8	0.5	12	1	1.57	Acrylic	9.8	9.85	1.00	11.43	1.17
14U/1	10	0.26	12	0.4	1.57	Acrylic	2.3	2.88	1.25	2.67	1.16
14U/2	10	0.5	12	0.4	1.57	Acrylic	3.8	3.95	1.04	3.82	1.01
14U/3	10	0.8	12	0.4	1.57	Acrylic	4.9	4.03	0.82	3.36	0.69
14U/4	10	0.26	24	0.4	1.57	Acrylic	4.3	6.17	1.43	5.78	1.34
14U/5	10	0.5	24	0.4	1.57	Acrylic	7.5	8.45	1.13	7.04	0.94
14U/6	10	0.8	24	0.4	1.57	Acrylic	10.2	8.62	0.85	6.96	0.68
14DU/2	10	0.8	24	0.4	0.79	Acrylic	5.3	4.18	0.79	2.32	0.44
14DU/3	10	0.8	24	0.4	1.05	Acrylic	8.5	6.07	0.71	4.61	0.54
TJOINT 1	16	0.25	12	1	1.57	Acrylic	4	6.84	1.71	6.41	1.60
TJOINT 2	16	0.5	12	1	1.57	Acrylic	9.8	9.94	1.01	9.74	0.99
TJOINT 3	16	0.75	12	1	1.57	Acrylic	8	10.13	1.27	10.16	1.27
TJOINT 5	16	0.25	16	1	1.57	Acrylic	7	9.38	1.34	9.11	1.30
TJOINT 6	16	0.5	16	1	1.57	Acrylic	13	13.63	1.05	12.50	0.96
TJOINT 7	16	0.75	16	1	1.57	Acrylic	14.8	13.88	0.94	13.29	0.90
TJOINT 10	16	0.33	24	1	1.57	Acrylic	12.5	19.16	1.53	16.77	1.34
TJOINT 11	16	0.5	24	1	1.57	Acrylic	20.2	21.26	1.05	19.02	0.94
TJOINT 12	16	0.67	24	1	1.57	Acrylic	23.2	21.61	0.93	19.93	0.86
2T/0	8	0.5	23.1	1	1.57	Acrylic	18.1	20.21	1.12	17.98	0.99
T-AC	9.3	0.67	15	0.8	1.57	Acrylic	8.1	10.25	1.27	10.08	1.24
Y-AC	9.3	0.67	15	0.8	0.79	Acrylic	5.3	5.32	1.00	5.58	1.05

**Table 5.11 Validation of SCF Distribution Parametric Equation for Y and T-joint
under Axial Loading at Brace Crown Position**

Equation	Steel/ Acrylic	No of Pts	Database		Pred SCF/Recorded SCF			Decision
			Mean	%st dev of Enq	%P/R< 0.8	%P/R< 1.0	%P/R> 1.5	
HCD	Steel	1	1.41	N/A	0.0%	0.0%	0.0%	accept
	Acrylic	17	1.37	40.3%	0.0%	5.9%	23.5%	
	Pooled	18	1.37	39.1%	0.0%	5.6%	22.2%	
SCF Dis	Steel	1	2.22	N/A	0.0%	0.0%	100.0%	accept
	Acrylic	17	1.35	48.2%	0.0%	11.8%	29.4%	
	Pooled	18	1.40	51.0%	0.0%	11.1%	33.3%	

**Table 5.12 Validation of SCF Distribution Parametric Equation for Y and T-joint
under Axial Loading at Brace Saddle Position**

Equation	Steel/ Acrylic	No of Pts	Database		Pred SCF/Recorded SCF			Decision
			Mean	%st dev of Enq	%P/R< 0.8	%P/R< 1.0	%P/R> 1.5	
HCD	Steel	13	1.51	24.5%	0.0%	0.0%	53.8%	accept but borderline
	Acrylic	34	1.16	26.7%	8.8%	23.5%	14.7%	
	Pooled	47	1.25	30.3%	6.4%	17.0%	25.5%	
SCF Dis	Steel	13	1.56	20.3%	0.0%	0.0%	53.8%	accept
	Acrylic	34	1.24	27.2%	5.9%	20.6%	20.6%	
	Pooled	47	1.33	29.1%	4.3%	14.9%	29.8%	

**Table 5.13 Validation of SCF Distribution Parametric Equation for Y and T-joint
under Axial Loading at Chord Crown Position**

Equation	Steel/ Acrylic	No of Pts	Database		Pred SCF/Recorded SCF			Decision
			Mean	%st dev of Enq	%P/R< 0.8	%P/R< 1.0	%P/R> 1.5	
HCD	Steel	4	0.96	14.7%	0.0%	50.0%	0.0%	reject
	Acrylic	23	0.97	15.9%	4.3%	60.9%	0.0%	
	Pooled	27	0.97	15.5%	3.7%	59.3%	0.0%	
SCF Dis	Steel	4	0.94	27.6%	50.0%	75.0%	0.0%	reject
	Acrylic	23	0.77	18.6%	69.6%	87.0%	0.0%	
	Pooled	27	0.79	20.5%	66.7%	85.2%	0.0%	

Table 5.14 Validation of SCF Distribution Parametric Equation for Y and T-joint
under Axial Loading at Chord Saddle Position

Equation	Steel/ Acrylic	No of Pts	Database		Pred SCF/Recorded SCF			Decision
			Mean	%st dev of Enq	%P/R< 0.8	%P/R< 1.0	%P/R> 1.5	
HCD	Steel	29	1.19	25.3%	10.3%	24.1%	13.8%	reject
	Acrylic	51	1.10	26.1%	13.7%	37.3%	11.8%	
	Pooled	80	1.13	26.1%	12.5%	32.5%	12.5%	
SCF Dis	Steel	29	1.19	20.7%	0.0%	17.2%	6.9%	accept
	Acrylic	51	1.14	24.9%	7.8%	27.5%	7.8%	
	Pooled	80	1.16	23.4%	5.0%	23.8%	7.5%	

Table 5.15 Validation of SCF Distribution Parametric Equation for Y and T-joint
under IPB Loading on Brace Side

Equation	Steel/ Acrylic	No of Pts	Database		Pred SCF/Recorded SCF			Decision
			Mean	%st dev of Enq	%P/R< 0.8	%P/R< 1.0	%P/R> 1.5	
HCD	Steel	7	1.40	24.1%	0.0%	0.0%	42.9%	accept
	Acrylic	28	1.31	19.7%	0.0%	3.6%	14.3%	
	Pooled	35	1.33	20.7%	0.0%	2.9%	20.0%	
SCF Dis	Steel	7	1.43	30.7%	0.0%	0.0%	42.9%	accept
	Acrylic	28	1.30	16.5%	0.0%	0.0%	14.3%	
	Pooled	35	1.33	20.3%	0.0%	0.0%	20.0%	

Table 5.16 Validation of SCF Distribution Parametric Equation for Y and T-joint
under IPB Loading on Chord Side

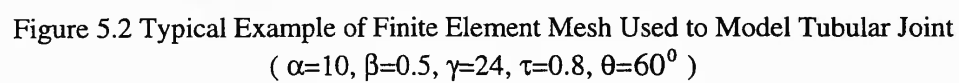
Equation	Steel/ Acrylic	No of Pts	Database		Pred SCF/Recorded SCF			Decision
			Mean	%st dev of Enq	%P/R< 0.8	%P/R< 1.0	%P/R> 1.5	
HCD	Steel	6	1.42	20.8%	0.0%	0.0%	50.0%	accept
	Acrylic	38	1.24	16.9%	0.0%	2.6%	5.3%	
	Pooled	44	1.26	18.4%	0.0%	2.3%	11.4%	
SCF Dis	Steel	6	1.53	21.5%	0.0%	0.0%	33.3%	accept
	Acrylic	38	1.38	20.9%	0.0%	0.0%	23.7%	
	Pooled	44	1.40	21.4%	0.0%	0.0%	25.0%	

Table 5.17 Validation of SCF Distribution Parametric Equation for Y and T-joint
under OPB Loading on Brace Side

Equation	Steel/ Acrylic	No of Pts	Database		Pred SCF/Recorded SCF			Decision
			Mean	%st dev of Enq	%P/R< 0.8	%P/R< 1.0	%P/R> 1.5	
HCD	Steel	7	1.62	17.9%	0.0%	0.0%	57.1%	accept
	Acrylic	35	1.13	16.5%	0.0%	14.3%	2.9%	
	Pooled	42	1.21	24.8%	0.0%	11.9%	11.9%	
SCF Dis	Steel	7	1.68	13.8%	0.0%	0.0%	85.7%	accept
	Acrylic	35	1.22	25.3%	0.0%	14.3%	14.3%	
	Pooled	42	1.30	29.2%	0.0%	11.9%	26.2%	

Table 5.18 Validation of SCF Distribution Parametric Equation for Y and T-joint
under OPB Loading on Chord Side

Equation	Steel/ Acrylic	No of Pts	Database		Pred SCF/Recorded SCF			Decision
			Mean	%st dev of Enq	%P/R< 0.8	%P/R< 1.0	%P/R> 1.5	
HCD	Steel	13	1.22	13.8%	0.0%	0.0%	7.7%	accept
	Acrylic	51	1.11	22.4%	3.9%	31.4%	3.9%	
	Pooled	64	1.13	21.3%	3.1%	25.0%	4.7%	
SCF Dis	Steel	13	1.17	20.8%	0.0%	23.1%	7.7%	reject
	Acrylic	51	1.04	24.5%	11.8%	47.1%	5.9%	
	Pooled	64	1.06	24.3%	9.4%	42.2%	6.3%	



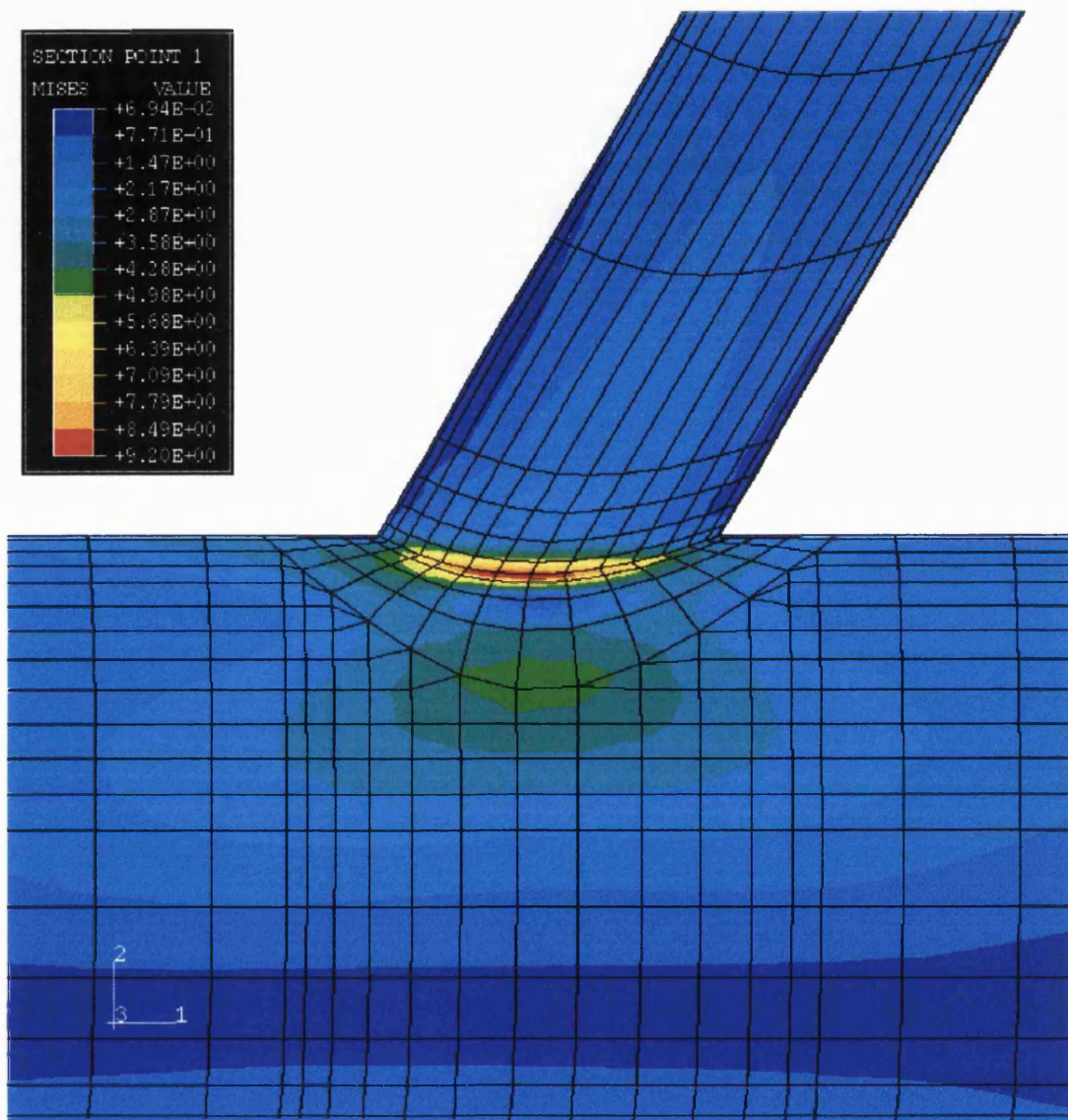


Figure 5.3 Plot of Typical External Stress Distribution around the Intersection of Tubular Y-joint under Axial Loading

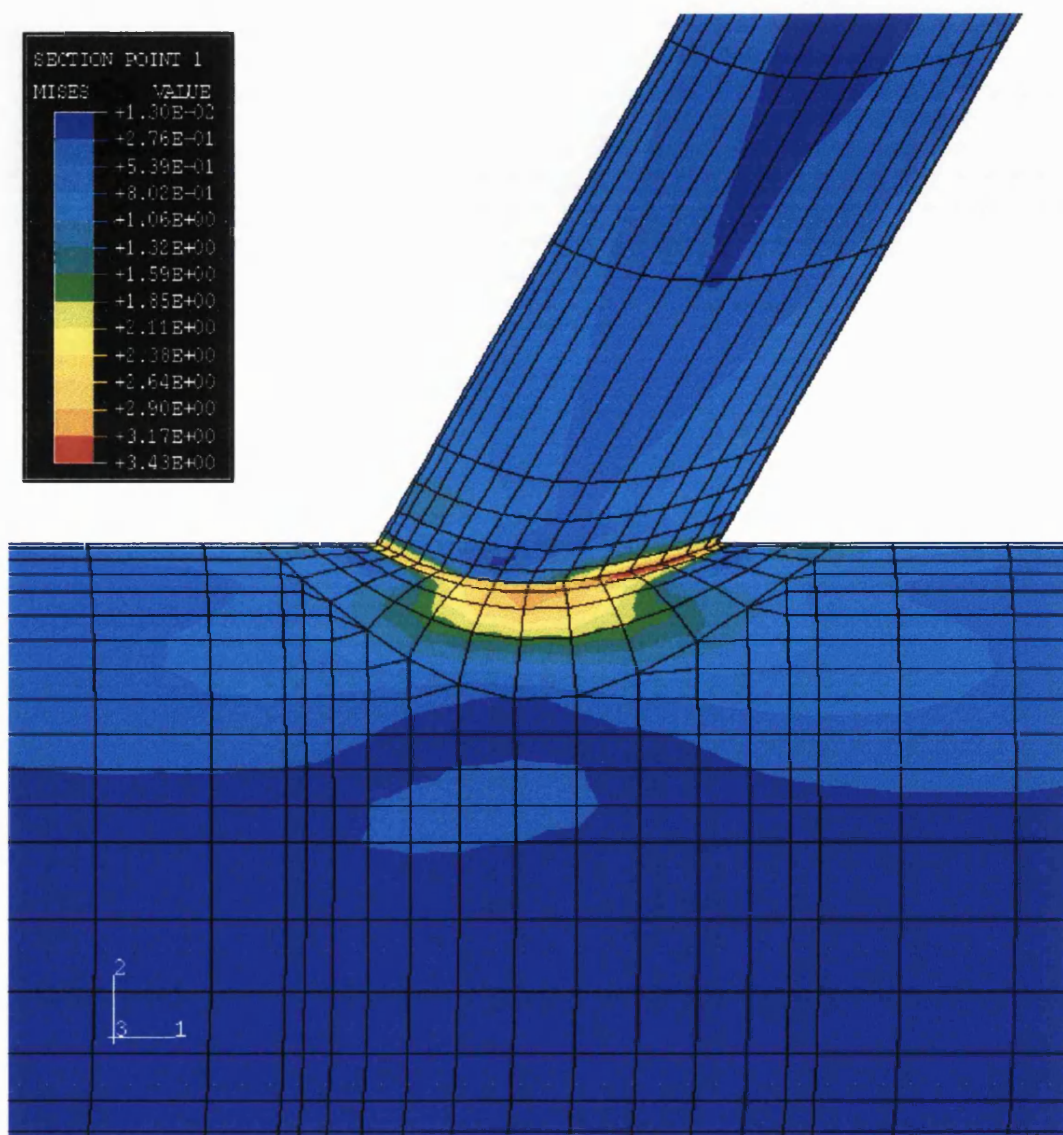


Figure 5.4 Plot of Typical External Stress Distribution around the Intersection of Tubular Y-joint under IPB Loading

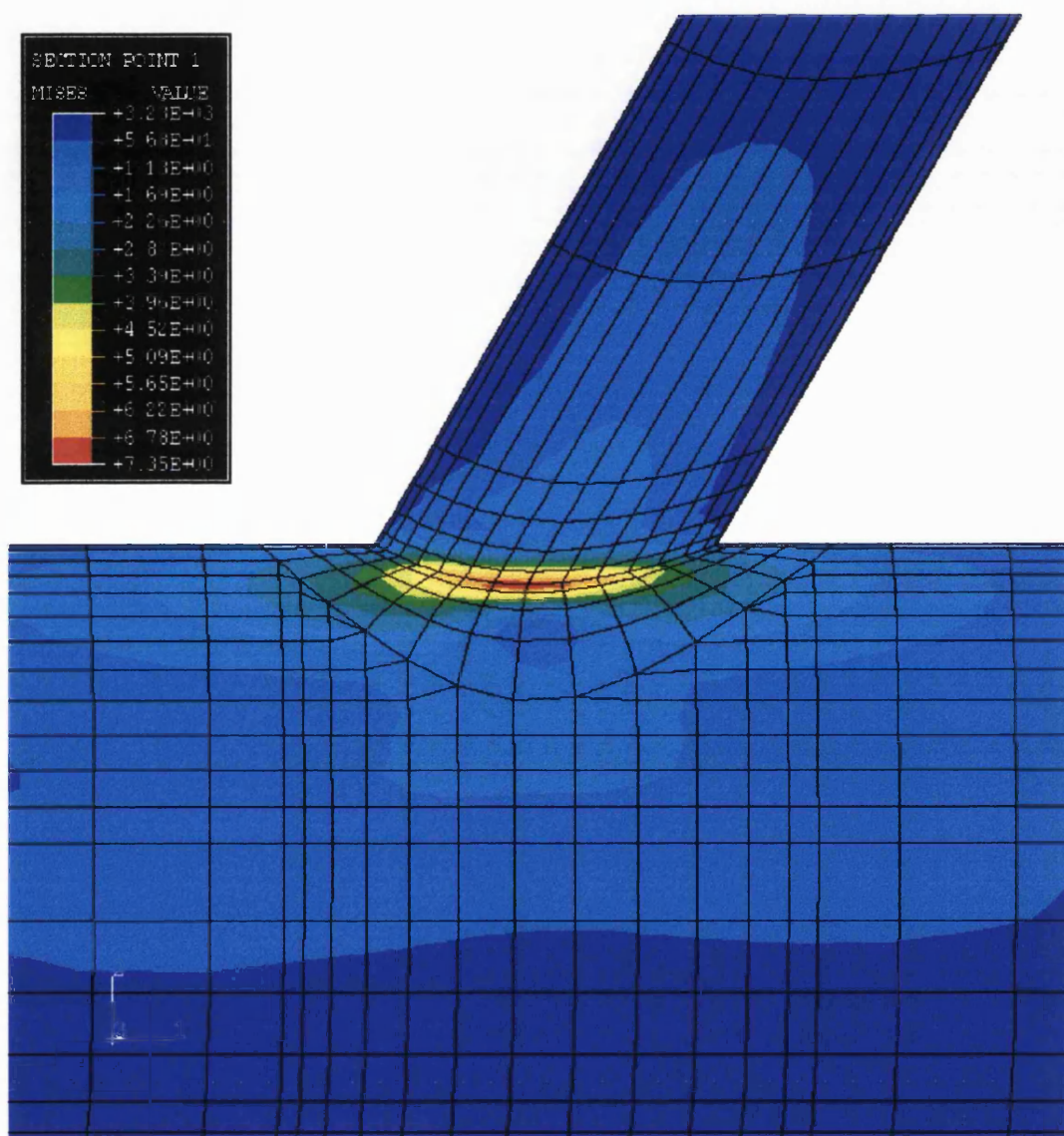


Figure 5.5 Plot of Typical External Stress Distribution around the Intersection of Tubular Y-joint under OPB Loading

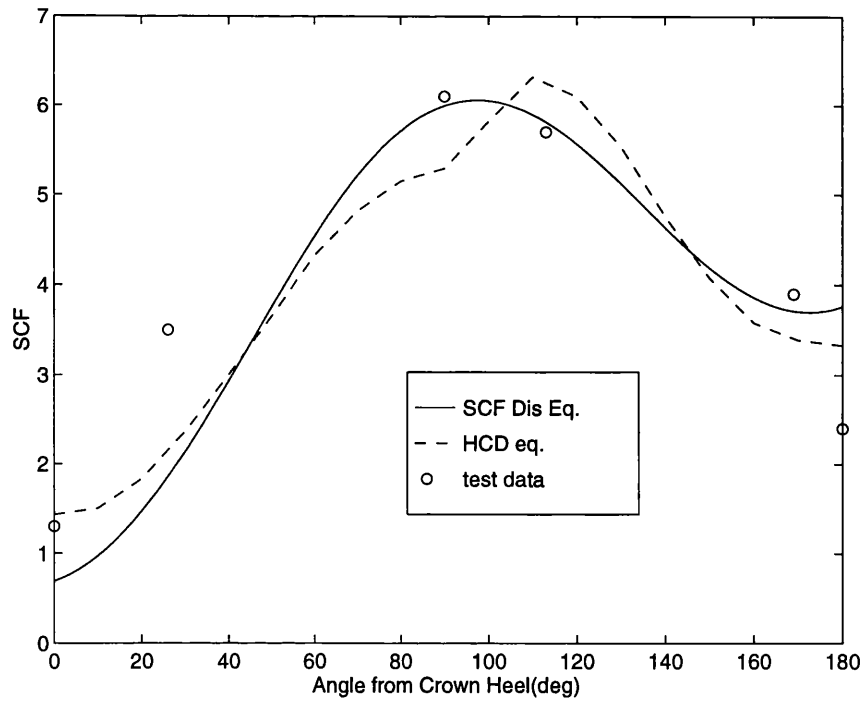


Figure 5.6 Comparison of Predicted External Surface SCF Distribution on Brace Toe with Acrylic Model Test Results for the Axially Loaded Y-joint ($\alpha=9.33$, $\beta=0.67$, $\gamma=15.0$, $\tau=0.8$, $\theta=45^\circ$)

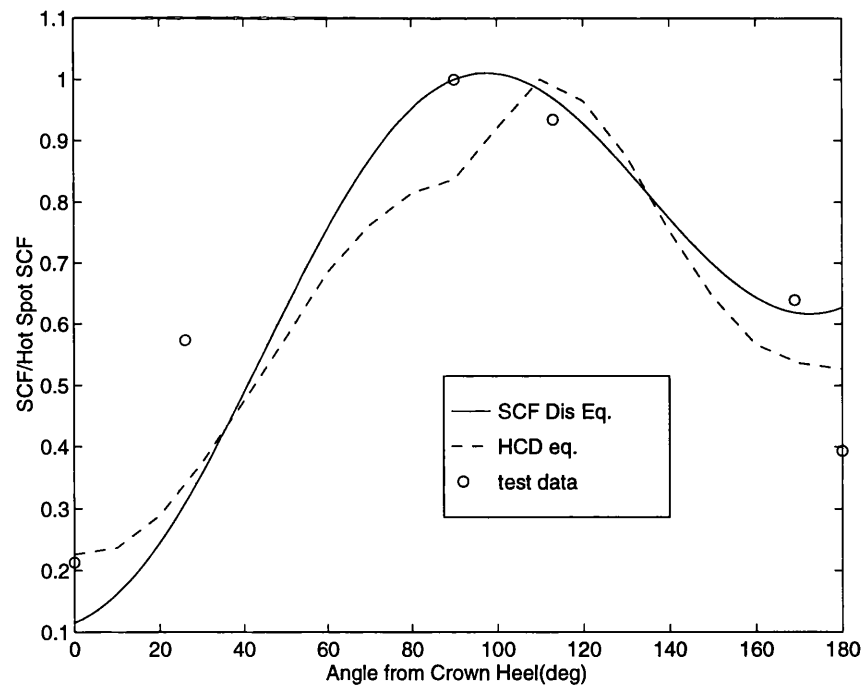


Figure 5.7 Comparison of Predicted Normalised External Surface SCF Distribution on Brace Toe with Acrylic Model Test Results for the Axially Loaded Y-joint ($\alpha=9.33$, $\beta=0.67$, $\gamma=15.0$, $\tau=0.8$, $\theta=45^\circ$)

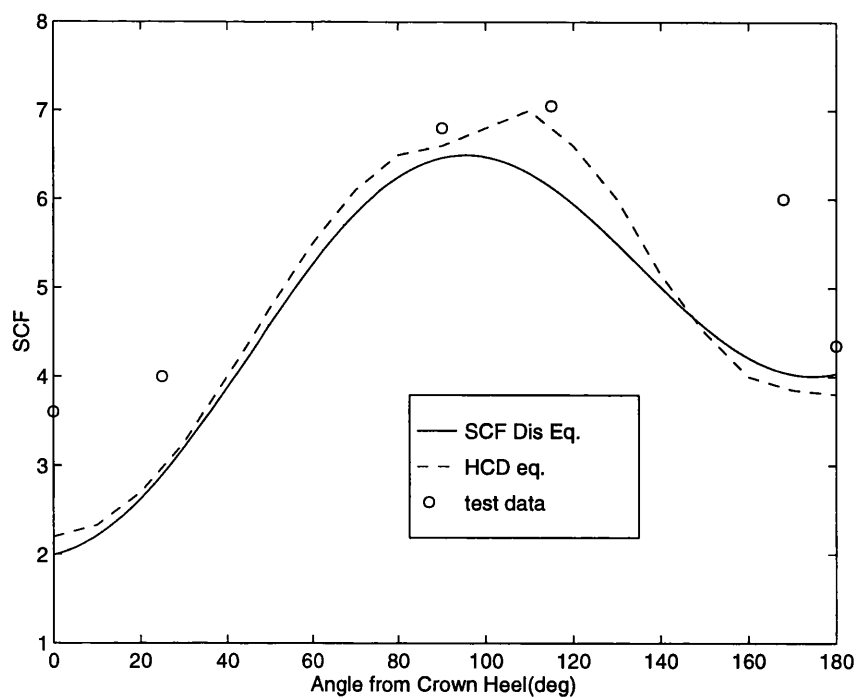


Figure 5.8 Comparison of Predicted External Surface SCF Distribution on Chord Toe with Acrylic Model Test Results for the Axially Loaded Y-joint ($\alpha=9.33$, $\beta=0.67$, $\gamma=15.0$, $\tau=0.8$, $\theta=45^\circ$)

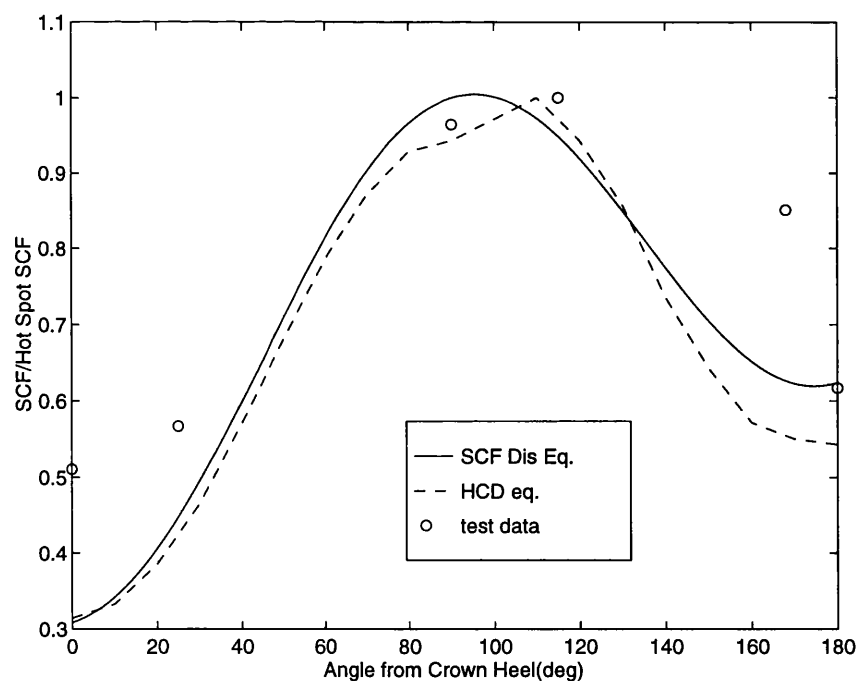


Figure 5.9 Comparison of Predicted Normalised External Surface SCF Distribution on Chord Toe with Acrylic Model Test Results for the Axially Loaded Y-joint ($\alpha=9.33$, $\beta=0.67$, $\gamma=15.0$, $\tau=0.8$, $\theta=45^\circ$)

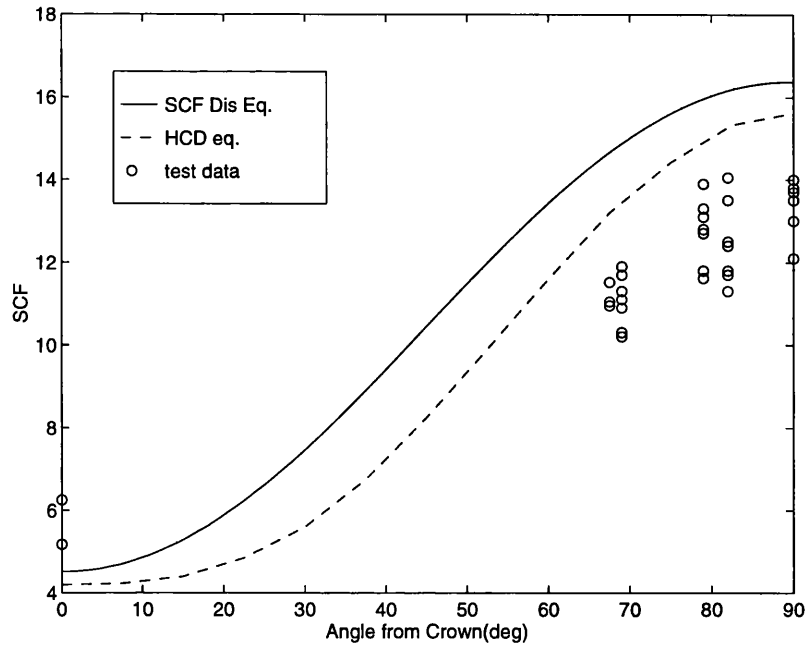


Figure 5.10 Comparison of Predicted External Surface SCF Distribution on Chord Toe with Steel Model Test Results for the Axially Loaded T-joint ($\alpha=7.26$, $\beta=0.71$, $\gamma=14.28$, $\tau=1.0$, $\theta=90^\circ$)

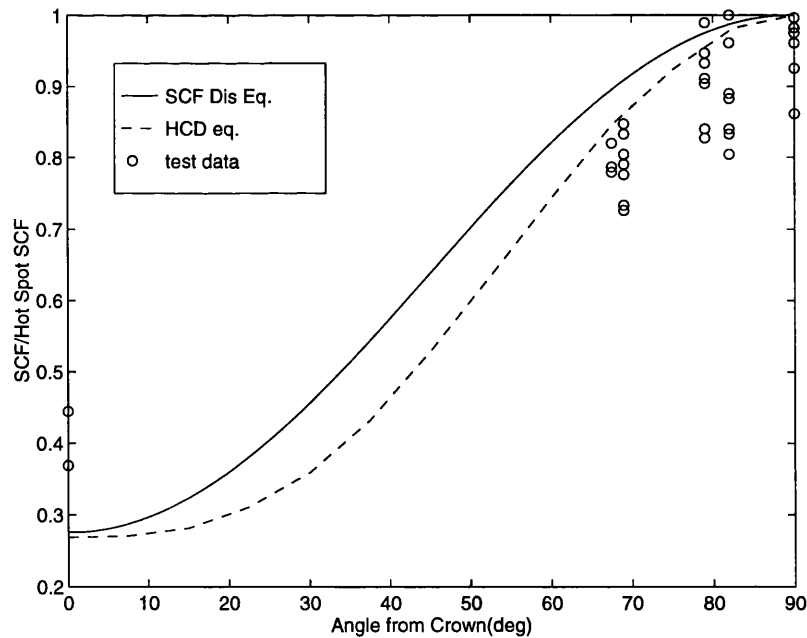


Figure 5.11 Comparison of Predicted Normalised External Surface SCF Distribution on Chord Toe with Steel Model Test Results for the Axially Loaded T-joint ($\alpha=7.26$, $\beta=0.71$, $\gamma=14.28$, $\tau=1.0$, $\theta=90^\circ$)

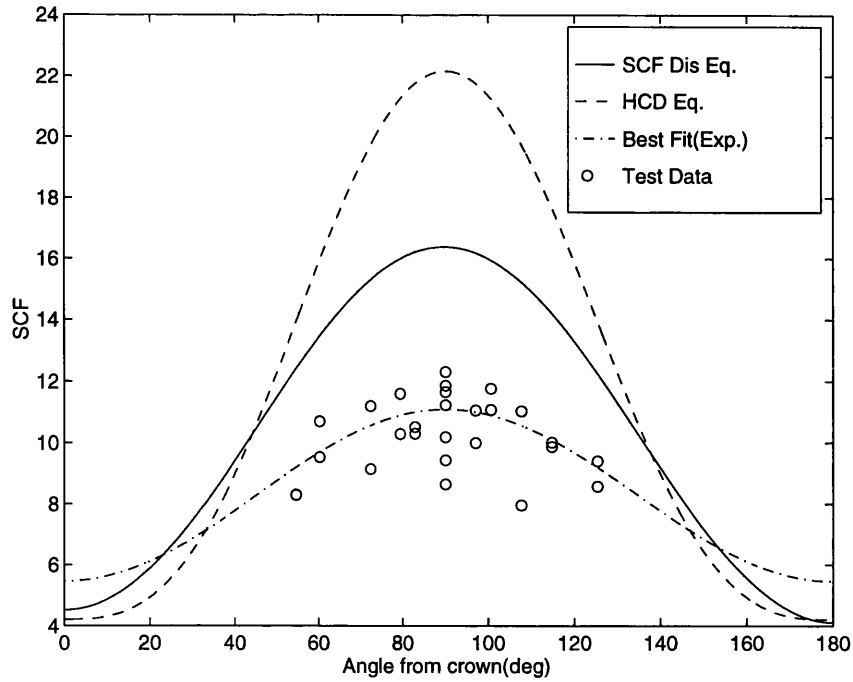


Figure 5.12 Comparison of Predicted External Surface SCF Distribution on Chord Toe with Recently Steel Model Test Results for the Axially Loaded T-joint ($\alpha=7.26$, $\beta=0.71$, $\gamma=14.28$, $\tau=1.0$, $\theta=90^\circ$)

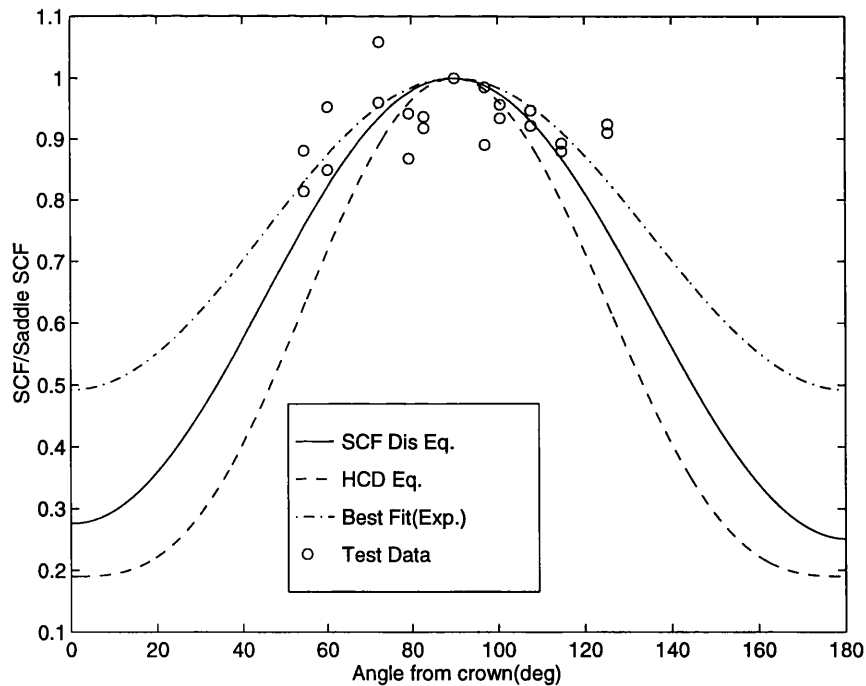


Figure 5.13 Comparison of Predicted Normalised External Surface SCF Distribution on Chord Toe with Recently Steel Model Test Results for the Axially Loaded T-joint ($\alpha=7.26$, $\beta=0.71$, $\gamma=14.28$, $\tau=1.0$, $\theta=90^\circ$)

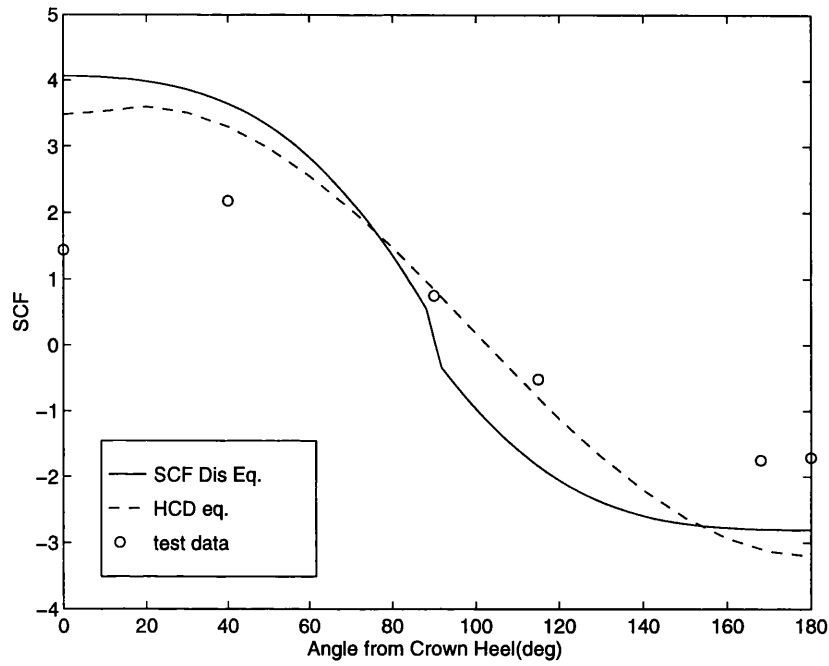


Figure 5.14 Comparison of Predicted External Surface SCF Distribution on Brace Toe with Acrylic Model Test Results for the IPB-Loaded Y-joint ($\alpha=9.33$, $\beta=0.67$, $\gamma=15.0$, $\tau=0.8$, $\theta=45^\circ$)

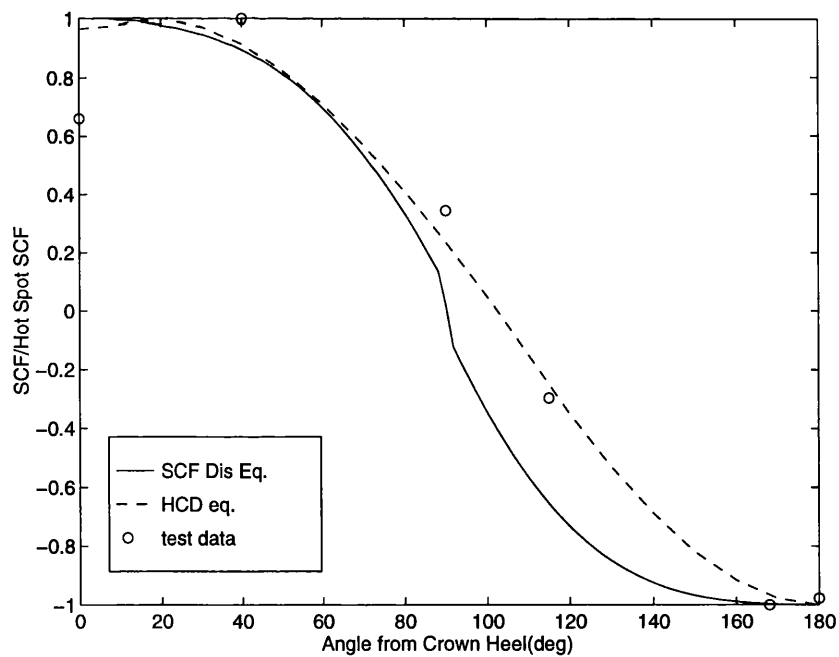


Figure 5.15 Comparison of Predicted Normalised External Surface SCF Distribution on Brace Toe with Acrylic Model Test Results for the IPB-Loaded Y-joint ($\alpha=9.33$, $\beta=0.67$, $\gamma=15.0$, $\tau=0.8$, $\theta=45^\circ$)

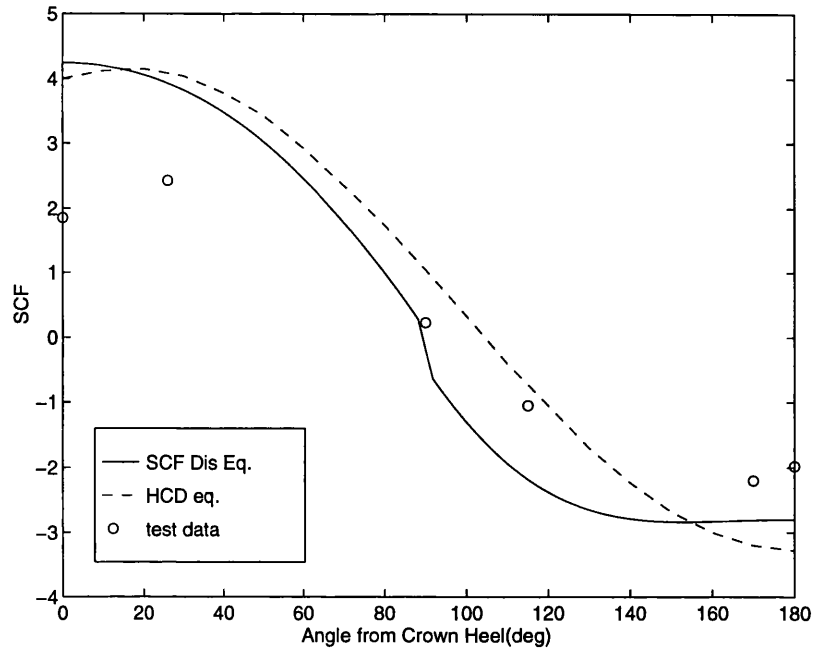


Figure 5.16 Comparison of Predicted External Surface SCF Distribution on Chord Toe with Acrylic Model Test Results for the IPB-Loaded Y-joint ($\alpha=9.33$, $\beta=0.67$, $\gamma=15.0$, $\tau=0.8$, $\theta=45^\circ$)

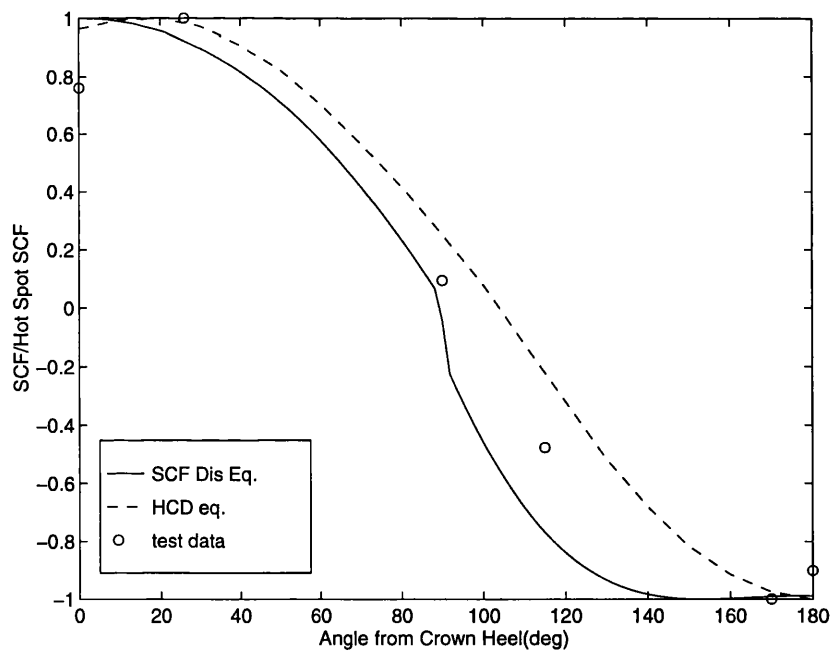


Figure 5.17 Comparison of Predicted Normalised External Surface SCF Distribution on Chord Toe with Acrylic Model Test Results for the IPB-Loaded Y-joint ($\alpha=9.33$, $\beta=0.67$, $\gamma=15.0$, $\tau=0.8$, $\theta=45^\circ$)

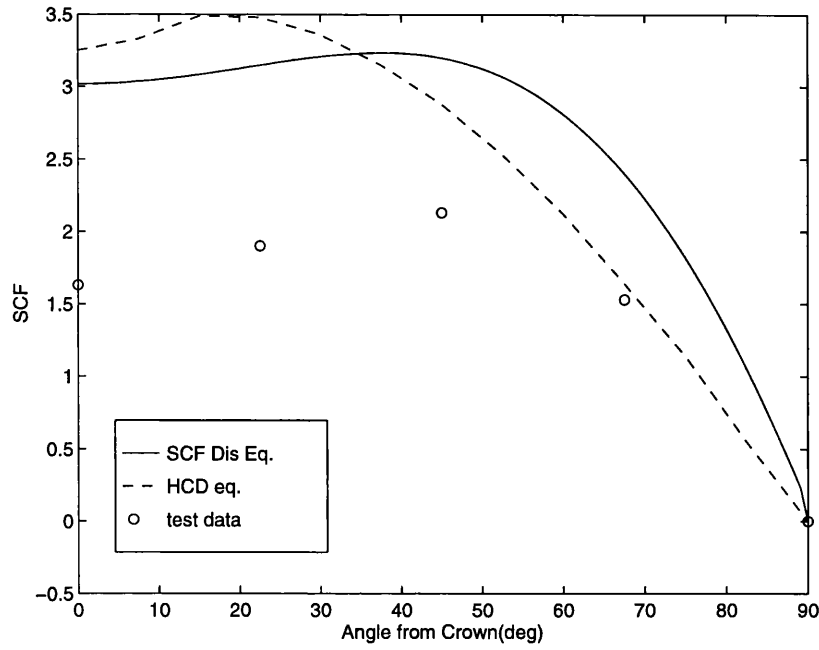


Figure 5.18 Comparison of Predicted External Surface SCF Distribution on Brace Toe with Steel Model Test Results for the IPB-Loaded T-joint ($\alpha=8.01$, $\beta=0.71$, $\gamma=14.28$, $\tau=0.78$, $\theta=90^\circ$)

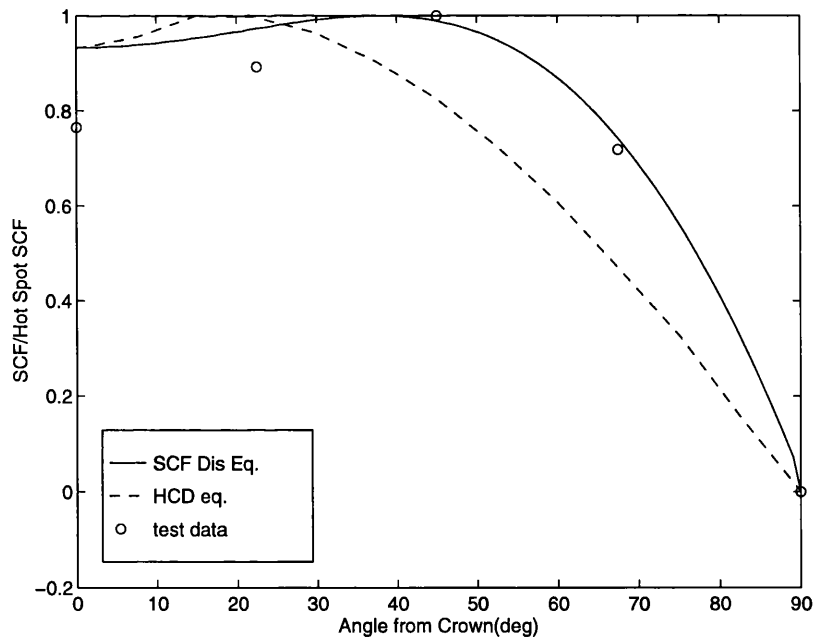


Figure 5.19 Comparison of Predicted Normalised External Surface SCF Distribution on Brace Toe with Steel Model Test Results for the IPB-Loaded T-joint ($\alpha=8.01$, $\beta=0.71$, $\gamma=14.28$, $\tau=0.78$, $\theta=90^\circ$)

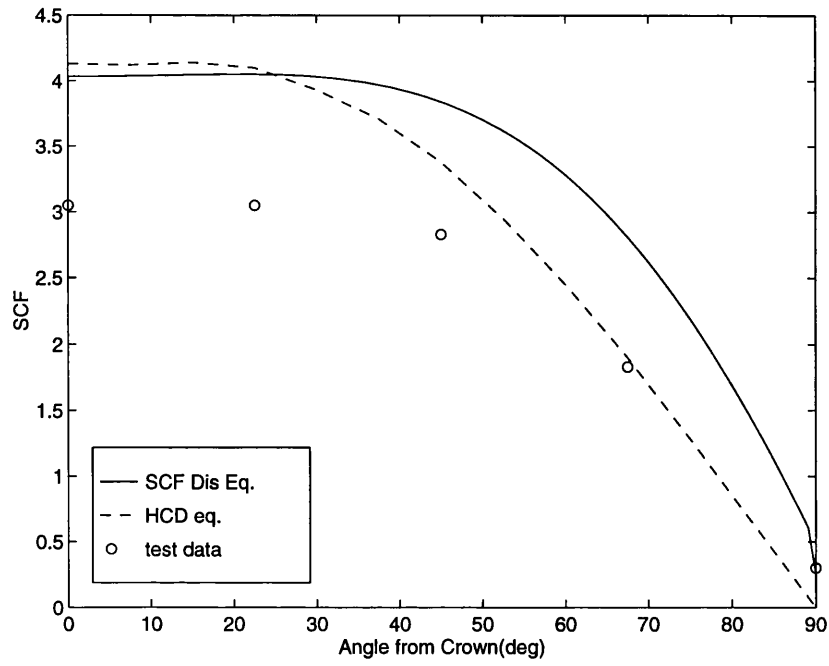


Figure 5.20 Comparison of Predicted External Surface SCF Distribution on Chord Toe with Steel Model Test Results for the IPB-Loaded T-joint ($\alpha=8.01$, $\beta=0.71$, $\gamma=14.28$, $\tau=0.78$, $\theta=90^\circ$)

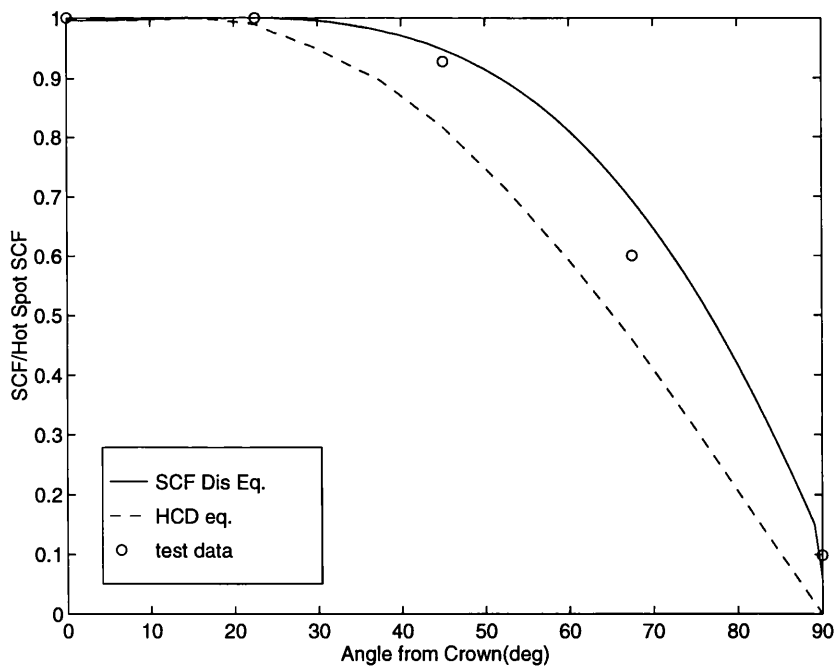


Figure 5.21 Comparison of Predicted Normalised External Surface SCF Distribution on Chord Toe with Steel Model Test Results for the IPB-Loaded T-joint ($\alpha=8.01$, $\beta=0.71$, $\gamma=14.28$, $\tau=0.78$, $\theta=90^\circ$)

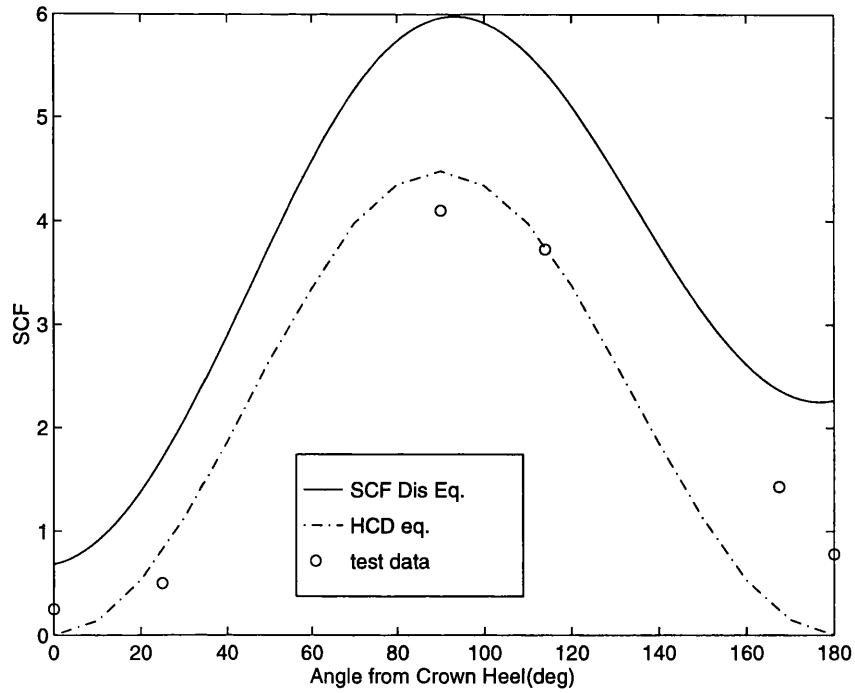


Figure 5.22 Comparison of Predicted External Surface SCF Distribution on Brace Toe with Acrylic Model Test Results for the OPB-Loaded Y-joint ($\alpha=9.33$, $\beta=0.67$, $\gamma=15.0$, $\tau=0.8$, $\theta=45^\circ$)

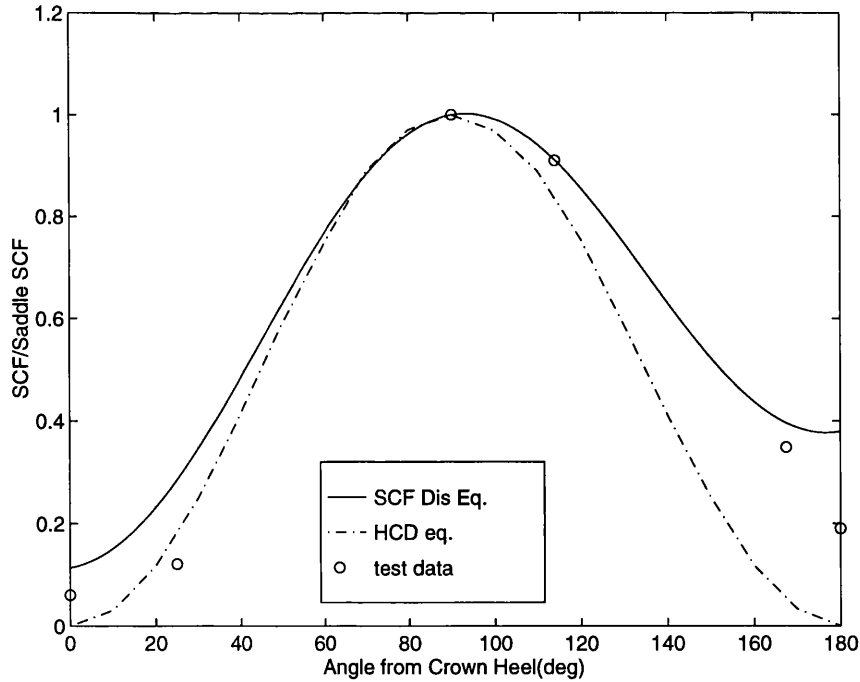


Figure 5.23 Comparison of Predicted Normalised External Surface SCF Distribution on Brace Toe with Acrylic Model Test Results for the OPB-Loaded Y-joint ($\alpha=9.33$, $\beta=0.67$, $\gamma=15.0$, $\tau=0.8$, $\theta=45^\circ$)

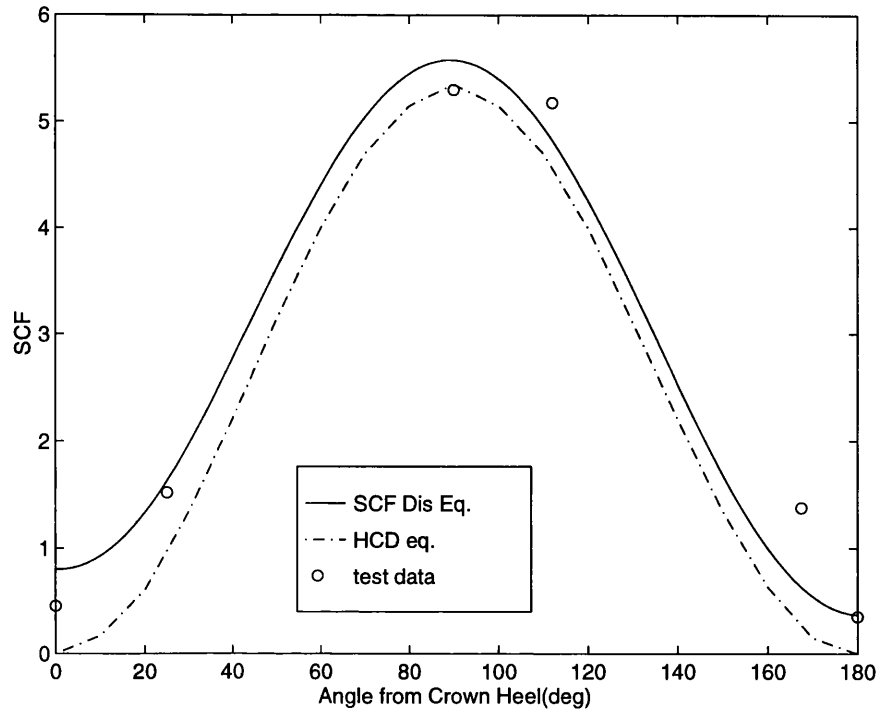


Figure 5.24 Comparison of Predicted External Surface SCF Distribution on Chord Toe with Acrylic Model Test Results for the OPB-Loaded Y-joint ($\alpha=9.33$, $\beta=0.67$, $\gamma=15.0$, $\tau=0.8$, $\theta=45^\circ$)

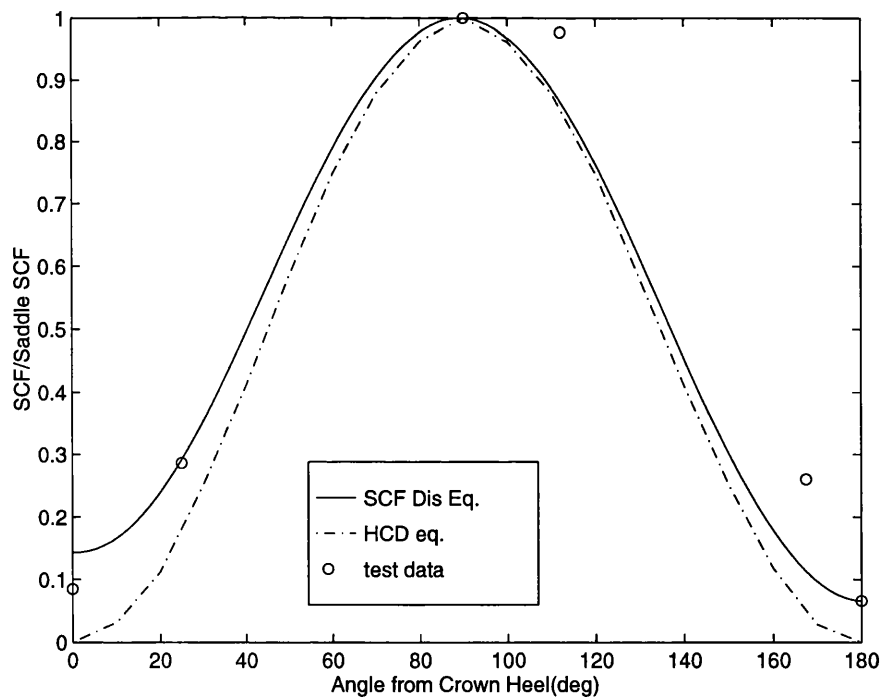


Figure 5.25 Comparison of Predicted Normalised External Surface SCF Distribution on Chord Toe with Acrylic Model Test Results for the OPB-Loaded Y-joint ($\alpha=9.33$, $\beta=0.67$, $\gamma=15.0$, $\tau=0.8$, $\theta=45^\circ$)

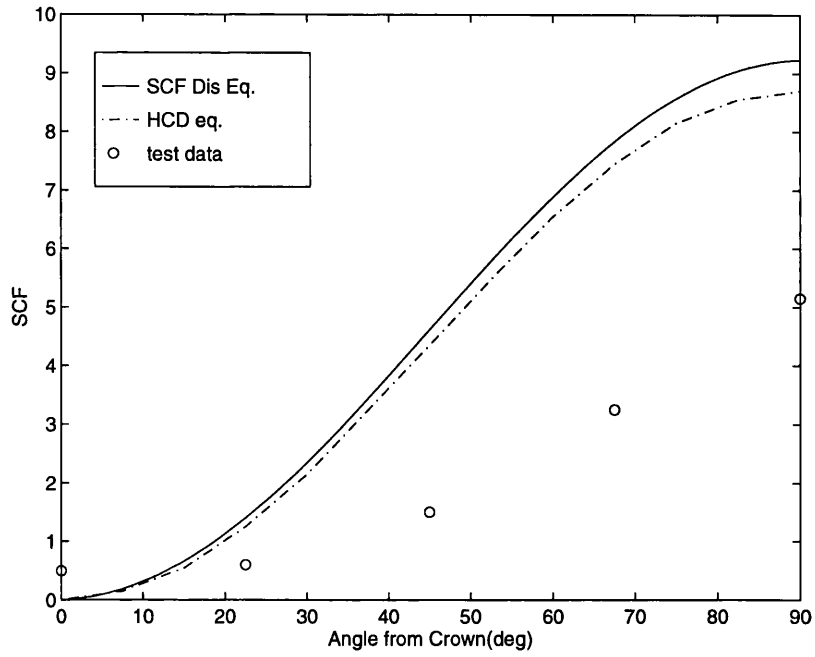


Figure 5.26 Comparison of Predicted External Surface SCF Distribution on Brace Toe with Steel Model Test Results for the OPB-Loaded T-joint ($\alpha=8.01$, $\beta=0.71$, $\gamma=14.28$, $\tau=0.78$, $\theta=90^\circ$)

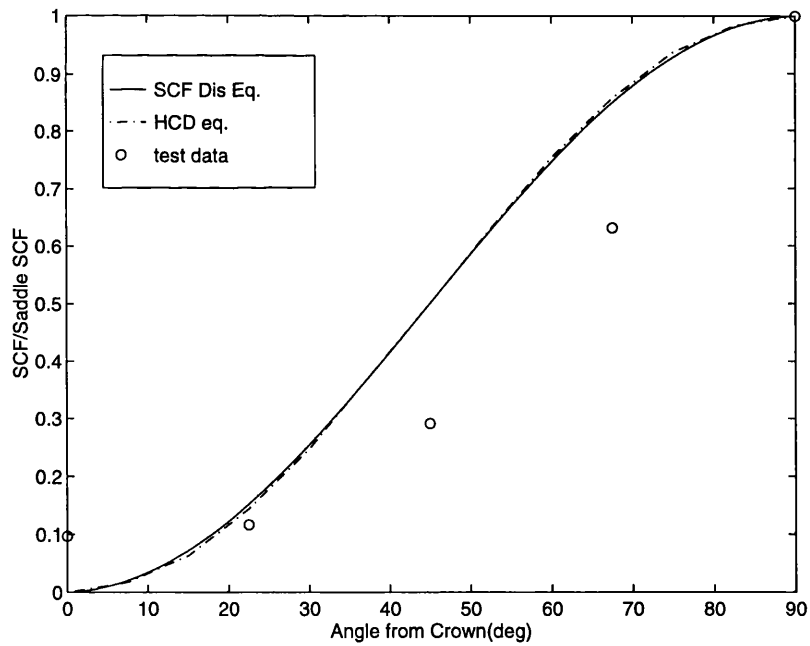


Figure 5.27 Comparison of Predicted Normalised External Surface SCF Distribution on Brace Toe with Steel Model Test Results for the OPB-Loaded T-joint ($\alpha=8.01$, $\beta=0.71$, $\gamma=14.28$, $\tau=0.78$, $\theta=90^\circ$)

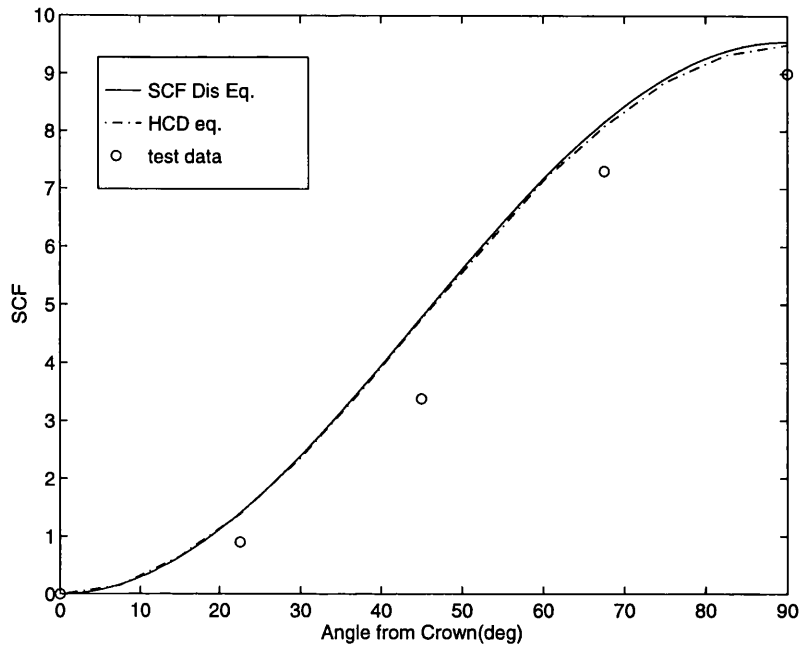


Figure 5.28 Comparison of Predicted External Surface SCF Distribution on Chord Toe with Steel Model Test Results for the OPB-Loaded T-joint ($\alpha=8.01$, $\beta=0.71$, $\gamma=14.28$, $\tau=0.78$, $\theta=90^\circ$)

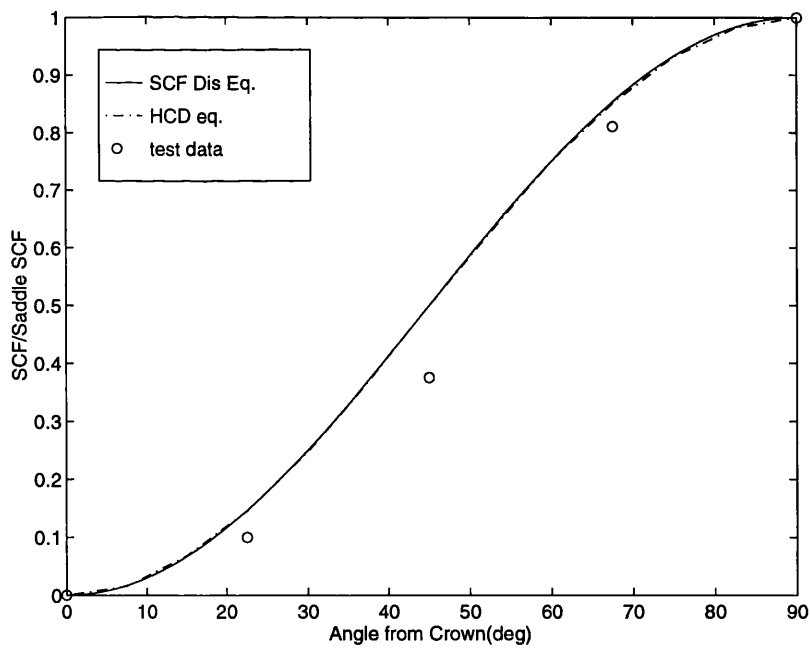


Figure 5.29 Comparison of Predicted Normalised External Surface SCF Distribution on Chord Toe with Steel Model Test Results for the OPB-Loaded T-joint ($\alpha=8.01$, $\beta=0.71$, $\gamma=14.28$, $\tau=0.78$, $\theta=90^\circ$)

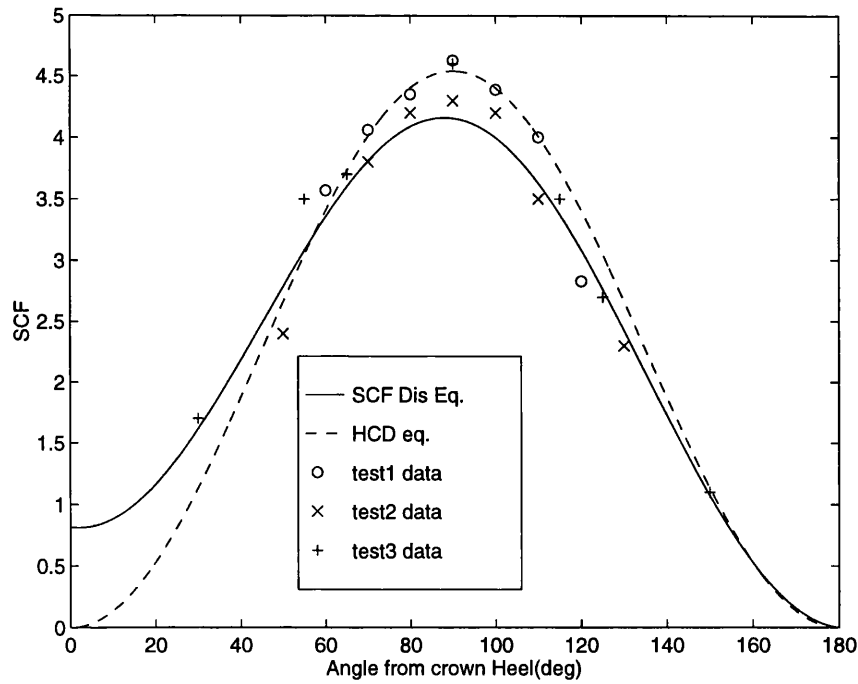


Figure 5.30 Comparison of Predicted External Surface SCF Distribution on Chord Toe with Recently Steel Model Test Results for the OPB-Loaded Y-joint ($\alpha=10.85$, $\beta=0.71$, $\gamma=14.28$, $\tau=1.0$, $\theta=35^\circ$)

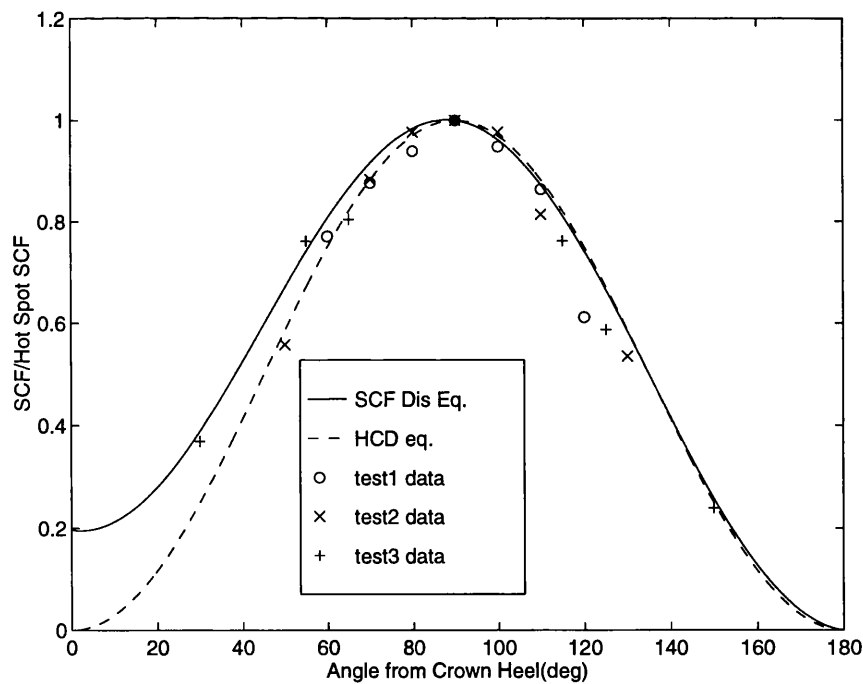


Figure 5.31 Comparison of Predicted External Surface SCF Distribution on Chord Toe with Recently Steel Model Test Results for the OPB-Loaded Y-joint ($\alpha=10.85$, $\beta=0.71$, $\gamma=14.28$, $\tau=1.0$, $\theta=35^\circ$)

CHAPTER SIX

CHARACTERISTIC PARAMETERS FOR STRESS DISTRIBUTION ALONG THE INTERSECTION OF TUBULAR Y, T, X AND DT-JOINTS

6.1 Introduction

The hot spot stress has been used to characterise the intensity of the stress field around the intersection and to provide a useful means for estimating the relative fatigue strengths of tubular welded joints. However, early fatigue tests have shown that the crack growth rate for a T-joint under axial loading was higher than that of a similar joint under out-of-plane bending for a similar hot spot stress range. It would seem that the hot spot stress range is not sufficient to describe the behaviour of crack growth under different types of loading. There are several other parameters which influence the crack growth behaviour in tubular joints. One of most important factor is the stress distribution along the intersection.

The characteristic parameters representing the whole stress distribution along the intersection are convenient for use in advanced fracture mechanics modelling. Dharmavasan and Dover(1987) suggested one of these parameters in terms of an average stress and proposed an AVS model based on early fatigue growth data of welded tubular joints. This study will extend this concept and will allow more complex interpretations to be made.

Furthermore, it is extremely valuable to the overall methodology that these parameters could be used as an alternative to the single value of hot spot stress for evaluating stress/life or remaining life(fatigue crack growth) as they provide the information on both magnitude and shape of the stress distribution around the intersection of tubular joint.

Despite the fact that these parameters are valuable, they can only be calculated from stress distribution data obtained by using either simple interpolation equations or fitting limited experimental data along the intersection in current practice, which would lead to inaccurate results. Systematic finite element analyses have been conducted for tubular Y, T, X and DT-joints as reported in last three chapters. Based on these results, regression analyses have been carried out to derive parametric equations for these important parameters.

6.2 Characteristic Parameters for Stress Distribution along Intersection of tubular Joints

Due to the geometry of a tubular joint, the SCF distribution curve has a bell shape. A typical example is shown in Figure 6.1 for the stress distribution along the chord toe of a tubular welded Y-joint under axial, IPB and OPB loading respectively. A pair of characteristic parameters can be defined to represent the magnitude and spread of SCF distribution along the intersection of tubular welded joints respectively(Figure 6.2).

Measure of Magnitude

As representing the magnitude of SCF distribution along the intersection, the concept of the average SCF has been proposed before(Dharmavasan and Dover 1987) as follows:

$$\overline{SCF} = \frac{1}{\pi} \int_0^{\pi} SCF(\theta) d\theta \quad \text{for Axial and OPB Loading} \quad (6-1)$$

$$\overline{SCF}_{Toe} = \frac{1}{\pi} \int_{-\frac{\pi}{2}}^{\frac{\pi}{2}} SCF(\theta) d\theta \quad \text{for IPB Loading around the Crown Toe side} \quad (6-2)$$

$$\overline{SCF}_{Heel} = \frac{1}{\pi} \int_{\frac{\pi}{2}}^{\frac{3\pi}{2}} SCF(\theta) d\theta \quad \text{for IPB Loading around the Crown Heel side} \quad (6-3)$$

This useful parameter has been used in the empirical Stress Intensity Factor(SIF) models such as AVS(Dharmavasan and Dover 1987) and TPM(Kam et al 1987) for tubular joints.

Measure of Spread

So far there is no proposed parameter to describe the spread of stress distribution along the intersection of a tubular joint. However, experimental results showed that apart from the hot spot SCF and average SCF, the number of initiation cracks and the subsequent crack shape development are very much dependent on the spread of stress distribution. Therefore it is valuable to propose a characteristic parameter to represent the spread of stress distribution.

Following similar form used for the spectrum width in spectrum analysis, the non dimensional SCF Distribution Concentration Factor(SDCF), ρ_{SCF} is proposed below to provide the relative measurement on spread of stress or SCF distribution curve along the intersection of tubular welded joints.

$$\rho_{SCF} = \sqrt{\frac{\int_0^{\pi} SCF(\theta)(\theta - \bar{\theta})^2 d\theta}{\pi^2 \int_0^{\pi} SCF(\theta) d\theta}} \quad \text{for Axial and OPB Loading} \quad (6-4)$$

$$\rho_{SCF}^{Toe} = \sqrt{\frac{\int_{\frac{\pi}{2}}^{\frac{\pi}{2}} SCF(\theta)(\theta - \bar{\theta}_{Toe})^2 d\theta}{\pi^2 \int_{\frac{\pi}{2}}^{\frac{\pi}{2}} SCF(\theta) d\theta}} \quad \text{for IPB Loading around the Crown Toe side} \quad (6-5)$$

$$\rho_{SCF}^{Heel} = \sqrt{\frac{\int_{\frac{\pi}{2}}^{\frac{3\pi}{2}} SCF(\theta)(\theta - \bar{\theta}_{Heel})^2 d\theta}{\pi^2 \int_{\frac{\pi}{2}}^{\frac{3\pi}{2}} SCF(\theta) d\theta}} \quad \text{for IPB Loading around the Crown Heel side} \quad (6-6)$$

where θ is the geometry centre(usually hot spot position) for a stress or SCF curve along the intersection of tubular joint under Axial and OPB loading.

$\bar{\theta}_{Toe}$, $\bar{\theta}_{Heel}$ are the geometry centres(usually hot spot locations) for the stress or SCF curve around the crown toe and heel side of the intersection of tubular joint respectively under IPB loading.

Finite element analysis results for tubular Y and X-joints already showed that the hot spot stress location is not necessary at the saddle for axial and OPB loading, or at crown position for IPB loading. Thus effort is made to define the centre of stress distribution along the intersection as below.

$$\bar{\theta} = \frac{\int_0^{\pi} SCF(\theta)\theta d\theta}{\int_0^{\pi} SCF(\theta) d\theta} \quad \text{for Axial and OPB Loading} \quad (6-7)$$

$$\bar{\theta}_{Toe} = \frac{\int_{-\frac{\pi}{2}}^{\frac{\pi}{2}} SCF(\theta) \theta d\theta}{\int_{-\frac{\pi}{2}}^{\frac{\pi}{2}} SCF(\theta) d\theta} \quad \text{for IPB Loading around the Crown Toe side} \quad (6-8)$$

$$\bar{\theta}_{Heel} = \frac{\int_{\frac{\pi}{2}}^{\frac{3\pi}{2}} SCF(\theta) \theta d\theta}{\int_{\frac{\pi}{2}}^{\frac{3\pi}{2}} SCF(\theta) d\theta} \quad \text{for IPB Loading around the Crown Heel side} \quad (6-9)$$

6.3 Regression Analyses

The SCF distributions along the intersection were extracted from the ABAQUS output files for tubular Y, T, X and DT-joints. FORTRAN programs were written to calculate the average SCF and SDCF for 330 tubular Y, T, X and DT-joints respectively. As only magnitude of SCF is interested, all SCFs along the intersection are assigned to be absolute value under each loading including IPB loading. Thus all average SCF values are positive for all cases.

This database of finite element analysis results was used to derive parametric equations for the average SCF and SDCF in tubular Y, T, X and DT-joints by using a statistical regression package known as 'MINITAB'(1991). The regression analysis methodology is similar to that used for deriving SCFs and is listed as follows:

a) The variations of the average SCF and SDCF were plotted as a function of the parameters α , β , γ and τ and θ in order to determine the best forms of the terms required, and also to ascertain if any cross-correlation existed between the terms.

b) A first attempt at the equation was made using the following simple form:

$$\overline{SCF} = A_1 \alpha^{A_2} \beta^{A_3} \gamma^{A_4} \tau^{A_5} \theta^{A_6} \quad (6-10)$$

$$\rho = A_1 \alpha^{A_2} \beta^{A_3} \gamma^{A_4} \tau^{A_5} \theta^{A_6} \quad (6-11)$$

where A_1 to A_6 were determined from the regression analysis.

c) Process adopted to get the final form:

The above equations were then modified by using other (e.g. exponential) terms, and regressions performed until a suitable equation with a large product moment correlation coefficient was obtained.

The parametric equations for average SCF and SDCF have been derived for both chord and brace toes under three different modes of loading for tubular Y and T-joints and six different modes of loading for tubular X and DT-joints by carrying out regression analysis. They are given in Appendix D. These equations can be easily programmed and enable the stress distribution characteristic parameters, average SCF and SDCF, to be calculated both for the brace and chord toes for all modes of loading. A summary of the degree of fit for each equation is presented in Tables 6.1-6.4. The tables show that these equations fit the original finite element data very well and the correlation coefficient R^2 is greater than 95% for the majority of cases.

As there is very little experimental data on SCF along the intersection of tubular joints, it is difficult to validate fully these parametric equations, especially for SDCF. An effort has been made to collect all available early UCL steel test data (Dharmavasan 1983) (Kam 1989) and other recent experimental data (Monahan 1994) in order to test the average SCF equations. Data from early tests were obtained by using simple interpolation equations to fit limited experimental data along the intersection. Recently experimental tests involved several multiple (M) plane and X-joints and test data were calculated by best-fitting these steel test data. A comparison of predictions from derived parametric equations with test data has been made (Table 6.5) and shown in Figure 6.3. From this figure, one can see that reasonable agreement has been achieved. It should be noted that the test data are obtained by combining some experimental data and the simple interpolation equations and therefore are not very accurate.

6.4 Conclusions

The new concept, SCF distribution concentration factor (SDCF) was proposed. The systematic finite element results have been used to derive the parametric equations for average SCF and SDCF by regression analysis. These equations describe average SCF and SDCF as a function of non-dimensional joint geometric ratios α , β , γ , τ and θ for each mode of loading, and for both the chord and brace sides of the intersection of tubular welded Y, T, X and DT-joints. The stress distribution characteristic parameters, average SCF and SDCF, together with hot-spot SCF and DoB, can be used to define fully the two dimensional stress distribution of a tubular joint. They are useful parameters to develop new advanced fracture mechanics modelling and are also valuable for fatigue design of offshore tubular welded joints.

Table 6.1 Summary of Degree of Fit for Parametric Equations for Average SCF
Along the Intersection of Tubular Y and T-Joints

Loading Case	Location	R ² (%)	Equation
Single Axial	Brace Side	97.29	Appendix E1.1
Single Axial	Chord Side	98.41	Appendix E1.2
Single IPB	Brace Side(around Crown Toe)	95.19	Appendix E2.1
Single IPB	Brace Side(around Crown Heel)	95.83	Appendix E2.2
Single IPB	Chord Side(around Crown Toe)	97.36	Appendix E2.3
Single IPB	Chord Side(around Crown Heel)	97.7	Appendix E2.4
Single OPB	Brace Side	96.41	Appendix E3.1
Single OPB	Chord Side	96.36	Appendix E3.2

Table 6.2 Summary of Degree of Fit for Parametric Equations for Average SCF
Along the Intersection of Tubular X and DT-Joints

Loading Case	Location	R ² (%)	Equation
Single Axial	Brace Side	96.2	Appendix F1.1
Single Axial	Chord Side	97.8	Appendix F1.2
Single IPB	Brace Side(around Crown Toe)	97.6	Appendix F2.1
Single IPB	Brace Side(around Crown Heel)	95.8	Appendix F2.2
Single IPB	Chord Side(around Crown Toe)	98.0	Appendix F2.3
Single IPB	Chord Side(around Crown Heel)	98.4	Appendix F2.4
Single OPB	Brace Side	97.4	Appendix F3.1
Single OPB	Chord Side	94.3	Appendix F3.2
Balanced Axial	Brace Side	95.6	Appendix F4.1
Balanced Axial	Chord Side	95.8	Appendix F4.2
Balanced IPB	Brace Side(around Crown Toe)	97.6	Appendix F5.1
Balanced IPB	Brace Side(around Crown Heel)	95.8	Appendix F5.2
Balanced IPB	Chord Side(around Crown Toe)	97.8	Appendix F5.3
Balanced IPB	Chord Side(around Crown Heel)	98.2	Appendix F5.4
Balanced OPB	Brace Side	98.4	Appendix F6.1
Balanced OPB	Chord Side	99.4	Appendix F6.2

Table 6.3 Summary of Degree of Fit for Parametric Equations of Stress Distribution
Concentration Factor Along the Intersection of Tubular Y and T-Joints

Loading Case	Location	R ² (%)	Equation
Single Axial	Brace Side	95.34	Appendix G1.1
Single Axial	Chord Side	96.49	Appendix G1.2
Single IPB	Brace Side(around Crown Toe)	96.31	Appendix G2.1
Single IPB	Brace Side(around Crown Heel)	96.04	Appendix G2.2
Single IPB	Chord Side(around Crown Toe)	95.18	Appendix G2.3
Single IPB	Chord Side(around Crown Heel)	95.51	Appendix G2.4
Single OPB	Brace Side	95.18	Appendix G3.1
Single OPB	Chord Side	95.5	Appendix G3.2

Table 6.4 Summary of Degree of Fit for Parametric Equations of Stress Distribution
Concentration Factor Along the Intersection of Tubular X and DT-Joints

Loading Case	Location	R ² (%)	Equation
Single Axial	Brace Side	96.6	Appendix H1.1
Single Axial	Chord Side	96.6	Appendix H1.2
Single IPB	Brace Side(around Crown Toe)	95.5	Appendix H2.1
Single IPB	Brace Side(around Crown Heel)	95.6	Appendix H2.2
Single IPB	Chord Side(around Crown Toe)	89.3	Appendix H2.3
Single IPB	Chord Side(around Crown Heel)	96.2	Appendix H2.4
Single OPB	Brace Side	96.4	Appendix H3.1
Single OPB	Chord Side	96.0	Appendix H3.2
Balanced Axial	Brace Side	96.0	Appendix H4.1
Balanced Axial	Chord Side	95.1	Appendix H4.2
Balanced IPB	Brace Side(around Crown Toe)	95.6	Appendix H5.1
Balanced IPB	Brace Side(around Crown Heel)	96.4	Appendix H5.2
Balanced IPB	Chord Side(around Crown Toe)	90.1	Appendix H5.3
Balanced IPB	Chord Side(around Crown Heel)	95.5	Appendix H5.4
Balanced OPB	Brace Side	97.0	Appendix H6.1
Balanced OPB	Chord Side	97.2	Appendix H6.2

Table 6.5 Comparison of Predicted Average SCF with Test Data for Tubular Joints

Ref	Joint Type	Mode of Loading	α	β	γ	τ	θ (deg)	Test Data	Pred
(Dharmavasan 1983)	T	Axial	7.20	0.71	14.30	0.79	90	6.35	6.68
(Dharmavasan 1983)	T	OPB	7.30	0.71	14.40	0.80	90	4.10	4.08
(Dharmavasan 1983)	Y	IPB	9.10	0.71	14.28	0.78	45	1.51	2.27
(Dharmavasan 1983)	Y	Axial	13.0	0.48	15.90	0.63	45	4.45	4.32
(Kam 1989)-UCX1	X	Balanced Axial	4.44	0.51	10.00	0.44	90	3.94	3.74
(Kam 1989)-UCX2	X	Balanced Axial	5.33	0.61	10.70	0.54	90	5.29	4.69
(Kam 1989)-UCX3	X	Balanced Axial	6.67	0.76	12.00	0.50	90	4.17	4.36
(Monahan 1994)	M-T	IPB	4.44	0.51	14.06	0.63	90	2.08	2.39
(Monahan 1994)	M-Y	OPB	4.44	0.36	14.06	0.56	35	2.03	1.23
(Monahan 1994)	M-T	OPB	4.44	0.51	14.06	0.63	90	4.10	3.46
(Monahan 1994)	M-Y	IPB	4.44	0.36	14.06	0.56	35	1.58	1.64
(Monahan 1994)	X	OPB	7.86	0.90	12.73	1.00	90	3.42	3.93

Note: M-T: T-brace/chord intersection of multiple-brace M-node

M-Y: Y-brace/chord intersection of multiple-brace M-node

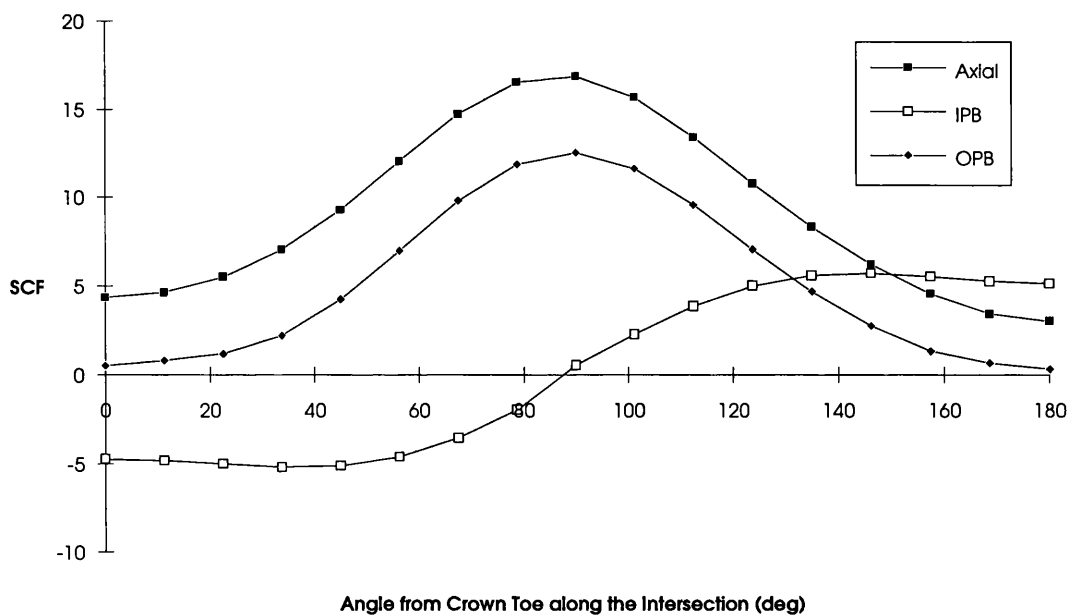


Figure 6.1 Typical Example of SCF Distribution along the Intersection of Tubular Y-Joint

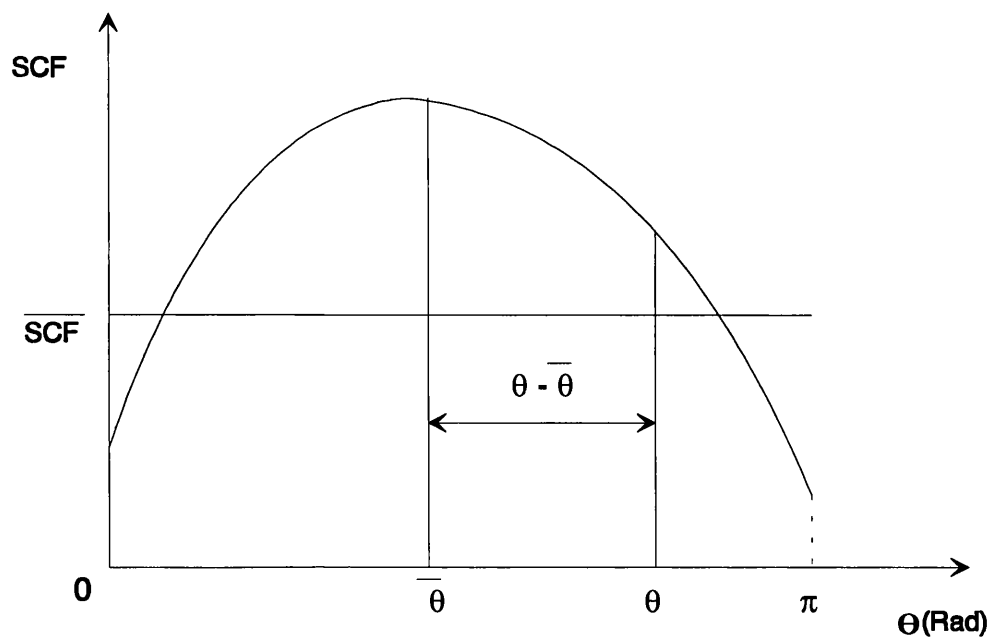


Figure 6.2 Illustration of Characteristic Parameters for SCF Distribution along the Intersection of Tubular Joint

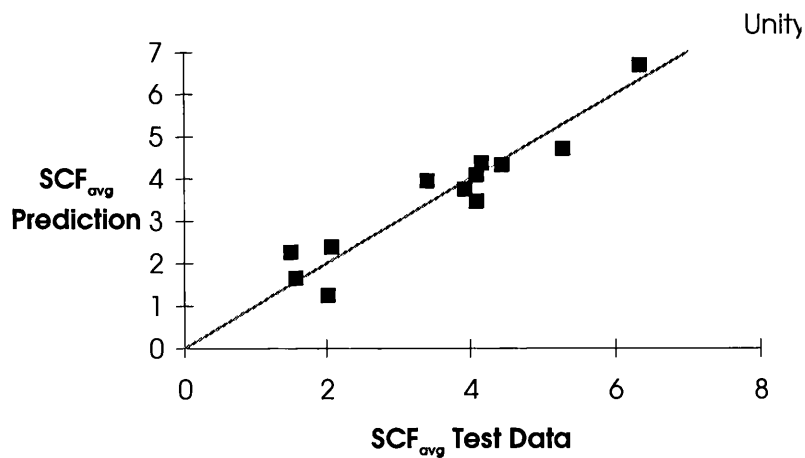


Figure 6.3 Comparison of Predictions from Derived Parametric Equations with Test Data for Average SCF along the Intersection of Tubular Joint

CHAPTER SEVEN

DEEPEST POINT SIF PARAMETRIC EQUATIONS FOR THE SEMI-ELLIPTICAL SURFACE CRACKS IN T-BUTT WELDED JOINTS

7.1 Introduction

The accurate solution for Stress Intensity Factor (SIF) is the essential element for predicting fatigue crack growth rate in offshore structures using a fracture mechanics approach. In particular, it is important to have the deepest point SIF for semi-elliptical surface cracks which are the most frequently observed crack shape in welded joints, such as T-butt and tubular welded joints. Many SIF solutions(Newman and Raju 1981)(Holdbrook and Dover 1979)(Oore and Burns 1980) have been derived for flat plates. However, for T-butt welded joints, there are not many solutions available as one has to consider the surface stress concentration influence at the weld toe. Currently there are two approaches to determine the deepest point SIF of surface semi-elliptical cracks in T-butt welded joints(Figure 7.1). One method is to use the Niu-Glinka weight function(Niu and Glinka 1989) that can incorporate weld angle and weld toe radius influences. This method also requires the through thickness stress distribution information at the weld toe for the joint in question in order to integrate them together to obtain the SIF. Therefore it is not convenient to use this method, especially at design stage, due to the complexity of the equations and heavy computational requirement. Recently, using the Niu-Glinka weight function and many finite element stress analysis results, a set of deepest point SIF parametric equations for T-butt welded joints for both membrane and bending loading have been derived by Hall, Topp and Dover(HTD)(Hall et al 1990). This set of equations include the influence of crack size and shape, weld toe radius and weld angle and have been included into new fatigue guidance for offshore structures(MaTSU 1996).

The other approach is to use a plate solution with a modification factor due to presence of weld toe, known as M_k . The M_k factor was obtained from the two dimensional finite element analysis of edge cracks at the weld toe and comparing the results with the corresponding results for the same crack in a flat plate. By curve fitting these values, expressions for M_k (Maddox 1975) have been derived. Much work was carried out to enhance the accuracy of M_k at The Welding Institute(TWI). The final results were included as part of the PD6493(1991). It should be noted that this approach is limited to a weld angle

of 45° and a sharp weld toe and only considers the variation of the ratio of overall weld attachment length to wall thickness(L/T).

One problem with the HTD approach is that it excludes the effect of attachment size. This parameter has been demonstrated to be quite important for SIF in the Mk approach. Thus it was considered valuable to carry out a study in order to extend the HTD equations to include the effect of attachment size. Having done this, it is of value to compare the results from these two different approaches with the available finite element data.

7.2 Niu-Glinka Weight Function

The weight function method is a powerful technique for the calculation of SIFs for a variety of complex loading conditions. Based on Petroski-Achenbach crack opening displacement expression and using Newman-Raju solutions as the reference SIF solution, Niu-Glinka(1990) has derived a weight function in closed form for calculating the SIF at the deepest point of a crack emanating from the weld toe of a T-butt welded connection. This weight function is capable of incorporating weld profile effects due to different weld angle α and weld toe radius ρ under any mode I type of loading.

The key idea in the Niu and Glinka weight function is to assume that the influence of the weld toe, i. e. the weld angle α , was the same for an edge crack and for the deepest point of a semi-elliptical crack with the same depth under the same stress system. This assumption can be explained as equivalence of the two-dimensional Mk and three dimensional Mk. This enabled Niu and Glinka to set up following relationship:

$$K_s^\alpha = \frac{K_e^\alpha}{K_e^p} K_s^p \quad (7-1)$$

where K_s^α is the SIF for a surface crack in a welded joint

K_s^p is the SIF for a surface crack in a flat plate subjected to the same stress distribution

K_e^α is the SIF for an edge crack in a welded joint

K_e^p is the SIF for an edge crack in a flat plate subjected to the same stress distribution

In order to derive a weight function for a surface crack emanating from the weld toe of a T-butt welded joint, the other three weight functions are needed. The only one available in the literature is the two-dimensional weight function for an edge crack. For this reason, Niu-Glinka initially derived a two-dimensional weight function m_e^α (Niu and Glinka 1987) for an edge crack emanating from the weld toe in a T-butt joint. Then, they derived a three dimensional weight function m_s^p for the deepest point of a surface semi-elliptical crack in a plate using Newman-Raju solution as reference data(Niu and Glinka 1989).

With all these weight functions available, Relation (7 - 1) can be expressed in terms of derived weight functions as following:

$$\int_0^a \sigma(x) m_s^\alpha(x, a/t, a/c, a/w, \alpha) dx = \frac{\int_0^a \sigma(x) m_e^\alpha(x, a, a/t, \alpha) dx}{\int_0^a \sigma(x) m_e^p(x, a, a/t) dx} \int_0^a \sigma(x) m_s^p(x, a, a/t, a/c, c/w) dx \quad (7-2)$$

The reference SIF for a uniform tensile local stress system can be easily obtained from (7 - 2). Using the Petroski-Achenbach method again, Niu and Glinka derived the following closed form weight function for calculation of the SIF at the deepest point of a crack emanating from the weld toe of a T-butt welded joints.

$$m_s^\alpha(x, a/t, a/c, c/w, \alpha) = \frac{2}{\sqrt{2\pi(a-x)}} \left[1 + m_{s1}^\alpha \left(\frac{a-x}{a} \right) + m_{s2}^\alpha \left(\frac{a-x}{a} \right)^2 \right] \quad (7-3)$$

where

$$m_{s1}^\alpha = A_s^\alpha + 3B_s^\alpha - 4 \quad (7-4)$$

$$m_{s2}^\alpha = 5 \left[\frac{\sqrt{2\pi}}{4} F_r - \frac{A_s^\alpha - 1}{3} - B_s^\alpha \right] \quad (7-5)$$

$$A_s^\alpha = \frac{2F_r' a}{F_r} \quad (7-6)$$

$$B_s^\alpha = \frac{5\sqrt{2\pi} \int_0^a F_r^2 a da}{8a^2 F_r} \quad (7-7)$$

This weight function is supposedly valid for weld angles $\pi/6 \leq \alpha \leq \pi/3$ (α in radians), crack aspect ratios $0 \leq a/c \leq 1$ and crack depths $0 \leq a/t \leq 0.5$. However, as deep cracks should not be significantly affected by the weld, the Niu-Glinka method should also be used for cracks of depth $a/t > 0.5$. The result from the Niu-Glinka weight function were found to be substantially the same as those from Newman-Raju for all values of a/T in a flat plate. This is because this weight function is based on the Newman-Raju solution. It should be noted that Niu-Glinka itself only considers the influence of weld angle. The other effects of weld toe, such as weld toe radius and attachment size will be incorporated into the stress distribution later on.

7.3 Systematic SIF Calculation

The weight function is a unique property of crack shape and component geometry and is independent of loading. It needs to be integrated with the uncracked stress distribution in order to calculate the SIF. The Stress Intensity Factor(SIF), K , can be expressed as follows:

$$K = \int_0^a m(a/c, a/T, x) \sigma(\alpha, \rho/T, L/T, a/T, x) dx \quad (7-8)$$

It is well known that through-wall stress distributions at the weld toes are well-represented by combining the results of models loaded in pure tension and pure bending. In order to simplify the use of the weight function method, the deepest point SIF parametric equations for T-butt welded joints in tension and bending would be desirable. Therefore, it is necessary to carry out the stress analysis of the uncracked body for this type of joint with different geometries under pure tension and pure bending respectively to obtain the stress distribution information. For this reason, systematic two dimensional finite element analyses (Brennan et al 1996) for wide range of T-Butt welded joints were conducted using the IDEAS package. Based on these results, the uncracked through-wall stress distribution database which allows all weld toe effects to be incorporated, has recently been established. This database covers T-butts within the following parameter ranges:

Parameter	Range
Weld Toe Angle (α)	$\alpha=30^\circ, 45^\circ, 60^\circ$
Weld Toe Radius/Wall Thickness (ρ/T)	$0.01 \leq \rho / T \leq 0.066$
Attachment Width/Wall Thickness (L/T)	$0.1577 \leq L / T \leq 4$
Location Along Wall Thickness (x)	$0 < x \leq T$

Combining this uncracked T-butt weld toe through-wall stress distribution database with the closed form Niu-Glinka weight function, it is possible to produce a new set of deepest point SIF parametric equations for semi-elliptical surface cracks in T-butt welded joints under tension and bending. A FORTRAN program was written to integrate the Niu-Glinka weight function with the uncracked through-wall stress distribution to generate SIF database for the deepest point of semi-elliptical surface cracks in T-butt welded joints.

The database used for each parameter in this SIF database is shown in following table.

Parameter	Range
Weld Angle α (deg)	30, 45, 60
Weld Radius Ratio ρ/T	0.01, 0.02, 0.04, 0.066
Attachment Ratio L/T	Many data between 0.1577 and 4
Aspect Ratios a/c	0.01, 0.05, 0.08, 0.1, 0.12, 0.15, 0.18, 0.2, 0.4, 0.6, 0.8, 1.0

As can be seen from this table, this SIF database includes the cracks within whole range of aspect ratio ($0 \leq a/c \leq 1$). In particular, sufficient data have been generated in the range $a/c \leq 0.2$ since most fatigue cracks in welded joints are long and shallow and their aspect ratios are often lower than 0.2. A study of the effect of plate width was carried out. As a result, the ratio of c/w was fixed to be 0.25 for conservative reasons in this database. Also it

should be noted that due to a limitation from the Newman-Raju SIF solution(Newman and Raju 1986), this weight function is not valid for long cracks with low aspect ratios and the validated relative crack depth ratio ranges is as follows:

$$\text{if } 0 \leq a/c \leq 0.2 \quad \text{then } a/T \leq 1.25(a/c + 0.6) \quad (7-9a)$$

$$\text{if } a/c \geq 0.2 \quad \text{then } a/T < 1 \quad (7-9b)$$

7.4 Deriving Parametric Equations

The above large database has been used to derive the parametric equations. The regression analyses have been carried out by using the Minitab statistical package(MINITAB 1991). Due to the two dimensional nature, the curve-fitting has to be divided into two steps. The first step is to find suitable expression for both tension and bending loading cases. The results have shown that SIF data can be fitted very well by the following expressions for tension and bending respectively.

$$K = Y\sigma\sqrt{(\pi a)} \quad (7-10)$$

$$Y = \text{Exp}\left(C_0 + C_1\left(\frac{a}{T}\right) + C_2\left(\frac{a}{T}\right)^2\right)\left(\frac{a}{T}\right)^{C_3} \quad \text{under Tension Loading } (7-11)$$

$$Y = C_0 + C_1\left(\frac{a}{T}\right) + C_2\left(\frac{a}{T}\right)^2 + C_3 \text{Ln}\left(\frac{a}{T}\right) \quad \text{under Bending loading } (7-12)$$

Efforts have been concentrated on the fitting the coefficients C_0 , C_1 , C_2 , C_3 from the first step regression analysis results. Regression has been performed until a suitable equation with a large product moment correlation coefficient was obtained.

As a result, the parametric equations to predict the SIF at the deepest point of semi-elliptical surface cracks in T-butt welded joints under tension and bending loading, have been derived in the form of continuous single functions by carrying out the regression analysis and they are given in Appendix I.

As a series of SIF parametric equations in this study were derived in the same way, i.e. by combining weight functions with the UCL database of T-butt through wall stress analysis results, it was decided that the names of these SIF solutions were referred in the form of "abbreviation of particular weight function*S" where * and S stand for the integration process and T-butt through stress distributions respectively and they are explained in footnotes.

A summary of degree of fit for this set of parametric equations(N&G*S)¹ is presented in Table 7.1. It shows that these equations fit the original SIF data extremely well and the correlation coefficient R² is greater than 96% for all cases including both the form of equation and the coefficients C₀, C₁, C₂, C₃. This set of parametric equations is valid for the following parameter ranges:

$$\frac{\pi}{6} \leq \alpha \leq \frac{\pi}{3} \quad (7-13)$$

$$0.01 \leq \frac{\rho}{T} \leq 0.066 \quad (7-14)$$

$$0.1577 \leq \frac{L}{T} \leq 4 \quad (7-15)$$

$$0 \leq \frac{a}{c} \leq 1 \quad (7-16)$$

$$\text{if } 0 \leq a/c \leq 0.2 \text{ then } a/T \leq 1.25(a/c + 0.6) \quad (7-17a)$$

$$\text{if } a/c > 0.2 \quad \text{then } a/T < 1 \quad (7-17b)$$

It is worth noting that this set of equations is appropriate for the whole crack aspect ratio range and works well for cracks with low aspect ratio as sufficient data in database have been generated in the range $a/c < 0.2$ where the coefficients vary rapidly for this aspect ratio range.

7.5 Validation

By using the Niu-Glinka weight function with the through-wall stress distribution information, a set of parametric equations(N&G*S) have been derived to calculate SIF at the deepest point of surface semi-elliptical cracks in T-butt welded joints under tension and bending respectively. In order to establish the accuracy of prediction, it is necessary to carry out the assessment for this set of parametric equations. Two and three dimensional finite element data available in the literature(Bell 1985)(Nykanen 1987)(Straalen et al 1988)(Dijkstra et al 89)(Dijkstra et al 93) have been collected for validation. However, comparison of the results from both the N&G*S and Mk(PD6493) approaches could produce useful information for future guidance. Thus, the predictions from the N&G*S and Mk(PD6493) methods were compared with available two and three dimensional finite element data(Figures 7.2-7.20). The validated ranges of parameters used for this comparison are listed in Table 7.2. The results of validation are presented for three and two dimensional cases in turn.

¹ N&G represent Niu and Glinka weight function, S denotes the T-butt through Stress distributions database, * stands for the integration process.

a) Three Dimensional Surface Cracks

The comparison of the N&G*S and Mk(PD6493) predictions with three dimensional finite element data are presented in the format of SIF calibration factor, Y , for surface cracks with different aspect ratios in T-butts with different weld angles. The predictions from the N&G*S equations were first compared with the results from the flat plate Newman-Raju(N&R) equations for tension and bending respectively(Figures 7.2-7.3). The stress concentration effect of a weld toe is clearly shown in the results from N&G*S as it decays quickly and disappears at about $a/T=0.1$. The figures also show the undershoot for N&G*S predictions as required by the self equilibrating nature of the stresses across the section.

A comparison of Y predictions from N&G*S and Mk(PD6493) solutions with increasing L/T is made for the shallow cracks($a/T=0.01$) with two different aspect ratios under tension and bending respectively(Figures 7.4-7.5)(as the attachment size is the only weld toe variable considered in PD6493). They show that there is a critical attachment size beyond which Y remains same for the PD 6493 approach, whilst a continuously changing curve is observed for the N&G*S predictions.

Figures 7.6-7.7 show comparison of predictions from N&G*S and PD6493 with Bell's three dimensional finite element results for the T-butt with $\alpha=45^\circ$. For tension, the N&G*S predictions agree very well with Bell's data while the PD6493 results are slightly conservative. For bending, the predictions from both methods are quite good. Also it was found that the predictions from the N&G*S are quite close to Bell's data for the T-butt with $\alpha=30^\circ$ (Figures 7.8-7.9). A comparison of the N&G*S results with Bell's data for the T-butt with $\alpha=70^\circ$ is shown in Figures 7.10-11. As the weld angle upper limitation for the N&G*S is 60° , the N&G*S results for both $\alpha=60^\circ$ and $\alpha=70^\circ$ were produced. The results indicated that they were very close to each other and agree extremely well with Bell's results. It should be noted that Bell's data and PD6493 predictions are based on a T-butt with $\rho/T=0$ and the minimum validated value $\rho/T=0.01$ for N&G*S equations were used for comparison in Figures 7.6-7.11.

Nykanen's three dimensional data(Nykanen 1987) were also used to compare with the N&G*S prediction for the T-butt under tension(Figure 7.12). The agreement between these data is not good, especially for high aspect ratios. This may due to that fact that the T-butt model considered in Nykanen data does not include the attachment, which is different to the conventional one used in the N&G*S method. The weld radius used by Nykanen, $\rho/T=0.17$, is well beyond the validated range($0.01 \leq \frac{\rho}{T} \leq 0.066$) for the N&G*S method.

b) Two dimensional Edge Cracks

Dijkstra's two dimensional finite element data were used to compare with the predictions from the N&G*S equations for the T-butt with different weld radius and attachment expressed in the form of Mk factors for convenience(Figures 7.13-17). Again, the values for $\alpha=70^\circ$ (Figures 7.13-14, 7.17-18) were produced although the N&G*S equations are normally only valid up to $\alpha=60^\circ$. The results show that there is little difference between the cases with $\alpha=60^\circ$ and $\alpha=70^\circ$ for the N&G*S predictions. They all agree very well with Dijkstra's data(Figures 7.13-18). Again, the minimum validated value $\rho/T=0.01$ for the N&G*S equations was used to compare with the Dijkstra's results with $\rho/T=0.0071$ in Figures 7.15-7.16.

Finally, the results from both the N&G*S and HTD equations were compared in Figures 7.19-7.20. In tension, the N&G*S results are higher, especially for large cracks while the HTD predictions are slightly higher in bending. However, they follow the same tendency and are quite close up to $a/T=0.25$.

Validation of the predictions from this set of parametric equations(N&G*S) has been carried out by comparing with the results from the PD6493 approach and available two dimensional and three dimensional finite element data. As a summary, excellent agreement is achieved for the N&G*S equations when compared with a variety of available finite element results for both tension and bending. As can be seen from this validation, it seems that the predictions from PD6493 are conservative under tension.

7.6 Conclusions

Based on the closed form Niu-Glinka weight function and UCL uncracked T-butt weld toe through-wall stress distribution database, a new set of SIF parametric equations(N&G*S) for deepest point of surface semi-elliptical cracks in T-butt welded joints have been derived. These equations have included the influence of crack aspect ratios, weld toe angle, weld attachment length and weld radius. They are available for both membrane and bending loading. The comprehensive assessment shows that this set of equations can give the reliable predictions within their broad validated parameter ranges. These equations can be easily programmed and used in application of fracture mechanics to welds.

Table 7.1 Summary of Degree of Fit for the Deepest Point SIF Parametric

Equations(N&G*S) for Semi-elliptical Cracks in T-butt Welded Joints

Loading	Equations	Form of Expression		C_0	C_1	C_2	C_3
		Descriptive Statistics (%)					
		Mean R^2	Std. Dev.	R^2			
Tension	Appendix I1	99.85	0.25	98.23	97.26	99.26	97.52
Bending	Appendix I2	99.71	0.32	96.83	97.78	99.46	97.55

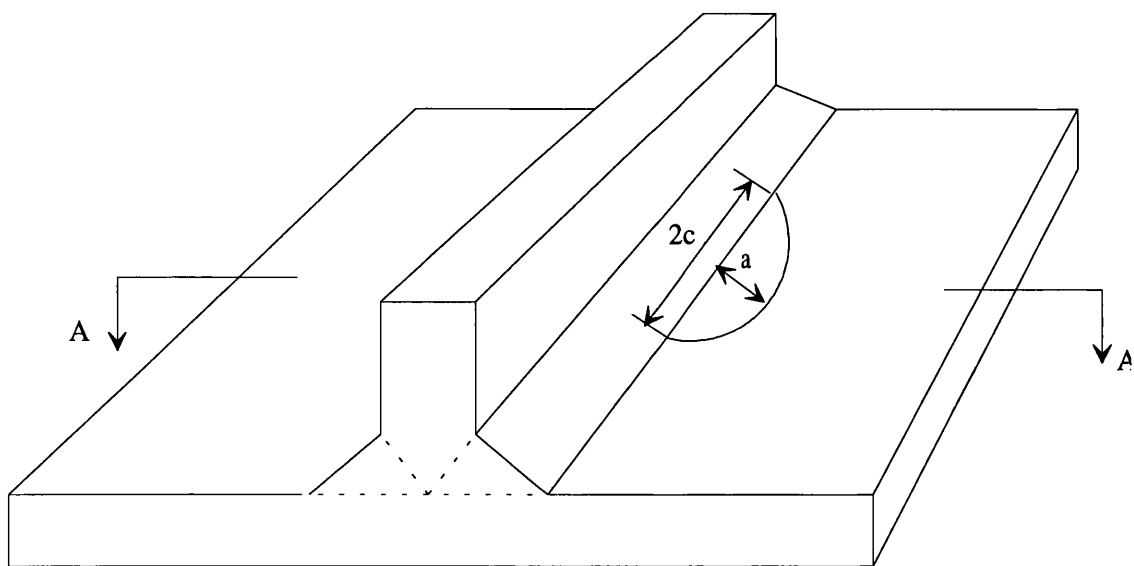
Table 7.2 Comparison of the validated parameter ranges for N&G*S and PD6493(Mk) methods together with available FE data

Solutions	α	ρ/T	L/T	a/c	a/T	Mode of Loading	Form
N&G*S	$30^\circ \leq \alpha \leq 60^\circ$	$0.01 \leq \rho/T \leq 0.066$	$0.1577 \leq L/T \leq 4$	$0 \leq a/c \leq 1.0$	* see note	Tension, Bending	Y
PD6493(Mk)	45°	N/A	$L/T > 0$	$0 \leq a/c \leq 1.0$	$0 < a/T \leq 1.0$	Tension, Bending	Mk

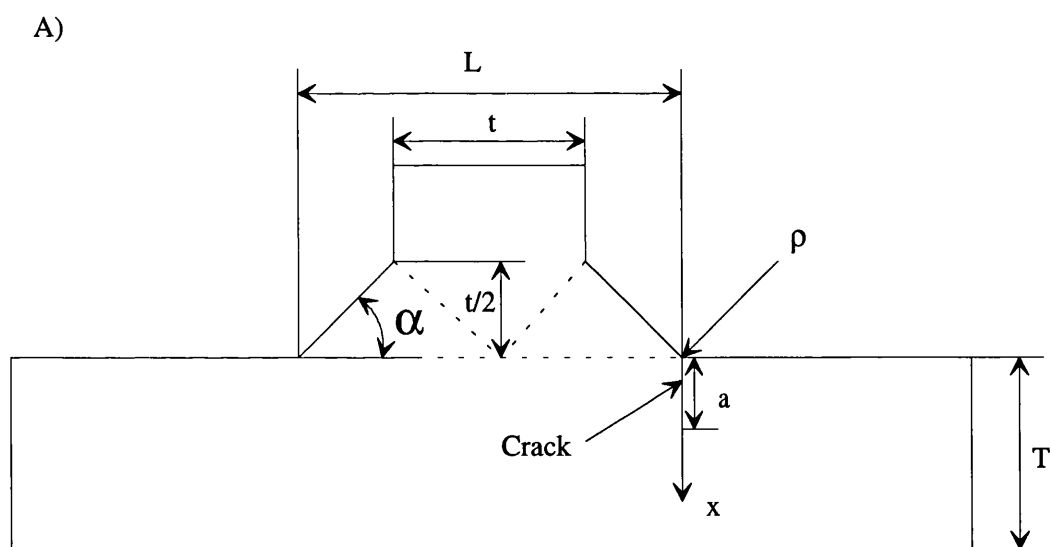
3D FE Data	α	ρ/T	L/T	a/c	a/T	Loading	Form
Bell	30°	0	2.3	0.25, 0.33, 0.5, 0.67, 1	$0.005 \leq a/T \leq 0.4$	Tension, Bending	Y
Bell	45°	0	2.3	0.25, 0.33, 0.5, 0.67, 1	$0.005 \leq a/T \leq 0.4$	Tension, Bending	Y
Bell	70°	0	2.3	0.25, 0.33, 0.5, 0.67, 1	$0.005 \leq a/T \leq 0.4$	Tension, Bending	Y
Nykanen	45°	0.17	1.952	0.2, 0.4, 0.6, 1	0.2, 0.4, 0.6	Tension	Y
Straalen	70°	0.125	1.31	0.64, 0.566, 0.458, 0.393	0.162, 0.224, 0.296, 0.4	Tension, Bending	MK

2D FE Data	α	ρ/T	L/T	a/c	a/T	Loading	Form
Dijkstra'89	70°	0	1.312	N/A	$0.0071 \leq a/T \leq 0.5$	Tension, Bending	Y
Dijkstra'89	70°	0.0071	1.319	N/A	$0 \leq a/T \leq 0.5$	Tension, Bending	Y
Dijkstra'89	70°	0.0125	1.322	N/A	$0 \leq a/T \leq 0.5$	Tension, Bending	Y
Dijkstra'89	70°	0.0714	1.383	N/A	$0 \leq a/T \leq 0.5$	Tension, Bending	Y
Dijkstra'89	70°	0.125	1.434	N/A	$0 \leq a/T \leq 0.5$	Tension, Bending	Y
Dijkstra'89	45°	0.0071	1.864	N/A	$0 \leq a/T \leq 0.5$	Tension, Bending	Y
Dijkstra'93	70°	0	0.562	N/A	$0.0071 \leq a/T \leq 0.5$	Tension, Bending	Y
Dijkstra'93	70°	0	0.812	N/A	$0.0071 \leq a/T \leq 0.5$	Tension, Bending	Y
Dijkstra'93	70°	0	1.062	N/A	$0.0071 \leq a/T \leq 0.5$	Tension, Bending	Y
Dijkstra'93	70°	0	1.312	N/A	$0.0071 \leq a/T \leq 0.5$	Tension, Bending	Y

Note: * if $0 \leq a/c \leq 0.2$ then $a/t \leq 1.25(a/c + 0.6)$, if $a/c > 0.2$ then $a/t < 1$



(a) T-butt Welded Joint (3D)



(b) Local Weld Geometry (2D)

Figure 7.1 Semi-elliptical Crack in T-butt Welded Joint

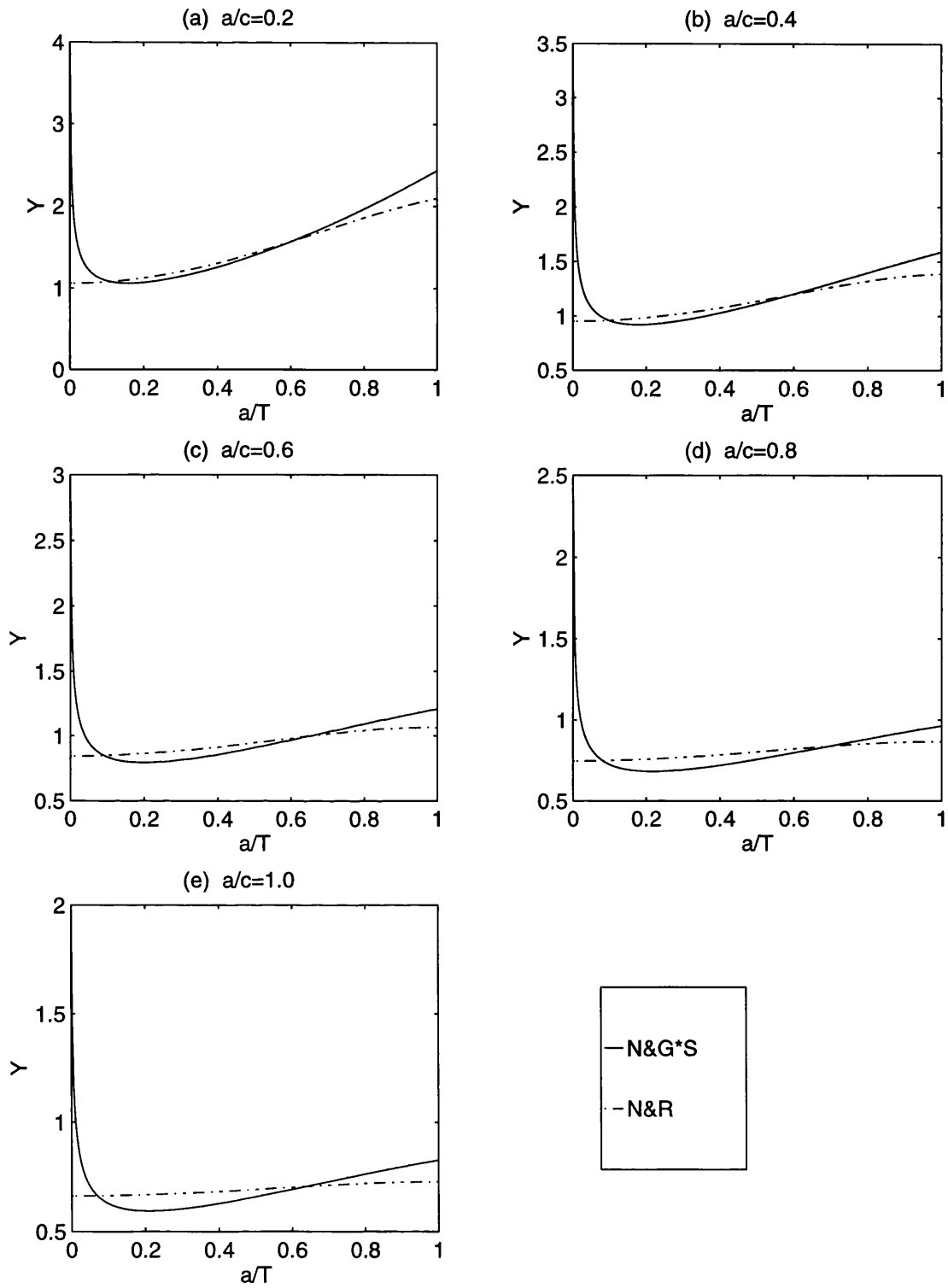


Figure 7.2 Comparison of Deepest Point SIF Predictions from N&G*S for Semi-elliptical Cracks in T-Butt Welded Joint ($\alpha=45^\circ$, $\rho/T=0.02$ and $L/T=2$) with N&R for Flat Plate under Tension

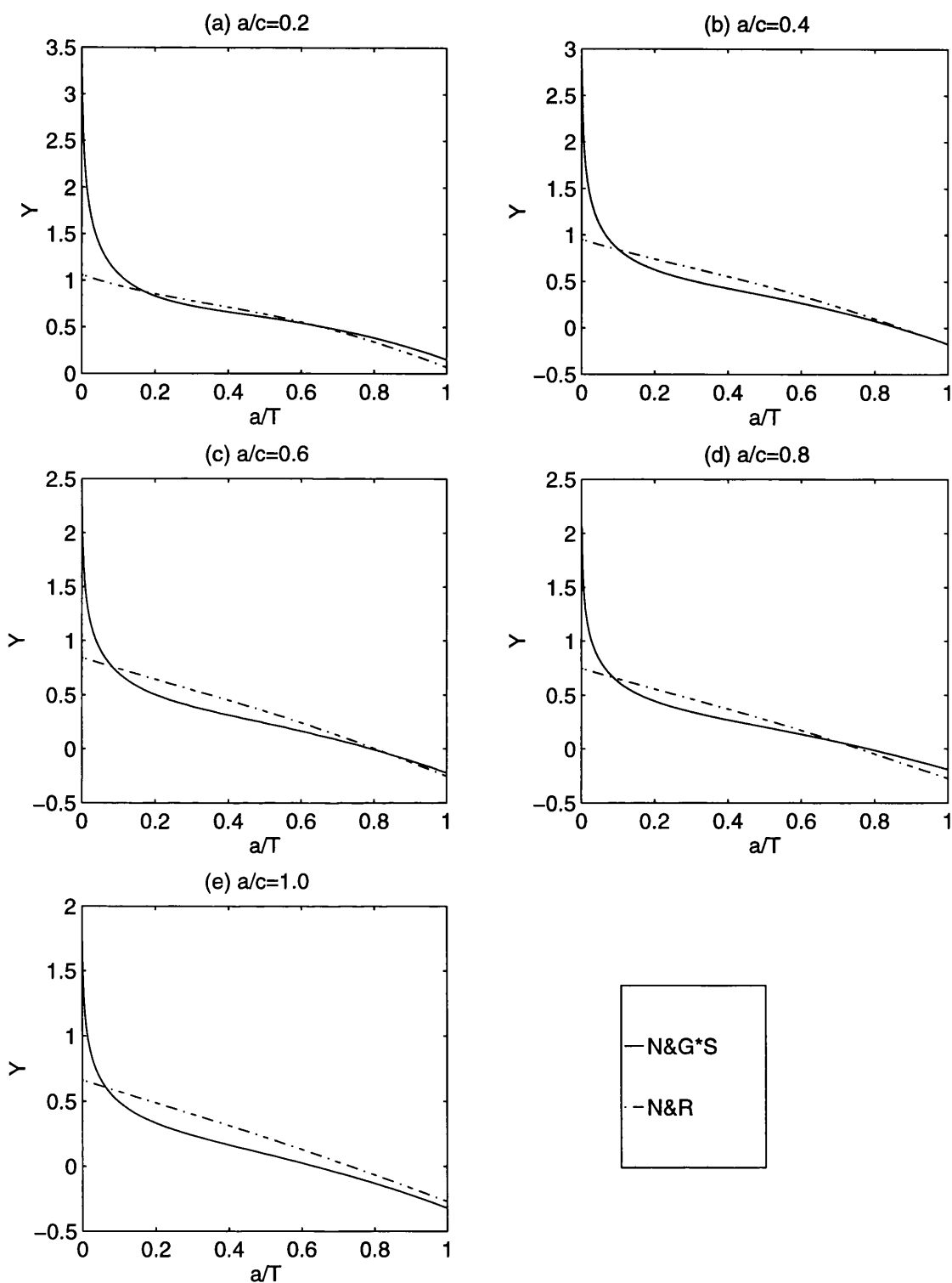


Figure 7.3 Comparison of Deepest Point SIF Predictions from N&G*S for Semi-elliptical Cracks in T-Butt Welded Joint ($\alpha=45^\circ$, $\rho/T=0.02$ and $L/T=2$) with N&R for Flat Plate under Bending

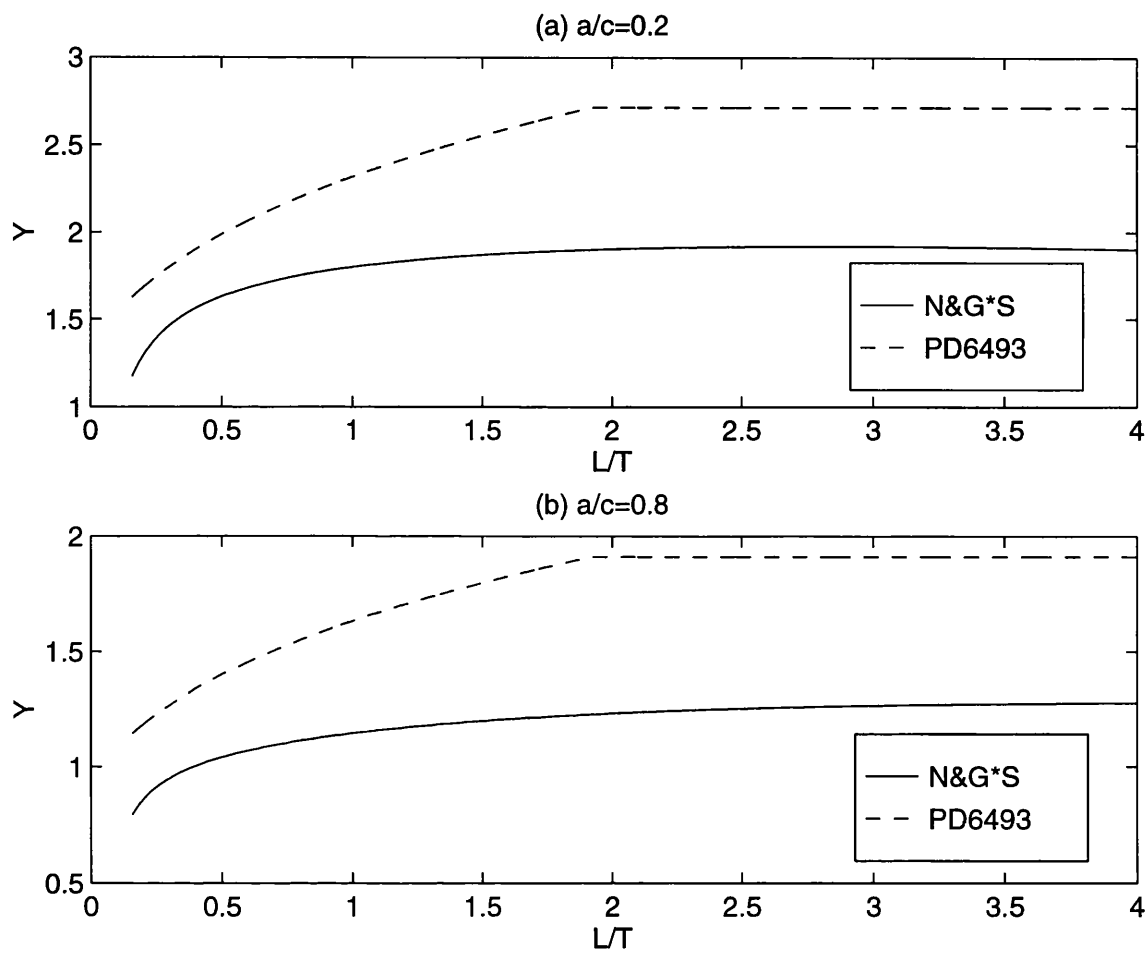


Figure 7.4 Comparison of Deepest Point SIF Predictions from N&G*S and PD6493 for Semi-elliptical Cracks in T-Butt Welded Joint ($\alpha=45^\circ$, $\rho/T=0.01$ and $a/T=0.01$) against L/T under Tension

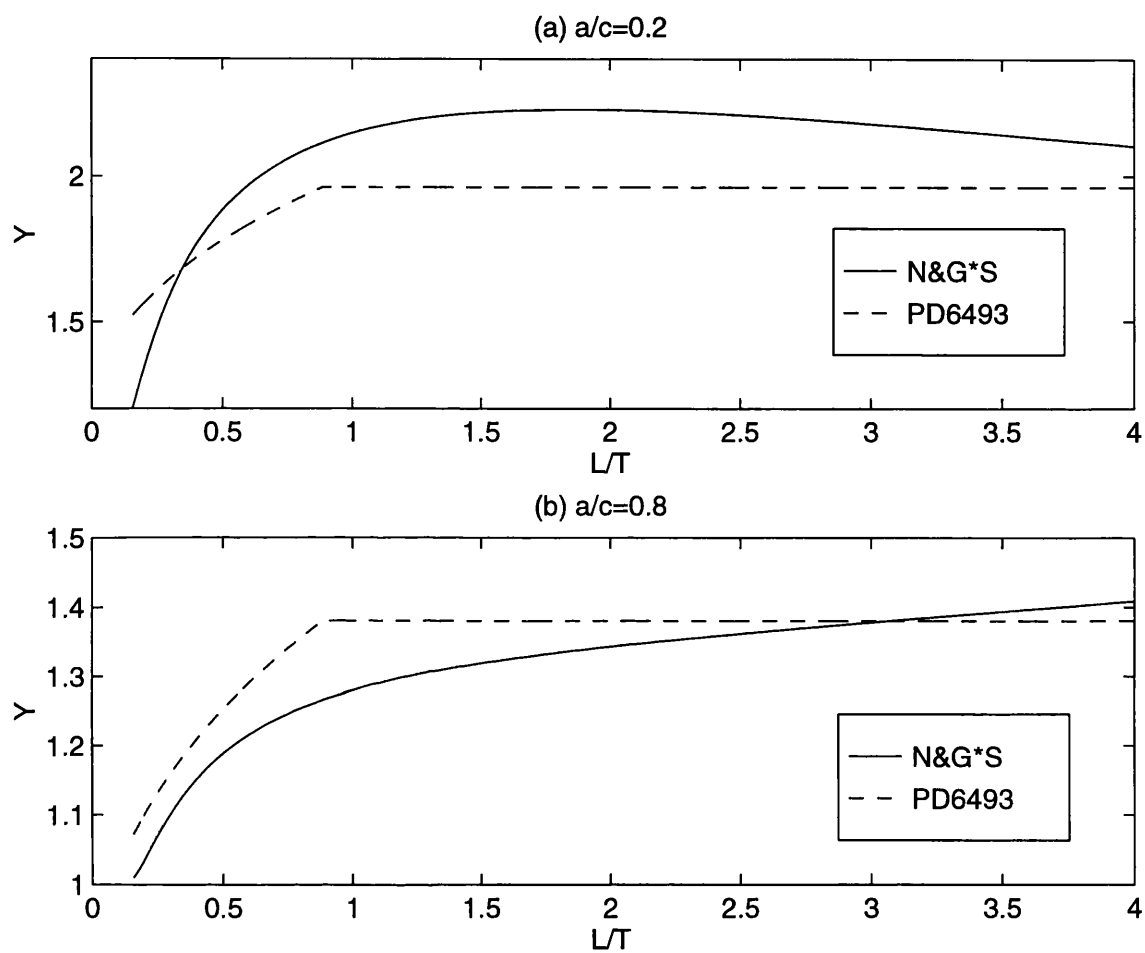


Figure 7.5 Comparison of Deepest Point SIF Predictions from N&G*S and PD6493 for Semi-elliptical Cracks in T-Butt Welded Joint ($\alpha=45^\circ$, $\rho/T=0.01$ and $a/T=0.01$) against L/T under Bending

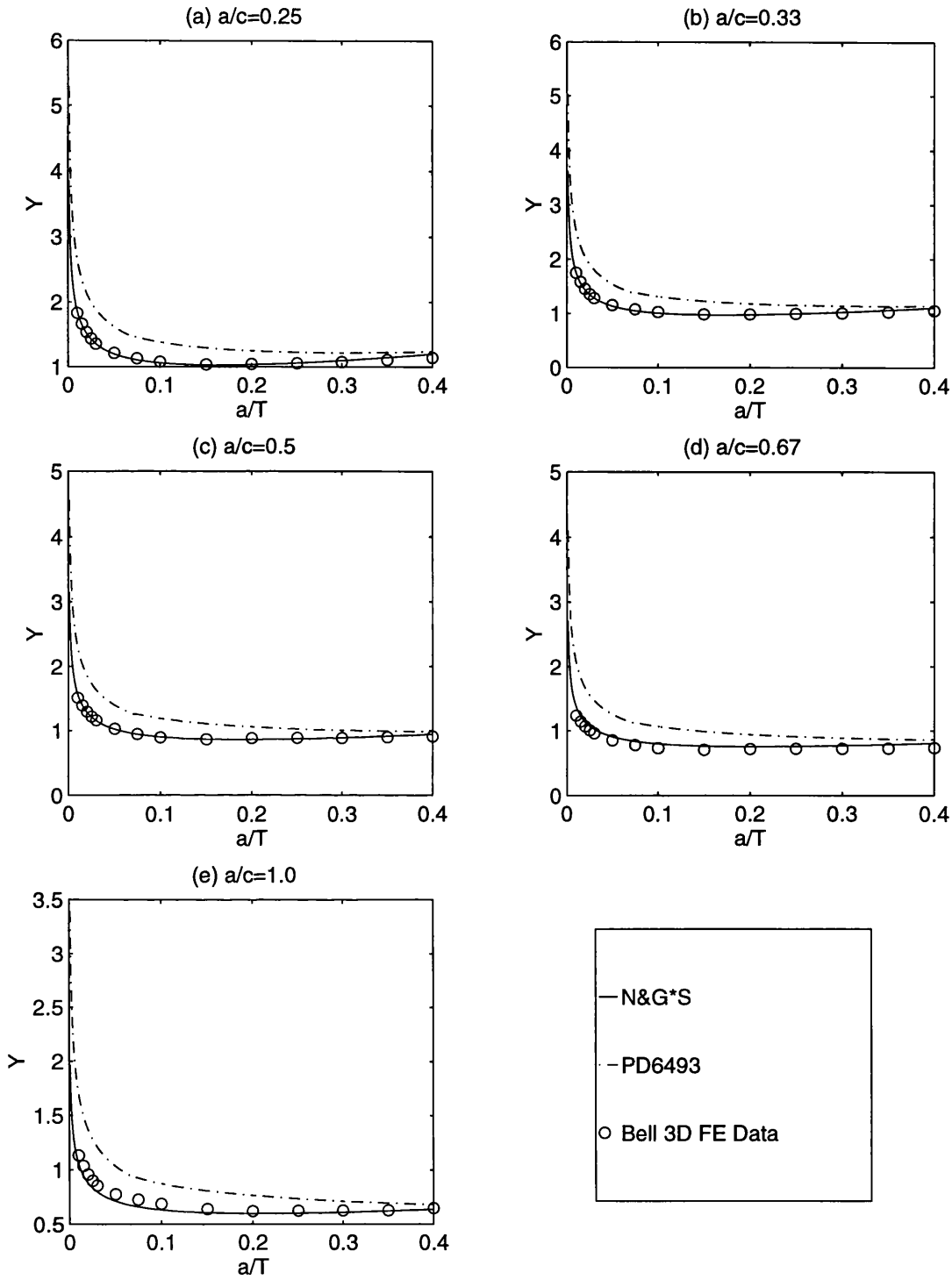


Figure 7.6 Comparison of Deepest Point SIF Predictions from N&G*S and PD6493 with Bell's 3D FE Data($p/T=0$) for Semi-elliptical Cracks in T-Butt Welded Joint ($\alpha=45^\circ$, $L/T=2.3$ and $p/T=0.01$) under Tension

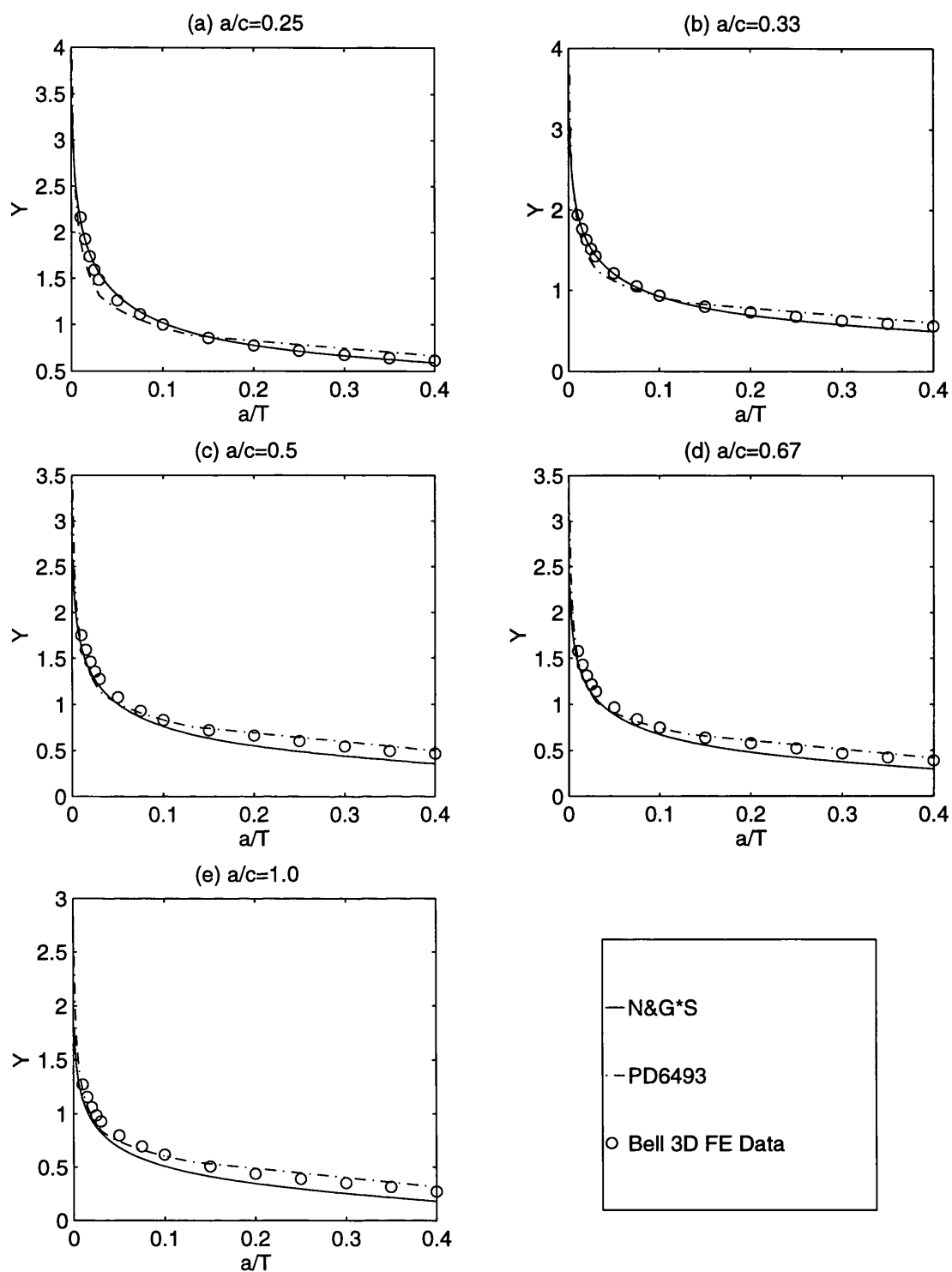


Figure 7.7 Comparison of Deepest Point SIF Predictions from N&G*S and PD6493 with Bell's 3D FE data($\rho/T=0$) for Semi-elliptical Cracks in T-Butt Welded Joint ($\alpha=45^\circ$, $L/T=2.3$ and $\rho/T=0.01$) under Bending

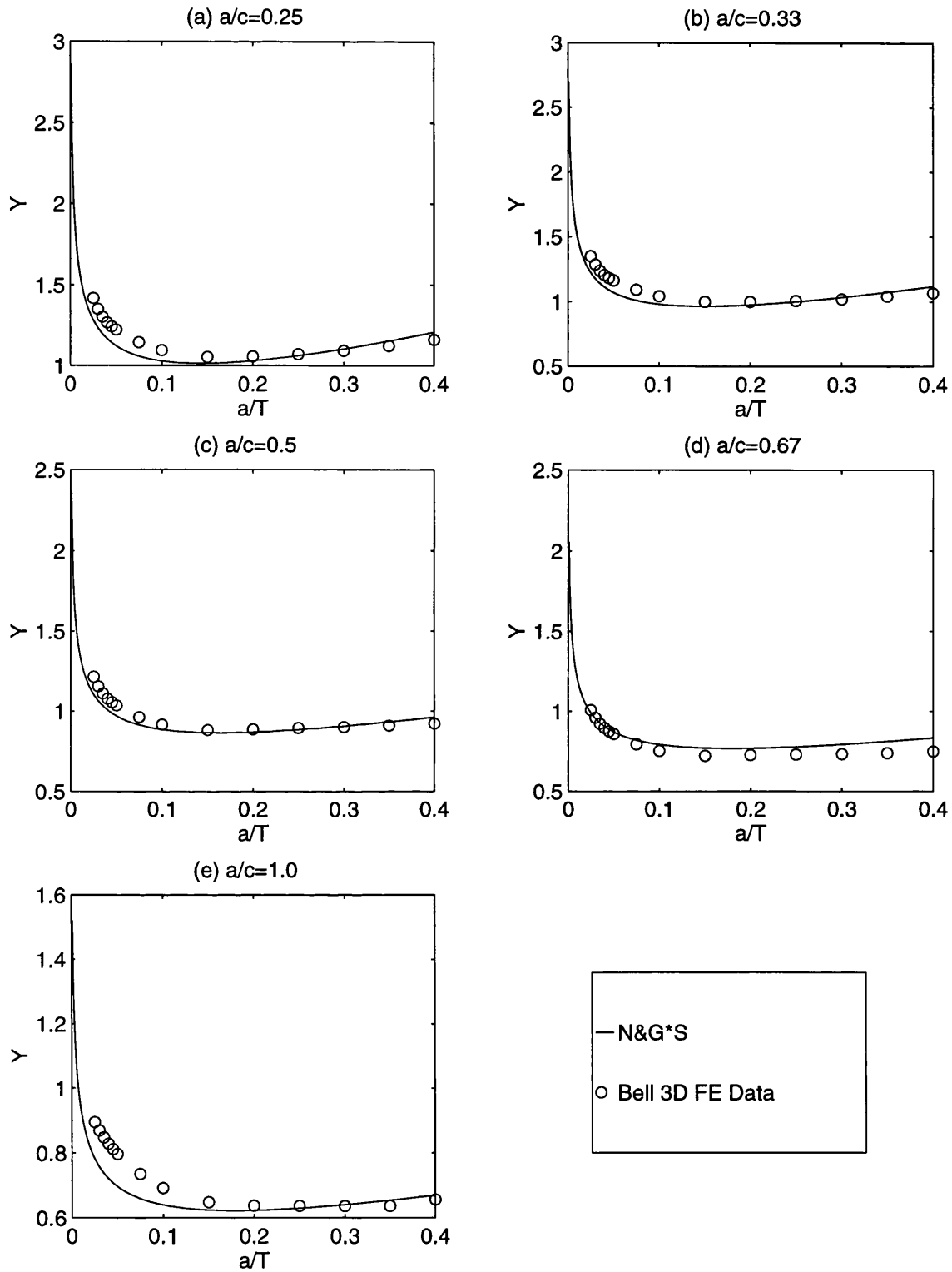


Figure 7.8 Comparison of Deepest Point SIF Predictions from N&G*S and PD6493 with Bell's 3D FE Data($\rho/T=0$) for Semi-elliptical Cracks in T-Butt Welded Joint ($\alpha=30^\circ$, $L/T=2.3$ and $\rho/T=0.01$) under Tension

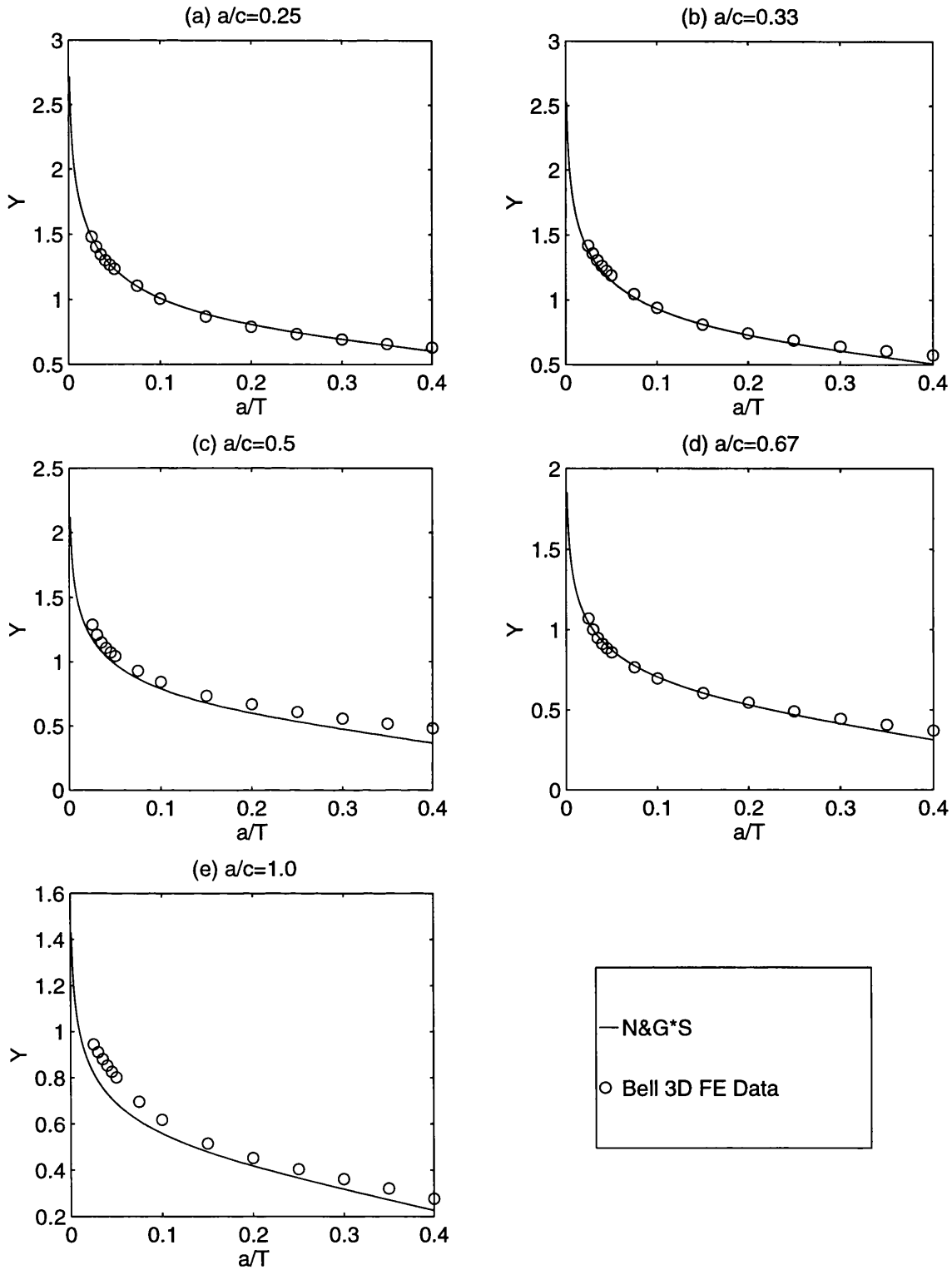


Figure 7.9 Comparison of Deepest Point SIF Predictions from N&G*S and PD6493 with Bell's 3D FE data($\rho/T=0$) for Semi-elliptical Cracks in T-Butt Welded Joint ($\alpha=30^\circ$, $L/T=2.3$ and $\rho/T=0.01$) under Bending

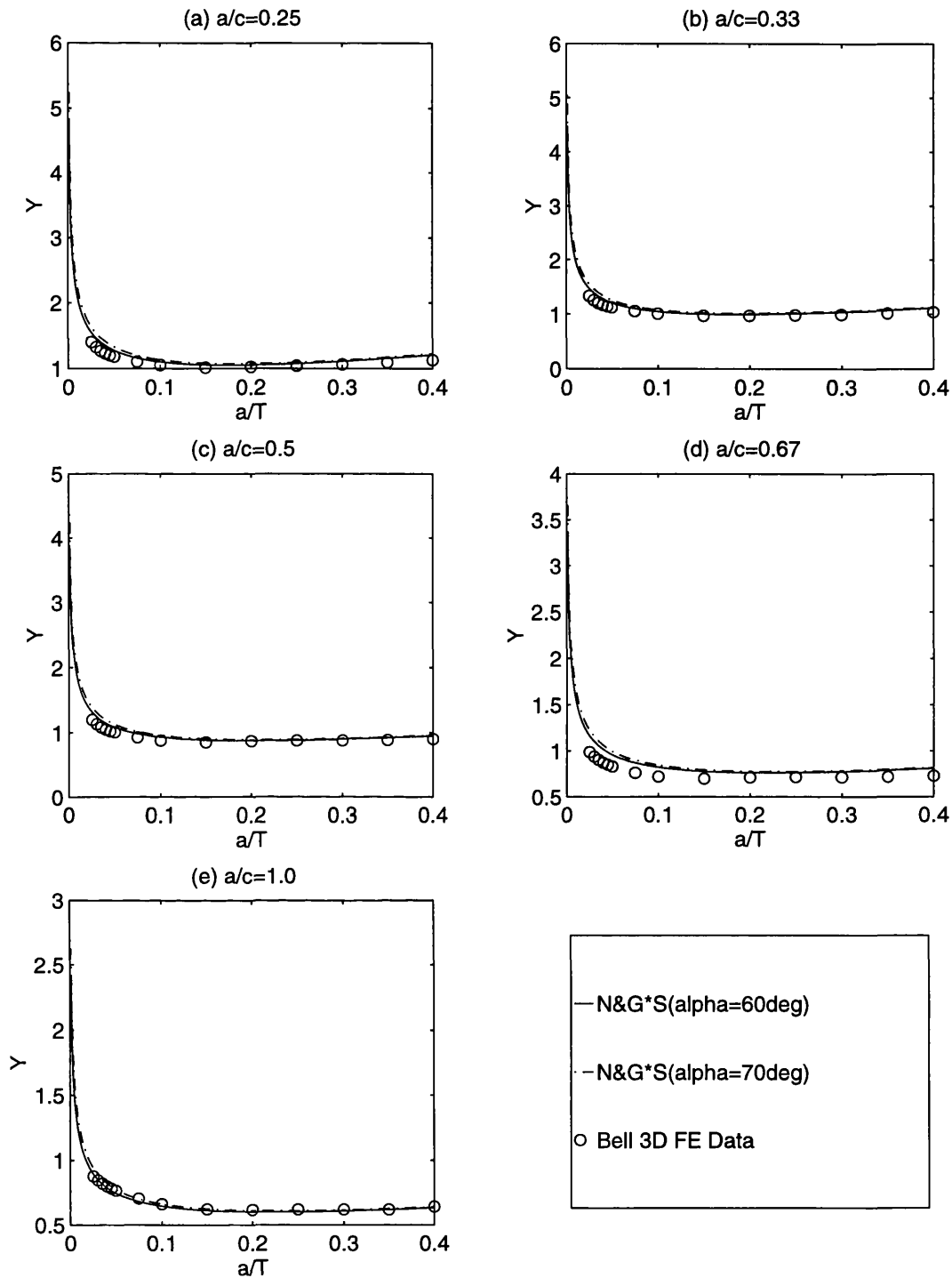


Figure 7.10 Comparison of Deepest Point SIF Predictions from N&G*S with Bell's 3D FE Data($\alpha=70^\circ$, $\rho/T=0$) for Semi-elliptical Cracks in T-Butt Welded Joint($L/T=2.3$ and $\rho/T=0.01$) under Tension (Note: α - Weld Angle in degree)

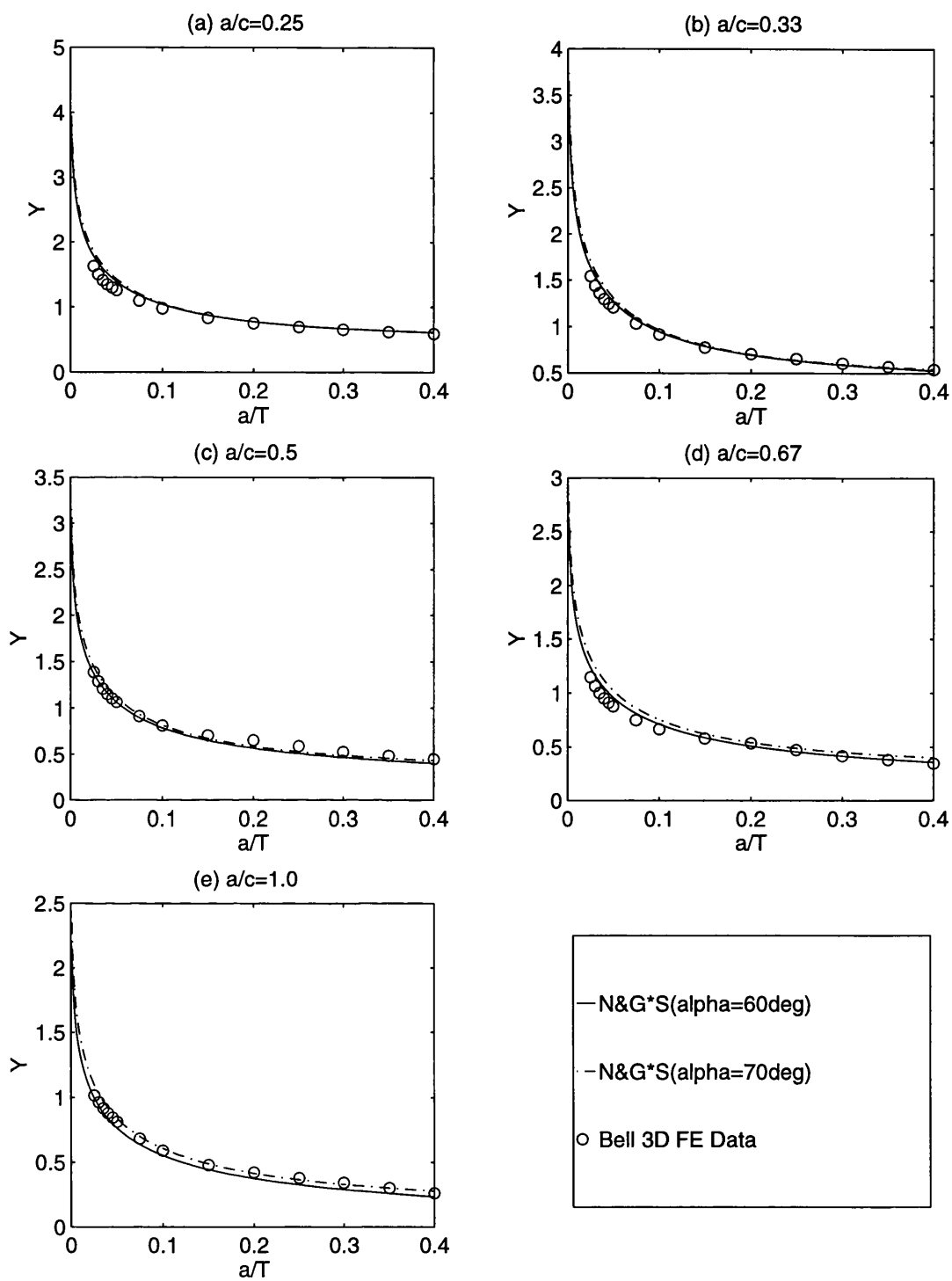


Figure 7.11 Comparison of Deepest Point SIF Predictions from N&G*S with Bell's 3D FE Data($\alpha=70^\circ$, $\rho/T=0$) for Semi-elliptical Cracks in T-Butt Welded Joint($L/T=2.3$ and $\rho/T=0.01$) under Bending (Note: α - Weld Angle in degree)

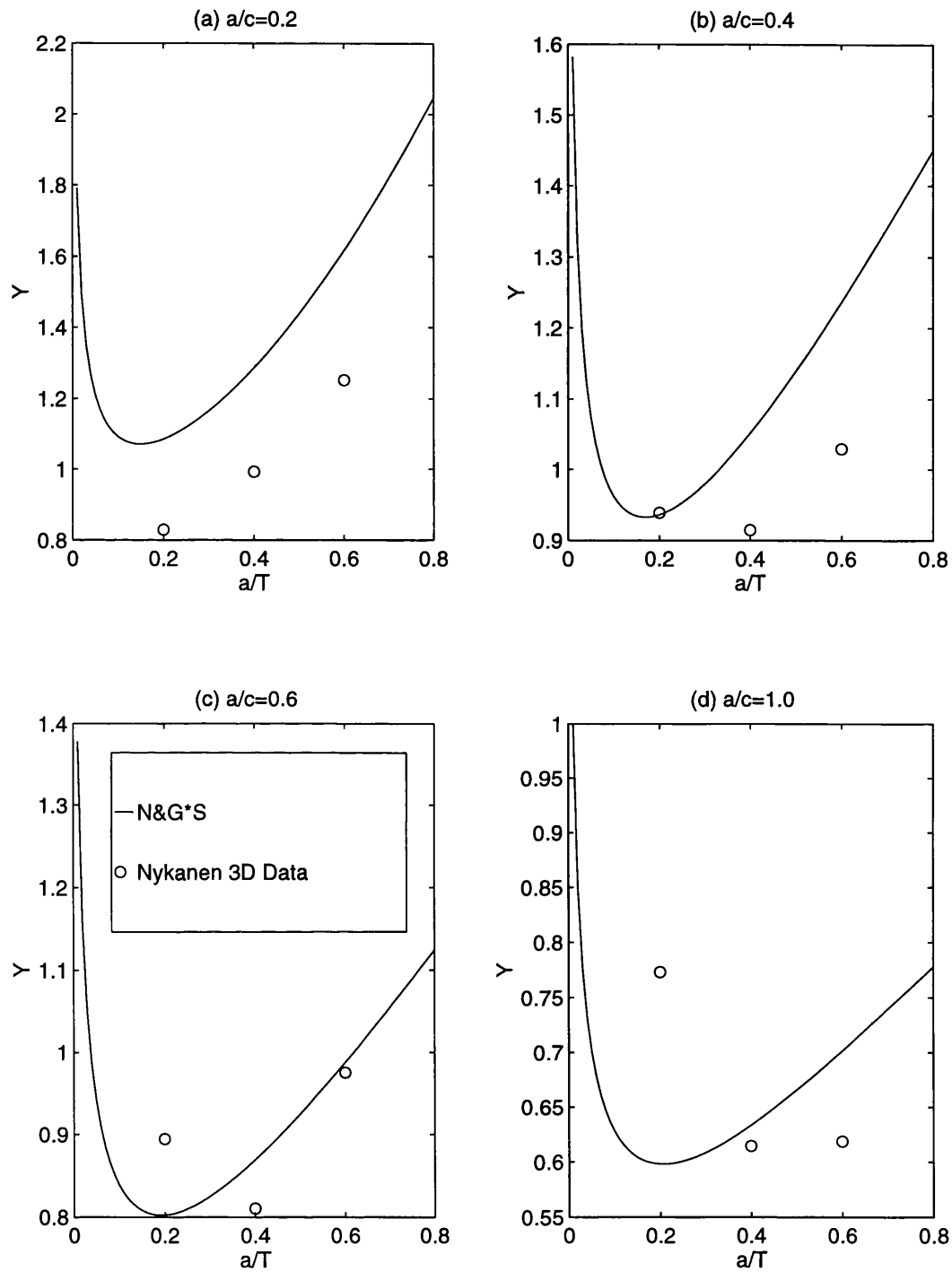


Figure 7.12 Comparison of Deepest Point SIF Predictions from N&G*S with Nykanen FE Data($\rho/T=0.17$) for Semi-elliptical Cracks in T-Butt Welded Joint ($\alpha=45^\circ$, $L/T=1.952$ and $\rho/T=0.066$) under Tension

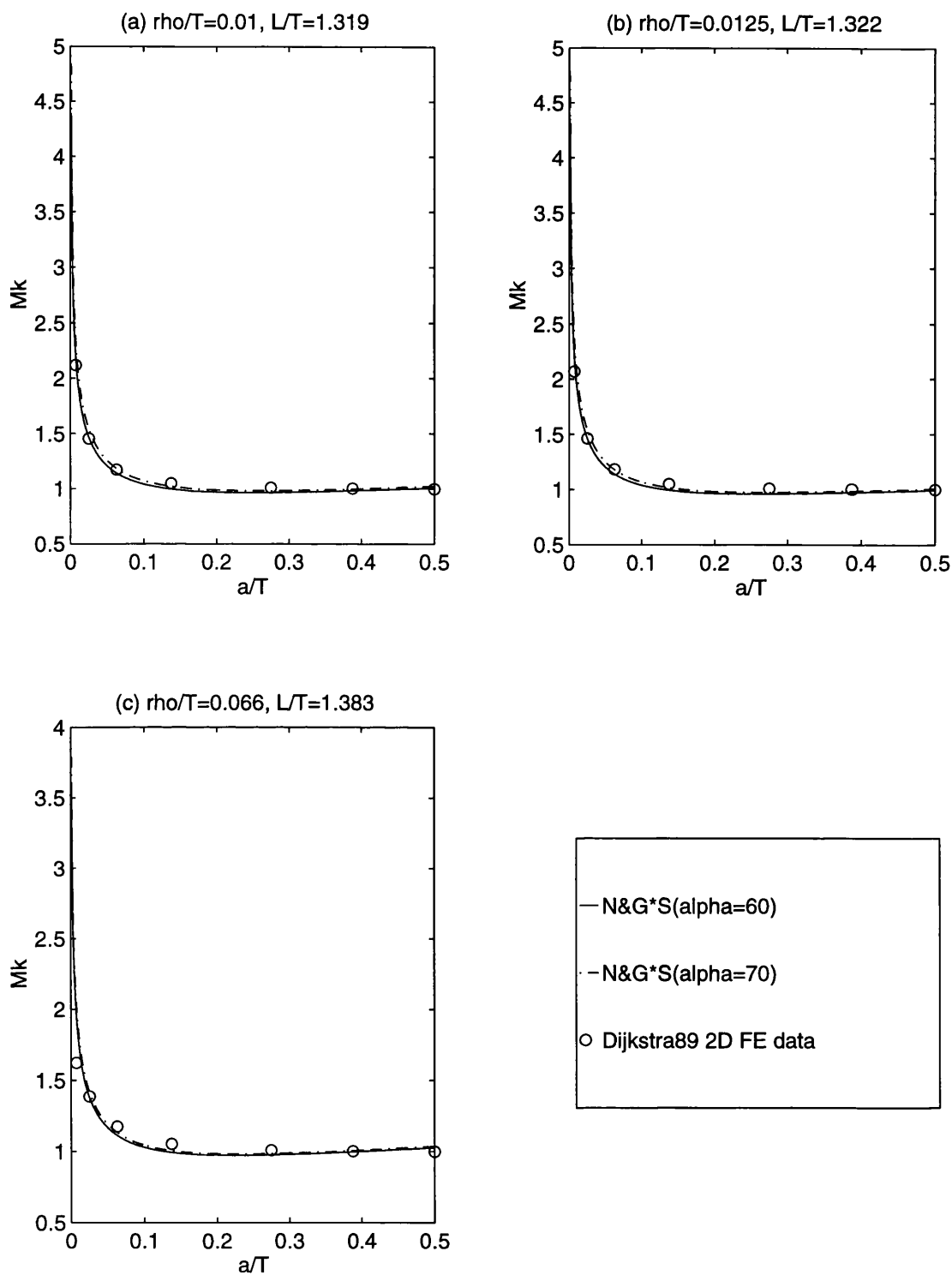


Figure 7.13 Comparison of Deepest Point SIF Predictions from N&G*S with Dijkstra'89 FE Data ($\alpha=70^\circ$) for Semi-elliptical Cracks in T-Butt Welded Joint under Tension
(Note: α - Weld Angle in degree, ρ - Weld Radius ρ)

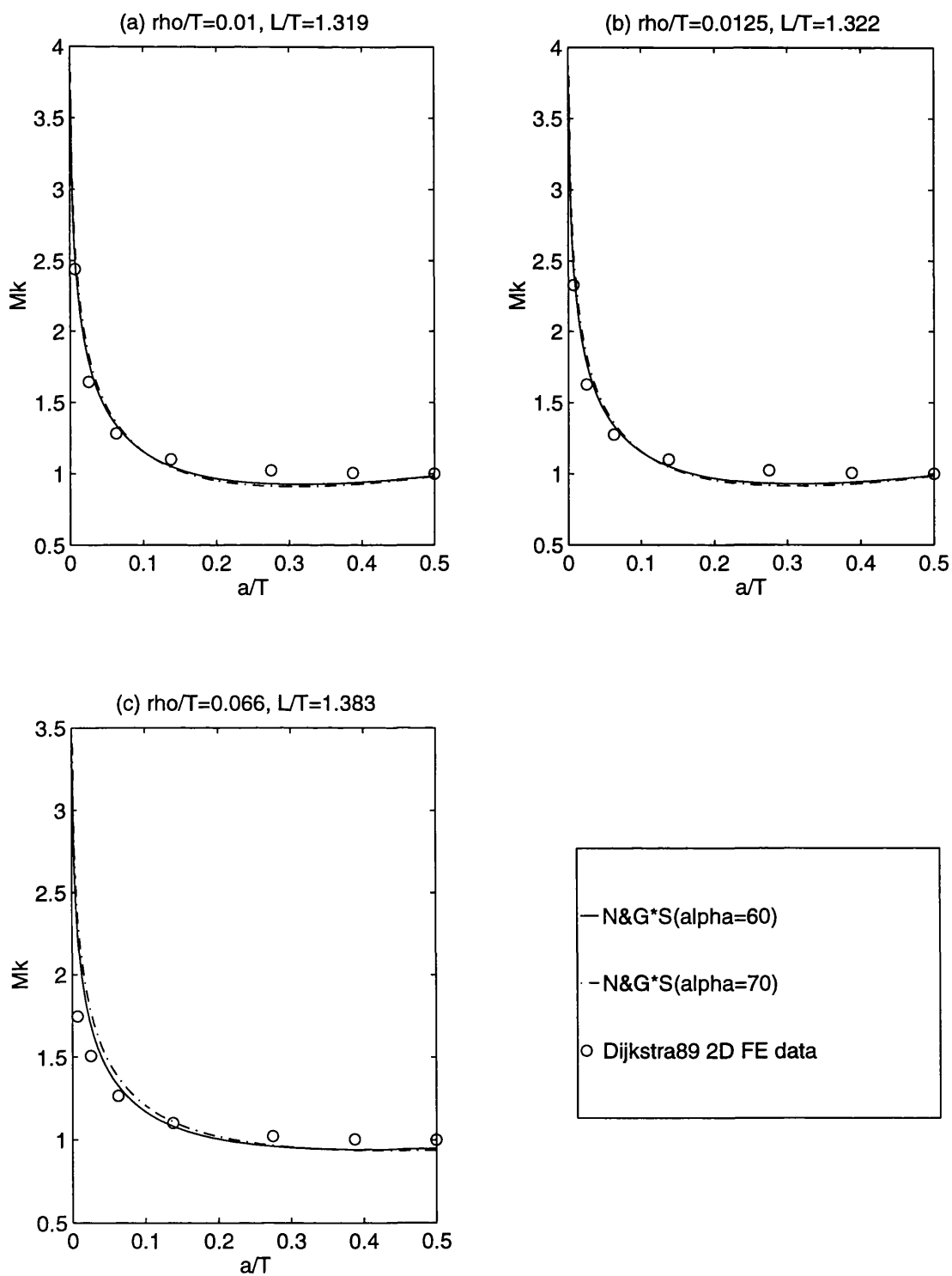


Figure 7.14 Comparison of Deepest Point SIF Predictions from N&G*S with Dijkstra'89 FE Data ($\alpha=70^\circ$) for Semi-elliptical Cracks in T-Butt Welded Joint under Bending (Note: α - Weld Angle in degree, ρ - Weld Radius p)

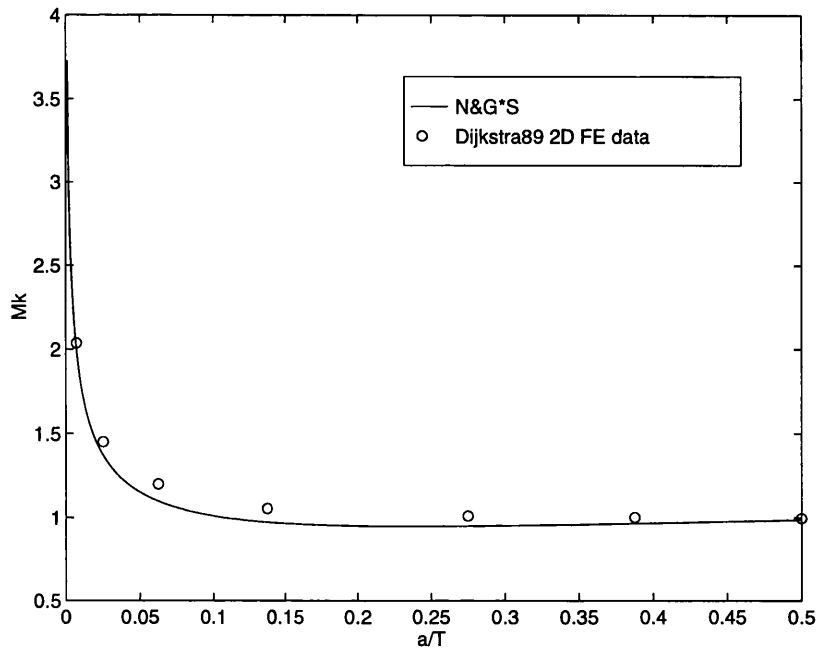


Figure 7.15 Comparison of Deepest Point SIF Predictions from N&G*S with Dijkstra'89 FE Data ($\rho/T=0.0071$) for Semi-elliptical Cracks in T-Butt Welded Joint ($a/c=0.2$, $\alpha=45^\circ$, $L/T=1.864$ and $\rho/T=0.01$) under Tension

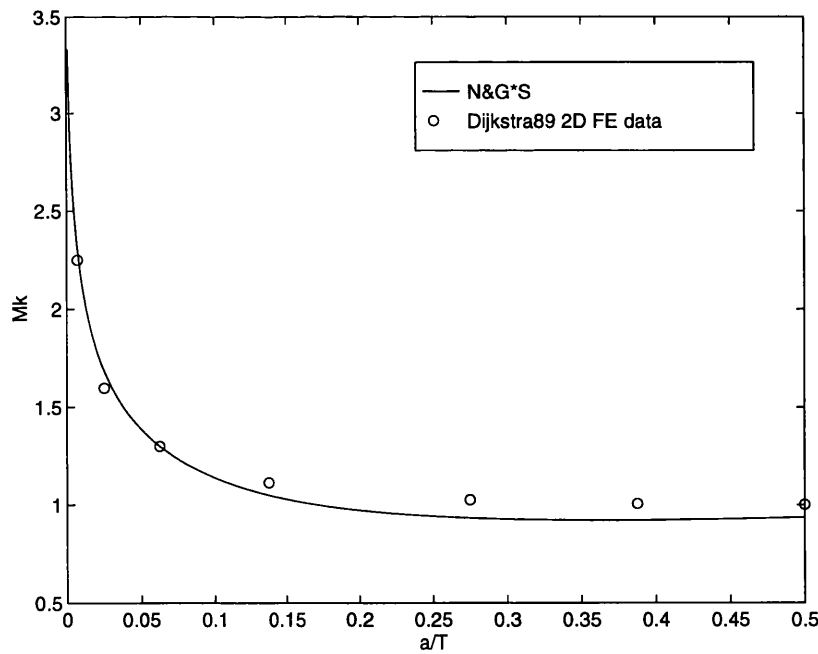


Figure 7.16 Comparison of Deepest Point SIF Predictions from N&G*S with Dijkstra'89 FE Data ($\rho/T=0.0071$) for Semi-elliptical Cracks in T-Butt Welded Joint ($a/c=0.2$, $\alpha=45^\circ$, $L/T=1.864$ and $\rho/T=0.01$) under Bending

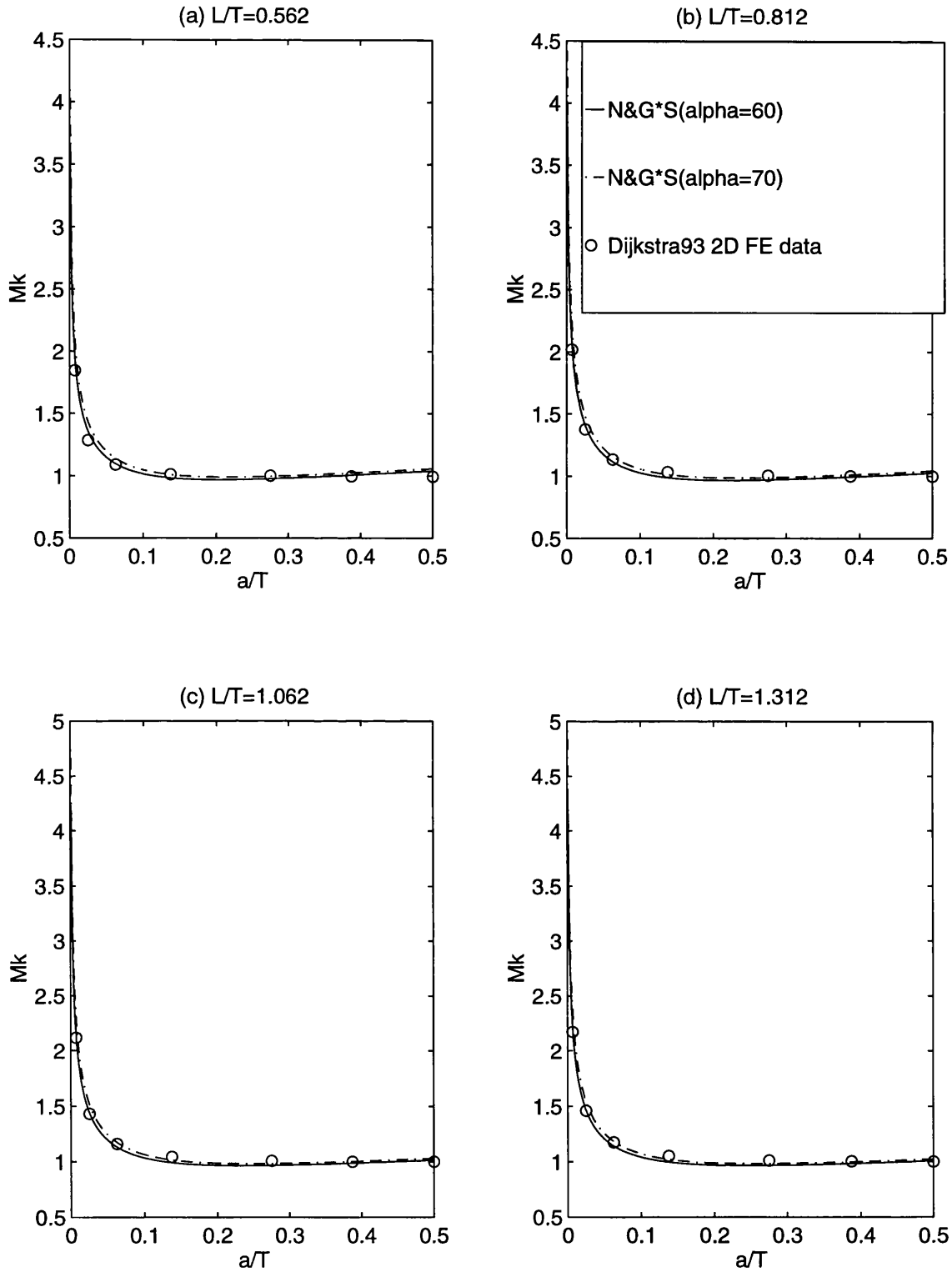


Figure 7.17 Comparison of Deepest Point SIF Predictions from N&G*S with Dijkstra'93 FE Data ($\alpha=70^\circ$, $\rho/T=0$) for Semi-elliptical Cracks in T-Butt Welded Joint ($a/c=0.2$, $\rho/T=0.01$) under Tension (Note: α - Weld Angle in degree)

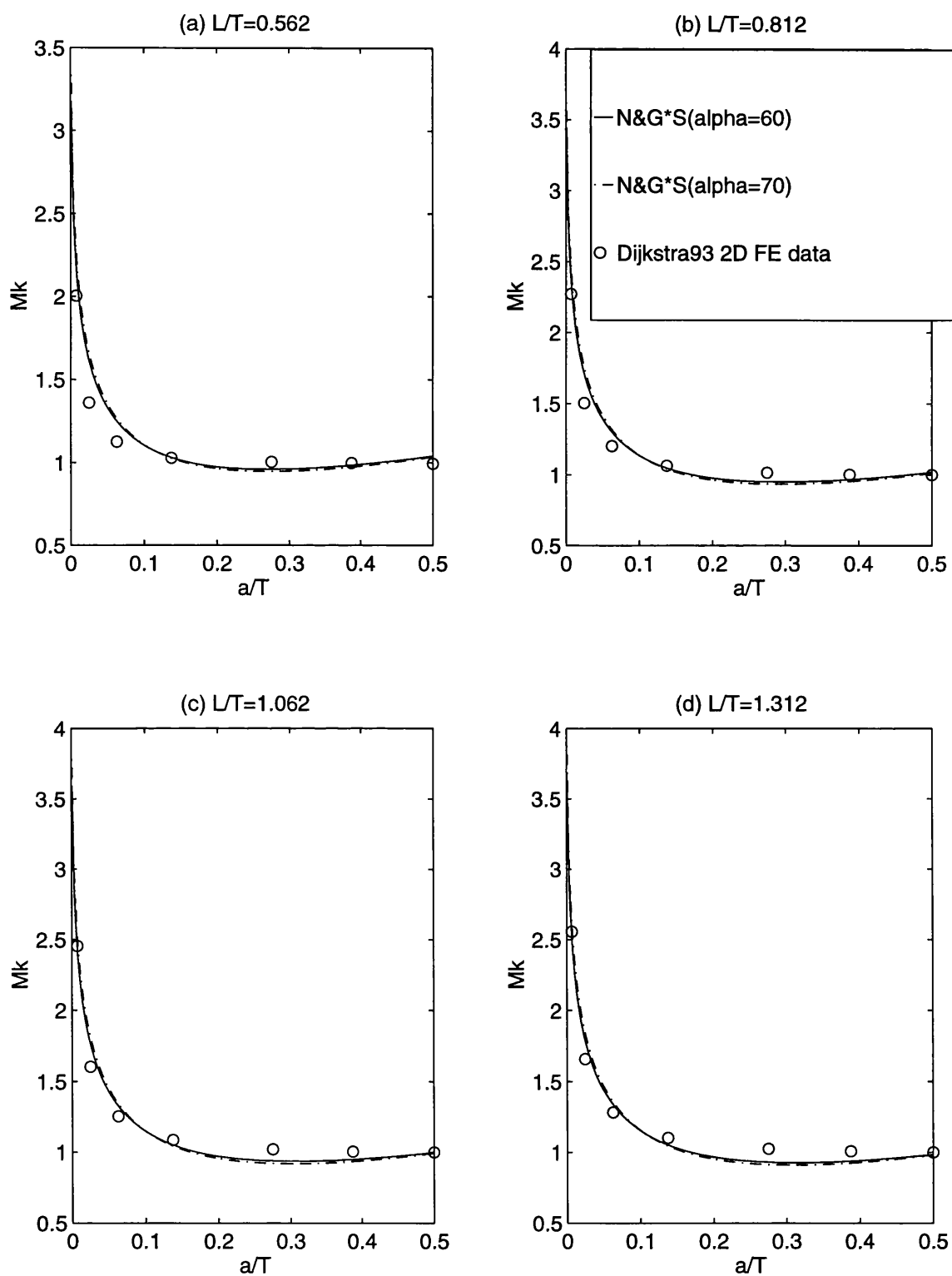


Figure 7.18 Comparison of Deepest Point SIF Predictions from N&G*S with Dijkstra'93 FE Data ($\alpha=70^\circ$, $\rho/T=0$) for Semi-elliptical Cracks in T-Butt Welded Joint ($a/c=0.2$, $\rho/T=0.01$) under Bending (Note: α - Weld Angle in degree)

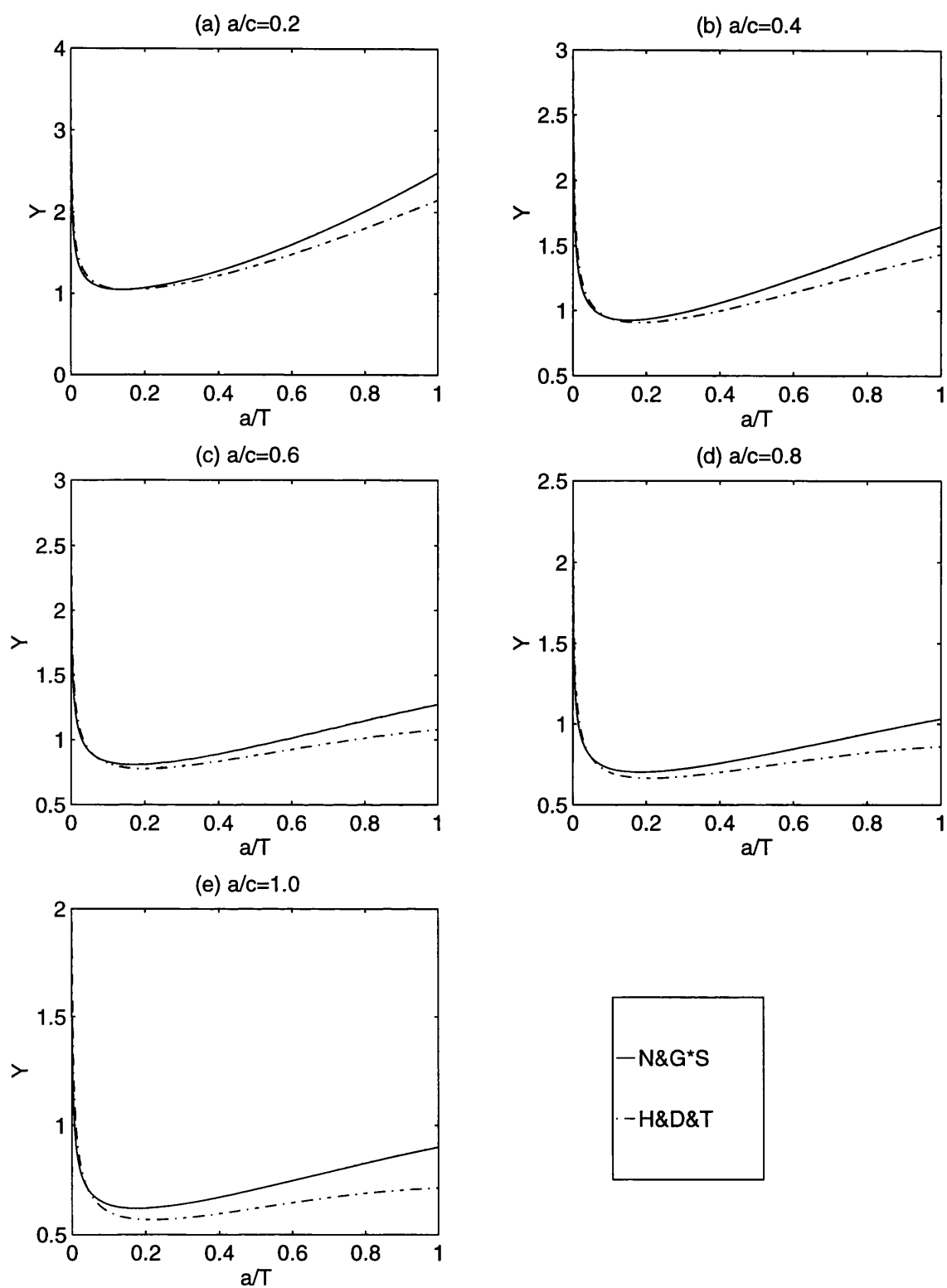


Figure 7.19 Comparison of Deepest Point SIF Predictions from N&G*S and H&D&T for Semi-elliptical Cracks in T-Butt Welded Joint ($\alpha=30^\circ$, $p/T=0.02$ and $L/T=2.8$) under Tension

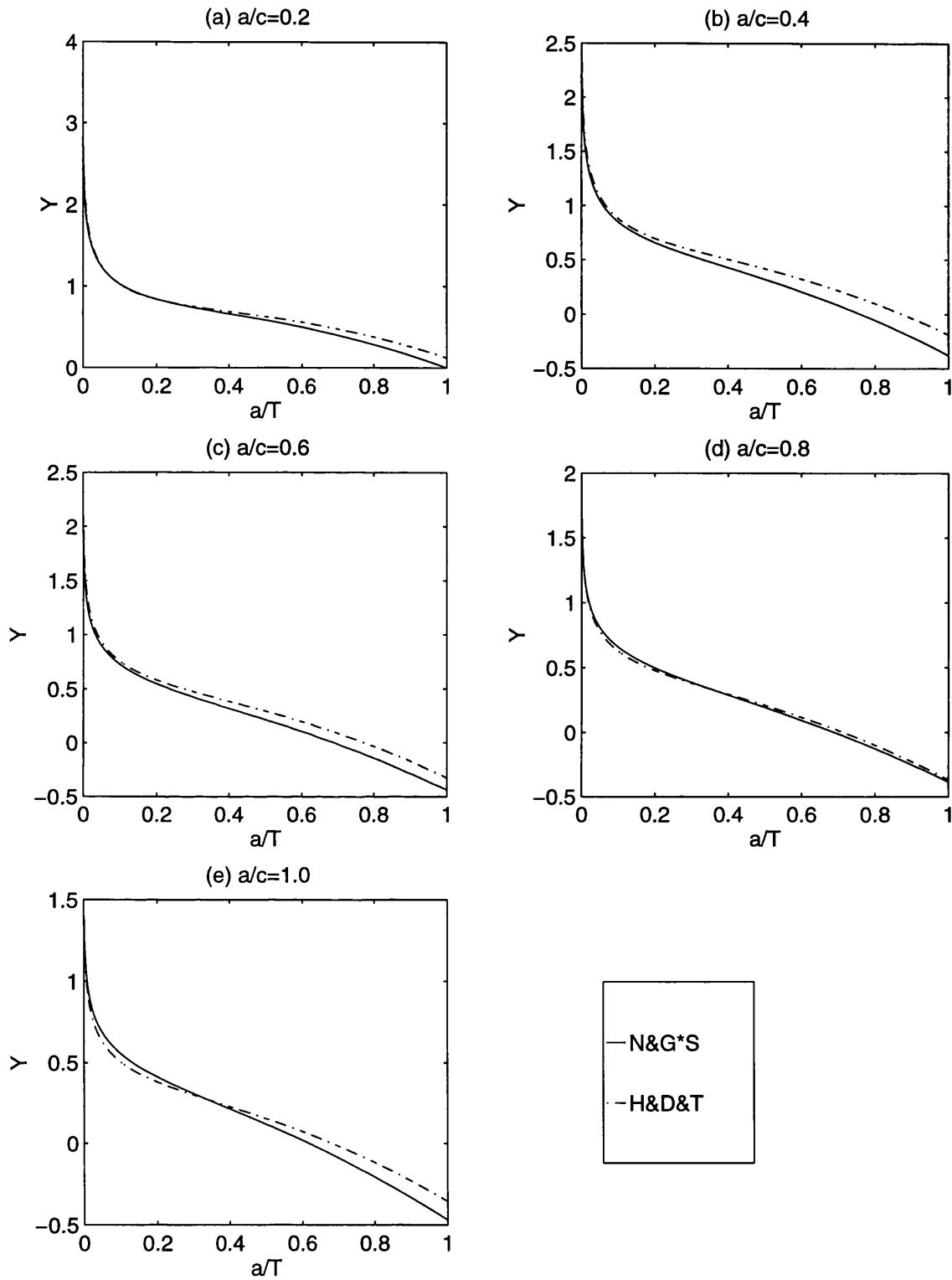


Figure 7.20 Comparison of Deepest Point SIF Predictions from N&G*S and H&D&T for Semi-elliptical Cracks in T-Butt Welded Joint ($\alpha=30^\circ$, $\rho/T=0.02$ and $L/T=2.8$) under Bending

CHAPTER EIGHT

SURFACE POINT SIF PARAMETRIC EQUATIONS FOR SEMI-ELLIPTICAL SURFACE CRACK IN T-BUTT WELDED JOINTS

8.1 Introduction

The key for application of fracture mechanics to offshore welded joints is to have the correct Stress Intensity Factor(SIF) solution for semi-elliptical surface cracks. The determination of SIFs for the surface intersection point of surface semi-elliptical cracks in welded joints has not attracted as much as attention as those for the deepest point since these cracks always grow rapidly along the weld toe and the fatigue crack length is easy to be detected and measured by NDT technique such as MPI. However, surface point SIFs would be useful for predicting crack aspect ratio development during fatigue crack growth. Using surface point SIFs, one can calculate the aspect ratio of fatigue crack for each particular crack depth and thus simulate the fatigue crack growth step by step.

Based on finite element analysis results, surface point SIF parametric equations have been derived for flat plates(Newman and Raju 1986). However there is no parametric equation available for T-butt or tubular welded joints. With the recent developments on the multiple reference data approach, it has proved to be possible to produce weight functions for the surface point of semi-elliptical surface crack in finite thickness plate(Shen, Plumtree and Glinka 1991)(Wang and Lambert 1995). Using these new weight functions and the UCL T-butt weld toe through-wall stress distribution database, it is possible to produce a set of surface point SIF parametric equations for semi-elliptical surface crack in T-butt welded joints under tension and bending. This chapter will present the work on the derivation and validation of this set of equations.

8.2 Wang-Lambert Weight Function

The weight function is a unique property of crack shape and component geometry and is independent of loading. With the uncracked weld toe through-thickness stress distribution at hand, it can be used to obtain SIFs. However, previous weight functions were only derived for the deepest point of semi-elliptical cracks in welded joints. By using the universal weight function form and two reference SIFs, Shen, Plumtree and Glinka(1991) have derived the closed form weight function for the surface point of a semi-elliptical surface crack in a plate of finite thickness.

Unfortunately Shen-Plumtree-Glinka weight functions are only valid for $a/c \geq 0.2$. However, most fatigue cracks on welded joints are long and shallow and their aspect ratios are often lower than 0.2. Recently, work has been done on improving Shen-Plumtree-Glinka weight function by Wang and Lambert(1995). They conducted the three dimensional finite element analyses for low aspect ratio semi-elliptical surface cracks. Combining these results with the existing finite element data(Newman and Raju 1981)(Shiratori et al 1987) for high aspect ratio and following the same procedure for deriving Shen-Plumtree-Glinka weight functions, the Wang and Lambert weight functions covering the entire range of aspect ratios were derived as follows:

$$m(x,a) = \frac{2}{\sqrt{\pi x}} \left[1 + M_1 \left(\frac{x}{a} \right)^{1/2} + M_2 \left(\frac{x}{a} \right) + M_3 \left(\frac{x}{a} \right)^{3/2} \right] \quad (8-1)$$

$$M_1 = \frac{\pi}{\sqrt{4Q}} (30F_1 - 18F_0) - 8 \quad (8-2)$$

$$M_2 = \frac{\pi}{\sqrt{4Q}} (60F_0 - 90F_1) + 15 \quad (8-3)$$

$$M_3 = -(1 + M_1 + M_2) \quad (8-4)$$

$$F_0 = \left[C_0 + C_1 \left(\frac{a}{T} \right)^2 + C_2 \left(\frac{a}{T} \right)^4 \right] \sqrt{\frac{a}{c}} \quad (8-5)$$

$$F_1 = \left[D_0 + D_1 \left(\frac{a}{T} \right)^2 + D_2 \left(\frac{a}{T} \right)^4 \right] \sqrt{\frac{a}{c}} \quad (8-6)$$

$$C_0 = 1.2972 - 0.1548 \left(\frac{a}{c} \right) - 0.0185 \left(\frac{a}{c} \right)^2 \quad (8-7)$$

$$C_1 = 1.5083 - 1.3219 \left(\frac{a}{c} \right) + 0.5128 \left(\frac{a}{c} \right)^2 \quad (8-8)$$

$$C_2 = -1.101 + \frac{0.879}{0.157 + \frac{a}{c}} \quad (8-9)$$

$$D_0 = 1.2687 - 1.0642 \left(\frac{a}{c} \right) + 1.4646 \left(\frac{a}{c} \right)^2 - 0.725 \left(\frac{a}{c} \right)^3 \quad (8-10)$$

$$D_1 = 1.1207 - 1.2289 \left(\frac{a}{c} \right) + 0.5876 \left(\frac{a}{c} \right)^2 \quad (8-11)$$

$$D_2 = 0.19 - 0.608 \left(\frac{a}{c} \right) + \frac{0.199}{0.035 + \frac{a}{c}} \quad (8-12)$$

8.3 Deriving SIF Parametric Equations

The weight function method is a powerful technique for the calculation of SIFs for a variety of complex loading conditions. Weight functions need to be integrated with the uncracked stress distribution to obtain the SIF. However, this procedure is not convenient to use at the design stage. The early finite element results have demonstrated that weld toe stress distributions in welded joints are well-represented by combining the results of T-butt models loaded in pure tension and pure bending, provided the weld geometries are the same in both cases. In order to simplify the use of weight function method, the surface point SIF parametric equations for T-butt welded joint in tension and bending would be desirable.

As the first step in the process, one would have to obtain the SIF results database by combining the above weight function with the T-butt through wall stress distribution database. The Stress Intensity Factor(SIF), K , can be expressed as follows:

$$K = \int_0^a m(a/c, a/T, x) \sigma(\alpha, \rho/T, L/T, a/T, x) dx \quad (8-13)$$

The UCL uncracked through-wall stress distribution database(Brennan et al 1996) was used again. It was based on the results of systematic two dimensional finite element analyses for T-Butt welded joints and allow all weld toe effects to be incorporated. This database covers T-butts with the following parameter ranges:

Parameter	Range
Weld Toe Angle (α)	$\alpha=30^\circ, 45^\circ, 60^\circ$
Weld Toe Radius/Wall Thickness (ρ/T)	$0.01 \leq \rho/T \leq 0.066$
Attachment Width/Wall Thickness (L/T)	$0.1577 \leq L/T \leq 4$
Location Along Wall Thickness (x)	$0 < x \leq T$

The SIF database was establish by integrating the Wang-Lambert closed form surface point flat plate weight function with the UCL uncracked through-wall stress distribution of T-butt welded joints. The database used for each parameter in this SIF database is shown in following table.

Parameter	Range
Weld Angle α (deg)	$30^\circ, 45^\circ, 60^\circ$
Weld Radius Ratio ρ/T	0.01, 0.02, 0.04, 0.066
Attachment Ratio L/T	Many data between 0.1577 and 4
Aspect Ratios a/c	0.01, 0.05, 0.08, 0.1, 0.12, 0.15, 0.18, 0.2, 0.4, 0.6, 0.8, 1.0

As can see from the above table, this SIF database includes the cracks within the whole range of aspect ratio($0 \leq a/c \leq 1$). Most fatigue cracks in welded joints are long and shallow and

their aspect ratios are often lower than 0.2. For this reason, sufficient data have been generated in the range $a/c \leq 0.2$.

This new large database was used to derive the surface point SIF parametric equations SIF for semi-elliptical surface cracks in T-butt welded joints under tension and bending respectively. The regression analyses were carried out by using Minitab statistical package (MINITAB 1991). This two-dimensional curve-fitting process is split into following two levels.

1) Performing numerous regressions until the best form of expression for the variations of the SIF, i.e. the equation with a large product moment correlation coefficient, was found for all joints under tension and bending. After numerous tries, the following appropriate expressions were found under each mode of loading.

$$K = Y\sigma \sqrt{(\pi a) / Q} \quad (8 - 14)$$

$$Q = 1 + 1.464 \left(\frac{a}{c} \right)^{1.65} \quad (8 - 15)$$

$$Y = \text{Exp} \left(C_0 + C_1 \left(\frac{a}{T} \right) + C_2 \left(\frac{a}{T} \right)^2 \right) \left(\frac{a}{T} \right)^{C_3} \quad \text{For Tension Loading (8 - 16)}$$

$$Y = C_0 + C_1 \left(\frac{a}{T} \right) + C_2 \left(\frac{a}{T} \right)^2 + C_3 \text{Ln} \left(\frac{a}{T} \right) \quad \text{For Bending loading (8 - 17)}$$

2) Fitting the coefficients in the above equations as a function of the parameters α , β , γ , τ and θ .

As a result, the parametric equations (W&L(FP)*S)¹ to predict the SIF at the surface point of semi-elliptical surface crack in T-butt welded joints under tension and bending loading, have been derived in the form of continuous single functions by carrying out the regression analysis and they are given in Appendix J. A summary of the degree of fit for this set of parametric equations is presented in Table 8.1. From this table, one can see that SIF data are fitted very well by this set of parametric equations. The correlation coefficient R^2 is greater than 96% for all cases including both the form of equation and the coefficients C_0 , C_1 , C_2 , C_3 . These equations are valid for the following parameter ranges:

$$\frac{\pi}{6} \leq \alpha \leq \frac{\pi}{3} \quad (8 - 18)$$

$$0.01 \leq \frac{\rho}{T} \leq 0.066 \quad (8 - 19)$$

¹ W&L(FP) represents Wang and Lambert Flat Plate weight function, S denotes the T-butt through thickness Stress distribution database, * stands for the integration process

$$0.1577 \leq \frac{L}{T} \leq 4 \quad (8-20)$$

$$0 \leq \frac{a}{c} \leq 1 \quad (8-21)$$

$$0 < \frac{a}{T} \leq 0.8 \quad (8-22)$$

8.4 Validation

Strictly speaking, it is not correct to calculate the SIF for semi-elliptical cracks in a T-butt welded joint by combining the flat plate weight function with the T-butt stress distribution. The weld toe effects are considered only in the uncracked through-wall stress distribution database rather than also in the weight function. Hence before use, it is necessary to carry out validation work to show whether the approach is a reasonable approximation.

The predictions from this set of equations(W&L(FP)*S) were first compared with the results from the flat plate Newman-Raju(N&R) equations for tension and bending respectively(Figures 8.2-8.3). The stress concentration effect of weld toe is clearly shown in the results for W&L(FP)*S and it decays quickly and disappears at about $a/T=0.1$. These figures also show that the W&L(FP)*S results are much higher than the flat plate data(N&R), especially for tension.

Bell's three dimensional finite element data(Bell 1985), generally considered to be the most accurate when compared with other numerical methods, were used to compare with the predictions from the parametric equations(W&L(FP)*S). The results are shown in Figures 8.4-8.9 for the T-butt with three different weld angles under tension and bending respectively. In these figures, the minimum validated value $p/T=0.01$ were used for W&L(FP)*S equations as Bell's data were based on T-butts with $p/T=0$. As can be seen from these figures, this set of equations derived by using a hybrid method gave good modelling of the several trend but quite conservative values when compared with Bell's three dimensional data, especially under tension. For this reason, modification factors(8 - 23)(8 - 24) were developed. The new W&L(FP)*S results show excellent agreement with Bell's data irrespective of weld angles and aspect ratios.

$$\left(\frac{K}{\sigma \sqrt{\frac{\pi a}{Q}}} \right)_{\text{Modified}} = \frac{K}{3.5\sigma \sqrt{\frac{\pi a}{Q}}} \quad \text{for tension} \quad (8-23)$$

$$\left(\frac{K}{\sigma \sqrt{\frac{\pi a}{Q}}} \right)_{Modified} = \frac{K}{\sigma \sqrt{\frac{\pi a}{Q}}} - 0.5 \quad \text{for bending} \quad (8 - 24)$$

It should be noted that these modification factors have been developed for the particular case of $L/T=2.3$. When more three dimensional finite element data becomes available, it should be possible to fit modification factors as functions of weld toe parameters, such as attachment size.

As a summary, the predictions from the W&L(FP)*S equations are very conservative when compared with Bell's finite element data. However excellent agreement can be achieved with the modified W&L(FP)*S equations for both tension and bending.

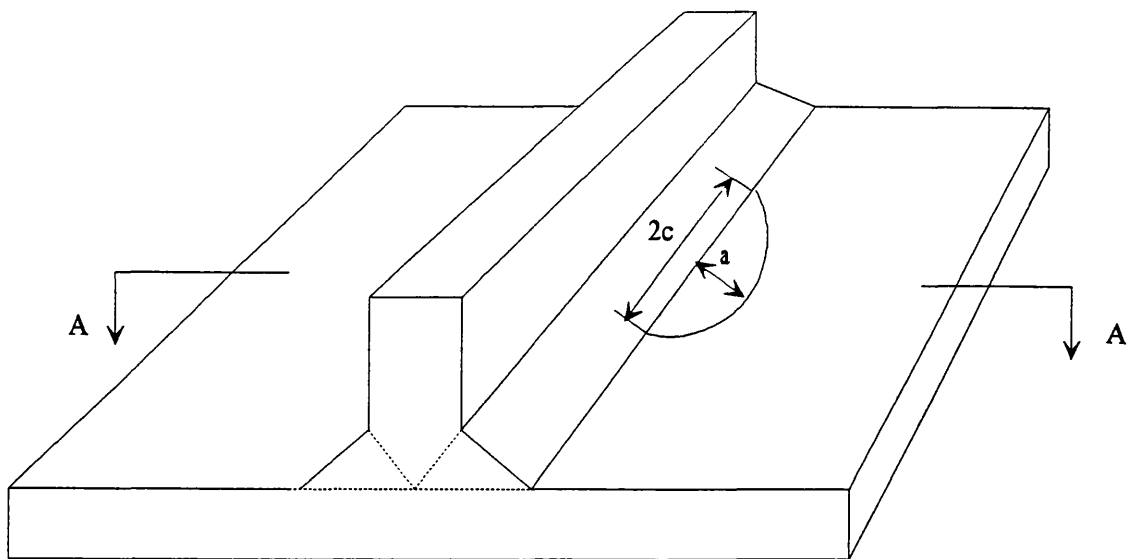
8.5 Conclusions

Based on the Wang-Lambert Flat Plate Weight function and the UCL uncracked through-wall stress distribution database for T-butt welded joints, a set of SIF parametric equations(W&L(FP)*S) for surface point of surface semi-elliptical cracks in T-butt welded joints have been derived for the first time. These equations have included the influence of crack aspect ratios, weld toe angle, weld attachment length and weld radius. They are available for both membrane and bending loading. The predictions from W&L(FP)*S equations are quite conservative when compared with Bell's three dimensional finite element data. Given the simple modification factors shown in equations(8 - 23)(8 - 24), they can give quite accurate estimations. These equations can be easily programmed and used in the prediction of fatigue crack growth along the welds and the fatigue crack shape development in T-butt welded joints.

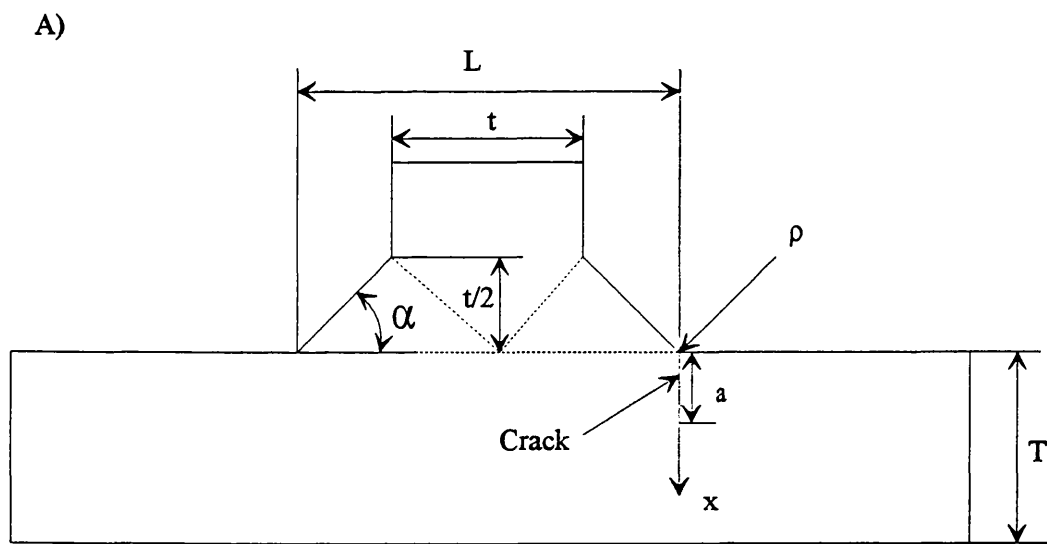
Table 8.1 Summary of Degree of Fit for the surface point SIF Parametric

Equations(W&L(FP)*S) for Semi-elliptical Crack in T-butt Welded Joints

Loading	Equations	Form of Expression		C_0	C_1	C_2	C_3
		Descriptive Statistics (%)					
		Mean R^2	Std. Dev.	R^2			
Tension	Appendix K1	99.60	1.86	97.96	99.30	99.52	98.50
Bending	Appendix K2	96.72	9.05	97.89	98.09	97.74	99.06



(a) T-butt Welded Joint (Three Dimension)



(b) Local Weld Geometry (Two Dimension)

Figure 8.1 Semi-elliptical Crack in T-butt Welded Joint

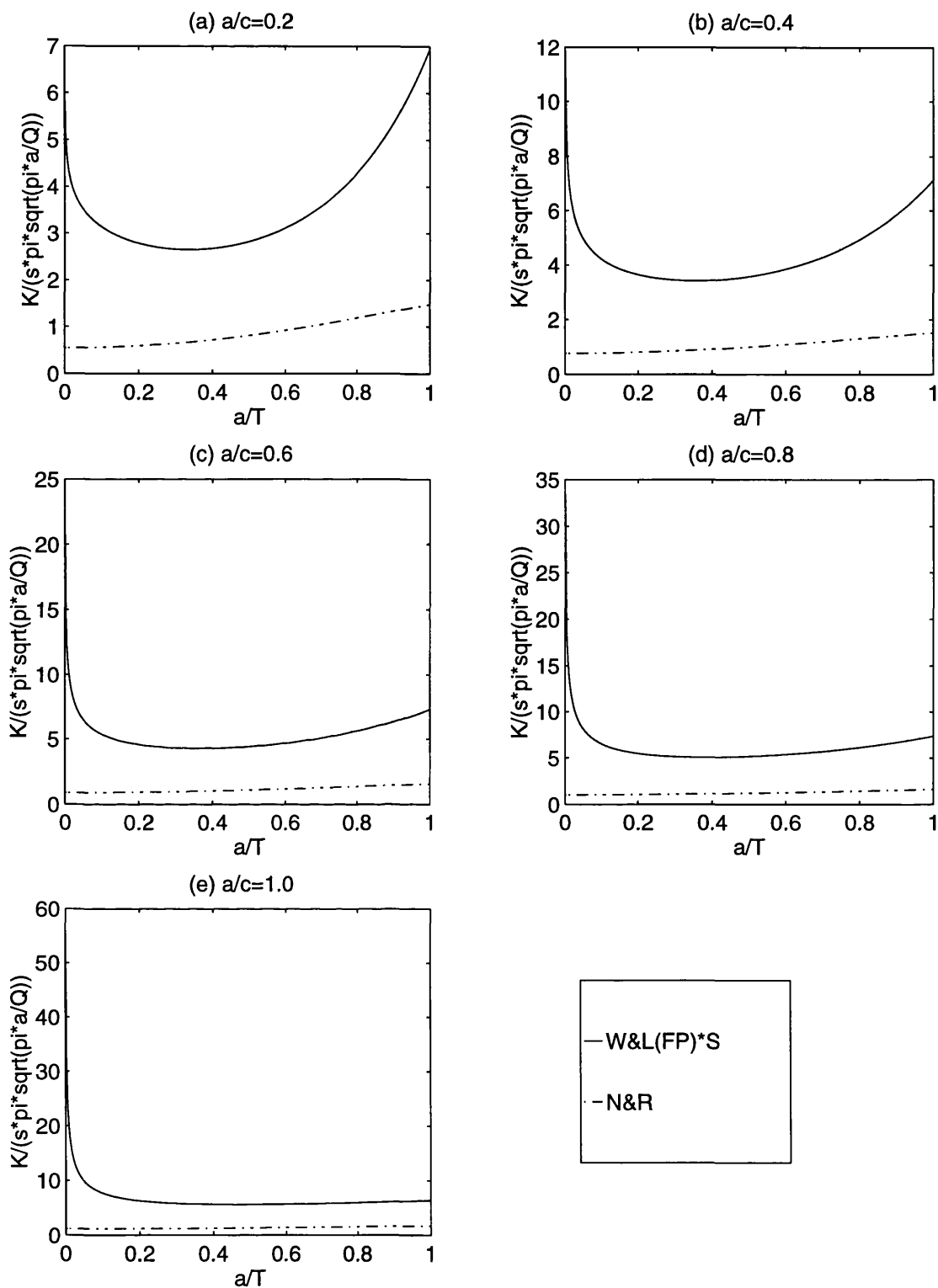


Figure 8.2 Comparison of Surface Point SIF Predictions from W&L(FP)*S for Semi-elliptical Cracks in T-Butt Welded Joint ($\alpha=45^\circ$, $\rho/T=0.02$, $L/T=2$) with N&R for Flat Plate under Tension

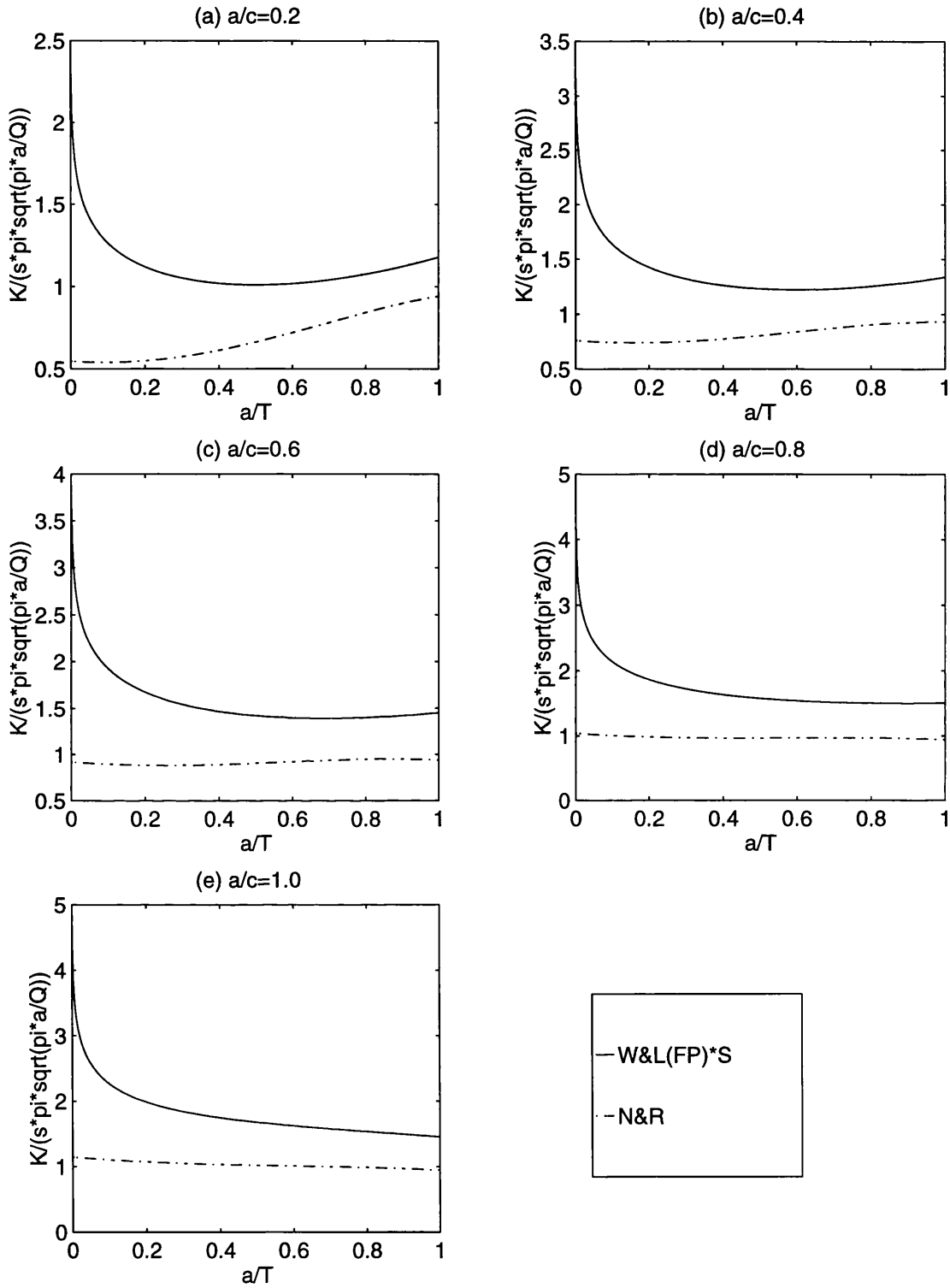


Figure 8.3 Comparison of Surface Point SIF Predictions from W&L(FP)*S for Semi-elliptical Cracks in T-Butt Welded Joint ($\alpha=45^\circ$, $\rho/T=0.02$, $L/T=2$) with N&R for Flat Plate under Bending

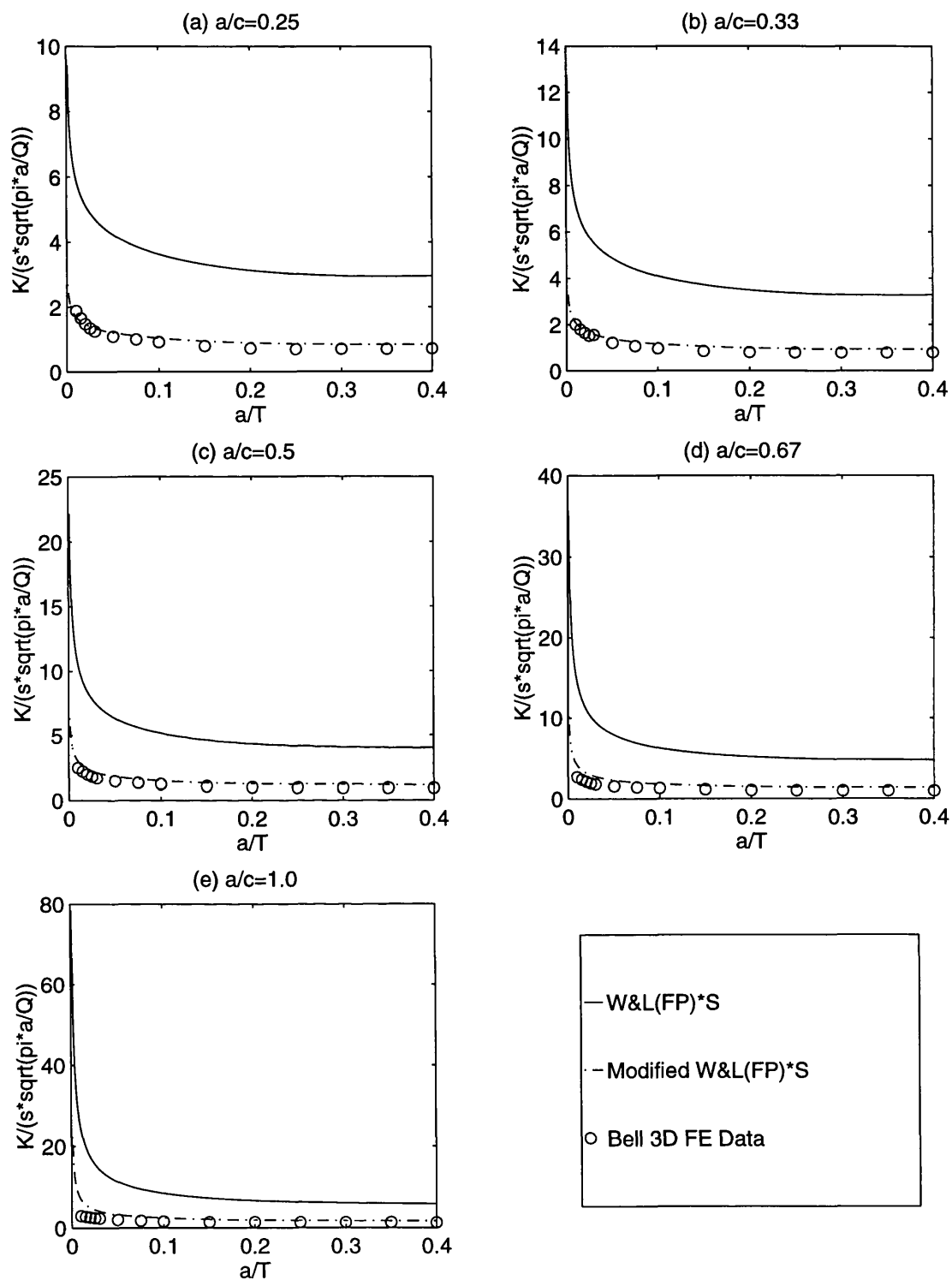


Figure 8.4 Comparison of Surface Point SIF Predictions from W&L(FP)*S and Modified W&L(FP)*S with Bell's 3D data for Semi-elliptical Cracks in T-Butt Welded Joint ($\alpha=45^\circ$, $\rho/T=0.01$, $L/T=2.3$) under Tension

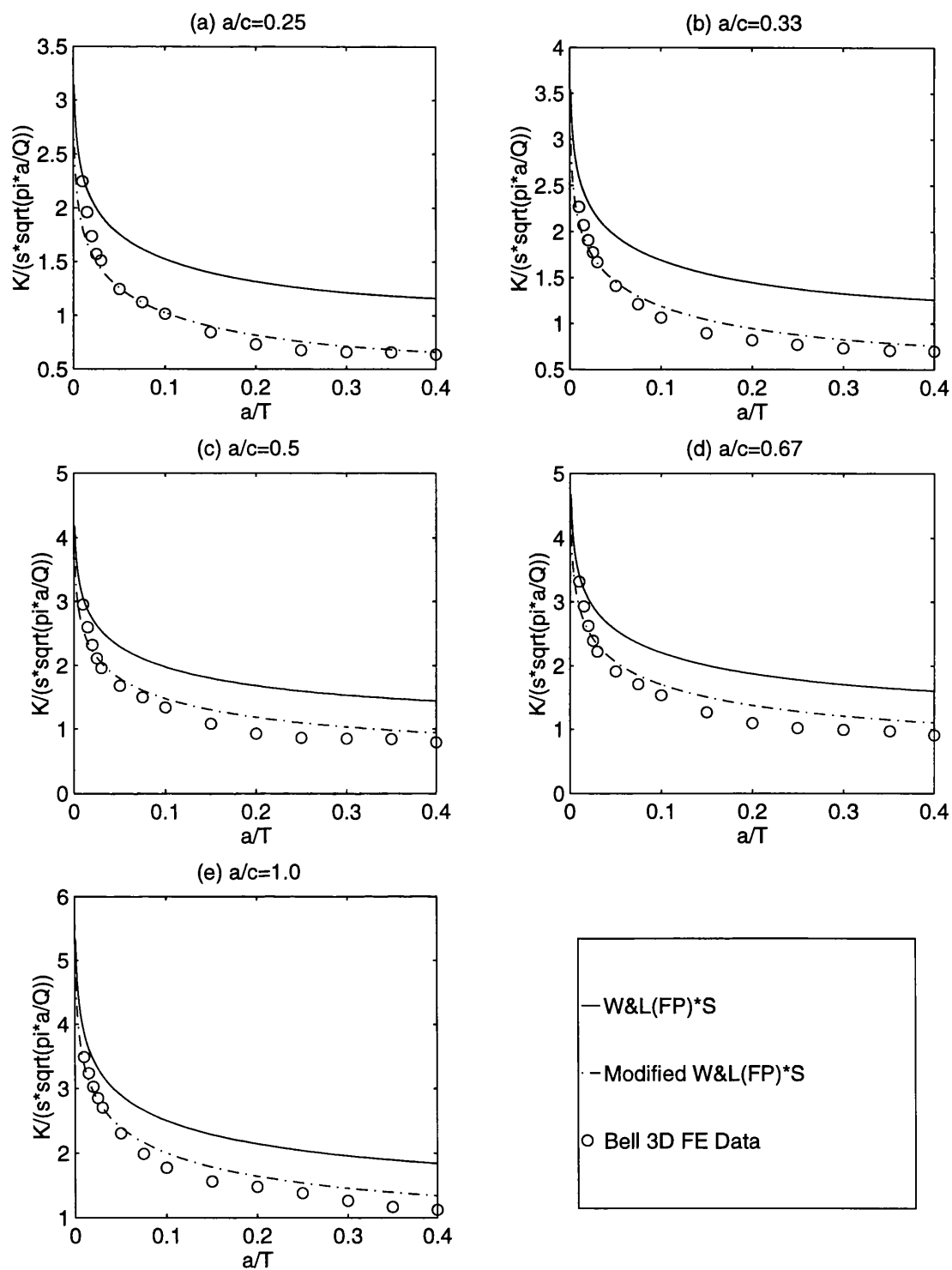


Figure 8.5 Comparison of Surface Point SIF Predictions from W&L(FP)*S and Modified W&L(FP)*S with Bell's 3D data for Semi-elliptical Cracks in T-Butt Welded Joint ($\alpha=45^\circ$, $\rho/T=0.01$, $L/T=2.3$) under Bending

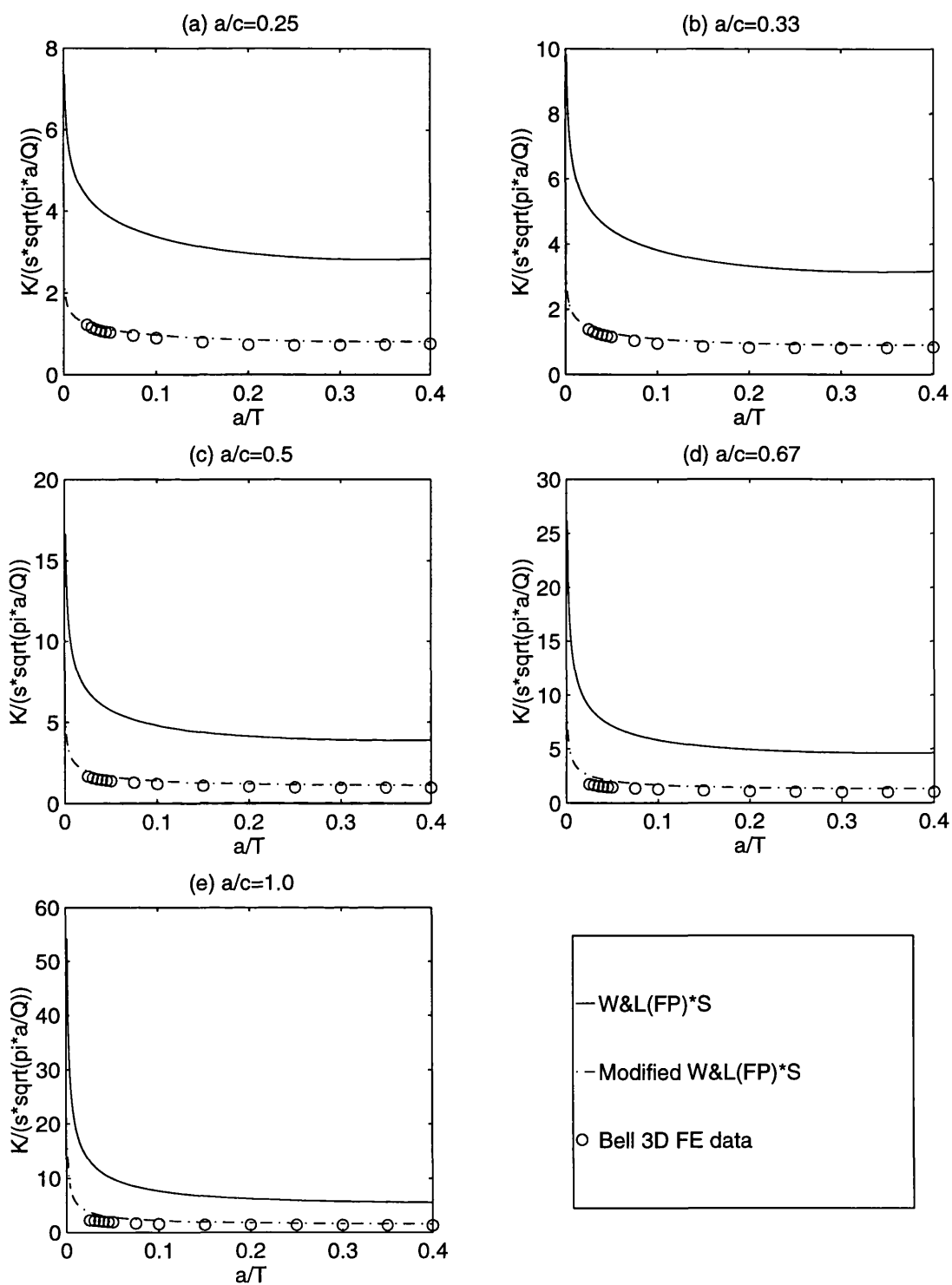


Figure 8.6 Comparison of Surface Point SIF Predictions from W&L(FP)*S and Modified W&L(FP)*S with Bell's 3D data for Semi-elliptical Cracks in T-Butt Welded Joint ($\alpha=30^\circ$, $\rho/T=0.01$, $L/T=2.3$) under Tension

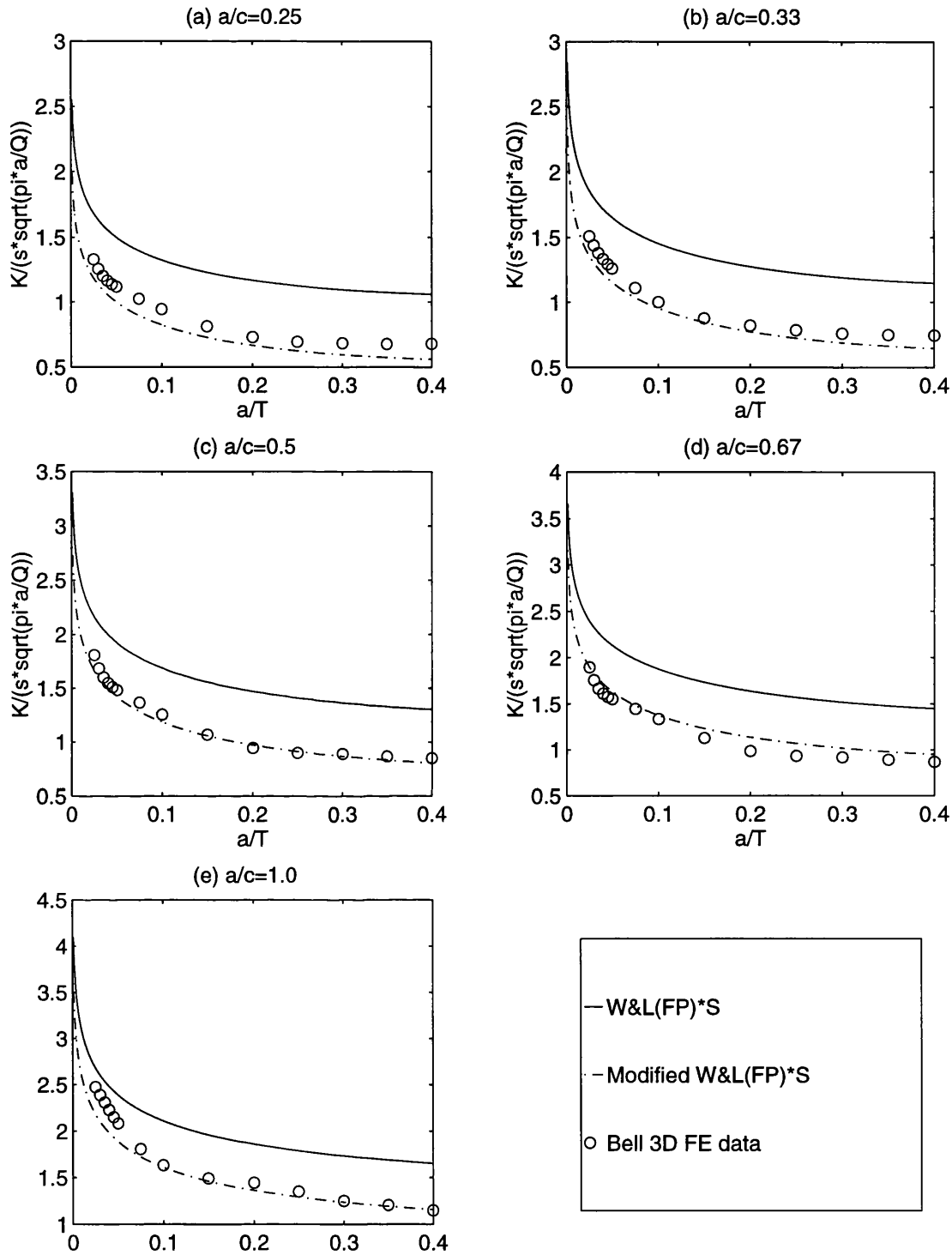


Figure 8.7 Comparison of Surface Point SIF Predictions from W&L(FP)*S and Modified W&L(FP)*S with Bell's 3D data for Semi-elliptical Cracks in T-Butt Welded Joint ($\alpha=30^\circ$, $p/T=0.01$, $L/T=2.3$) under Bending

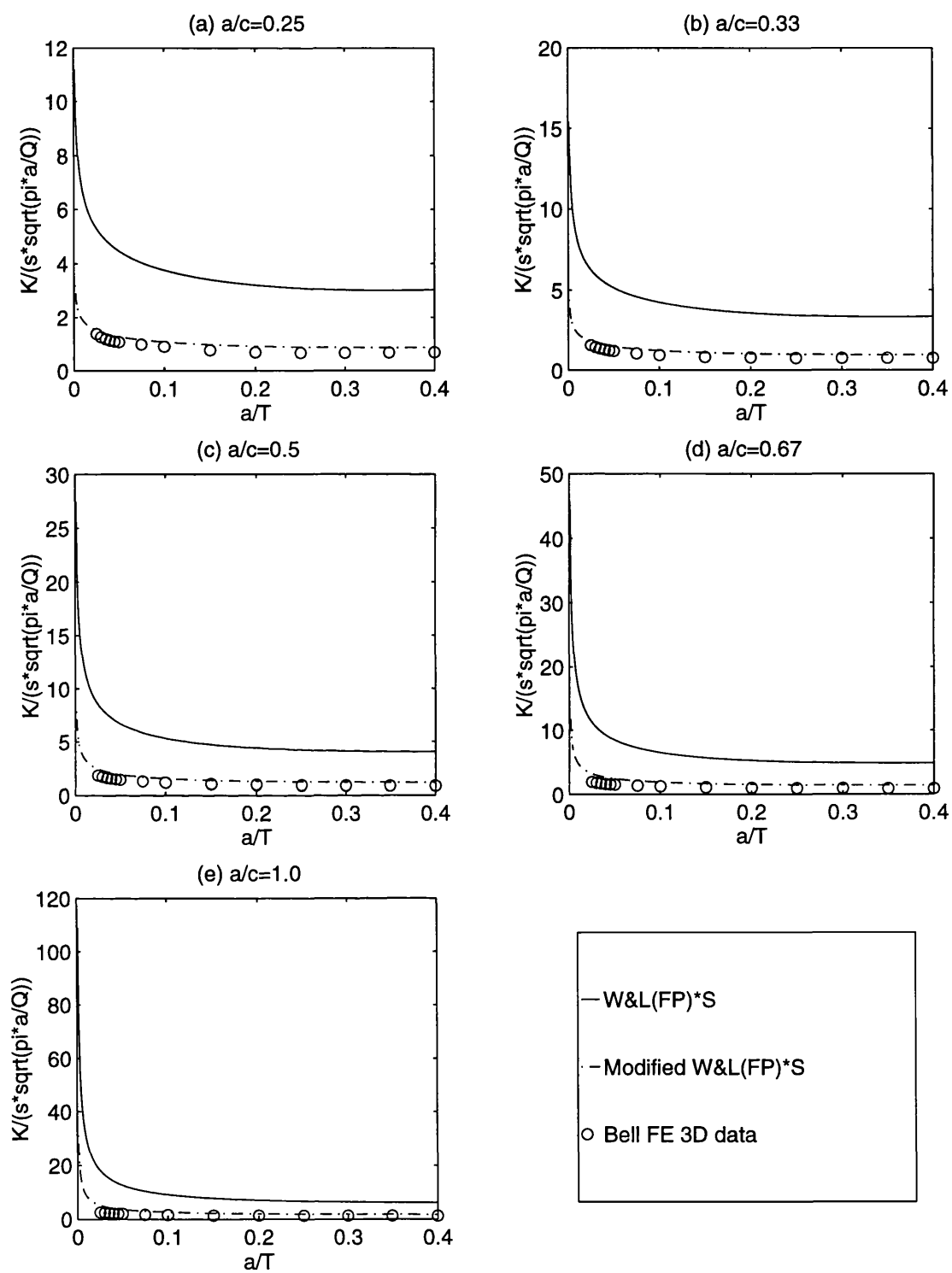


Figure 8.8 Comparison of Surface Point SIF Predictions from W&L(FP)*S and Modified W&L(FP)*S with Bell's 3D data for Semi-elliptical Cracks in T-Butt Welded Joint ($\alpha=70^\circ$, $\rho/T=0.01$, $L/T=2.3$) under Tension

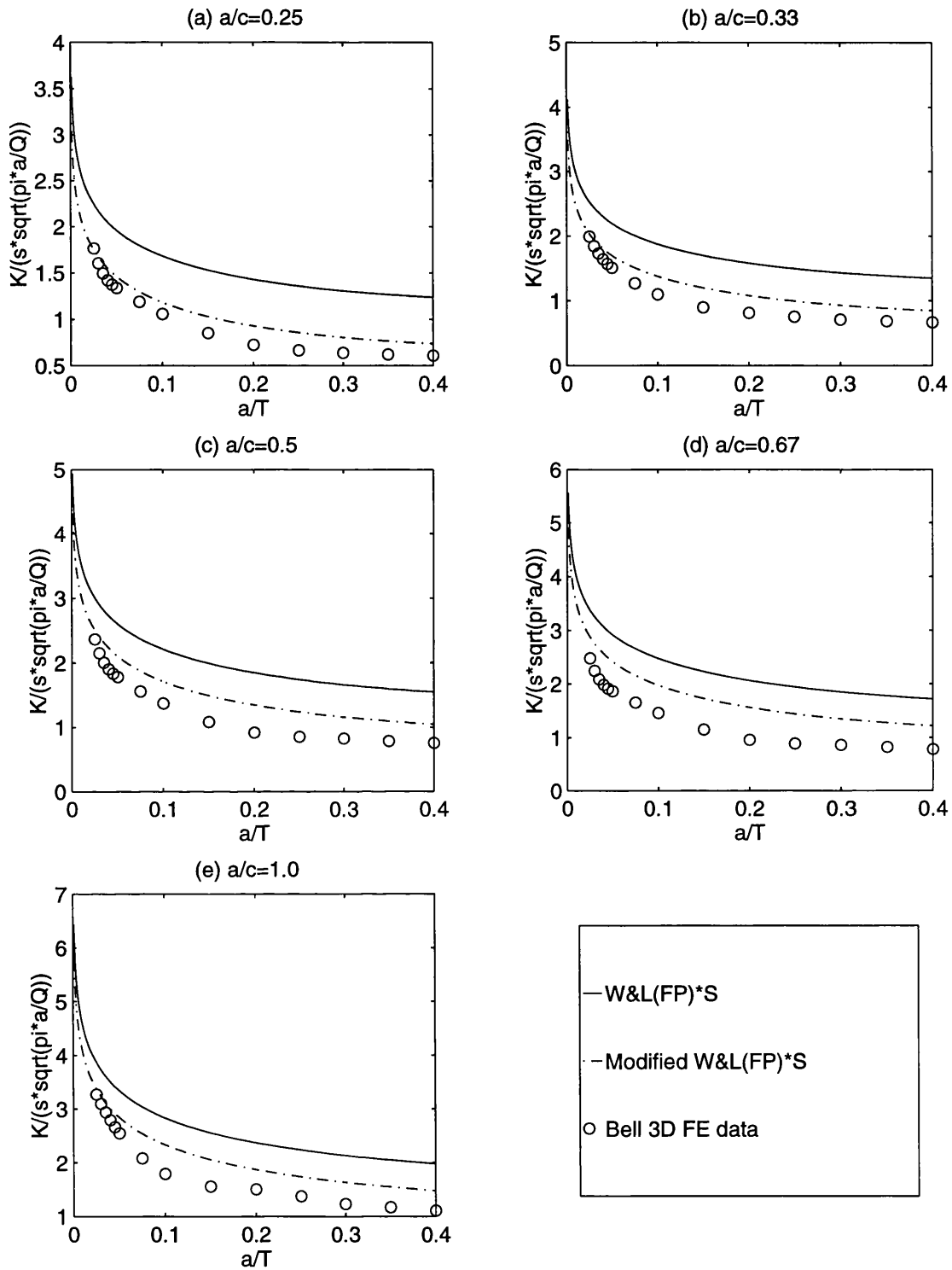


Figure 8.9 Comparison of Surface Point SIF Predictions from W&L(FP)*S and Modified W&L(FP)*S with Bell's 3D data for Semi-elliptical Cracks in T-Butt Welded Joint ($\alpha=70^\circ$, $\rho/T=0.01$, $L/T=2.3$) under Bending

CHAPTER NINE

SIF PARAMETRIC EQUATIONS

FOR SEMI-ELLIPTICAL SURFACE CRACKS

AT THE SADDLE OF TUBULAR WELDED T-JOINTS

9.1 Introduction

The stress analysis for tubular welded joints has been discussed in previous chapters. With this information at hand, it is necessary to develop the accurate fatigue crack growth modelling for rational inspection scheduling and maintenance of offshore jacket platform. The crack growth relationship such as Paris law, relates crack growth rate to the Stress Intensity Factor(SIF) range. Thus, accurate estimation of SIF for semi-elliptical cracks in tubular welded joints is of primary importance for the fatigue strength assessment of offshore tubular joints.

The occurring of through-thickness crack was been regarded as the fatigue failure of joints. Also fatigue cracks always grow rapidly along the weld toe and the crack length is easy to be measured by NDT technique such as MPI. Thus, much effort has been made to derive the deepest point SIF solutions to predict fatigue crack grow in thickness direction and to develop the advanced NDT techniques, such as ACPD and ACFM to size the depth of cracks.

The tubular joints of real structures are usually of complex geometric configuration and loading. As a result, currently there is no analytical solution for SIF for these joints. Although one can do three dimensional finite element analysis, it is very expensive. Instead, SIF for tubular joints is usually predicted using a simple flat plate or T-butt solution in conjunction with an appropriate load shedding model. Among them, the Niu-Glinka weight function based solution(N&G*S) with a linear release moment model is most successful for predicting fatigue crack growth in tubular welded joints.

However, all previous solutions including N&G*S do not consider the curvature of a tubular structure. Thus it is not accurate to assess the SIF for tubular joints using these simple models since weight function is the property of a geometry. Therefore, it is necessary to develop more accurate weight function based on real geometry of tubular joint. With the recent development of weight functions for longitudinal cracks in thin pipes, it is possible to develop a new weight function for the deepest point of a semi-elliptical crack at the saddle position of tubular welded T-joints. Furthermore, using the available UCL T-butt stress through-wall distribution database,

parametric equations can be derived to predict the deepest point SIFs for semi-elliptical cracks in tubular welded joints.

9.2 Weight Function for Semi-elliptical Cracks at the Saddle of Tubular Welded T-Joints

As an important development of the weight function technique, Niu and Glinka(1990) have proposed a closed form weight function for a semi-elliptical surface crack emanating from the weld toe of T-butt welded joint. This weight function is capable of incorporating weld profile effects due to different weld angles α and weld toe radii ρ under any mode I type of loading. But this solution does not consider the curvature of the tube as it uses the Newman and Raju flat plate solution(1986) as reference data. However, the effect of curvature is important for pipes, pressure vessels and tubular joints.

By using three dimensional finite elements, Raju and Newman(1982) and Shiratori(1989) obtained SIFs for constant, linear, parabolic or cubic stress distributions acting on the crack surface of internal and external longitudinal semi-elliptical surface cracks in pipes with a radius/thickness ratio of 10. Based on these reference data and using the generalised form of Mode I weight function expressions, Shen and Glinka(1993) derived the weight functions for the deepest and surface points of semi-elliptical cracks in thin pipes. However, these solutions are restricted to aspect ratios between 0.2 and 1.0. In order to overcome this difficulty, Wang and Lambert(1996) conducted a series of three dimensional finite element analyses to obtain the low aspect ratio crack data. Using these results together with existing finite element data for higher aspect ratios, they(Wang and Lambert 1996) derived the closed form weight functions for the deepest and surface points of longitudinal semi-elliptical surface cracks in thin pipes(Figure 9.1) which are valid for all aspect ratios as follows:

$$m_s^p(x, a) = \frac{2}{\sqrt{2\pi(a-x)}} \left[1 + M_{s1}^p \left(1 - \frac{x}{a} \right)^{1/2} + M_{s2}^p \left(1 - \frac{x}{a} \right) + M_{s3}^p \left(1 - \frac{x}{a} \right)^{3/2} \right] \quad (9-1)$$

$$M_{s1}^p = \frac{\pi}{\sqrt{2Q}} (4Y_0 - 6Y_1) - \frac{24}{5} \quad (9-2)$$

$$M_{s2}^p = 3 \quad (9-3)$$

$$M_{s3}^p = 2 \left(\frac{\pi}{\sqrt{2Q}} Y_0 - M_{s1}^p - 4 \right) \quad (9-4)$$

$$Y_0 = B_0 + B_1 \left(\frac{a}{t} \right)^2 + B_2 \left(\frac{a}{t} \right)^4 \quad (9-5)$$

$$Y_1 = A_0 + A_1 \left(\frac{a}{t} \right)^2 + A_2 \left(\frac{a}{t} \right)^4 \quad (9-6)$$

$$Q = 1 + 1.464 \left(\frac{a}{c} \right)^{1.65} \quad (9-7)$$

$$B_0 = 1.1492 - 0.4322 \left(\frac{a}{c} \right) + 0.2984 \left(\frac{a}{c} \right)^2 \quad (9-8)$$

$$B_1 = 4 - 8.98 \left(\frac{a}{c} \right) + 5.29 \left(\frac{a}{c} \right)^2 \quad (9-9)$$

$$B_2 = -7.44 + 14.559 \left(\frac{a}{c} \right) - 8.305 \left(\frac{a}{c} \right)^2 + \frac{1}{0.066 + \left(\frac{a}{c} \right)^{1.094}} \quad (9-10)$$

$$A_0 = 0.484 - 0.5211 \left(\frac{a}{c} \right) + 0.788 \left(\frac{a}{c} \right)^2 - 0.453 \left(\frac{a}{c} \right)^3 \quad (9-11)$$

$$A_1 = 2.4478 - 5.0937 \left(\frac{a}{c} \right) + 2.85 \left(\frac{a}{c} \right)^2 \quad (9-12)$$

$$A_2 = -5.69 + 9.653 \left(\frac{a}{c} \right) - 5.062 \left(\frac{a}{c} \right)^2 + \frac{1}{0.097 + \left(\frac{a}{c} \right)^{1.006}} \quad (9-13)$$

With the above weight function available, it was assumed that the relative influence of weld toe, i. e. weld angle α , was the same for an edge crack and the deepest point of a semi-elliptical surface crack with the same depth under the same stress system. This assumption is similar to that for the Niu and Glinka weight function but uses different reference data for the different geometries. It enables one to derive a weight function for the deepest point of semi-elliptical crack at the saddle position of a tubular welded T-joint (Figure 9.2) in the following relationship:

$$\frac{K_s^{ij}}{K_s^{ip}} = \frac{K_e^\alpha}{K_e^p} \quad (9-14)$$

where K_s^{ij} is the SIF for the deepest point of semi-elliptical surface crack at the saddle position of a tubular welded T-joint

K_s^{ip} is the SIF for an external longitudinal surface crack in a thin pipe subjected to the same stress distribution

K_e^α is the SIF for an edge crack in a welded joint

K_e^p is the SIF for an edge crack in a plate subjected to the same stress distribution

In order to derive a new weight function for the deepest point of a semi-elliptical crack at the saddle position of a tubular welded T-joint, the other three weight functions are needed. The weight functions for an edge crack in plate(m_e^p) and an edge crack emanating from the weld toe in a T-butt joint (m_e^α) were available in reference(Niu and Glinka 1987). With the recently derived Wang-Lambert thin pipe weight function, relations (9 - 14) can be expressed in terms of derived weight functions as follow:

$$\int_0^a \sigma(x) m_s^j(x, a/t, a/c, \alpha) dx = \frac{\int_0^a \sigma(x) m_e^\alpha(x, a, a/t, \alpha) dx}{\int_0^a \sigma(x) m_e^p(x, a, a/t) dx} \int_0^a \sigma(x) m_s^{tp}(x, a, a/t, a/c) dx \quad (9 - 15)$$

The reference SIF (K_r^j) for uniform tensile local stress system(σ_0) can be easily obtained from (9 - 15) as below:

$$K_r^j = \sigma_0 \frac{\int_0^a m_e^\alpha(x, a, a/t, \alpha) dx}{\int_0^a m_e^p(x, a, a/t) dx} \int_0^a m_s^{tp}(x, a, a/t, a/c) dx \quad (9 - 16)$$

By substituting all three available weight functions into the above equations, the reference SIF(K_r^j) can be given as :

$$K_r^j = F_r^j \sigma_0 \sqrt{\pi a} \quad (9 - 17)$$

$$F_r^j = \frac{\sqrt{2}}{6\pi} \frac{F^\alpha}{F^{90}} \left(\frac{15 + 5M_{e1}^{90} + 3M_{e2}^{90}}{15 + 5M_{e1}^p + 3M_{e2}^p} \right) (12 + 6M_{s1}^{tp} + 4M_{s2}^{tp} + 3M_{s2}^{tp}) \quad (9 - 18)$$

where the geometric correction factor ratio(Niu and Glinka 1990):

$$\frac{F^\alpha}{F^{90}} = 1 + \left(\frac{6}{\pi} \alpha - 2 \right) \left[1 - f\left(\frac{a}{t}\right) \right] \quad \text{for } \alpha \text{ in radians} \quad (9 - 19a)$$

$$f\left(\frac{a}{t}\right) = 1.0355 - 3.3324\left(\frac{a}{t}\right)^{0.5} + 21.5999\left(\frac{a}{t}\right) - 58.8513\left(\frac{a}{t}\right)^{1.5} \\ + 81.6246\left(\frac{a}{t}\right)^2 - 56.9396\left(\frac{a}{t}\right)^{2.5} + 15.8784\left(\frac{a}{t}\right)^3 \quad (9 - 19b)$$

the parameters in the weight function for an edge crack emanating from the right corner in a finite thickness plate(Niu and Glinka 1990):

$$M_{e1}^{90} = 0.6643 - 12.7438\left(\frac{a}{t}\right)^{1.5} + 397.8081\left(\frac{a}{t}\right)^3 - 3285.181\left(\frac{a}{t}\right)^{4.5} \\ + 14162.587\left(\frac{a}{t}\right)^6 - 30127.158\left(\frac{a}{t}\right)^{7.5} + 258119.535\left(\frac{a}{t}\right)^9 \quad (9 - 20a)$$

$$M_{e2}^{90} = 0.1117 - 3.857\left(\frac{a}{t}\right)^{1.5} + 30127.158\left(\frac{a}{t}\right)^3 + 285.4393\left(\frac{a}{t}\right)^{4.5} \\ - 647.6118\left(\frac{a}{t}\right)^6 + 934.4538\left(\frac{a}{t}\right)^{7.5} - 596.8319\left(\frac{a}{t}\right)^9 \quad (9 - 20b)$$

the parameters in the weight function for an edge crack in a plate of finite thickness t (Bueckner 1971):

$$M_{e1}^P = 0.6147 + 17.1944\left(\frac{a}{t}\right)^2 + 8.4822\left(\frac{a}{t}\right)^6 \quad (9 - 21a)$$

$$M_{e2}^P = 0.2502 + 3.2899\left(\frac{a}{t}\right)^2 + 70.0444\left(\frac{a}{t}\right)^6 \quad (9 - 21b)$$

Using the Petroski-Achenbach method again, the following closed form weight function for calculation of SIF at the deepest point of a semi-elliptical surface crack emanating from the saddle position of a Tubular welded T-joint was derived.

$$m_s^j(x, a/t, a/c, \alpha) = \frac{2}{\sqrt{2\pi(a-x)}} \left[1 + M_{s1}^j \left(\frac{a-x}{a} \right) + M_{s2}^j \left(\frac{a-x}{a} \right)^2 \right] \quad (9 - 22a)$$

where $m_{s1}^j = A_s^j + 3B_s^j - 4 \quad (9 - 22b)$

$$m_{s2}^j = 5 \left[\frac{\sqrt{2\pi}}{4} F_r^j - \frac{A_s^j - 1}{3} - B_s^j \right] \quad (9 - 22c)$$

$$A_s^j = \frac{2(F_r^j)' a}{F_r^j} \quad (9 - 22d)$$

$$B_s^j = \frac{5\sqrt{2\pi} \int_0^a (F_r^j)^2 ada}{8a^2 F_r^j} \quad (9 - 22e)$$

Instead of Newman Raju's flat plate solution, Wang-Lambert thin pipe weight function has been used as new reference data to derive the new weight function for a tubular welded T-joint, following the same procedure adopted by Niu and Glinka. This weight function can be used to

calculate the SIF for tubular welded T-joints containing semi-elliptical chord saddle cracks with different aspect ratios which were usually generated under axial and OPB loading.

This weight function is valid for weld angles $\pi/6 \leq \alpha \leq \pi/3$, aspect ratios $0 \leq a/c \leq 1$ and relative crack depths $0 \leq a/t \leq 0.8$. It should also be noted that this new function was derived for the tubular joint with $\gamma=9$ and only considers the influence of weld angle. The other effects of weld toe, such as weld toe radius and attachment size and global geometry effect in the form of Degree of Bending(DoB) can be incorporated into a SIF solution subsequently. It is also be aware that the effect of through-wall curvature of the crack, caused by the mode II contribution to crack opening is ignored at the deepest point of the semi-elliptical surface cracks.

9.3 SIF Parametric Equations for the Deepest Point of Semi-elliptical Surface Cracks at the Saddle of Tubular Welded T-Joints

Based on the Petroski-Achenbach crack opening displacement expression and using the Wang-Lambert thin pipe weight function as the reference SIF solution, a new weight function in closed form for calculation of SIF at the deepest point of a semi-elliptical crack emanating from the saddle position of a tubular welded T-connection has been derived. This weight function needs to be integrated with the uncracked stress distribution to obtain the SIF. However, this numerical integration procedure is not convenient to use at design stage. Finite element analysis results(Kare 1989) have demonstrated that weld toe stress distributions in tubular welded joints are well-represented by combining the results of T-butt models loaded in pure tension and pure bending, provided the weld geometries are the same in both cases. Therefore simple two dimensional finite element models can be used to calculate the weld toe through-wall stress distribution in tubular welded joints. The proportion of bending to total stress is characterised by Degree of Bending(DoB). In order to simplify the use of the weight function method, the deepest point SIF parametric equations for semi-elliptical saddle crack in tubular welded T-joint in tension and bending would be desirable.

To derive parametric equations, one would have to produce the SIF results database by combining the above weight function with the T-butt through wall stress distribution database. Stress Intensity Factor(SIF), K , can be expressed as follows:

$$K = \int_0^a W(a/c, a/t, x) \sigma(\alpha, \rho/t, L/t, a/t, x) dx \quad (9-23)$$

The UCL uncracked through-wall stress distribution database(Brennan et al 1996) was used again. It was based on the results of systematic two dimensional finite element analyses for T-

Butt welded joints and allow all weld toe effects to be incorporated. This database covers the T-butts with the following parameter ranges:

Parameter	Range
Weld Toe Angle (α)	$\pi / 6 \leq \alpha \leq \pi / 3$
Weld Toe Radius/Wall Thickness (ρ/T)	$0.01 \leq \rho / T \leq 0.066$
Attachment Width/Wall Thickness (L/T)	$0.1577 \leq L / T \leq 4$
Location Along Wall Thickness (x)	$0 < x \leq T$

The SIF database was establish by integrating the new derived closed form weight function for the deepest point of semi-elliptical saddle cracks in tubular welded T-joints with the UCL uncracked through-wall stress distribution of T-butt welded joints. The database used for each parameter in this SIF database is shown in following table.

Parameter	Range
Weld Toe Angle α	$\pi/6, \pi/4, \pi/3$
Weld Radius Ratio ρ/T	0.01, 0.02, 0.04, 0.066
Attachment Ratio L/T	Many data between 0.1577 and 4
Aspect Ratios a/c	0.01 0.05 0.08 0.1 0.12 0.15 0.18 0.2 0.4 0.6 0.8 1.0

As can see from the above table, this SIF database includes cracks within the whole range of aspect ratios($0 \leq a / c \leq 1$). In particular, sufficient data have been generated in the range $a / c \leq 0.2$, i.e. applicable to most fatigue cracks in tubular welded joints.

This new large database was used to derive the deepest point SIF parametric equations(TJ*S)¹ for semi-elliptical surface saddle cracks in tubular welded T-joints under tension and bending respectively. The regression analyses were carried out by using the Minitab statistical package(MINITAB 1991).

This two-dimensional curve-fitting process was conducted along the same lines as explained in section 8.3. The following forms of expression were fitted:

$$K_s^{ij} = (Y_T^{ij} R_T + DoB \bullet Y_B^{ij} R_B) \sigma_{hotspot} \sqrt{(\pi a)} \quad (9 - 24)$$

$$Y_T^{ij} = Exp \left(C_0 + C_1 \left(\frac{a}{T} \right) + C_2 \left(\frac{a}{T} \right)^2 \right) \left(\frac{a}{T} \right)^{C_3} \quad \text{For the Tension Loading} \quad (9 - 25)$$

¹ TJ represents Tubular Joint weight function, S denotes the T-butt through thickness stress distribution database, * stands for the integration process.

$$Y_B^{ij} = C_0 + C_1 \left(\frac{a}{T} \right) + C_2 \left(\frac{a}{T} \right)^2 + C_3 \ln \left(\frac{a}{T} \right) \quad \text{For the Bending loading} \quad (9 - 26)$$

The coefficients C_0 , C_1 , C_2 , C_3 are provided in appendix K as a function of the crack aspect ratio and weld toe parameters. As a result, the parametric equations(TJ*S) to predict the SIF at the deepest point of semi-elliptical surface crack at saddle position of tubular welded T-joint under tension and bending loading, were derived in the form of continuous single function. The degree of fit is indicated in Table 9.1 where it can be seen that the correlation coefficient R^2 is greater than 96% for all cases. The force(tension stress) release component release function(R_T) and moment(bending stress) release component release function(R_B) in above formulae will be identified in next section. This set of equations is valid in the following parameter ranges:

$$\frac{\pi}{6} \leq \alpha \leq \frac{\pi}{3} \quad (9 - 27)$$

$$0.01 \leq \frac{\rho}{T} \leq 0.066 \quad (9 - 28)$$

$$0.1577 \leq \frac{L}{T} \leq 4 \quad (9 - 29)$$

$$0 \leq \frac{a}{c} \leq 1 \quad (9 - 30)$$

$$0 < \frac{a}{T} \leq 0.8 \quad (9 - 31)$$

9.4 Models for Load Shedding and Crack Shape Development

As the crack grows, the cracked region could gradually lose the local bending stiffness and rotational constraints, and the excess bending load could be transmitted through the uncracked part of the joint. It is thought that the reduction in local bending moment due to cracking, and allied increase in local flexibility can be modelled by a systematic moment release. Thus, in order to have a realistic SIF solution for a tubular joint, the load shedding mechanism has to be taken into account. Unfortunately, it is not fully understood for tubular joints due to the complex geometry. However, so far there are several load shedding models available.

Assuming the tensile stress component does not change while the bending stress component decreases, moment release models have been proposed(Aaghaakouchak 1989). They include the parabolic and the linear release models. The parabolic release model is derived from the studies

of edge cracks in plates and rings. The following linear moment release model(LRM) is proposed as a "limiting case".

$$R_B^{LMR} = \left(1 - \frac{a}{T}\right) \quad (9 - 32)$$

Although the simplified SIF model combined with linear moment release model gives good agreement with the experimental data, there is no solid theoretical foundation for the linear moment release model(LRM). It is just the borderline for load shedding. It could be that this improved agreement is due to the over-prediction of simplified SIF solution in conjunction with severe linear moment release model and the usually high DoB for tubular joints.

Du and Hancock(1989) found the non-linear sigmoidal load shedding both for force and moment for tubular joints by using line spring finite element model and it is relatively insensitive to crack shape or loading mode. As a result of further study of these finite element results, the non-linear sigmoidal moment release model(NMR) was suggested by Kam(1989) as below:

$$R_B^{NMR} = 0.5 \cos\left(\frac{\pi a}{T}\right) + 0.5 \quad (9 - 33)$$

Comparison of these two moment release models is shown in Figure 9.3. It shows that NMR is higher than LRM for the crack up to half-through wall and lower for the large cracks($a/T > 0.5$). This confirms that LRM is severe when used to predict early small crack growth($a/T < 0.5$).

Apart from the moment release, the force release was also found by Du and Hancock(1989). However, it is secondary effect compared with moment release as the proportion of tensile stress component is usually small. As a compromise, the constant release force(CRF) which is equal to DoB, i.e. $R_T = \text{DoB}$, was proposed in this study.

The empirical equations such as AVS and TPM, do not need crack shape information since they include this information implicitly. However, for all fracture mechanics solutions, fatigue crack aspect ratio data is crucial. By fitting the UCL experimental data for tubular joint under axial and OPB loading, Hancock and co-worker derived the following relationship(Du and Hancock 1989):

$$\frac{a}{c} = 0.167 \left(\frac{a}{T}\right) + 0.05 \quad \left(\frac{a}{T} > 0.2\right) \quad (9 - 34)$$

Based on the study of a series of fatigue test results for X joints and multiple-brace nodes, Dover and co-worker(Dover et al 1988) also suggested a lower bound value as a forcing function as below:

$$\text{When } 0 < \frac{a}{T} < 0.1 \text{ then } \frac{a}{c} = \frac{a}{T} \quad (9 - 35a)$$

$$\text{When } 0.1 < \frac{a}{T} < 1.0 \text{ then } \frac{a}{c} = 0.2 \frac{a}{T} \quad (9 - 35b)$$

Figure 9.4 presents the comparison of these two different models. The fatigue crack often grows initially as several small cracks which eventually join up to form a single crack at about $a/T=0.1$. This feature is reflected in Dover model. However, sometimes, the linking up process may not be particular significant if individual cracks are fairly close. In this case, the single relationship such as Hancock model may be more appropriate. This model was extrapolated into the area $0 < \frac{a}{T} < 0.2$ in this study as shown below.

$$\frac{a}{c} = 0.167 \left(\frac{a}{T} \right) + 0.05 \quad \left(0 < \frac{a}{T} < 1.0 \right) \quad (9 - 36)$$

9.5 Validation

Based on ideas similar to those used for deriving the Niu-Glinka weight function and using the Wang-Lambert thin tube weight function as reference data, the weight function for the deepest point of semi-elliptical saddle cracks in tubular welded T-joints has been derived. Furthermore the SIF parametric equations were derived. It is necessary to assess the accuracy of this new set of equations by comparing them with experimental data and the predictions from other methods.

The predictions from this new set of equations(TJ*S) were firstly compared with the results from the N&G*S T-butt and Newman-Raju plate solutions for a particular case($\alpha=45^\circ$, $\rho/T=0.02$ and $L/T=2$) with different aspect ratios for tension and bending respectively(Figures 9.5-9.6). The stress concentration effect of weld toe is clearly shown in the TJ*S and N&G*S predictions and it decays quickly and disappears at about $a/T=0.1$. These figures show that the results from the new model follow the tendency of that of the N&G*S and are general slightly lower except for the large crack with lower aspect ratio($a/c=0.2$).

A direct comparison of plate and thin pipe SIF solutions is not made in this chapter. However, it can be demonstrated from the Figures 9.5-9.6 as the only difference between TJ*S and N&G*S is that they use these two different reference data. For low aspect ratio($a/c=0.2$) which is quite common for the fatigue cracks in tubular joints, the values from TJ*S are lower than that from the N&G*S for the small cracks($a/T<0.5$) and higher for the large cracks($a/T>0.5$). Two load shedding models, the LMR and NMR were used for TJ*S solution initially. The results

indicated that NMR is a suitable load shedding model for TJ*S. Thus NMR is used with TJ*S when compared with experimental data.

The available UCL in-air fatigue crack growth data(Dharmavasan 1983)(Kam 1989)(Monahan 1994)(Smith 1995) were re-analysed(the general information about these tests is shown in Table 9.2). They include one T joint under axial loading, one T joint under OPB loading and several DT and Multiple plane(M) joints under OPB and IPB loading. As both TJ*S and N&G*S solutions include the influence of weld toe, the emphasis is on the early fatigue crack growth. However, it is difficult to collect weld toe information for most of fatigue test data. As a result, the average weld angle and radius taken from the reference(Kare 1989) were used in this study.

Figures 9.7-9.20 show the comparison between the predictions from the new model(TJ*S) and N&G*S with these experimental results together with the most sophisticated empirical equation, i.e. the TPM solution. From these figures, one can see that the N&G*S works well with LMR whilst the TJ*S predictions fits well with experimental data with CRF and NMR. With suitable load release models, excellent agreement is achieved between the predictions from both TJ*S and N&G*S. They agree very well with test data as well.

All TJ*S and N&G*S data are calculated by using the experimental crack shape evolution information. However, they are available only for limited number of different crack depths. In order to obtain the complete fatigue crack grow curve, crack shape development information is needed. Two different crack shape evolution models were tried initially. It was found that the predictions using Dover model were too conservative for $a/T > 0.1$. The Hancock model was therefore chosen in the comparison(Figures 9.7-9.20). The results indicated that this crack shape development model work very well for the tubular T-joints under axial and OPB loading(Figures 9.7-9.8) as this model was derived from the test data of these joints. For other cases(Figures 9.9-9.20), it is shown that it can be used as a reasonable low bound estimations of aspect ratio as it produces the conservative values for SIFs. As a summary, Figures 9.7-9.20 demonstrated that this single aspect ratio relationship can be used in conjunction with TJ*S and N&G*S solutions to predict the SIFs for tubular welded joints. The advantage of the TJ*S and N&G*S solutions is that they can incorporate the aspect ratio information. With the accurate crack shape development relationship available, they can provide reliable SIF predictions.

It is not surprising that the predictions from TMP solutions agree well with some experimental data(Figures 9.7-9.11) as they are the data used to derive these equations. However, they are quite conservative for other cases(Figures 9.15-9.18 and 9.20).

Although the TJ*S was derived for the deepest point of semi-elliptical surface cracks at the saddle positions of tubular welded T-joints under axial and OPB loading, it was found that it

could work well for many other cases such as X(Figures 9.9-9.11) and multiple-brace nodes(Figures 9.12-9.19) and IPB loading(Figures 9.19) as long as the DoB and crack shape evolution information for these cases was accurate.

The differences between the predictions of TJ*S+CRF+NRM and N&G*S+LRM are very small for majority cases and they agree with the experimental data very well except for Figure 9.20 where the prediction accuracy can be improved by approximately 11% at $a/T=0.2$ and up to 13% at $a/T=0.46$ by using the TJ*S+CRF+NRM model when compared with those from the N&G*S+LRM solution.

9.6 Conclusions

Based on the Petroski-Achenbach crack opening displacement expression and using the Wang-Lambert thin pipe weight function as the reference SIF solution, a new weight function in closed form for calculating the SIF at deepest point of a semi-elliptical surface crack emanating from the saddle position of a tubular welded T-connection has been derived. Using this new weight function and the UCL T-butt through-wall stress distribution database, parametric equations(TJ*S) in the form of continuous single functions were derived for tension and bending loading. With the DoB information, they can be used to predict the deepest point SIF for semi-elliptical surface crack in tubular welded joints.

Available UCL in-air tubular joint fatigue test results, especially early crack growth data, were used to validate this new model. Considering the curvature of tube, TJ*S was found to work very well with the non-linear load shedding relationship derived from line spring finite element model(Du and Hancock 1989). In conjunction with the constant force release(CRF) and non-linear moment(NRM) release models, a new analytical model(TJ*S+CRF+NRM) has been developed for predicting the deepest point SIF for semi-elliptical surface fatigue cracks in tubular welded joints.

The predictions from this model agree very well with the experimental results, especially for early fatigue crack growth. In one case(Figure 9.20), the results showed that the predictions from this model are more accurate than those from the N&G*S+LRM when compared with experimental data. This new model can incorporate the influence of the local weld geometry and allows a rapid modelling of fatigue crack growth in tubular welded joints.

Table 9.1 Summary of Fitting Degree for the SIF Parametric Equations(TJ*S)

for the Deepest point of Semi-elliptical Crack at Saddle Position of Tubular Welded Joint

Loading	Equations	Form of Expression		C ₀	C ₁	C ₂	C ₃
		Descriptive Statistics (%)					
		Mean R ²	Std. Dev.	R ²			
Tension	Appendix K1	99.74	0.523	97.8	98.56	98.53	98.07
Bending	Appendix K2	99.54	0.809	96.84	97.44	98.49	97.72

Table 9.2 The Details of UCL Steel Tests for Tubular Joints

Ref	Joint Type	Mode of Loading	Geometry		Stress Information			Weld Toe Details		
			T (mm)	β	SCF_{hs}	$\frac{SCF_{hs}}{SCF}$	DoB	α (deg)	ρ (mm)	L (mm)
(Dharmavasan 1983)	T	Axial	16	0.71	8.70	1.37	0.82	47	0.75	20.70
(Dharmavasan 1983)	T	OPB	16	0.71	9.10	2.22	0.84	47	0.75	20.70
(Kam 1989)-UCX1	DT	Axial	45	0.51	6.70	1.70	0.84	47	0.75	28.62
(Kam 1989)-UCX2	DT	Axial	35	0.61	9.40	1.78	0.86	47	0.75	27.65
(Kam 1989)-UCX3	DT	Axial	25	0.76	7.70	1.85	0.82	47	0.75	21.25
(Monahan 1994)	T1-M	OPB	32	0.508	6.57	1.57	0.88	38	1.65	36.00
(Monahan 1994)	T2-M	OPB	32	0.508	6.29	1.57	0.88	39	1.25	36.00
(Monahan 1994)	T4b-DT	OPB	20	0.898	8.43	2.52	0.85	33	1.58	30.00
(Monahan 1994)	Y1a-M	OPB	32	0.359	3.36	1.52	0.94	40	1.63	32.00
(Monahan 1994)	Y1c-M	OPB	32	0.359	2.96	1.52	0.94	41	1.89	32.00
(Monahan 1994)	Y2a-M	OPB	32	0.359	2.87	1.52	0.94	41	1.38	32.00
(Monahan 1994)	Y2c-M	OPB	32	0.359	2.94	1.52	0.94	39	1.66	32.00
(Monahan 1994)	T1-M	IPB	32	0.508	2.73	1.31	0.83	54	1.28	36.00
(Smith, 1995)	TS-DT	OPB	19	0.8	6.4	1.55	0.89	23	2.10	50.00

Note: X-Y: X-brace/chord intersection of Y-node

M: Multiple-brace M-node

SCF_{hs} : Hot spot SCF

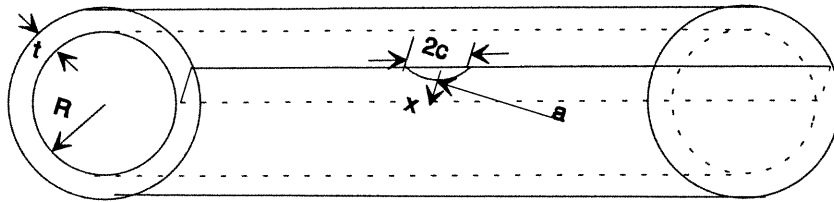


Figure 9.1 External Longitudinal Semi-elliptical Surface Crack in Thin Pipe

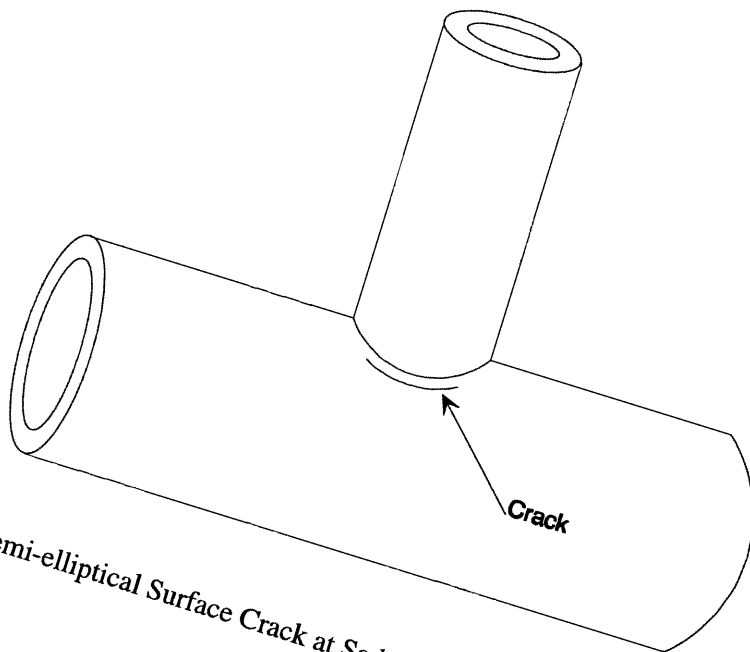


Figure 9.2 Semi-elliptical Surface Crack at Saddle Position of Tubular Welded Joint

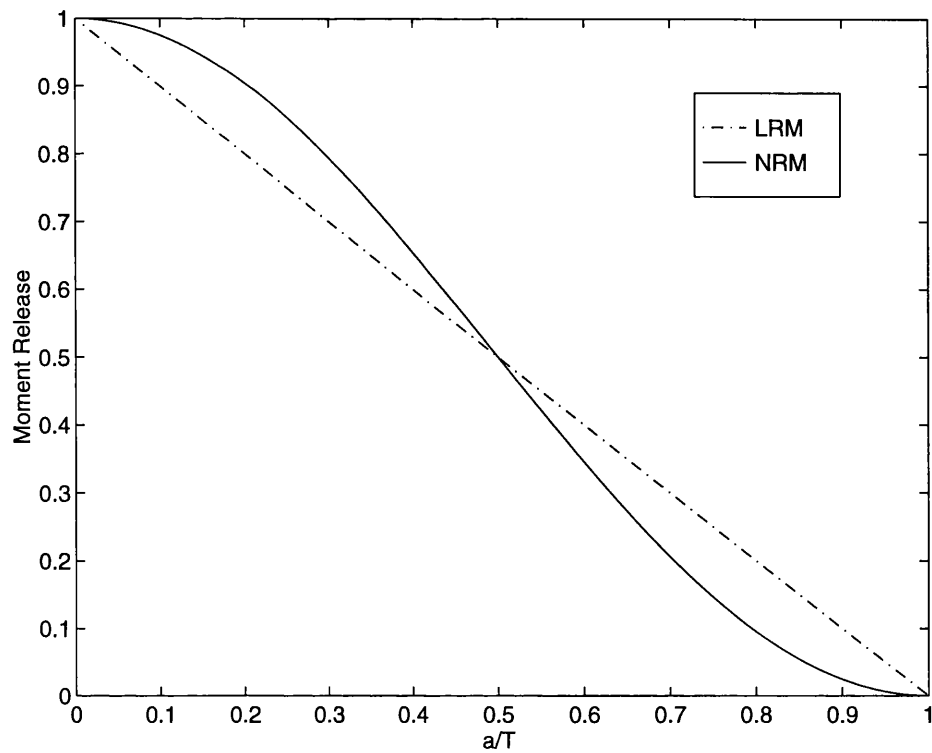


Figure 9.3 Comparison of Two Different Load Shedding Models for Tubular Joints

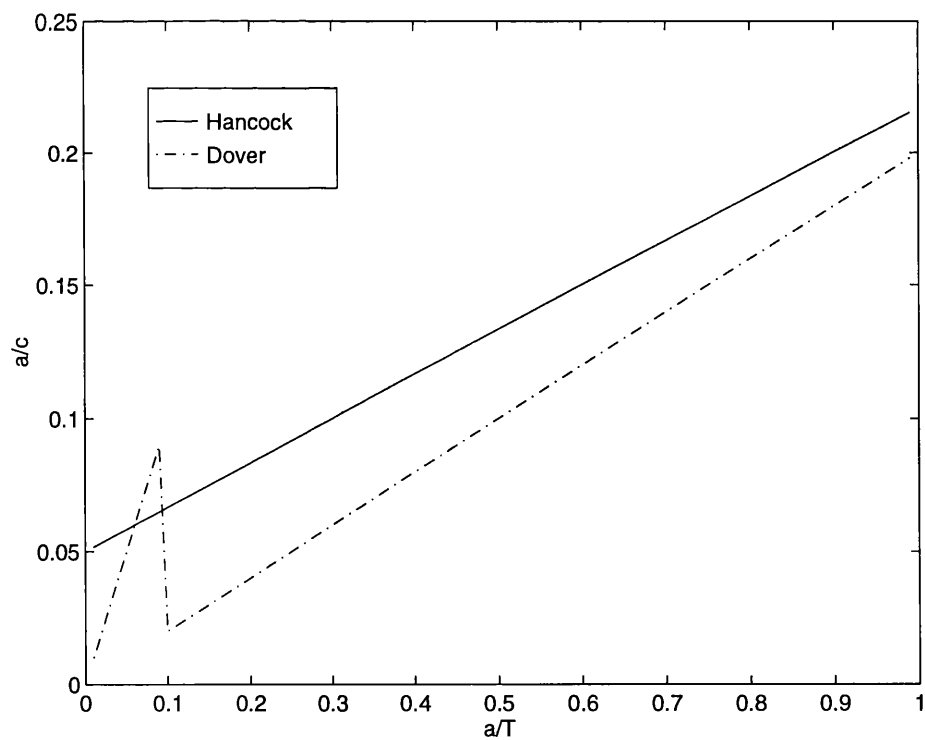


Figure 9.4 Comparison of Two Different fatigue Crack Shape Development Models for Tubular Joints

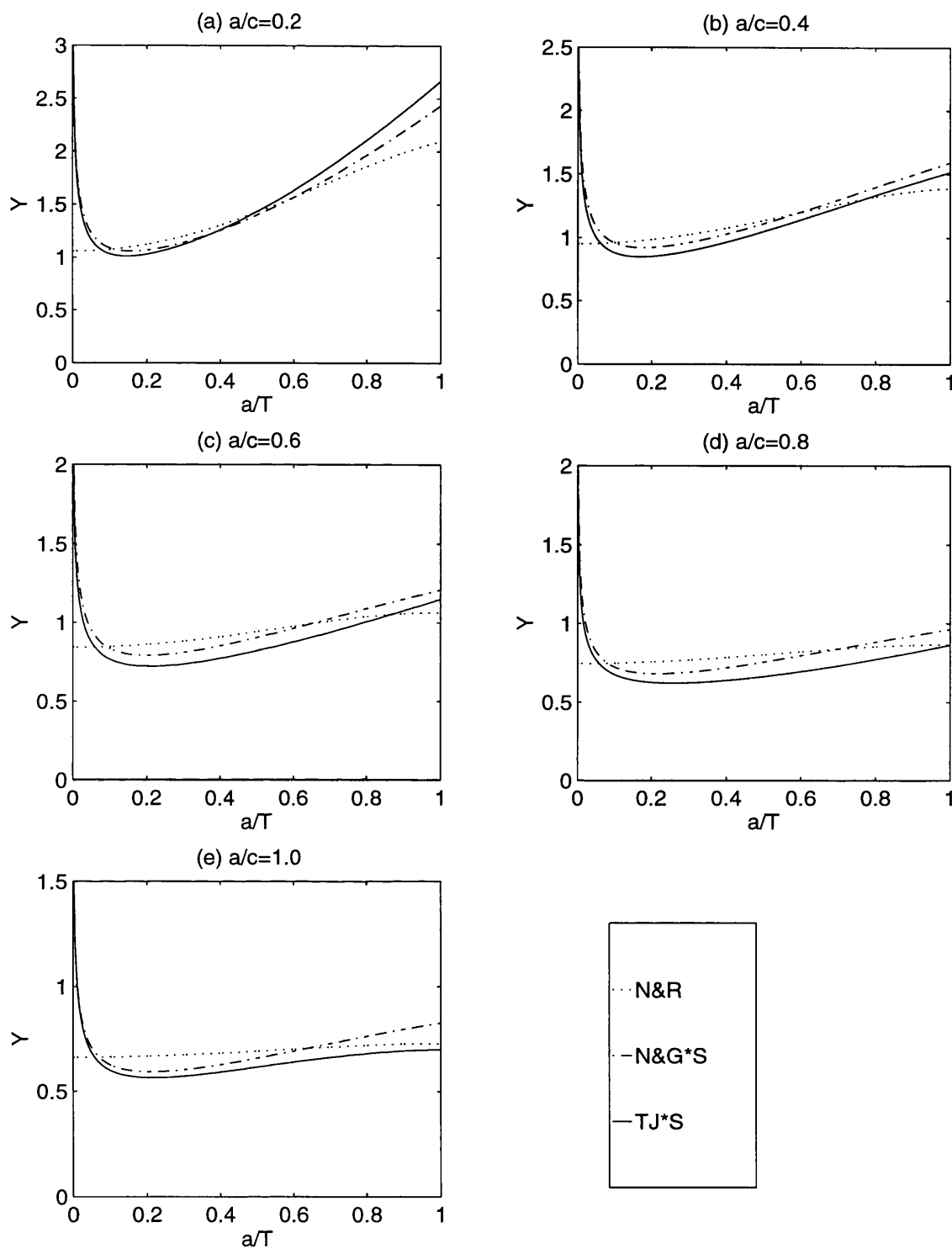


Figure 9.5 Comparison of Deepest Point SIF Predictions from N&G*S and TJ*S for Semi-elliptical Cracks in Welded Joint ($\alpha=45^\circ$, $\rho/T=0.02$ and $L/T=2$) with N&R for Flat Plate under Tension

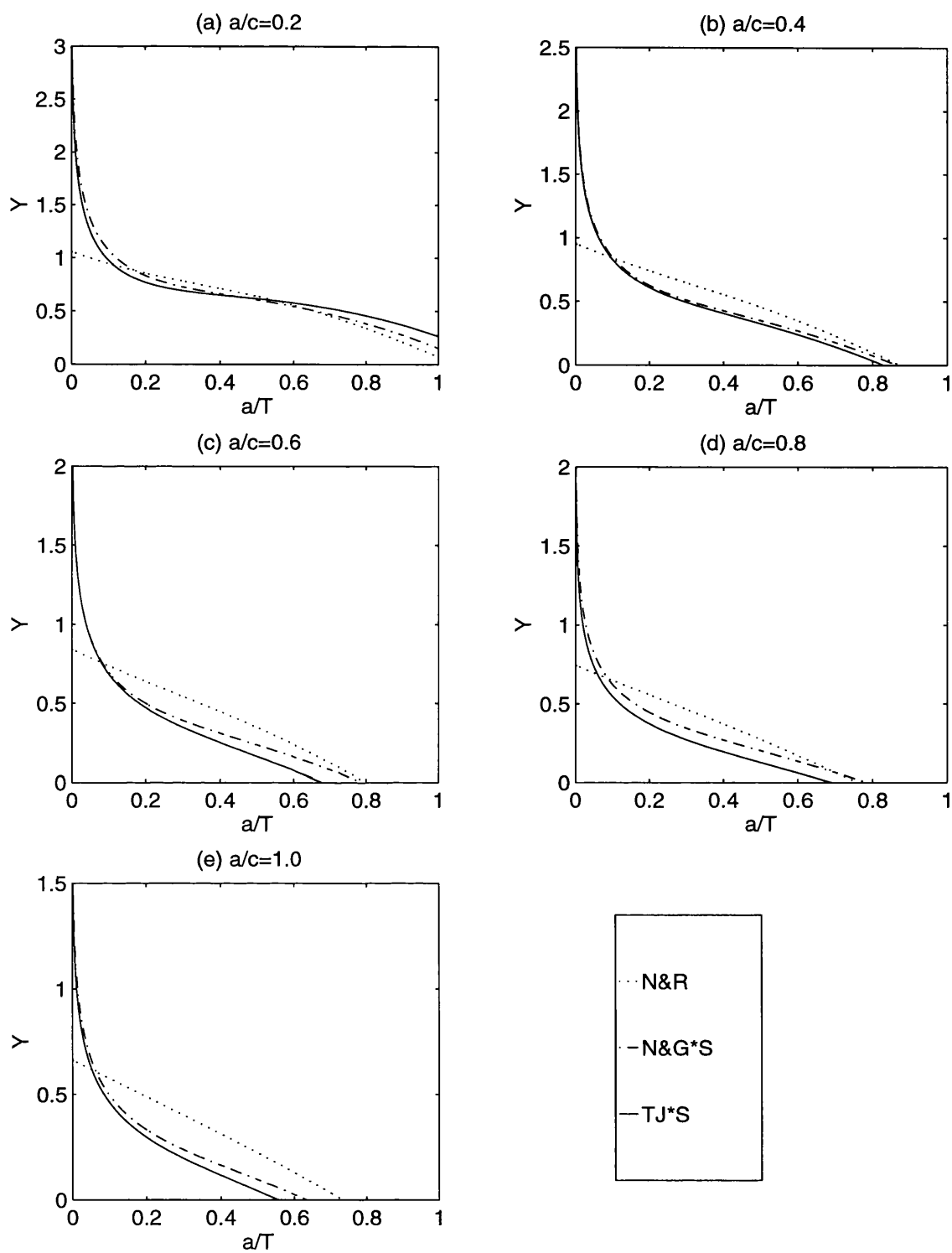


Figure 9.6 Comparison of Deepest Point SIF Predictions from N&G*S and TJ*S for Semi-elliptical Cracks in Welded Joint ($\alpha=45^\circ$, $\rho/T=0.02$ and $L/T=2$) with N&R for Flat Plate under Bending

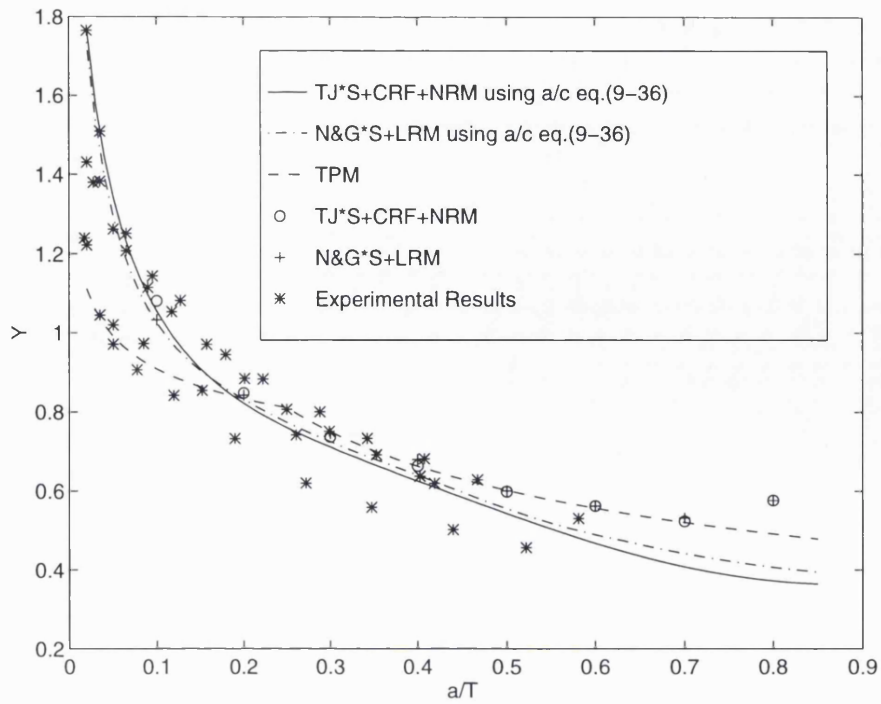


Figure 9.7 Comparison of Deepest Point SIF Predictions from N&G*S and TJ*S for Semi-elliptical Cracks in Tubular Welded T-Joint under Axial Loading ($\alpha=47^\circ$, $p/T=0.047$ and $L/T=1.294$)

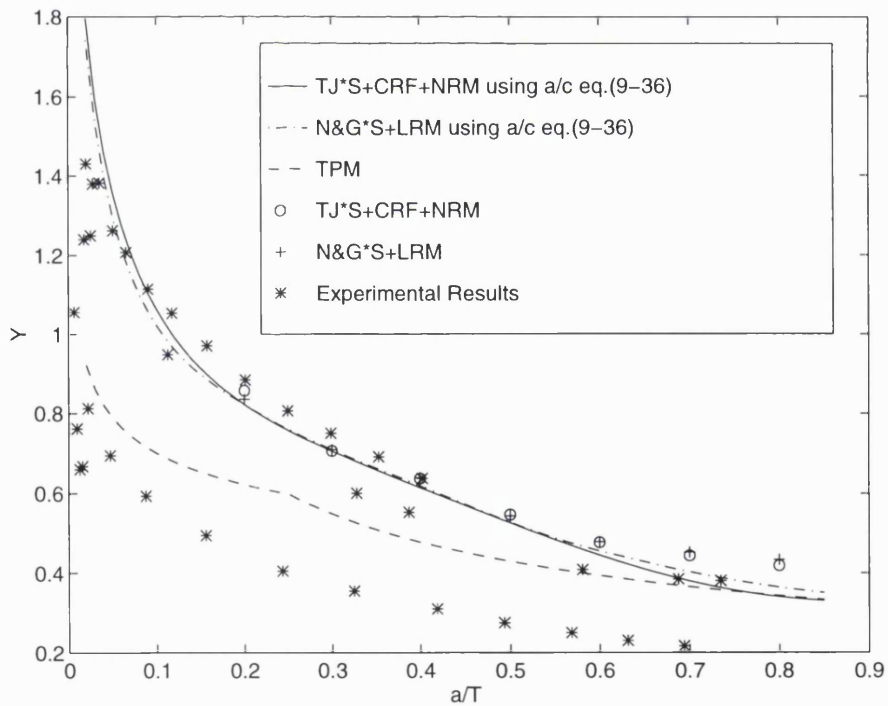


Figure 9.8 Comparison of Deepest Point SIF Predictions from N&G*S and TJ*S for Semi-elliptical Cracks in Tubular Welded T-Joint under OPB Loading ($\alpha=47^\circ$, $p/T=0.047$ and $L/T=1.294$)

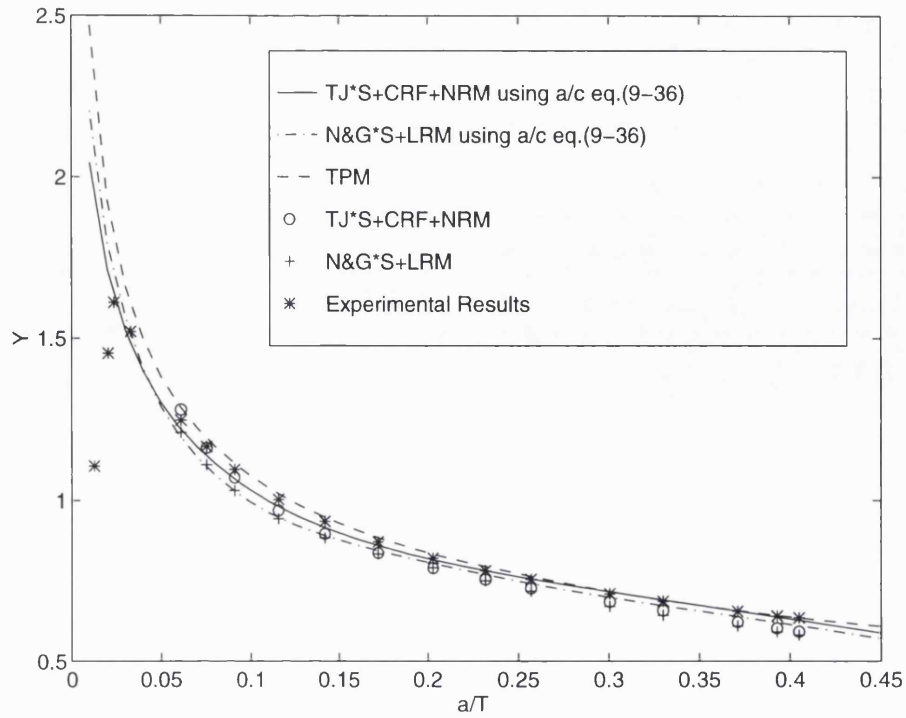


Figure 9.9 Comparison of Deepest Point SIF Predictions from N&G*S and TJ*S for Semi-elliptical Cracks in Tubular Welded DT-Joint(UCX1) under Axial Loading ($\alpha=47^\circ$, $\rho/T=0.017$ and $L/T=0.636$)

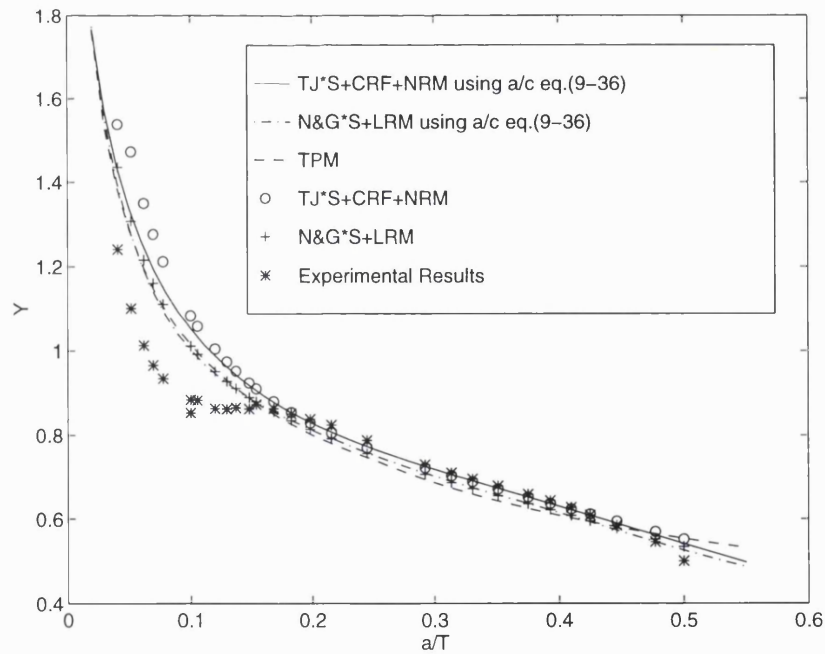


Figure 9.10 Comparison of Deepest Point SIF Predictions from N&G*S and TJ*S for Semi-elliptical Cracks in Tubular Welded DT-Joint(UCX2) under Axial Loading ($\alpha=47^\circ$, $\rho/T=0.021$ and $L/T=0.79$)

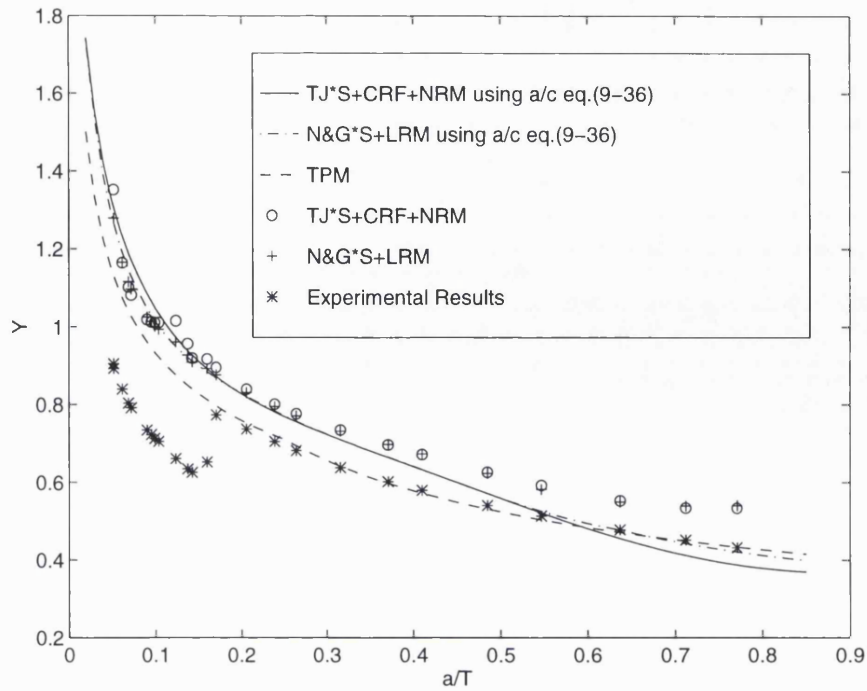


Figure 9.11 Comparison of Deepest Point SIF Predictions from N&G*S and TJ*S for Semi-elliptical Cracks in Tubular Welded DT-Joint(UCX3) under Axial Loading ($\alpha=47^\circ$, $\rho/T=0.03$ and $L/T=0.85$)

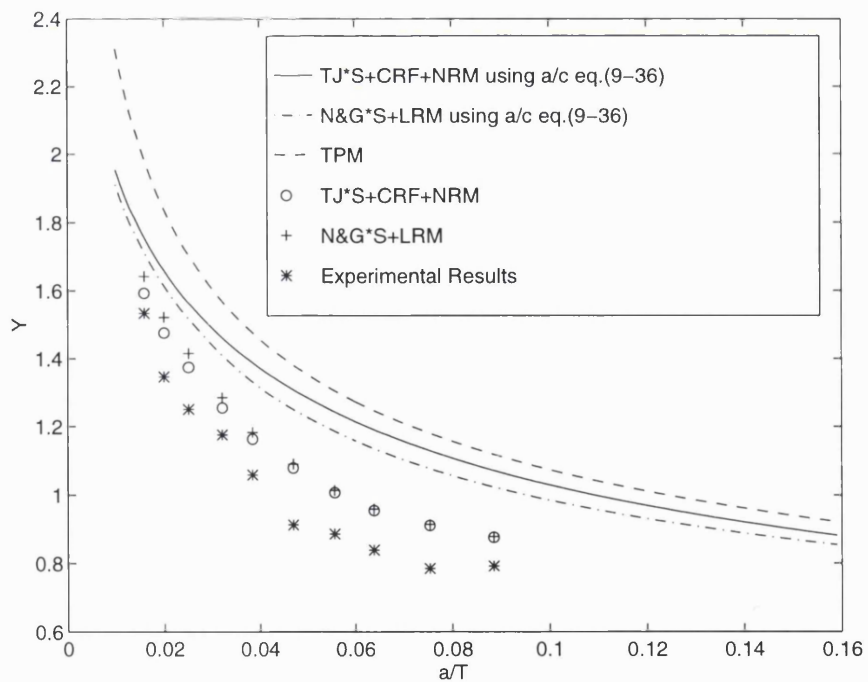


Figure 9.12 Comparison of Deepest Point SIF Predictions from N&G*S, TJ*S and TPM for Semi-elliptical Cracks in Tubular Welded Joint(T1-M) under OPB Loading ($\alpha=38^\circ$, $\rho/T=0.052$ and $L/T=1.125$)

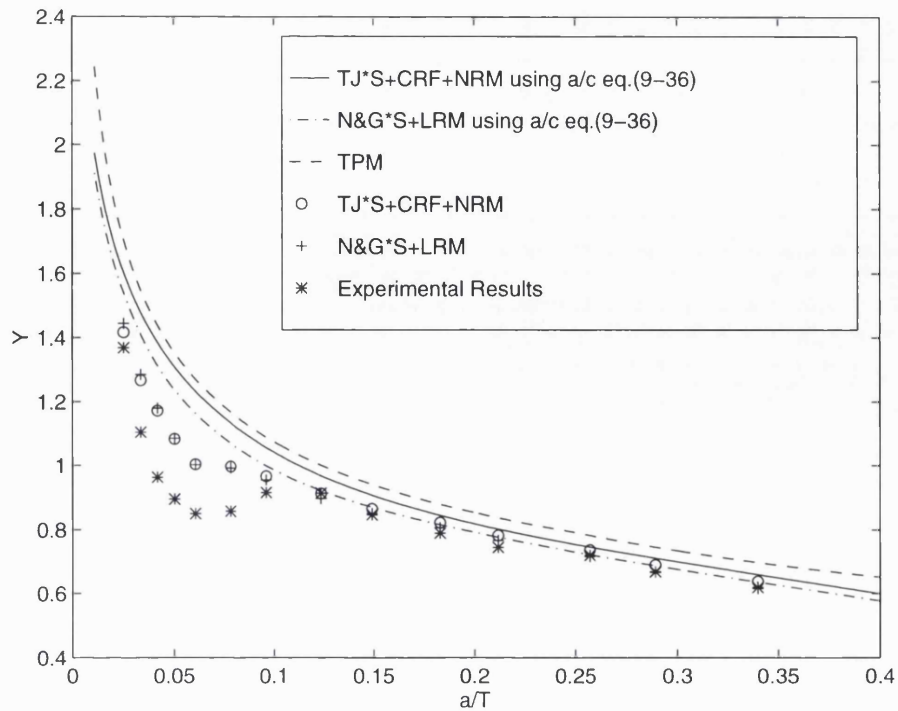


Figure 9.13 Comparison of Deepest Point SIF Predictions from N&G*S, TJ*S and TPM for Semi-elliptical Cracks in Tubular Welded Joint(T2-M) under OPB Loading ($\alpha=39^\circ$, $p/T=0.039$ and $L/T=1.125$)

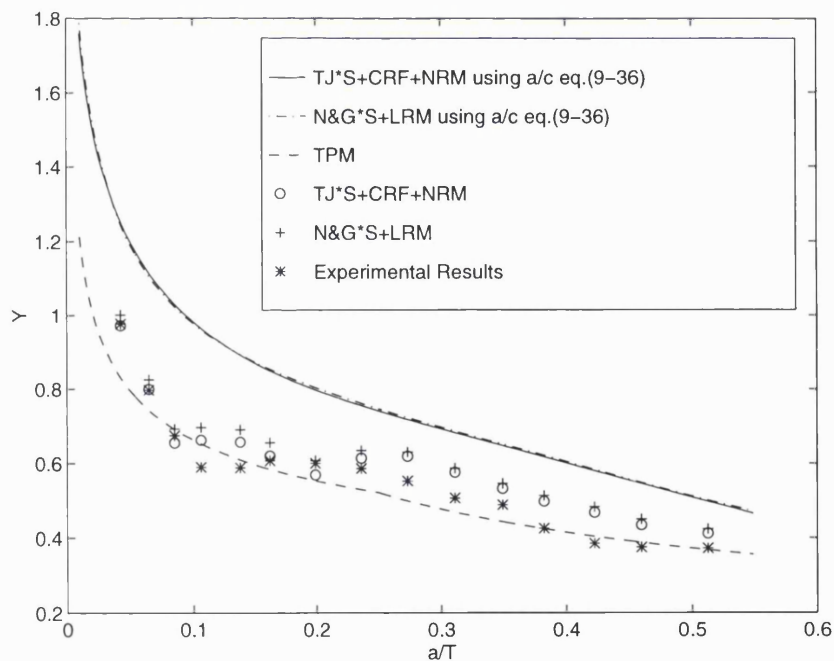


Figure 9.14 Comparison of Deepest Point SIF Predictions from N&G*S, TJ*S and TPM for Semi-elliptical Cracks in Tubular Welded Joint(T4b-DT) under OPB Loading ($\alpha=33^\circ$, $p/T=0.079$ and $L/T=1.5$)

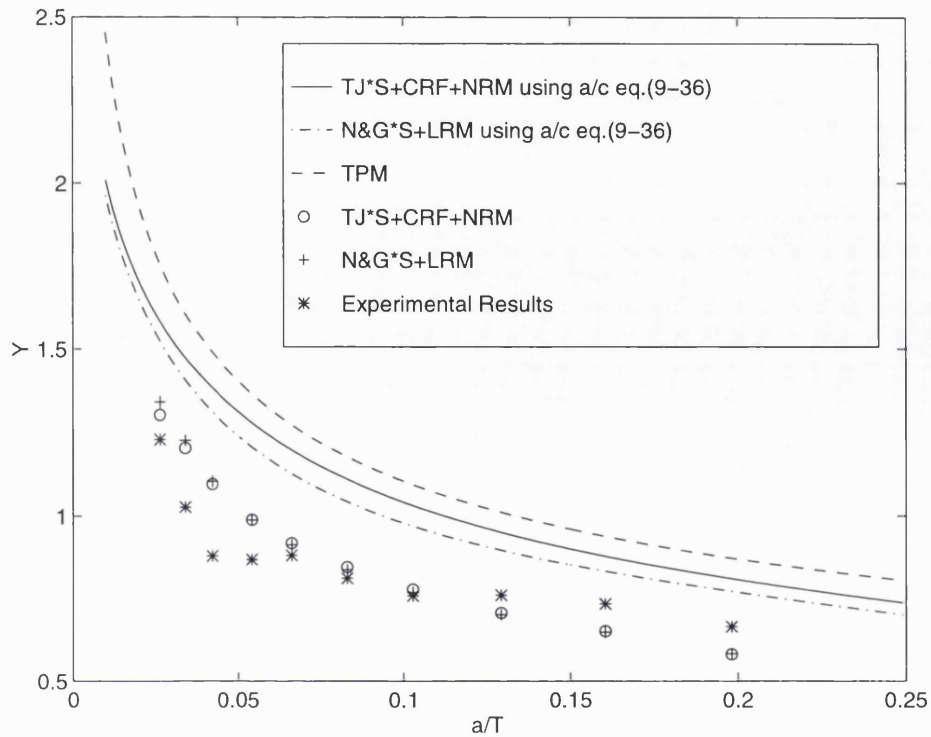


Figure 9.15 Comparison of Deepest Point SIF Predictions from N&G*S, TJ*S and TPM for Semi-elliptical Cracks in Tubular Welded Joint(Y1a-M) under OPB Loading ($\alpha=40^\circ$, $\rho/T=0.051$ and $L/T=1.0$)

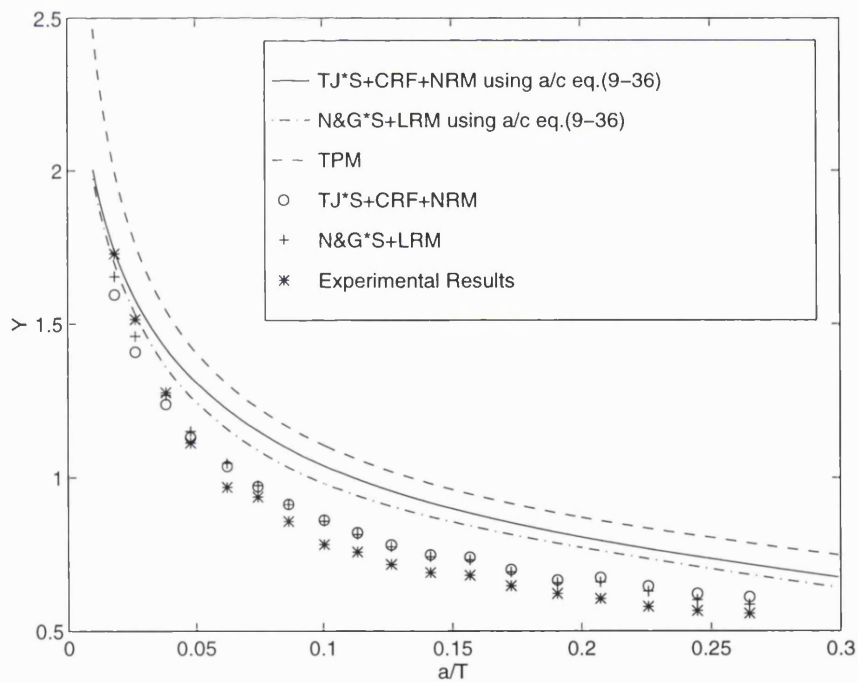


Figure 9.16 Comparison of Deepest Point SIF Predictions from N&G*S, TJ*S and TPM for Semi-elliptical Cracks in Tubular Welded Joint(Y1c-M) under OPB Loading ($\alpha=41^\circ$, $\rho/T=0.059$ and $L/T=1.0$)

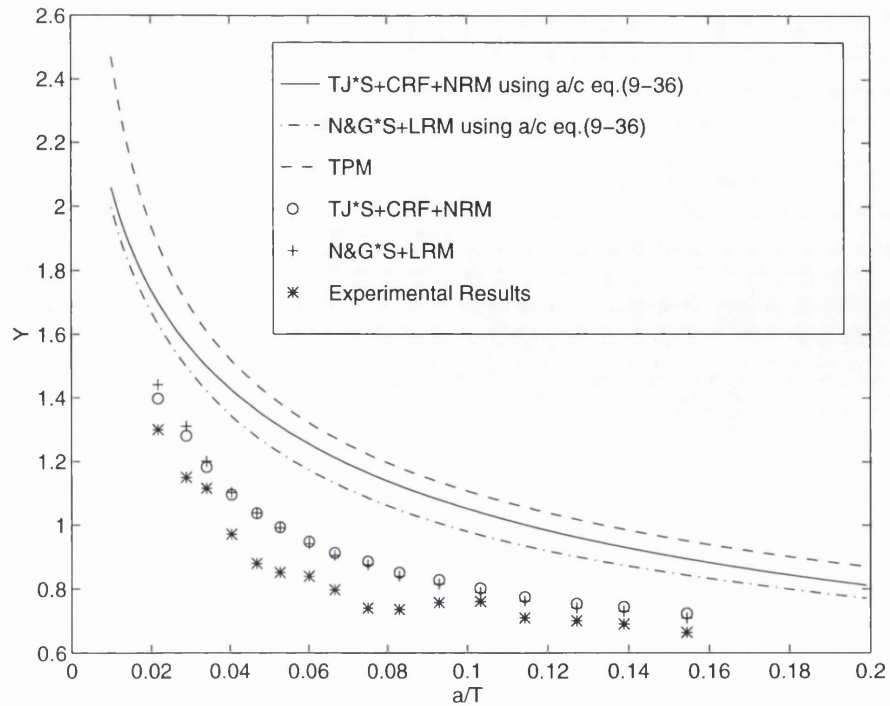


Figure 9.17 Comparison of Deepest Point SIF Predictions from N&G*S, TJ*S and TPM for Semi-elliptical Cracks in Tubular Welded Joint(Y2a-M) under OPB Loading ($\alpha=41^\circ$, $p/T=0.043$ and $L/T=1.0$)

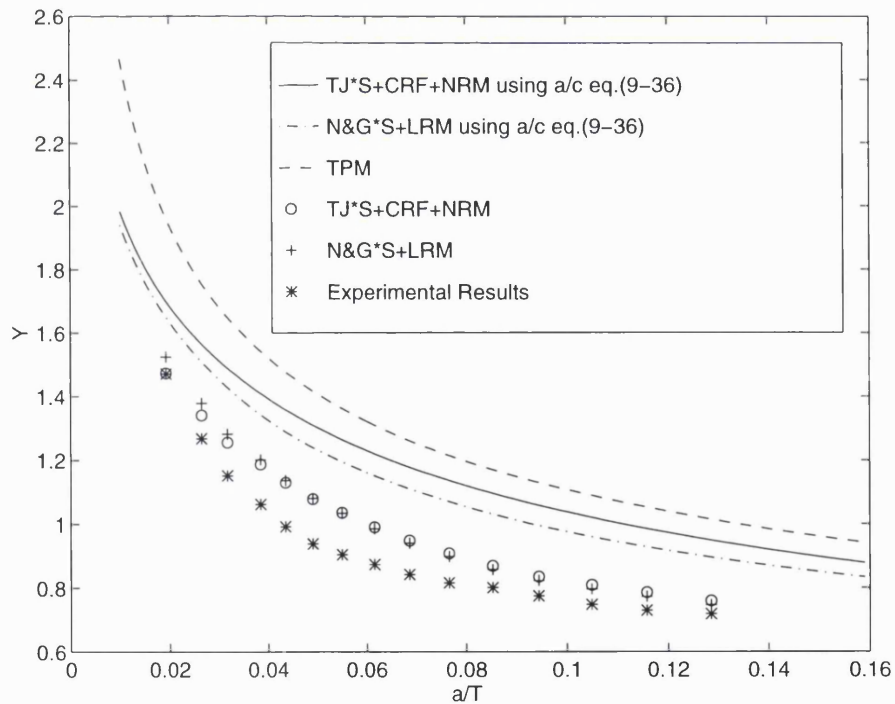


Figure 9.18 Comparison of Deepest Point SIF Predictions from N&G*S, TJ*S and TPM for Semi-elliptical Cracks in Tubular Welded Joint(Y2c-M) under OPB Loading ($\alpha=39^\circ$, $p/T=0.052$ and $L/T=1.0$)

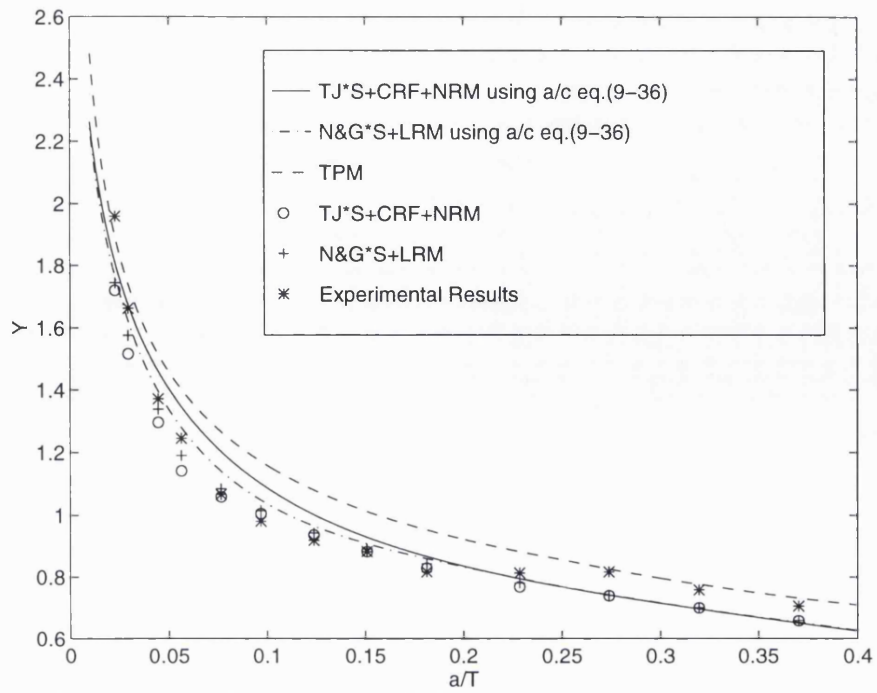


Figure 9.19 Comparison of Deepest Point SIF Predictions from N&G*S, TJ*S and TPM for Semi-elliptical Cracks in Tubular Welded Joint(T1-M) under IPB Loading ($\alpha=54^0$, $\rho/T=0.04$ and $L/T=1.125$)

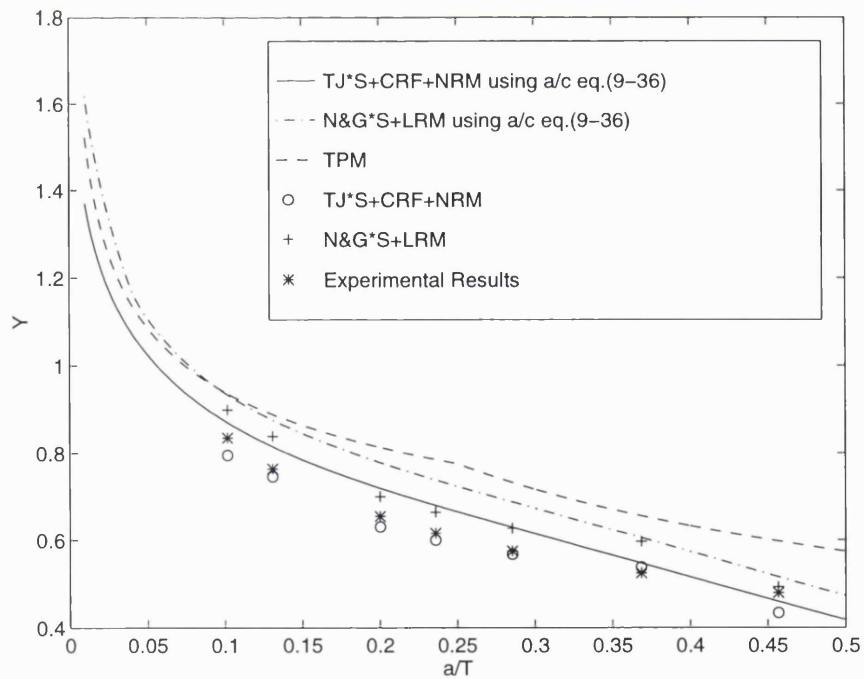


Figure 9.20 Comparison of Deepest Point SIF Predictions from N&G*S, TJ*S and TPM for Semi-elliptical Cracks in Tubular Welded DT-Joint(S) under OPB Loading ($\alpha=23^0$, $\rho/T=0.111$ and $L/T=2.632$)

CHAPTER TEN

CONCLUSIONS

10.1 Overall Summary

Fatigue damage has been recognised as one of most important failure modes for offshore tubular joints in the hostile North Sea environment. Periodic inspection using NDT techniques is necessary to ensure the integrity of offshore platform. Given crack detection, remedial methods such as grinding can be used to extend the life before the fatigue crack reach an unacceptable size. The methodology of non-destructive fatigue strength assessment for offshore tubular joints is illustrated in Figure 10.1. An appropriate inspection, repair and maintenance strategy relies on the accuracy of stress and fracture mechanics modelling to predict the fatigue crack growth behaviour and the ability of non destructive techniques to reliably detect and size fatigue cracks in tubular welded joints. Research work on these areas was reviewed in Chapter 1. It was concluded that more basic information and tools are needed in order to derive more advanced fatigue strength modelling and apply the sophisticated methodology to offshore structures.

Aiming toward this purpose, comprehensive parametric studies have been conducted on the major areas of non-destructive fatigue strength evaluation of offshore welded tubular joints. As a result, these studies have produced much useful information in the form of databases and parametric equations and they are fully reported in the preceding chapters(Figure 10.1). A summary of these developments are given below in turn.

NDT Measurement and Underwater Inspection Reliability

- i) Fatigue cracks on tubular welded joints were re-measured using MPI, ACPD and ACFM techniques in order to clarify some UCL crack library characterisation data. The effect of using different versions of WAMI(ACFM crack detection and sizing software) and sizing procedures for the underwater ACFM results were investigated. The results showed that the sizing accuracy of ACFM technique depends on not only the theoretical model but also the correct procedures to interpret ACFM inspection results.
- ii) The underwater POD trials results for ACFM and MPI were compared. The POD performance for these two techniques is close. The ACFM technique is preferred to use as this technique offers many benefits to industries for the inspection of offshore structures. However, it does sometimes miss small cracks near the end of a long crack.

iii) The UCL underwater non destructive inspection reliability trial results (POD data) were re-analysed to make them suitable for reliability fracture mechanics procedures for the first time. A new crack classification D was suggested. The POD in terms of both the crack length and the maximum crack depth for MPI and two well-known eddy current systems (Hocking and EMD III) using classification B, B1 and D were produced. These data, especially the crack depth based POD data, formed the inspection reliability database and were incorporated into the UCL Reliability based Inspection Scheduling (RISC) system for reliability fracture mechanics based inspection planning of offshore jacket structures.

Stress Analysis of Tubular Welded Joints

Many sets of stress parametric equations have been derived for tubular welded joints during the last two decades. Except for the UCL HCD equations, all these equations can only be used to predict hot spot SCFs. However, for the fracture mechanics calculation of remaining life for in-service cracked joints, information is required on the magnitude and distribution of the stress acting along the anticipated crack path, not just the peak stress at one location. Thus it was necessary to derive parametric equations which can predict the full two dimensional stresses for tubular joints. For this reason, comprehensive thin shell finite element analyses were conducted for 660 tubular X and DT, Y and T-joints typical of those used in offshore structures, subject to principal modes of loading. The results from this work have been used to produce by regression analysis a family of stress parametric equations as a function of non-dimensional joint geometric ratios α , β , γ , τ and θ . They are listed in Table 10.1 and summarised below.

I) Comprehensive stress parametric equations were derived for tubular X and DT-joints. They can be used to predict SCFs and DoBs at all critical positions for each mode of loading, for both chord and brace, as well as the angular location of the hot-spot stress site around the intersection. Furthermore, the parametric equations to predict the full stress distribution along the intersection were also derived as a function of non-dimensional joint geometric ratios α , β , γ , τ and θ for each mode of loading. They can be used to predict the normalised distribution but also provide an alternative method for calculation of hot spot SCFs. This set of parametric equations has been assessed by comparing the predicted values with results from steel and acrylic model tests and also with the predictions from existing parametric formulae given in the literature. All these equations are directly compatible with each other. Thus the full two dimensional stress distribution can be recreated for tubular X and DT-joints.

ii) So far, the UCL HCD equations are the only ones which can predict not only hot spot SCFs but also the degree of bending and the characteristic stress distribution for tubular Y and T-joints. However, they were not recommended for estimating hot spot SCFs as they were

borderline in terms of the proposed acceptance criteria(they were unconservative at the chord saddle under axial loading). The problem with the UCL HCD stress distribution equations is that they were derived by observing a limited number of typical sample results rather than whole database and therefore they can not provide enough accuracy to all other cases for detailed analyses. Thus it was desirable to enhance the capability of this set of equations.

For this reason, systematic thin shell finite element analyses have been conducted for tubular Y, T-joints following similar procedures for tubular X and DT-joints. A regression analysis of the computed results has been carried out to produce a new set of parametric equations. This set of equations can be used to predict the full SCF distribution along both chord and brace toe for each mode of loading. The validation against experimental data has shown that they can provide SCF distribution predictions along the intersection under all modes of loading with reasonably good accuracy. Moreover, the results of assessment indicate that this set of equations also has the capability to reliably estimate the hot spot SCFs on both brace and chord toes under all modes of loading except for the chord saddle under OPB loading. For this particular case, the HCD SCF parametric equations can be used instead. Thus, combining this new set of equations with the original UCL HCD DoB and SCF(only for the chord saddle under OPB loading) equations, one can predict the full two dimensional stress distribution at any location around the tubular intersection.

iii) A new concept, i.e. stress distribution concentration factor(SDCF), was proposed to characterise the degree of concentration(or the spread) of stress distribution along the intersection. Based on the systematic finite element database, parametric equations were derived to predict average SCF and SDCF for Y and T, X and DT-joints. Availability of the parametric equations to predict average SCF would promote the use of the fast empirical fatigue crack growth modelling such as the AVS and TPM models. The average SCF and SDCF can also be used to estimate stress distributions at the design stage and used to develop advanced fracture mechanics modelling. Furthermore, it is extremely valuable to the overall methodology that these parameters could be used as an alternative to the single value of hot spot stress for evaluating stress/life or remaining life(fatigue crack growth) as they provide the measurement on magnitude and spread of the stress distribution around the intersection of tubular joint.

As a summary, comprehensive stress parametric equations were derived for tubular Y, T, X and DT-joints. These equations can be used to recreate the two dimensional stress distribution around intersection. They are valuable for multiple-axis stress analysis, fatigue design, fatigue strength assessment and fatigue crack growth analysis(e.g. application of advanced fracture mechanics modelling, especially for those considering 2D stress distribution).

SIF Parametric Equations for Semi-elliptical Surface Cracks in Welded Joints

Based on the weight function approach, a series of SIF parametric equations was derived for the deepest and surface point of semi-elliptical surface cracks in T-butts and deepest point of semi-elliptical surface cracks in tubular welded joints, by using the UCL database of T-butt through wall stress analysis results. These equations are listed in Table 10.2 and summarised as follows in turn.

i) Using the three dimensional Niu-Glinka weight function and the stress analysis results for T-butts, the new SIF parametric equations have been derived for the deepest point of semi-elliptical cracks for T-butts under tension and bending loading. Apart from a number of factors such as crack shape ratio, weld angle, weld radius, these solutions also include the effect of attachment width. The predictions from these equations were validated against known finite element results and predictions from Mk factor approach as given in PD 6493.

ii) The SIF parametric equations for the surface point of semi-elliptical cracks for T-butts under tension and bending loading were derived by combining the Wang Lambert surface point weight function for semi-elliptical cracks in plates and the T-butt through wall stress analysis results. The validation of this set of SIF parametric equations was conducted by comparing the predictions with finite element analysis results from literature. Given the simple modification factors, they give quite accurate estimations and can be used to predict the fatigue crack growth along the welds. Combination of this set of equations with the deepest point SIF equations, such as those derived in chapter 7, allows one to predict the fatigue crack shape development in T-butt welded joints.

iii) Using the Wang-Lambert thin pipe weight function as reference data and assuming that the contributions of the weldment geometry to the SIF for edge cracks in plates is the same as those of semi-elliptical cracks in thin pipes, a new weight function for the deepest point of a semi-elliptical surface crack at the saddle of tubular welded joints was derived. Combining this new weight function and the UCL database of T-butt through wall stress analysis results, a new set of SIF parametric equations(TJ*S) in the form of continuous single functions was derived for tension and bending. With the DoB information and a suitable load shedding model, they can be used to predict SIFs for fatigue cracks in tubular joints.

Available UCL in-air tubular joint fatigue test results, especially early crack growth data, were used to validate this new model. Considering the curvature of tube, TJ*S works very well with the non-linear load shedding relationship derived from line spring finite element analysis(Du and Hancock 1989). In conjunction with the constant force release(CRF) and non-linear moment(NRM) release models, a new model(TJ*S+CRF+NRM) has been developed for predicting the deepest point SIF for semi-elliptical surface fatigue cracks in tubular welded joints.

The predictions from this model agree very well with the experimental results, especially for early fatigue crack growth. In one case (Figure 9.20), the results showed that the predictions from this model are more accurate than those from the N&G*S+LRM when compared with experimental data. This new model can incorporate the influence of the local weld geometry and allows a rapid modelling of fatigue crack growth in tubular welded joints.

In overall terms, this study has produced an improved underwater NDT Inspection reliability database and new parametric equations for predicting stresses in tubular joints and SIFs of semi-elliptical surface cracks in welded joints. They can be used for non destructive evaluation of fatigue strength of offshore tubular welded joints. Availability of these tools also creates the base to develop more sophisticated methodology. It will lead to a better understanding of fatigue crack growth in tubular welded joints and, in turn, permits more rational inspection scheduling to be planned with respect to the assessment of fatigue cracks in offshore structures, including decision on potential remedial work.

10.2 Recommendations for Further Research

Recommendation for future work that would contribute to a better understanding of the fatigue properties of tubular joints based on the understanding of this study are outlined below:

Stress Parametric Equations for Tubular Joints:

- a) Extending comprehensive finite element stress studies to K and KT and furthermore multiple-plane joints.
- b) Improving the accuracy of stress parametric equations by fitting the finite element database with available steel and acrylic test results together in order to reduce the uncertainty when used for predicting fatigue life.

Fatigue Design of Offshore Tubular Joints

The accuracy of using S-N curve, such as T' curve to predict fatigue life, can be improved by deriving the semi-empirical fatigue life equation based on experimental data which incorporate not only the hot spot SCF, but also the DoB, \overline{SCF} and SDCF to consider the stress variations through the wall thickness and along the intersection.

Tools for Whole Methodology

An artificial neural network (ANN) neural network can be used to fit the computational and experimental data into parametric equations and empirical relationships for examples the SCF and DoB equations, and fatigue crack growth rate.

Table 10.1 Stress Parametric Equations for Simple Tubular Joints

Parametric Equations	Type of Simple Tubular Joint	
	T/Y	DT/X
Hot spot SCFs	Hellier Connolly and Dover 1990	Appendix A
DoB	Connolly et al 1990	Appendix B
SCF Distributions	Appendix D	Appendix C
Average SCF	Appendix E	Appendix F
SDCF	Appendix G	Appendix H

Table 10.2 SIF Solutions for Semi-elliptical Cracks in Welded Joints

Parametric Equations	Type of Welded Joints	
	T-Butts	Tubular Joints
Deepest Point SIF	Appendix I	Appendix K
Surface Point SIF	Appendix J	Rhee et al 1991

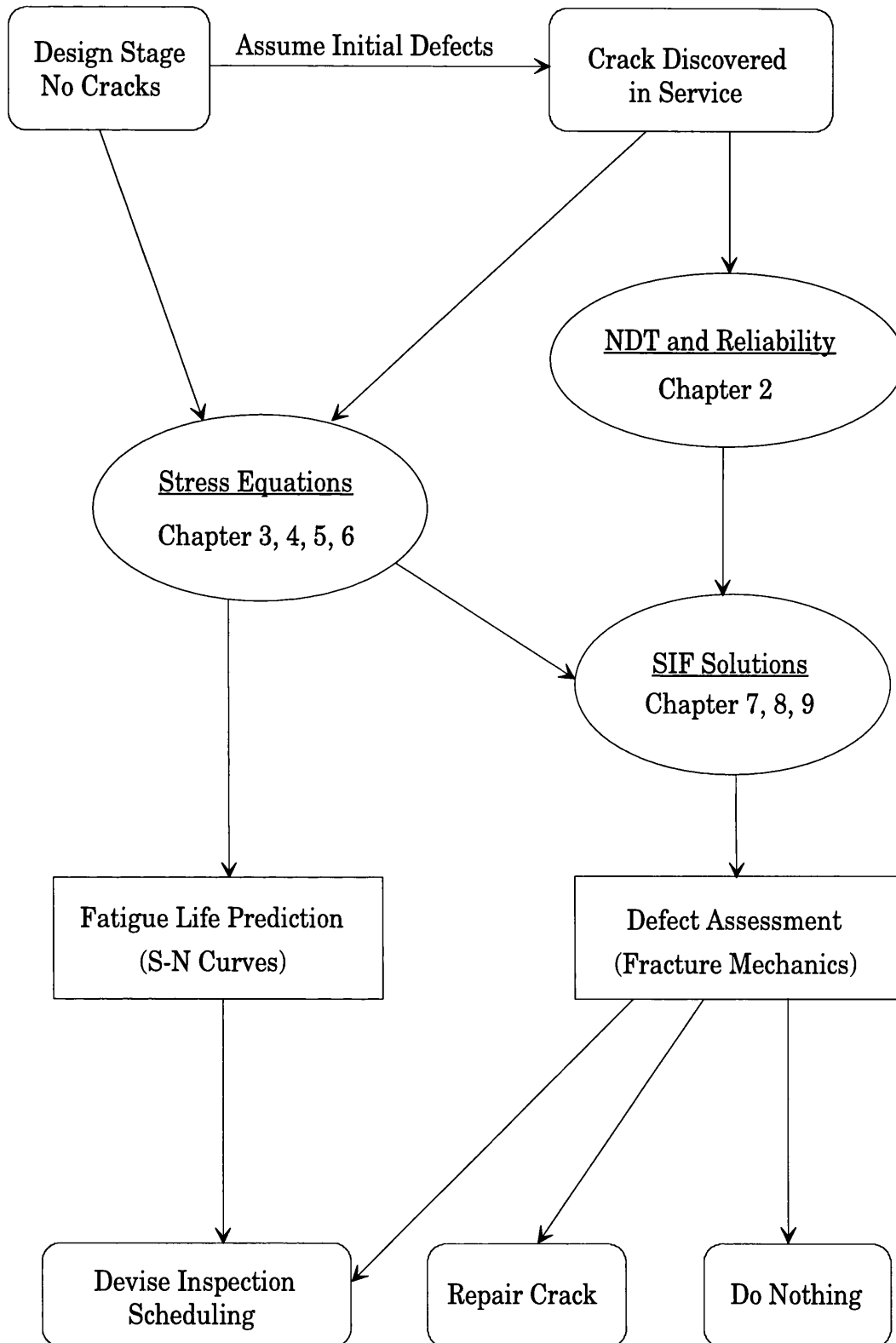


Figure 10.1 Illustration of Non-Destructive Fatigue Strength
Assessment Methodology for Offshore Tubular Joints

References

- Aaghaakouchak, A. (1989), Fatigue Fracture Mechanics Analysis of Ring-Stiffened and Simple Tubular Joints for Offshore Structure, PhD Thesis, University of London 1989.
- Ahmad S, Irons B.M. and Zienkiewicz O.C. (1970), "Analysis of Thick and Thin Shell Structures by Curved Elements", *IJNME* 2, pp. 419-451, 1970.
- American Petroleum Institute(API) (1993), *Recommended Practice for Planning, Design and Constructing Fixed Offshore Platforms*, API RF2A 20th Edition, 1993.
- American Welding Institute(AWI) (1984), Structural Welding Code AWS D1.1-84, 1984.
- Austin, J.A., " The Role of Corrosion Fatigue Crack Growth Mechanisms in Predicting the Fatigue Life of Offshore Tubular Joints", PhD Thesis, University College London. October, 1994.
- Bell, R., "Determination of Stress Intensity Factors for Weld Toe Defects", final report BSS 22ST, 23440-2-1083/7, Faculty of Engineering, Carlton University, Ottawa, Canada, October 1985.
- Berge, S. (1985), "On the Effect of Plate Thickness in Fatigue on Welds", *Engineering Fracture Mechanics*, Vol. 21, No. 2, pp423-435, 1985.
- Bijlaard, P.P., August (1955), "Stress from Local Loadings in Cylindrical Pressure Vessels", *Transaction ASME*, 1955.
- Brennan, F.P. (1994), "Evaluation of Stress Intensity Factors by Multiple Reference State Weight Function Approach", *Theoretical and Applied Fracture Mechanics*, Vol. 20, pp249-256, 1994.
- Brennan, F.P., Dover, W.D., Kare, R.F. and Hellier A.K. (1995), "Development of Parametric Equations for Weld Toe Stress Intensity Factors", The Atomic Energy Authority's Marine and Technology Support Unit, Project No 8707-HSEP3317, Culham, UK, 1995.
- Bueckner, H.F. (1970), "A Novel Principle for the Computation of Stress Intensity Factors", *Zeitschrift der Angewandte Mathematik und Mechanik*, 50, pp. 529-546, 1970.
- Bueckner, H.F. (1971), "Weight Function for the Notched Bar", *Zeitschrift Angewandte und Mechanik*, 51, pp. 97-109, 1971.
- CAN/CSA-S473-92 (1992), *Steel Structures, Code for the Design, Construction and Installation of Fixed Offshore Structures*, June 1992.
- Carter, R.M., Marshall, P.W., Swanson, T.M., and Thomas, P.D. (1969), "Material Problems in Offshore Platforms." OTC 1043, Proc., First Annual Offshore Technology Conference, Houston Vol. 1. II, 443-470, May 1969.
- Chang, E., Rudlin, J.R. and Dover, W.D. (1991 a), "POD Trial Results using a New Classification", NDE Centre Internal Report, September 1991.
- Chang, E., Rudlin, J.R. and Dover, W.D. (1991 b), "Further POD Trial Results in Classification D", NDE Centre Internal Report, September 1991.

Chang, E and Dover, W.D. (1991 c), "MPI POD Trial Results Using a New Classification", NDE Centre Internal Report, December 1991.

Chang, E and Dover, W.D. (1992 a), "Hocking Eddy Current Inspection POD Trial Results Using a New Classification", NDE Centre Internal Report, January 1992.

Chang, E and Dover, W.D. (1992 b), "EMD III Eddy Current Inspection POD Trial Results Using a New Classification", NDE Centre Internal Report, February 1992.

Chang, E., Rudlin, J.R. and Dover, W.D. (1992 c), "Crack Measurement", NDE Centre Internal Report, March 1992.

Chang, E., Rudlin, J.R. and Dover, W.D. (1992 d), "Comparison of the Underwater ACFM Sizing Results using Different WAMI Versions", NDE Centre Internal Report, March 1992.

Chang, E and Dover, W.D. (1992 e), "Draft Report for MPI POD Trial Results", NDE Centre Internal Report, November 1992.

Chang E. and Dover, W. D. (1992), "Inspection Reliability Database", Chapter 5.3, Section 2: Theory, Reliability based Inspection Scheduling for Fixed Offshore Platforms, THERMIE Project OG/0019/90/UK-IT-NL.

Chang E. and Dover, W. D. (1996), "Stress Concentration Factor Parametric Equations for Tubular X and DT-Joints", Int. J. Fatigue Vol. 18, No. 6, pp363-387, 1996.

Cheaitani, M.J., Thurlbeck, S.D. and Burdekin, F.M. (1995), "Fatigue, Fracture, and Plastic Collapse of Offshore Tubular Joints using BSI PD 6493:1991", OMAE, 1995.

Clayton, A.M. and Irine, N.M. (1978), "Stress Analysis Methods for Tubular Connections", Paper 30, European Offshore steels Research Seminar, 1978.

Connolly, M.P.M. (1986), A Fracture Mechanics Approach To the Fatigue Assessment of Tubular Welded Y and K Joints, PhD Thesis, University of London, 1986.

Connolly, M.P.M., Hellier, A.K., Dover, W.D. and Sutomo, J. (1990), "A Parametric Study of the Ratio of Bending to Membrane Stress in Tubular Y- and T-Joint", Int. J. Fatigue, Vol. 12, No. 1, 1990, pp 3-11.

Department of Energy (1983), Background Notes to the Fatigue Guidance of Offshore of Offshore Tubular Joints, HMSO, London, 1983.

Department of Energy (1984 a), Offshore Installations: Guidance on Design, Construction and Certification, third Edition, London, 1984.

Department of Energy (1984 b), "Background to new fatigue design guidance for steel welded joints in offshore structures", HMSO, 1984

Dharmavasan, S. (1983), "Fatigue Fracture Mechanics Analysis of Tubular Welded Y-Joints", PhD Thesis, University College London, 1983.

Dharmavasan, S., Dover, W.D. (1988), "Nondestructive Evaluation of Offshore Structures using Fracture Mechanics", Applied Mechanics Review, Vol. 41, No. 2, February, 1988.

Dijkstra, O.D. (1981), "Comparison of Strain Distribution in Three X Joints Determined by Strain Gauge Measurements and Finite Element Calculations", Paper TS6.2, Steel in Marine Structures, Paris, October 1981.

Dijkstra, O.D., Snijder, H.H., Van Straalen, I.J. (1989), "Fatigue Crack Growth Calculations using Stress Intensity Factors for Weld Toe Geometries", OMAE Conference Proceeding, The Hague, 1989.

Dijkstra, O.D., Straalen I.J. and Noordhoek C. (1993), "A fracture Mechanics Approach of Fatigue of Welded Joints in Offshore Structures", OMAE Conference Proceeding, Vol. III-B, 1993.

Doonnel, L.H. (1934), "Stability of Thin Walled Tubes under Torsion", Nat. Adv. Committee on Aeronautics (NASA), Report No. 479, 1934.

Dover W. D., Petrie J. R. (1976), "In-Plane Bending Fatigue of a Tubular Welded T Joints", Proc. Int. Conf. on Fatigue Testing and Design, SEE, Vol. 1, Paper 19, London, 1976.

Dover, W.D. and Connolly, M.P.M. (1986), "Fatigue Fracture Mechanics Assessment of Tubular Welded Y and K Joints", Int. Conf. on Fatigue and Crack Growth in Offshore Structures, I Mech E, London, 1986.

Dover, W.D. and Dharmavasan S. (1987), "Fatigue Fracture Mechanics Analysis of T and Y Joints", Proc. 14th Offshore Technology Conference, Houston 1987.

Dover, W.D., Niu, X., Aaghaakouchak, A., Kare, R. and Topp, D.A. (1988), "Fatigue Crack Growth in X Joints and Multi-Brace Nodes", Proc. of Conference (Fatigue of Offshore Structures), London, 1988.

Dover, W.D. (1992), "Degree of Bending", UCL NDE Centre News, May 1992.

Dover, W.D., Chang, E. and Rudlin, J.R. (1994), "Underwater Inspection Reliability for Offshore Structures", Presented on 1994 OMAE.

Du, Z.Z., Hancock, J.W. (1989), "Moment and Force Release Calculations for Tubular Welded Joints", Report to the Fatigue Software Working Group, May, 1989.

Dundrova, V. (1965), "Stress at Intersection of Tubes: Cross and T-Joints", SFRL Tech. Report, Structures Fatigue Research Laboratory, Dept. of Civil Engineering, U. of Texas, Austin, July 1965.

Efthymiou, M., Durkin F. (1988), "Development of SCF Formulae and Generalised Influence Functions for use in Fatigue Analysis". OTJ Conference, Surrey, 1988.

Eide, O.I., Skallerud, B. and Berge, S. 1993, "Fatigue of Large Scale Tubular Joints - Effects of Sea Water and Spectrum Loading", Proceedings of Fatigue under Spectrum Loading and in Corrosive Environments Conference, 26-27th August 1993, The Technical University of Denmark, Lyngby.

Etube, L. (1996), Private communication, University College London, 1996.

Fatigue Handbook (1985), (Offshore Steel Structure), Edited by A. Almar-Nøβss, 1985.

Fatigue of Offshore Structures (1988), ed. by W. D. Dover and G.. Glinka, Engineering materials Advisory Services Ltd., Warle, United Kingdom, 1988.

Fett, T., Mattheck, C. and Munz., D. (1987), "On the Calculation of Crack Opening Displacement from the Stress Intensity Factor", *Engineering Fracture Mechanics*, Vol. 27, pp697-715, 1987.

Flugge, W. (1934), Statik and Dynamik der Shalen, Springer, Berlin, 1934.

Gibstein, M B (1978), "Parametrical Studies of T-Joints", European Offshore Steels Research Seminar, Cambridge, Nov., 1978.

Gibstein, M.B. (1981), "Stress Concentration in Tubular Joints, Its Definitions, Determination and application", *Proc. Int. Conf. Steel in Marine Structures*, ECSC, Paris, 1981.

Greimann. L.F., De hart, R.C., Blackstone, W.R., Stewart, B., Scalees, R.E. (1973), "Finite Element Analysis of Complex Joints", *Proc. Int. Offshore Tech. Conf. Paper OTC 1823*, Houston, 1973.

Gurney, T.R. (1979), "The Inference of Thickness on the Fatigue Strength of Welded Joints", paper 41, BOSS Conference, London, August 1979.

Hall, M.S., Topp, D.A. and Dover, W.D. (1990), "Parametric Equation for Stress Intensity Factors", Technical Software Consultants Ltd., Report No. TSC/MSH/0224 for Department of Energy, March 1990.

Hamilton, W (1984), "The Structural Integrity of Tubular Joints", MSc Thesis, University College London, Sept., 1984.

Haswell, J. and Dover, W.D. (1991), "Stress Intensity Factor Solutions for Tubular Joints(FACTS)", 1991 OMAE, Vol. III-B, Materials Engineering, ASME, 1991.

Haswell, J. and Hopkins, P. (1991), "A Review of Fracture Mechanics Models of Tubular Joints", *Int. J. of Fatigue and Fracture Engineering Materials and Structures*, Vol. 14, No. 5, pp. 483-497, 1991.

Health and Safety Executive(HSE) Report, OTH 87 265 (1987), United Kingdom Offshore Steels Research Project - Phase II, Final Summary Report, Her Majesty's Stationery Office, London, 1987.

Health and Safety Executive(HSE) Report, OTH 88 282 (1988), United Kingdom Offshore Steels Research Project - Phase I: Final Report, ed. R Peckover, , Her Majesty's Stationery Office, London, 1988.

Health and Safety Executive (1990), Offshore Installations: Guidance on Design, Construction and Certification, fourth Edition, , London, 1990.

Health and Safety Executive (1995), Offshore Installations: Guidance on Design, Construction and Certification. Third Amendment to Fourth Edition, London, 1995.

Hellier A.K., Connolly M.P. and Dover W.D. (1990 a), "Stress Concentration Factors for Tubular Y and T Joints", *Int. J fatigue*, Vol. 12, No. 1, pp 13-23, 1990.

Hellier, A.K., Connolly, M.P., Kare, R.F., and Dover, W.D. (1990 b), "Prediction of the Stress Distribution in Tubular Y- and T-joints", *Int. J Fatigue* Vol. 12, No. 1, pp 25-33, 1990.

Hibbitt Karlsson & Sorensen(HKS) Inc. (1992 a), ABAQUS/Standard, User's Manual, Version 5.2, 1992.

Hibbitt Karlsson & Sorensen(HKS) Inc. (1992 b), ABAQUS/Post, Manual, Version 5.2, 1992.

Hoff, N.J. et al (1953), "Deformation and Stresses in Circular Shells Caused by Pipe Attachments", Knolls Atomic Power Laboratory, Reports KAPL 921-926 and 1025, Nov. 1953.

Holdbrook, S.J. and Dover, W.D. (1979), "The Stress Intensity Factors for A Deep Surface Cracks in a Finite Plate", *Engineering Fracture Mechanics*, Vol. 12, 1979.

Huang, X. and Hancock, J.W. (1988), "The Stress Intensity Factors of Semi-Elliptical Cracks in a Tubular Welded T-Joint under axial loading", *J. Engng Fract. Mech.*, 1, pp. 25-35, 1988.

Irons B.M. (1976), "The Semiloof Shell Element Chapter 11" in Finite Element for Thin shells and Curved Membranes, edit by Ashwell D.G. and Gallagher R.H., Wiley, 1976.

Irvine, N.M. (1981), "Review of Stress Analysis Techniques Used in UKOSRP I", *Fatigue in Offshore Structural Steels*, Proceedings of a Conference Organised by the Institution of Civil Engineering, London, February 24-25 1981.

Irwin, G.R. (1962), "Crack Extension Force for a Part-Through Crack in a Plate", *J. of Applied Mechanics*, ASME, Vol. 29, No. 4, 1962.

Kam, J.C.P., Topp, D.A. and Dover, W.D. (1987), "Fracture Mechanics Modelling and Structural Integrity of Welded tubular Joints in Fatigue", *Proc. 6th Int. Symp-OMAE*, ASME, Houston 1987.

Kam, J.C.P. (1989), "Structural Integrity of Offshore Tubular Joints Subject to Fatigue", PhD Thesis, University of London, 1989.

Kam, J.C.P. (1989), "A Study of the Effect of Releasing Tensile/Bending Stress Components in Fatigue Crack Growth Predictions", *Special Report(2) to Fatigue Software Working Group (FACTS)*, 1989.

Kare, R.F. (1989), "Influence of Weld Profile on Fatigue Crack Growth in Tubular Welded Joints", PhD Thesis, The City University, London, 1989.

Kellogg, Col M.W. (1956), Design of Piping System, 2nd. ed., Wiley, 1956.

Kuang, J.G., Potvin, A.B. (1975), "Stress Concentrations in Tubular joints", *Proc. Int. Offshore Tech. Conf.*, Paper OTC 2609, Houston, 1975.

Kuang, J G et al. (1977), "Stress Concentration in Tubular Joints", *Society of Petroleum Engineers*, 1977.

Levy, N., Marcal, P.V., Ostergren, W. and Rice, J. (1971), "Small Scale Yielding near a Crack in Plane Strain: a Finite Element Analysis", *Int. J. Frac. Mech.*, Vol. 7, No. 2, pp143-157, 1971.

Maddox, S.J. (1975), "An Analysis of Fatigue Cracks in Fillet Welded Joints", *Int. J. Fracture*, 1975, Vol. 11, No. 2, pp221-243, 1975.

MaTSU (1996), "Fatigue Background Guidance Document", by HSE Books as a Offshore Technology Report, 1996.

Miner, M.A. (1945), "Cumulative Damage in Fatigue", *J. of Applied Mechanics*, Vol. 112, pp A159-A164, 1945.

Minitab Inc. (1991), *MINITAB Reference Manual*(Version 8), 3081 Enterprise Drive, State College, PA 16801, Nov., 1991.

Monahan, C. C., Rudlin, J.R. and Dover, W.D. (1991), "Library Partial Replacement Project", NDE Centre Internal Report, November 1991.

Monahan, C. C. (1994), "Early Fatigue Crack Growth in Offshore Structures", PhD Thesis, University College London, May 1994.

Mshana, Y. (1993), "The Influence of Multiple Axis Fatigue Loading on Structural Integrity of Offshore Tubular Joints", PhD Thesis, City University, June 1993.

Murakami, Y. (1987), *Stress Intensity Handbook*, Ed., Pergamon Press, 1987.

Myers, P. (1996), Private communication, University College London, 1996.

Newman, J.C. and Raju, I.S. (1981), "An Empirical Stress Intensity Factor Equation for the Surface Crack", *Engineering Fracture Mechanics*, Vol. 15, NO. 1-2, pp 185-192, 1981.

Newman, J. C. and Raju, I. S. (1986), "Stress Intensity Factors Equations for Cracks in three dimensional finite bodies subjected to tension and bending loads", *Computational Methods in the Mechanics of Fracture*, Edited by Naluri, pp311-334, North-Holland, Amsterdam, 1986.

Niu, X. (1987), "Effect of Local Stresses on Fatigue Strength of Tubular Welded Joints", PhD Thesis, University of London, 1987.

Niu, X. and Glinka, G., (1987), "The Weld Profile Effect on Stress Intensity Factors in Weldments", *Int. J. of Fracture*, 35 pp 3-20, 1987.

Niu, X. and Glinka, G. (1989), "Stress Intensity Factors for semi-elliptical Surface Cracks in Welded Joints", *Int. J. Fracture*, Vol. 40, pp 255-270, 1989.

Niu, X. and Glinka, G. (1990), "Weight Functions for Edge and Surface Semi-elliptical Cracks in Flat Plates and Plates with Corners", *Engineering Fracture Mechanics* Vol. 36, No. 3, pp459-475, 1990.

Nykanen, T, " On the Effect of Weld Shape on the Crack Shape Development at the Toe of Fillet Weld", Department of Mechanical Engineering, Lappeenranta University of Technology, Finland, 1987.

- Ojdrovic Rasko, P. and Petroski, H.J. (1991), "Weight Functions from Multiple Reference States and Crack Profile Derivatives", *Engineering Fracture Mechanics*, Vol. 39, pp105-pp111, 1991.
- Oore, M. and Burns, D.J. (1980), "Estimation of Stress Intensity Factors for Irregular Cracks Subjected to arbitrary Normal Stress Field", *Proc. 4th Int. Conf. on Pressure Vessel Technology*, London, I. Mech. E., Vol. 1, 1980.
- Pang, H.L. (1990), "A Review of Stress Intensity Factors for a Semi-elliptical Surface Crack in a Plate and Fillet Welded Joint", *Welding Institute Members Report* 426, 1990.
- Paris, P.C. and Erdogan, F. (1963), "A Critical Analysis of Crack Propagation Laws", *Trans. ASME J. of Bas. Engineering*, 85, 1963.
- Parks, D.M. (1974), "A Stiffness Derivative Finite Element Technique for Determination of Elastic Crack Tip Stress Intensity Factors ", *Int. J. of Fracture*, 10, pp. 487-502, 1974.
- Parks, D.M. and White, C.S. (1982), "Elastic Plastic Line-Spring Finite Elements for Surface-Cracked Plates and Shells", *Trans. ASME, J. Press. Vess. Tech.*, Vol. 104, No. 4, pp. 287-292, Nov., 1982.
- Parkhouse, J.G. (1981), "Improved Modelling of tube wall intersection using Brick Elements", *Paper TS1.3, Steel in Marine Structures*, Paris, October 1981.
- PD6493 (1991), Guidance on Methods for Assessing the acceptability of Flaws in Fusion Welded Structures, British Standards Institute(BSI), 1991
- Petroski, H.J. and Achenbach, J.D. (1978), "Computation of the weight function from a stress intensity factor", *Engineering Fracture Mechanics*, Vol. 10, No. 2, pp 257-266, 1978.
- Potvin A.B., Kuang J.G., Leick R.D., Kahlich J.L. (1977), "Stress Concentration in Tubular Joints". *Trans. Soc. Petroleum Engineering*, August 1977.
- Raju, I.S. and Newman, J.C. (1979), "Stress Intensity Factors for a Wide Range of Semi-Elliptical Cracks in Finite Thickness Plates", *Engineering Fracture Mechanics*, Vol. 11, pp 817-829, 1979.
- Raju, I.S. and Newman, J.C. (1982), "Stress Intensity Factors for Internal and External Surface Cracks in Cylindrical Vessels", *Journal of Pressure Vessel Technology*, Vol. 104, pp293-298, 1982.
- Remzi, E.M. and Blackburn, W.S. (1987), "Propagation crack in a T-junction", In *Proceeding of the 4th International Conference on Numerical Methods in Fracture Mechanics*, San Antonio, Texas, U.S.A., 1987.
- Reynolds, A.G. (1987), "Fatigue Performance Comparison of Simple, Over-lapped and Stiffened Welded Tubular Joints", *International Symposium on integrity of Offshore Structure*, 1987.
- Rhee, H.C., Han, S. and Gipson, G.S. (1991), "Reliability of Solution Method and Empirical Formulas of Stress Intensity Factors for Weld Toe Cracks of Tubular Joints", Vol. III-B, 1991 OMAE, 1991.

Rice, J.R. and Levy, N. (1972), "The Part-through Surface Crack in an Elastic Plate", J. Appl. Mech., 39, pp. 185-194, 1972

Ritchie D. and Voermans C.W.M. (1987), "Stress Intensity Factors in an Offshore Tubular Joint Test Specimen", Proc. of the 4th Int. Conf. on Numerical Methods in Fracture Mechanics, San Antonio, Texas, U.S.A., 1987.

Rook, D.P. and Cartwright, D.J. (1976), Compendium of Stress Intensity Factors, HMSO, London, 1976.

Rudlin, J.R. and Dover, W.D. (1990 a), Underwater Trials of Magnetic Particle Inspection technique, Final Report, UCL NDE Centre, June, 1990.

Rudlin, J.R. and Dover, W.D. (1990 b), Underwater Inspection Reliability Trials for Hocking and EMD III Eddy Current Inspection Methods, Final Report, UCL NDE Centre, August, 1990.

Rudlin, J.R., Dover, W.D. and Sheppard, J. (1992), "Probability of Detection and sizing for the TSC U11 ACFM Crack Microgauge", NDE Centre Internal Report, June 1992.

Rudlin, J.R., Chang, E. and Dover, W.D. (1992 a), "Comparison of POD Trial Data for the TSC U11 ACFM Underwater Crack Microgauge and Underwater MPI", NDE Internal Report, July 1992.

Rudlin, J.R., Chang, E. and Dover, W.D. (1992 b), "Investigation of Procedures for the ACFM Crack Sizing", NDE Internal Report, August 1992.

Scordelis, A.C. and Bouwkamp, J.G. (1970), "Analytic Study of Tubular Tee-Joints", Proc. ASCE, J. Structural Div., Vol. 96, 1970.

Shen, G. and Glinka, G. (1991), "Weight Function for a surface Semi-elliptical Crack in a Finite Thickness Plate", Theoretical Applied Fracture Mechanics, Vol. 15, pp247-255, 1991.

Shen, G., Plumtree, A. and Glinka G. (1991), "Weight Function for the Surface Point of Semi-elliptical Surface Crack in a Finite Thickness Plate", Engineering Fracture Mechanics, Vol. 40, pp167-176, 1991.

Shen, G., Liebster, T.D. and Glinka, G. (1993), "Calculation of Stress Intensity Factors for Cracks in Pipes", Proceedings of the 12th International Conference on Offshore Mechanics and Arctic Engineering, ASME, Vol. III-B, pp847-851, 1993.

Shiratori, M., Miyoshi T. and Tanikawa K. (1987), "Analysis of Stress Intensity Factors for Surface Cracks subjected to Arbitrarily Distribution Surface Stresses, in Stress Intensity Factors Handbook (Editor-in-Chief Murakami Y.), Vol. 2, pp. 725-727, Pergamon Press, Oxford.

Shiratori, M. (1989), "Analysis of Stress Intensity Factors for Surface Cracks in Pipes by an Influence Function Method", Advances in Fracture and Fatigue for the 1990's, PVP-167, ASME, Vol. 2, pp45-50, 1989.

Smedley, P. and Fisher, P. (1991), "Stress Concentration Factors for Simple Tubular Joints", Proceedings of the first(1991) International Offshore and Polar Engineering Conference, Edinburgh, UK, Page 475-483, 1991.

Smith, A. (1995), "The Effect of Cathodic Overprotection on the Corrosion Fatigue Behaviour of Offshore Tubular Joints", PhD Thesis, City University, 1995.

Sneddon, I.N. (1946), "The Distribution of Stresses in the Neighbourhood of a Crack in an Elastic Solid", Proc. of Royal Society London, A, 187, 1946.

Steel in Marine Structures (1987), Proceedings of the Third International ECSC Offshore Conference, Delft, ed. by C. Noordhoek and J. de Back, Elsevier, June 1987.

Straalen, V., Dijkstra O.D. and Snijder, H.H. (1988), "Stress Intensity Factors and Fatigue Crack Growth of Semi-elliptical Surface Cracks at Weld Toes", Paper 15 Weld Failures, November, 1988.

Tracey, D. and Cook, T.S. (1977), "Analysis of Power Type Singularities using Finite Elements", Int. J. Num. Math. Engng., Vol. 11, No. 8, pp1225-1235, 1977.

Underwater Engineering Group(UEG) (1985), "Design of Tubular Joints for Offshore Structures", UEG Publication UR-33, Volume 2, 1985.

Vinas-Pich, Jordi (1994), "Influence of Environment, Loading and Steel Composition on Fatigue of Tubular Connections", PhD Thesis, University College London, 1987.

Vughts, J.H. and Kinra, R.K. (1976), "Probabilistic Fatigue Analysis of Fixed Offshore Structures", Offshore Technology Conference, Houston, 1976.

Wang, X. and Lambert, S.B. (1995), "Stress Intensity Factors for Low Aspect ratio Semi-elliptical Surface Cracks in Finite-Thickness Plates Subjected to Nonuniform Stresses", Engineering Fracture Mechanics, Vol. 51, No. 4, pp517-532, 1995.

Wang, X. and Lambert, S.B. (1996), "Stress Intensity Factors and Weight Functions for Longitudinal Semi-elliptical Surface Cracks in Thin Pipes", Int. J. Pres. Ves. & Piping, Vol. 65, pp75-87, 1996.

Wordsworth A.C., Smedley G.P. (1981), "Stress Concentration Factors at K and K T Tubular Joints". Conference on Fatigue in Offshore Structural Steel, Institute of Civil Engineers, London, 1981.

Wordsworth A.C. (1987), "Aspects of the Stress Concentration Factors at Tubular Joints", Steel in Marine Structures, Amsterdam, 1987.

Yamamoto, Y., Tokuda, N. and Sumi, Y. (1973), "Finite Element Treatment of Singularities of Boundary Value Problems and Its Application to Analysis of Stress Intensity Factors", Theory and Practice in Finite Element Structural Analysis, University of Tokyo Press, Tokyo, 1973.

Appendix A

Stress Concentration Factor Parametric Equations for Tubular X and DT-Joints

Appendix A1 - Single brace axial loading, brace toe SCF

A1.1 Parametric equation for SCF at the brace crown toe position ($\phi = 0^0$)

$$SCF_c^0 = 17.8143\alpha^{-0.152}\beta^{0.424/\theta-1.07}\gamma^{0.388/\theta}\tau^{0.495+0.195/\theta}\theta^{1.83}\exp(-0.0358\gamma - 0.969\tau - 1.34\theta)$$

A1.2 Parametric equation for SCF at the brace saddle position

$$SCF_s = 0.963\alpha^{0.305}\beta^{-0.193}\gamma^{0.692}\tau^{0.812}\sin^{2.25}\theta$$

A1.3 Parametric equation for SCF at the brace crown heel position ($\phi = 180^0$)

$$SCF_c^{180} = 0.1188\beta^{0.432/\theta-1.2}\gamma^{0.209/\theta}\exp(0.895\beta^5 - 0.000403\gamma^2 - 0.134\tau^4 + 2.1\sin\theta)$$

A1.4 Parametric equation for SCF at the brace hot-spot stress position

$$SCF_{hs} = 1.1549\alpha^{0.272}\beta^{-0.13}\gamma^{0.642}\tau^{0.652}\sin^{1.77}\theta$$

A1.5 Parametric equation for position of brace hot-spot stress site

$$\phi_{hs} = -333.4 + 51.4\theta + 646.9\sin\theta - 326\sin^2\theta + 0.26\frac{\alpha}{\theta} + 1567\frac{\gamma}{\theta} + 48.9\frac{\tau}{\theta} - 1.47\gamma\tau$$

Appendix A2 - Single brace axial loading, chord toe SCF

A2.1 Parametric equation for SCF at the chord crown toe position ($\phi = 0^0$)

$$SCF_c^0 = 1.6145\alpha^{0.202}\beta^{-0.126}\gamma^{0.232}\tau^{0.923}\sin^{0.189}\theta$$

A2.2 Parametric equation for SCF at the chord saddle position

$$SCF_s = 0.8504\alpha^{0.224}\beta^{-0.272}\gamma^{0.871}\tau^{1.35}\sin^{2.09}\theta$$

A2.3 Parametric equation for SCF at the chord crown heel position ($\phi = 180^0$)

$$SCF_c^{180} = 1.0937\alpha^{0.257}\beta^{-0.212}\gamma^{0.262}\tau^{0.822}\sin^{1.34}\theta$$

A2.4 Parametric equation for SCF at the chord hot-spot stress position

$$SCF_{hs} = 1.061\alpha^{0.215}\beta^{-0.199}\gamma^{0.807}\tau^{1.28}\sin^{1.88}\theta$$

A2.5 Parametric equation for position of chord hot-spot stress site

$$\phi_{hs} = -189.1 - 0.00002\gamma^4 - 17.9\tau^4 + 403\sin\theta - 140\sin^2\theta - 33.3\frac{\beta}{\theta} + 2.17\frac{\gamma}{\theta} + 38.8\frac{\tau}{\theta} - 0.0074\frac{\gamma^2}{\beta}$$

Appendix A3 - Single brace in-plane bending loading, brace toe SCF

A3.1 Parametric equation for SCF at the brace crown toe position ($\phi = 0^\circ$)

$$SCF_c^0 = -45.6042\beta^{0.32/\theta}\gamma^{0.115+0.194/\theta}\tau^{0.789-0.197/\theta}\sin^{3.07}\theta\exp(-1.1\beta-0.812\tau-1.81\sin\theta)$$

A3.2 Parametric equation for SCF at the brace saddle position

$$SCF_s \approx 0$$

A3.3 Parametric equation for SCF at the brace crown heel position ($\phi = 180^\circ$)

$$SCF_c^{180} = 3.2871\gamma^{0.742-0.382/\theta}\tau^{0.582}\sin^{-1.43}\theta\exp(-0.793\beta-0.0169\gamma-0.708\tau)$$

A3.4 Parametric equation for SCF at the brace negative hot-spot stress position

$$SCF_{hs}^- = -5.9895\beta^{0.609}\gamma^{0.452}\tau^{0.827-0.282/\theta}\sin^{1.32}\theta\exp(-1.43\beta-0.517\tau)$$

A3.5 Parametric equation for SCF at the brace positive hot-spot stress position

$$SCF_{hs}^+ = 3.1268\beta^{0.484-0.182/\theta}\gamma^{0.647-0.38/\theta}\tau^{0.518-0.0759/\theta}\sin^{-1.07}\theta\exp(-0.996\beta-0.127\tau^4)$$

A3.6 Parametric equation for position of brace negative hot-spot stress site

$$\phi_{hs}^- = -72.54 + 0.283\alpha + 79.1\beta - 37\beta^5 + 1.267\gamma + 27.9\tau^2 + 12.2\theta$$

A3.7 Parametric equation for position of brace positive hot-spot stress site

$$\phi_{hs}^+ = 269.7 - 0.404\alpha - 61.6\beta - 1.253\gamma - 28.5\tau - 35.4\sin\theta$$

Appendix A4 - Single brace in-plane bending loading, chord toe SCF

A4.1 Parametric equation for SCF at the chord crown toe position ($\phi = 0^\circ$)

$$SCF_c^0 = -1.3258\gamma^{0.482}\tau^{0.899}\sin^{1.28}\theta$$

A4.2 Parametric equation for SCF at the chord saddle position

$$SCF_s \approx 0$$

A4.3 Parametric equation for SCF at the chord crown heel position ($\phi = 180^\circ$)

$$SCF_c^{180} = 2.0077\alpha^{-0.0322}\beta^{-0.0603}\gamma^{0.364}\tau^{0.97}\sin^{0.622}\theta$$

A4.4 Parametric equation for SCF at the chord negative hot-spot stress position

$$SCF_{hs}^- = -1.0784\alpha^{0.0469}\gamma^{0.537}\tau^{0.944}\sin^{1.33}\theta$$

A4.5 Parametric equation for SCF at the chord positive hot-spot stress position

$$SCF_{hs}^+ = 1.7006\beta^{-0.0367}\gamma^{0.422}\tau^{1.01}\sin^{0.683}\theta$$

A4.6 Parametric equation for position of chord negative hot-spot stress site

$$\phi_{hs}^- = 38.99 + 67.3\beta^2 - 0.00003\gamma^4 - 48.2\sin\theta - 58.2\frac{\beta}{\theta} - 3.2\frac{\tau}{\beta} + 13.76\beta^2\gamma - 17.28\beta^3\gamma + 1.995\gamma\tau$$

A4.7 Parametric equation for position of chord positive hot-spot stress site

$$\phi_{hs}^+ = 199.2 + 0.00001\gamma^4 - 11.91\theta - 0.0125\alpha\gamma - 7.24\beta^2\gamma + 9.19\beta^3\gamma + 7.4\frac{\tau}{\theta} - 2.46\beta\gamma\tau$$

Appendix A5 - Single brace out-plane bending loading, brace toe SCF

A5.1 Parametric equation for SCF at the brace crown toe position ($\phi = 0^\circ$)

$$SCF_c^0 \approx 0$$

A5.2 Parametric equation for SCF at the brace saddle position

$$SCF_s = 0.8896\alpha^{0.179}\beta^{0.567}\gamma^{0.864}\tau^{0.605}\sin^{2.07}\theta$$

A5.3 Parametric equation for SCF at the brace crown heel position ($\phi = 180^\circ$)

$$SCF_c^{180} \approx 0$$

A5.4 Parametric equation for SCF at the brace hot-spot stress position

$$SCF_{hs} = 0.8781\alpha^{0.177}\beta^{0.568}\gamma^{0.863}\tau^{0.555}\sin^2\theta$$

A5.5 Parametric equation for position of brace hot-spot stress site

$$\phi_{hs} \approx 90$$

Appendix A6 - Single brace out-plane bending loading, chord toe SCF

A6.1 Parametric equation for SCF at the chord crown toe position ($\phi = 0^\circ$)

$$SCF_c^0 \approx 0$$

A6.2 Parametric equation for SCF at the chord saddle position

$$SCF_s = 0.8694\alpha^{0.173}\beta^{0.432}\gamma^{0.946}\tau^{1.11}\sin^{1.96}\theta$$

A6.3 Parametric equation for SCF at the chord crown heel position ($\phi = 180^\circ$)

$$SCF_c^{180} \approx 0$$

A6.4 Parametric equation for SCF at the chord hot-spot stress position

$$SCF_{hs} = 0.8851\alpha^{0.173}\beta^{0.425}\gamma^{0.937}\tau^{1.11}\sin^{1.94}\theta$$

A6.5 Parametric equation for position of chord hot-spot stress site

$$\phi_{hs} \approx 90$$

Appendix A7 - Double brace balanced axial loading, brace toe SCF

A7.1 Parametric equation for SCF at the brace crown toe position ($\phi = 0^\circ$)

$$SCF_c^0 = 8.35 - 8.52\beta - \frac{0.174}{\beta^2} - 0.00426\gamma^2 - 0.129\alpha\tau + 0.172\beta^3\gamma + 0.0736\frac{\alpha}{\theta} + 0.0157\frac{\gamma}{\theta} + \frac{0.182}{\beta\tau} + 0.0127\frac{\gamma}{\beta^2}$$

A7.2 Parametric equation for SCF at the brace saddle position

$$SCF_s = 1.6922\alpha^{0.0523}\beta^{0.0382}\gamma^{0.899}\tau^{0.891}\sin^{2.17}\theta$$

A7.3 Parametric equation for SCF at the brace crown heel position ($\phi = 180^\circ$)

$$SCF_c^{180} = -9.37 - 13.6\beta + 8.44\beta^2 - 0.102\gamma - 2.65\tau + 3.43\theta + 22.1\sin\theta - 10.7\sin^2\theta - 0.115\alpha\beta - 0.0715\gamma\tau + 0.0491\frac{\alpha}{\theta} + 4.07\frac{\beta}{\theta} + 0.0544\frac{\gamma}{\theta} + 1.43\frac{\tau}{\theta} - 0.101\beta^2\gamma\tau$$

A7.4 Parametric equation for SCF at the brace hot-spot stress position

$$SCF_{hs} = 1.8313\alpha^{0.046}\beta^{0.0896}\gamma^{0.866}\tau^{0.754}\sin^{1.84}\theta$$

A7.5 Parametric equation for position of brace hot-spot stress site

$$\phi_{hs} = 59.7399\beta^{0.0943/\theta}\gamma^{0.236/\theta}\tau^{0.323/\theta-0.192}\sin^{1.22}\theta\exp(-0.152\beta^2 - 0.00796\gamma + 0.14\theta)$$

Appendix A8 - Double brace balanced axial loading, chord toe SCF

A8.1 Parametric equation for SCF at the chord crown toe position ($\phi = 0^\circ$)

$$SCF_c^0 = -2.54 - \frac{0.109}{\beta^2} - 1.08\tau^2 - 1.05\theta + 3.72\sin\theta - 0.0953\gamma\tau + 0.0292\frac{\gamma}{\theta} + 1.99\frac{\tau}{\beta} + 1.42\frac{\tau}{\theta} + \frac{0.092}{\beta\tau}$$

A8.2 Parametric equation for SCF at the chord saddle position

$$SCF_s = 1.3539\alpha^{0.0547}\gamma^{1.06}\tau^{1.37}\sin^{2.04}\theta$$

A8.3 Parametric equation for SCF at the chord crown heel position ($\phi = 180^\circ$)

$$SCF_c^{180} = 0.121 - 4.35\beta - 0.00441\gamma^2 + 0.000003\gamma^4 + 2.5\sin\theta + 0.081\beta^3\gamma + 1.98\frac{\beta}{\theta} + 0.0272\frac{\gamma}{\theta} + 0.904\frac{\tau}{\beta} - 1.05\frac{\tau}{\theta}$$

A8.4 Parametric equation for SCF at the chord hot-spot stress position

$$SCF_{hs} = 1.5129\alpha^{0.0487}\beta^{0.0508}\gamma^{1.04}\tau^{1.34}\sin^{1.95}\theta$$

A8.5 Parametric equation for position of chord hot-spot stress site

$$\phi_{hs} = -30.28 - \frac{4855}{\gamma^3} + 69.6\tau - 37.3\tau^2 + 192\sin\theta - 85\sin^2\theta - 27.7\frac{\beta}{\theta} + 0.939\frac{\gamma}{\theta} + 12.9\frac{\tau}{\theta} - 3.58\frac{\tau}{\beta} - 1.49\gamma\tau + 0.68\beta\gamma\tau^2$$

Appendix A9 - Double brace balanced in-plane bending loading, brace toe SCF

A9.1 Parametric equation for SCF at the brace crown toe position ($\phi = 0^\circ$)

$$SCF_c^0 = -41.6791\beta^{0.258/\theta}\gamma^{0.129+0.206/\theta}\tau^{0.825-0.239/\theta}\sin^{3.36}\theta\exp(-1.01\beta-0.818\tau-1.85\sin\theta)$$

A9.2 Parametric equation for SCF at the brace saddle position

$$SCF_s \approx 0$$

A9.3 Parametric equation for SCF at the brace crown heel position ($\phi = 180^\circ$)

$$SCF_c^{180} = 6.0497\alpha^{-0.0784}\beta^{0.295}\gamma^{0.798-0.369/\theta}\tau^{0.617}\sin^{-1.36}\theta\exp(-1.37\beta-0.0195\gamma-0.748\tau)$$

A9.4 Parametric equation for SCF at the brace negative hot-spot stress position

$$SCF_{hs}^- = -5.8709\beta^{0.626}\gamma^{0.464}\tau^{0.796-0.273/\theta}\sin^{1.36}\theta\exp(-1.51\beta-0.486\tau)$$

A9.5 Parametric equation for SCF at the brace positive hot-spot stress position

$$SCF_{hs}^+ = 3.0957\beta^{0.464-0.188/\theta}\gamma^{0.599-0.334/\theta}\tau^{0.515-0.0659/\theta}\sin^{-0.854}\theta\exp(-0.908\beta-0.13\tau^4)$$

A9.6 Parametric equation for position of brace negative hot-spot stress site

$$\phi_{hs}^- = -85.04 + 145.9\beta - 44\beta^2 + 1.182\gamma + 12.5\theta - 34.3\frac{\beta}{\theta} + 31.7\frac{\tau}{\theta} + 0.442\alpha\tau$$

A9.7 Parametric equation for position of brace positive hot-spot stress site

$$\phi_{hs}^+ = 174.164\beta^{0.146/\theta-0.421}\gamma^{-0.133}\tau^{-0.181}\sin^{-0.349}\theta\exp\left(-\frac{0.0163}{\beta\tau}\right)$$

Appendix A10 - Double brace balanced in-plane bending, chord toe SCF

A10.1 Parametric equation for SCF at the chord crown toe position ($\phi = 0^\circ$)

$$SCF_0 = -1.2399\beta^{-0.0228}\gamma^{0.502}\tau^{0.893}\sin^{1.37}\theta$$

A10.2 Parametric equation for SCF at the chord saddle position

$$SCF_s \approx 0$$

A10.3 Parametric equation for SCF at the chord crown heel position ($\phi = 180^\circ$)

$$SCF_c^{180} = 2.0647\alpha^{-0.0486}\beta^{-0.0468}\gamma^{0.377}\tau^{0.971}\sin^{0.644}\theta$$

A10.4 Parametric equation for SCF at the chord negative hot-spot stress position

$$SCF_{hs}^- = -1.0292\alpha^{0.056}\gamma^{0.544}\tau^{0.939}\sin^{1.38}\theta$$

A10.5 Parametric equation for SCF at the chord positive hot-spot stress position

$$SCF_{hs}^+ = 1.7126\beta^{-0.0277}\gamma^{0.424}\tau\sin^{0.682}\theta$$

A10.6 Parametric equation for position of chord negative hot-spot stress site

$$\phi_{hs}^- = -20.68 + 99\beta^5 - 0.00003\gamma^4 + 0.0115\alpha\gamma + 1.685\gamma\tau + 17.73\beta^2\gamma - 24.6\beta^3\gamma$$

A10.7 Parametric equation for position of chord positive hot-spot stress site

$$\phi_{hs}^+ = 212 - 66\beta^4 - \frac{0.37}{\beta^2} + 0.00001\gamma^4 - 17.8\sin^2\theta - 0.018\alpha\gamma - 11.3\beta^2\gamma + 15.7\beta^3\gamma - 1.87\beta\gamma\tau$$

Appendix A11 - Double brace balanced out-plane bending, brace toe SCF

A11.1 Parametric equation for SCF at the brace crown toe position ($\phi = 0^\circ$)

$$SCF_c^0 \approx 0$$

A11.2 Parametric equation for SCF at the brace saddle position

$$SCF_s = 0.697\alpha^{0.157}\beta^{0.422}\gamma^{0.918}\tau^{0.615}\sin^{2.16}\theta$$

A11.3 Parametric equation for SCF at the brace crown heel position ($\phi = 180^\circ$)

$$SCF_c^{180} \approx 0$$

A11.4 Parametric equation for SCF at the brace hot-spot stress position

$$SCF_{hs} = 0.6998\alpha^{0.155}\beta^{0.445}\gamma^{0.914}\tau^{0.556}\sin^{2.04}\theta$$

A11.5 Parametric equation for position of brace hot-spot stress site

$$\phi_{hs} \approx 90$$

Appendix A12 - Double brace balanced out-plane bending, chord toe SCF

A12.1 Parametric equation for SCF at the chord crown toe position ($\phi = 0^\circ$)

$$SCF_c^0 \approx 0$$

A12.2 Parametric equation for SCF at the chord saddle position

$$SCF_s = 0.6818\alpha^{0.138}\beta^{0.309}\gamma^{1.02}\tau^{1.12}\sin^{2.02}\theta$$

A12.3 Parametric equation for SCF at the chord crown heel position ($\phi = 180^\circ$)

$$SCF_c^{180} \approx 0$$

A12.4 Parametric equation for SCF at the chord hot-spot stress position

$$SCF_{hs} = 0.6914\alpha^{0.137}\beta^{0.306}\gamma^{1.01}\tau^{1.12}\sin^{1.99}\theta$$

A12.5 Parametric equation for position of chord hot-spot stress site

$$\phi_{hs} \approx 90$$

Notes:

1) All equations are valid in the following ranges of the geometric parameters:

$$6.0 \leq \alpha \leq 40.0$$

$$0.2 \leq \beta \leq 0.8$$

$$7.6 \leq \gamma \leq 32.0$$

$$0.2 \leq \tau \leq 1.0$$

$$0.1944\pi \leq \theta \leq \frac{\pi}{2}$$

2) The following minimum SCF applies for predicting the SCF at critical points such as hot spot, saddle, crown toe and crown heel.

2a: For Single Brace/Balanced Axial and OPB loading,

if $SCF < 1.5$ then $SCF = 1.5$

2b: For Single Brace/Balanced IPB loading

if $|SCF| < 1.5$ and $SCF > 0$ then $SCF = 1.5$

if $|SCF| < 1.5$ and $SCF < 0$ then $SCF = -1.5$

3) θ in radians

ϕ_{hs} , ϕ_{hs}^- and ϕ_{hs}^+ in degrees

Appendix B

Parametric Equations for Degree of Bending in Tubular X and DT-Joints

B1 - Single brace subjected to axial loading

B1.1 Parametric equation for degree of bending at the brace saddle position

$$\frac{\sigma_B}{\sigma_T} = 1.125 - 0.185\beta^5 + 0.0926Ln\gamma - 0.462\tau + 0.29Ln\tau + 0.138 \frac{Ln\tau}{\theta} - 0.0903\theta + \frac{0.0065}{\beta\tau}$$

B1.2 Parametric equation for degree of bending at the chord saddle position

$$\frac{\sigma_B}{\sigma_T} = 0.8202 - 0.253\beta^5 + 0.00671\gamma - 0.00014\gamma^2 + 0.0577\tau - 0.0888 \sin \theta + 0.00494\beta^2\gamma$$

B2 - Single brace subjected to in-plane bending loading

B2.1 Parametric equation for degree of bending at the brace crown toe position ($\phi = 0^\circ$)

$$\frac{\sigma_B}{\sigma_T} = 0.5122\gamma^{0.186}\tau^{0.425} \exp(0.301\beta - 0.506\tau + 0.401\sin\theta - 0.0189\beta^2\gamma)$$

B2.2 Parametric equation for degree of bending at the brace crown heel position ($\phi = 180^\circ$)

$$\frac{\sigma_B}{\sigma_T} = 1.004\beta^{0.126}\gamma^{0.196}\tau^{0.319+0.217/\theta} \exp(-0.537\tau - 0.018\beta^2\gamma)$$

B2.3 Parametric equation for degree of bending at the brace crown toe position ($\phi = 0^\circ$)

$$\frac{\sigma_B}{\sigma_T} = 0.778\beta^{-0.0907}\gamma^{0.0451/\theta-0.0368} \sin^{0.449} \theta$$

B2.4 Parametric equation for degree of bending at the brace crown heel position ($\phi = 180^\circ$)

$$\frac{\sigma_B}{\sigma_T} = 0.8261\alpha^{-0.024/\theta}\beta^{-0.0843-0.055/\theta}\gamma^{0.0566-0.121/\theta} \sin^{-0.7} \theta$$

B3 - Single brace subjected to out-plane bending loading on brace toe

B3.1 Parametric equation for degree of bending at the brace saddle position

$$\frac{\sigma_B}{\sigma_T} = 0.8781\beta^{0.0633/\theta}\gamma^{0.101+0.0411/\theta}\tau^{0.334}\exp(-0.115\beta^5 - 0.354\tau - 0.00737\beta^2\gamma)$$

B3.2 Parametric equation for degree of bending at the chord saddle position

$$\frac{\sigma_B}{\sigma_T} = 0.8816\beta^{0.0171/\theta-0.0341}\sin^{-0.118}\theta\exp(-0.0684\beta^2 + 0.00185\beta\gamma\tau^2)$$

B4 - Double braces subjected to balanced axial loading

B4.1 Parametric equation for degree of bending at the brace saddle position

$$\frac{\sigma_B}{\sigma_T} = 0.06561 + 0.01149\gamma + 2.25\tau - 2.18\tau^2 + 0.606\tau^4 - 0.219\frac{\beta}{\theta} - 0.0233\frac{\tau}{\beta} + 0.215\frac{\tau}{\theta} - 0.0085\gamma\tau$$

B4.2 Parametric equation for degree of bending at the chord saddle position

$$\frac{\sigma_B}{\sigma_T} = 0.8472 - 0.2551\beta^5 + 0.00508\gamma - 0.0001\gamma^2 + 0.0467\tau - 0.0674\sin\theta + 0.00437\beta^2\gamma$$

B5 - Double braces subjected to balanced in-plane bending loading

B5.1 Parametric equation for degree of bending at the brace crown toe position ($\phi = 0^\circ$)

$$\frac{\sigma_B}{\sigma_T} = 0.9716\beta^{0.102}\gamma^{0.174}\tau^{0.453-0.0319/\theta}\sin^{0.349}\theta\exp(-0.503\tau - 0.0152\beta^2\gamma)$$

B5.2 Parametric equation for degree of bending at the brace crown heel position ($\phi = 180^\circ$)

$$\frac{\sigma_B}{\sigma_T} = 1.1388\beta^{0.0601+0.0719/\theta}\gamma^{0.185}\tau^{0.296+0.232/\theta}\exp(-0.53\tau - 0.0864\theta - 0.0177\beta^2\gamma)$$

B5.3 Parametric equation for degree of bending at the brace crown toe position ($\phi = 0^\circ$)

$$\frac{\sigma_B}{\sigma_T} = 1.0876\beta^{0.0521/\theta-0.205}\gamma^{0.0127/\theta}\sin^{0.597}\theta\exp(0.125\beta - 0.507\sin\theta)$$

B5.4 Parametric equation for degree of bending at the brace crown heel position ($\phi = 180^\circ$)

$$\frac{\sigma_B}{\sigma_T} = 0.4431\alpha^{-0.0259/\theta}\beta^{-0.0985-0.0514/\theta}\gamma^{0.0642-0.126/\theta}\sin^{-1.2}\theta\exp(0.607\sin\theta)$$

B6 - Double braces subjected to balanced out-plane bending loading

B6.1 Parametric equation for degree of bending at the brace saddle position

$$\frac{\sigma_B}{\sigma_T} = 0.3606\beta^{0.155}\gamma^{0.188+0.0237/\theta}\tau^{0.335}\exp(-0.426\beta^2 - 0.00559\gamma - 0.341\tau)$$

B6.2 Parametric equation for degree of bending at the chord saddle position

$$\frac{\sigma_B}{\sigma_T} = 1.0034 - 0.1658\beta^2 - 0.0905\sin\theta + 0.00223\beta^2\gamma + 0.0017\beta\gamma\tau^2$$

Notes:

1) All equations are valid in the following ranges of the geometric parameters:

$$6.0 \leq \alpha \leq 40.0$$

$$0.2 \leq \beta \leq 0.8$$

$$7.6 \leq \gamma \leq 32.0$$

$$0.2 \leq \tau \leq 1.0$$

$$0.1944\pi \leq \theta \leq \frac{\pi}{2}$$

2) θ in radians

Appendix C

Parametric Equations for the SCF Distribution around the Intersection of Tubular X and DT-Joints

C1 - Single Brace Axial Loading

C1.1 Parametric equation for SCF Distribution on Brace Toe

$$SCF(\phi) = C_0 + C_1\phi + C_2\cos\phi + C_3\cos 2\phi \quad (0 \leq \phi \leq \pi)$$

$$C_0 = 29.54 + 0.468\alpha + 0.214\gamma + 8.52\tau + 8.54\theta - 76.3\sin\theta + 34.5\sin^2\theta - 0.7\alpha\beta + 0.17\beta^3\gamma - 0.195\beta^2\gamma\tau - 1.92\frac{\beta}{\theta} - 0.283\frac{\gamma}{\theta} - 2.19\frac{\tau}{\theta} - \frac{0.266}{\beta^2} + 0.0145\frac{\gamma}{\beta^2}$$

$$C_1 = \beta^{0.8/\theta}\gamma^{1.51+0.858/\theta}\tau^{0.42}\exp(-3.294 + 2.07\beta - 0.055\gamma - 13.6\theta - 1.59\tau^2 + 18.18\sin^2\theta - 0.13\beta^2\gamma + 0.069\beta\gamma\tau^2) - 0.1$$

$$C_2 = \beta^{0.506/\theta}\gamma^{0.688}\exp(19.252 - 29.85\theta - 33.3\sin\theta + 54.55\sin^2\theta) - 0.01$$

$$C_3 = -0.2801 - 0.162\alpha - 0.131\gamma + 2.98\beta^5 + 0.0703\frac{\alpha}{\theta} + 0.1512\frac{\gamma}{\theta} + 1.17\frac{\tau}{\theta} - 0.2739\gamma\tau + \frac{0.0495}{\beta^2}$$

C1.2 Parametric equation for SCF Distribution on Chord Toe

$$SCF(\phi) = C_0 + C_1\phi + C_2\cos\phi + C_3\cos 2\phi \quad (0 \leq \phi \leq \pi)$$

$$C_0 = \gamma^{0.856-0.262/\theta}\tau^{1.246-0.096/\theta}\exp(0.37875 + 0.366\sin^2\theta - 1.674\beta^4)$$

$$C_1 = \alpha^{-0.516}\beta^{-1.038+1.058/\theta}\gamma^{0.842/\theta}\sin^{7.5}\theta\exp(3.576 + 2.26\beta - 0.97\theta - 3.98\sin\theta + 0.00077\alpha^2 - 0.00065\gamma^2 - 0.203\tau^4 - 0.0747\beta^2\gamma + 0.0539\beta\gamma\tau^2) - 0.6$$

$$C_2 = \alpha^{-0.58}\beta^{1.2/\theta}\gamma^{1.101/\theta}\tau^{0.57/\theta}\theta^{6.1}\exp(5.306 + 1.09\beta - 11.78\theta + 0.00084\alpha^2 - 0.00053\gamma^2 + 8.23\sin^2\theta - 0.099\beta^2\gamma + 0.0303\beta\gamma\tau^2) - 0.11$$

$$C_3 = -16.8 - 0.189\gamma + 28.5\sin\theta - 5.09\tau^2 - 0.369\gamma\tau - 12.5\sin^2\theta + 0.2504\beta^3\gamma + \frac{0.0785}{\beta^2} + 6.68\frac{\tau}{\theta} + 0.191\frac{\gamma}{\theta}$$

C2 - Single Brace In-Plane Bending Loading

C2.1 Parametric equation for SCF Distribution on Brace Toe

$$SCF(\phi) = C_0 + C_1 \cos \phi + C_2 \cos 2\phi$$

when $0 \leq \phi < \frac{\pi}{2}$ Crown Toe Side

$$C_0 = 7.295 + 3.47\beta + 0.1114\gamma - 16.7\sin\theta + 0.032\alpha\beta - 2.77\frac{\beta}{\theta} - 0.1287\frac{\gamma}{\theta} + 8.05\sin^2\theta + 0.49\beta\gamma\tau - 0.33\beta^2\gamma\tau$$

$$C_1 = -5.011 - 0.176\gamma - 0.0725\alpha\beta - 0.4365\gamma\tau + 2.19\frac{\beta}{\theta} + 1.709\frac{\tau}{\beta} + 0.2387\frac{\gamma}{\theta} + \frac{0.25}{\beta\tau} - \frac{0.094}{\beta^2}$$

$$C_2 = 7.777 + 3.44\beta + 0.1155\gamma - 17.3\sin\theta + 0.0315\alpha\beta - 2.85\frac{\beta}{\theta} - 0.13\frac{\gamma}{\theta} + 8.31\sin^2\theta + 0.479\beta\gamma\tau - 0.312\beta^2\gamma\tau$$

when $\frac{\pi}{2} < \phi \leq \pi$ Crown Heel Side

$$C_0 = -0.2774 - 0.85\sin\theta - 0.00086\alpha\gamma + 0.0565\frac{\gamma}{\theta} + 1.457\frac{\tau}{\theta} + \frac{0.038}{\beta^2} + \frac{402}{\gamma^3} - 0.6\beta\gamma\tau + 0.369\beta^2\gamma\tau$$

$$C_1 = 3.557 - 0.453\frac{\ln\alpha}{\theta} - 4.05\ln\beta - 6.916\ln\gamma + 2.349\frac{\ln\gamma}{\theta} - 2.13\ln\tau + 3.1\tau^4 + 0.378\beta^2\gamma - 0.475\beta\gamma\tau^2$$

$$C_2 = -1.339 - 0.00085\alpha\gamma + 0.0557\frac{\gamma}{\theta} + 1.884\frac{\tau}{\theta} + \frac{0.032}{\beta^2} + \frac{385}{\gamma^3} + 0.407\beta^2\gamma\tau - 0.643\beta\gamma\tau$$

when $\phi = \frac{\pi}{2}$ Saddle Position

C_0, C_1, C_2 are taken to be the average of two values from above two side equations

C2.2 Parametric equation for SCF Distribution on Chord Toe

$$SCF(\phi) = C_0 + C_1 \cos \phi + C_2 \cos 2\phi$$

when $0 \leq \phi < \frac{\pi}{2}$ Crown Toe Side

$$C_0 = \beta^{2.71-0.762/\theta} \gamma^{1.055} \tau^{0.553} \sin^{2.511}\theta \exp(1.651 - 3.74\beta - 1.693\beta^5 - 0.000001\gamma^4 + 0.0343\beta\gamma\tau^2) - 0.8$$

$$C_1 = -\beta^{2.868-0.441/\theta} \gamma^{1.544} \tau^{0.927+0.438/\theta} \sin^{2.17}\theta \exp(3.146 - 5.27\beta - 0.0271\gamma)$$

$$C_2 = \beta^{1.612-0.828/\theta} \gamma^{1.527-0.262/\theta} \tau^{0.872} \sin^{1.016}\theta \exp(-1.5615 - 2.806\beta^4 - 0.00054\gamma^2 + 0.0344\beta\gamma\tau^2) - 0.5$$

when $\frac{\pi}{2} < \phi \leq \pi$ Crown Heel Side

$$C_0 = -7.1463 - 2.55\tau + 15.3\sin\theta - 0.2463\gamma\tau + 0.0682\frac{\gamma}{\theta} + 5.11\frac{\tau}{\theta} - 7.19\sin^2\theta + 0.000001\gamma^4 - 0.864\beta^2\gamma + 0.982\beta^3\gamma$$

$$C_1 = 0.44369 - 7.92\tau - 0.631\gamma\tau + 0.722\frac{\tau}{\beta} + 0.089\frac{\gamma}{\theta} + 8.53\frac{\tau}{\theta} + 0.000001\gamma^4 - 1.212\beta^2\gamma + 1.504\beta^3\gamma$$

$$C_2 = -8.489 - 2.76\tau + 17.36\sin\theta - 0.2654\gamma\tau + 0.0859\frac{\gamma}{\theta} + 5.19\frac{\tau}{\theta} - 7.87\sin^2\theta + 0.000001\gamma^4 - 0.893\beta^2\gamma + 0.989\beta^3\gamma$$

when $\phi = \frac{\pi}{2}$ Saddle Position

C_0, C_1, C_2 are taken to be the average of two values from above two side equations

C3 - Single Brace Out-Plane Bending Loading

C3.1 Parametric equation for SCF Distribution on Brace Toe

$$SCF(\phi) = C_0 + C_1\sin\phi + C_2\sin 2\phi + C_3\cos 2\phi \quad (0 \leq \phi \leq \pi)$$

$$C_0 = \beta^{1.433+0.37/\theta} \gamma^{1.582} \tau^{0.971+0.261/\theta} \sin^{2.105} \theta \exp(-0.49474 - 0.399\tau^4 - 0.0723\beta^2\gamma)$$

$$C_1 = -71.08 - 15.72\beta - 0.4\gamma - 5.56\tau + 11.94\theta + 142.9\sin\theta - 83\sin^2\theta - 0.182\alpha\beta + 15.89\frac{\beta}{\theta} + 0.423\frac{\gamma}{\theta} + 7.74\frac{\tau}{\theta} - 0.818\beta\gamma\tau$$

$$C_2 = \beta^{1.523/\theta-0.91} \gamma^{0.882/\theta} \tau^{0.876-0.636/\theta} \sin^{6.43} \theta \exp(1.0075 + 1.56\beta - 0.933\tau^2 - 2.057\theta - 0.0866\beta^2\gamma + 0.025\beta\gamma\tau^2) - 0.4$$

$$C_3 = 0.3 - \alpha^{0.145/\theta} \beta^{1.445+0.443/\theta} \gamma^{1.6} \tau^{0.88+0.171/\theta} \sin^{2.677} \theta \exp(-0.9126 - 0.285\tau^4 - 0.0741\beta^2\gamma)$$

C3.2 Parametric equation for SCF Distribution on Chord Toe

$$SCF(\phi) = C_0 + C_1\sin\phi + C_2\sin 2\phi + C_3\cos 2\phi \quad (0 \leq \phi \leq \pi)$$

$$C_0 = \alpha^{0.118/\theta} \beta^{2.093-0.295/\theta} \gamma^{1.837} \tau^{2.2+0.592/\theta} \exp(-4.3011 - 1.45\beta^5 - 1.19\tau + 4.3\sin\theta - 0.0485\beta\gamma\tau^2) - 0.03$$

$$C_1 = -123.2 - 21.5\beta + 18.1\theta + 223.6\sin\theta - 0.473\alpha\tau + 0.224\frac{\alpha}{\theta} + 21.09\frac{\beta}{\theta} + 0.696\frac{\gamma}{\theta} + 13.51\frac{\tau}{\theta} - 0.0208\gamma^2 - 124.9\sin^2\theta + 0.00001\gamma^4 - 2.47\beta\gamma\tau + 1.24\beta^2\gamma\tau$$

$$C_2 = -0.3422 + 0.205\theta - 0.0295\alpha\beta + 0.0242\alpha\tau + 0.464\frac{\beta}{\theta} + 0.00229\frac{\gamma}{\theta} - 0.607\frac{\tau}{\theta} + \frac{0.00713}{\beta^2} + \frac{26.3}{\gamma^3} - 0.00026\frac{\gamma}{\beta^2} + 0.015\beta^2\gamma\tau$$

$$C_3 = 0.1 - \beta^{2.187} \gamma^{1.972} \tau^{1.546+0.528/\theta} \sin^{2.737} \theta \exp(-1.0809 - 1.76\beta^4 - 0.0578\beta\gamma\tau^2)$$

C4 - Double Brace Balanced Axial Loading

C4.1 Parametric equation for SCF Distribution on Brace Toe

$$SCF(\phi) = C_0 + C_1\phi + C_2\cos\phi + C_3\cos 2\phi \quad (0 \leq \phi \leq \pi)$$

$$C_0 = 76.07 - 8.61\frac{\beta}{\theta} + 6.8\tau^2 + 10.3\theta - 145\sin\theta - 0.454\frac{\gamma}{\theta} + 0.0065\frac{\gamma^2}{\beta} - \frac{0.398}{\beta^2} + 68.2\sin^2\theta - \frac{855}{\gamma^3}$$

$$-0.00156\frac{\gamma^2}{\beta^2} - 4.23\frac{\tau}{\theta} - \frac{0.324}{\beta\tau} + 0.036\frac{\gamma}{\beta^2} - 3.8\beta$$

$$C_1 = \exp(1.4879 + 1.79\frac{\beta}{\theta} - \frac{369}{\gamma^3} - 11.06\theta + 14.9\sin^2\theta - 0.617\frac{\tau}{\beta} + 0.0431\frac{\gamma}{\theta} + 0.064\beta^2\gamma\tau$$

$$- \frac{0.075}{\beta\tau} + 0.00171\frac{\gamma}{\beta^2} - 0.106\beta^2\gamma) - 0.25$$

$$C_2 = \beta^{0.801/\theta} \gamma^{0.735/\theta} \tau^{0.218/\theta} \exp(15.943 - 31.31\theta + 54.46\sin^2\theta - 26.7\sin\theta - 0.444\tau^4) - 0.01$$

$$C_3 = 0.5 - \beta^{1.16 - 0.098/\theta} \gamma^{0.988 + 0.117/\theta} \tau^{0.961 + 0.74/\theta} \sin^{3.446}\theta \exp(2.564 - 1.767\beta^2 + 0.45\tau^4 - 1.4\tau^2 - 1.1\sin\theta)$$

C4.2 Parametric equation for SCF Distribution on Chord Toe

$$SCF(\phi) = C_0 + C_1\phi + C_2\cos\phi + C_3\cos 2\phi \quad (0 \leq \phi \leq \pi)$$

$$C_0 = 54.9 + 0.401\gamma\tau - 7.79\frac{\beta}{\theta} - 2.405\beta^2\gamma\tau - 0.244\frac{\gamma}{\theta} - 12.47\frac{\tau}{\theta} - 93.9\sin\theta + 11.39\tau^2 + 58.3\sin^2\theta$$

$$- 9.74\theta + 2.62\beta\gamma\tau - 0.746\beta\gamma\tau^2 + 0.244\beta^2\gamma$$

$$C_1 = -11.947 + 5.99\frac{\beta}{\theta} - 0.0156\frac{\alpha}{\theta} + 0.605\beta^2\gamma\tau + 25.14\sin\theta - 13\beta - 0.347\frac{\tau}{\beta} + 1.68\frac{\tau}{\theta} + 9.9\beta^2$$

$$- 0.284\beta^3\gamma - 0.397\beta\gamma\tau - \frac{188}{\gamma^3} - 15.2\sin^2\theta + 2.83\theta + 0.032\gamma$$

$$C_2 = -24.86 + 8.02\frac{\beta}{\theta} - 0.000001\gamma^4 - 0.0204\frac{\alpha}{\theta} - 1.37\tau^4 + 40.7\sin\theta + 3.62\frac{\tau}{\theta} - 23.9\sin^2\theta + 3.46\theta$$

$$- 1.7\beta + 0.938\beta^2\gamma\tau - 0.246\beta^2\gamma - 1.087\beta\gamma\tau + 0.17\gamma + 0.386\beta\gamma\tau^2$$

$$C_3 = 0.1 - \beta^{2.42} \gamma^{1.142 + 0.42/\theta} \tau^{1.16 + 0.665/\theta} \sin^{4.21}\theta \exp(2.848 - 4.32\beta - 0.0325\beta\gamma\tau^2)$$

C5 - Double Brace Balanced In-Plane Bending Loading

C5.1 Parametric equation for SCF Distribution on Brace Toe

$$SCF(\phi) = C_0 + C_1 \cos \phi + C_2 \cos 2\phi$$

$$\text{when } 0 \leq \phi < \frac{\pi}{2} \quad \text{Crown Toe Side}$$

$$C_0 = 5.9116 - 0.00299\alpha^2 + 0.102\gamma - 13.09\sin\theta + 0.262\alpha\beta - 1.95\frac{\beta}{\theta} - 0.1247\frac{\gamma}{\theta} + 6.52\sin^2\theta \\ + 0.49\beta\gamma\tau - 0.332\beta^2\gamma\tau$$

$$C_1 = -3.469 - 0.231\gamma - 3.68\tau - 0.078\alpha\beta - 0.3109\gamma\tau + 3.1\frac{\beta}{\theta} + 0.2167\frac{\gamma}{\theta} + 2.128\frac{\tau}{\beta} + \frac{0.226}{\beta\tau} - \frac{0.116}{\beta^2}$$

$$C_2 = 6.6489 + 2.97\beta + 0.0988\gamma - 14.71\sin\theta - 2.9\frac{\beta}{\theta} - 0.117\frac{\gamma}{\theta} + 0.101\alpha\beta - 0.00087\alpha^2 \\ + 6.98\sin^2\theta + 0.501\beta\gamma\tau - 0.354\beta^2\gamma\tau$$

$$\text{when } \frac{\pi}{2} < \phi \leq \pi \quad \text{Crown Heel Side}$$

$$C_0 = 2.292 - 0.425\ln\alpha - 2.209\ln\beta - 2.481\ln\gamma + 0.847\frac{\ln\gamma}{\theta} - 0.664\ln\tau + 1.314\tau^4 \\ + 0.1507\beta^2\gamma + 0.2382\beta\gamma\tau^2$$

$$C_1 = 2.913 - 0.623\ln\alpha - 4.43\ln\beta - 6.298\ln\gamma + 1.909\frac{\ln\gamma}{\theta} - 2.33\ln\tau + 3.04\tau^4 \\ + 0.385\beta^2\gamma - 0.456\beta\gamma\tau^2$$

$$C_2 = 1.415 - 0.46\ln\alpha - 2.12\ln\beta - 1.663\ln\gamma - 1.895\ln\tau + 1.199\frac{\ln\tau}{\theta} - 4.784\ln(\sin\theta) \\ + 1.253\tau^4 + 0.1298\beta^2\gamma - 0.222\beta\gamma\tau^2$$

$$\text{when } \phi = \frac{\pi}{2} \quad \text{Saddle Position}$$

C_0, C_1, C_2 are taken to be the average of two values from above two side equations

C5.2 Parametric equation for SCF Distribution on Chord Toe

$$SCF(\phi) = C_0 + C_1 \cos \phi + C_2 \cos 2\phi$$

$$\text{when } 0 \leq \phi < \frac{\pi}{2} \quad \text{Crown Toe Side}$$

$$C_0 = \alpha^{0.162} \gamma^{1.363} \tau^{0.929} \sin^{1.277} \theta \exp(-2.5584 - \frac{0.0533}{\beta^2} - 0.1512\beta^3\gamma - 0.0603\beta\gamma\tau + 0.149\beta^2\gamma\tau) - 0.5$$

$$C_1 = -\gamma^{1.164} \tau^{1.326+0.407/\theta} \sin^{1.345} \theta \exp(-0.02281 - 0.3079\frac{\tau}{\beta} - 0.0639\beta^3\gamma)$$

$$C_2 = \alpha^{0.137} \beta^{0.762-0.437/\theta} \gamma^{1.179} \tau^{0.903} \text{Sin}^{1.492} \theta \exp(-1.79 - \frac{0.0257}{\beta^2} - 0.047\beta\gamma\tau - 0.1524\beta^3\gamma + 0.149\beta^2\gamma\tau) - 0.5$$

when $\frac{\pi}{2} < \phi \leq \pi$ Crown Heel Side

$$C_0 = -2.735 + 0.105\alpha - 0.108\gamma + 7.9\text{Sin}\theta - 0.28\alpha\tau + 0.00199\alpha^2 - 4.54\text{Sin}^2\theta - 2.03\frac{\beta}{\theta} + 0.056\frac{\gamma}{\theta}$$

$$+ 4.13\frac{\tau}{\theta} - 0.603\beta\gamma\tau + 0.26\beta^3\gamma + 0.000001\gamma^4 - 3.01\beta^5 + 0.437\beta^2\gamma\tau$$

$$C_1 = 1.5 - \alpha^{0.121/\theta} \beta^{0.716/\theta} \gamma^{0.524+0.756/\theta} \tau^{1.073-0.419/\theta} \text{Sin}^{11.98} \theta \exp(8.352 + 0.8\beta + 1.21\theta - 10.5\text{Sin}\theta - 0.0987\beta^2\gamma + 0.0297\beta\gamma\tau^2)$$

$$C_2 = -6.778 + 12.7\text{Sin}\theta + 0.00192\alpha^2 - 0.00326\gamma^2 - 1.08\tau^2 - 5.78\text{Sin}^2\theta - 0.1426\alpha\tau + 0.065\frac{\gamma}{\theta}$$

$$+ 4.22\frac{\tau}{\theta} - 0.304\beta^2\gamma - 0.616\beta\gamma\tau + 0.000001\gamma^4 + 0.615\beta^3\gamma + 0.387\beta^2\gamma\tau - 5.8\beta^5$$

when $\phi = \frac{\pi}{2}$ Saddle Position

C_0, C_1, C_2 are taken to be the average of two values from above two side equations

C6 - Double Brace Out-Plane Bending Loading

C6.1 Parametric equation for SCF Distribution on Brace Toe

$$SCF(\phi) = C_0 + C_1\text{Sin}\phi + C_2\text{Sin}2\phi + C_3\text{Cos}2\phi \quad (0 \leq \phi \leq \pi)$$

$$C_0 = \alpha^{0.087} \beta^{3.045} \gamma^{1.3} \tau^{1.687} \text{Sin}^{2.79} \theta \exp(3.8862 - 4.46\beta - 1.28\tau)$$

$$C_1 = -70.13 - 8.96\beta + 10.7\theta + 128\text{Sin}\theta - 0.00542\gamma^2 - 74.4\text{Sin}^2\theta - 0.0615\alpha\tau + 13.39\frac{\beta}{\theta}$$

$$+ 0.438\frac{\gamma}{\theta} + 6.22\frac{\tau}{\theta} - 0.381\beta^2\gamma - 1.832\beta\gamma\tau + 1.205\beta^2\gamma\tau$$

$$C_2 = \alpha^{0.259/\theta-0.203} \beta^{1.549/\theta-1} \gamma^{0.712/\theta} \tau^{0.691-0.485/\theta} \theta^{7.66} \exp(3.88 + 1.59\beta - 6.47\theta - 0.808\tau^2 + 0.78\text{Sin}^2\theta - 0.0748\beta^2\gamma + 0.0192\beta\gamma\tau^2) - 0.4$$

$$C_3 = 0.3 - \beta^{1.202+0.365/\theta} \gamma^{1.329} \tau^{0.957+0.244/\theta} \text{Sin}^{2.168} \theta \exp(-0.21389 - 0.481\tau^2 - 2.17\beta^5)$$

C6.2 Parametric equation for SCF Distribution on Chord Toe

$$SCF(\phi) = C_0 + C_1\text{Sin}\phi + C_2\text{Sin}2\phi + C_3\text{Cos}2\phi \quad (0 \leq \phi \leq \pi)$$

$$C_0 = \beta^{2.065-0.304/\theta} \gamma^{1.873} \tau^{2.28+0.488/\theta} \sin^{2.824} \theta \exp(0.13723 - 1.79\beta^4 - 1.43\tau - 0.0282\beta\gamma\tau^2) - 0.05$$

$$C_1 = -114.12 - 26.9\beta^5 + 16\theta + 200.4\sin\theta - 112.1\sin^2\theta + 18.73\frac{\beta}{\theta} + 0.733\frac{\gamma}{\theta} + 12.7\frac{\tau}{\theta} - \frac{0.2}{\beta^2}$$

$$-3.066\beta\gamma\tau - 4.59\beta^2\gamma + 4.99\beta^3\gamma + 1.66\beta^2\gamma\tau$$

$$C_2 = -1.712 + 1.94\beta + 0.0343\gamma + 0.724\theta - 2.24\beta^2 + 1.45\beta^5 - 0.332\sin^2\theta + 0.00396\frac{\alpha}{\theta} + 1.021\frac{\beta}{\theta} - 0.0059\frac{\gamma}{\theta}$$

$$-0.346\frac{\tau}{\theta} - 0.04\gamma\tau + 0.185\frac{\tau}{\beta} - 0.0657\beta^2\gamma + 0.0698\beta^2\gamma\tau$$

$$C_3 = 0.1 - \beta^{3.665} \gamma^{1.833} \tau^{2.64} \sin^{3.055} \theta \exp(4.022 - 5.28\beta - 1.69\tau)$$

Note:

1) All equations are valid in the following ranges of the geometric parameters:

$$6.0 \leq \alpha \leq 40.0$$

$$0.2 \leq \beta \leq 0.8$$

$$7.6 \leq \gamma \leq 32.0$$

$$0.2 \leq \tau \leq 1.0$$

$$0.1944\pi \leq \theta \leq \frac{\pi}{2}$$

2) If the negative SCF value is predicted at crown positions under single/balanced axial and OPB loading, the compensation factor D for whole stress distribution is assigned in following rules:

$$SCF_{new}(\phi) = SCF(\phi) + D$$

a) if $SCF(0) \leq 0$ and $SCF(\pi) > 0$ then $D = -SCF(0)$

b) if $SCF(0) > 0$ and $SCF(\pi) \leq 0$ then $D = -SCF(\pi)$

c) if $SCF(0) \leq 0$ and $SCF(\pi) \leq 0$, and

if $SCF(0) \leq SCF(\pi)$, $D = -SCF(0)$

if $SCF(\pi) \leq SCF(0)$, $D = -SCF(\pi)$

3) When used to predict the SCF at critical points such as hot spot, saddle, crown toe and crown heel, the following minimum SCF applies.

if $|SCF| < 1.5$ and $SCF > 0$ then $SCF = 1.5$

if $|SCF| < 1.5$ and $SCF < 0$ then $SCF = -1.5$

4) ϕ and θ in radians

Appendix D

Parametric Equations of SCF Distribution along the Intersection of Tubular Y and T-Joints

D1 - Axial Loading

D1.1 Parametric equation for SCF Distribution on Brace Toe

$$SCF(\phi) = C_0 + C_1\phi + C_2\cos 2\phi \quad (0 \leq \phi \leq \pi)$$

$$\begin{aligned} C_0 &= 6.644 + 0.305\gamma\tau + 2.85\frac{\beta}{\theta} + 0.653\alpha\tau - 2.39\frac{\tau}{\theta} - 0.757\alpha\beta - \frac{0.114}{\beta\tau} + 0.00018\frac{\gamma^2}{\beta^2} \\ &\quad - \frac{941}{\gamma^3} - 0.0981\frac{\gamma}{\theta} - 0.895\frac{\tau}{\beta} - 3.55\theta + 6.08\sin^2\theta - 0.195\beta\gamma\tau^2 - 1.1\tau^4 \\ C_1 &= 0.7016 + 1.39\theta - 6.4\sin\theta + 0.207\frac{\tau}{\beta} - \frac{104}{\gamma^3} + 0.11\beta^2\gamma + \frac{0.0512}{\beta\tau} + 0.0614\alpha\beta \\ &\quad - 0.293\frac{\tau}{\theta} + 2.98\sin^2\theta - 0.099\beta^3\gamma - 0.0083\frac{\gamma}{\theta} - 0.033\alpha - 0.00066\frac{\gamma}{\beta^2} \\ C_2 &= 19.55 - 16.7\sin^2\theta - 0.152\beta\gamma\tau^2 - 3.51\ln(\alpha) + 2.89\beta^4 - 2.55\ln(\gamma) + 3.52\frac{\ln(\gamma)}{\theta} \\ &\quad + 20.1\ln(\sin\theta) - 2.37\ln(\tau) + 2.16\frac{\ln(\tau)}{\theta} - 2.49\ln(\beta) + 9.37\ln(\theta) + 1.9\frac{\ln(\alpha)}{\theta} \\ &\quad + 0.68\frac{\ln(\beta)}{\theta} + 2.07\tau^4 + 0.153\beta^2\gamma - 0.322\gamma + 0.000001\gamma^4 - 4.9\tau \end{aligned}$$

D1.2 Parametric equation for SCF Distribution on Chord Toe

$$SCF(\phi) = C_0 + C_1\phi + C_2\cos 2\phi \quad (0 \leq \phi \leq \pi)$$

$$\begin{aligned} C_0 &= -0.1326 + 0.417\gamma\tau - 0.1501\frac{\gamma}{\theta} - 0.316\beta^2\gamma\tau + 0.01351\alpha\gamma + 1.75\tau^4 \\ &\quad - 5.1\frac{\tau}{\theta} + 8.45\tau + 4.16\frac{\beta}{\theta} - 0.362\alpha\beta \\ C_1 &= 3.629 - 1.056\frac{\tau}{\theta} + 0.228\theta - 7.66\sin\theta + 0.0376\frac{\tau}{\beta} - 0.00696\frac{\alpha}{\theta} + 3.94\sin^2\theta \\ &\quad + 0.555\tau - 0.116\tau^4 - 0.00478\frac{\gamma}{\theta} + 0.0107\beta^2\gamma - 0.208\frac{\beta}{\theta} - \frac{0.91}{\alpha} \end{aligned}$$

$$C_2 = -25.362 - 0.341\gamma\tau + 0.21\frac{\gamma}{\theta} + 7.8\frac{\tau}{\theta} + 0.284\beta^3\gamma - 1.41\frac{\beta}{\theta} - 5.52\tau^2 - 0.308\gamma$$

$$+ 0.000001\gamma^4 + 48.34\sin\theta + \frac{0.169}{\beta\tau} - 30.3\sin^2\theta + 4.26\theta + \frac{10.3}{\alpha}$$

D2 - In-Plane Bending Loading

D2.1 Parametric equation for SCF Distribution on Brace Toe

$$SCF(\phi) = C_0 + C_1\cos\phi + C_2\cos 2\phi$$

when $0 \leq \phi < \frac{\pi}{2}$ Crown Toe Side

$$C_0 = -3.6487 + 0.2156\beta\gamma\tau + 1.61\theta - 0.203\frac{\gamma}{\theta} + 0.22\gamma + 3.51\frac{\tau}{\theta} - 1.79\tau^2$$

$$- 0.00194\frac{\gamma}{\beta^2} - 0.0181\frac{\alpha}{\theta}$$

$$C_1 = -1.8399 - 0.822\beta\gamma\tau + 0.431\beta^2\gamma\tau + 0.3532\frac{\gamma}{\theta} - 0.388\gamma + \frac{0.193}{\beta\tau}$$

$$C_2 = -2.9616 + 0.21\beta\gamma\tau - 0.1894\frac{\gamma}{\theta} + 0.213\gamma + 2.54\frac{\tau}{\theta} - 0.00185\frac{\gamma}{\beta^2} + 1.21\theta - 1.04\tau^2$$

when $\frac{\pi}{2} < \phi \leq \pi$ Crown Heel Side

$$C_0 = 5.2337 - 0.5614\beta\gamma\tau - 5.94\sin\theta + 0.366\beta^2\gamma\tau + 0.512\frac{\tau}{\beta}$$

$$C_1 = -0.2456 - 1.765\beta\gamma\tau - 5.23\sin\theta + 1.346\beta^2\gamma\tau + 0.445\frac{\tau}{\beta} + \frac{1454}{\gamma^3}$$

$$+ 0.1427\frac{\gamma}{\theta} + 2.39\tau^4$$

$$C_2 = 2.0402 - 0.5643\beta\gamma\tau - 2.87\sin\theta - 0.00124\alpha\gamma + \frac{0.0528}{\beta^2} + 0.355\beta^2\gamma\tau + 1.39\frac{\tau}{\theta}$$

when $\phi = \frac{\pi}{2}$ Saddle Position

C_0, C_1, C_2 are taken to be the average of two values from above two side equations

D2.2 Parametric equation for SCF Distribution on Chord Toe

$$SCF(\phi) = C_0 + C_1\cos\phi + C_2\cos 2\phi$$

when $0 \leq \phi < \frac{\pi}{2}$ Crown Toe Side

$$C_0 = 2.3106 - 0.1086 \frac{\gamma}{\theta} + 0.111\gamma - 0.00031 \frac{\gamma^2}{\beta} - 0.853\beta^2\gamma\tau + 0.171\beta\gamma\tau^2 \\ + 0.736\beta\gamma\tau - 1.26 \frac{\tau}{\theta} - 2.73\sin\theta$$

$$C_1 = -3.939 - 0.6697\gamma\tau + 0.147 \frac{\gamma}{\theta} + 3.57 \frac{\tau}{\theta} + 7.55\beta^5 + \frac{0.169}{\beta^2} - 2.2\tau^4$$

$$C_2 = 3.7474 + 0.2713\gamma\tau - 0.1237 \frac{\gamma}{\theta} - 0.439 \frac{\tau}{\beta} + 0.849\beta^2\gamma - 0.896\beta^3\gamma \\ - 0.000001\gamma^4 + \frac{0.063}{\beta\tau} - 3.85\sin\theta - 1.94 \frac{\beta}{\theta}$$

when $\frac{\pi}{2} < \phi \leq \pi$ Crown Heel Side

$$C_0 = 0.3909 - 0.3352\gamma\tau + 3.637 \frac{\tau}{\theta} + 0.00461\gamma^2 + 1.1579\beta^3\gamma - 1.006\beta^2\gamma$$

$$C_1 = 0.6957 - 3.028\beta\gamma\tau + 2.799\beta^2\gamma\tau - 10.88\ln(\sin\theta) + 0.000001\gamma^4 + 1.74 \frac{\ln\tau}{\theta}$$

$$C_2 = 1.7333 - 1.218\beta\gamma\tau - 5.63\ln(\sin\theta) + 1.103\beta^2\gamma\tau + 1.565 \frac{\ln\tau}{\theta} + 0.000001\gamma^4$$

when $\phi = \frac{\pi}{2}$ Saddle Position

C_0, C_1, C_2 are taken to be the average of two values from above two side equations

D3 - Out-Plane Bending Loading

D3.1 Parametric equation for SCF Distribution on Brace Toe

$$SCF(\phi) = C_0 + C_1\phi + C_2\cos 2\phi \quad (0 \leq \phi \leq \pi)$$

$$C_0 = 1.6749 + 0.416\gamma - 1.324 \frac{\ln(\gamma)}{\theta} + 0.117\beta\gamma\tau^2 + 0.0114\alpha - 1.76\beta^5$$

$$+ 1.904\ln(\beta) + 2.48\ln(\tau) - 1.22 \frac{\ln(\tau)}{\theta} - 0.171\beta^2\gamma - 1.31\tau^4$$

$$+ 3.76\sin^2\theta - 3.8\ln(\theta) + 0.28 \frac{\ln(\beta)}{\theta} - 0.00463\gamma^2$$

$$C_1 = \alpha^{0.204/\theta} \beta^{-0.402+1.464/\theta} \gamma^{1.14/\theta} \tau^{0.786-0.719/\theta} \theta^{14.8} \exp(10.399 - 9.82\theta - 0.0922\beta^2\gamma \\ - 0.0209\gamma + 0.0305\beta\gamma\tau^2 - 3.65\sin\theta + 0.58\beta^4 - 0.726\tau^2 - 0.009\alpha)$$

$$\begin{aligned}
C_2 = & 7.8816 - 0.168\beta\gamma\tau^2 - 8.23\sin^2\theta - 0.514\gamma + 2.64\frac{\ln(\gamma)}{\theta} - 0.017\alpha \\
& + 8.36\ln(\sin\theta) - 3.46\ln(\beta) + 1.34\frac{\ln(\beta)}{\theta} + 0.075\beta^2\gamma + 1.25\frac{\ln(\tau)}{\theta} \\
& + 7.49\tau^2 + 0.00585\gamma^2 + 4.16\ln(\theta) + 2.53\beta^4 - 12.17\tau
\end{aligned}$$

D3.2 Parametric equation for SCF Distribution on Chord Toe

$$SCF(\phi) = C_0 + C_1\phi + C_2\cos 2\phi \quad (0 \leq \phi \leq \pi)$$

$$\begin{aligned}
C_0 = & 4.814 + 0.2551\gamma\tau - 3.79\sin\theta - 0.0853\frac{\gamma}{\theta} - 4.45\frac{\tau}{\theta} + 1.12\tau^2 - 0.532\beta^3\gamma \\
& + 0.408\beta^2\gamma - \frac{389}{\gamma^3} + 4.23\tau - 0.421\frac{\tau}{\beta}
\end{aligned}$$

$$\begin{aligned}
C_1 = & 0.4117 + 0.356\frac{\tau}{\theta} - 0.0079\beta\gamma\tau - 0.227\frac{\beta}{\theta} - 0.178\tau + 0.128\beta^2 - 0.339\sin\theta \\
& - 0.00477\frac{\gamma}{\theta} + 0.00399\gamma - 0.00114\frac{\alpha}{\theta} - \frac{0.0034}{\beta\tau} - \frac{11.2}{\gamma^3}
\end{aligned}$$

$$\begin{aligned}
C_2 = & -24.41 - 0.283\gamma\tau - 26.4\sin^2\theta + 0.1793\frac{\gamma}{\theta} + 5.61\frac{\tau}{\theta} - 0.016\alpha\gamma - 0.92\tau^4 \\
& + 44.3\sin\theta + 0.0024\alpha^2 + 4.11\theta - 10.65\tau + 1.338\frac{\tau}{\beta} + 2.27\frac{\beta}{\theta} + 0.296\alpha\tau
\end{aligned}$$

Notes:

1) All equations are valid in the following ranges of the geometric parameters:

$$6.0 \leq \alpha \leq 40.0$$

$$0.2 \leq \beta \leq 0.8$$

$$7.6 \leq \gamma \leq 32.0$$

$$0.2 \leq \tau \leq 1.0$$

$$0.1944\pi \leq \theta \leq \frac{\pi}{2}$$

2) If the negative SCF value is predicted at crown positions under single/balanced axial and OPB loading, the compensation factor D for whole stress distribution is assigned in following rules:

$$SCF_{new}(\phi) = SCF(\phi) + D$$

a) if $SCF(0) \leq 0$ and $SCF(\pi) > 0$ then $D = -SCF(0)$

b) if $SCF(0) > 0$ and $SCF(\pi) \leq 0$ then $D = -SCF(\pi)$

c) if $SCF(0) \leq 0$ and $SCF(\pi) \leq 0$, and

if $SCF(0) \leq SCF(\pi)$, $D = -SCF(0)$

if $SCF(\pi) \leq SCF(0)$, $D = -SCF(\pi)$

3) When used to predict the SCF at critical points such as hot spot, saddle, crown toe and crown heel, the following minimum SCF applies.

if $|SCF| < 1.5$ and $SCF > 0$ then $SCF = 1.5$

if $|SCF| < 1.5$ and $SCF < 0$ then $SCF = -1.5$

4) ϕ and θ in radians

Appendix E

Parametric Equations of Average SCF Along the Intersection of Tubular Y and T-Joints

E1 - Axial Loading

E1.1 Parametric equation for Average SCF on Brace Toe

$$\overline{SCF} = \alpha^{0.218} \gamma^{0.618} \tau^{0.543} \sin^{1.545} \theta \exp(0.08261 - 0.03125\beta^2\gamma)$$

E1.2 Parametric equation for Average SCF on Chord Toe

$$\overline{SCF} = \alpha^{0.223} \gamma^{0.5656} \tau^{1.148} \sin^{1.485} \theta \exp(0.6787 - 0.639\beta)$$

Appendix E2 - IPB Loading

E2.1 Parametric equation for Average SCF on Brace Toe at Crown Toe Side

$$\begin{aligned} \overline{SCF}_{Toe} = & 0.6636 + 1.03Ln\gamma + 2.612Ln(\sin \theta) + 1.26Ln\tau - \frac{0.0535}{\beta^2} \\ & + 0.00007\frac{\gamma^2}{\beta^2} - 0.55\frac{Ln\tau}{\theta} - 0.387\beta^4 \end{aligned}$$

E2.2 Parametric equation for Average SCF on Brace Toe at Crown Heel Side

$$\begin{aligned} \overline{SCF}_{Heel} = & \exp(0.8406 + 0.0237\gamma\tau - \frac{183.3}{\gamma^3} - 0.00975\frac{\gamma}{\theta} - 0.368\tau^4 - \frac{0.03539}{\beta^2} \\ & + 0.00145\frac{\gamma}{\beta^2} + 0.508\tau - 0.392\beta^4) \end{aligned}$$

E2.3 Parametric equation for Average SCF on Chord Toe at Crown Toe Side

$$\overline{SCF}_{Toe} = \beta^{0.078} \gamma^{0.607} \tau^{1.039} \sin^{1.007} \theta \exp(-0.1593)$$

E2.4 Parametric equation for Average SCF on Chord Toe at Crown Heel Side

$$\overline{SCF}_{Heel} = \gamma^{0.617} \tau^{1.076} \sin^{0.565} \theta \exp(-0.20561)$$

Appendix E3 - OPB Loading

E3.1 Parametric equation for Average SCF on Brace Toe

$$\overline{SCF} = 0.94563 + 0.1209\gamma\tau + 1.27 \sin \theta - 0.499 \frac{\tau}{\beta} - 0.1096\beta^3\gamma + 0.00079\alpha\gamma \\ - 0.1099 \frac{\gamma}{\theta} + 0.1639\gamma - \frac{0.107}{\beta\tau}$$

E3.2 Parametric equation for Average SCF on Chord Toe

$$\overline{SCF} = 2.5215 + 0.2825\gamma\tau - 0.0698 \frac{\gamma}{\theta} - 2.14 \frac{\tau}{\theta} + 1.17\tau^4 + 0.0255\alpha\tau \\ - 2.67\beta^5 - \frac{0.0582}{\beta^2}$$

Note:

1) All equations are valid in the following ranges of the geometric parameters:

$$6.0 \leq \alpha \leq 40.0$$

$$0.2 \leq \beta \leq 0.8$$

$$7.6 \leq \gamma \leq 32.0$$

$$0.2 \leq \tau \leq 1.0$$

$$0.1944\pi \leq \theta \leq \frac{\pi}{2}$$

2) θ in radians

Appendix F

Parametric Equations of Average SCF Along the Intersection of Tubular X and DT-Joints

Appendix F1 - Single Brace Subjected to Axial Loading

F1.1 Parametric equation for Average SCF on Brace Toe

$$\overline{SCF} = 1.1185\alpha^{0.252}\beta^{-0.372}\gamma^{0.403}\tau^{0.579}\sin^{1.48}\theta$$

F1.2 Parametric equation for Average SCF on Chord Toe

$$\overline{SCF} = 1.0846\alpha^{0.229}\beta^{-0.306}\gamma^{0.57}\tau^{1.14}\sin^{1.45}\theta$$

Appendix F2 - Single Brace Subjected to IPB Loading

F2.1 Parametric equation for Average SCF on Brace Toe at Crown Toe Side

$$\overline{SCF}_{Toe} = 1.3553\beta^{0.332}\gamma^{0.662}\tau^{0.726}\sin^{1.21}\theta\exp(-0.656\tau - 0.0334\beta^2\gamma)$$

F2.2 Parametric equation for Average SCF on Brace Toe at Crown Heel Side

$$\overline{SCF}_{Heel} = 0.4809\beta^{0.264}\gamma^{0.521}\tau^{0.559}\sin^{1.08}\theta\exp(-0.532\tau^2 - 0.0418\beta^2\gamma + 0.0204\beta\gamma\tau^2)$$

F2.3 Parametric equation for Average SCF on Chord Toe at Crown Toe Side

$$\overline{SCF}_{Toe} = 0.7657\gamma^{0.62}\tau^{1.05}\sin^{1.27}\theta$$

F2.4 Parametric equation for Average SCF on Chord Toe at Crown Heel Side

$$\overline{SCF}_{Heel} = 0.7953\gamma^{0.609}\tau^{1.08}\sin^{1.11}\theta$$

Appendix F3 - Single Brace Subjected to OPB Loading

F3.1 Parametric equation for Average SCF on Brace Toe

$$\overline{SCF} = 30.5694\beta^{1.75}\gamma^{0.725}\tau^{1.07}\sin^{1.66}\theta\exp(-3.27\beta - 1.04\tau)$$

F3.2 Parametric equation for Average SCF on Chord Toe

$$\overline{SCF} = 0.894\beta^{0.128}\gamma^{0.707}\tau^{0.986}\sin^{1.53}\theta$$

Appendix F4 - Double Braces Subjected to Axial Loading

F4.1 Parametric equation for Average SCF on Brace Toe

$$\overline{SCF} = 1.7402\beta^{-0.291}\gamma^{0.562}\tau^{0.622}\sin^{1.56}\theta$$

F4.2 Parametric equation for Average SCF on Chord Toe

$$\overline{SCF} = 1.5699\beta^{-0.299}\gamma^{0.693}\tau^{1.13}\sin^{1.5}\theta$$

Appendix F5 - Double Braces Subjected to IPB Loading

F5.1 Parametric equation for Average SCF on Brace Toe at Crown Toe Side

$$\overline{SCF}_{Toe} = 1.2751\beta^{0.319}\gamma^{0.681}\tau^{0.718}\sin^{1.28}\theta\exp(-0.654\tau - 0.0338\beta^2\gamma)$$

F5.2 Parametric equation for Average SCF on Brace Toe at Crown Heel Side

$$\overline{SCF}_{Heel} = 0.6873\beta^{0.321}\gamma^{0.559}\tau^{0.746}\exp(-0.714\tau + 1.01\sin\theta - 0.0327\beta^2\gamma)$$

F5.3 Parametric equation for Average SCF on Chord Toe at Crown Toe Side

$$\overline{SCF}_{Toe} = 0.7611\gamma^{0.622}\tau^{1.05}\sin^{1.32}\theta$$

F5.4 Parametric equation for Average SCF on Chord Toe at Crown Heel Side

$$\overline{SCF}_{Heel} = 0.8328\gamma^{0.595}\tau^{1.08}\sin^{1.07}\theta$$

Appendix F6 - Double Braces Subjected to OPB Loading

F6.1 Parametric equation for Average SCF on Brace Toe

$$\overline{SCF} = 1.3771\beta^{0.562}\gamma^{0.754}\tau^{0.821}\sin^{1.73}\theta\exp(-1.92\beta^5 - 0.47\tau^2)$$

F6.2 Parametric equation for Average SCF on Chord Toe

$$\overline{SCF} = 1.0754\beta^{0.464}\gamma^{0.776}\tau^{0.985}\sin^{1.61}\theta\exp(-1.97\beta^5)$$

Note:

1) All equations are valid in the following ranges of the geometric parameters:

$$6.0 \leq \alpha \leq 40.0$$

$$0.2 \leq \beta \leq 0.8$$

$$7.6 \leq \gamma \leq 32.0$$

$$0.2 \leq \tau \leq 1.0$$

$$0.1944\pi \leq \theta \leq \frac{\pi}{2}$$

2) θ in radians

Appendix G

Parametric Equations of SCF Distribution Concentration Factor(SDCF) Along the Intersection of Tubular Y and T-Joints

Appendix G1 - Axial Loading

G1.1 Parametric equation for SDCF on Brace Toe

$$\rho_{SCF} = \alpha^{-0.0386} \beta^{-0.2138+0.0963/\theta} \gamma^{-0.1891+0.0757/\theta} \tau^{-0.2026} \exp(-1.392-0.00843\beta\gamma\tau^2+0.226\beta^4+0.277\tau+0.000001\gamma^4)$$

G1.2 Parametric equation for SDCF on Chord Toe

$$\rho_{SCF} = \alpha^{-0.0638} \gamma^{-0.1775} \tau^{-0.1294} \sin^{-0.2386} \theta \exp(-0.9816+0.2609\beta^5+0.00011\gamma^2+0.0359\frac{\tau}{\beta}+0.0001\alpha^2)$$

Appendix G2 - IPB Loading

G2.1 Parametric equation for SDCF on Brace Toe at Crown Toe Side

$$\rho_{SCF}^{Toe} = 0.5515+0.0731\theta-0.00473\frac{\gamma}{\theta}+0.1159\frac{\tau}{\theta}+0.01536\beta^2\gamma+0.00336\gamma-0.0107\beta^3\gamma$$

G2.2 Parametric equation for SDCF on Brace Toe at Crown Heel Side

$$\rho_{SCF}^{Heel} = 1.099+0.0236Ln\gamma+0.087Ln\beta+0.805Ln(\sin\theta)+0.0561\frac{Ln\gamma}{\theta}+0.0189\frac{Ln\alpha}{\theta}-0.0934\frac{Ln\tau}{\theta}+0.0928Ln\tau-0.0755\beta^4-0.441Sin\theta$$

G2.3 Parametric equation for SDCF on Chord Toe at Crown Toe Side

$$\begin{aligned}\rho_{SCF}^{Toe} = & 0.7651 - 0.00443 \frac{\gamma}{\theta} + 0.0872 \frac{\tau}{\theta} + 0.00622\gamma - 0.4963\tau^2 - 0.115\beta^5 \\ & + 0.00202\beta^2\gamma\tau - 0.0267 \frac{\tau}{\beta} - 0.0918 \frac{\beta}{\theta} - 0.607 \sin \theta + 0.562\tau + \frac{0.00327}{\beta^2} \\ & + 0.168\beta - 0.00012 \frac{\gamma}{\beta^2} + 0.359 \sin^2 \theta - 0.0524\theta + 0.124\tau^4 + \frac{0.0057}{\beta\tau}\end{aligned}$$

G2.4 Parametric equation for SDCF on Chord Toe at Crown Heel Side

$$\begin{aligned}\rho_{SCF}^{Heel} = & 0.5664 + 0.0609 \ln \gamma + 0.2557 \ln(\sin \theta) + 0.00253\beta\gamma\tau^2 + 0.0206 \frac{\ln \alpha}{\theta} \\ & - 0.0825\beta^5 + 0.0648 \ln \beta - 0.0399 \frac{\ln \beta}{\theta}\end{aligned}$$

Appendix G3 - OPB Loading

G3.1 Parametric equation for SDCF on Brace Toe

$$\rho_{SCF} = \alpha^{-0.0294} \beta^{-0.2389+0.098/\theta} \gamma^{-0.0936} \sin^{-0.3995} \theta \exp(-1.442 - 0.01109\beta^2\gamma\tau)$$

G3.2 Parametric equation for SDCF on Chord Toe

$$\rho_{SCF} = \alpha^{-0.052} \beta^{-0.35+0.216/\theta} \gamma^{-0.1116} \tau^{-0.0708} \sin^{-0.594} \theta \exp(-1.418 - 0.00868\beta^2\gamma)$$

Note:

1) All equations are valid in the following ranges of the geometric parameters:

$$6.0 \leq \alpha \leq 40.0$$

$$0.2 \leq \beta \leq 0.8$$

$$7.6 \leq \gamma \leq 32.0$$

$$0.2 \leq \tau \leq 1.0$$

$$0.1944\pi \leq \theta \leq \frac{\pi}{2}$$

2) θ in radians

Appendix H

Parametric Equations of SCF Distribution Concentration Factor(SDCF) Along the Intersection of Tubular X and DT-Joints

Appendix H1 - Single Brace Subjected to Axial Loading

H1.1 Parametric equation for SDCF on Brace Toe

$$\rho_{SCF} = 0.3135\alpha^{-0.0347}\beta^{0.0962/\theta-0.234}\gamma^{0.0759/\theta-0.199}\tau^{-0.0809}\exp(0.224\beta^4 - 0.00375\beta\gamma\tau^2)$$

H1.2 Parametric equation for SDCF on Chord Toe

$$\rho_{SCF} = 0.3814\beta^{-0.0784}\gamma^{0.046/\theta-0.294}\tau^{-0.0861}\exp(0.000038\alpha^2 + 0.343\beta^5 + 0.0076\gamma)$$

Appendix H2 - Single Brace Subjected to IPB Loading

H2.1 Parametric equation for SDCF on Brace Toe at Crown Toe Side

$$\rho_{SCF}^{Toe} = 0.1381\alpha^{0.0142/\theta}\beta^{-0.0539/\theta}\gamma^{-0.066/\theta}\tau^{0.0897/\theta}\sin^{-0.5}\theta\exp(0.264\beta + 0.00595\gamma + 0.433\sin\theta)$$

H2.2 Parametric equation for SDCF on Brace Toe at Crown Heel Side

$$\rho_{SCF}^{Heel} = 0.2322\beta^{0.124}\gamma^{0.0944/\theta}\tau^{0.122-0.114/\theta}\sin^{0.669}\theta\exp(-0.105\beta^4 + 0.00123\beta^2\gamma)$$

H2.3 Parametric equation for SDCF on Chord Toe at Crown Toe Side

$$\rho_{SCF}^{Toe} = 0.3296\beta^{0.119-0.089/\theta}\gamma^{0.0879-0.0621/\theta}\tau^{0.0478/\theta}\exp(-0.159\beta^5 - 0.00000003\gamma^4 - 0.0527\tau^4 + 0.00722\beta\gamma\tau^2 - 0.396\sin\theta)$$

H2.4 Parametric equation for SDCF on Chord Toe at Crown Heel Side

$$\rho_{SCF}^{Heel} = 0.2165\alpha^{0.0161}\beta^{0.139}\gamma^{0.0996}\tau^{0.0444}\sin^{0.233}\theta\exp(-0.209\beta)$$

Appendix H3 - Single Brace Subjected to OPB Loading

H3.1 Parametric equation for SDCF on Brace Toe

$$\rho_{SCF} = 0.2276\beta^{0.0932/\theta-0.299}\gamma^{-0.142}\tau^{-0.0634}\sin^{-0.376}\theta$$

H3.2 Parametric equation for SDCF on Chord Toe

$$\rho_{SCF} = 0.2753\alpha^{-0.0364}\beta^{0.176/\theta-0.382}\gamma^{0.104/\theta-0.271}\tau^{-0.0749}$$

Appendix H4 - Double Braces Subjected to Axial Loading

H4.1 Parametric equation for SDCF on Brace Toe

$$\rho_{SCF} = 0.1959\beta^{-0.198}\tau^{-0.138}\sin^{-0.241}\theta\exp(0.278\beta^5 - 0.00933\gamma + 0.12\tau^4 - 0.0169\beta\gamma\tau^2)$$

H4.2 Parametric equation for SDCF on Chord Toe

$$\rho_{SCF} = 0.3166\beta^{-0.234}\gamma^{-0.265}\tau^{-0.176}\sin^{-0.363}\theta$$

Appendix H5 - Double Braces Subjected to IPB Loading

H5.1 Parametric equation for SDCF on Brace Toe at Crown Toe Side

$$\rho_{SCF}^{Toe} = 0.2276\alpha^{0.0147/\theta}\beta^{0.072-0.0729/\theta}\gamma^{-0.0385/\theta}\tau^{0.0896/\theta}\exp(0.156\beta+0.00443\gamma)$$

H5.2 Parametric equation for SDCF on Brace Toe at Crown Heel Side

$$\rho_{SCF}^{Heel} = 0.2187\alpha^{0.0193/\theta}\beta^{0.0686+0.0457/\theta}\gamma^{0.0168+0.071/\theta}\tau^{0.11-0.102/\theta}\sin^{0.536}\theta$$

H5.3 Parametric equation for SDCF on Chord Toe at Crown Toe Side

$$\rho_{SCF}^{Toe} = 0.2346\beta^{0.13-0.0973/\theta}\gamma^{0.0792-0.0478/\theta}\tau^{0.0519/\theta}\theta^{-0.137}\exp(-0.18\beta^5 - 0.00000003\gamma^4 - 0.0542\tau^4 + 0.00712\beta\gamma\tau^2)$$

H5.4 Parametric equation for SDCF on Chord Toe at Crown Heel Side

$$\rho_{SCF}^{Heel} = 0.1864\alpha^{0.0252}\beta^{0.0542}\gamma^{0.0852}\tau^{0.0441}\sin^{0.205}\theta$$

Appendix H6 - Double Braces Subjected to OPB Loading

H6.1 Parametric equation for SDCF on Brace Toe

$$\rho_{SCF} = 0.2894\beta^{0.0542/\theta}\tau^{-0.0683}\sin^{-0.314}\theta\exp(-0.539\beta - 0.00886\gamma)$$

H6.2 Parametric equation for SDCF on Chord Toe

$$\rho_{SCF} = 0.2592\beta^{0.181/\theta-0.275}\gamma^{0.106/\theta-0.228}\tau^{-0.084}\exp(-0.0143\beta^2\gamma)$$

Note:

1) All equations are valid in the following ranges of the geometric parameters:

$$6.0 \leq \alpha \leq 40.0$$

$$0.2 \leq \beta \leq 0.8$$

$$7.6 \leq \gamma \leq 32.0$$

$$0.2 \leq \tau \leq 1.0$$

$$0.1944\pi \leq \theta \leq \frac{\pi}{2}$$

2) θ in radians

Appendix I

Deepest Point SIF Parametric Equations for

Semi-Elliptical Surface Crack in T-Butt Welded Joints

using Niu-Glinka Weight Function

Appendix I1 -Subjected to Tension Loading

$$K = Y\sigma\sqrt{(\pi a)}$$

$$Y = \exp(C_0 + C_1 \frac{a}{T} + C_2 \left(\frac{a}{T}\right)^2) \left(\frac{a}{T}\right)^{C_3}$$

$$C_0 = -\left(\frac{a}{c}\right)^{0.056} \left(\frac{L}{T}\right)^{-0.0459/\alpha} \exp(0.3653 - \frac{0.0888}{\left(\frac{L}{T}\right)} + 0.267\left(\frac{a}{c}\right)^{3/2} - \frac{0.2234}{\sin(\alpha)} + \frac{0.00002}{\left(\frac{a}{c}\right)^2}$$

$$- 2.307\left(\frac{\rho}{T}\right) + 1.74\left(\frac{a}{c}\right)\left(\frac{\rho}{T}\right)\left(\frac{L}{T}\right) + 3.26\frac{\left(\frac{\rho}{T}\right)^2}{\left(\frac{L}{T}\right)} - 1.39\alpha\left(\frac{\rho}{T}\right)\left(\frac{L}{T}\right)\left(\frac{a}{c}\right)$$

$$C_1 = 3.88 - 3.024\left(\frac{a}{c}\right) - 2.528\frac{\left(\frac{\rho}{T}\right)}{\alpha} - \frac{0.153}{\left(\frac{L}{T}\right)} + 0.0603\frac{\left(\frac{L}{T}\right)}{\alpha} + \frac{0.0114}{\left(\frac{a}{c}\right)} + 0.927\left(\frac{a}{c}\right)^3$$

$$+ 0.00001\frac{\alpha}{\left(\frac{\rho}{T}\right)^2} + 0.0571\left(\frac{L}{T}\right)\left(\frac{a}{c}\right) - 0.1501\ln\left(\frac{L}{T}\right) + 0.0494\frac{\ln\left(\frac{\rho}{T}\right)}{\alpha}$$

$$- 0.1313\frac{\ln\left(\frac{L}{T}\right)}{\alpha} + 0.474\ln\left(\frac{a}{c}\right)$$

$$C_2 = -16.6786 - 4.5188\ln\left(\frac{a}{c}\right) - 7.749\left(\frac{a}{c}\right) - \frac{0.0489}{\left(\frac{a}{c}\right)} + 23.98\sqrt{\left(\frac{a}{c}\right)}$$

$$+ 0.0417\frac{\ln\left(\frac{L}{T}\right)}{\alpha} + 1.559\left(\frac{\rho}{T}\right)$$

$$C_3 = -0.4069 + \frac{0.02388}{\left(\frac{L}{T}\right)} - 0.123Ln(\alpha) - 0.26\left(\frac{\rho}{T}\right)\left(\frac{a}{c}\right) + 0.0874\left(\frac{a}{c}\right) + 0.802\alpha\left(\frac{\rho}{T}\right) \\ + 0.00951\frac{\left(\frac{L}{T}\right)}{\alpha} - 0.00738\left(\frac{L}{T}\right)\left(\frac{a}{c}\right) - \frac{0.00001}{\left(\frac{a}{c}\right)^2} + \frac{0.00113}{\left(\frac{a}{c}\right)} - 0.0173Ln\left(\frac{L}{T}\right)$$

Appendix I2 -Subjected to Bending Loading

$$K = Y\sigma\sqrt{(\pi a)}$$

$$Y = C_0 + C_1\frac{a}{T} + C_2\left(\frac{a}{T}\right)^2 + C_3Ln\left(\frac{a}{T}\right)$$

$$C_0 = -1.228 + \frac{0.0402}{\left(\frac{L}{T}\right)} - \frac{0.00019}{\left(\frac{a}{c}\right)^2} + 7.71\alpha\left(\frac{\rho}{T}\right) - 0.801\left(\frac{a}{c}\right)^2\alpha + 0.3245\frac{Ln\left(\frac{L}{T}\right)}{\alpha} \\ - 0.691Ln\left(\frac{L}{T}\right) + \frac{0.02991}{\left(\frac{a}{c}\right)} + 1.523\alpha\left(\frac{a}{c}\right) - 12.81\frac{\left(\frac{\rho}{T}\right)^2}{\left(\frac{L}{T}\right)} + 0.2723\left(\frac{L}{T}\right) \\ - 4.25\left(\frac{\rho}{T}\right)\alpha\left(\frac{a}{c}\right) - 1.296Ln(\alpha) - 0.115\frac{\left(\frac{L}{T}\right)}{\alpha} \\ C_1 = 2.54 + \frac{0.00122}{\left(\frac{a}{c}\right)^2} + 0.517\frac{\left(\frac{a}{c}\right)}{\alpha} - \frac{0.2154}{\left(\frac{L}{T}\right)} - 10.87\left(\frac{a}{c}\right) - 13.73\alpha\left(\frac{\rho}{T}\right) - 2.054\left(\frac{a}{c}\right)^4 \\ - \frac{0.18}{\left(\frac{a}{c}\right)} - 0.3533\frac{Ln\left(\frac{L}{T}\right)}{\alpha} + 3.166Sin(\alpha) + 8.51\left(\frac{a}{c}\right)^2 + 0.405Ln\left(\frac{L}{T}\right) + 29.1\frac{\left(\frac{\rho}{T}\right)^2}{\left(\frac{L}{T}\right)}$$

$$\begin{aligned}
C_2 &= 0.2593 + \frac{0.44237}{\left(\frac{a}{c}\right)} - 0.866\left(\frac{a}{c}\right)^2 - \frac{0.00285}{\left(\frac{a}{c}\right)^2} + 2.211\text{Ln}\left(\frac{a}{c}\right) - 0.1571\frac{\text{Ln}\left(\frac{a}{c}\right)}{\alpha} \\
&+ 0.1224\text{Ln}\left(\frac{\rho}{T}\right) + \frac{0.0348}{\left(\frac{L}{T}\right)} \\
C_3 &= -\exp\left(0.3346 - \frac{0.1517}{\left(\frac{L}{T}\right)} - 5.76\left(\frac{a}{c}\right)^2 - 0.00046\frac{\left(\frac{\rho}{T}\right)}{\left(\frac{a}{c}\right)^2} - \frac{0.00194}{\left(\frac{a}{c}\right)\left(\frac{L}{T}\right)} - 3.59\left(\frac{\rho}{T}\right)\right. \\
&- 4.2\left(\frac{a}{c}\right)^4 + 0.1981\frac{\text{Ln}\left(\frac{a}{c}\right)}{\alpha} - 0.0828\frac{\left(\frac{L}{T}\right)}{\alpha} + 9.09\left(\frac{a}{c}\right)^3 + 0.085\alpha\left(\frac{L}{T}\right)\left(\frac{a}{c}\right) \\
&\left. + 0.086\frac{\text{Ln}\left(\frac{L}{T}\right)}{\alpha} - 0.472\frac{\left(\frac{a}{c}\right)}{\alpha} + \frac{0.00416}{\left(\frac{a}{c}\right)}\right)
\end{aligned}$$

Note:

1) All equations are valid in the following ranges of the geometric parameters:

$$\frac{\pi}{6} \leq \alpha \leq \frac{\pi}{3}$$

$$0.01 \leq \frac{\rho}{T} \leq 0.066$$

$$0.1577 \leq \frac{L}{T} \leq 4$$

$$0 \leq \frac{a}{c} \leq 1$$

$$\text{if } 0 \leq a/c \leq 0.2 \text{ then } a/T \leq 1.25(a/c + 0.6)$$

$$\text{if } a/c \geq 0.2 \text{ then } a/T < 1$$

2) α in radians

Appendix J

Surface Point SIF Parametric Equations for

Semi-Elliptical Surface Crack in T-Butt Welded Joints

using Wang-Lambert Weight Function

Appendix J1 -Subjected to Tension Loading

$$K = Y\sigma\sqrt{(\pi a) / Q}$$

$$Q = 1 + 1.464\left(\frac{a}{c}\right)^{1.65}$$

$$Y = \exp\left(C_0 + C_1\left(\frac{a}{T}\right) + C_2\left(\frac{a}{T}\right)^2\right)\left(\frac{a}{T}\right)^{C_3}$$

$$\begin{aligned} C_0 = & \left(\frac{L}{T}\right)^{0.054/\alpha} \exp(0.1733 - \frac{0.01333}{\left(\frac{a}{c}\right)} - \frac{0.021}{\left(\frac{L}{T}\right)} + 2.71\left(\frac{\rho}{T}\right)\left(\frac{a}{c}\right) - 0.674\alpha\left(\frac{a}{c}\right) \\ & - 1.427\frac{\left(\frac{\rho}{T}\right)^2}{\left(\frac{a}{c}\right)} + \frac{0.00009}{\left(\frac{a}{c}\right)^2} + 1.51\alpha\left(\frac{\rho}{T}\right)\left(\frac{L}{T}\right)\left(\frac{a}{c}\right) - 0.00112\frac{\left(\frac{\rho}{T}\right)}{\left(\frac{a}{c}\right)^2} + 0.0223\frac{\left(\frac{\rho}{T}\right)^2}{\left(\frac{a}{c}\right)^2} \\ & - \frac{0.00142}{\left(\frac{\rho}{T}\right)} + 0.471\left(\frac{a}{c}\right)^2\alpha - 0.0256\frac{\left(\frac{L}{T}\right)}{\alpha} - 0.192\left(\frac{\rho}{T}\right)\left(\frac{a}{c}\right)\left(\frac{L}{T}\right)^2 \\ & + 0.05\frac{\left(\frac{a}{c}\right)}{\alpha} - 0.111\left(\frac{a}{c}\right)^4) \\ C_1 = & -1.66 + 3.992\left(\frac{a}{c}\right) + \frac{0.00007}{\left(\frac{a}{c}\right)^2} - 24.06\left(\frac{\rho}{T}\right)\left(\frac{a}{c}\right) - 0.925\left(\frac{a}{c}\right)^3 + 0.00002\frac{\alpha}{\left(\frac{\rho}{T}\right)^2} \\ & + 11.41\frac{\left(\frac{\rho}{T}\right)^2}{\left(\frac{L}{T}\right)} - 0.1688\frac{\left(\frac{a}{c}\right)}{\alpha} + 13.32\left(\frac{a}{c}\right)^2\left(\frac{\rho}{T}\right) \end{aligned}$$

$$\begin{aligned}
C_2 &= 3.668 - 17.689 \left(\frac{a}{c} \right)^{1.5} - \frac{0.00204}{\left(\frac{a}{c} \right)} + 18.339 \left(\frac{a}{c} \right)^2 - \frac{0.00152}{\left(\frac{\rho}{T} \right)} - \frac{0.0193}{\left(\frac{L}{T} \right)} \\
&+ 0.462 \operatorname{Ln} \left(\frac{a}{c} \right) - 4.34 \left(\frac{a}{c} \right)^3 \\
C_3 &= 0.411 - 0.6355 \left(\frac{a}{c} \right)^{0.5} + 0.0795 \operatorname{Ln} \left(\frac{\rho}{T} \right) - 0.0283 \alpha \left(\frac{L}{T} \right) \left(\frac{a}{c} \right) \\
&+ 0.356 \alpha \left(\frac{\rho}{T} \right) \left(\frac{L}{T} \right) \left(\frac{a}{c} \right) - 0.133 \frac{\left(\frac{\rho}{T} \right)^2}{\left(\frac{a}{c} \right)} + \frac{0.01848}{\left(\frac{L}{T} \right)} - 0.016 \frac{\operatorname{Ln} \left(\frac{\rho}{T} \right)}{\alpha} \\
&+ 2.44 \left(\frac{\rho}{T} \right) \left(\frac{a}{c} \right) - \frac{0.00015}{\left(\frac{a}{c} \right) \left(\frac{L}{T} \right)} - 2.95 \frac{\left(\frac{\rho}{T} \right)^2}{\left(\frac{L}{T} \right)} + 0.01195 \frac{\operatorname{Ln} \left(\frac{a}{c} \right)}{\alpha}
\end{aligned}$$

Appendix J2 -Subjected to Bending Loading

$$K = Y\sigma\sqrt{(\pi a) / Q}$$

$$Q = 1 + 1.464\left(\frac{a}{c}\right)^{1.65}$$

$$Y = C_0 + C_1\left(\frac{a}{T}\right) + C_2\left(\frac{a}{T}\right)^2 + C_3\ln\left(\frac{a}{T}\right)$$

$$C_0 = \left(\frac{a}{c}\right)^{0.0346/\alpha - 0.2513} \left(\frac{L}{T}\right)^{0.2789} \exp(-0.9655 + 2.065\left(\frac{a}{c}\right) + 14.13\left(\frac{\rho}{T}\right)\left(\frac{a}{c}\right) - 10.59\left(\frac{a}{c}\right)^2\left(\frac{\rho}{T}\right) - 4071\left(\frac{\rho}{T}\right)^4 - 0.00001\frac{\alpha}{\left(\frac{\rho}{T}\right)^2} - 0.00143\frac{\left(\frac{\rho}{T}\right)}{\left(\frac{a}{c}\right)^2} + 0.0135\frac{\left(\frac{\rho}{T}\right)^2}{\left(\frac{a}{c}\right)^2} - 0.899\left(\frac{a}{c}\right)^2 - 0.0572\alpha\left(\frac{L}{T}\right)\left(\frac{a}{c}\right) + 1.11\alpha\left(\frac{\rho}{T}\right)\left(\frac{L}{T}\right)\left(\frac{a}{c}\right) - 0.1546\left(\frac{L}{T}\right) + 0.00047\left(\frac{L}{T}\right)^4),$$

$$C_1 = 2.8658 + 1.1187\ln\left(\frac{a}{c}\right) - 21.35\left(\frac{\rho}{T}\right)\left(\frac{a}{c}\right) + 11.8\left(\frac{a}{c}\right)^2\left(\frac{\rho}{T}\right) + 9.59\frac{\left(\frac{\rho}{T}\right)^2}{\left(\frac{L}{T}\right)}$$

$$+ 0.00002\frac{\alpha}{\left(\frac{\rho}{T}\right)^2} - 0.271\frac{\left(\frac{a}{c}\right)}{\alpha} - 0.515\left(\frac{a}{c}\right)^4 + 4.271\left(\frac{a}{c}\right)^2 + \frac{0.00009}{\left(\frac{a}{c}\right)^2} - 5.4\left(\frac{a}{c}\right)$$

$$- 3.92\alpha\left(\frac{\rho}{T}\right)\left(\frac{L}{T}\right)\left(\frac{a}{c}\right) + 0.00041\frac{\left(\frac{\rho}{T}\right)}{\left(\frac{a}{c}\right)^2} - 0.0232\frac{\ln\left(\frac{a}{c}\right)}{\alpha} + 0.499\left(\frac{\rho}{T}\right)\left(\frac{a}{c}\right)\left(\frac{L}{T}\right)^2$$

$$C_2 = -8.866 - 2.672\ln\left(\frac{a}{c}\right) - \frac{0.00118}{\left(\frac{\rho}{T}\right)} - 4.125\left(\frac{a}{c}\right)^{1.5} - \frac{0.02893}{\left(\frac{a}{c}\right)} + 13.07\left(\frac{a}{c}\right)^{0.5}$$

$$+ 0.081\ln\left(\frac{\rho}{T}\right) + 0.0235\frac{\ln\left(\frac{a}{c}\right)}{\alpha} - 0.0387\frac{\ln\left(\frac{\rho}{T}\right)}{\alpha} - \frac{0.099}{\sin(\alpha)}$$

$$+ 0.0722\ln\left(\frac{L}{T}\right) - 0.0293\left(\frac{L}{T}\right)$$

$$C_3 = 0.07 - \left(\frac{\rho}{T}\right)^{0.1048/\alpha - 0.4478} \left(\frac{a}{c}\right)^{0.404 - 0.0959/\alpha} \exp\left(-1.703 - \frac{0.03625}{\left(\frac{a}{c}\right)} - \frac{0.109}{\left(\frac{L}{T}\right)}\right) \\ + \frac{0.0019}{\left(\frac{a}{c}\right)\left(\frac{L}{T}\right)} - 0.00562 \frac{\left(\frac{\rho}{T}\right)}{\left(\frac{a}{c}\right)^2} + 0.056 \frac{\left(\frac{\rho}{T}\right)^2}{\left(\frac{a}{c}\right)^2} + \frac{0.00021}{\left(\frac{a}{c}\right)^2} - 0.759 \left(\frac{\rho}{T}\right)\left(\frac{L}{T}\right)$$

Note:

1) All equations are valid in the following ranges of the geometric parameters:

$$\frac{\pi}{6} \leq \alpha \leq \frac{\pi}{3}$$

$$0.01 \leq \frac{\rho}{T} \leq 0.066$$

$$0.1577 \leq \frac{L}{T} \leq 4$$

$$0 \leq \frac{a}{c} \leq 1$$

$$0 < \frac{a}{T} \leq 0.8$$

2) α in radians

Appendix K
The Deepest Point SIF Parametric Equations
for Semi-Elliptical Surface Cracks
at Saddle Position of Tubular Welded Joint

$$K_s^{ij} = (Y_T^{ij} R_T + DoB \bullet Y_B^{ij} R_B) \sigma_{hotspot} \sqrt{(\pi a)}$$

$$R_T = DoB; \quad R_B = 0.5 \cos\left(\frac{\pi a}{T}\right) + 0.5$$

Appendix K1 -Subjected to Tension Loading

$$Y_T^{ij} = \exp\left(C_0 + C_1\left(\frac{a}{T}\right) + C_2\left(\frac{a}{T}\right)^2\right)\left(\frac{a}{T}\right)^{C_3}$$

$$C_0 = -\left(\frac{a}{c}\right)^{0.271+0.0108/\alpha} \left(\frac{L}{T}\right)^{-0.02714/\alpha} \exp\left(0.6805 - \frac{0.07525}{\left(\frac{L}{T}\right)} - \frac{0.1702}{\sin(\alpha)} - \frac{0.00016}{\left(\frac{a}{c}\right)^2} + 1.7858\left(\frac{a}{c}\right)^4 - 1.274\left(\frac{\rho}{T}\right) - 1.871\left(\frac{a}{c}\right)^3 + \frac{0.02618}{\left(\frac{a}{c}\right)}\right)$$

$$C_1 = 2.833 - 0.144\sqrt{\left(\frac{a}{c}\right)} + 9.63\left(\frac{a}{c}\right)^4 - 10.49\left(\frac{a}{c}\right)^3 - 2.051\frac{\left(\frac{\rho}{T}\right)}{\alpha} + \frac{0.00459}{\left(\frac{a}{c}\right)} - \frac{0.0781}{\left(\frac{L}{T}\right)} - 0.0428\frac{\left(\frac{L}{T}\right)}{\alpha}$$

$$C_2 = -6.798 - 3.289 \ln\left(\frac{a}{c}\right) + 9.034\left(\frac{a}{c}\right) + \frac{0.00106}{\left(\frac{a}{c}\right)^2} - 2.772\left(\frac{a}{c}\right)^4 - \frac{0.1858}{\left(\frac{a}{c}\right)} + 0.0185\frac{\left(\frac{L}{T}\right)}{\alpha} + 1.248\left(\frac{\rho}{T}\right)$$

$$C_3 = -0.09611 + \frac{0.02331}{\left(\frac{L}{T}\right)} - 0.2307 \sin(\alpha) - 0.1577 \sqrt{\left(\frac{a}{c}\right)} + 0.671\alpha \left(\frac{\rho}{T}\right) - 0.663 \left(\frac{a}{c}\right)^4$$

$$+ 0.757 \left(\frac{a}{c}\right)^3 + 0.0315 \ln\left(\frac{a}{c}\right) + 0.00956 \frac{\left(\frac{L}{T}\right)}{\alpha} - 0.0237 \ln\left(\frac{L}{T}\right)$$

Appendix K2 -Subjected to Bending Loading

$$Y_B^{ij} = C_0 + C_1 \left(\frac{a}{T}\right) + C_2 \left(\frac{a}{T}\right)^2 + C_3 \ln\left(\frac{a}{T}\right)$$

$$C_0 = -1.525 - 0.481\alpha \left(\frac{L}{T}\right) + 0.2098 \left(\frac{L}{T}\right)^2 - \frac{0.00018}{\left(\frac{a}{c}\right)^2} + 2.035 \left(\frac{a}{c}\right) - 0.055 \frac{\ln\left(\frac{a}{c}\right)}{\alpha} + \frac{0.1316}{\left(\frac{L}{T}\right)} - 3.07 \left(\frac{a}{c}\right)^3 + \frac{0.658}{\sin(\alpha)}$$

$$+ \frac{0.0246}{\left(\frac{a}{c}\right)} + 1.96 \left(\frac{a}{c}\right)^4 + 0.264 \frac{\ln\left(\frac{L}{T}\right)}{\alpha} - 0.344 \frac{\left(\frac{L}{T}\right)}{\alpha} - 0.00419 \left(\frac{L}{T}\right)^4 + 6.59\alpha \left(\frac{\rho}{T}\right) - 11.49 \frac{\left(\frac{\rho}{T}\right)^2}{\left(\frac{L}{T}\right)} - 2.59 \left(\frac{\rho}{T}\right) \left(\frac{a}{c}\right)$$

$$C_1 = 4.042 - 13.72 \left(\frac{a}{c}\right)^{1.5} - \frac{0.0938}{\left(\frac{a}{c}\right)} + \frac{0.279}{\sin(\alpha)} - \frac{0.1831}{\left(\frac{L}{T}\right)} + 23.32 \left(\frac{a}{c}\right)^3 - 13.4\alpha \left(\frac{\rho}{T}\right) + \frac{0.00066}{\left(\frac{a}{c}\right)^2} - 13.1 \left(\frac{a}{c}\right)^4$$

$$- 0.3483 \frac{\ln\left(\frac{L}{T}\right)}{\alpha} + 0.434 \ln\left(\frac{L}{T}\right) + 25.4 \frac{\left(\frac{\rho}{T}\right)^2}{\left(\frac{L}{T}\right)} + 0.1231 \frac{\ln\left(\frac{a}{c}\right)}{\alpha} + 1.33 \ln(\alpha) + 6.12 \left(\frac{\rho}{T}\right) \alpha \left(\frac{a}{c}\right)$$

$$C_2 = -4.006 + \frac{0.21729}{\left(\frac{a}{c}\right)} - 2.926\left(\frac{a}{c}\right)^2 - \frac{0.00154}{\left(\frac{a}{c}\right)^2} + 5.56\left(\frac{a}{c}\right) + \frac{0.38}{\sin(\alpha)} + 3.47\alpha\left(\frac{\rho}{T}\right) + \frac{0.0325}{\left(\frac{L}{T}\right)}$$

$$C_3 = -\left(\frac{a}{c}\right)^{0.1457/\alpha} \left(\frac{L}{T}\right)^{0.146} \exp\left(0.521 - 0.566\frac{\left(\frac{a}{c}\right)}{\alpha} - \frac{0.1272}{\left(\frac{L}{T}\right)} - 1.1\sqrt{\left(\frac{a}{c}\right)} - 0.0751\frac{\left(\frac{L}{T}\right)}{\alpha} + 0.0798\left(\frac{a}{c}\right)^2\left(\frac{L}{T}\right) - \frac{0.00049}{\left(\frac{a}{c}\right)\left(\frac{L}{T}\right)} - 3.303\left(\frac{\rho}{T}\right)\right)$$

Note:

1) All equations are valid in the following ranges of the geometric parameters:

$$\frac{\pi}{6} \leq \alpha \leq \frac{\pi}{3}$$

$$0.01 \leq \frac{\rho}{T} \leq 0.066$$

$$0.1577 \leq \frac{L}{T} \leq 4$$

$$0 \leq \frac{a}{c} \leq 1$$

$$0 < \frac{a}{T} \leq 0.8$$

2) α in radians